Bulk continuum generation:
The ultimate tool for laser applications and spectroscopy

From new insights to ultrafast amplifiers and spectrometers

Maximilian Bradler

Dissertation
an der Fakultät für Physik
der Ludwig-Maximilians-Universität
München

vorgelegt von
Maximilian Bradler
aus Burghausen

München, im Juli 2014

Erstgutachter: Prof. Dr. Eberhard Riedle
Zweitgutachter: Dr. habil. Thomas Udem

Tag der mündlichen Prüfung: 16. September 2014

Kurzfassung

Weißlichterzeugung in Festkörpern ist eine faszinierende Konsequenz der extremen Wechselwirkung zwischen Licht und Materie und führt zur Erzeugung neuer Frequenzen. Die vorteilhaften Eigenschaften der ultrakurzen Eingangsimpulse werden dabei erhalten. Die einfache Handhabung und hohe Robustheit machen Weißlichterzeugung zu einer exzellenten Quelle für die Erzeugung neuer Frequenzen und zu einem beliebten Werkzeug im Bereich der Optik. Im Rahmen dieser Arbeit werden die Mechanismen während der Weißlichterzeugung erläutert und neue Erkenntnisse aufgezeigt. Zusätzlich wird die Verwendung in optisch parametrischen Verstärkern und transienten Spektrometern demonstriert.
Um Festkörper-Weißlichter sinnvoll nutzen zu können, müssen die Mechanismen während der Erzeugung verstanden und die Eigenschaften der Weißlichter kontrolliert werden können. Eine der zentralen Erkenntnisse dieser Arbeit ist, dass die Wellenlängen nahe der Fundamentalen während des gesamten Prozesses erzeugt werden, wohingegen Wellenlängen am Rand des Kontinuums nur zu Beginn erzeugt werden. Die verbleibende nichtlineare Propagation im Medium führt dann zu einer zeitlichen Versetzung der einzelnen Farben und zu einem Wellenlängen abhängigen Bündelprofil.
Mithilfe dieses Wissens ist es möglich, direkt sub-10 fs Weißlichter in Festkörpern zu erzeugen, ohne dass eine Kompression notwendig ist. Die Eingangsimpulse haben dabei Energien im µJ Bereich und Pulsdauern von 200 fs. Solch kurze Pulse konnten bis jetzt nur durch Filamentation intensivster Impulse mit wenigen Zyklen in Gasen erreicht werden. Des Weiteren werden alle relevanten geometrischen Parameter untersucht und optimiert, um best mögliche Weißlichterzeugung zu garantieren. Dazu werden die Wellenlänge, Energie und Dauer des Pumpimpulses, sowie das Bündelprofil untersucht. Aufgrund der neu gewonnen Erkenntnisse ist es möglich, Weißlicht mit Impulsdauern über den gesamten Femtosekundenbereich zu erzeugen. Ebenfalls wird die Erzeugung von Weißlichtern mit Wellenlängen von 258 nm bis hin zu 3 µm gezeigt, wodurch eine lückenlose spektrale Abdeckung vom Ultravioletten bis ins Infrarote erreicht werden kann. Alle untersuchten Weißlichter zeigen hervorragende Eigenschaften wie ein glattes Spektrum, hohe Impuls-zu-Impuls Stabilität, ein ausgezeichnetes Bündelprofil, sowie spektrale und örtliche Kohärenz. Des Weiteren wird das Phänomen der multiplen Fokussierung und deren Konsequenzen für die Eigenschaften der Weißlichter studiert. Dadurch wird der Ursprung von Phasenfluktuationen gefunden und diese werden auf ein Minimum reduziert.
Durch die Verwendung von Weißlichtern in parametrischen Verstärkern können Impulse mit sub-zwei Zyklen und ein enormer Abstimmbereich von 215 nm bis hin zu 10 µm erzeugt werden. Es wird gezeigt, dass limitierenden Faktoren wie schmalbandige Phasenanpassung, niedrige Verstärkung, fehlendes Seed-Licht oder kleine Akzeptanzwinkel oder -bandbreiten kompensiert werden können. Dies führt zu einem bisher unerreichten Abstimmbereich über vier Oktaven, Quanteneffizienzen von bis zu 40 % und Ausgangsleistungen von bis zu 700 mW. Sichtbare Vorverstärkung, duale Verstärkung, Anpassen der Pumpintensität und breitbandiges Frequenzmischen von sichtbaren und infraroten Impulsen sind Techniken, um die erwähnten Einschränkungen zu überwinden. Sowohl die Weißlichterzeugung, als auch die optisch parametrischen Verstärker funktionieren sehr gut mit verschiedenen Pumplasern mit Wiederholraten bis zum MHz Regime.
Aufgrund ihrer herausragenden Eigenschaften sind Weißlichter bestens als Problicht in ultraschnellen, transienten Breitbandspektrometern geeignet. Die in dieser Arbeit vorgestellten Weißlichter ermöglichen es, komplexe Systeme vom Ultravioletten ab 225 nm bis ins Infrarote bis hin zu 1700 nm mit einer Zeitauflösung von 60 fs für den gesamten Bereich zu untersuchen. In Kombination mit den beschrieben Verstärkersystemen kann der Wellenlängenbereich bis 5 µm erweitert werden. Durch die Synchronisierung mit einem zusätzlichen Nanosekunden Oszillator zur primären Laserquelle können Verzögerungszeiten von wenigen Femtosekunden bis in den Millisekundenbereich realisiert werden. Somit ist es möglich, zur Aufklärung aller relevanten Prozesse nahezu jeder untersuchten Probe beizutragen.

Short summary

Bulk continuum generation is a fascinating consequence of extreme light-matter interaction and leads to the generation of new frequencies beside the pump wavelength. The advantageous properties of the ultrashort input pulse are maintained or even improved by this process. The easy handling, the good performance, and the high robustness in the daily operation favor continuum generation as an excellent source for new frequencies and make it a very popular tool for experiments in optics and photonics.
In this thesis the mechanisms during bulk filamentation and continuum generation are reviewed and new insights are given. In addition, the use of such continua in optical parametric amplifiers and transient spectrometers is demonstrated.
For the proper use of bulk continua, the generation mechanisms have to be understood and the properties of the continua should be controllable. Therefore, intense studies on the processes involved in the generation are performed. One of the central new findings in this work is that wavelengths close to the fundamental are generated over the entire process, whereas wavelengths close to the cut-off are just generated in the beginning. The remaining nonlinear propagation in the bulk material leads to temporal shifts and spatial changes of the new frequencies. With this knowledge, it is possible to generate sub-10 fs pulses directly from bulk continuum generation with superior optical properties and without any need of compression. The input pulses only have a few µJ's of pulse energy at most and a long pulse duration of nearly 200 fs. Up to now, this has only been achieved by filamentation of intense few-cycle pulses in gases. In addition, all relevant external and geometrical parameters are discussed and optimized to guarantee best continuum generation. A wide range of input light parameters such as the central wavelength, pulse duration, pump energy, and beam profile are investigated. Based on the new insights gained in this work, continuum generation with nearly any pulse in the femtosecond regime is achievable. Pulse durations from few femtoseconds up to above one picosecond and central wavelengths from 266 nm up to 3 µm permit bulk continuum generation with needed pulse energies of at most a few µJ. All presented continua show superior properties such as a smooth, gap free spectrum, high pulse-to-pulse stability, a brilliant beam profile, and a wide spectral and spatial coherence. With this method, previously not directly accessible wavelength ranges can be covered. Furthermore, the phenomenon of multiple focusing and its relation to the continuum properties are studied. By this, the origin of phase fluctuations is found and they can be reduced to a minimum.
Using these continua as seed in advanced amplifier systems allows the generation of extremely short pulses down to sub-two cycles and an enormous tuning range starting from the deep ultraviolet at 215 nm to the midinfrared up to 10 µm at highest repetition rates. It is shown, that limiting factors such as narrowband phase-matching, low gain coefficients, the absence of seed light, or small acceptance angles and bandwidths can be overcome. This leads to an unprecedented tuning range over four octaves, quantum efficiencies of up to 40 %, and output powers of up to 700 mW. Visible pre-amplification, dual amplification, the matching of the pump intensity, and broadband frequency mixing between visible and infrared pulses with different pulse durations are techniques to overcome these limitations. Continuum generation as well as optical parametric amplification work well for various laser sources and for a wide range of repetition rates up to the MHz regime.
In addition, due to their superior properties, bulk continua are brilliantly suited as probe light in ultrafast broadband transient spectrometers. The continua presented in this work allow the investigation of complex molecules from the ultraviolet starting from 225 nm to the infrared up to 1700 nm with an extremely high time resolution of approximately 60 fs for the entire range. In combination with the described amplifiers, this wavelength range is even extended up to 5 µm. By synchronizing an additional nanosecond oscillator to the primary laser source, delay times from a few femtoseconds up to the millisecond regime can be realized and this will help to uncover all relevant processes of nearly any investigated system.

Publications

This thesis is based on the following publications sorted in chronological order. They are re-printed in part II (publications 1 to 16).

1 **Femtosecond continuum generation in bulk laser host materials with sub-µJ pump pulses**
M. Bradler, P. Baum, and E. Riedle
Appl. Phys. B **97**, 561 - 574 (2009).

2 **Widely Tunable Infrared Pulse Generation up to 5 µm with Novel Optical Parametric Amplifiers at 100 kHz Repetition Rate**
M. Bradler, E. Riedle, and C. Homann
Ultrafast Phenomena XVII, M. Chergui, D. Jonas, E. Riedle, R.W. Schoenlein, A. Taylor, eds. (Oxford University Press, Inc., New York 2011), 733 - 735.

3 **Continuum Generation in Laser Host Materials towards Table-Top OPCPA**
M. Bradler, P. Baum, and E. Riedle
Ultrafast Phenomena XVII, M. Chergui, D. Jonas, E. Riedle, R.W. Schoenlein, A. Taylor, eds. (Oxford University Press, Inc., New York 2011), 712 - 714.

4 **Mid-IR femtosecond pulse generation on the microjoule level up to 5 µm at high repetition rates**
M. Bradler, C. Homann, and E. Riedle
Opt. Lett. **36**, 4212 - 4214 (2011).

5 **Carrier-envelope phase stable sub-two-cycle pulses tunable around 1.8 µm at 100 kHz**
C. Homann, M. Bradler, M. Förster, P. Hommelhoff, and E. Riedle
Opt. Lett. **37**, 1673 - 1675 (2012).

6 **Ultrafast photo-induced charge transfer unveiled by two-dimensional electronic spectroscopy**
O. Brixner, V. Lukes, T. Mancal, J. Hauer, F. Milota, M. Fischer, I. Pugliesi, M. Bradler, W. Schmid, E. Riedle, H. F. Kauffmann, and N. Christensson
J. Chem. Phys. **136**, 204503 (2012).

7 **Electronic transient spectroscopy from the deep UV to the NIR: unambiguous disentanglement of complex processes**
E. Riedle, M. Bradler, M. Wenninger, C. F. Sailer and I. Pugliesi
Faraday Discuss. **163**, 139 - 158 (2013).

8 **Internal Conversion vs. Intersystem Crossing – What Drives the Dynamics of Cyclic α,β-Enones?**
O. Schalk, P. Lang, M. S. Schuurman, G. Wu, M. Bradler, E. Riedle, and A. Stolow
Proceedings of the XVIIIth International Conference on Ultrafast Phenomena, Lausanne, Switzerland. EPJ Web of Conferences **41**, 05029 (2013).

9 **Continuum generation in bulk materials from the deep UV to the infrared with pump pulse durations over the entire femtosecond regime**
M. Bradler and E. Riedle
Proceedings of the XVIIIth International Conference on Ultrafast Phenomena, Lausanne, Switzerland. EPJ Web of Conferences **41**, 10011 (2013).

10 **Generation of sub-two-cycle pulses tunable around 1.8 µm with passively stabilized carrier-envelope phase at 100 kHz repetition rate**
C. Homann, M. Bradler, M. Förster, P. Hommelhoff, and E. Riedle
Proceedings of the XVIIIth International Conference on Ultrafast Phenomena, Lausanne, Switzerland. EPJ Web of Conferences **41**, 10012 (2013).

11 **Broadband difference frequency mixing between visible and near-infrared pulses for few-cycle pulse generation with stable carrier-envelope phase**
M. Bradler, C. Homann, and E. Riedle
Appl. Phys. B **113**, 19 - 25 (2013).

12 **Ultrafast Dynamics of meso-Tetraphenylmetalloporphyrins: the Role of Dark States**
Y. Liang, M. Bradler, M. Klinger, O. Schalk, M. C. Balaban, T. S. Balaban, E. Riedle, and A. N. Unterreiner
Chem. Plus. Chem.**78**, 1244 - 1251 (2013).

13 **A novel setup for femtosecond pump-repump-probe IR spectroscopy with few cycle CEP stable pulses**
M. Bradler, J. C. Werhahn, D. Hutzler, S. Fuhrmann, R. Heider, E. Riedle, H. Iglev, and R. Kienberger
Opt. Express **21**, 20145 - 20158 (2013).

14 **A broad and tunable 250- to 430-nm source for microscopy and lifetime measurements by frequency doubling of a 78-MHz-picosecond white-light laser**
M. Bradler, F. D. Nielsen, C. E. Eckert, and E. Riedle
Appl. Phys. B, published online, DOI 10.1007/s00340 014 5774 5 (2014).

15 **Sub-20 fs μJ-energy pulses tunable down to the near-UV from a 1 MHz Yb-fiber laser system**
M. Bradler and E. Riedle
Opt. Lett. **39**, 2588 - 2591 (2014).

16 **Temporal and spectral correlations in bulk continua and improved use in transient spectroscopy**
M. Bradler and E. Riedle
J. Opt. Soc. Am. B **31**, 1465 (2014).

Patent applications and forthcoming publications

This thesis is based on the following forthcoming publications and patent applications sorted in chronological order. They are reprinted in part II (publications 17 to 20).

17 **Relaxation dynamics of the OH stretching overtones in isolated HDO molecules studied by IR pump-repump-probe spectroscopy**
J. C. Werhahn, D. Hutzler, R. Heider, M. Bradler, R. Kienberger, E. Riedle, and H. Iglev
to be submitted to Phys Rev. Lett (2014)

18 **Small-scale filamentation and continuum generation in solids with femtosecond pump sources from the ultraviolet to the infrared**
M. Bradler, E. Wittmann, and E. Riedle
to be submitted to Opt. Express (2014)

19 **Transient Spectroscopy covering three Octaves in Spectrum and 11 orders of Magnitude in Time**
M. Bradler, C. Sailer, N. Krebs, M. Wenninger, P. Lang, D. Herrmann, I. Pugliesi, and E. Riedle
to be submitted to Appl. Phys. B (2014)

20 **Direct Generation of 7 fs Whitelight Pulses from Bulk Sapphire**
E. Wittmann, M. Bradler, and E. Riedle
submitted to book of proceedings for Ultrafast Phenomena XIX (2014)

21 **Pushing the NOPA to New Frontiers: Output to below 400 nm, MHz Operation and ps Pump Duration**
M. Bradler, L. Kasmi, P. Baum, and E. Riedle
submitted to book of proceedings for Ultrafast Phenomena XIX (2014)

22 **Pulsed UV-light source**
C. L. Thomsen, F. D. Nielsen, S. Hauser, E. Riedle, and M. Bradler
Danish patent application DK 2012 70597 A1

Content

Part I:

1. Introduction

The invention of the laser over 50 years ago [Maiman60, Zinth11] substantially changed the daily life in science and industry. The novel light source is used in a large number of applications and opened the door for many groundbreaking studies and experiments. With the development of shorter and shorter laser pulses the fastest processes in nature could be resolved. Nowadays, even the attosecond regime is reached by the help of nonlinear conversion [Hentschel01, Corkum07, Krausz09]. Basically all transparent material and the very fastest phenomena in physics, biology, medicine, and chemistry can be investigated. One of the main challenges is that laser systems have a limited spectral operation range which is often not easily tunable. For many investigations, the provided laser wavelengths do not fit the experimental needs. New concepts had to be found to convert the laser light to the desired wavelength without loosing its advantageous properties such as the short pulse duration, the good spatial quality, or the coherence. The key parameter leading to new frequencies is the interaction of light and matter. At intensities in the TW/cm^2 regime all transparent materials show nonlinear effects which can lead to the generation of new frequencies. Such intensities are quadrillion times higher than the intensity of the sunlight on earth and would be reached by concentrating the entire sunlight irradiating Germany on one DIN A4 sheet. For short pulses not only the peak intensity is extremely high, but also the peak power. For instance during the 150 fs, which is a typical pulse duration for a Ti:sapphire based laser system, the emitted energy of 1 mJ leads to a peak power of 10 GW. Several atomic power plants would be necessary to achieve such a peak power. Only the combination of high peak power and a good focusability allows generating highest intensities which launch nonlinear processes. Under theses extreme conditions the interaction of light with matter can become very complex, but still controllable and with a well suited output for many applications.

In the beginning, frequency doubling of laser pulses [Franken61, Giordmaine62, Maker62] followed by the generation of further harmonics [Maker66, Burnett77] was (and is) a well established technique to generate light at other frequencies. However, the produced wavelengths depend on the fundamental light and are still not freely tunable. A further approach which allows the generation of tunable light is optical parametric oscillation [Giordmaine65, Myers95]. In this process, quantum fluctuations are amplified to a macroscopic power level by the laser light in a nonlinear crystal. The generated parametric superfluorescence can be further amplified and is widely tunable. Unfortunately, it only produces pulses with wavelengths longer than that of the pump. In addition, it is incompressible and depends on phase-matching conditions.

A very successful method for generating new frequencies which overcomes all these limitations is continuum generation. If ultrashort pulses propagate in nonlinear transparent media such as gases [Braun95, Kasparian03, Hauri04, Berge07, Couairon07], liquids [Fork83], solids [Alfano06, Couairon07, Chin10], or fibers [Ranka00, Russell03, Dudley06] the dynamic interplay of several nonlinear effects leads to octave wide and gap free spectral broadening. Especially, when generating such continua in solids, broadband spectra reaching from

the ultraviolet (UV) to the infrared can be produced by modest pump energies. In addition, the process does not depend on phase-matching conditions and the produced light shows outstanding properties. This favors it as excellent source to seed an amplifier or to be used in an ultrafast transient spectrometer.

This work focuses on the generation mechanisms and the conditions for bulk continuum generation and its manifold application possibilities. The phenomenon was first observed by Alfano in 1970 [Alfano70a, Alfano70b] and is still subject of many investigations. To get an impression of the potential which such continua have for the generation of new frequencies, selected continua achieved in this work are shown in Fig 1.1. The pump wavelengths range from the UV to the infrared and allow a gap free spectral coverage.

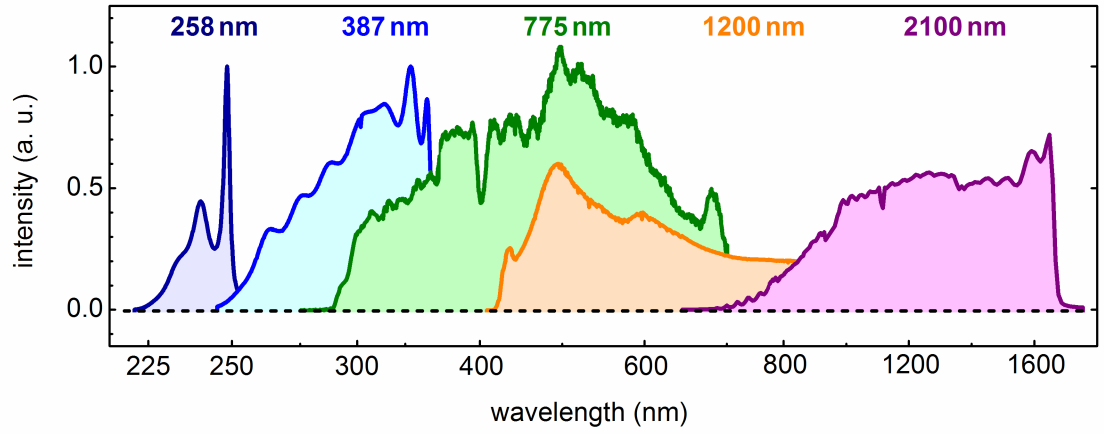

Fig. 1.1: Spectrum of continua generated in a 5 mm moving CaF_2 plate with various pump wavelengths. The 2100 nm continuum is generated in a 4 mm YVO_4 plate. The pump region is blocked by a dielectric mirror in each case.

All these continua show an excellent beam profile, a high stability, and a gap free spectrum. This renders them as ideal source for many applications. For example, these continua can be used as seed source in optical parametric amplifiers (OPAs). These OPAs are widely tunable and can range from the UV to the infrared. Figure 1.2 shows pulses with an extreme spectral bandwidth achieved in this thesis.

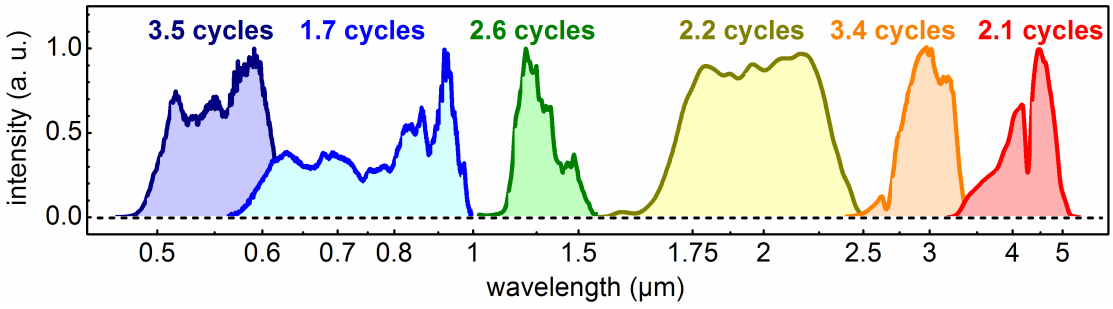

Fig. 1.2: Broadband pulses from various OPAs with few-cycle pulse duration limit.

These pulses have Fourier limits in the few-cycle regime. With the proper approach, they can be generated even at highest repetition rates with reasonable pulse energy as it will be shown in the following chapters. The wide tuning range of the input parameter and its high applicability make continuum generation in solids a highly attractive source for the genera-

tion of new wavelengths beside the laser fundamental. Furthermore, also ultrafast spectrometers benefit from such continua since a previously not achieved spectral coverage will be shown. In combination with an extremely wide range of delay times up to the millisecond regime, this allows unraveling the complete inner life of most investigated samples.

The thesis is structured as followed. In the first part I will describe the new findings in the generation processes of bulk continua and show the applications of such continua in broadest OPAs and transient spectrometers. After the short introduction in this chapter 1, which shows the potential of continuum generation, I will describe the mechanism of continuum generation and the single steps of bulk filamentation in chapter 2.

In chapter 3 it will be shown that continuum generation works for a wide range of input parameters. Pulses with durations up to picoseconds and central wavelengths from the UV up to the infrared will be applied for continuum generation. In addition, the properties of these continua will be characterized in full detail and results will be presented which reveal new aspects of the generation process of the new wavelengths. This knowledge will be used to produce shortest pulses directly from bulk continuum generation with superior spatial properties.

With the help of these continua and various mixing processes tunable ultrafast optical parametric amplifiers will be built which deliver short and tunable pulses from the deep UV up to the mid-infrared in chapter 4. The presented concepts enable the operation of ultrafast amplifiers from the UV to the infrared with previously not observed tuning ranges, pulse durations, and efficiencies. Starting with two typical laser wavelengths at 775 and 1025 nm, UV, visible, and infrared pulses will be generated.

Chapter 5 shows that bulk continuum generation can be excellently used as probe light in pump-probe experiments. A full statistical characterization of the whitelight pulses will also be given. Broadband transient spectrometers from the deep UV to the midinfrared allow capturing the entire dynamic of the investigated sample and unraveling the complete inner life of these complexes. Furthermore, beside the extension of the wavelength range, also the extension of the delay time between pump and probe pulses will be presented. In addition, the extension to the mid-infrared with highest time resolution and multi MHz repetition rates will be demonstrated. To show the potential of this extended spectrometer, examples will be presented for every wavelength region and time range. Studies about intermediate states in malachite green, sensitizing-based formation of benzhydryl cations, cooling processes in isotopically diluted aqueous lithium nitrate trihydrate, a C-nucleoside with benzophenone as chromophore, and fluorescence lifetimes of benzothiazole will clearly show the wide range of applicability for these continua. To conclude this chapter, the temporal resolution will be discussed in more detail since this is a crucial parameter for uncovering the fastest processes.

In the end of part I a summary of the obtained results will be given, including a conclusion for modern amplifiers and transient spectrometers. As an outlook on upcoming experiments, novel approaches will be shown that discuss the potential and future perspectives of bulk continuum generation.

The thesis is cumulative. The main part is the publications reprinted in part II. The first part summarizes the achieved developments and gained knowledge of the publications. In addition, it gives a guideline for building amplifiers and spectrometers which fit best to the experimental demands. Furthermore, it shows previously not regarded key aspects of bulk continuum generation.

2. Mechanisms of small-scale filamentation and continuum generation

2.1 The Kerr effect and related processes in continuum generation

During continuum generation many processes interact dynamically. Due to the various material properties and boundary conditions the generation of the new frequencies depends rather strongly on the chosen medium. To get a view inside the mechanisms of whitelight generation, the participating processes will be described followed by an explanation of their significance for continuum generation. The most important process is the optical Kerr effect [Buckingham56, Maker64, Ho79]. It describes the dependence of the refractive index n on the intensity I. The relation is shown in Eq. (1).

$$n = n_0 + n_2 \cdot I \tag{1}$$

n_0 is the linear and n_2 the nonlinear refractive index. If intense linearly polarized laser light propagates in an isotropic medium, the disturbance of the atomic motions from equilibrium and the distortion of the electron clouds induce temporary birefringence described with a nonlinear refractive index term. Typical values for gases for n_2 are 3 x 10^{-19} cm^2/W for air [Liu05c] and 6.9 x 10^{-16} cm^2/W for solids as for YAG crystals [Koechner06]. The variation of the refractive index according to the intensity has several consequences for the beam and its propagation. For a correct description, the peak intensity of laser pulses has to be known. It is not as trivial as it seems to be. For details, see part II Appendix A0.

A well known consequence of the Kerr effect is self-focusing [Marburger75, Shen75]. The refractive index becomes larger in areas where the intensity is higher. For a Gaussian shaped laser pulse, this is the central part. Therefore these parts have a lower phase velocity which leads to a significant curvature of the phase front and the pulse starts to self-focus. Figure 2.1 illustrates this.

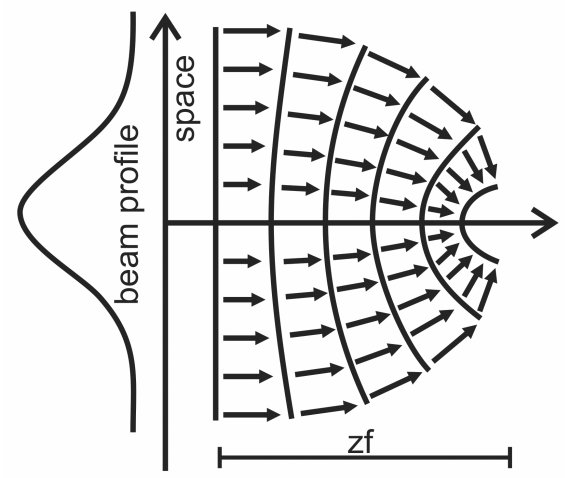

Fig 2.1: Gaussian beam profile in space and Kerr effect leading to a curvature of the phase front and self-focusing. This leads to a self focus after the distance z_f

This focusing effect is called a Kerr lens and can be used in lasers for mode-locking [Morgner99]. The self-focusing has to be stronger than the natural divergence of the beam to obtain a substantial decrease of the beam size. Therefore, there is a threshold power P_{crit} for self-focusing [Marburger75, Fibich00] which depends on the wavelength λ and is shown in Eq. (2).

$$P_{crit} = \frac{3.77 \cdot \lambda^2}{8\pi \cdot n_0 \cdot n_2} \tag{2}$$

If the nonlinear medium is long enough, self-focusing can lead to a self-focus which is reached theoretically after a distance z_f [Marburger75]. The formula for z_f is given in Eq. (3) and strongly depends on the input peak power P and the beam radius a.

$$z_f = \frac{0.367 \cdot 2\pi / \lambda \cdot a^2}{\sqrt{\left(\sqrt{P/P_{crit}} - 0.852\right)^2 - 0.219}} \tag{3}$$

After this distance the beam would collapse to a singularity. However, there are several mechanisms which counteract the self-collapse such as multi-photon absorption from the valence to the conduction band [Kosareva11], group velocity dispersion [Chernev92, Rothenberg92b, Ranka96], the saturation of the Kerr effect [Fibich99, Akoezbek00, Couairon03, Bree11], nonlinear absorption [Vlasov89, Kosmatov91, Dyachenko92, Couairon06a, Dubietis06], nonlocal effects [Bang02], avalanche breakdown [Kennedy95, Noack99, Vogel99], or vectorial and nonparaxial effects [Fibich01]. Which process is dominant depends on the material and is controversially discussed [Koleski10, Teleski10, Kosareva11]. For gases, it is plasma defocusing and the influence of the higher order Kerr terms [Vincotte04, Kosareva11]. In solids, it is supposed to be group velocity dispersion and plasma defocusing [Chernev92, Rothenberg92b]. How the group velocity dispersion can stop the collapse can be seen in Eq. (4).

$$v_g = \frac{c}{n - \lambda \cdot \frac{\partial n}{\partial \lambda}} = \frac{c}{n_0 + n_2 \cdot I - \lambda \cdot \frac{\partial (n_0 + n_2 \cdot I)}{\partial \lambda}} \tag{4}$$

This means that the group velocity v_g does not only depend on the change of the linear refractive index with the wavelength ($\delta n_0/\delta\lambda$), but also on the change of the nonlinear term ($\delta n_2/\delta\lambda$) and on the spectrum ($\delta I/\delta\lambda$).

The balance between self-focusing and the defocusing effects is called filamentation. The interesting key feature is the non Gaussian pulse propagation without diffraction. This allows highest intensities exceeding 10^{13} W/cm² to be conveyed over long distances in strong contrast to the natural Gaussian propagation and maintaining the advantageous properties such as superior beam quality and the short pulse durations. In addition, there is a unique beam profile during filamentation. Independently from the input beam profile there is always a Townes profile obtained [Chiao64, Moll03]. Figure 2.2 compares a Gaussian and a Townes profile.

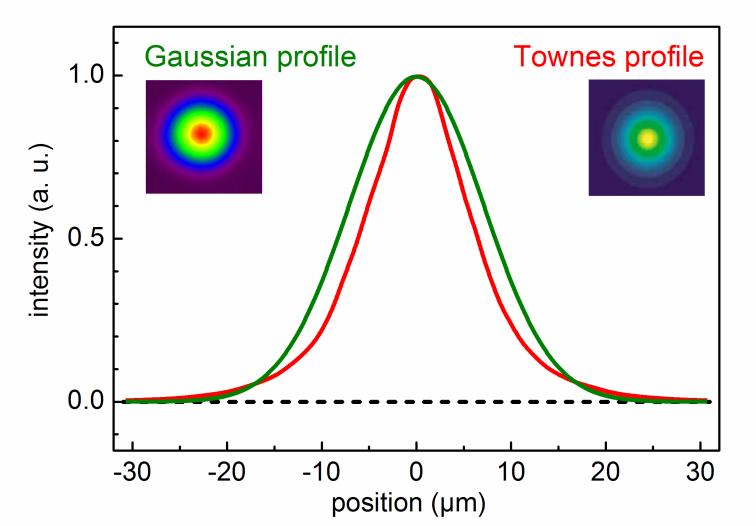

Fig. 2.2: Comparison of a Townes (redesigned from [Moll03]) and a Gaussian profile including beam profiles.

In gases, filaments typically have diameters of 100 µm and can even last over several kilometers [Mechain04, Rodriguez04, Mechain05]. At this point it should be mentioned that only about 10% of the energy are contained in the filament [Brodeur97, Chin99, Liu05a]. The main part is contained in the surrounding photon reservoir. To understand this surprising spatial distribution, the initial beam profile has to be regarded. Let's assume a Gaussian temporal intensity profile. This profile is then cut in thin temporal slices so that every slice has its own peak power. The central slice has the highest peak power. According to Eq. 3 this slice will have the shortest self-focal distance. The other slices with a lower peak power will have longer self-focal distances. Therefore, the impression of a moving focus arises [Brodeur97]. However, this leads to the effect that at each position in the nonlinear material only a small part of the beam is actually focused and most of the energy is contained in the surrounding area – the reservoir. It has been shown that this reservoir is essential for maintaining the filament [Liu05a, Liu05b, Scheller14]. It even allows the self-reconstruction and healing of an interrupted filament [Dubietis04b, Kolesik04b]. The decrease of the energy reservoir and the losses due to multi-photon or plasma absorption lead to the end of the filament. In solids, the losses are significantly higher [Dubietis06] due to the higher density. This allows filamentation distances of only a few millimeters. The longest reported filament in bulk ranges over 2 cm [Tzortzakis01, Dubietis03].

Another key feature of filamentation is intensity clamping [Becker01, Liu02, Kandidov11]. Since there is an extremely stable equilibrium between self-focusing and defocusing effects, also the peak intensity is extreme stable and will not exceed a maximum value or otherwise the defocusing effects dominate. In addition, this leads to self-spatial filtering [Chin07]. The exact value of the intensity depends on the material properties – mainly on the nonlinear refractive index and the multi-photon and plasma absorption coefficients and the group velocity dispersion. Typical values for the clamped intensity in air are $2-4$ x 10^{13} W/cm^2 [Kasparian00, Couairon07, Daigle10]. The nonlinear refractive index in solids is a factor of 1,000 higher, which lead to critical self-focusing powers in the Megawatt re-

gime instead of in the Gigawatt regime as for gases. However, also the probability for multiphoton absorption is around a factor 1,000 higher [Liu03a]. This leads to the interesting fact that the clamping intensities in solids and gases are roughly in the same range and on the order of 10^{13} W/cm^2.

A completely different picture arises if the dimensions are considered. Whereas filamentation in gases have a diameter of about 100 µm and can range over several kilometer, filaments in solids only range several millimeters and have diameters of several µm [Yablonovitch72, Tzortzakis01, A18]. The reason for this fact is the high amount of losses in solids and the low energy which can be contained inside a filament. Whereas filaments in gases can carry energies up to several mJ inside the filament channel, in solids only energies in the order of 100 nJ can be contained inside a filament although there are similar clamping intensities. This discrepancy originates from the high nonlinear refractive index in solids. Whereas in gases a smooth transition from the initially larger input beam profile to the Townes mode with 100 µm diameter is given, the high nonlinear refractive index in solids leads to strong self-focusing. Unavoidable smallest impurities and defects in the beam profile or material as well as not round beam profiles [Dubietis04a] lead to many small-scale filaments side by side [Schroeder04]. To demonstrate this, the propagation of a 1 mJ, 150 fs, 775 nm laser beam with a $1/e^2$ intensity radius of 3.5 mm in a 10 cm SF75 glass block is imaged from the side. The result can be seen in Fig. 2.3.

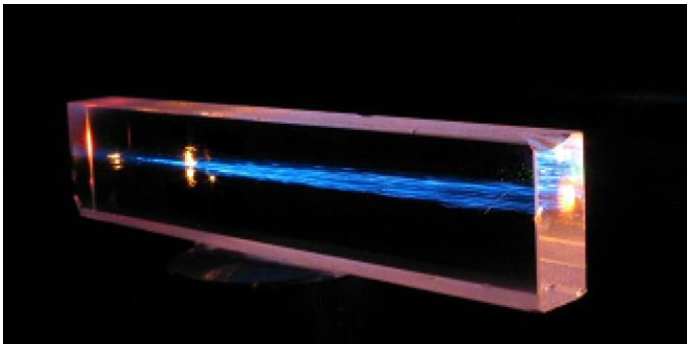

Fig 2.3: Side view of multi-filamentation. A 775 nm, 150 fs unfocussed laser beam with 1 mJ pulse energy propagates through a 10 cm long SF57 glass block

Many laterally and vertically displaced filaments are obtained. Each of them has a length of several millimeters and a diameter of just a few µm. If the initial intensity would already be on the level of the clamping intensity [Kiran10], the surface would be destroyed and this permanent damage would hinder filamentation with larger diameter. There are ongoing investigations on the phenomenon of multifilamentation. The interaction of the individual filaments could give an insight in the involved processes [Berge10, Beruge10]. Only input beam radii in the range of a few tens of µm with powers slightly above the threshold of self-focusing will lead to single filamentation in bulks. Therefore, external focusing is needed for bulk filamentation [Brodeuer99, A1, A18]. Since the first observations of filamentation in air [Braun95, Nibbering96], there have been many applications such as waveguides [Davis96, Watanabe03, Chin05], remote sensing and further analysis of the atmosphere [Rairoux00 Kasparian03, Stelmaszczyk04, Chin05, Kasparian08], the generation of ultrashort pulses

[Hauri04, Hauri05, Theberge06, Fuji07], or laser induced water condensation [Rohwetter10] where filamentation is used for experimental studies.

Another nonlinear effect which is a direct consequence of the Kerr effect and appears during filamentation is self-steepening [DeMartini67]. Assuming a Gaussian shape in time, the front and trailing part of the pulse see a lower refractive and group index and therefore propagate faster than the center of the pulse. This means that the back of the pulse will catch up with the center of the pulse and will form a steep slope at the end of the pulse. The front of the pulse will escape and there will be a long flat rise. Self-steepening appears instantaneously during filamentation [Schroeder06] and can be used for the generation of few cycle pulses since it dramatically shortens the pulse duration [Hauri04, Hauri05, Couairon06b, Uryupina10, Bethge11]. This self-shortening is possible in solids as well [Krebs13]. Figure 2.4 illustrates this behavior and shows the deformation of the on-axis temporal intensity profile during self-steepening.

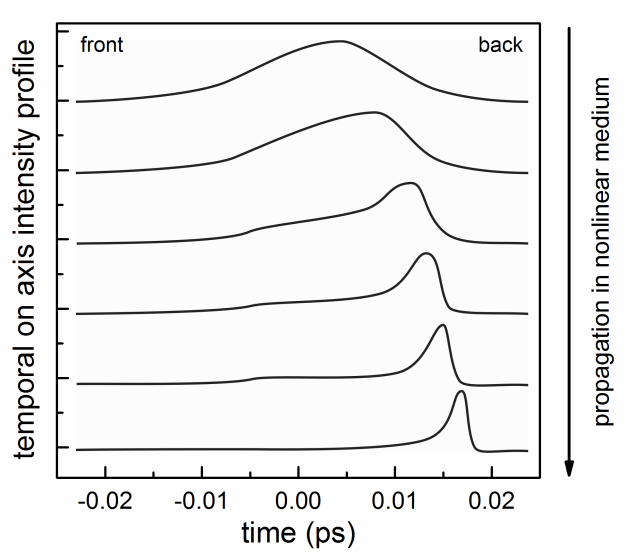

Fig. 2.4: Evolution of the temporal intensity profile of an initial Gaussian pulse in time due to self-steepening (redesigned from [Rothenberg92a])

A third effect which is also directly connected to the Kerr effect is self-phase-modulation [Shimizu67, Alfano70b, Stolen78]. Since the phase φ is related to the refractive index, also the phase of the pulse is influenced by the temporal varying intensity as can be seen in Eq. (5).

$$\varphi = \omega_0 t + kz = \omega_0 t + \frac{2\pi L}{\lambda}(n_0 + n_2 I) \tag{5}$$

ω_0 the central frequency of the pulse, k is the wave vector, z the propagation distance, and L the length of the nonlinear medium. This relation allows the generation of new colors in the pulse since a changing phase results in new frequencies. Equation (6) shows the formula for the new frequencies ω.

$$\omega = -\delta_t \varphi = -\omega_0 - \frac{2\pi L}{\lambda}\delta_t (n_2 \cdot I) \tag{6}$$

A change of the temporal intensity profile also changes the phase of the pulses and leads to the generation of new frequencies. Figure 2.5 illustrates this and shows that the redder frequencies are generated at the front of the pulse and the bluer at the back of the pulse.

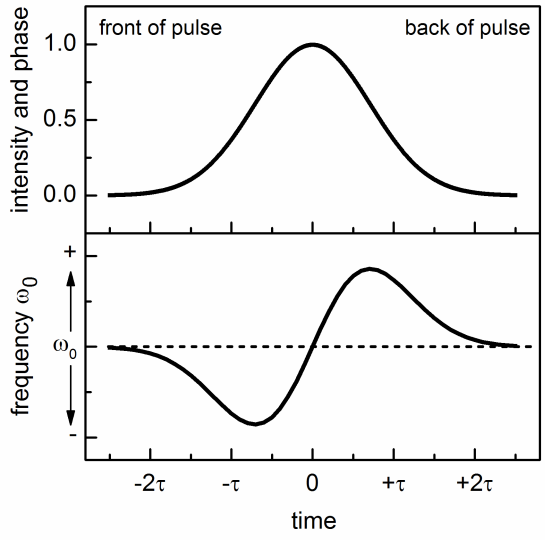

Fig. 2.5: Self-phase modulation of a laser pulse with a temporal Gaussian intensity profile. The redder frequencies are generated at the front of the pulse, the bluer at the back

To get an impression of the strength of this effect, an 800 nm pulse with a duration of 150 fs and a peak intensity of 1.0 TW/cm^2 is considered which propagates in a 4 mm thick YAG plate. According to Eq. (6) the maximum frequency depends on the maximum temporal variation of the intensity as shown in Eq. (7):

$$\begin{aligned}\Delta\omega_{max} &= -\omega_0 - \frac{2\pi L}{\lambda}\delta_t(n_2 \cdot I)_{max} \\ \partial_t I = \partial_t &\left(1\frac{TW}{cm^2}\cdot\exp\left(-\frac{t^2}{\left(150fs/2\sqrt{\ln 2}\right)^2}\right)\right) \\ = 1\frac{TW}{cm^2}&\cdot\exp\left(-\frac{t^2}{\left(150fs/2\sqrt{\ln 2}\right)^2}\right)\cdot\frac{-2t}{\left(150fs/2\sqrt{\ln 2}\right)^2}\end{aligned} \tag{7}$$

The extrema of this function are at $t = \pm 150fs/\sqrt{\ln 256} = \pm 63.7fs$ (calculated from the zero points of the second derivation) and the maximum intensity change there is ± 9.5 GW/cm²/fs. With the central frequency, the crystal length and the nonlinear refractive index, the maximum shift of the frequency is 206 THz which corresponds to 70 nm at 800 nm. However, the spectrum of a continuum generated in a 4 mm thick YAG crystal [A1] covers a significant broader spectral range and is not symmetric. The spectral shape can be explained if self-steepening is taken into account [Gaeta00]. An asymmetric temporal intensity profile with a steep slope at the back of the pulse is obtained (see Fig. 2.4) which leads to the typically observed spectrum.

2.2 Description of continuum generation in bulk material

All the involved processes interact with each other and lead to the generation of new wavelengths. The first significant process is self-focusing. If the initial beam profile is small and clean enough and the peak power of the pulse exceeds the threshold, self-focusing decreases the beam size and dramatically increases the intensity of the beam. The group velocity dispersion is delaying the onset of self-focusing [Luther94a], but does not prevent it. The dynamic interplay between these two processes can lead to pulse splitting [Rothenberg92a, Chernev92, Ranka96, Trippenbach97, Faccio06, Faccio08b]. Self-steepening is already present and shifts the central part towards the back of the pulse. This leads to asymmetric pulse-splitting [Fibich97, Ranka98]. The trailing pulse further undergoes self-steepening and self-focusing until multi-photon absorption from the valence to the conduction band appears and arrests the collapse at the clamped intensity. This catastrophic collapse is often described as the formation of an optical shock wave [Gaeta00, Akoezbek01]. The electrons which are excited from the valence to the conduction band can move nearly freely and be described as a plasma. They add a negative contribution to the refractive index which is equal to the nonlinear term and a stable equilibrium between self-focusing and plasma defocusing is formed. This negative contribution occurs very quickly and according to Eq. (6) new frequencies are generated. Self-phase modulation is enhanced by the fast change of the refractive index due to multi-photon excitation and plasma generation [Bloembergen73, Chin99, Kandidov03]. New wavelengths are also generated by self-phase modulation enhanced by self-steepening. Equation (6) shows that the new frequencies are also generated due to a temporally changing intensity [Gaeta00]. Due to the steep edge at the back of the pulse, the continuum spectrum develops a plateau on the short wavelength side. At the front of the pulse, there is a smooth increase in the temporal intensity profile. Therefore, the Stokes side of the continuum shows an exponential drop-off.

According to the moving focus model, only 10% of the energy is in the central filament. The remaining 90% are contained in the surrounding photon bath which continuously feeds the filament. The filament ends if the losses due to multi-photon absorption are too high or if the reservoir cannot provide enough photons any more to feed the filament. Additional processes which are involved in continuum generation are four-wave mixing [Xing93, Luther04], Cherenkov radiation, [Golub90], formation of X-waves [Kolesik04a, Couairon06a, Faccio06, Faccio08a, Faccio08b, Majus11a], self-phase modulation in the plasma [Kosareva97], and Raman processes [Zozulya98, Kardas13]. They contribute to the generation of the new frequencies, but play a minor role. Typically sub-μJ pulses are needed for bulk continuum generation. About 1 % of the input energy is converted. This means, only some nJ of light is generated at new frequencies.

If the input energy is high enough, multiple refocusing occurs. This means that two or more distinctive light bullets can be observed from the side lining up sequentially along the propagation axis. It has been shown that this is the result of the complex spatio-temporal transformation of the radiation due to Kerr self-focusing, ionization and plasma-induced defocusing, material dispersion and diffraction [Kandidov03, Liu03b].

2.3 Theoretical consideration and simulation of small-scale filamentation

One of the main challenges of modeling the continuum generation process is the dynamic interplay of the processes. They do not happen after each other and are strongly intermingled. There are several models to describe the process such as the moving focus model [Brodeur97], the slowly varying envelope approach [Brabec97] including its breakdown [Rothenberg92b, Ranka98], the description with solitons [Wise02, Chekalin13, Smetalina13], or X-waves [Kolesik04a, Faccio06, Couairon06a, Faccio08a, Faccio08b]. The most promising approach to simulate continuum generation is the description with the nonlinear Schrödinger equation [Vlasov89, Ranka98, Fibich99, Jukna13].

Even seemingly small contributions like the higher order terms of the Kerr effect contribute to the process [Berge04, Kolesik10, Bejot10, Borchers12] and can play an essential role. All these processes happen on a very fast time scale. Although many investigations focus on filamentation in gases, there are a couple of studies on continuum generation in liquids and solids [Brodeur99, Gaeta00, Kandidov03, Ashcom06, Chekalin13, Darginavicius13]. A full theoretical description including simulating and modeling filamentation and continuum generation is beyond the scope and dimension of this work. However, since this topic can be of interest for the readership, they are pointed to comprehensive encyclopedias on these topics [Brabec00, Chin05, Alfano06, Berge07, Couairon07, Kasparian08, Chin10]. This research field is still heavily investigated [Chekalin13, Darginavicius13, Durand13, Gong13, Kardas13, Jukna13, Majus13, Smetanina13a, Smetanina13b] and there is a vivid discussion about the role of the single phenomena for the process of filamentation and continuum generation [Kolesik10, Teleski10, Kosareva11, Kardas13]. Therefore, different aspects of filamentation and continuum generation in solids will be analyzed experimentally in the following chapter. In addition, the influence of the input pulse parameter will be studied.

3. New aspects of bulk continuum generation

3.1 Universal features of bulk continuum generation

The goal of this chapter is to find the optimum conditions for continuum generation so that it can be used in ambitious applications. Therefore, all external parameters and pump pulse properties are pushed to the extreme and their influence on continuum generation is studied [A1, A18]. In addition, the generation and propagation of the new frequencies are studied with the highest possible precision. This allows continuum generation in various media, with picosecond pulses, and with UV or infrared pump wavelengths. Even few-cycle pulses can be directly produced. A fascinating observation is that all continua have universal features independent from the used material. Fig. 3.1 shows a typical bulk continuum generated in a 4 mm YAG plate with a Ti:sapphire laser system (CPA2001, Clark MXR) which delivers nominal 150 fs pulses at 775 nm at 1 kHz with a pulse energy of 0.9 mJ.

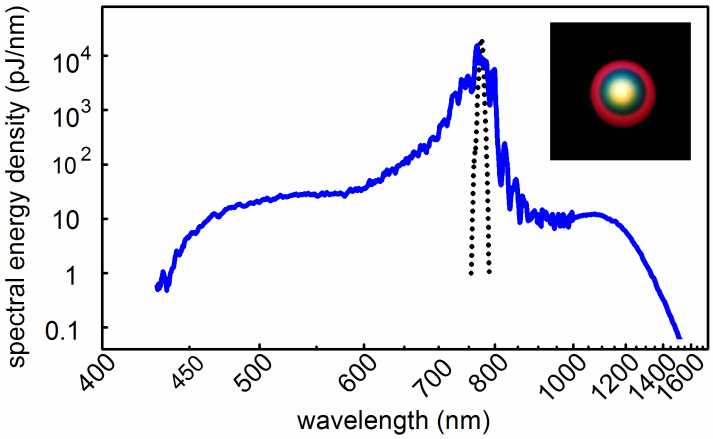

Fig. 3.1: Spectrum of continuum generation in a 4 mm YAG plate and visual appearance [A1].

- A smooth gap-free plateau on the short wavelength side and a more exponential drop off on the long wavelength side appear. The region around the fundamental wavelength is highly structured and strongly fluctuating. Only 1% of the total input energy is converted into new colors. Taking into account that only 10% of the energy is contained in the filament, this corresponds to a conversion efficiency of 10%. Fig. 3.1 shows the spectrum of the filament and the energy reservoir.
- When increasing the pump energy, the short wavelength side stays rather constant and no spectral changes are observed. On the long wavelength side an increasing energy leads to an increased amount of newly generated colors. If the energy exceeds the threshold for multiple refocusing, the spectral behavior and the visible appearance change significantly [A1, A9, A18]. For single filamentation, the beam profiles of the new colors have a high spatial quality (see inset in Fig. 3.1).
- The interaction of the various nonlinear processes leads to a strongly structured spectrum and high fluctuations in the pump region. On the other side, the new frequencies show pulse-to-pulse fluctuations in the order of only 1 to 2 % rms.

3.2 External focusing, material properties, and crystal selection

To find the optimum continuum which is best suited for the specific application, first the influence of the external conditions needs to be investigated. Therefore, the initial focusing, the material, and its dimensions are studied. To ensure that all measured values are fairly comparable, care is taken to obtain absolute spectral energy densities [A1].

To achieve self-focusing and hence continuum generation without destroying the crystal surface or achieving multiple filamentation, external focusing is needed. This ensures a sufficient small beam diameter and a sufficiently high intensity at the crystal entrance. The propagation properties for a Gaussian beam (with $M^2 = 1$) are given by the numerical aperture and its wavelength. Therefore, various numerical aperture are investigated. If the numerical aperture is above 0.1, a stable operation of the continuum is critical because optical breakdown and surface destruction occur. Therefore, the numerical aperture should remain below this limit. A further decrease leads to an enhanced blue broadening of the continuum [Ashcom06] and more newly generated light [A1]. In addition, the probability of permanent damage is reduced [Ashcom06]. However, if the numerical aperture is set below 0.015, the input beam size is too large at the entrance surface of the crystal. Then, a high pulse energy is needed to achieve sufficiently strong self-focusing so that a self-focal is reached within the crystal length and filamentation can start. However, such a high pulse energy leads to multiple filaments and crystal damage. To demonstrate this, a 70 cm lens is used to focus the 775 nm pump light onto a 10 mm YAG plate. For the 3.5 mm beam radius ($1/e^2$ intensity level), this corresponds to a numerical aperture of 0.005 and a beam waist radius of 60 µm at the YAG entrance surface. When exceeding the threshold for continuum generation by increasing the energy sufficiently, instantaneously many single filaments are generated side by side. With a further increased pump energy, electrons are liberated from the surface and permanent damage occurs. This can be seen in the attached video [Video01]. The spectrum of this continuum is shown in Fig. 3.2 The input energy is 250 µJ. This corresponds to 2 TW/cm^2 at the crystal entrance surface.

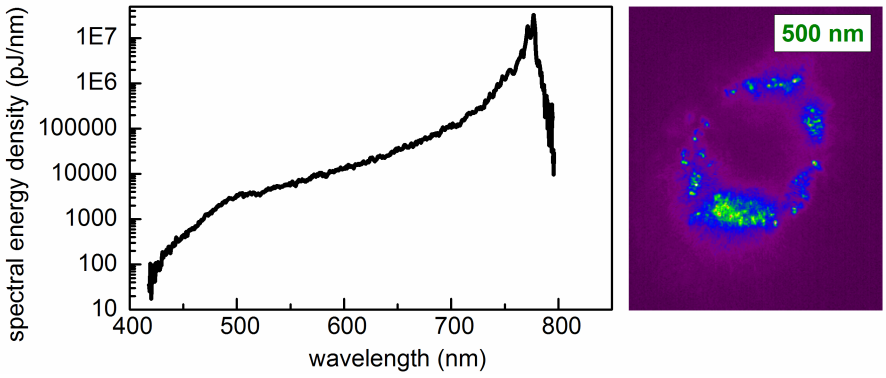

Fig. 3.2: Spectrum of continuum generation in a 10 mm YAG plate when focusing 250 µJ of the 775 nm laser light with a 700 mm lens. The right panel shows the beam profile of the 500 nm part for the multiple generated filaments.

Although the generated spectrum in Fig. 3.2 looks smooth and has a 1,000 times higher spectral energy density (compare to Fig. 3.1), it is not suitable for most applications. The

filaments are generated side by side. This can be seen by bare eye if the 500 nm part of the continuum is considered. Each single spot in the graph corresponds to a small single filament. The main challenge with such continua is that the spatial and spectral coherence gets lost and that the temporal and spatial structure is distorted. A focal length of 8 to 10 cm turns out to be best to achieve the highest amount of new frequencies. For the used laser beam, this corresponds to a numerical aperture of approximately 0.04.

Another approach for a proper pre-focusing is the use of Bessel beams which are generated by focusing with axicons. Bessel beams have the advantageous property that the beam stays short in time and space over a long distance [Bowlan09]. To demonstrate the spatial robustness of Bessel beams, the beam profiles for different positions behind a 2.0° axicon are shown as inset in Fig. 3.3. The central part of the beam has a diameter of 10 µm FWHM for a nearly 20 cm distance. The idea behind filamentation with Bessel beams is that the beam propagation is already close to the filamentary beam propagation. Especially, an enhanced energy reservoir is generated which feeds the filament continuously. Thereby, a propagation distance of the filament can be achieved which is a magnitude longer than typical [Scheller14]. However, this is only realized with an additional background pulse. When only using one pulse, no significant differences are obtained compared to continuum generation with Gaussian input beams. Figure 3.3 shows the spectrum of a continuum generated in a 10 mm YAG plate when focusing the laser light with a 2.0° axicon and a 10 cm lens.

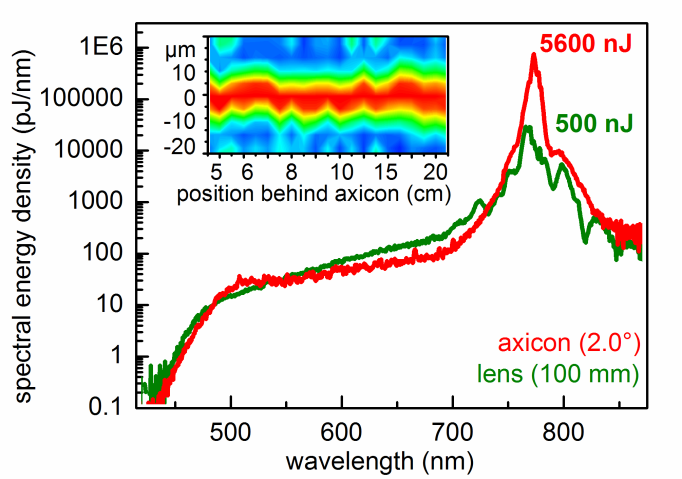

Fig. 3.3: Spectrum of continuum generation in a 10 mm YAG plate when focusing the laser light with a 2.0° axicon (red) and a 10 cm lens (green). The inset shows the spatial profile of the pump in dependence on the distance behind the axicon.

Except the higher amount of energy needed for continuum generation, no significant differences between the continua are found. There are several studies about filamentation in solids with Bessel beams [Dubietis07, Clerici10, Majus13] which support the obtained observations. The reason why the Bessel beam does not improve the situation in solids is the robustness of filamentation against external influences. Once the filament has been formed, the influence of additional light is suppressed by the dynamic interplay of the filament and the energy reservoir. In conclusion, the best continuum generation is obtained, if lenses with

a fairly short focal length are used to focus the laser light. The numerical aperture should be in the range between 0.015 and 0.1.

Beside the focusing geometry, surprisingly, also the crystal length is essential for the amount of generated continuum light. An increased crystal length allows the formation of the full filament and leads to increased continuum generation [A1]. To prove this, a continuum is generated in a YAG wedge. By laterally moving the wedge, the crystal length is varied and the continuum generation is characterized for different material thicknesses. The apex angle of the wedge is so small (2.0°) that the tilted exit surface does not effect the continuum generation. The front surface is kept perpendicularly to the input beam and the front surface of the wedge is placed in the focus of the beam. The 500, 600, and 700 nm part of the continuum (selected with interference filers) are focused on a photo diode and the amount of generated light is measured [A1]. The setup is shown in Fig. 3.4, too.

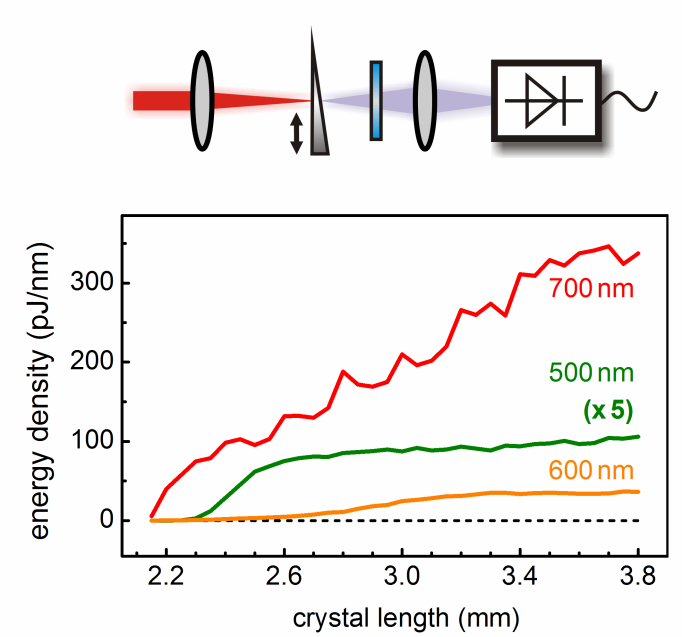

Fig. 3.4: 500, 600, and 700 nm part of a YAG continuum for a varying crystal thickness.

In the first 300 µm of the filament, self-phase modulation enhanced by self-steepening is dominant and all colors are generated. Then, self-phase modulation enhanced by multi-photon excitation becomes relevant and leads to the generation of new light during the entire filamentation process for wavelengths close to the pump. This means that the 500 nm part has fully built up after the first 300 µm, whereas the 700 nm part continuously increases over the entire filament. At 600 nm a mixture of both cases is present. There, only a continuous rise within the first 800 µm is observed. To get a better impression of the discussed influences, Fig. 3.5 shows the continuum spectra for various crystal thicknesses.

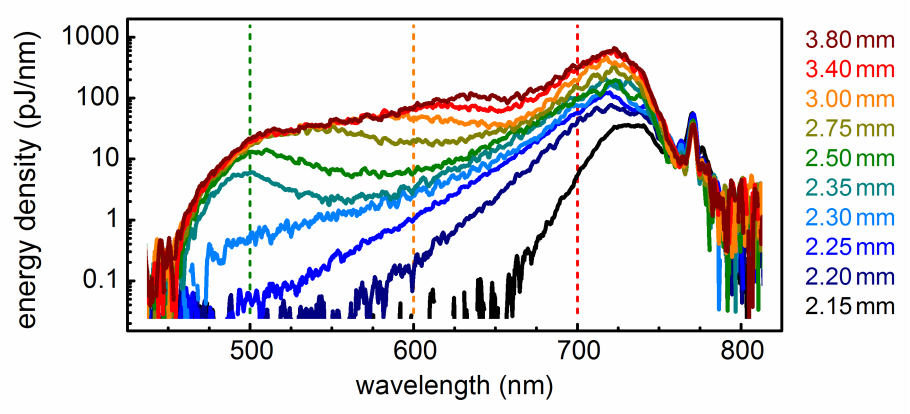

Fig. 3.5: Spectra of continua generated in a YAG wedge for various effective crystal lengths

Studies on the influence of the crystal length have been performed by moving the focusing lens in front of the crystal [Brodeur99]. Since in these experiments the movement of the lens also changes the starting position for filamentation, the position of the lens cannot be transferred to the crystal thickness. Experiments, in which fused silica wedges are used for continuum generation were also performed [Smetanina12b, Smetanina13a], but for other research goals. In conclusion, it has been shown for the first time that the shorter wavelengths are generated only at the beginning of the filament, whereas wavelengths close to the pump are produced during the entire filamentation. This complex temporal structure of the new colors should be kept in mind when the compressibility of such continua is studied.

Another key feature is the selection of the nonlinear medium. It is essential for the spectral range, which should be covered by the continuum, and for the available pump energy. The short wavelength continuum cut-off is mainly determined by the bandgap of the material and the necessary pump energy by the linear and nonlinear refractive index [Brodeur98, A1]. Therefore, a large number of crystals have been tested to find the optimum medium for each purpose. Figure 3.6 shows the spectrum and the power threshold for various materials in dependence on the linear and nonlinear refractive index.

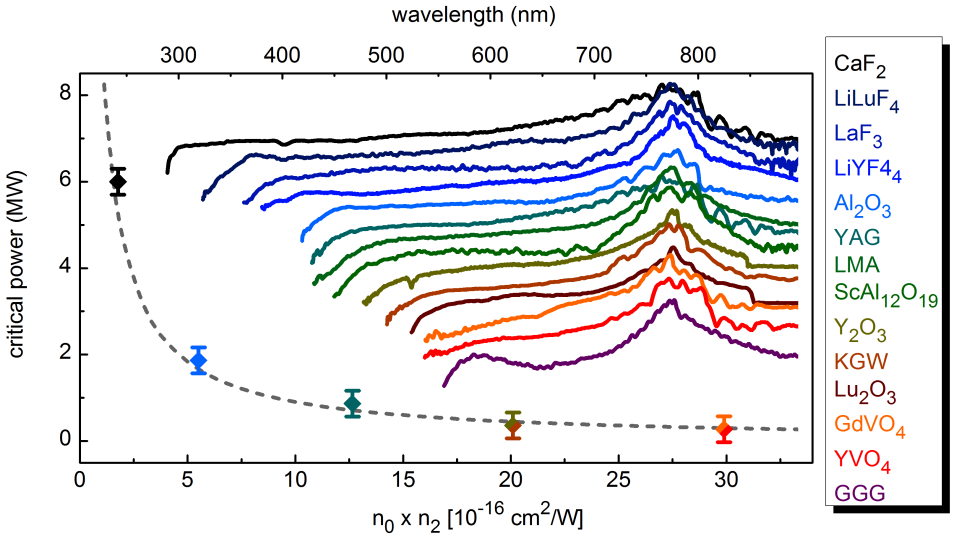

Fig. 3.6: Critical power and spectrum for continuum generation in various media in dependence on the refractive indices. The color of the squares indicates the material.

Beside the now well known materials for continuum generation such as calcium fluoride (CaF_2), sapphire (Al_2O_3), or YAG, there are plenty of other well-suited materials for continuum generation. For example, there are:

- Further fluorides (lanthan fluoride (LaF_3), lithium lutetium fluoride ($LiLuF_4$), yttrium lithium fluoride),
- Sesquioxide crystals (yttrium oxide (Y_2O_3), lutetium oxide (Lu_2O_3))
- Vanadate crystals (gadolinium vanadate ($GdVO_4$), yttrium vanadate (YVO_4))
- Garnet crystals (gadolinium gallium garnet (GGG))
- Tungstate crystals (potassium gadolinium tungstate (KGW))
- Aluminum oxides (scandium aluminum oxide ($ScAl_{12}O_{19}$), lanthan magnesium aluminum oxide ($LaMgAl_{11}O_{19}$, LMA))

This means that for nearly any available pump energy, a suited material can be found for continuum generation.

- If UV light is needed, as in many transient spectrometers, CaF_2 is a well-suited choice.
- If visible light is needed, as for most OPAs, sapphire or YAG should be chosen.
- At high repetition rate on the other side, where only modest pulse energies are available, $GdVO_4$, YVO_4, or KGW are recommended due to the low threshold.

The search for suited materials was only performed among laser host materials because they show a superior crystalline quality, a high damage threshold, and good thermal properties. However, nearly any transparent medium can be used for continuum generation which shows the uniqueness of this process. When looking for the proper material, the following relations were derived:

- The lower the linear refractive index, the lower the nonlinear refractive index, the higher the bandgap.
- The higher the bandgap, the shorter the transmission cut-off, the shorter the continuum cut-off, the higher the energy threshold for continuum generation [A1], and the shorter the maximum pulse duration allowing continuum generation [A18].

With these relations in mind, nearly always a suited material can be found for proper continuum generation.

3.3 Influence of the pump wavelength on bulk continuum generation

Beside the adequate choice of the focusing geometry, material, and crystal thickness, also the correct parameters for the pump pulses are essential for proper continuum generation. Therefore, all relevant pump pulse parameter are studied in this thesis. At first, the central wavelength of the pump pulses is regarded. Often, bulk continua are generated with Ti:sapphire lasers, but also with the upcoming Ytterbium based lasers systems. One of the main attractive features of bulk continuum generation is that the short wavelength cut-off stays nearly constant when generating the continua with pump wavelengths longer than the typically used 800 nm Ti:sapphire wavelength [A1]. This can be utilized to obtain octave-spanning continua. Figure 3.7 (b) shows continua generated with pump wavelengths from 1.1 to 1.6 µm in a 4 mm YAG plate and a continuum generated with a pump wavelength of 2.1 µm in a 10 mm sapphire plate.

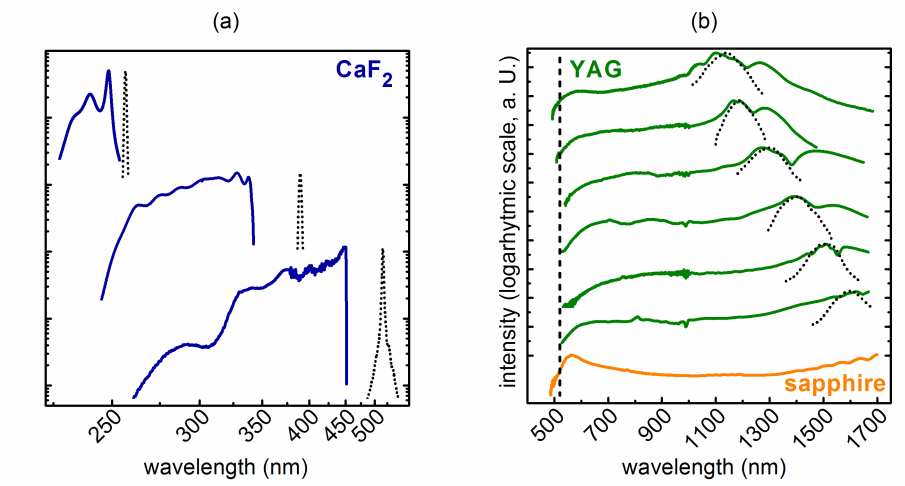

Fig. 3.7: Spectrum of a continuum generated in (a) a 5 mm CaF_2 plate with UV pump pulses and (b) in a 4 mm YAG plate and a 10 mm sapphire plate (2.1 µm) with various infrared pump pulses.

It can be seen that for continuum generation with infrared pump pulses the cut-off is always close to 500 nm. This means the main criteria for the blue extension of continua generated with wavelengths longer than 800 nm are the material properties and not the pump wavelength. The dominating generation mechanism is self-phase modulation enhanced by multi-photon excitation because it strongly depends on the material properties and therefore can lead to an independent continuum cut-off. Self-phase modulation enhanced by self-steepening also contributes to the new frequencies, but will not lead to such an immense blue broadening.

This changes, if continua with short wavelengths are generated. Then, the continuum cut-off strongly shifts with the pump wavelength as can be seen in Fig. 3.7 (a). It shows continuum generation in a 5 mm CaF_2 plate with pump wavelengths below 800 nm. These continua allow the generation of broadband UV light down to 225 nm which can otherwise only be achieved with great effort and by complex mixing schemes. The reason for the different behavior of the continuum cut-off compared to the long wavelength continua is the generation mechanism. For these short pump wavelength, self-phase modulation enhanced by self-

steepening has a larger broadening effect than self-phase modulation enhanced by multi-photon excitation. Therefore, the continuum cut-off shifts with the wavelength. The main challenge with short wavelength pumped continua is the visual impression. The 800 and 1000 nm pumped continua have the advantageous property that the fundamental region is barely observable although 99% of the energy is contained in this spectral range. However, the newly generated light is clearly visible by bare eye. This is different for continua pumped by shorter wavelengths. The 99% contained in the fundamental region dominate the visual impression and the newly generated wavelengths are only visible after spectral selection, which makes the daily operation more demanding. The advantageous properties of continua pumped by short and long wavelengths will be utilized in chapter 5. There, these continua are used as stable probe light in ultrafast transient spectrometers.

Another point which should be mentioned is the energy threshold for continuum generation. Since self-focusing is the first important process, the threshold for continuum generation coincides with that for self-focusing. Therefore, it scales quadratically with the wavelength. In addition, the achievable minimum beam radius has to be taken into account. The beam waist radius depends besides the numerical aperture and the M^2 also on the wavelength and increases linearly with it. This means that the intensity in the focus decreases quadratically for longer wavelengths, if the same focusing is used.

From all these studies, it can be concluded that bulk continuum generation is possible with nearly any pump wavelength from the UV to the infrared without loosing the advantageous features. This is extremely helpful if additional frequencies at the current wavelength regime are needed or other pump lasers as Ti:sapphire based systems are available. Especially when using the newly evolving Yb based laser systems, continuum generation is a very attractive source to produce new frequencies. Based on our work [A1, A2, A3, A4, A5, A9, A10, A11, A15, A21] and recommendation, continuum generation with Yb based systems has become practicable and is used for many purposes [Emons10, Schulz11, Harth12, Riedel13, Liebel14, Nillon14]. There are further studies which investigate and utilize bulk continuum generation with pump wavelengths beyond the typical laser wavelengths [Riedle00, Baltuska02a, Nagura02, Ziolek04, Saliminia05, Saeki07, Faccio08b, Muecke09a, Bethge10, Etzold12, Silva12a, Smetanina12b, Darginavicius13, Liao13, Smetanina13a, A6, A7, A13, A18, A19]. These continua are used in broadband amplifiers, carrier envelope phase measurements, or transient spectrometers, mainly to extend the spectral range. By this method, for example, the UV probe range of the our ultrafast transient spectrometer [Megerle09] could be significantly extended from 280 nm down to 225 nm [A7, A8, A19].

In addition, it has been shown for the first time that the continuum cut-off depends on the pump wavelength. For infrared pump pulses, a constant continuum cut-off is observed. For visible or UV pump pulses, it strongly shifts with the pump wavelength.

3.4 Influence of the pump energy on bulk continuum generation

An important parameter influencing continuum generation is the pump pulse energy. When increasing the pump energy, the short wavelength side stays nearly constant and minor spectral changes are observed. On the long wavelength side, an increased energy leads to a higher amount of newly generated colors [Gaeta00, A1]. This is valid until about twice the threshold for self-focusing is reached. Then, multiple refocusing occurs [Liu03b, Dharmadhikari09, A9, A18]. Further filaments are generated on the same pathway as the first filament. This strongly influences the spectral and spatial properties of the continuum. To demonstrate this, for the first time the spectrum, the beam profile, and the side view of continuum generation in a 6 mm YAG plate are simultaneously recorded and displayed. The side view is possible without any further modifications of the crystal because a part of the recombination luminescence spectrum is in the visible [Hayes80, Muerk95, Babin05]. Figure 3.8 shows the spectrum after a Calflex-X filter that blocks the 800 nm pump region, the beam profile, and the visible appearance of multiple refocusing in a 6 mm YAG plate. The numbers indicate how many filaments are present. In addition, a video synchronously showing spectrum, beam profile and side view of the crystal for an increasing pump energy is attached to this work [Video02].

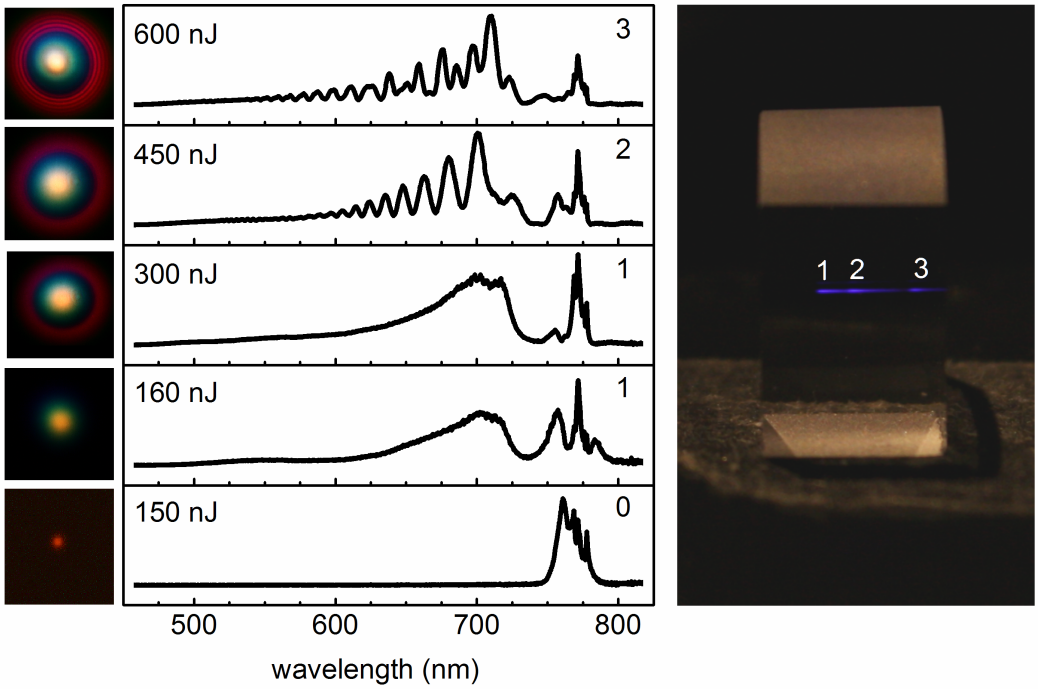

Fig. 3.8: Spectrum, beam profile, and side view for various input energies during continuum generation in a 6 mm YAG plate showing multiple refocusing.

When continuum generation starts, first a weak broadening due to self-phase modulation is observed. Once a single filament has been formed, no difference between 160 or 300 nJ input energy is observed except of the rise of the conical emission [Luther94b, Nibbering96, Kosareva97, Faccio06, A1] and an increasing infrared continuum (not shown) [A1]. If the pump energy exceeds twice the threshold for continuum generation, a second filament appears. A clear interference structure in the spectrum can be observed. The period of this

structure originates from the interference between the two temporary delayed filaments on the detector. With additionally arising filaments, the spectrum is fluctuating strongly and shows no clear structure. The beam profile on the other side, shows an interference pattern in the conical emission for multiple refocusing, whereas in the central part no substructures can be observed. For even higher pump energies, a beam break up occurs. The interference pattern for the conical emission is due to the fact that the single filaments diverge from the same small area. The side view can be used to characterize the dimensions of the filament channel [A18]. To achieve the best image quality and highest spatial resolution, a reflex camera (EOS 60D; Canon) and a five time enlarging objective (MP-E 65mm f/2.8 1-5x Macro Photo, Canon) is used. The focus is optimized with a linear micrometer translation stage and a computer is used to control the camera. A micro objective (micro objective 200 in 2 mm; Qioptiq Inc.) is utilized as scale and a resolution of 0.85 µm per pixel can be estimated. This is in good agreement with the calculated resolution from the pixel size and the enlargement factor (4.3 µm pixel size and 5:1 enlargement on sensor). With the help of neutral density filters the system is calibrated and a linear intensity scale is ensured. This allows for the first time directly measuring the dimensions of the filament channel inside the YAG plate. Figure 3.9 shows the length (b), the lateral profile (c), and the fluorescence spectrum (d) of single filamentation in a 6 mm YAG plate with an unprecedented µm resolution.

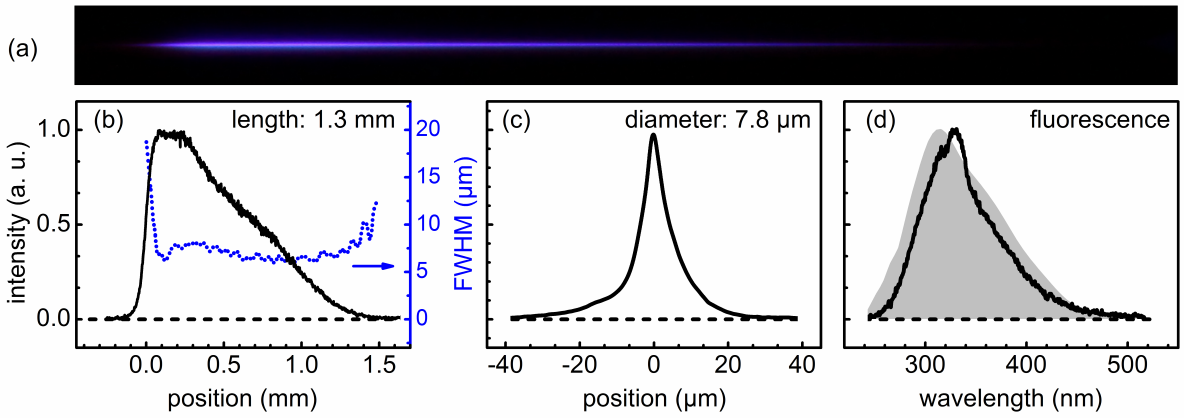

Fig. 3.9: (a) Photography of a single filament in YAG with (b) length and diameter, (c) lateral profile, and (d) measured spectrum of observable recombination light (black) compared to the reported luminescence spectrum of YAG (gray area, from [Babin05]).

The characteristic behavior of filamentation of a long propagation with a small beam diameter is observed. For a beam diameter of 7.8 µm (FWHM) the Raleigh length would be 180 µm which is 7 times shorter than the observed filament length of 1.3 mm. The lateral spatial profile also shows the mentioned Townes mode. In addition, the surrounding photon bath is indicated. The fact that the observable visible light of the side view originates from the recombination can be seen if its spectrum is measured. It is in good agreement with the luminescence spectrum (gray area in Fig. 3.9 (d)) [Babin05].

Beside the dimension, also the position of the filament in the crystal can be determined. This can be used to improve the phase fluctuations of the continuum [A18]. Figure 3.10 shows the filament position in a 6 mm YAG plate in dependence on the pump energy.

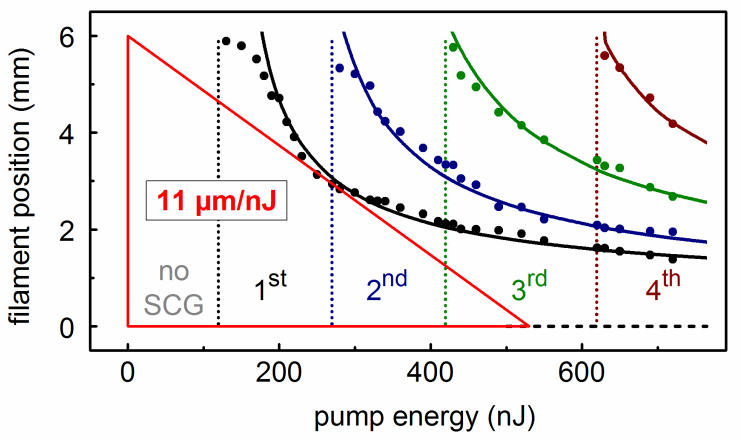

Fig. 3.10: Filament position in dependence on the input pulse energy in a 6 mm YAG plate. The solid lines are fits for the self-focal distances assuming multiple self-focusing thresholds

The solid lines show the theoretical self-focal distance, assuming one, two, three, or four times the self-focusing threshold as critical power. Since the energy of the laser is fluctuating, also the position of the filament is fluctuating, according to the slope of the tangent (red line in Fig. 3.10). This means that for example for 250 nJ the position is varying 11 µm if the pump energy is varied by 1 nJ. The variation of the generation position results in temporal and hence phase fluctuations of the newly generated frequencies. Depending on the actual generation position, the propagation pathways inside the crystal for fundamental and newly generated light are different. And since both are propagating with different group velocities the traveling time and phase become different. The phase fluctuations in dependence on the energy fluctuations ($\Delta\varphi/\Delta E$) can be written as

$$\frac{\Delta\varphi}{\Delta E} = \frac{2\pi c}{\lambda_{SCG}} \cdot \frac{\Delta t}{\Delta E} = \frac{2\pi c}{\lambda_{SCG}} \cdot \left| \frac{1}{v_{group}^{pump}} - \frac{1}{v_{group}^{SCG}} \right| \cdot \frac{\Delta z}{\Delta E} \tag{8}$$

λ_{SCG} is the continuum wavelength which is considered, c the speed of light, $\Delta t/\Delta E$ the time fluctuation in dependence on the energy fluctuation, v_{group} the group velocity for pump and continuum wavelength, and $\Delta z/\Delta E$ the position variation in dependence on the energy fluctuations. The optimum condition with minimum temporal and phase jitter is reached, if strong energy fluctuations lead to weak position variations. This is always the case, when the pump energy is slightly below multiple refocusing. With the proper adjustment phase fluctuations down to 100 mrad are achieved [A5] which is necessary for phase stable OPA pulses and carrier envelope phase (CEP) sensitive experiments. This is in good agreement with previous measurements in which the jitter and the phase relations between continuum seeded NOPA pulses are measured [Baum03, Baum05]. Both are clearly below one optical cycle. The jitter is determined to below 1 fs and the phase fluctuation to 250 mrad. This means that due to the high quality of the side view one main origin of continuum phase fluctuations is found and these are minimized by the proper combination of pump energy and crystal length. There is also an influence of the CEP of the input pulse on filamentation [Berge11, Riedel13, Gong13]. However, all used laser sources have no stable CEP and up to hundred optical cycles. Therefore, this issue will not be further investigated in this work.

3.5 Influence of the pump pulse duration and the chirp on bulk continuum generation

Also a very critical parameter for bulk filamentation and continuum generation is the pump pulse duration. Ti:sapphire laser systems typically have pulse durations below 200 fs, which is well suited for bulk continuum generation. Upcoming Yb amplifiers have pulse durations of several hundreds of femtoseconds up to picoseconds. With such long pulses, the generation of new colors is challenging due to parasitic effects such as avalanche ionization, the evolution of an electron plasma, optical breakdown, or the appearance of turbulent regimes [Berge10, Sun10, Schulz11]. These processes suppress filamentation, hinder the build up of a clean channel, and lead to permanent damage of the crystal. An influence of the pump pulse duration on filamentation is also observed for gases [Hauri05]. To see the effect on bulk continuum generation, filamentation in solids with different pulse durations is studied [A1, A3, A9, A18]. Therefore, continuum generation with various crystals, pulse durations and laser sources is performed. If a high pump energy is applied, always new colors are generated. As main criterion for proper continuum generation, the pulse-to-pulse fluctuations of the new frequencies are considered. Only if they are in the range of a few % rms, the newly generated light is regarded as suitable continuum generation. Therefore, continuum generation with various laser sources is performed [A1, A9, A18]. It works best in YAG and KGW crystals and is possible over the entire femtosecond regime. The maximum pulse duration where still suitable continuum generation is obtained is 2.6 ps [A9, A18]. All of the advantageous features of bulk continuum generation are maintained when generating the continua with picosecond pulses. This means bulk continuum generation is a suited method to generate new frequencies, even with picosecond pulses.

Beside the sole pulse duration, for the first time, also the influence of the chirp of the pump pulses on the continuum is investigated here. It should be clarified, if there is a difference between the generation with Fourier limited pulses or with chirped pulses of the same duration [A18]. Therefore, pulses with long durations are generated in two different ways. One method is chirping the Ti:sapphire pulses by inserting glass. In the other method, the pulses are spectrally narrowed. This increases the Fourier limit and leads to transform limited pulses with similar pulse durations. Figure 3.11 shows the necessary pump energy for proper continuum generation and the spectrum in the pump region for both cases.

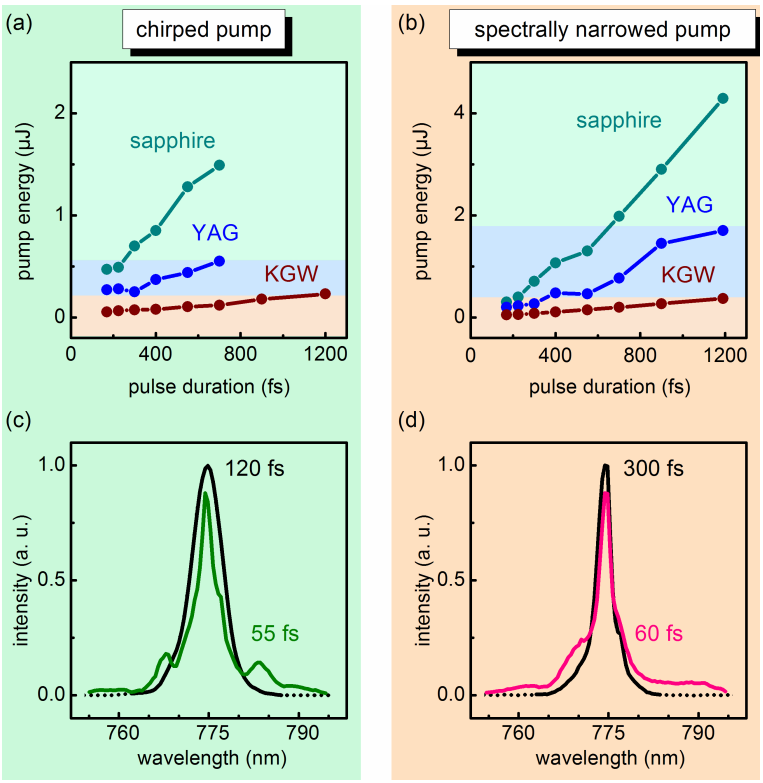

Fig. 3.11: Pump energy for continuum generation in various crystals on dependence of the input pulse duration and spectral chirp ((a) and (b)). (c) and (d) show the spectrum close to the pump region before and after continuum generation in a 4 mm YAG including Fourier limits (for the region from 755 to 795 nm).

For all investigated materials, the needed pump energy linearly grows with the pulse duration. This corresponds to a constant peak power and is in good agreement with the power dependence of the self-focusing threshold. However, the pump energy for spectrally narrowed pulses is always significantly higher than for chirped pulses. In this case, stronger self-phase modulation of the pump has to take place to achieve the same self-steepening effect and shockwave formation as in the case without pump pulse modification. The stronger broadening can be seen from the Fourier limit of the pump region (755 – 795 nm). This is reduced from 300 fs to 60 fs during continuum generation for the spectrally narrowed pump (see Fig. 3.11 (d)). Since the Fourier limit of the entire continuum would always be in the range of a few femtoseconds, no reasonable conclusion could be drawn from this. Therefore, only the part around the pump wavelength is considered. In the case of chirped pump pulses, the Fourier limit of the pump region reduces to a similar value during continuum generation (55 fs). The initial pulse has the same spectral widths as the not modified 150 fs pump pulse. Therefore, the reduction of the Fourier limit is significantly lower (from 120 to 55 fs). This only explains why a higher pump energy is needed for continuum generation. No useful conclusion on the maximum pulse duration can be drawn from Fig. 3.11(a) and 3.11(b).

When regarding the newly generated light, practically no differences are observed. Figure 3.12 shows the spectrum (a) and the corresponding group delay (b) of continuum generation in a 4 mm YAG plate for 150 fs and 400 fs Fourier limited pump pulses and for 400 fs pulses with a Fourier limit of 150 fs.

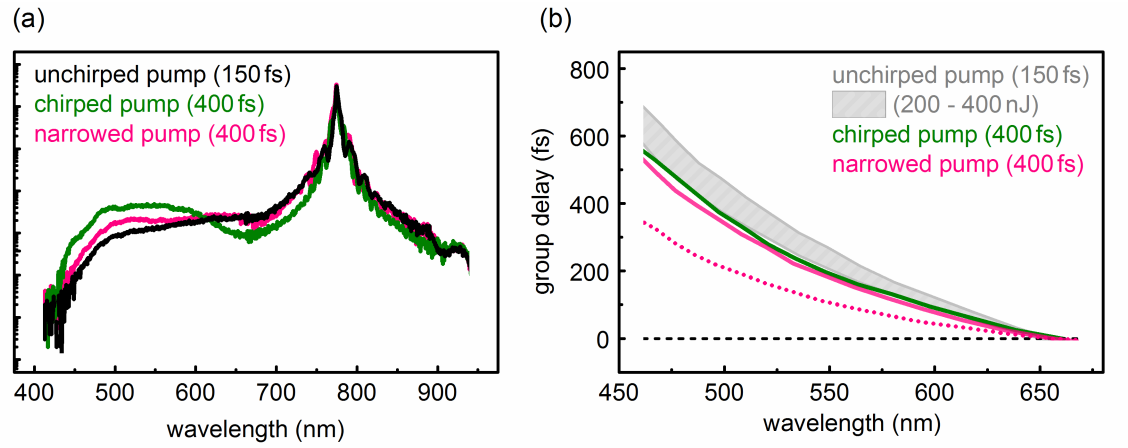

Fig. 3.12: (a) Spectrum and (b) corresponding chirp of continua generated in a 4 mm YAG plate with pump pulses with various pulse durations and chirp

The spectral distribution is very similar independent from the duration and the chirp of the pump pulse. The group delay of the new colors is about 500 fs from 450 to 650 nm. This is in good agreement with previous measurements [Cerullo00, Cerullo99, Ziolek04]. If the input energy of the 150 fs pulses is varied, the filament is generated at a different position in the crystal. For higher pump energies, the filament is generated earlier in the crystal and the remaining propagation in the crystal enhances the continuum chirp. The gray area in Fig. 3.12 shows the group delay of the continuum for pump energies between 200 and 400 nJ (b). The green and pink curves are the continuum spectrum and chirp for spectrally narrowed (pink) and chirped (green) pump pulses They show that there is no influence of the pump pulse duration or chirp on the spectrum and the chirp of the new colors. With the spectrally narrowed pulses, the filament can even be generated close to the end of the crystal. The reduced remaining propagation of the new colors in the crystal leads to a decreased spectral chirp (dotted pink line). The chirp of the continuum therefore depends on the remaining propagation in the crystal after the filament has ended [Cerullo97, Ziolek04].

The important message of this section is that continuum generation is possible even with picosecond pulses, if a proper material such as YAG or KGW is chosen. There are several research groups which use filamentation in YAG crystals to generate broadband continua with long pump pulses due to our recommendation [Schulz11, Dobner12, Harth12, Riedel13] or based on our work [Anitpenkov11, Stanislauskas14]. Especially, high power lasers which pump optical parametric chirped parametric amplifiers (OPCPA's) often have pulse durations in the picosecond regime and can benefit from these findings. When using these pump lasers also to generate the seed, synchronization issues and jitter problems can be drastically reduced. This will lead to table top TW-class OPCPA systems [Stanislauskas14] as predicted [A3, A18].

3.6 Generation of sub-10 fs bulk continua and astigmatism free imaging

The chirp of the new colors mainly originates from the remaining propagation in the crystal. Many applications would benefit from a chirp free continuum. For example, the temporal resolution of a transient spectrometer could be enhanced or these continua could be used as a seed source in a broadband OPA. Therefore, the generation of ultrashort continua is studied. Chapter 3.2 shows that a small part of all new colors is generated in the beginning and that wavelengths close to the fundamental are additionally generated over the entire filament. This leads to a rather complex temporal distribution of the new colors. This and the fact that all colors have a different propagation, make a straight forward compression of the newly generated frequencies hardly possible. If the continuum is used as seed for an optical parametric amplifier, the amplified pulses can be compressed close to the Fourier limit and few-cycle pulses can be generated [Shirakawa99, Kobayashi00, Baltuska02b, Baum06]. However, the most practicable solution would be, if short continuum pulses could be directly produced by bulk continuum generation.

A further challenge when working with multiple colors, beside the chirp, is the chromatic beam propagation. Even when a continuum is imaged with a high quality objective (Canon EF 50mm / 1:1,8 II), which is corrected for all chromatic aberrations, the single colors have different focus positions and beam waist radii. To understand this behavior, see Fig. 3.13.

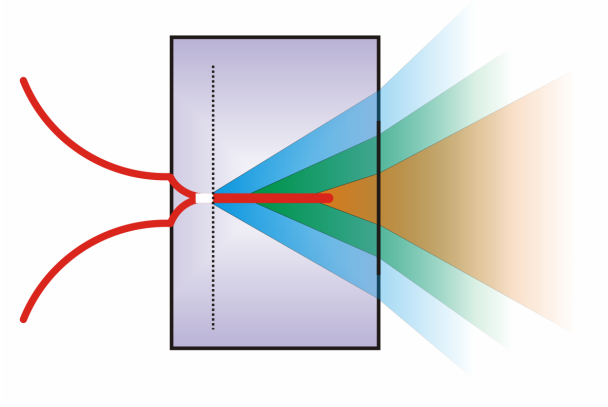

Fig 3.13: Continuum generation in a crystal and beam propagation of the newly generated colors

During and also after filamentation, the pump light shows a self-guided propagation [Dubietis03]. The newly generated colors follow the pump light channel because the pump light temporary modifies the refractive index due to the Kerr effect. The lower the wavelength of the newly generated light is, the higher is the difference of the group velocity compared to that of the pump. Therefore, the light of this wavelength falls behind the channel earlier and also start to diverge earlier.

To demonstrate this, the following experiment is performed. A continuum in ethanol is generated and it is monitored from the side [A20]. To visualize the propagation of single colors, small amounts of Rhodamine 6G (530 nm) or Oxazine 1 (627 nm) are added. These laser dyes partly absorb the newly generated light and fluoresce so that the beam propagation can be recorded from the side [Liu03b, Schroeder04, A18, A20]. Figure 3.14 shows the fluo-

rescence signal of the 530 and 627 nm light and the sideview from filamentation in ethanol enriched with Rhodamine 6G or Oxazine 1.

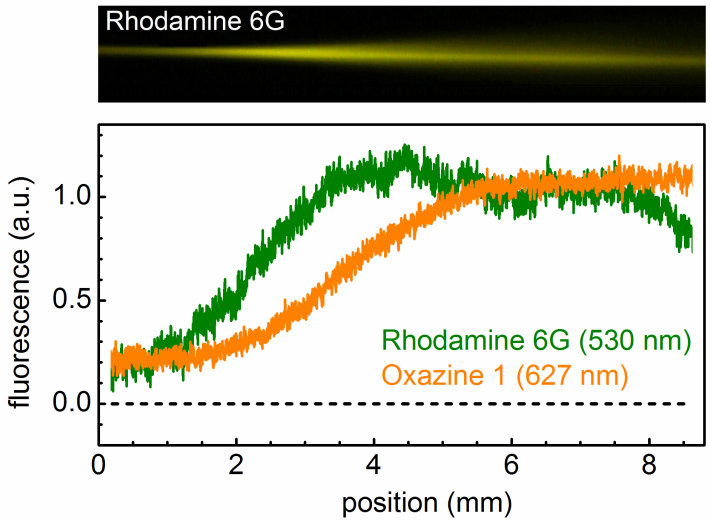

Fig. 3.14: Fluorescence of Rhodamine 6G (green) and Oxazine 1 (orange) to monitor the beam propagation of the 530 and 627 nm part during filamentation in ethanol

Please note that the fluorescence level is not easily transferable to the size of the propagating light. The region before filamentation is not shown. At the beginning of the filament (position 0 mm) multi-photon absorption of the pump and one-photon absorption of the newly generated light are observed. This happens within a channel of a few µm. Therefore, the absorption is saturated and the fluorescence is on a constant – but low – level. At 1.5 mm, the 530 nm light falls behind the pump light and starts to diverge. Due to this divergence, a larger area in which the 530 nm light is absorbed contributes to the fluorescence and the signal rises. However, the absorption is still partially saturated. At 4 mm the absorption is not saturated anymore because the larger area due to divergence is now compensated by the lower absorption per area. Therefore, the fluorescence is on a constant level. The same is true for the 637 nm light. However, this wavelength part follows the pump channel longer and diverges later. This means that different colors start diverging at different positions in the “crystal” and this explains the difficulty of proper imaging. After the filament has ended, the beam diameter increases. Since the wavelengths close to the pump wavelength still follow the pump light, the beam waist radii for these colors are also larger. Ethanol has very similar properties compared to bulk crystals such as the linear and nonlinear refractive index, the material density, the absorption spectrum, or the multi-photon-absorption probability. Therefore, the obtained results in ethanol can be transferred to solids [Brodeur99, Dubietis03, Dubietis06, Couairon07].

To avoid the chromatic propagation and the complex temporal distribution of the new wavelengths, a short crystal length should be used. A small part of all colors is already generated at the beginning of the filament. Therefore, the crystal should end immediately after this point (dashed line in Fig. 3.13) so that no spectral components can fall behind and all colors start to diverge simultaneously. This should lead to a nearly chirp free continuum. In addition, the new wavelengths would have the same spatial properties.

To demonstrate this, a continuum in a 1 mm sapphire is generated. Only reflective optics are used to avoid additional chirp. To minimize astigmatism and coma, a combination of spherical mirrors in a Schiefspiegler geometry is utilized [Kutter53]. This allows focusing all new colors on the same position with similar beam waist radii [A20].

To show that this continuum indeed has nearly no chirp, an autocorrelation [Kozma04] of the newly generated frequencies is performed. Due to the improved imaging with the Schiefspiegler geometry, only a few nanojoules are needed for a proper autocorrelation. Figure 3.15 shows the autocorrelation of a 7.5 fs pulse from the newly generated wavelengths directly obtained from continuum generation in a 1 mm sapphire plate [A20] including the very short Fourier limit of 3.8 fs (green line in Fig. 3.15).

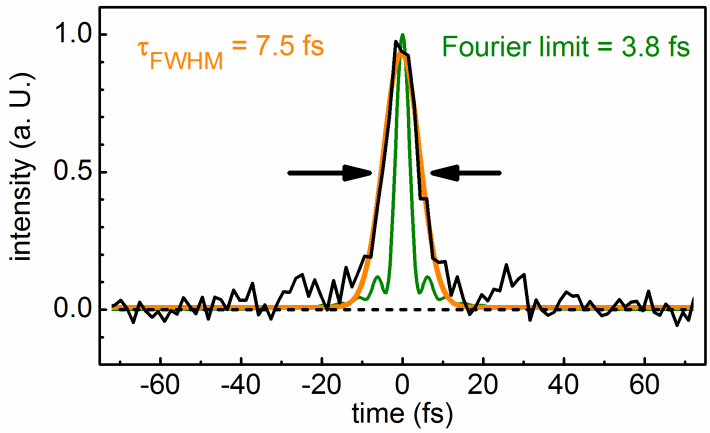

Fig. 3.15: Autocorrelation trace of a 7.5 fs pulse (black) directly obtained from the newly generated colors of a 1 mm sapphire continuum including Fourier limit (3.8 fs, green) and fit (orange)

To get a better insight in the spectro-temporal distribution of the continuum, the chirp of the sapphire continuum is determined with our transient spectrometer [Megerle09]. A 25 fs, 200 nJ pulse at 480 nm is used as pump and a 130 µm thin GG400 filter as sample. Figure 3.16 shows the transient signal of this measurement.

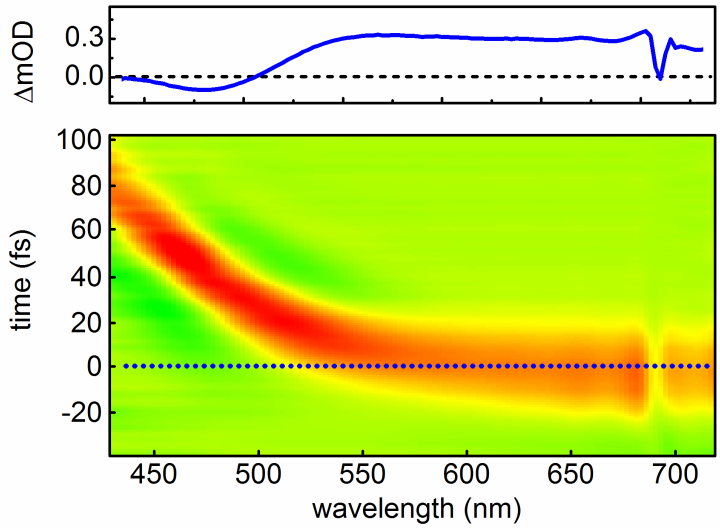

Fig. 3.16: Transient absorption of a 130 µm thin GG400 to determine the chirp of a continuum generated in a 1 mm sapphire plate

The minimum at 680 nm is due to the used continuum filter positioned between the GG400 sample and the detector. This does not transmit enough light at this wavelength for a reasonable signal. The combined two photon absorption of the pump pulse and the probe continuum is present from 500 to 700 nm (see panel above). It allows determining the time zero for every wavelength. Since no transmissive optics is in the probe beam path, this represents the spectral chirp of the continuum at the sample and hence after 50 cm propagation in air. Figure 3.17 shows this group delay for the 1 mm sapphire continuum at the sample and hence after propagation of 0.5 m in air (blue). To determine only the chirp of the continuum, the group delay of the propagation of 0.5 m in air is calculated and then subtracted (green).

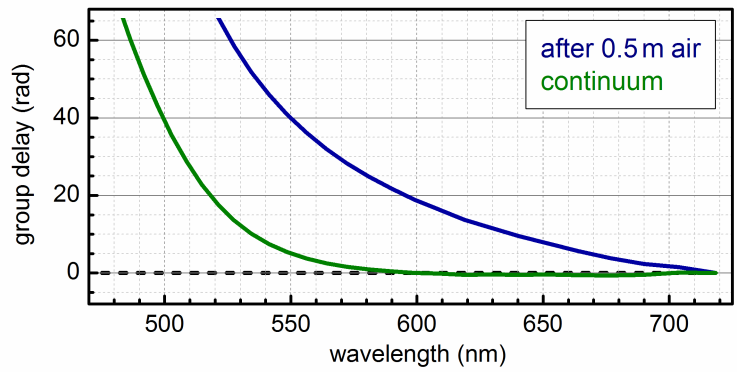

Fig. 3.17: Group delay of 1 mm sapphire continuum at sample (blue, after propagation of 0.5 m in air) and directly behind the continuum generation (green).

This means that the wavelengths from 550 – 750 nm are all generated at once. For shorter wavelength, the beginning fall back behind the fundamental can be observed. For the first time, few-cycle pulses are directly obtained from bulk continuum generation.

No further compression is needed and the setup is extremely simple. The group delay for the short wavelengths originate from the propagation in air and by the beginning fall back of the blue frequencies in the short filament channel. An even shorter crystal would lead to less generated whitelight and to strong pulse-to-pulse fluctuations of the new components. With the proper imaging, also any chromatic aberrations can be avoided. Such pulses are highly interesting for broadband amplification, ultrafast 2D spectroscopy, or pulse compression. If the complexity of the generation of such short pulses by others [Shikarawa98b, Cerullo98, Cerullo99, Kobayashi00, Baltuska02b, Baum06] is regarded, this is an extremely convenient method for producing sub-10 fs pulses. Once the optimum conditions are found, the setup is very robust and nearly no adjustment is needed. Even in the rare case of damage on the surface or inside the crystal is not critical, since the active area of the crystal is just a few square micrometer and the dimensions of such a crystal typically is some square millimeter.

3.7 Influence of the repetition rate and further pulse parameters on bulk continuum generation

There are further light parameters which effect continuum generation such as the wavefront, the polarization, the phase of the pump pulses, or the influence of induced birefringence [Marceau10]. Since in most experiments, these parameters are standard or not stable, their influence is not studied here.

The repetition rate of the laser should be mentioned at last. For filamentation, the peak intensity is important. It depends on the pulse energy and not on the average power or the repetition rate of the laser. Therefore, this parameter should not influence the continuum generation. In addition according to the mechanisms discussed so far, no light is stored in the crystal. This means no light induced damage as observed for BBO crystals by two-photon absorption should occur. The highest repetition rate with which continuum generation is tested, is 80 MHz and a stable long-term operation is observed [A1]. Also continuum generation with an average power of 2.0 W [A15, A21] does not lead to damage of the crystal. The important issue at high repetition rates is thermal lensing. However, after a short warm up time and appropriate tweaking, continuum generation works stable for long times. For special crystals, the recovery time can be longer than the time between two pump pulses. This hinders a stable long term continuum generation. For example, for calcium fluoride, the relaxation time after continuum generation is about 20 ms. If during this time filamentation takes place again, color centers are generated and a stable long term operation of the continuum is not possible. To avoid this problem, the repetition rate of the laser can be lowered which leads to dramatically increased averaging and a demanding handling of the system. Otherwise the crystal can be moved so that for every laser pulse a new area is provided. There are several techniques for an adequate lateral change of the crystal position. It should be noted that rotation of the calcium fluoride plate leads to depolarization [Buchvarov07, Johnson09]. Therefore, translating the plate is preferred [Megerle09].

This part of the work has given new insights in the generation mechanism for continuum generation in solids. For the first time, it has been shown that a small part of all new colors is generated at the beginning of the filamentation process. Then, during the remaining filamentation process only colors close to the pump wavelength are increased. This means, whereas the bluer part of the continuum is only generated at the beginning, the redder part (of the short wavelength side) is generated during the entire process. This complex temporal distribution of the new colors complicates a straight forward compression. The new frequencies follow the pump light in the filamentation channel. Due to the lower group velocity, the new colors fall behind and start to diverge. This also explains the seemingly different generation location and the wavelength dependent beam propagation. By the proper choice of focusing geometry, material thickness, and pump parameters, sub-10-fs continua without any chromatic aberrations can be generated. The use of a Schiefspiegler geometry even allows astigmatism and coma free imaging of all colors to the same focus size and position.

4. Bulk continuum generation as seed for broadband optical parametric amplifiers

4.1 Visible noncollinear optical parametric amplification with Ti:sapphire pump sources

The generation of a broadband femtosecond light source such as bulk continua enables many interesting investigations. However, for most experiments, more light as the few nJ provided by bulk continuum generation is needed. Optical parametric amplification is a very powerful method to enhance the energy of weak seed light. All aspects of this process are comprehensively reviewed in [Riedle00, Cerullo03, Homann12a]. Bulk continua are well suited as seed for optical parametric amplifiers (OPAs). Although the seed continua are only in the visible, it will be shown that this is no limitation to access the various wavelength regimes. In addition, concepts will be presented that allow the operation at highest repetition rates with reasonable pulse energies and broadband spectra. To explain the basic layout and the needed ingredients, a visible noncollinear OPA (NOPA) pumped by a Ti:sapphire laser is shown in Fig. 4.1. All presented amplifiers in this chapter are based on this layout. By modifying the seed, the pump, and the pump-seed angle, other wavelength regimes will be accessible.

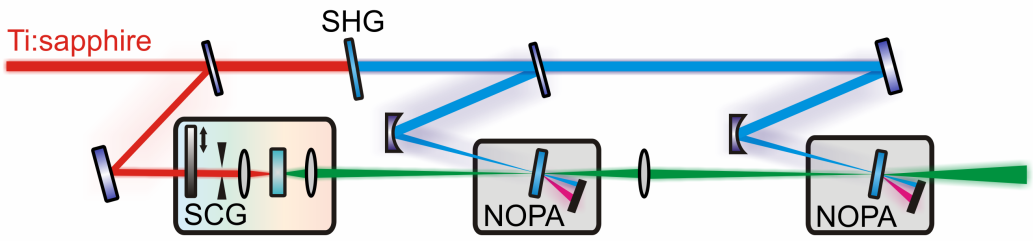

Fig. 4.1: Layout of a two-stage visible NOPA. A small portion of the Ti:sapphire pump laser is used to generate a bulk continuum. The main part is frequency doubled and then used to amplify the continuum seed in two subsequent noncollinear amplifier stages.

To operate a visible NOPA, an adequate seed is needed. This can be the output of a fiber, of an oscillator, of an optical parametric generator, or bulk continuum generation. The latter is perfectly suited for this purpose. It covers the full visible region, has an excellent beam profile, low pulse-to-pulse fluctuations, and only a modest pump energy is needed. Using a bulk continuum as seed has already been proposed in the 90's [Reed94, Reed95a, Reed95b, Greenfield95]. Beside the seed, a short wavelength pump is necessary. Often, the light from second harmonic generation (SHG) of the Ti:sapphire is applied. Using the light from third harmonic generation (THG) as pump can lead to two-photon absorption and limits this approach [Tzankov02, Tanigawa11, A15]. When a suitable seed and pump source is found, the amplifier material has to be determined. Negative uniaxial crystals such as β-barium-borate (BBO) have turned out to fit best. Especially BBO has a high damage threshold, a wide transparency range, a high nonlinear coefficient, and enables a broad phase-matching.

To obtain optical parametric amplification, energy and momentum conservation must be fulfilled beside the temporal and spatial overlap of seed and pump [Riedle00, Kobayashi00, Cerullo03]. However, this phase-matching is often only possible for a small spectral range. Equation 9 shows the achievable spectral $\Delta\nu$ width for a collinear OPA [Cerullo03].

$$\Delta\nu = \frac{2\sqrt{\ln 2}}{\pi}\left(\frac{\Gamma}{L}\right)^{1/2} \times \frac{1}{\left|\frac{1}{\nu_{gs}} - \frac{1}{\nu_{gi}}\right|} \tag{9}$$

L is the crystal length, Γ the gain coefficient (defined in Eq. (10)), υ_{gs} and υ_{gi} the group velocity of signal and idler. This means that the spectral width depends on the group velocity mismatch between signal and idler. For visible signal and infrared idler pulses, this term will not vanish and limits the spectral width in a collinear geometry. By introducing an angle between seed and pump, a further degree of freedom is added so that the group velocity mismatch can be minimized for a broad spectral range [Riedle00, Cerullo03]. To appreciate the difference between both configurations, Fig. 4.2 shows spectra obtained from a collinear (black) and a noncollinear (blue to red) optical parametric amplifier (NOPA) with a 2 mm type I BBO crystal (cut at 32.5°) as amplifier material.

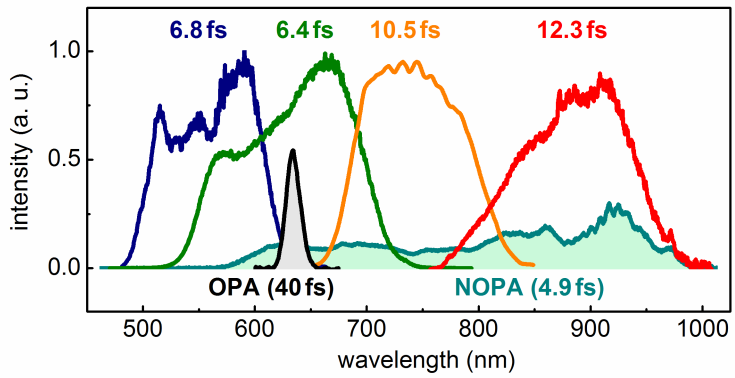

Fig. 4.2: Collinear (black) and noncollinear (blue to red) OPA pulses and Fourier limits.

Pulses with Fourier limits of a few femtoseconds are obtained. The noncollinear geometry was first proposed by Gale et al. [Driscoll94, Gale 95, Gale98]. Shortly after this, NOPAs with sub-20-fs pulses were developed [Willhelm97, Cerullo97, Wilson97, Shikarawa98a, Shikarawa98b, Cerullo99, Shirakawa99, Cerullo00, Riedle00, Huber01]. Then, even few-cycle pulses with sub-5 fs pulse durations in the visible were obtained [Shirakawa99, Kobayashi00, Baltuska02b, Baum06]. The next step was increasing the pulse energy [Tzankov06, Cirmi12]. Therefore, pumping with long pulses and subsequent compression is used to produce powerful, and ultrashort pulses [Dubietis92, Ross97, Shirakawa99, Brabec00, Witte06, Ishii05, Dubietis06, Adachi08, Herrmann09, Witte12]. In these optical parametric chirped pulse amplifiers (OPCPAs) synchronized Ti:sapphire oscillators are used as seed. When using bulk continua as seed, table top OPCPAs with terawatt peak powers can be built [Stanislauskas14] as predicted [A3]. This approach also avoids an active synchronization [Schwarz12] and increases the contrast of the pulse to the amplified spontaneous emission by several magnitudes [Homann13b, Stanislauskas14].

4.2 Collinear amplification and the ideal pump intensity

Since the success of the NOPA, the approach of a collinear visible amplifier [Reed94, Reed95a, Reed95b, Greenfield95] is not any longer pursued in the scientific literature. However, the collinear approach can be used to determine a proper pump intensity. This is due to the fact that the spectral width in Eq. 9 depends on the parametric gain G and on the pump intensity I_p, as can be seen from Eq. 10 [Cerullo03].

$$G = \frac{1}{4}\exp\left(2 \cdot L \cdot \sqrt{\frac{8\pi^2 \cdot d_{eff}^2 \cdot I_p}{n_p \cdot n_s \cdot n_i \cdot \lambda_s \cdot \lambda_i \cdot \varepsilon_0 \cdot c_0}}\right) \tag{10}$$

n_p, n_s, and n_i are the linear refractive indices for pump, signal, and idler, λ_s and λ_i the signal and idler wavelengths, d_{eff} the nonlinear coefficient, ε_0 the vacuum permittivity, and c_0 the speed of light. This means that the spectral width increases with higher pump intensities. To find an ideal pump intensity, the limit of the spectral broadening effect is determined in a visible collinear OPA. In the noncollinear case, also spectral broadening would occur, but due to the broadband phase-matching the analysis becomes more challenging. As pump, the SHG light at 387 nm with a pulse duration of 140 fs is used. Pump pulse energies of 6 – 60 µJ are applied. The $1/e^2$ radius at the entrance surface of the amplifier crystal is 150 µm. This leads to peak intensities from 100 to 900 GW/cm^2. The calculation of the peak intensity is far from trivial and explained in Appendix A0. As amplifier material a 2 mm thick type I BBO crystal (cut at 32.5°) is used. Figure 4.3 shows the spectra (a) and the corresponding autocorrelations (b) of the OPA pulses for different pump intensities.

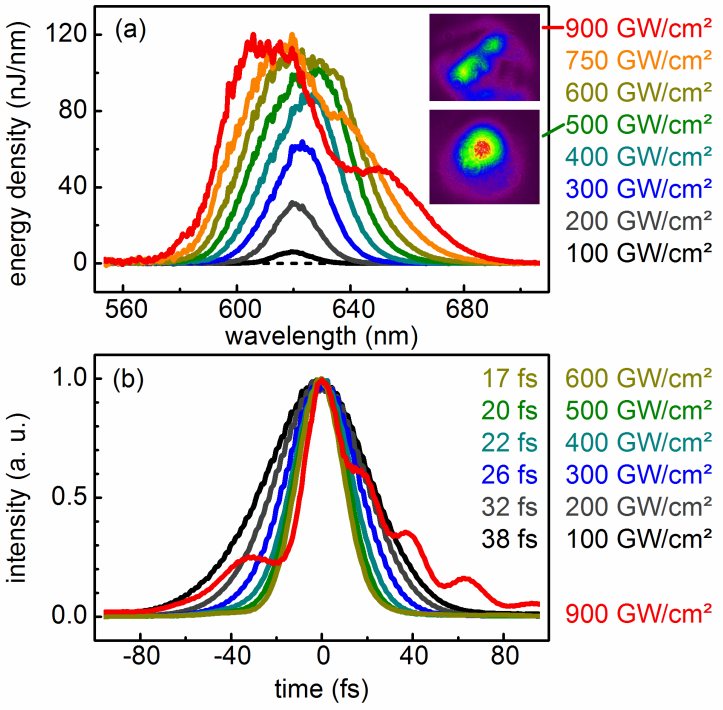

Fig. 4.3: Spectra (a) and autocorrelations (b) of visible pulses from a collinear OPA for an increasing pump intensity.

The spectral broadening works fine until a peak intensity of 500 GW/cm^2 is reached. For higher pump intensities, back conversion, two-photon-absorption, self-focusing, self-steepening, self-phase modulation of the pump, and the generation of superfluorescence background [Homan13a] hinder the use of the amplified pulses. This can be seen from the distorted spectrum, autocorrelation signal, and beam profile shown in Fig. 4.3 for a pump intensity of 900 GW/cm^2. The distorted beam profile is also the reason for the not symmetric autocorrelation signal. For comparison, the beam profile for 500 GW/cm^2 pumping is shown, too. For a peak intensity of 600 GW/cm^2, the spectrum and the autocorrelation are still fine, but the beam profile starts to break up and distorts. To emphasize the problem of a too high pump intensity, Fig. 4.4 shows the pulse-to-pulse fluctuations (a) and the Fourier limit and pulse duration after a prism compressor (b).

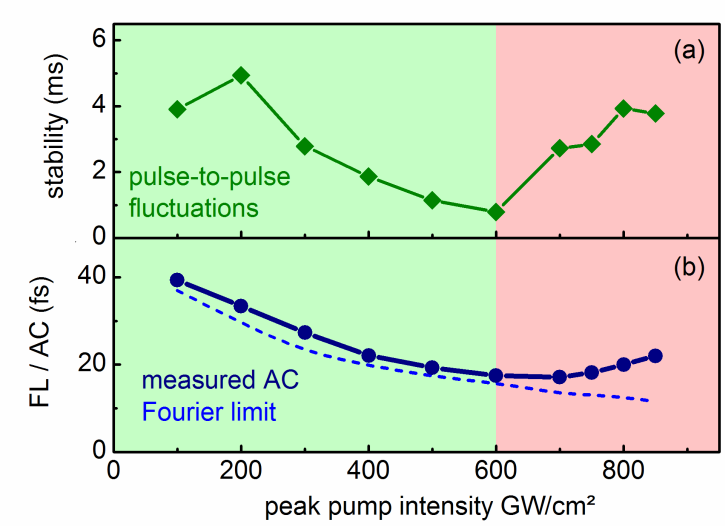

Fig. 4.4: (a) Pulse-to-pulse fluctuations, (b) Fourier limits and compressed pulse durations for various pump intensities.

The green area indicates pump intensities which are suitable for amplification. For intensities above 600 GW/cm^2, the spectrum, the temporal intensity profile including pulse duration, and the stability are not favorable and the parasitic effects dominate the amplification. This means that the peak intensity of the pump pulses of OPAs can be close to 500 GW/cm^2 for an maximum spectral broadening effect and the highest gain without any distortion of the amplified pulses. A good compromise between a stable long term operation and a reasonable spectral broadening and gain is a peak pump intensity of 300 GW/cm^2.

4.3 Visible noncollinear optical parametric amplification with Yb based pump sources

Beside the established Ti:sapphire laser systems, also Yb based systems are suited to operate an OPA. Bulk continuum generation is possible with these systems and renders an octave-wide seed spectrum. Such lasers often operate at repetition rates of several hundred kHz or even a few MHz. For Ti:sapphire laser systems, the generation of short pulses in the visible at high repetition rate is more challenging due to the reduced pump energy of the available laser sources [Reed94, Reed95a, Reed95b, Piel06, Shen11]. Typically, such systems operate at 100 to 250 kHz and have a pulse energy of only a few µJ. A main advantage of the longer wavelength of the Yb based lasers is that the THG light can be used as pump source [A15, A21]. Using SHG light as pump allows the generation of visible and near-infrared pulses [Steinmann06, Schriever08, Homann08, Emons10, Herrmann10, Harth12, Antipenkov11, Nillon14, Liebel14, A15, A21]. For a THG pumped NOPA, phase-matching down to 400 nm is possible. The 1030 nm pumped seed continuum or other seed sources only range down to about 500 nm [Schriever08, Homann08, Liebel14, A1, A15, A21]. To fill the gap down to below 400 nm, the SHG light of the Yb systems is used to generate a bulk seed continuum. By this approach, for the first time, 20 fs pulses tunable to below 400 nm with average powers of several 100 mW can be produced [A15, A21]. As pump laser, a fiber amplifier (Tangerine fs; Amplitude Systems Inc.) is used delivering 300 fs pulses at 1030 nm and 20 W output with a high beam quality. Figure 4.5 shows pulses from 395 to 650 nm from a THG pumped NOPA at 200 kHz seeded with a fundamental (red) and a SHG (green) pumped continuum.

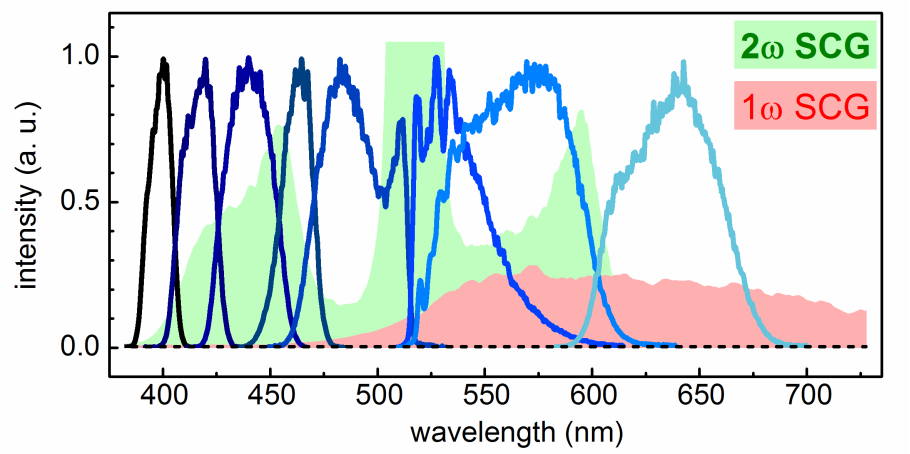

Fig. 4.5: Tunable pulses from 400 to 650 nm from a 343 nm pumped NOPA at 200 kHz seeded by a 1ω pumped (red area) and 2ω pumped (green area) seed continuum in a 4 mm YAG plate.

The energy of the NOPA pulses is in the µJ regime. This leads to average powers of 200 mW at 200 kHz [A15, A21]. Taking into account that the pump energy is approximately 3.5 µJ at 343 nm and the NOPA pulse energy 1.2 µJ at 425 nm, quantum efficiencies of up to 42 % are reached. This is the highest documented value for visible NOPAs. At 1 MHz repetition rate, average powers of up to 700 mW are obtained. Fourier limits down to 10 fs and pulse durations of below 20 fs are achieved. When combining this tuning range with that

of a SHG pumped NOPA (650 – 950 nm), pulses from 400 to 950 nm without a gap can be generated. For the first time, more than an octave is covered without further nonlinear processes [A15, A21].

A main challenge when operating with UV pump light at high repetition rates is the two-photon absorption of the pump in the amplifier crystal. For example, an amplifier crystal in a NOPA pumped by the third harmonic of a Ti:sapphire laser already absorbs 50% of the pump light, even at a low peak intensity of 10 GW/cm^2 [A15, A21]. This may work at low repetition rates. At high repetition rates, however, the thermal load will permanently damage the crystal. On the other side, when pumping with the 343 nm THG light of Yb based laser systems, the two-photon-absorption is reduced to 15% for 100 GW/cm^2 peak intensity. This renders the THG light as ideal pump source for short-wavelength amplification with reasonable two-photon absorption.

Another advantage of the use of the Yb based laser systems is the long pump pulse duration. Since the chirp of continua generated with such long pulses is comparable to that of continua produced with short pulses, the long pump pulses can be used to amplify the entire visible range. Usually this is achieved by chirping the pump pulses [Baltuska02b, Baum06]. A visible picosecond NOPA on the other side, inherently delivers broadband amplification without any modifications. Figure 4.6 shows the spectrum of a visible NOPA pumped with the THG light of a 1.0 ps laser system.

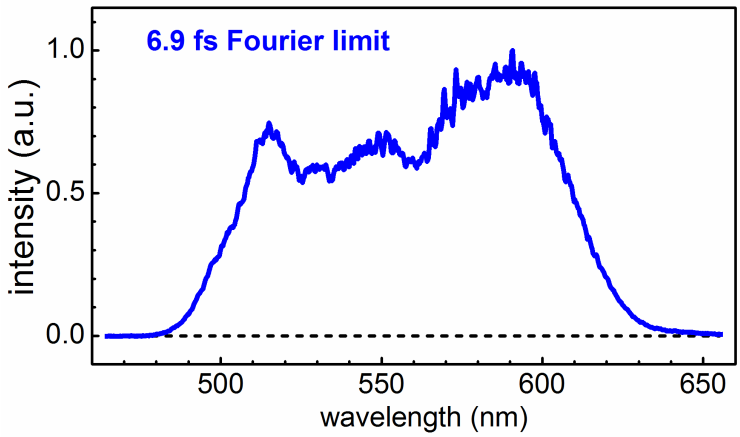

Fig. 4.6: Spectrum of a visible pulse from a THG pumped picosecond NOPA at 300 kHz with an average output of 300 mW and a few-cycle Fourier limit of 6.9 fs.

The pulses are compressed down to 25 fs with a pair of fused silica prisms. This corresponds to a 40 time reduction of the input pulse duration of 1.0 ps and favors such pulses, for example, to be frequency doubled and used for single-electron generation by two-photon photoemission experiments. The advantage of picosecond pump lasers is that such lasers combine a high pulse energy and repetition rate. The used laser source delivers 1 mJ pulses at a repetition rate of 300 kHz. This corresponds to a total output power of 300 W. Only 20 µJ are used for the NOPA. With suited compression techniques, these pulses can be brought close to the few fs Fourier limit [Liebel14, Nillon14]. This correspond to a 140 times reduction of the input pulse duration and shows that a long pulse duration is no limitation for the generation of few-cycle pulses due to bulk continuum generation.

4.4 Extension to the UV via nonlinear mixing

In many spectroscopic experiments, the investigated samples have absorption bands in the UV. To study these materials, tunable pulses in this spectral region are needed. Visible amplifiers reach down to 450 nm for Ti:sapphire pumping [Riedle00, Cerullo03]. To access wavelengths in the UV with NOPA pulses, additional nonlinear processes such as the generation of harmonics or sum frequency mixing [Wilson97, Ziegler98, Cerullo03, Kozma03, Beutler09] or even a combination of both is necessary to reach shortest wavelength below 200 nm [Petrov98, Homann12b]. One of the main challenges of this concept is the low bandwidth and energy of these pulses due to the nonlinear processes. To overcome the low bandwidth, achromatic phase-matching can be used to transfer an immense bandwidth to the UV [Kanai03, Nabekawa03, Baum04a, Baum04b, Zhao09, A14, A22]. Pulse durations of sub-10 fs can be achieved with this approach. To generate highly energetic pulses, powerful visible pulses must be provided to counteract the limited efficiency of the nonlinear processes [Kanai03, Beutler09].

A further challenge is the characterization of the duration of the UV pulses. Since the usually used nonlinear processes such as frequency doubling or sum frequency mixing can not be applied for the UV pulses, alternatives have to be found. Two photon absorption [Nishioka93, Kleimeier10, Homann11, Heisel13], spontaneous parametric down conversion [Michelberger13], surface SHG [Kintzer87, Plass92], and Kerr gating [Kane94, Michelmann96] can be used to measure the pulse duration. Prism and grating compressors [Durfee99, Baum04] or the use of self-phase modulation and self-steepening [Krebs13] are well-suited methods to bring the UV pulses close to their Fourier limit. Acousto optical modulators even allow shaping UV pulses and the generation of complex pulse trains [Krebs10].

Due to the wide tuning range of the visible NOPA pumped by the SHG and THG light of the Yb based laser from to 400 to 950 nm, tunable UV pulses down to 215 nm can be generated via SHG. This permits a unprecedented gap free tuning range from 215 to 950 nm at MHz repetition rates with only one additional SHG stage. Figure 4.7 shows 215 nm UV pulses generated by frequency doubling of a 430 nm NOPA output in a 30 µm thick BBO cut at 70° [A15, A21]. Such pulses still have an energy of a few tens of nJ and are therefore well suited for sensitive experiments due to the high repetition rate.

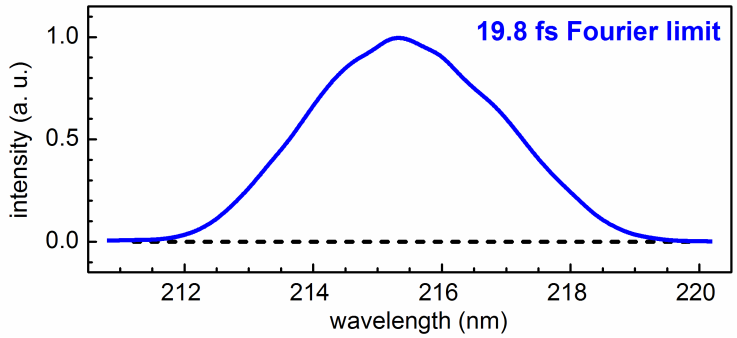

Fig. 4.7: 215 nm SHG of a visible NOPA pulse at 1 MHz repetition rate.

4.5 Broadband optical parametric amplification in the infrared

Besides the visible and the UV region, also infrared pulses can be used to unravel the inner life of molecules. Time resolved vibrational spectroscopy, carrier dynamics in monolayer graphene, high harmonic generation, and tunneling ionization are interesting research fields that benefit from investigations with infrared pulses. To generate such pulses, various methods have to be used. Up to 1.6 µm, the direct amplification of infrared seed light is well suited [Riedle00, Cerullo03, Ghotbi09, Isaienko10]. In this spectral range, the phase-matching in BBO or bismuth triborate (BiB_3O_6) even enables the generation of extreme broad pulses with few-cycle pulse durations [Vozzi06, Cirmi07, Nikolov07, Brida08, Gaydardzhiev08, Isaienko08, Brida10, Li11, Isaienko13]. Figure 4.8 shows broadband pulses from an infrared OPA with a 2 mm type I BBO crystal (cut at 20°) and a 3 mm type I BiB_3O_6 crystal (cut at 11°) as amplifier crystal. Pulses with spectral widths of 400 to 500 nm are obtained. This would allow pulse durations in the two cycle regime.

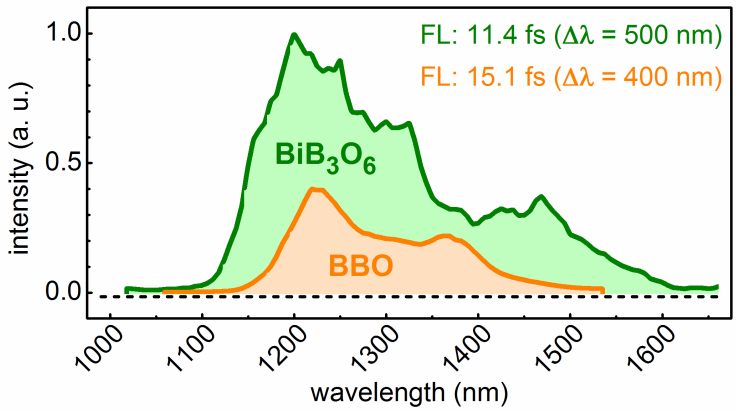

Fig. 4.8: Broadband near-infrared amplification in BBO (cut at 20°) and BiB_3O_6 (cut at 36°) including Fourier limit.

Furthermore, a visible OPA seeded by light near 450 nm and pumped by the SHG of a Ti:sapphire system, the idler is located in the infrared near 3 µm. However, this approach only allows narrowband phase-matching. For the generation of broadband infrared pulses, the generation of an adequate seed is essential, but challenging. Bulk continua show an exponential drop off on the long wavelength side and are therefore not suited as mid-infrared seed source. One approach to overcome this limitation is quasi cw-seeding with an additional laser [Petrov95, Petrov97, Rotermund99, Homann13b]. However, the achievable spectral widths are then limited by the pump pulse duration. This is also the case if superfluorescence is used as tunable seed. Fibers could render a suitable seed but their experimental handling is very challenging. However, when using OPAs for spectral regions with wavelengths longer than that of the laser source, the laser itself can be used as pump. When near-infrared seed light is amplified with the fundamental of the laser system, the related idler is located in the midinfrared. The phase-matching for this wavelength configuration supports broadband amplification even in a collinear geometry for the proper amplifier material. Figure 4.9 shows calculated Fourier limits for midinfrared amplification for two pump wavelengths

with a peak pump intensity of 100 GW/cm^2 in various materials of 1.5 mm thickness. The Fourier limits are derived from the spectral widths according to Eq. 9.

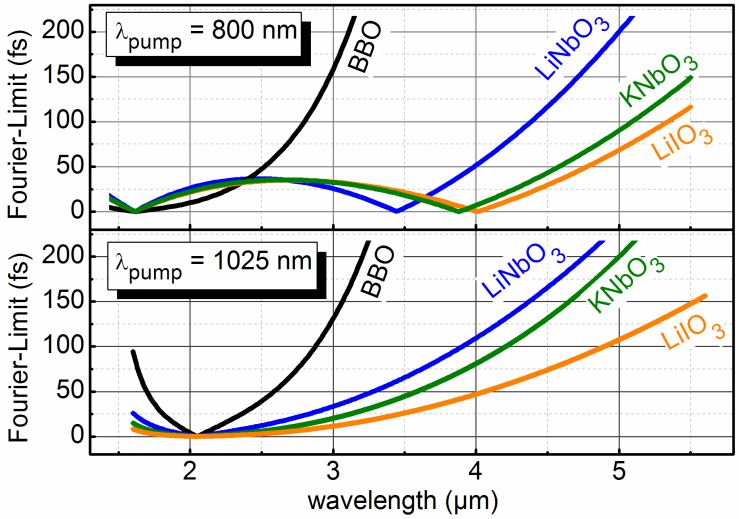

Fig. 4.9: Calculated Fourier limits for infrared amplification in a 1.5 mm thick BBO, lithium niobate ($LiNbO_3$), potassium niobate ($KNbO_3$), and lithium iodate ($LiIO_3$).

Infrared OPAs with proper amplifier crystals enable the generation of broadband and widely tunable pulses up to 5 µm with high average powers and without additional difference frequency generation [Petrov96, Gale97, Cussat00, Fecko04, Ghotbi06, Brida07, Petrov07, Vozzi07, Cerullo11, A2, A4]. However, the efficiency for amplification of long wavelengths close to the absorption bands of the crystal (for example for 5 µm in $LiNbO_3$) decreases dramatically due to the following reasons [A4]:

- The absorption of the idler suppresses the amplification. Pump, signal, and idler have to be present to achieve a significant amplification. For example, $LiNbO_3$ has an absorption coefficient of 3 cm^{-1} at 5 µm [Jiangou92]. This means that 45% of the idler is already absorbed in a 2 mm $LiNbO_3$ crystal.
- When approaching the absorption bandwidth, the refractive index increases. This leads to a large group velocity mismatch between signal, idler, and pump and according to Eq. 9 to a strong reduction of the spectral bandwidth . The fast temporal separation of the pulses only allows a short part of the crystal to be used for amplification. For example, for amplification of 5 µm in $LiNbO_3$ with 775 nm pump light, the signal (920 nm) and idler are completely separated after 0.5 mm when assuming a pump pulse duration of 150 fs.
- A long idler wavelength decreases the parametric gain G (see Eq. 10). For example, the gain coefficient for amplification of 2.5 µm light is 25% higher than for amplification of 5 µm (for 775 nm pumping) [A4]. And since the gain coefficient enters exponential in the amplification [Cerullo03], this significantly reduces the output energy.

To compensate these limiting issues, often high pump energies are used. However, this is not possible for high repetition rate laser systems which typically have a limited output en-

ergy. There are selected laser systems which can provide such high pump energies at multi 100 kHz and then infrared pulse generation with high average powers is possible [Erny09a, Erny09b, Chalus09, Chalus10], but these systems are rare and very expensive.

However, high repetition rates are demanded for ambitious experiments. Up to now, the use of optical parametric oscillators [Emmerichs94, Lohner94, Holtom95, Reed95a] or periodically poled lithium niobate [Manzoni09, Heese10] allows the generation of tunable mid-infrared pulses at high repetition rates, but with limited bandwidths and hence long pulse durations. Also OPAs can be used to generate tunable infrared pulses at highest repetition rates. To achieve an efficient generation of such pulses with sufficient bandwidth for short pulse durations, the near infrared seed has to be pre-amplified. This pre-amplifier is pumped by SHG light since only near-infrared light must be provided for the main-amplifier. Figure 4.10 shows the concept of this hybrid pumping scheme which has previously only been implemented for low repetition rates [Gale97, Petrov01, Brida07, Muecke09a, Pilles14].

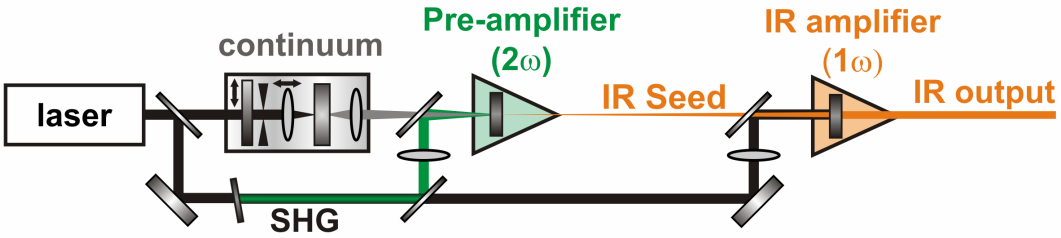

Fig 4.10: Concept of hybrid pumping. A SHG pumped pre-amplifier delivers a strong near-infrared seed for the main amplifier. The desired infrared output is the idler of the main-amplifier.

The advantage of the pre-amplifier is that no idler absorption occurs, the group-velocity-mismatch is reduced, and that no long wavelength is involved which would limit the amplification. In addition, the gain in the main amplifier can be low because a strong seed is provided. To use all photons from the pre-amplifier as seed in the main amplifier, the bandwidth of the near-infrared seed light has to be matched to the acceptance bandwidth of the main amplifier. This is done by inserting glass and hence adequately chirping the seed continuum in the pre-amplifier. It should be mentioned that continuum generation with 1030 nm, 300 fs pulses has a very weak infrared side. Therefore, the visible part of the continuum is amplified and the idler of the pre-amplifier is used to seed the main amplifier. The needed collinear geometry for the pre-amplifier does not limit the spectral bandwidth of the final midinfrared output.

Therefore, for the first time, widely tunable, ultrashort, infrared pulses are generated from a 100 kHz Ti:sapphire system providing 6 µJ pump pulse energy (RegA 9050; Coherent Inc.) [A2, A4]. These pulses are used to study low-bandgap polymers for photovoltaics [Tautz12]. Combining the visible pulses from the pre-amplifier with the infrared pulses from the main amplifier, a three octave wide tuning range from the 450 nm to 5.5 µm without gap is achieved from one amplifier system. Figure 4.11 shows this extreme wide tuning range.

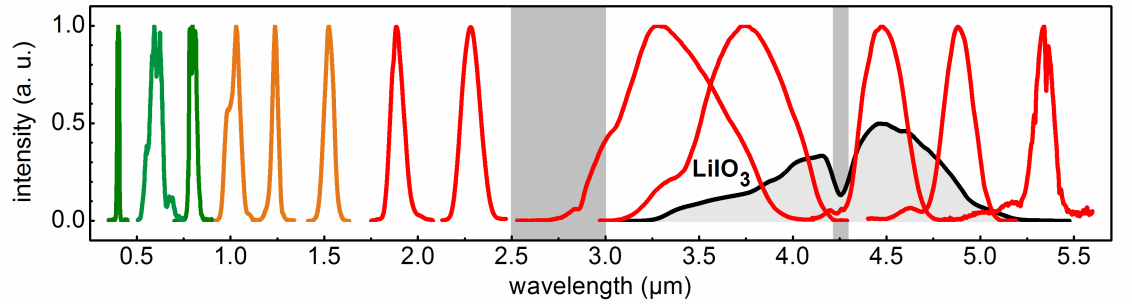

Fig. 4.11: Tuning range of a hybrid OPA pumped by a 100 kHz Ti:sapphire laser system from the visible to the midinfrared. The gray areas indicate the absorption of air. The infrared pulses are generated in a 2 mm type I $LiNbO_3$ (cut at 45°). The black curve shows broadband amplification in a 3 mm type $LiIO_3$ (cut at 20°).

The gray areas indicate the absorption of air. The black curve shows broadband amplification in a 3 mm type $LiIO_3$ (cut at 45°) which would render sub-two-cycle pulses in the infrared. By this hybrid pumping concept, also sub-40 fs pulses at 3.8 µm with an energy of 5 µJ from our 1 kHz laser system are generated. Figure 4.12 shows the spectrum, beam profile, stability, autocorrelation, and Fourier limit of these three cycle pulses.

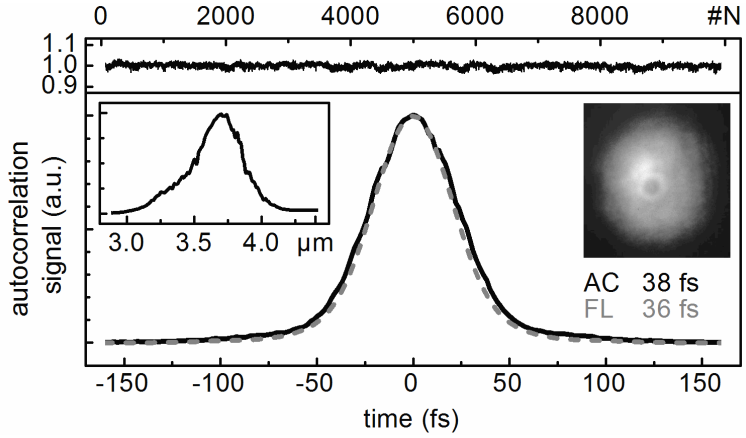

Fig. 4.12: Spectrum, beam profile, stability, autocorrelation, and Fourier limit of a 5 µJ, 38 fs pulse at 3.8 µm obtained from a hybrid OPA pumped by a 1 kHz Ti:sapphire laser system.

The pulse-to-pulse stability is measured with a mercury cadmium telluride diode and determined to 1.25 % rms. At 3.8 µm, the 36 fs correspond to three cycles of the electric field. To obtain such a short pulse duration, a compression is needed. The output of the OPA has the same duration as the pump pulses (~170 fs). In the infrared, the handling of a prism or grating compressor is challenging. Fortunately, the properties of many materials can help to shorten the pulses. Silicium and germanium for example have a negative dispersion between 3 and 5 µm. This means that the pulses can be shortened by adding substrates in the beam path [Demirdoeven02, A13]. A 500 µm thick Germanium plate is placed under the Brewster angle in the beam path to compress the pulses. Due to the high refractive indices of these materials, an antireflection coating or the use of the Brewster angle is necessary or high reflection losses of up to 50% occur.

A main advantage of the presented concept is that it can be applied to various laser sources. Beside the Ti:sapphire based laser system, also a Yb based laser system (Jenlas D2.fs; JENOPTIK Laser GmbH) is used as pump source. The system delivers 300 fs pulses at 1025nm with an energy of 40 µJ at 100 kHz. Output energies between 1 and 2 µJ are achieved for infrared pulses between 1 and 4.5 µm with Fourier limits in the 50 fs regime [A2, A4].

For selected crystals, wavelength combinations of pump, signal, and idler can be found so that the group velocity mismatches nearly vanish. This allows the use of long amplifier crystals of up to 10 mm [Petrov01]. However, long crystal lengths have a negative influence on the spectral widths and additional amplifier stages complicate the setup. An efficient way to enhance the energy from a single stage infrared collinear OPA is the insertion of a second amplifier crystal. Typically, the amplifier crystal is placed slightly behind the focus. For a collinear geometry and a low group velocity mismatch, a second amplifier crystal can just be added in front of the focus of the pump. The collinearity ensures that all pulses have spatial overlap in both crystals and the low group velocity mismatches maintain the temporal overlap. By the use of two crystals, the intensity for both crystals can be optimized separately, whereas for one long crystal only one intensity adjustment can be done. Figure 4.13 shows the improvement of the pulse energy of a single infrared collinear OPA when adding an identical amplifier crystal in front of the focus. As amplifier crystal a 3 mm type I BBO (cut at 20°) is used.

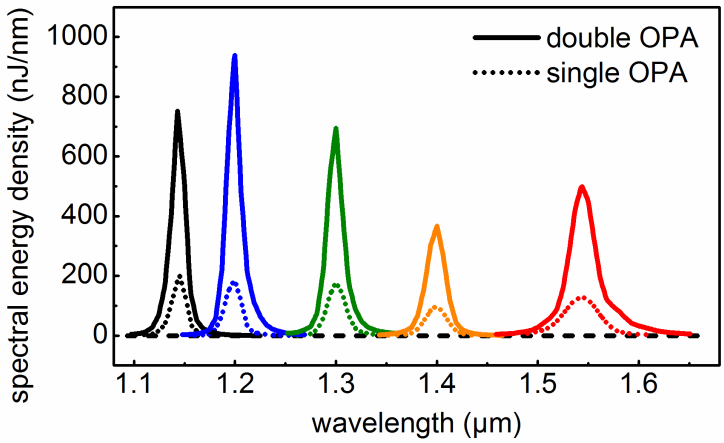

Fig. 4.13: Infrared collinear optical parametric amplifier with one (dotted) and two (solid) amplifier crystals.

The idea behind this concept is the increase of the output energy of an infrared OPA without setting up an additional amplifier stage. Up to a 5 times enhancement in the output energy (from 3.8 to 19 µJ for the 1200 nm pulse with 96 µJ pumping) is achieved by this method. It would also allow the broadening of the infrared pulses [Hong13]. Herby, material is inserted between the two amplifier crystals to compensate the remaining group velocity mismatch.

4.6 Broadband difference frequency mixing in the infrared

Optical parametric amplification is a good method for the generation of tunable and ultrashort pulses in the mid-infrared up to 5 µm. The low conversion limit of OPA is DFG. To generate infrared pulses with DFG, two equally strong pulses with similar central wavelengths are mixed in a nonlinear crystal [Elsaesser91, Hamm93, Lohner94, Seifert94, Golubovic98, Kaindl00, Petrov01]. The photons of the short wavelength pulse are converted into two photons. One has the wavelength of the pulse with the longer wavelength. The wavelength of the second photon is determined by energy conservation and typically located in the infrared. DFG at high repetition rates is extremely demanding, because two pulses with reasonable energies have to be provided. Otherwise, a low output energy result. In our approach the nearinfrared output of the pre-amplifier is on the µJ level. Therefore, efficient DFG with the µJ laser pulses is possible. A 1 mm thick silver thiogallate ($AgGaS_2$) crystal is used to perform DFG between the nearinfrared seed and the laser fundamental. Pulses with central wavelengths of 8 and 10 µm at 100 kHz repetition rate are produced. Due to the modest focusing and the ideal combination of input pulses, two-photon absorption can be avoided and the 8 and 10 µm pulses can be directly generated without further mixing stages. Figure 4.14 shows the spectrum, the energy, and the Fourier limit of infrared pulses obtained by DFG between the 1030 nm laser pulses and the 1140 and 1180 nm pre-amplifier pulses.

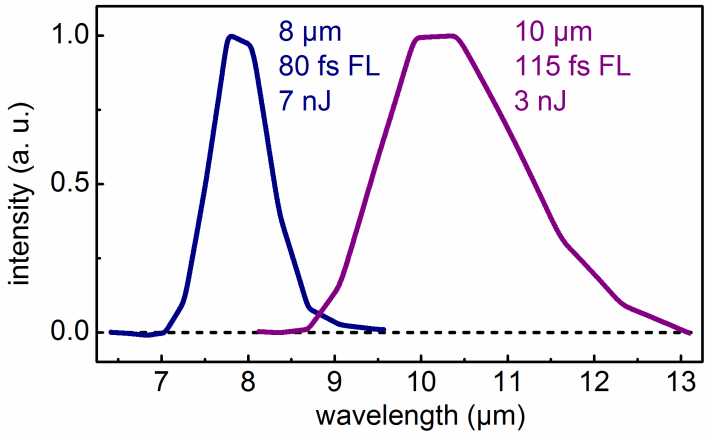

Fig. 4.14: Spectrum, Fourier limit, and pulse energy of the midinfrared DFG output of a 1 mm $AgGaS_2$ crystal.

Beside the generation of midinfrared pulses, also pulses at 2 µm with few-cycle pulse duration are of great interest. Such pulses are needed in strong field science to study high harmonic generation, attosecond physics, tunneling ionization, or electron emission. However, the generation of few cycle infrared pulses is still a challenging task. Broadband laser materials such as Holmium and Thulium for the direct generation of infrared few-cycle pulses are still in their early steps of development [Lagatsky10, Krylov12, Wan13]. A very successful and comely used method is optical parametric amplification [Kaindl00, Cirmi07, Brida08a, Brida08b, Cirmi08, Moses09, Brida10, Hong11, Li11, Silva12b, A2, A4, A5, A10, A11, A13], often with chirped pulses [Fuji06, Kramer07, Erny09a, Erny09b, Gu09, Chalus09, Chalus10, Andriukaitis11, Thai11, Biegert12, Deng12, Pelletier12, Mayer13], comprehen-

sively reviewed in [Cerullo11]. Also hollow core fibers and filamentation are used for spectral broadening and compression down to a few cycles [Manzoni06a, Vozzi06, Vozzi07, Giguere09, Muecke09b, Schmidt10, Schmidt11]. Further approaches are parametric generation [Heese10], difference frequency generation between nearinfrared pulses [Manzoni04], and single mode fibers [Anashkina11, Thomas12]. Most recently, sub-10 fs pulses with a spectral coverage from 2 to 10 µm were achieved from conical emission from a filament created with 800 and 400 nm light [Nomura12]. These concepts work well for low repetition rates and for lasers with high average powers. However, most of the mentioned experiments would benefit from high repetition rates. In addition, often lasers with a limited pulse energy are available. To still obtain few cycle pulses with a reasonable pulse energy under these conditions, a novel approach is proposed. It is based on broadband DFG between a short and visible NOPA pulse and the 1030 nm pump laser [A5, A10, A11]. Figure 4.15 shows the setup for the generation of sub two cycle pulses near 2 µm.

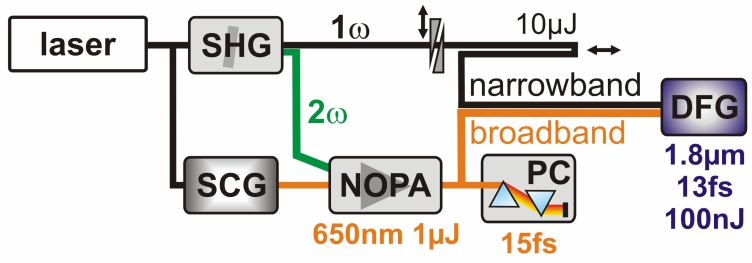

Fig 4.15: Setup for broadband DFG between a 15 fs visible NOPA pulse and the narrowband 1030 nm laser source for few cycle pulse generation near 2 µm.

A small fraction of the nearinfrared laser light is used to generate a visible seed continuum. A SHG pumped NOPA generates pulses at 650 nm which are compressed to a sub-20 fs pulse duration with a pair of fused silica prisms. This corresponds to 5 to 8 cycles of the electric field. These pulses are then difference frequency mixed with the not frequency doubled part of the 1030 nm laser light in a 800 µm thick BBO crystal cut at 20°. Without any further compression 150 nJ, CEP stable, sub-two-cycle pulses near 2 µm are produced at 100 kHz. This corresponds to an average power of 14.5 mW which is sufficient for most experiments. Figure 4.16 shows the spectrum of these pulses (green).

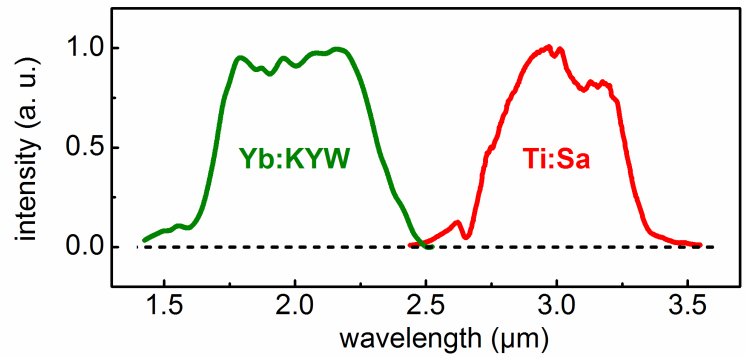

Fig. 4.16: Broadband DFG between a short visible NOPA pulse and the laser fundamental. The concept works well for various pump laser sources such as Ti:sapphire (red) or Yb:KYW (green) based laser systems.

When working with few cycle pulses the phase of the electric field in relation to the envelope – the carrier envelope phase (CEP) – becomes relevant. The maximum strength of the electric field significantly varies for not CEP stable pulses and hence influences the experiment. For pulses with long pulse durations, this effect can be neglected. Few-cycle pulses, on the other side, have to be CEP stable. Here, this condition is fulfilled because the NOPA pulses have the same fluctuations as the 1030 nm pump laser. The DFG signal is then CEP stable [A5, A10, A11].

A great advantage of this technique is that it can also be applied to various pump sources. Figure 4.16 additionally shows the spectrum of a pulse with a few-cycle Fourier limit when applying the concept to a Ti:sapphire based system (red). Again an output energy of above 100 nJ is achieved. Further energy scaling with higher input pulses [Darginavicius12a, Darginavicius12b] or in subsequent broadband infrared OPAs [Manzoni06a] is possible as demonstrated for low repetition rates. The broadband DFG is further used as seed for OPCPA systems [Moses12, Fattahi13] The most impressive key feature of this method is that the infrared pulses already have the few cycle pulse duration directly after the DFG although the input pulses have only sub-20 fs and 300 fs pulse durations. This corresponds to an overall shortening of an factor of 30. To understand, how this is possible with the simple setup, the following issues should be taken into account.

- The continuum generation in the visible provides a broadband seed which would be sufficient for few-cycle pulses in the visible.
- The noncollinear geometry of the visible NOPA supports amplification of this broad bandwidth so that pulses with Fourier limits of sub-10 fs are generated without great effort.
- A pair of prisms is sufficient to compress the NOPA pulses down to a sub-15 fs pulse duration. A compression closer to the Fourier limit is not needed.
- The narrowband laser pulses are then difference frequency mixed with the short visible NOPA pulses. This requires temporal overlap. Therefore, the infrared pulses inherit the pulse duration of the short visible NOPA pulses.
- An optical cycle of the electric field is longer in the infrared than in the visible. Therefore, even multi-cycle pulses in the visible are sufficient to generate two-cycle pulses in the infrared.
- In addition, the infrared pulse inherits the phase of the visible pulse [A11] because the fundamental laser pulse has a flat phase. Due to the dispersion properties of BBO, the infrared pulses are compressed close to the Fourier limit by the remaining propagation in the crystal.

No additional compression is needed and for the first time, few-cycle pulses at 2 µm at 100 kHz repetition rate are generated from only one pump source so that no synchronization is needed. In addition, no active CEP control is necessary since DFG passively stabilizes the CEP. As mentioned in Chapter 3.5, a proper continuum generation is necessary for a stable CEP. A phase stability of sub-100 mrad is therewith achievable [A5].

4.7 Broadband pulse generation from the visible to the infrared with high average output powers

The presented methods allow the generation of tunable pulses from the visible to the infrared with an immense bandwidth for each pulse. All these pulses can be generated with various laser sources and at high repetition rates. Figure 4.17 shows an overview about the OPA pulses supporting few-cycle pulse durations achieved in this work.

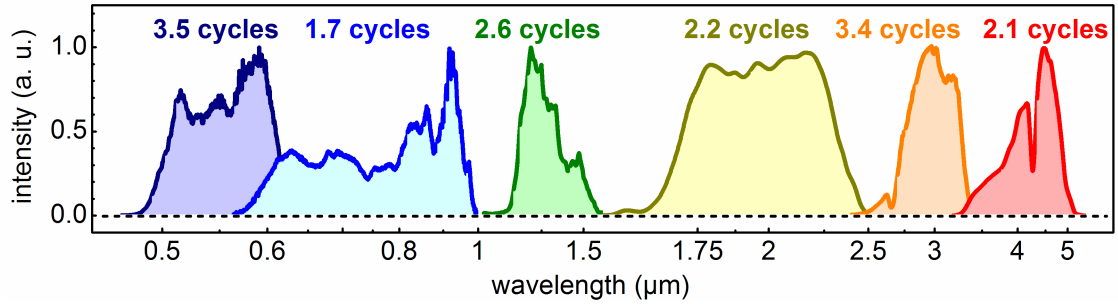

Fig. 4.17: Broadband OPA pulses from the visible to the infrared.

The generation of broadband UV pulses is well documented [Kanai03, Nabekawa03, Baum04a, Baum04b, Zhao09]. For the generation of the infrared pulses, a near-infrared pre-amplifier is used. This allows counteracting the large velocity mismatch, the narrowband phase-matching, the temporal pulse separation, and the low parametric gain in the main amplifier. The infrared pulses could be compressed close to the Fourier limit with the simplest compression technique. The insertion of various materials in the pathway is sufficient to reduce the pulse duration close to the Fourier limit. These pulses are well suited for a daily operation and can be used in highly ambitious experiments [A5, A13, A17].

The optimized conditions and concepts for OPAs found in this thesis allows achieving the highest conversion efficiencies and output powers. Figure 4.18 shows the photon conversion efficiency for the various OPA pulses shown in this thesis. The photon conversion efficiency relates the number of photons generated at the new wavelength to the number of total pump photons. This allows a fair comparison of pulses at different wavelengths and from laser sources with differing pump energies. In Fig. 4.18, only OPA pulses with more than 100 nJ at repetition rates of at least 100 kHz are regarded.

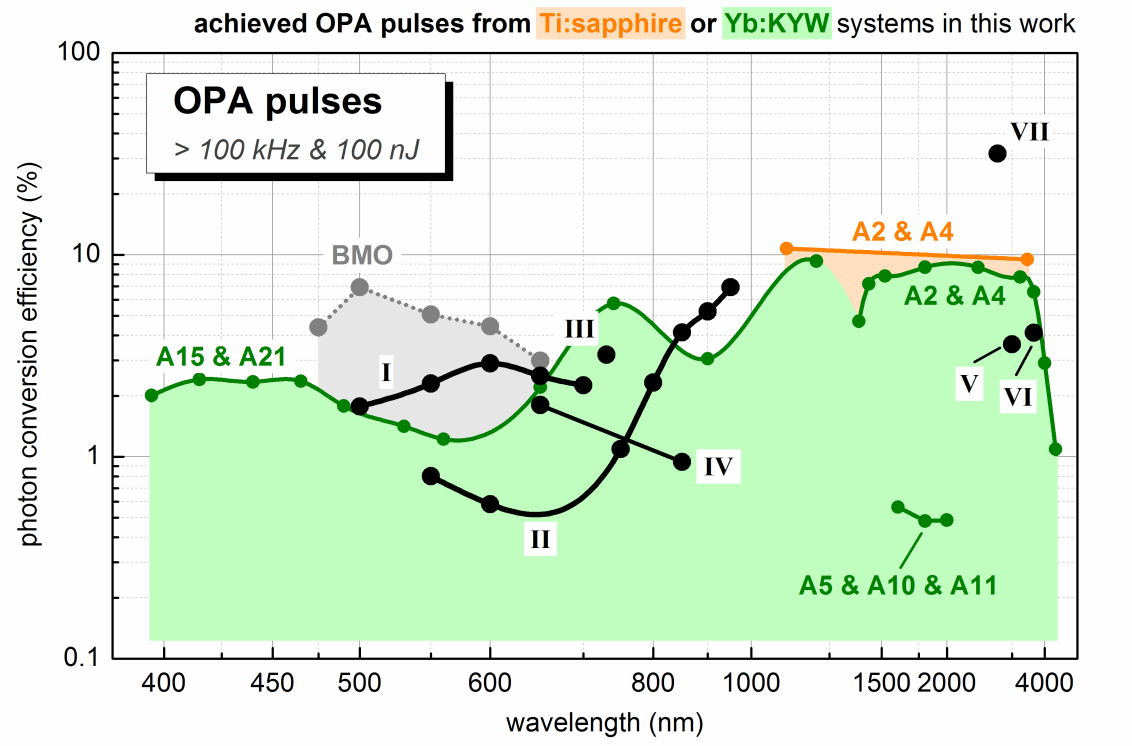

Fig. 4.18: Photon conversion efficiency of OPA pulses from the visible to the infrared with a pulse energy of above 100 nJ at a repetition rate of at least 100 kHz. The efficiencies of pulses achieved in this work are shown in green (Yb based systems) and orange (Ti:sapphire based systems), these of pulses achieved previously at the institute in gray (BMO : [Piel06]). The remaining curves (black) are obtained by others. I : [Reed94, Reed95a, Reed95b], II : [Nillon14], III : [Herrmann09], IV : [Emons10, Harth12], V : [Erny09a, Erny09b, Heese10], VI : [Chalus09, Chalus10, Thai11, Biegert12], VII : [Holtom95].

OPA pulses with high average powers and best photon conversion efficiencies are achieved in this work for a wide spectral range (green and orange, [A2, A4, A5, A10, A11, A15, A21]). Especially in the region between 400 and 480 nm, such pulses are generated exclusively in this work. In the visible range, highest conversion efficiencies of up to 7% have been achieved previously by our group [Piel06]. OPA pulses close to the 1030 nm pump wavelength (850 – 1000 nm for II [Nillon14]) should be considered carefully since the spectrally broadened pump region is often not suitable for most applications due to the structured spectrum and temporal intensity profile. In the infrared region from 1 to 4 µm, very high 10% are obtained in this work due to the use of a visible pre-amplifier. Only optical parametric oscillators with limited wavelength tunability and spectral width can render higher conversion efficiencies (VII, [Holtom95]). If few-cycle-pulses are generated, significantly lower conversion efficiencies are obtained (II, IV, V, VI) [Erny09a, Erny09b, Heese10, Chalus09, Chalus10, Emons10, Thai11, Biegert12, Harth12, Nillon14, A5, A10, A11].

In summary, this chapter has shown that the wide spectral coverage of the OPA pulses in this work originates always from visible continuum generation. Covering only the visible range is no limitation to produce shortest pulses at any wavelength. This underlines the importance of bulk continuum generation as adequate seed source in broadband OPAs.

5. Bulk continua as probe light in ultrafast transient spectrometers

5.1 Spectral coverage from the UV to the infrared and temporal extension up to milliseconds

The goal of many investigations in ultrafast spectroscopy is to reveal the path of a chemical reaction or biological process or to uncover the inner life of a complex molecule. Therefore, molecules are excited and their ultrafast response is monitored. All relevant processes modify characteristically the transmission of the investigated sample. These various signatures are then temporally and spectrally resolved. By this, the inner life of the studied system can be understood. Typical processes which happen on the femtosecond or picosecond time scale are the relaxation to other states, energy or charge transfers, the change of the geometric structure, or the interaction with the environment. To analyze the transmission change with highest temporal resolution and over a wide spectral range, an adequate light source for probing has to be provided. Broadband bulk continua are ideally suited for this purpose due to their favorable properties such as a smooth, gap free spectrum, the high pulse-to-pulse stability, and the excellent beam profile. For excitation, often femtosecond UV pulses are used to bring a molecule in an excited state. After this, many of the mentioned processes show transmission changes in the visible. However, also the UV and the infrared region show signatures which explain the molecular dynamic. Further, signatures of various processes can overlap in the visible so that only infrared or UV spectroscopy will lead to unambiguous results. This means that a wide temporal and spectral coverage is essential for a complete analysis of the studied system. Therefore, our setup for time-resolved absorption spectroscopy with a sub-50 fs resolution [Megerle09] is modified so that 11 magnitudes in time and over 3 octaves in spectrum are covered [A7, A19]. Figure 5.1 shows the upgraded setup.

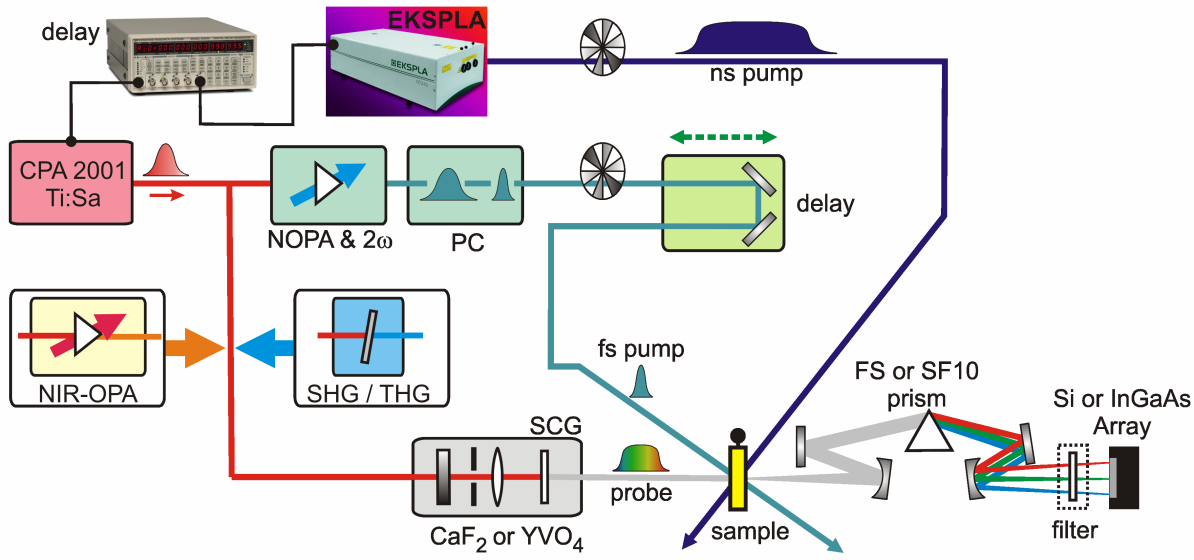

Fig. 5.1: Setup of the broadband transient absorption spectrometer covering 11 magnitudes in time (femto- to milliseconds) and 3 octaves in spectrum (UV, visible, and infrared).

As pump source for time delays between femtoseconds and a few nanoseconds, UV and visible pulses generated in a two stage NOPA with subsequent frequency doubling are used. To obtain a high temporal resolution, a prism compressor is utilized to achieve sub-30 fs pump pulse durations. The delay time is set geometrically by varying the path length of the pump with respect to the fixed path length of the probe.

For time delays from a few nanoseconds up to the millisecond regime, a geometrical delay cannot be applied due to the divergence of the pump pulses. Therefore, a tunable optical parametric oscillator (NT242-SH/SFG; EKSPLA Inc.) delivering nanosecond pulses from the UV to the infrared is synchronized to the Ti:sapphire laser system and used as pump source. This allows setting the time between pump and probe pulses electronically. Thereby, any time interval between a few nanoseconds and a millisecond can be realized. The minimum delay time which can be set electronically is in the order of one nanosecond and overlaps with the geometrically achievable delay times. This allows a gap free tuning from femto- to millisecond delay times. The jitter between both laser systems is below 200 ps and does therefore not affect the nanosecond temporal resolution.

The probe continuum is generated with the 775 nm Ti:sapphire pulses in a moving 5 mm CaF_2 plate. An effective probe range from 285 – 730 nm [Megerle09] is obtained. Near the pump wavelength (730 – 820 nm), the spectrum is strongly structured and the pulse-to-pulse fluctuations are very high [A1]. Therefore, this part is not used as probe light. To extend the spectral region, continua generated with various central wavelengths are used. The second and third harmonic of the laser, as well the signal and idler output of a nearinfrared OPA are used as continuum pump. Figure 5.2 shows the spectrum and the pulse-to-pulse fluctuations of bulk continua generated with various pump wavelengths and used in various broadband transient spectrometers [A6, A7, A8, A12, A19].

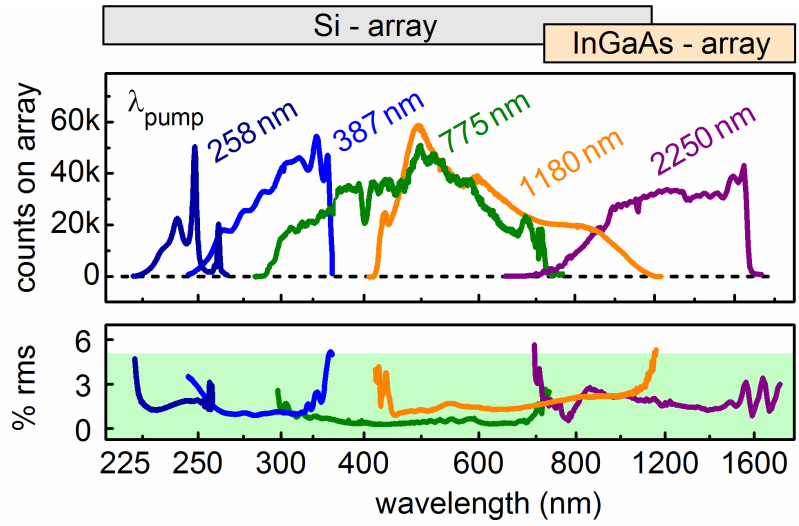

Fig. 5.2: Spectrum and pulse-to-pulse fluctuations of bulk continua generated with various pump wavelengths and used in transient spectroscopy to extend the spectral coverage. The gray and orange areas indicate in which spectral region silicon and InGaAs array are used for detection.

All continua, except the 2250 nm pumped one, are generated in CaF_2 plates. For the 2250 nm pulses, an YVO_4 crystal is used due to the limited output of the infrared OPA. After the probe light has passed the sample, it is dispersed with a prism and then imaged onto a silicium or indium gallium arsenide (InGaAs) array. This allows obtaining the transmission change for the entire probe spectrum at once. To compare the excited and the not excited molecules, a chopper is used which alternatingly blocks the pump pulses. To improve the signal-to-noise ratio, several transient spectra are averaged.

The extensions into the UV and infrared, as well as to long delay times allow investigations with an unprecedented spectral and temporal coverage. For the first time, an ultrafast transient spectrometer is presented which can monitor processes over several magnitudes in spectrum and time with highest resolution. The entire molecular dynamic and ultrafast response of almost any systems after excitation can be monitored [A19]. To demonstrate the potential of the developed ultrafast transient spectrometer, selected experiments will be shown. In these measurements, the newly implemented spectral and temporal extensions are used to understand the complex processes in the studied molecules.

5.2 Infrared time-resolved transient spectroscopy of malachite green

One of the main advantages of the spectral extension towards the infrared is that selected processes can be monitored exclusively. In the visible, transient signals are often a combination of several contributions and the correct interpretation turns into a challenge. In the infrared, wavelength regions can be found where the signals only originate from one state or process. To demonstrate this, a transient measurement of the laser dye malachite green in ethanol is performed. To study its dynamics, the molecule is excited into the S_1 state by pumping with 620 nm [A7]. Figure 5.3 shows the transient signal of this measurement.

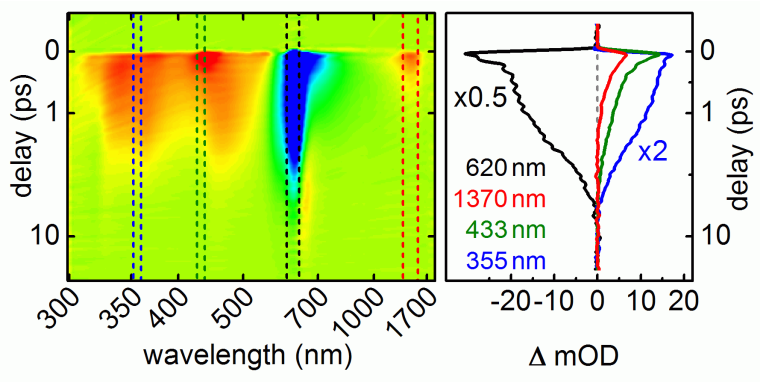

Fig. 5.3: Transient signal of malachite green (in ethanol) after 620 nm excitation.

Early studies of malachite green concentrate on the ground state bleach (GSB) recovery. Complex kinetics with a main time constant of 2.1 ps in methanol and a strong solvent dependence are found [Ippen76, Nagasawa99]. After relaxation to the ground state, the geometrical relaxation and cooling of the hot S_0 are thought to complete the cycle. However, the main problem is that the strong transient signal around the 620 nm pump wavelength is the sum of GSB, stimulated emission (SE) and excited state absorption (ESA). This hinders an unambiguous interpretation of the dynamics of malachite green.

When using the extended probe range up to 1700 nm, the S_1 population can be explicitly probed through the S_1 to S_2 ESA at 1370 nm. A relaxation time of 440 fs is found which nicely matches with previous fluorescence measurements [Gottfried97]. Only the extension of the probe range allows for this clear determination of the S_1 dynamics. At 355 nm, on the other side, no ground state absorption or bleach is present. At this wavelength, the intermediate state S_x that the S_1 state relaxes to with the 440 fs time constant can be exclusively probed. A decay time of 2.0 ps is found. This is, within experimental accuracy, identical to the 1.7 ps component obtained at 433 nm. However, at 433 nm, the relaxation signal is overlapped by the ESA from the S_1 to the S_4. This could lead to false decay times and an ambiguous interpretation. With the decay times extracted from 355 and 1370 nm, the complex dynamic of the 620 nm signal can be determined now. Beside the mentioned 440 fs and 2.2 ps decay time – the latter is a little higher due to cooling processes – a further time constant of 100 fs can be evaluated. In addition, temporal signal oscillations of about 226 cm^{-1} are found that can be attributed to a symmetric carbon–phenyl stretch vibration [Rosker86, Nelson87]. Table 1 shows the obtained time constants for single wavelengths.

Table 1: Decay times in malachite green after S_1 excitation. "--" means that this time constant has no amplitude and "?" means that the time constant can not be determined due to the overlapping signals.

	λ (nm) S_0 to S_n	λ (nm) S_1 to S_n	λ (nm) TA exp	τ_1 (ps)	τ_2 (ps)	τ_3 (ps)
S_1	622			0.1	0.44	2.2
S_2	428	1372	1400	--	0.44	--
S_3	315	638	635	?	?	?
S_4	255	432	433	--	0.33	1.7
ESA			355	--	--	2.0

The found time constants can be interpreted as followed. At first, with a time constant of 100 fs an inertial motion of the optically prepared wavepacket away from the Franck–Condon point towards the equilibrium geometry of the excited electronic state S_1 takes place. Then, with a 440 fs time constant the S_1 relaxes to an intermediate state S_x. From this intermediate state, the molecule relaxes to the ground state with a time constant of 2.2 ps. Only due to the extended probe range, the single steps of the relaxation dynamics of malachite green can be monitored exclusively and an unambiguous interpretation is possible [A7]. After the S_1 excitation, malachite green relaxes to a state S_x that neither fluoresces below 900 nm nor carries any oscillator strength to the known higher electronic states. Instead of this, a nearly 2 eV broad ESA band is found decaying with a time constant very close to the GSB recovery. This fact points to a charge transfer character of the S_x state. Indeed, recent calculations predict such a character even for the S_1 state [Nakayama11]. The initially excited state could have an electronic character more similar to the ground state. This would explain the strong S_0 to S_1 absorption. The often discussed torsion of the phenyl rings [Hirsch78, Ben87, Mokhtari87, Mokhtari90, Nagasawa99, Nagasawa02] starts after the initial 100 fs geometric relaxation and leads to a simultaneous change in the electronic character towards a charge transfer state on the 500 fs time scale. Then, charge recombination takes approximately 2 ps to repopulate the ground state with little optical signature from the reverse torsion of the phenyl rings.

Further applications of the extended infrared probe wavelength are the investigations of ultrafast photo-induced charge transfers [A6], the study of the ultrafast dynamics of meso-tetraphenylmetalloporphyrins and the role of the dark states [A12], or the research on hybrid polythiophene silicium photovoltaics [Herrmann11a, Herrmann11b]. Also experiments on the effect of solvent additives on morphology and excited-state dynamics in PCPDTBT:PCBM photovoltaic blends benefit from an extended infrared probe range [Etzold12]. Only due to the here presented infrared extension, the dynamic and molecular processes and reaction paths can be unraveled in full detail.

5.3 Ultraviolet time-resolved transient spectroscopy of Cyclohexadiene and α,β-enones

Beside the infrared extension, also the spectral expansion to the UV can be essential to determine the molecular dynamic. Especially when pumping with UV pulses, the recovery of the ground state can be monitored to identify the end of the molecular interaction. To demonstrate the potential of the UV probe continua, 1,3-cyclohexadiene in ethanol after excitation at 250 nm is studied. The transient signal is shown in Fig. 5.4.

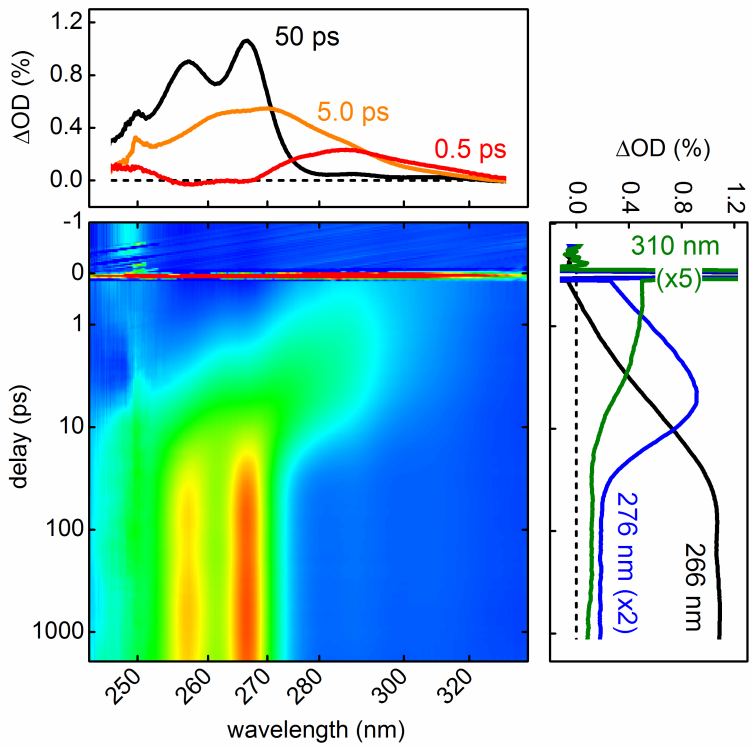

Fig. 5.4: Transient spectra of 1,3-cyclohexadiene in ethanol after excitation at 250 nm.

This system has already been investigated with laborious experiments [Lochbrunner98] in which the pump and probe pulses were produced by a traveling wave OPA seeded by superfluorescence. With the help of the UV probe continuum, a more complete picture is achieved with only one measurement. A repopulation of the ground state, accompanied by ring opening to Z-hexatriene, occurs in less than 300 fs. In addition, the analysis of the long-wavelength wings of the ground-state spectra reveals a cooling time constant of 7 ps for the hot product Z-hexatriene. Furthermore, the single-bond isomerization of this product to different conformers can be deduced from the transient signal. The measurement nicely agrees with the previously obtained results [Lochbrunner98].

The UV extension down to 225 nm can further be used to determine which process is dominating after the excitation of a,ß-enones including the triplet yield [A7, A8]. For this, 2,3,4,5-tetramethyl-2-cyclopentenone (TMCPO) in cyclohexane is excited at 227 nm and the transient absorption is measured (see Fig. 5.5).

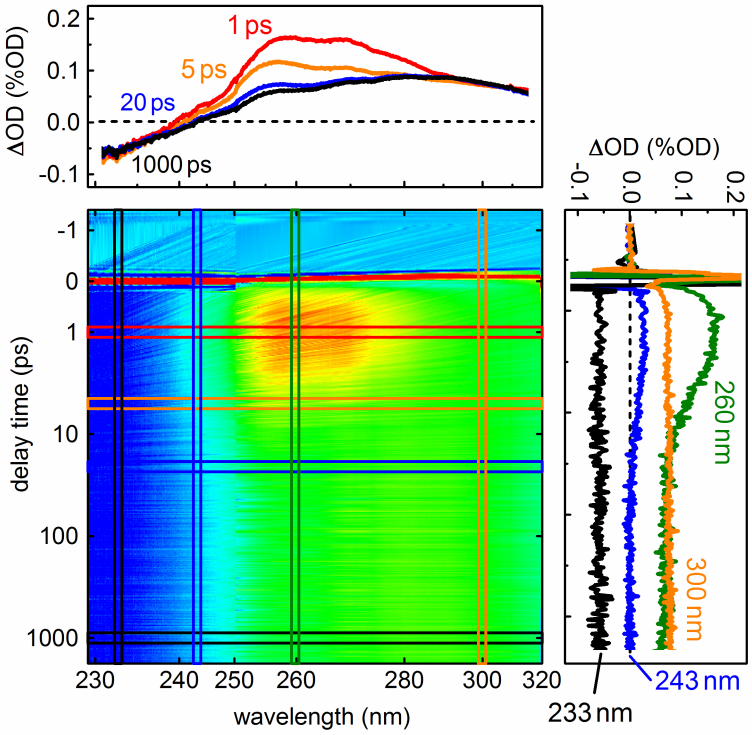

Fig. 5.5: Transient spectra of TMCPO in cyclohexane after excitation at 227 nm down to 230 nm showing that intersystem crossing is the main reaction channel.

In combination with time-resolved photoelectron spectroscopy and ab initio calculations [A8], it can be determined that the main reaction channel after excitation is intersystem crossing and not internal conversion as for acrolein [Lee07]. In addition, it is shown [A7], that the molecule relaxes to the S_1 state (0.25 ps) and subsequently to the triplet manifold (4 ps) after S_2 excitation. With the help of the extended UV probe range, the lack of the GSB recovery is observed. From this, it can be concluded that the triplet yield after S_2 excitation is near unity. Such high triplet yields are already observed for similar systems [Bonneau80].

If the fundamental pumped continuum is used solely, this information can not be obtained. Only with the help of the second and third harmonic pumped continuum and the therewith gained extended spectral probe range, an unambiguous statement on the molecular dynamic of these systems can be given.

5.4 Time-resolved spectroscopy up to the microsecond regime of the sensitizing-based formation of benzhydryl cations

The temporal extension up to the millisecond regime allows monitoring the full dynamics of complex systems. Many molecular reactions do not only consist of ultrafast components on the picosecond time scale, but also show a dynamical behavior on the nano- or even microsecond scale. Typical processes which take place on these time scales are the relaxation to the triplet state or intramolecular charge transfers. We study the sensitizing-based formation of benzhydryl cations. The idea behind this approach is that a bond breaking is induced in a precursor molecule leading to the formation of the benzhydryl cations [Das93, Ammer12, Sailer13a, Sailer13b]. To avoid unwanted concurring reactions when exciting the precursor, it is possible excite an additional sensitizer instead of the precursor [Hauser13]. The sensitizer acts then as catalyst and initializes the reaction. 9,10-Dimethylanthracen (DMA) is used as sensitizer, 4-4'-dimethoxybenzhydryltriphenylphosphonium ($(ani)_2CH\text{-}PPh_3^+$) as precursor, and dichloromethane (DCM) as solvent. The extended temporal coverage is necessary to capture the full dynamic of the system. Figure 5.6 shows the transient spectra and time traces at selected wavelengths.

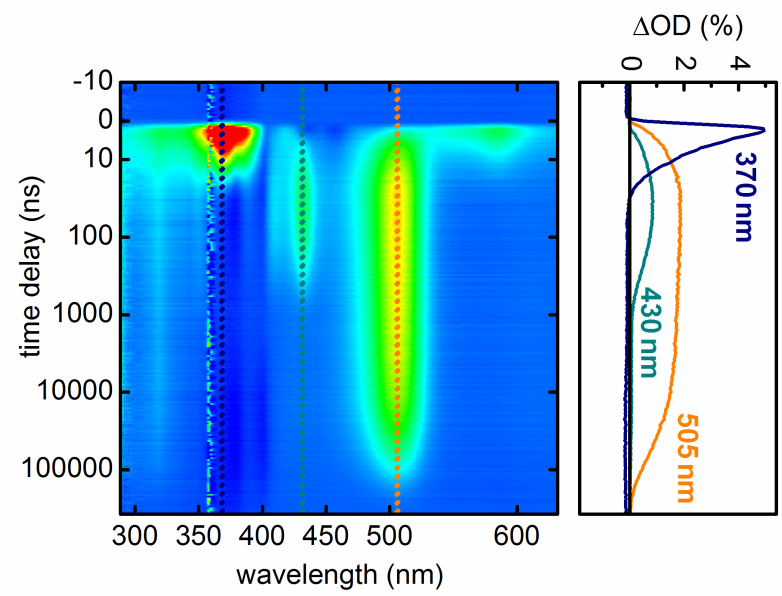

Fig. 5.6: Transient absorption spectra of DMA and $(ani)_2CH\text{-}PPh_3^+$ solved in DCM.

DMA is excited in the S_1 state by excitation with 360 nm. This decays with 9 ns (370 nm, blue curve) either into the triple state T_1 (430 nm, cyan) by intersystem crossing or when an $(ani)_2Ch\text{-}PPh_3^+$ molecule is present, an electron is transferred from the DMA to the $(ani)_2Ch\text{-}PPh_3^+$. This electron transfer induces a bound breaking in $(ani)_2Ch\text{-}PPh_3^+$ and the benzhydryl cation is formed (505 nm, orange curve). Only the temporal extension of the transient spectrometer up to delay times of 100 µs allows capturing the entire dynamic and evaluating the quantum yields of the individual processes.

5.5 Midinfrared pump-repump-probe experiments with few-cycle pulses

With the transient setup in Fig. 5.1, broadband pump probe spectroscopy can be performed from the deep UV to 1.7 µm. However, midinfrared pump-probe and two dimensional spectroscopy are very powerful tools to elucidate the complex ultrafast dynamics for many condensed systems [Graener91, Wouterson97, Zanni01, Khalil03]. For systems with hydrogen bonds, high-lying stretching vibrations of the hydrogen bond donors can be used as local probe of the chemical environment of the donor group [Nibbering04, Kramer08, Bakker10, Werhahn11]. Also studies on monolayer of graphene or investigations on the tunneling effect require infrared spectrometers. Although such spectrometers are used in many scientific fields, a full description of the setups is rare [Hamm94, Nibbering04, Bingaman12, Donaldson12]. Therefore, we presented a full description of the first pump-repump-probe setup operating completely in the infrared and using only few-cycle pulses. The ultrashort, infrared pulses from chapter 4.5 are used as pump and probe and a high temporal resolution of 60 fs is achieved [A13, A17]. The setup is comparable to Fig. 5.1 and shown in Fig. 5.7.

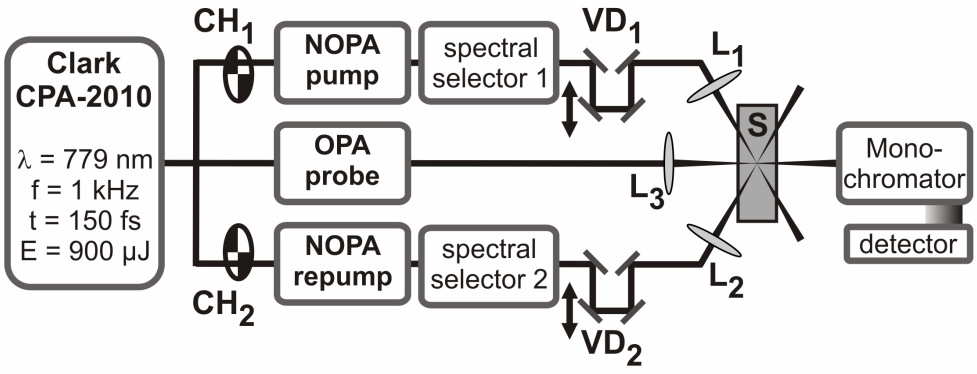

Fig. 5.7: Setup for midinfrared pump-repump-probe-spectroscopy with CEP stable few-cycle pulses and a time resolution of 60 fs.

Instead of the frequency doubled NOPA pulses, the infrared few-cycles pulses from chapter 4.5 are used as pump. The probe continuum is replaced by an infrared collinear OPA. All infrared pulses have been characterized by SHG based frequency resolved optical gating [Trebino97]. All of them have a few-cycle pulse duration and a stable CEP [A13]. For detection an infrared monochromator and a nitrogen cooled multichannel infrared mercury cadmium telluride sensor is used. Spectral selectors behind the amplifiers allow setting the spectral width of pump and repump pulses down to 20 cm^{-1} so that a selective excitation becomes possible. To get an impression of the operation principle of the spectral selector, Fig. 5.6 shows the selector setup and the resulting spectra.

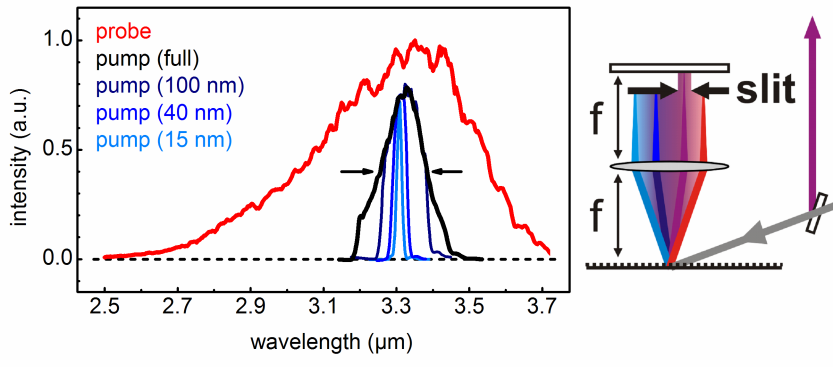

Fig. 5.8: Setup of spectral selector and generated spectra (blue and black). In addition, a typical probe spectrum is shown (red).

In addition, a typical probe spectrum is shown (red). To demonstrate the pump-repump capability of the setup, a 5M HDO in H_2O sample at 230 K is pumped at 4.1 µm and with 4.5 ps delay repumped at 3.1 µm. The probe is centered at the wavelength of the pump. Figure 5.9 shows the time dependent transmission change at the pump wavelength without (black) and with (red) repump and its difference (blue).

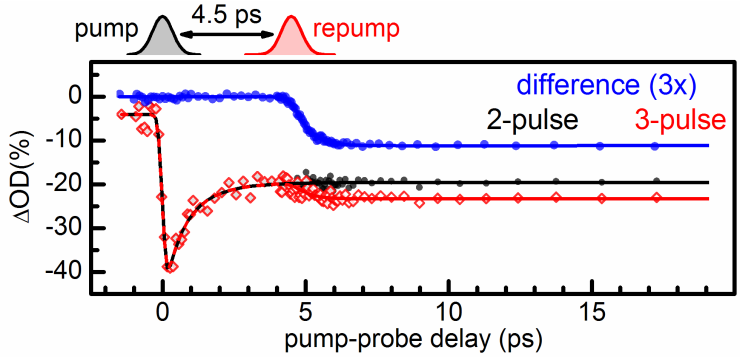

Fig. 5.9: Transient signal of 5M HDO H_2O at 4.1 µm after pumping at 4.1 µm and repumping at 3.1 µm after 4.5 ps (red). The transient signal without repump is shown (black) and the difference between both (blue).

The signal of the pump-repump experiment (red) consists of a GSB of the OD stretching vibration which increases with the instrumental response function of the system. The GSB signal relaxes with 1.1 ps to an offset caused by the local heating of the sample. The excitation of the OH oscillations is not instantaneously observable at the OD stretching mode. The heating induced by the repump leads to a delayed transmission change at the pump wavelength with a rise time of 0.5 ps. Only the repump shows the influence of the OH stretching mode on the OD stretching vibration. Further studies on the relaxation dynamics of the OH stretching overtones in isolated HDO molecules are performed [A17]. A continuous decrease of the energy separation for the first four states is observed. The population lifetime of the first excited state is 7.2 ps, while the one of the second excited state is 5 times shorter. The large acceleration factor indicates a stronger coupling of the OH stretching overtones with the low-frequency bath of the hydrate crystal [A17]. These observations are only possible due to the enormous spectral and temporal resolution and the full operation in the infrared.

A main feature of this thesis is the generation of short tunable infrared pulses at high repetition rates. This opens a novel field of research possibilities. The infrared OPA with visible pre-amplification delivering two-cycle pulses around 2 µm [A5, A10, A11] for example is used to investigate electron emission from a tungsten tip. This is interesting since the emission of the electron can originate either from multi-photon excitation or by tunneling. This is a CEP sensitive experiment which has to be performed at high repetition rates since the emission rate is very low. Up to now, these experiments are carried out with pulses at 800 nm. However, the theory predicts that for longer wavelengths interesting new effects will be observed as for example the scaling of the electron energy [Krueger11, Thomas13]. The experiment requires highly repetitive, CEP stable few-cycles pulses. Up to now, only Ti:sapphire oscillators could be used as pump source. With the here presented visible to infrared broadband frequency conversion [A5, A10, A11], pulses with longer central wavelengths are available and can give new insights in the involved processes. First experiments have just been performed and indicate a different behavior of the liberated electrons as for the 800 nm measurements since the tunneling is more dominant than the unwanted multi-photon excitation at longer wavelengths.

Another interesting field is the study of organic photovoltaics. With the help of the shown infrared OPA with visible pre-amplification [A2, A4] the structural correlations in the generation of polaron pairs in low-bandgap polymers for photovoltaics is uncovered [Tautz12] and the obtained results provide an useful input for the understanding of polaron pair photogeneration in low-bandgap co-polymers for the wide field of renewable energies. The challenge in this experiment is that widely tunable infrared pulses from 1 to 5 µm with a pulse duration of 50 fs must be provided at a high repetition rate of at least 100 kHz. This is only possible due to the here presented infrared OPA system with a visible pre-OPA. The results from these studies will help to unravel the primary step in light to currency transformation.

5.6 Spectral and temporal correlations of bulk continuum generation

The shown measurements are based on the spectrally and temporally resolved transmission change between an excited sample and a sample in the ground state. Every deviation from zero transmission change can be a hint for ultrafast dynamic in an investigated sample. Therefore, it is important to analyze the statistical properties of the spectrometer itself to check its performance [Dobryakov10, A16]. This can be tested best, if no sample and no pump light is present. Then all transmission changes should be zero for all times and over the entire spectrum. Such measurements are performed with a visible continuum and transient signals are found which deviate from unity. Figure 5.10 shows a typical transient spectrum from our spectrometer without pump and sample. S_{2k} and S_{2k+1} indicate that two subsequent continuum pulses are compared.

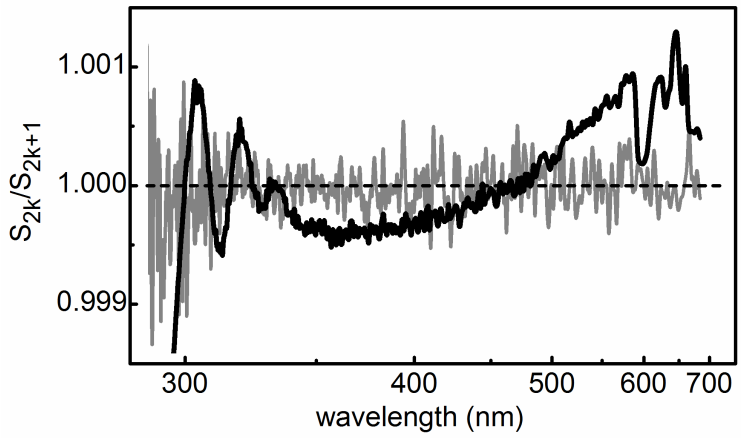

Fig. 5.10: Typically obtained S_{2k}/S_{2k+1} spectrum (black) from the transient absorption spectrometer without pump pulse and sample. A simulated spectrum expected from the pulse-to-pulse fluctuations (gray) is shown.

The shown S_{2k}/S_{2k+1} spectrum is an average of 500 consecutive single ratios. In addition, a spectrum expected from the pulse-to-pulse stability (gray) is shown in Fig. 5.10. The main challenge with the obtained S_{2k}/S_{2k+1} spectrum is that the low local fluctuations and strong global fluctuations can be misinterpreted as molecular response and therefore lower the effective sensitivity. These systematic deviations or pseudo-structures originate from the continuum generation process. There are only a few shapes and they appear random in time. This impedes averaging to improve the signal and no model for a reliable prediction has so far been found. A helpful mean to quantify this issue is the Pearson product moment correlation coefficient. It describes the relation between two series of numbers (X and Y) and is shown in Eq. (11).

$$\rho_{X,Y} = \frac{\mathrm{cov}(X,Y)}{\sigma_X \cdot \sigma_Y} = \frac{\sum_{i=1}^{n}\left(x_i - \overline{X}\right)\cdot\left(y_i - \overline{Y}\right)}{\sqrt{\sum_{i=1}^{n}\left(x_i - \overline{X}\right)^2}\cdot\sqrt{\sum_{i=1}^{n}\left(y_i - \overline{Y}\right)^2}} \tag{11}$$

$\mathrm{cov}(X,Y)$ is the covariance between series X and Y, σ_X and σ_Y are the standard deviations of X and Y, $\bar{X}$ and $\bar{Y}$ are the mean values, and x_i and y_i the values for i-th pulse. A high correlation coefficient means that the deviation from the mean is similar for many values of the series. The spectral and temporal Pearson correlations for the CaF_2 continuum used in our broadband transient spectrometer are evaluated [A16]. High correlations for neighboring wavelengths and a decreasing correlation to later continuum pulses are found. More interesting are the correlations in the ratio between subsequent continua. There are still high spectral correlations and random correlations to later times. To eliminate these, referencing is needed. Therefore, a second identical camera is set up. This allows referencing the signal from the sample camera (the one with pumped sample) to the signal from the reference camera (no pump) for the same continuum pulse. The spectral correlations can be eliminated by that. However, when not using the high temporal correlation to the next continuum pulse, temporal correlations in the sample/reference camera ratio arise. To avoid these, the referencing to the subsequent pulse is still necessary. To show that the improved sensitivity and avoidance of the pseudo-structures is indeed decisive, the transient signals of an artificial C-nucleoside with benzophenone as chromophore are measured [A16] and shown in Fig 5.11.

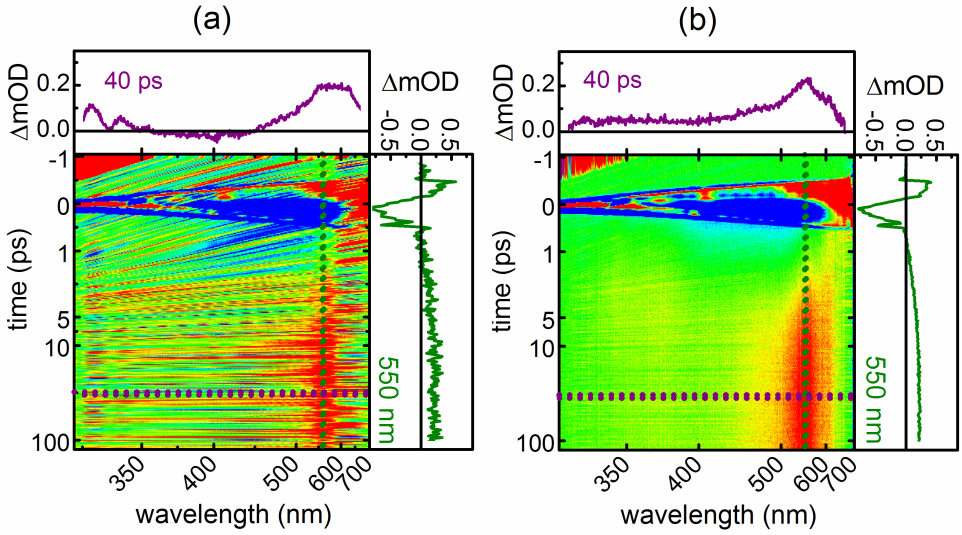

Fig. 5.11: Transient absorption spectra of an artificial C-nucleoside with benzophenone as chromophore after 310 nm excitation (a) with referencing to the subsequent continuum pulses and (b) with additional referencing to a second camera.

When referencing to a second camera (see Fig. 5.9(b)), all signatures are clearly visible. A quantitative measure describing the improvement is the confidence interval [Dobryakov10]. It is the minimum obtainable change of the optical density which can be detected effectively. This can be reduced from 100 µOD [Megerle09] to 20 µOD [A16] without increasing the measuring or acquisition time, when the referencing camera is used. Only the combination of referencing to the second camera and referencing to the subsequent pulse allows such an improvement of the transient spectrometer. In addition, all systematic errors are uncovered and eliminated by these measurements and techniques.

5.7 An 80 MHz setup for fluorescence lifetime measurements with tunable UV picosecond pulses

Referencing is a good method to reduce the detection limit and increase the sensitivity of a spectrometer. Another approach is increasing the averaging. However, many biological sample degrade with the time and change their properties and no useful conclusions can be drawn from such long term measurements. A favorable alternative is the use of high repetition rates. However, high repetition rates leads to low energies and modest peak intensities for the single pulses and complicate the generation of wavelength tunable pulses. At repetition rates close to 100 MHz for example, the generation of UV light is limited to small spectral ranges near the harmonics of the pump laser [Nebel91, Ellingson92, Ghotbi08, Zhou10]. Also the broadening in fibers only ranges down to approximately 400 nm [Birks00, Russell03, Dudley06, Russell06] and for additional nonlinear processes the peak power seems to be too low. Multiple applications in chemistry and biology such as fluorescence lifetime imaging, total internal reflection fluorescence microscopy, stimulated Raman scattering, broadband spectroscopy, optical coherence tomography, nano photonics, flow cytometry, or single molecule and bio-imaging would benefit from UV pulses at such high repetition rates. For the first time, UV pulses at 78 MHz tunable from 250 up to 430 nm with picosecond pulse durations are shown. They are obtained by frequency doubling of a commercially available whitelight laser (EXR-15; NKT Photonics A/S) [A14, A22]. For SHG with such low intensities, tight focusing and long doubling crystals are needed. At first sight, both of these requirements seem to be counterproductive because both exceed the acceptance angle and bandwidth limit. However, due to the tight focusing and hence the high numerical aperture, achromatic phase-matching occurs [Ashworth95]. This leads to frequency doubled light in the UV with output powers up to 70 µW and spectral widths far beyond the acceptance bandwidth [A14, A22]. Spectral widths of up to 20 nm are obtained. Figure 5.12 shows the tunable SHG pulses and the spectrum of the whitelight laser transferred to the UV enclosing the acceptance bandwidth and angle of the SHG process.

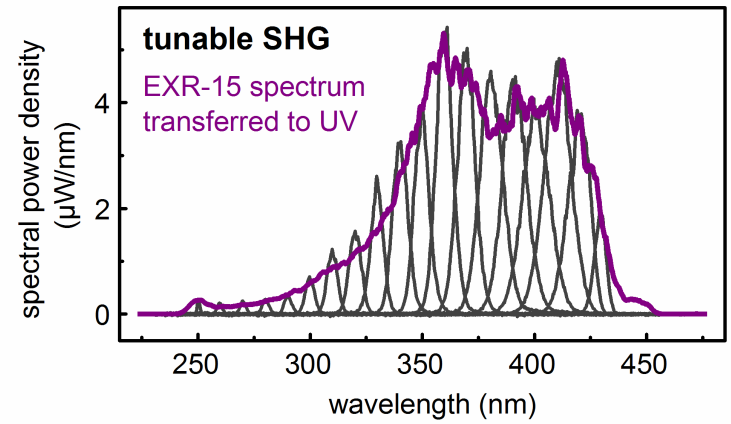

Fig. 5.12: Tunable SHG light from 250 to 430 nm at 78 MHz and spectrum of the whitelight laser transferred to the UV enclosing the acceptance angle and bandwidth (purple).

Although the obtained 70 µW only correspond to 900 fJ per pulse, the high repetition rate and single photon counting technology allow using the UV light in many experiments as pump or probe light. To show the potential of UV light at high repetition rates, the fluorescence lifetime of 2-(2'-hydroxyphenyl) benzothiazole (HBT) is measured. This molecule is of high interest since ultrafast photochemical processes such as coherent skeletal motion, proton transfer, or internal conversion and their interplay can be investigated [Frey91, Lochbrunner00, Lochbrunner03, Mintova04, Barbatti09, A14, A22]. It is excited at 330 nm and the fluorescence is captured with a streak camera (C5680; Hamamatsu Photonics) for two different wavelength regions. The emission of the HBT after the ultrafast excited state proton transfer is found in the range above 470 nm. This proton transfer can be blocked because the intramolecular hydrogen bond can be substituted by a hydrogen bond to an ethanol molecule. Then, the emission is observed from 360 to 410 nm. Both spectral regions are measured separately by inserting suited colored glass filters in the emission. Figure 5.13 shows the temporally resolved fluorescence (solid) and the excellent agreement to previous measurements performed with a 1 kHz Ti:sapphire laser (dotted) [Barbatti09, Mintova04].

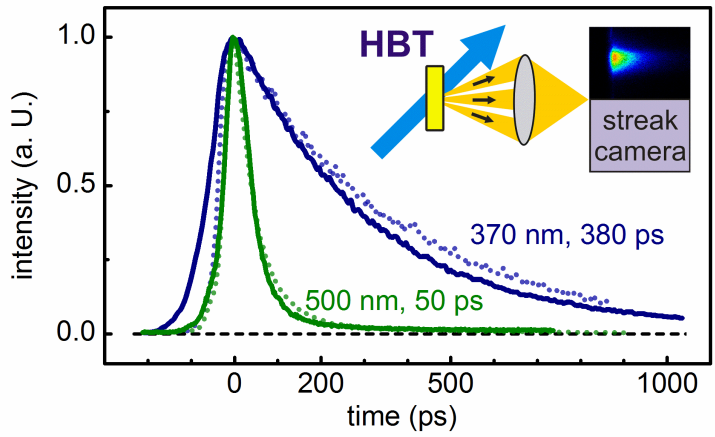

Fig 5.13: Time resolved fluorescence of HBT in two different spectral regions after 330 nm excitation (solid) and excellent agreement to previous 1 kHz measurements (dotted).

The high repetition rate of 78 MHz in combination with the previously not achievable UV tunability and the established detection techniques makes this simple and robust setup a unique tool to measure fastest processes with multi MHz repetition rate of even single molecules. Since the whitelight pulses can be used multiples times for SHG generation, even UV pump UV probe experiments at multi-MHz with picosecond time resolution are possible.

5.8 Temporal resolution in broadband spectrometers

The presented transient absorption spectrometers are well suited to measure the fastest processes and to uncover the inner life of molecules. To obtain the best results, a high temporal resolution is required. This is defined by the instrumental response function and is the cross correlation between the pump and the probe pulse [Vardeny81] as described in Eq. (12).

$$\Delta\tau_{CC} = \sqrt{\Delta\tau_{pump}^2 + \Delta\tau_{SCG}^2} \tag{12}$$

$\Delta\tau_{SCG}$ is the Fourier limit of the spectral part which temporally overlaps with the pump pulse. Due to the chirp of the probe continua and the pulse duration of the pump even theoretically instantaneous processes show a rise or decay time above "zero". Processes with durations shorter than the instrumental response function can not be resolved unambiguously. Therefore, it is crucial to know the time zero and the resolution for the measurements. Otherwise, misinterpretations and assignments to not existing ultrafast processes result. These values can be obtained from the measurements of ultrafast processes which do not show any remarkable delay. To find the time resolution, the full width half maximum (FWHM) of the coherent artifact can be analyzed. This artifact originates from the interaction between the pump and the probe pulses such as cross-phase modulation, two-photon absorption, four-wave mixing, or stimulated Raman amplification [Kovalenko99, Lorenc02]. For all presented spectrometers the coherent artifacts and fastest initial rise times are evaluated and therewith the temporal resolution of the particular spectrometer could be determined. Figure 5.14 shows the time resolution for the various spectral regions covered by the transient broadband spectrometers. The group velocity mismatch in a finite thick sample is not included and can deteriorate the temporal resolution.

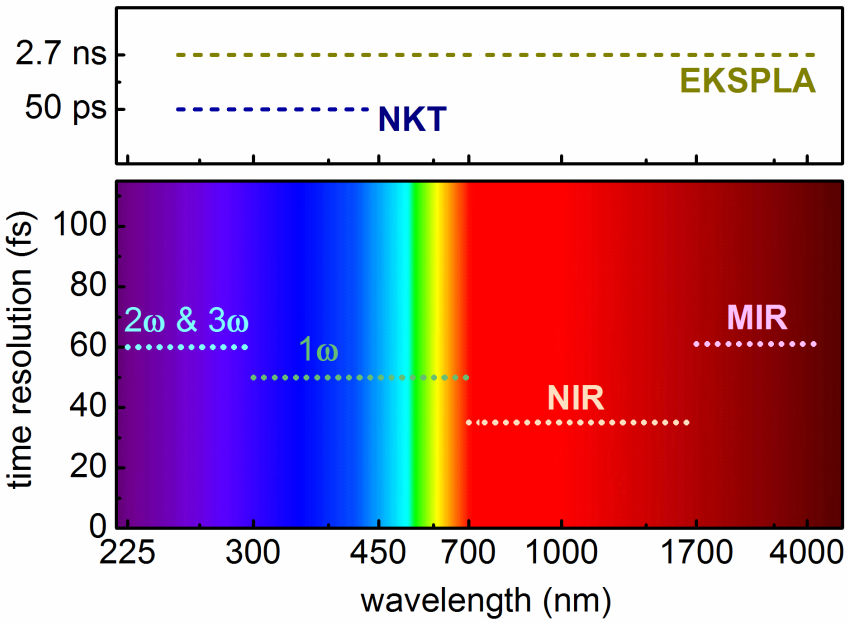

Fig. 5.14: Time resolution of the various transient spectrometers for UV, visible and infrared wavelength range.

1ω, 2ω, and 3ω stands for fundamental, SHG, and THG pumped continua, NIR for the continuum pumped by the infrared OPA, and MIR for the midinfrared pump repump probe system with. NKT indicates the second harmonic light from the 78 MHz whitelight laser. EKSPLA represents the kHz absorption spectrometer with ns pump pulses from the tunable OPO synchronized to the Ti:sapphire system. As sample thin glasses or colored filters with sub-200 µm thickness are used. Materials with pure two-photon absorption are found to be best for the precise determination of the time zero and the time resolution. For the 1 kHz Ti:sapphire system, the use of continuum generation as seed in optical parametric amplifier for the generation of pump pulses and as probe light allow building transient absorption spectrometers with pump and probe pulses from 225 nm up to 5 µm. For the entire spectral range, a time resolution below 60 fs can be reached. In the nearinfrared region even a temporal resolution of 35 fs is achieved. The dependence of the FWHM on the cross correlation and therefore the instrumental response function allows optimizing the pump pulse duration at the sample position. Short temporal coherent artifacts also lead to spectrally narrow coherent artifacts. This simplifies the search for shortest pump pulse durations since the spectral shape of the artifacts can be observed in situ. From the performed measurements it can be concluded that the time resolution in a broadband transient spectrometer is enhanced with shorter pump and probe pulses. With the use of the 10 fs continuum from chapter 3.6 (see Fig. 3.16) as probe light time resolutions down to 30 fs are achieved. For the visible and nearinfrared, experiments have been reported with a higher time resolution [Manzoni06b, Polli07, Brida09, Takeushi09, Polli10], but not for the complete spectral range from the UV to the infrared. In addition, the use of fully compressed probe pulses leads to very large coherent artifacts which overlap with the ultrafast response of the studied system.

The use of the frequency doubled UV light of a whitelight laser at 78 MHz allows measuring the fluorescence life time of HBT with a time resolutions of 50 ps which is in partly limited by the streaking technology. For proper pump probe experiments, a temporal resolutions of 25 ps is expected since pump and probe pulses will have a pulse duration of 15 ps. For measurements up to millisecond delay times, the pump pulses are generated in a nanosecond OPO. Therefore, also the temporal resolution of the kHz spectrometer with the synchronized laser systems is on the 3 nanosecond level. The great advantage is that the entire spectrometer is contained in one setup. This means that the various combinations of spectral and temporal coverage can be realized in the daily operation and that the shown coverage over several magnitudes is not only hypothetical.

6. Summary, conclusion, and future perspectives

In this thesis, bulk continuum generation is presented in its full manifoldness and studied in detail. The involved processes during the generation are reviewed and the influence of the input light parameters is investigated and new insights in the generation are given. Then, the experimental realization and utilization in optical parametric amplifiers and ultrafast broadband transient absorption spectrometers are demonstrated. Broadest pulses from the UV to the infrared with highest efficiencies are obtained. A transient spectrometer with an extreme spectral and temporal coverage and a high temporal resolution is presented. The generation of new colors beyond the fundamental wavelength of the laser and its harmonic is indispensable for time-resolved studies in physics, chemistry, biology, or medicine. Filamentation and the accompanying continuum generation are well suited for this purpose due to the advantageous properties of the newly generated light. A smooth, gap-free, and broadband spectrum with a superior beam profile and high stability is obtained. The simple setup, easy handling, and high robustness favor bulk continuum generation as ideal broadband source for various applications.

First, the involved processes in continuum generation in solids are investigated in detail. The Kerr effect describes the dependence of the refractive index on the intensity. Self-focusing is a consequence of the Kerr effect in space and dramatically increases the intensity and launches further nonlinear processes. Self-focusing is stopped by multi-photon excitation and plasma generation. The balance between these processes is called filamentation and allows high intensities to be conveyed over very long distances. Hereby, the surrounding photon reservoir continuously feeds the filament and maintains it. A further consequence of the Kerr effect is self-steepening. This shortens the pulses and completely restructures the temporal intensity profile. As consequence, self-phase modulation – which also results from the Kerr effect – is enhanced by self-steepening and multi-photon excitation. This is the origin of the newly generated colors during continuum generation.

All geometrical conditions and pump pulse parameters are investigated and optimized. External focusing down to a few tens of µm with numerical apertures between 0.015 and 0.1 is necessary. Otherwise, high pulse energies are needed which lead to surface damage and multi-filamentation. The detailed beam profile of the input pulse is not substantial. Even Bessel beams are sufficient for a proper continuum generation. Filament channels last over several millimeters in bulk material. Therefore, the crystal thickness is important, because it determines the amount of generated light, the chirp, and whether multiple refocusing occurs or not. New insights in the mechanism of continuum generation are given. A small amount of all colors is generated at the beginning of the filament due to the abrupt self-steepening. Then, colors close to the pump wavelength are generated constantly over the entire filament, whereas colors close to the continuum cut-off are generated only in the first few hundred µm. However, all new colors have initially the same properties. Only the remaining propagation in the material leads to the spectral chirp and to different spatial properties for the single wavelengths. When the filament is generated at the end of the crystal so that it can only de-

velop several 100 µm's, there is nearly no chirp on the continuum. In combination with the use of a Schiefspiegler geometry, an astigmatism free, sub-10 fs pulse can be generated directly from bulk continuum generation. All colors of this pulse have the same size and divergence. Another important parameter is the pump wavelength of the pump. In combination with the material properties, this determines the spectral coverage of the continuum. With infrared pulses, octave spanning spectra can be produced with a continuum cut-off in the visible. With UV light as pump, the continuum cut-off shifts with the wavelength and continua down to 225 nm can be achieved in CaF_2. Materials with a high bandgap have a higher threshold for continuum generation, but also have a continuum cut-off deeper in the blue. The pump pulse energy, on the other side, influences the infrared spectrum of the continuum, the appearance of multiple refocusing, and the phase stability of the newly generated frequencies. All of them increase for higher pump energies. Finally, the duration and the chirp of the pump pulses are studied. There is no influence on the newly generated frequencies observed. Whether continuum generation takes place or not, depends on the appearance of avalanche ionization and optical breakdown. However, for the first time, pulse durations of clearly above one picosecond are found to be suited for proper continuum generation.

The presented continua are used as seed source in optical parametric amplifiers. Although only a small visible range is provided as seed, the use of nonlinear processes allow the generation of tunable pulses from the deep UV (215 nm) up to the infrared (10 µm) even at highest repetition rates and with limited available pump energies. The generated pulses can be compressed to a few-cycle pulse duration and have high average powers. All limiting factors such as narrowband phase-matching, idler absorption, or the lack of suited seed light are overcome. For example, UV pulses benefit from achromatic phase-matching, visible pulses from the use of a noncollinear geometry and infrared pulses from broadband difference frequency generation. In addition, the use of a dual amplifier crystal setup, visible preamplification, or the choice of the proper amplifier crystal allow achieving a high energy output and broadband spectra in the infrared. Therefore, an unrivaled tuning range over five octaves starting from a narrowband laser source is achieved in this work. Not even high repetition rates, different pump wavelengths, or low pump pulse energies limit the tuning range. Figure 6.1 shows this ultrawide tuning range from below 215 nm to over 10 µm of OPA pulses achieved in this thesis.

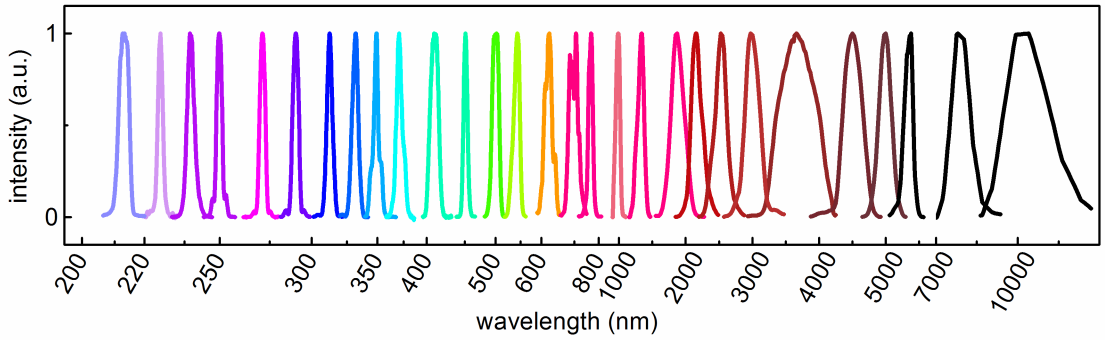

Fig. 6.1: Overall tuning range over five octaves of OPAs seeded by visible bulk continua.

In addition, the influence of the pump intensity on optical parametric amplification is studied. For peak intensities of up to 500 GW/cm^2, the advantageous properties of spectral broadening can be used without limitation. However, for a stable long term operation 300 GW/cm^2 should be applied to avoid a fast degradation of the amplifier crystals. For high repetition rates, two-photon absorption has to be taken into account. There, 100 GW/cm^2 is found to be the optimum peak intensity.

Furthermore, the presented continua are used in transient spectroscopy. Their advantageous properties favor them as ideal probe light. An ultimate transient spectrometer with a previously not shown spectral and temporal coverage is presented. Pump and probe pulses ranges from the deep UV (225 nm) up to the midinfrared (5 µm). A time resolution of 60 fs or better for the entire spectral range is achieved. Delay times over 11 magnitudes from single femtoseconds up to several hundred microseconds can be applied in a daily operation. Figure 6.2 shows an overview over the various techniques to cover these immense ranges.

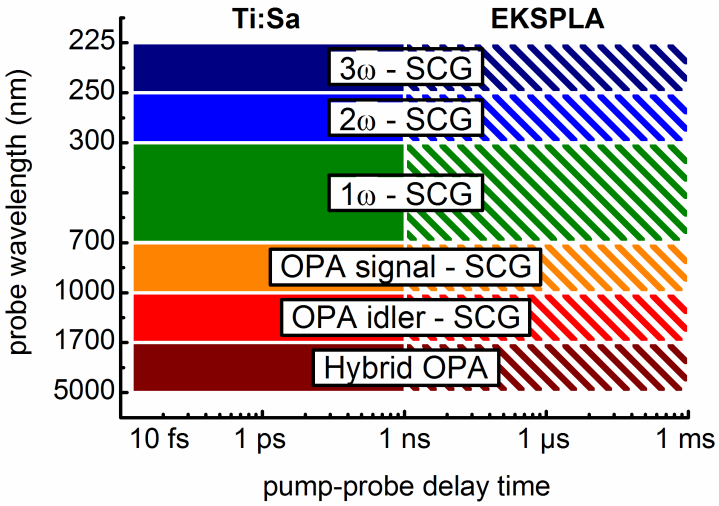

Fig. 6.2: Temporal and spectral coverage of the extended transient spectrometer consisting of a widely tunable pump, various probe continua, and a synchronized nanosecond laser.

The innumerous combination possibilities in spectrum and time of the presented spectrometer will uncover all relevant processes of any studied system. This makes the spectrometer a superior tool in ultrafast spectroscopy. The investigation of the intermediate states in malachite green, the dominating processes in of a,ß-enones, the ultrafast processes in cyclohexadiene, the interaction of anthracene with the surrounding, or the thermal relaxation of 5M HDO in H_2O benefit from the wide spectral and temporal coverage of the spectrometer. Without these modifications, the ultrafast processes of the systems could not be determined unambiguously. In addition, measurements without sample and pump show that referencing to the consecutive pulse and to a second camera eliminate the strong spectral and temporal correlations in transient spectra. This allows an improvement of the sensitivity down to 20 µOD.

In conclusion, bulk continuum generation is an extreme powerful tool and a unique source for the generation of new colors. The favorable properties, as well as the simple generation and handling allow a wide usage in the field of optics. Filamentation is still a topic of many investigations and continuum generation will benefit from these studies since both are closely connected. In addition, the development of new laser host materials will also push continuum generation in solids since these crystals are excellently suited for this purpose. Therefore, bulk continuum generation needs to be further examined and researched in detail in order to gain proper and complete knowledge of this fascinating phenomenon:

- For example, the increase of the pump wavelength even deeper into the infrared for obtaining a coherent femtosecond light source with a smooth and gap free spectrum, a good beam quality, and a high stability from the visible to the mid-infrared at once is a fascinating concept. The generation of bulk continua with 3 µm shows no indications that this might fail for longer pump wavelengths.
- Furthermore, the limiting processes of bulk continuum generation with longer pump pulses state a controversial issue of research. The current maximum pulse duration for continuum generation is increased by a factor of 5 in this work and enters the picosecond regime. New laser host materials might even increase this limit since the parasitic effects are also a challenge for this research field.
- An advantage of continuum generation with long pump pulses is that the chirp of the new frequencies is equal to the chirp as for short pump pulses. The chirp of the continuum is determined by the remaining propagation in the crystal. This fact allows broadband parametric amplification of the new frequencies when pumping with long pump pulses.
- Furthermore, the stretching of the pump pulses in OPAs can be avoided by the use of a 10 fs bulk continuum as seed. Broadband amplifiers can then be operated even with short pump pulses. This has the advantage that the parasitic superfluorescence background can be kept on a very low level. This favors bulk continuum generation as an excellent alternative in optical parametric chirped pulse amplification. The seed for the main amplifier is not an additional oscillator including the synchronization problems, but a femtosecond continuum. Such amplifier systems work well and already produce peak powers on the petawatt level.
- For the upcoming laser systems near 2 µm, bulk continuum generation is an excellent source for the generation of new colors down to the visible. The needed low input energy, the short continuum cut-off, and the still reasonable amount of newly generated light makes it superior to gas filamentation, spectral broadening in fibers, or optical parametric oscillators with subsequent nonlinear conversion.

Bulk continuum generation is an excellent method to generate new colors beside the fundamental wavelength of the used laser system and can be utilized in many areas of optic such as broadband amplifiers or ultrafast transient spectrometers. Its wide applicability renders it as perfect tool for numerous laser applications and ultrafast spectroscopy.

7. References

Adachi08 "5-fs, multi-mJ, CEP-locked parametric chirped-pulse amplifier pumped by a 450-nm source at 1 kHz," S. Adachi, N. Ishii, T. Kanai, A. Kosuge, J. Itatani, Y. Kobayashi, D. Yoshitomi, K. Torizuka, and S. Watanabe, Opt. Express **16**, 14341 (2008).

Akoezbek00 "Femtosecond pulse propagation in air: variational analysis," N. Aközbek, C. M. Bowden, A. Talebpour, and S. L. Chin, Phys. Rev. E **61**, 4540 (2000).

Akoezbek01 "White-light continuum generation and filamentation during the propagation of ultra-short laser pulses in air," N. Aközbek, M. Scalora, C. M. Bowden, and S. L. Chin, Opt. Commun. **191**, 353 (2001).

Alfano70a "Emission in the region 4000 to 7000 Å via four-photon coupling," R. R. Alfano and S. L. Shapiro, Phys. Rev. Lett. **24**, 584 (1970).

Alfano70b "Observation of self-phase modulation and small-scale filaments in crystals and glasses," R. R. Alfano and S. L. Shapiro, Phys. Rev. Lett **24**, 592 (1970).

Alfano06 "*The supercontinuum laser source,*" R. R. Alfano, (Springer, 2006).

Ammer12 "Photolytic generation of benzhydryl cations from quaternary phosphonium salts: how highly reactive carbocations survive their first nanoseconds," J. Ammer, C. F. Sailer, E. Riedle, and H. Mayr, J. Am. Chem. Soc. **134**, 11481 (2012).

Anashkina11 "All-fiber design of erbium-doped laser system for tunable two-cycle pulse generation," E. A. Anashkina, A. V. Andrianov, S. V. Muravyev, and A. V. Kim, Opt. Express **19**, 20141 (2011).

Andriukaitis11 "90 GW peak power few-cycle mid-infrared pulses from an optical parametric amplifier," G. Andriukaitis, T. Balciunas, S. Alisauskas, A. Pugzlys, A. Baltuska, T. Popmintchev, M. C. Chen, M. M. Murnane, and H. C. Kapteyn, Opt. Lett. **36**, 2755 (2011).

Antipenkov11 "Femtosecond Yb:KGW MOPA driven broadband NOPA as a frontend for TW few-cycle pulse systems," R. Antipenkov, A. Varanavicius, A. Zaukevicius, and A. P. Piskarskas, Opt. Express **19**, 3519 (2012).

Ashcom06 "Numerical aperture dependence of damage and supercontinuum generation from femtosecond laser pulses in bulk fused silica," J. B. Ashcom, R. R. Gattass, C. B. Schaffer, and E. Mazur, J. Opt. Soc. Am B **23**, 2317 (2006).

Ashworth95 "Generation of 16-fs pulses at 425 nm by extracavity frequency doubling of a mode-locked Ti:sapphire laser," S. H. Ashworth, M. Joschko, M. Woerner, E. Riedle, and T. Elsaesser, Opt. Lett. **20**, 2120 (1995).

Babin05 "Luminescence of undoped LuAG and YAG crystals," V. Babin, K. Blazek, A. Krasnikov, K. Nejezchleb, M. Nikl, T. Savikhina, and S. Zazubovich, Phys. Stat. Sol. **2**, 97 (2005).

Bakker10 "Vibrational spectroscopy as a probe of structure and dynamics in liquid water," H. J. Bakker and J. L. Skinner, Chem. Rev. **110**, 1498 (2010).

Baltuska02a "Controlling the carrier-envelope phase of ultrashort light pulses with optical parametric amplifiers," A. Baltuska, T. Fuji, and T. Kobayashi, Phys. Rev. Lett. **88**, 133901 (2002).

Baltuska02b "Visible pulse compression to 4 fs by optical parametric amplification and programmable dispersion control," A. Baltuska, T. Fuji, and T. Kobayashi, Opt. Lett. **27**, 306 (2002).

Bang02 "Collapse arrest and soliton stabilization in nonlocal nonlinear media," O. Bang, W. Krolikowski, J. Wyller, and J. J. Rasmussen, Phys. Rev. E **66**, 045519 (2002).

Barbatti09 "Ultrafast internal conversion pathway and mechanism in 2-(20-hydroxyphenyl)benzothiazole: a case study for excited-state intramolecular proton transfer systems," M. Barbatti, A. J. A. Aquino, H. Lischka, C. Schriever, S. Lochbrunner, and E. Riedle, Phys. Chem. Chem. Phys. **11**, 1406 (2009).

Baum03 "Phase-coherent generation of tunable visible femtosecond pulses," P. Baum, S. Lochbrunner, J. Piel, and E. Riedle, Opt. Lett. **28**, 185 (2003).

Baum04a "Tunable sub-10-fs ultraviolet pulses generated by achromatic frequency doubling," P. Baum, S. Lochbrunner, and E. Riedle, Opt. Lett. **29**, 1686 (2004).

Baum04b "Generation of tunable 7-fs ultraviolet pulses: achromatic phase matching and chirp management," P. Baum, S. Lochbrunner, and E. Riedle, Appl. Phys. B **79**, 1027 (2004).

Baum05 "Phase-locked ultrashort pulse trains at separate and independently tunable wavelengths," P. Baum, E. Riedle, M. Greve, and H. R. Telle, Opt. Lett. **30**, 2028 (2005).

Baum06 "Brewster-angled chirped mirrors for broadband pulse compression without dispersion oscillations," P. Baum, M. Breuer, E. Riedle, and G. Steinmeyer, Opt. Lett. **31**, 2220 (2006).

Becker01 "Intensity clamping and re-focusing of intense femtosecond laser pulses in nitrogen molecular gas," A. Becker, N. A. Aközbek, K. Vijayalakshmi, E. Oral, C. M. Bowden, and S. L. Chin, Appl. Phys. B **73**, 287 (2001).

Bejot10 "Higher-order Kerr terms allow ionization-free filamentation in gases", P. Bejot, J. Kasparian, S. Henin, V. Loriot, T. Vieillard, E. Hertz, O. Faucher, B. Lavorel, and J.-P. Wolf, Phys. Rev. Lett. **104**, 103903 (2010).

Ben87 "Torsional dynamics of molecules on barrierless potentials in liquids. I. Temperature and wavelength dependent picosecond studies of triphenyl methane dyes," D. Ben-Amotz and C. B. Harris, J. Chem. Phys. **86**, 4856 (1987).

Berge07 "Ultrashort filaments of light in weakly ionized, optically transparent media," L. Berge, S. Skupin, R. Nuter, J. Kasparian, and J.-P. Wolf, Rep. Prog. Phys. **70**, 1633 (2007).

Berge10 ",Multifilamentation of powerful optical pulses in silica," L. Berge, S. Mauger, and S. Skupin, Phys. Rev A. **81**, 013817 (2010).

Berge11 "Role of the carrier-envelope phase in laser filamentation," L. Berge, C. L. Soulez, C. Köhler, and S. Skupin, Appl. Phys. B **103**, 563 (2011).

Berube10 "Self and forced periodic arrangement of multiple filaments in glass," J. P. Berube, R. Vallee, M. Bernier, O. Kosareva, N. Panov, V. Kandidov, and S. L. Chin, Opt. Express **18**, 1801 (2010).

Bethge10 "Two-octave supercontinuum generation in a water-filled photonic crystal fiber," J. Bethge, A. Husakou, F. Mitschke, F. Noack, U. Griebner, G. Steinmeyer, and J. Herrmann, Opt. Express **18**, 6230 (2010).

Bethge11 "Self-compression of 120 fs pulses in a white-light filament," J. Bethge, C. Bree, H. Redlin, G. Stibenz, P. Staudt, G. Steinmeyer, A. Demircan, and S. Düsterer, J. Opt. **13**, 055203 (2011).

Beutler09 "Generation of high-energy sub-20 fs pulses tunable in the 250–310 nm region by frequency doubling of a high-power noncollinear optical parametric amplifier," M. Beutler, M. Ghotbi, F. Noack, D. Brida, C. Manzoni, and G. Cerullo, Opt. Lett. **34**, 710 (2009).

Biegert12 "New mid-infrared light sources," J. Biegert, P. K. Bates, and O. Chalus, IEEE Select. Topics Quantum. Electron. **18**, 531 (2012).

Bingaman12 "Time-resolved vibrational spectroscopy of [FeFe]-hydrogenase model compounds," J. L. Bingaman, C. L. Kohnhorst, G. A. Van Meter, B. A. McElroy, E. A. Rakowski, B. W. Caplins, T. A. Gutowski, C. J. Stromberg, C. E. Webster, and E. J. Heilweil, J. Phys. Chem. A **116**, 7261 (2012).

Birks01 "Supercontinuum generation in tapered fibers," T. A. Birks, W. J. Wadsworth, P. St. J. Russell: Opt. Lett. 25, 1415 (2000).

Blaga07 "Intense self-compressed, self-phase-stabilized few-cycle pulses at 2 μm from an optical filament," C. I. Blaga, K. D. Schultz, J. Cryan, R. Chirla, P. Colosimo, G. Doumy, A. M. March, C. Roedig, E. Sistrunk, J. Tate, J. Wheeler, and L. F. DiMauro, Opt. Lett. **32**, 868 (2007).

Bloembergen73 "The influence of electron plasma formation on superbroadening in light filaments," N. Bloembergen, Opt. Commun. **8**, 285 (1973).

Bonneau80 "Transient species in photochemistry of enones. The orthogonal triplet state revealed by laser photolysis," R. Bonneau, J. Am. Chem. Soc. **102**, 3816 (1980).

Borchers12 "Saturation of the all-optical Kerr effect in solids," B. Borchers, C. Bree, S. Birkholz. A. Demircan, and G. Steinmeyer, Opt. 37, 1541 (2012).

Bowlan09 "Measuring the spatiotemporal field of ultrashort Bessel-X pulses," P. Bowlan, H. Valtna-Lukner, M. Lohmus, P. Piksarv, P. Saari, and R. Trebino, Opt. Lett. **34**, 2276 (2009).

Brabec97 "Nonlinear optical pulse propagation in the single-cycle regime," T. Brabec and F. Krausz, Phys. Rev. Lett. **78**, 3282 (1997).

Brabec00 "Intense few-cycle laser fields: frontiers of nonlinear optics," T. Brabec and F. Krausz, Rev. Mod. Phys. **72**, 545 (2000).

Braun95 "Self-channeling of high-peak-power femtosecond laser pulses in air," A. Braun, G. Korn, X. Liu, D. Du, J. Squier, and, G. Mourou, Opt. Lett. **20**, 73 (1995).

Bree11 "Saturation of the all-optical Kerr effect," C. Bree, A. Demircan, and G. Steinmeyer, Phys. Rev. Lett. **106**, 183902 (2011).

Brida07 "Generation of broadband mid-infrared pulses form an optical parametric amplifier," D. Brida, C. Manzoni, G. Cirmi, M. Marangoni, S. De Silvestri, G. Cerullo, Opt. Exp. **15**, 15035 (2007).

Brida08a "Sub-two-cycle light pulses at 1.6 μm from an optical parametric amplifier," D. Brida, G. Cirmi, C. Manzoni, S. Bonora P. Villoresi, S. De Silvestri, and G. Cerullo, Opt. Lett. **33**, 741 (2008).

Brida08b "Two-optical-cycle pulses in the mid-infrared from an optical parametric amplifier," D. Brida, M. Marangoni, C. Manzoni, S. De Silvestri, and G. Cerullo, Opt. Lett. **32**, 2901 (2008).

Brida09 "Generation of 8.5-fs pulses at 1.3 μm for ultrabroadband pump-probe spectroscopy," D. Brida, S. Bonora, C. Manzoni, M. Marangoni, P. Villoresi, S. De Silvestri, and G. Cerullo, Opt. Express **17**, 12510 (2009).

Brida10 "Few-optical-cycle pulses tunable from the visible to the mid-infrared by optical parametric amplifiers," D. Brida, C. Manzoni, G. Cirmi, M. Marangoni, S. Bonora, P. Villoresi, S. De Silvestri, and G. Cerullo, J. Opt. **12**, 013001 (2010).

Brodeur97 "Moving focus in the propagation of ultrashort laser pulses in air," A. Brodeur, C. Y. Chien, F. A. Ilkov, S. L. Chin, O. G. Kosareva and V. P. Kandidov, Opt. Lett. **22**, 704 (1997).

Brodeur98 "Band-gap dependence of the ultrafast white-light continuum," A. Brodeur and S. L. Chin, Phys. Rev. Lett. **80**, 4406 (1998).

Brodeur99 "Ultrafast white-light continuum generation and self-focusing in transparent condensed media," A. Brodeur, S.L. Chin, J. Opt. Soc. Am. B **16**, 637 (1999).

Buchvarov07 "Toward an understanding of white-light generation in cubic media - polarization properties across the entire spectral range," I. Buchvarov, A. Trifonov, and T. Fiebig, Opt. Lett. 32, 1539 (2007)

Buckingham56 "Birefringence resulting from the application of an intense beam of light to an isotropic medium," A. D. Buckingham, Proc. Phys. Soc. London B **69**, 344 (1956).

Burnett77 "Harmonic-generation in CO_2-laser target interaction," N. H. Burnett, H. A. Baldis, M. C. Richardson, and G. D. Enright, Appl. Phys. Lett. **31**, 172 (1977).

Canto93 "Surface second-harmonic generation in Si(111) for autocorrelation measurements of 248-nm femtosecond pulses," E. J. Canto-Said, P. Simon, C. Jordan, and G. Marowsky, Opt. Lett. **18**, 2038 (1993).

Cerullo97 "Generation of 11 fs pulses tunable across the visible by optical parametric amplification," G. Cerullo, M. Nisoli, and S. De Silvestri, Appl. Phys. Lett. **71**, 3616 (1997).

Cerullo98 "Sub-8-fs pulses from an ultrabroadband optical parametric amplifier in the visible," G. Cerullo, M. Nisoli, S. Stagira, and S. De Silvestri, Opt. Lett. **23**, 1283 (1998).

Cerullo99 "Mirror-dispersion-controlled sub-10-fs optical parametric amplifier in the visible," G. Cerullo, M. Nisoli, S. Stagira, S. De Silvestri, G. Tempea, F. Krausz, and K. Ferencz, Opt. Lett. 24, 1529 (1999).

Cerullo00 "Mirror-dispersion-controlled OPA: a compact tool for sub-10-fs spectroscopy in the visible," G. Cerullo, M. Nisoli, S. Stagira, S. De Silvestri, G. Tempea, F. Krausz, and K. Ferencz, Appl. Phys. B: Lasers Opt. 70, S253 (2000).

Cerullo03 "Ultrafast optical parametric amplifiers," G. Cerullo and S. De Silvestri, Rev. Sci. Instrum. **74**, 1 (2003).

Cerullo11 "Few-optical-cycle light pulses with passive carrier-envelope phase stabilization," G. Cerullo, A. Baltuska, O . D. Mücke, and C. Vozzi, Laser Phot. Rev. **5**, 323 (2011).

Chalus09 "Mid-IR short-pulse OPCPA with micro-Joule energy at 100kHz," O. Chalus, P. K. Bates, M. Smolarski, and J. Biegert, Opt. Express **17**, 3587 (2009).

Chalus10 "Six-cycle mid-infrared source with 3.8 μJ at 100 kHz," O. Chalus, A. Thai, P. K. Bates, and J. Biegert, Opt. Lett. **35**, 3204 (2010).

Chekalin13 "Light bullets and supercontinuum spectrum during femtosecond pulse filamentation under conditions of anomalous group-velocity dispersion in fused silica," S. V. Chekalin, V. O. Kompanets, E. O. Smetanina, and V. P. Kandidov, Quant. Elec.**43**, 326 (2013).

Chernev92 "Self-focusing of light pulses in the presence of normal group-velocity dispersion," P. Chernev and V Petrov, Opt. Lett. **17**, 172 (1992).

Chiao64 "Self-trapping of optical beams," R. Y. Chiao, E. Garmire, and C. H. Townes, Phys. Rev. Lett. **13**, 479 (1964).

Chin99 "Filamentation and continuum generation during the propagation of powerful ultrashort laser pulses in optical media (white light laser)," S. L. Chin, A. Brodeur, S. Petit, O. G. Kosareva, and V. P. Kandidov, J. Nonlin. Opt. Phys. Mater. **8**, 121 (1991).

Chin05 "The propagation of powerful femtosecond laser pulses in optical media: physics, applications, and new challenges," S. L. Chin, S. A. Hosseini, W. Liu, Q. Luo, F. Theberge, N. Aközbek, A. Becker, V. P. Kandidov, O. G. Kosareva, and H. Schroeder, Can. J. Phys. **83**, 863 (2005).

Chin07 "Filamentation nonlinear optics," S. L. Chin, F. Theberge, and W. Liu, Appl. Phys. B **86**, 477 (2007).

Chin10 "*Femtosecond laser filamentation*," S. L. Chin, (Springer, 2010).

Cirmi07 "Few-optical-cycle pulses in the near-infrared from a noncollinear optical parametric amplifier," G. Cirmi, D. Brida, C. Manzoni, M. Marangoni, S. De Silvestri, and G. Cerullo, Opt. Lett. **32**, 2396 (2007).

Cirmi08 "Carrier-envelope phase stable, few-optical-cycle pulses tunable from visible to near IR," G. Cirmi, C. Manzoni, D. Brida, S. De Silvestri, and G. Cerullo, J. Opt. Soc. Am. B **25**, B62 (2008).

Cirmi12 "Cut-off scaling of high-harmonic generation driven by a femtosecond visible optical parametric amplifier," G. Cirmi, C. J. Lai, E. Granados, S. W. Huang, A. Sell, K. H. Hong, J. Moses, P. Keathley, and F. X Kärtner, J. Phys. B **45**, 205601 (2012).

Clerici10 "Space–time focusing of Bessel-like pulses," M. Clerici, D. Faccio, E. Rubino, A. Lotti, A. Couairon, and P. Di Trapani, Opt. Lett. **35**, 3267 (2010).

Corkum07 "Attosecond science," P. B. Corkum and F. Krausz, Nature Physics **3**, 381 (2007).

Couairon03 "Dynamics of femtosecond filamentation from saturation of self-focusing laser pulses," A. Couairon, Phys. Rev. A **68**, 015801 (2003).

Couairon05 "Filamentation and damage in fused silica induced by tightly focused femtosecond laser pulses," A. Couairon, L. Sudrie, M. Franco, B. Prade, and A. Mysyrowicz, Phys. Rev. B **71**, 125435 (2005).

Couairon06a "Nonlinear X-wave formation by femtosecond filamentation in Kerr media," A. Couairon, E. Gaizauskas, D. Faccio, A. Dubietis, and P. Di Trapani, Phys. Rev. E. **73**, 016608 (2006).

Couairon06b "Self-compression of ultra-short laser pulses down to one optical cycle by filamentation," A. Couairon, J. Biegert, C. P. Hauri, W. Kornelis, F. W. Helbing, U. Keller, and A. Mysyrowicz, J. Mod Opt. **53**, 75 (2006).

Couairon07 "Femtosecond filamentation in transparent media," A. Couairon and A. Mysyrowicz, Phys. Rep. **441**, 47 (2007).

Cussat00 "$KTiOPO_4$, $KtiOAsO_4$, and $KNbO_3$ crystals for mid-infrared femtosecond optical parametric amplifiers: analysis and comparison," S. Cussat-Blanc, A. Ivanov, D. Lupinski, E. Freysz, Appl. Phys. B **70**, S247 (2000).

Das93 "Transient carbocations and carbanions generated by laser flash photolysis and pulse radiolysis," P. K. Das, Chem. Rev. **93** 119 (1993).

Daigle10 "Intensity clamping measurement of laser filaments in air at 400 and 800 nm," J. F. Daigle, A. Jaron-Becker, S. Hosseini, T. J. Wang, Y. Kamali, G. Roy, A. Becker, and S. L. Chin, Phys. Rev. A **82**, 023405 (2010).

Darginavicius12a "Generation of carrier-envelope phase-stable two optical-cycle pulses at 2 μm from a noncollinear beta-barium borate optical parametric amplifier," J. Darginavicius, N. Garejev, and A. Dubietis, Opt. Lett. **37**, 4805 (2012).

Darginavicius12b "Generation of tunable few optical-cycle pulses by visible-to-infrared frequency conversion," J. Darginavicius, G. Tamosauskas, A. Piskarskas, G. Valiulis, and A. Dubietis, Appl. Phys. B **108**, 1 (2012).

Darginavicius13 "Ultrabroadband supercontinuum and third-harmonic generation in bulk solids with two optical-cycle carrier-envelope phase-stable pulses at 2 μm," J. Darginavicius, D. Majus, V. Junka, N. Garejev, G Valiulis, A. Couairon, and A. Dubietis, Opt. **21**, 25210 (2013).

Davis96 "Writing waveguides in glass with a femtosecond laser," K. M. Davis, K. Miura, N. Sugimoto, and K. Hirao, Opt. Lett. **21**, 1729 (1996).

DeMartini67 "Self-steepening of light pulses," F. De Martini, C. H. Townes, T. K. Gustafson, and P. L. Kelley, Phys. Rev. **164**, 312 (1967).

Demirdoeven02 "Dispersion compensation with optical materials for compression of intense sub-100-fs mid-infrared pulses," N. Demirdöven, M. Khalil, O. Golonzka, and A. Tokmakoff, Opt. Lett. **27**, 433 (2002).

Deng12 "Carrier-envelope-phase-stable, 1.2 mJ, 1.5 cycle laser pulses at 2.1 μm," Y. Deng, A. Schwarz, H. Fattahi, M. Ueffing, X. Gu, M. Ossiander, T. Metzger, V. Pervak, H. Ishizuki, T. Taira, T. Kobayashi, G. Marcus, F. Krausz, R. Kienberger, and N. Karpowicz, Opt. Lett, **37**, 4973 (2012).

Dharmadhikari09 "Visualization of focusing–refocusing cycles during filamentation in BaF2," A. K. Dharmadhikari, J. A. Dharmadhikari, and D. Mathur, Appl. Phys. B **94**, 259 (2009).

Diddams98 "Amplitude and phase measurements of femtosecond pulse splitting in nonlinear dispersive media," S. A. Diddams, H. K. Eaton, A. A. Zozulya, and T. S. Clement, Opt. Lett. **23**, 379 (1998).

Dobner12 "Interferometric background reduction for femtosecond stimulated Raman scattering loss spectroscopy," S. Dobner, C. Cleff, C. Fallnich, and Petra Gross, J. Chem. Phys. **137**, 174201 (2012).

Dobryakov10 "Femtosecond pump/supercontinuum-probe spectroscopy: optimized setup and signal analysis for single-shot spectral referencing," A. L. Dobryakov, S. A. Kovalenko, A. Weigel, J. L. Perez-Lustres, J. Lange, A. Müller, and N. P. Ernsting, Rev. Science. Instrum. **81**, 113106 (2010).

Donaldson12 "High sensitivity transient infrared spectroscopy: a UV/visible transient grating spectrometer with a heterodyne detected infrared probe," P. M. Donaldson, H. Strzalka, and P. Hamm, Opt. Express **20**, 12761 (2012).

Driscoll94 "Ti:sapphire second-harmonic-pumped visible range femtosecond optical parametric oscillator," T. J. Driscoll, G. M. Gale, and F. Hache, Opt. Commun. **110**, 638 (1994).

Dubietis92 "Powerful femtosecond pulse generation by chirped and stretched pulse parametric amplification in BBO crystal," A. Dubietis, G. Jonusauskas, and A. Piskarskas, Opt. Commun. **88**, 437 (1992).

Dubietis03 "Self-guided propagation of femtosecond light pulses in water," A. Dubietis, G. Tamosauskas, I. Diomin, and A. Varanavicius, Opt. Lett. **28**, 1269 (2003).

Dubietis04a "Multiple filamentation induced by input-beam ellipticity," A. Dubietis, G. Tamosauskas, G. Fibich, and B. Ilan, Opt. Lett. **29**, 1126 (2005).

Dubietis04b "Self-reconstruction of light filaments," A. Dubietis, E. Kucinskas, G. Tamosauskas, E. Gaizauskas, M. A. Porras, and P. Di Trapani, Opt. Lett, **29**, 2893 (2004).

Dubietis06 "Measurement and calculation of nonlinear absorption associated with femtosecond filaments in water," A. Dubietis, A. Couairon, E. Kucinskas, G. Tamosauskas, E. Gaizauskas, D. Faccio, and P. Di Trapani, Appl. Phys. B **84**, 439 (2006).

Dubietis07 "Axial emission and spectral broadening in self-focusing of femtosecond Bessel beams," A. Dubietis, P. Polesana, G. Valiulis, A. Stabinis, P. Di Trapani, and A. Piskarskas, Opt. Express **15**, 4168 (2007).

Dudley06 "Supercontinuum generation in photonic crystal fiber," J. M. Dudley, G. Genty, and S. Coen, Rev. Mod. Phys. **78**, 1135 (2006).

Durand13 "Blueshifted continuum peaks from filamentation in the anomalous dispersion regime," M. Durand, K. Lim, V. Jukna, E. McKee, M. Baudelet, A. Houard, M. Richardson, A. Mysyrowicz, and A. Couairon, Phys. Rev. A **87**, 043820 (2013).

Durfee99 "Intense 8-fs pulse generation in the deep ultraviolet," C. G. Durfee, S. Backus, H. C. Kapteyn, and M. M. Murnane, Opt. Lett. **24**, 697 (1999).

Dyachenko92 "Optical turbulence: weak turbulence, condensates and collapsing filaments in the nonlinear Schr6dinger equation," S. Dyachenko, A. C. Newell, A. Pushkarev and V. E. Zakharov, Physica D **57**, 96 (1992).

Ellingson92 "High-repetition-rate femtosecond pulse generation in the blue," R. J. Ellingson, and C. L. Tang, Opt. Lett. **17**, 343 (1992).

Elsaesser91 "Femtosecond pulses in the mid-infrared generated by down-conversion of a traveling-wave dye laser," T. Elsaesser, M. C. Nuss, Opt. Lett. **16**, 411, (1991).

Emmerichs94 "Generation of high-repetition rate femtosecond pulses tunable in the mid-infrared," U. Emmerichs, H. J. Bakker, and H. Kurz, Opt. Commun. **111**, 497 (1994).

Emons10 "Sub-10-fs pulses from a MHz-NOPA with pulse energies of 0.4 μJ," M. Emons, A. Steinmann, T. Binhammer, G. Palmer, M. Schultze, and U. Morgner, Opt. Express **18**, 1191 (2010).

Erny94 "Mid-infrared difference-frequency generation of ultrashort pulses tunable between 3.2 and 4.8 μm form a compact fiber source," C. Erny, K. Moutzouris, J. Biegert, D. Kühlke, F. Adler, A. Leitenstorfer, and U. Keller, Opt. Lett. **32**, 1138 (2007).

Erny09a "High-repetition-rate optical parametric chirped pulse amplifier producing 1-μJ, sub-100-fs pulses in the mid-infrared," C. Erny, C. Heese, M. Haag, L. Gallmann, and U. Keller, Opt. Express **17**, 1340 (2009).

Erny09b "High-repetition-rate femtosecond optical parametric chirped-pulse amplifier in the mid-infrared," C. Erny, L .Gallmann, and U. Keller, Appl. Phys. B **96**, 257 (2009).

Etzold12 "The effect of solvent additives on morphology and excited-state dynamics in PCPDTBT:PCBM photovoltaic blends," F. Etzold, I. A.

Howard, N. Forler, D. M. Cho, M. Meister, H. Mangold, J. Shu, M. R. Hansen, K. Müllen, F. Laquai, J. Am. Chem. Soc. **134**, 10569 (2012).

Faccio06 "Conical emission, pulse splitting, and x-wave parametric amplification in nonlinear dynamics of ultrashort light pulses," D. Faccio, M. A. Porras, A. Dubietis, F. Bragheri, A. Couairon, and P. Di Trapani, Phys. Rev. Lett. **96**, 193901 (2006).

Faccio08a "Ultrashort laser pulse filamentation from spontaneous X-wave formation in air," D. Faccio, A. Averchi, A. Lotti, P. Di Trapani, A. Couairon, D. Papazoglou, S. Tzortzakis, Opt. Express **16**, 1565 (2008).

Faccio08b "Generation and control of extreme blue shifted continuum peaks in optical Kerr media," D. Faccio, A. Averchi, A. Lotti, M. Kolesik, J. V. Moloney, A. Couairon, and P. Di Trapani, Phys. Rev. A **78**, 033825 (2008).

Fattahi13 "Efficient, octave-spanning difference-frequency generation using few-cycle pulses in simple collinear geometry," H. Fattahi, A. Schwarz, S. Keiber, and N. Karpowicz, Opt. Lett. **38**, 4216 (2013).

Fecko04 "Generation of 45 femtosecond pulses at 3 μm with a $KNbO_3$ optical parametric amplifier," C. F. Fecko, J. J. Loparo, and A. Tokmakoff, Opt. Com. **241**, 521 (2004).

Fibich97 "Self-focusing in the presence of small time dispersion and nonparaxiality," G. Fibich and G. C. Papanicolaou, Opt. Lett. **22**, 1379 (1997).

Fibich99 "Self-focusing in perturbed and unperturbed nonlinear Schrödinger equation in critical dimensions," G. Fibich and G. Papanicolaou, SIAM J. Appl. Math **60**, 183 (1999).

Fibich00 "Critical power for self-focusing in bulk media and in hollow waveguides," G. Fibich, A. L. Gaeta, Opt. Lett. **25**, 335 (2000).

Fibich01 "Vectorial and random effects in self-focusing and in multiple filamentation," G. Fibich, B. Ilan, Physica D **157**, 112 (2001).

Fork83 "Femtosecond white-light continuum pulses," R. L. Fork, C. V. Shank, C. Hirlimann, R. Yen, and W. J. Tomlinson, Opt. Lett. **8**, 1 (1983)

Franken61 "Generation of optical harmonics," P. A. Franken, G. Weinreich, C. W. Peters, and A. E. Hill, Phys. Rev. Lett. **7**, 118 (1961).

Frey91 "Femtosecond studies of excited-state proton and deuterium transfer in benzothiazole compounds," W. Frey, F. Lärmer, and T. Elsaesser, J. Phys. Chem. **95**, 10391 (1991).

Fuji06 "Parametric amplification of few-cycle carrier envelope phase-stable pulses at 2.1 μm," T. Fuji, N. Ishii, C. Y. Teisset, X. Gu, Th. Metzger, A. Baltuska, N. Forget, D. Kaplan, A. Galvanauskas, and F. Krausz, Opt. Lett. **31**, 1103 (2006).

Fuji07 "Generation of 12 fs deep-ultraviolet pulses by four-wave mixing through filamentation in neon gas," T. Fuji, T. Horio, and T. Suzuki, Opt. Lett. **32**, 2481, (2007).

Gaeta00 "Catastrophic collapse of ultrashort pulses," A. L. Gaeta, Phys. Rev. Lett. **84,** 3582 (2000).

Gale95 "Sub-20-fs tunable pulses in the visible from an 82-MHz optical parametric oscillator," G. M. Gale, M. Cavallari, T. J. Driscoll, and F. Hache, Opt. Lett. **20**, 1562 (2014).

Gale97 ”Generation of intense highly coherent femtosecond pulses in the mid infrared,” G. M. Gale, G. Gallot, F. Hache, and R. Sander Opt. Lett **22**, 1253 (1997).

Gale98 “Femtosecond visible optical parametric oscillator,” G. M. Gale, M. Cavallari, and F. Hache

Gaydardzhiev08 “Ultrabroadband operation of a femtosecond optical parametric generator based on BiB_3O_6 in the near-IR”, A. Gaydardzhiev, I. Nikolov, I. Buchvarov, V. Petrov, and F. Noack, Opt. Express **18**, 2363 (2008).

Ghotbi06 “Efficient 1 kHz femtosecond optical parametric amplification in BiB3O6 pumped at 800 nm,” M. Ghotbi, M. Ebrahim-Zadeh, V. Petrov, P. Tzankov, and F. Noack, Opt. Express **14**, 10621 (2006).

Ghotbi08 “Tunable, high-repetition-rate, femtosecond pulse generation in the ultraviolet,” M. Ghotbi, A. Esteban-Martin, and M. Ebrahim-Zadeh, Opt. Lett. **33**, 345 (2008).

Ghotbi09 “High-energy, sub-30 fs near-IR pulses from a broadband optical parametric amplifier based on collinear interaction in BiB_3O_6,” M. Ghotbi, M. Beutler, V. Petrov, A. Gaydardzhiev, and F. Noack, Opt. Lett. **34**, 689 (2009).

Giguere09 “Pulse compression of sub-millijoule few-optical cycle infrared laser pulses using chirped mirrors,” M. Giguere, B. E. Schmidt, A. D. Shiner, M. A. Houle, H. C. Bandulet, G. Tempea, D. M. Villeneuve, J. C. Kieffer, and F. Legare, Opt. Lett. **34**, 1894 (2009).

Giordmaine62 “Mixing light beams in crystals,” J. A. Giordmaine, Phys. Rev. Lett. **8**, 19 (1962).

Giordmaine65 “Tunable coherent parametric oscillation in $LiNbO_3$ at optical frequencies,” J. A. Giordmaine and R. C. Miller, Phys. Rev. Lett. **14**, 973 (1965).

Golub90 “Optical characteristics of supercontinuum generation,” I. Golub, Opt. Lett. **15**, 305 (1990).

Golubovic98 “All-solid-state generation of 100-kHz tunable mid-infrared 50-fs pulses in type I and type II $AgGaS_2$,” B. Golubovic and M. K. Reed, Opt. Lett. **23**, 1760 (1998).

Gong13 “Observation of CEP effect via filamentation in transparent solids,” C. Gong, J. Jiang, C. Li, L. Song, Z. Zeng, Y. Zheng, J. Miao, X. Ge, Y. Deng, R. Li, and Z. Xu, Opt. Express **21**, 24120 (2013).

Gottfried97 “New aspects of the ultrafast electronic decay of malachite green in solution,” N. H. Gottfried, B. Roither, and P. O. J. Scherer, Opt. Commun. **143**, 261 (1997).

Graener91 “New spectroscopy of water using tunable picosecond pulses in the infrared,” H. Graener, G. Seifert, and A. Laubereau, Phys. Rev. Lett. **66**, 2092 (1991).

Greenfield95 “Near-transform-limited visible and near-IR femtosecond pulses from optical parametric amplification using Type II β-barium borate,” S. R. Greenfield and M. R. Wasielewski, Opt. Lett. **20**, 1394 (1995).

Gu09 “Generation of carrier-envelope-phase-stable 2-cycle 740 μJ pulses at 2.1 μm carrier wavelength,” X. Gu,1, G. Marcus, Y. Deng, T. Metzger, C. Teisset, N. Ishii, T. Fuji, A. Baltuska, R. Butkus, V. Pervak, H. Ishizuki, T. Taira, T. Kobayashi, R. Kienberger, and F. Krausz, Opt. Express **17**, 62 (2009).

Hamm93 ”Generation of tunable subpicosecond light pulses in the midinfrared between 4.5 and 11.5 µm,” P. Hamm, C. Lauterwasser, W. Zinth, Opt. Lett. **18**, 1943 (1993).

Hamm94 “Highly sensitive multichannel spectrometer for subpicosecond spectroscopy in the midinfrared,” P. Hamm, S. Wiemann, M. Zurek, and W. Zinth, Opt. Lett. **19**, 1642 (1994).

Harth12 “Two-color pumped OPCPA system emitting spectra spanning 1.5 octaves from VIS to NIR,” A. Harth, M. Schultze, T. Lang, T. Binhammer, S. Rausch, and U. Morgner, Opt. Express **20**, 3076 (2012).

Hauri04 “Generation of intense, carrier-envelope phase-locked few cycle laser pulses through filamentation,” C. P. Hauri, W. Kornelis, F. W. Helbing, A. Heinrich, A. Couairon, A. Mysyrowicz, J. Biegert, and U. Keller, Appl. Phys. B **79**, 673 (2004).

Hauri05 “Generation of intense few-cycle laser pulses through filamentation – parameter dependence,” C. P. Hauri, A. Guandalini, P. Eckle, W. Kornelis, J. Biegert, U. Keller, Opt. Express **13**, 7541 (2005).

Hauser13 “Investigations of the sensitizing-based formation of benzhydryl cations,” M. Hauser, bachelor thesis at the LMU Munich (2013).

Hayes80 “Optical detection of EPR of recombination centers in YAG,”W Hayes, M. Yamaga, D. J. Robbins, and B. Cockayne, J. Phys. C **13**, L1085 (1980).

Heese10 “Ultrabroadband, highly flexible amplifier for ultrashort midinfrared laser pulses based on aperiodically poled Mg:$LiNbO_3$,” C. Heese, L. Gallmann, U. Keller, C. R. Phillips, and M. M. Fejer, Opt. Lett. **35**, 2340 (2010).

Heisel13 “197 nm femtosecond laser-pulse duration: comparison of autocorrelation measurements,” P. C. Heisel, J. Bergmann, W. Paa, W. Triebel, T. Zeuner, and H. Stafast, Appl. Phys. B **112**, 49 (2013).

Hentschel01 “Attosecond metrology,” M. Hentschel, R. Kienberger, C. Spielmann, G. A. Reider, N. Milosevic, T. Brabec, P. Corkum, U. Heinzmann, M. Drescher, and F. Krausz, Nature **414**, 509 (2001).

Herrmann09 “Generation of sub-three-cycle, 16 TW light pulses by using noncollinear optical parametric chirped-pulse amplification,” D. Herrmann, L. Veisz, R. Tautz, F. Tavella, K. Schmid, V. Pervak, and F. Krausz, Opt. Lett. **34**, 2459 (2009).

Herrmann10 “Approaching the full octave: Noncollinear optical parametric chirped pulse amplification with two-color pumping,” D. Herrmann, C. Homann, R. Tautz, M. Scharrer, P. St. J. Russell, F. Krausz, L. Veisz and E. Riedle, Optics Express **18**, 18752 (2010).

Herrmann11a “Role of structural order and excess energy on ultrafast free charge generation in hybrid polythiophene/Si photovoltaics probed in real time by NIR broadband transient absorption,” D. Herrmann, S. Niesar, C. Scharsich, A. Köhler, M. Stutzmann, and E. Riedle, J. Am. Chem. Soc. **133**, 18220 (2011).

Herrmann11b "Photonics at the frontiers: generation of few-cycle light pulses via NOPCPA and real-time probing of charge transfer in hybrid photovoltaics,” D. Herrmann, doctoral thesis at the LMU Munich (2011), http://edoc.ub.uni-muenchen.de/13685/

Hirsch79 “Luminescent decay kinetics of malachite green on a picosecond time scale,” M. D. Hirsch and H. Mahr, Chem. Phys. Lett. **60**, 299 (1979).

Ho79 "Optical Kerr effect in liquids," P. P. Ho and R. R. Alfano, Phys. Rev. A **20**, 2170 (1979).

Holtom95 "High-repetition-rate femtosecond optical parametric oscillator–amplifier system near 3 μm," G. R. Holtom, R. A. Crowell, and X. S. Xie, J. Opt. Soc. Am. B **12**, 1723 (1995).

Homann08 "Octave wide tunable UV-pumped NOPA: pulses down to 20 fs at 0.5 MHz repetition rate," C. Homann, C. Schriever, P. Baum, and E. Riedle, Opt. Express **16**, 5746 (2008).

Homann11 "Convenient pulse length measurement of sub-20-fs pulses down to the deep UV via two-photon absorption in bulk material," C. Homann, N. Krebs and E. Riedle, Appl. Phys. B **104**, 783 (2011).

Homann12a "Optical parametric processes to the extreme: From new insights in first principles to tunability over more than 4 octaves," C. Homann, doctoral thesis at the LMU Munich (2012), http://edoc.ub.uni-muenchen.de/16104/

Homann12b "Generation of 30 fs-pulses tunable from 189 to 240 nm with an all-solid-state setup," C. Homann, P. Lang, and E. Riedle, J. Opt. Soc. Am. B **29**, 2765 (2012).

Homann13a "Direct measurement of the effective input noise power of an optical parametric amplifier," C. Homann and E. Riedle, Laser. Phys. Rev. **7**, 580 (2013).

Homann13b "Seeding of picosecond and femtosecond optical parametric amplifiers by weak single mode continuous lasers" C. Homann, M. Breuer, F. Setzpfandt, T. Pertsch, and E. Riedle, Opt. Express **21**, 730 (2013).

Hong11 "High-energy, phase-stable, ultrabroadband kHz OPCPA at 2.1 μm pumped by a picosecond cryogenic Yb:YAG laser," K. H. Hong, S. W. Huang, J. Moses, X. Fu, C. J. Lai, G. Cirmi, A. Sell, E. Granados, P. Keathley, and F. X. Kärtner, Opt. Express **19**, 15538 (2011).

Hong13 "Compact dual-crystal optical parametric amplification for broadband IR pulse generation using a collinear geometry," Z. Hong, Q. Zhang, and P. Lu, Opt. Express **21**, 9491 (2013).

Huber01 "Noncollinear optical parametric amplifiers with output parameters improved by the application of a white light continuum generated in CaF_2," R. Huber, H. Satzger, W. Zinth, and J. Wachtveitl, Opt. Commun. **194**, 443 (2001).

Ippen76 "Picosecond recovery dynamics of malachite green," E. P. Ippen, C. V. Shank, and A. Bergman, Chem. Phys. Lett. **38**, 611 (1976).

Ishii05 "Multimillijoule chirped parametric amplification of few-cycle pulses," N. Ishii, L. Turi, V. S. Yakovlev, T. Fuji, F. Krausz, A. Baltuska, R. Butkus, G. Veitas, V. Smilgevicius, R. Danielius, and A. Piskarskas, Opt. Lett. **30**, 567 (2005).

Isaienko08 "Generation of ultra-broadband pulses in the near-IR by non-collinear optical parametric amplification in potassium titanyl phosphate," O. Isaienko and E. Borguet, Opt. Express **16**, 3949 (2008).

Isaienko10 "High-repetition-rate near-infrared noncollinear ultrabroadband optical parametric amplification in $KTiOPO_4$," O. Isaienko, E. Borguet, and P. Vöhringer, Opt. Lett. **35**, 3238 (2010).

Isaienko13 "Generation of ultra-broadband pulses in the near-IR by noncollinear optical parametric amplification in potassium titanyl phosphate," O. Isaienko and E. Borguet, J. Opt. Soc. Am. B **30**, 2075 (2013).

Jiangou92 "Optical absorption properties of doped lithium niobate crystals," Z. Jiangou, Z. Shipin, X. Dingquan, W. Xiu, and X. Guanfeng, J. Phys. Condens. Matter **4**, 2977 (1992).

Johnson09 "Stable UV to IR supercontinuum generation in calcium fluoride with conserved circular polarization states," P. J. M. Johnson, V. I. Prokhorenko, and R. J. D. Miller, Opt. Express **17**, 21488 (2009).

Jukna13 "Infrared extension of femtosecond supercontinuum generated by filamentation in solid-state media," V. Jukna, J. Galinis, G. Tamosauskas, D. Majus, A. Dubietis, Appl. Phys. B, DOI 10.1007/s00340-013-5723-8 (2013).

Kaindl00 "Generation, shaping, and characterization of intense femtosecond pulses tunable from 2 to 20 μm," R. A. Kaindl, M. Wurm, K .Reimann, P. Hamm, A. M. Weiner, M. Woerner, J. Opt. Soc. Am. B **17**, 2086 (2000).

Kanai03 "Generation of subterawatt sub-10-fs blue pulses at 1–5 kHz by broadband frequency doubling," T. Kanai, X. Zhou, T. Sekikawa, S. Watanabe, and T. Togashi, Opt. Lett. **28**, 1484 (2003).

Kandidov03 "Self-transformation of a powerful femtosecond laser pulse into a white-light laser pulse in bulk optical media (or supercontinuum generation)," V. P. Kandidov, O. G. Kosareva, I. S. Golubtsov, W. Liu, A. Becker, N. Aközbek, C. M. Bowden, and S. L. Chin, Appl. Phys. B **77**, 149 (2003).

Kandidov11 "Intensity clamping in the filament of femtosecond laser radiation," V. P. Kandidov, V .Y. Fedorov, O. V. Tverskoy, O. G. Kosareva, and S. L. Chin, Quantum Elec. **41**, 382 (2011).

Kane94 "Single-shot measurement of the intensity and phase of a femtosecond UV laser pulse with frequency-resolved optical gating," D. J. Kane, A. J. Taylor, R. Trebino, and K. W. DeLong, Opt. Lett. **19**, 1061 (1994). Lapini, and R. Righini, Opt. Express **21**, 24201 (2013).

Kardas13 "The role of stimulated Raman scattering in supercontinuum generation in bulk diamond," T. M. Kardas, B. Ratajska-Gadomska, W. Gadomski, A. Lapini, and R. Righini, Opt. Express **21**, 24201 (2013).

Kasparian00 "The critical laser intensity of self-guided light filaments in air," J. Kasparian, R. Sauerbrey, and S. L. Chin, Appl. Phys. B **71**, 877 (2000).

Kasparian03 "White-light filaments for atmospheric analysis," J. Kasparian, M. Rodriguez, G. Mejean, J. Yu, E. Salmon, H. Wille, R. Bourayou, S. Frey, Y.-B. Andre, A. Mysyrowicz, R. Sauerbrey, J.-P. Wolf, and L. Wöste, Science **301**, 61 (2003).

Kasparian08 "Physics and applications of atmospheric nonlinear optics and filamentation," J. Kasparian and J. P. Wolf, Opt. Express. **16**, 466 (2008).

Kennedy95 "A first-order model for computation of laser-induced breakdown thresholds in ocular and aqueous media. I. Theory," P. K. Kennedy, IEEE. J. of Quantum. Electron. **31**, 2241 (1995).

Khalil03 "Coherent 2D IR spectroscopy: molecular structure and dynamics in solution," M. Khalil, N. Demirdöven, and A. Tokmakoff, J. Phys. Chem. A **107**, 5258 (2003).

Kintzer87 "Near-surface second-harmonic generation for autocorrelation measurements in the UV," E. S. Kintzer and C. Rempel, Appl. Phys. B **42**, 91 (1987).

Kiran10 "Filamentation without intensity clamping," P. P. Kiran, S. Bagchi, C. L. Arnold, S. R. Krishnan, G. R. Kumar, and A. Couairon, Opt. Express 18, 21504 (2010).

Kleimeier10 "Autocorrelation and phase retrieval in the UV using two-photon absorption in diamond pin photodiodes," N. F. Kleimeier, T. Haarlammert, H. Witte, U. Schühle, J. F. Hochedez, A. BenMoussa, and H. Zacharias, Opt. Express **18**, 6945 (2010).

Kobayashi00 "Tunable visible and near-infrared pulse generator in a 5 fs regime," T. Kobayashi and A. Shirakawa, Appl. Phys. B: Lasers Opt. **70**, S239 (2000).

Koechner06 "*Solid-State Laser Engineering,*" W. Koechner, (Springer, 2006).

Kolesik04a "Dynamic nonlinear X-waves for femtosecond pulse propagation in water," M. Kolesik, E. M. Wright, and J.V. Moloney, Phys. Rev. Lett. **92**, 253901 (2004).

Kolesik04b "Self-healing femtosecond light filaments," M. Kolesik and J. V. Moloney, Opt. Lett, **29**, 590 (2004).

Kolesik10 "Femtosecond filamentation in air and higher-order nonlinearities," M. Kolesik, E. M. Wright, and J. V. Moloney, Opt. Lett. **35**, 2550 (2010).

Kosareva97 "Conical emission from laser–plasma interactions in the filamentation of powerful ultrashort laser pulses in air," O. G. Kosareva, V. P. Kandidov, A. Brodeur, C. Y. Chien, and S. L. Chin, Opt. Lett. **22**, 1332 (1997).

Kosareva11 "Arrest of self-focusing collapse in femtosecond air filaments: higher order Kerr or plasma defocusing?," O. Kosareva, J.-F. Daigle, N. Panov, T. Wang, S. Hosseini, S. Yuan, G. Roy, V. Makarov, and S. L. Chin, Opt. Lett. **36**, 1035 (2011).

Kosmatov91 "Computer simulation of wave collapses in the nonlinear Schr6dinger equation," N. E. Kosmatov, V. F. Shvets and V. E. Zakharov, Physica D **52**, 16 (1991).

Kovalenko99 "Femtosecond spectroscopy of condensed phases with chirped supercontinuum probing," S. A. Kovalenko, A. L. Dobryakov, J. Ruthmann, and N. P. Ernsting, Phys. Rev. A **59**, 2369 (1999).

Kozma03 "Widely tunable sub-30 fs ultraviolet pulses by chirped sum frequency mixing," I. Z. Kozma, P. Baum, S. Lochbrunner, and E. Riedle, Opt. Express **11**, 3110 (2003).

Kozma04 "Compact autocorrelator for the online measurement of tunable 10-femtosecond pulses," I. Z. Kozma, P. Baum, U. Schmidhammer, S. Lochbrunner, and E. Riedle, Rev. Sci. Instrum. **75**, 2323 (2004).

Kraemer07 "High-power femtosecond infrared laser source based on noncollinear optical parametric chirped pulse amplification," D. Kraemer, M. L. Cowan, R. Hua, K. Franjic, R. J. D. Miller, J. Opt. Soc. Am. B 24, 813 (2007).

Kraemer08 "Temperature dependence of the two-dimensional infrared spectrum of liquid H_2O," D. Kraemer, M. L. Cowan, A. Paarmann, N. Huse, E. T. J. Nibbering, T. Elsaesser, and R. J. D. Miller, Proc. Natl. Acad. Sci. U.S.A. **105**, 437 (2008).

Krausz09 "Attosecond physics", F. Krausz and M. Ivanov, Rev. Mod. Phys. **81**, 163 (2009).

Krebs10 "Sub-20 fs pulses shaped directly in the UV by an acousto-optic programmable dispersive filter," N. Krebs, R. A. Probst, E. Riedle, Opt. Express **18**, 6164 (2010).

Krebs13 "Pulse compression of ultrashort UV pulses by self-phase modulation in bulk material," N. Krebs, I. Pugliesi, E. Riedle, Appl. Sciences **3**, 153 (2013).

Krebs13 "Pulse compression of ultrashort UV pulses by self-phase modulation in bulk material," N. Krebs, I. Pugliesi, and E. Riedle, Appl. Sci. **3**, 153 (2013).

Krueger11 "Attosecond control of electrons emitted from a nanoscale metal tip," M. Krüger, M. Schenk, and P. Hommelhoff, Nature **475**, 58 (2011).

Krylov12 "High-power thulium-doped fiber laser with intracavity dispersion management," A. A. Krylov, M. A. Chernysheva, D. S. Chernykh, A. K. Senatorov, I. M. Tupitsyn, P. G. Kryukov, and E. M. Dianov, Quantum Electron. **42**, 427 (2012).

Kutter53 "*Der Schiefspiegler*," A. Kutter, (Weichhardt, 1953).

Lagatsky10 "Femtosecond pulse operation of a Tm,Ho-codoped crystalline laser near 2 μm," A. A. Lagatsky, F. Fusari, S. Calvez, S. V. Kurilchik, V. E. Kisel, N. V. Kuleshov, M. D. Dawson, C. T. A. Brown, and W. Sibbett, Opt. Lett. **35**, 172 (2010).

Lang13 "Broadband ultraviolet-visible transient absorption spectroscopy in the nanosecond to microsecond time domain with sub-nanosecond time resolution," B. Lang, S. Mosquera-Vazquez, D. Lovy, P. Sherin, V. Markovic, and E. Vauthey, Rev. Sci. Instrum **84**, 073107 (2013).

Lee07 "Substituent effects on dynamics at conical intersections: α,β-enones," A. M. D. Lee, J. D. Coe, S. Ullrich, M. L. Ho, S. J. Lee, B. M. Cheng, M. Z. Zgierski, I. C. Chen, T. J. Martinez, and A. Stolow, J. Phys. Chem. A **111**, 11948 (2007).

Liebel14 "Sub-10-fs pulses tunable from 480 to 980 nm from a NOPA pumped by an Yb:KGW source," M. Liebel, C. Schnedermann, and P. Kukura, Opt. Lett. **39**, 4112 (2014).

Li11 "Generation of carrier-envelope phase stabilized intense 1.5 cycle pulses at 1.75 μm," C. Li, D. Wang, L. Song, J. Liu, P. Liu, C. Xu, Y. Leng, R. Li, and Z. Xu, Opt. Express **19**, 6783 (2011).

Liao13 "Five-octave-spanning supercontinuum generation in fluoride glass," M. G. Liao, W. Gao, T. Cheng, X. Xue, Z. Duan, D. Deng, H. Kawashima, T. Suzuki, and Y. Ohishi, Appl. Phys. Express **6**, 032503 (2013).

Liu02 "Intensity clamping of a femtosecond laser pulse in condensed matter," W. Liu, S. Petit, A. Becker, N. Aközbek, C. M. Bowden, and S. L. Chin, Opt. Commun **202**, 189 (2002).

Liu03a "Femtosecond laser pulse filamentation versus optical breakdown in H_2O," W. Liu, O. Kosareva, I. S. Golubtsov, A. Iwasaki, A. Becker, V. P. Kandidov, and S. L. Chin, Appl. Phys. B. **76**, 215 (2003).

Liu03b "Multiple refocusing of a femtosecond laser pulse in a dispersive liquid (methanol)," W. Liu, S. L. Chin, O. Kosareva, I. S. Golubtsov, and V. P. Kandidov, Opt. Commun. **225**, 193 (2003).

Liu05a "Background reservoir: its crucial role for long-distance propagation of femtosecond laser pulses in air," W. Liu, J. F. Gravel, F. Theberge, A. Becker, and S. L. Chin, Appl. Phys. B **80**, 857 (2005).

Liu05b "Experiment and simulations on the energy reservoir effect in femtosecond light filaments," W. Liu, F. Theberge, E. Arevalo, J. F. Gravel, A. Becker, and S. L. Chin, Opt. Lett. **30** 2602 (2005).

Liu05c "Direct measurement of the critical power of femtosecond Ti:sapphire laser pulse in air," W. Liu and S.L. Chin, Opt. Express **13**, 5750 (2005).

Lochbrunner98 "Electronic relaxation and ground-state dynamics of 1,3-Cyclohexadiene and cis-Hexatriene in ethanol," S. Lochbrunner, W. Fuss, W. E. Schmid, and K. L. Kompa, J. Phys. Chem. A **102**, 9334 (1998).

Lochbrunner00 "Ultrafast excited state proton transfer and subsequent coherent skeletal motion of 2-(2'-hydroxyphenyl)benzothiazole," S. Lochbrunner, A. J. Wurzer, and E. Riedle, J. Chem. Phys. **112**, 10699 (2000).

Lochbrunner03 "The microscopic mechanism of ultrafast excited state intramolecular proton transfer: a 30 fs study of 2-(2'-hydroxyphenyl)benzothiazole," S. Lochbrunner, A. J. Wurzer, and E. Riedle, J. Phys. Chem. A **107**, 10580 (2003).

Lohner94 "Generation of 200 femtosecond pulses tunable between 2.5 and 5.5 μm," A. Lohner, P. Kruck. W. W. Rühle, Appl. Phys. B **59**, 211 (1994).

Lorenc02 "Artifacts in femtosecond transient absorption spectroscopy," M. Lorenc, M. Ziolek, R. Naskrecki, J. Karolczak, J. Kubicki, and A. Maciejewski, Appl. Phys. B. **74**, 19 (2002).

Luther94a "Self-focusing threshold in normal dispersive media," G. G. Luther, J. V. Moloney, A. C. Newell, and E. M. Wright, Opt. Lett. **19**, 862 (1994).

Luther94b "Short-pulse conical emission and spectral broadening in normally dispersive media," G. G. Luther, A. C. Newell, J. V. Moloney, and E. M. Wright, Opt. Lett. **19**, 789 (1994).

Maiman60 "Stimulated optical radiation in ruby," T. H. Maiman, Nature **187**, 493 (1960).

Majus11a "Spatiotemporal rogue events in femtosecond filamentation," D. Majus, V. Jukna, G. Valiulis, D. Faccio, and A. Dubietis, Phys. Rev. A. **83**, 025802 (2011).

Majus13 "Statistical properties of ultrafast supercontinuum generated by femtosecond Gaussian and Bessel beams: a comparative study," D. Majus and A. Dubietis, J. Opt. Soc Am. B **30**, 994 (2013).

Maker62 "Effects of dispersion and focusing on the production of harmonics,", P. D. Maker, R. W. Terhune, M. Nisenoff, and C. M. Savage, Phys. Rev. Lett. **8**, 21 (1962).

Maker64 "Intensity-dependent changes in the refractive index of liquids," P. D. Maker, R. W. Terhune, and C. W. Savage, Phys. Rev. Lett. **12**, 507 (1964).

Maker66 "Study of optical effects due to an induced polarization third order in the electric field strength," P. D. Maker and T. W. Terhune, Phys. Rev. **148**, 990 (1966).

Manzoni04 "Ultrabroadband self-phase-stabilized pulses by difference-frequency generation," C. Manzoni, G. Cerullo, and S. De Silvestri, Opt. Lett. **29**, 2668 (2004).

Manzoni06a "Generation of high-energy self-phase-stabilized pulses by difference-frequency generation followed by optical parametric amplification," C. Manzoni, C. Vozzi, E. Benedetti, G. Sansone, S. Stagira, O. Svelto, S. De Silvestri, M. Nisoli, and G. Cerullo, Opt. Lett. **31**, 963 (2006).

Manzoni06b "Two-color pump-probe system broadly tunable over the visible and the near infrared with sub-30 fs temporal resolution," C. Manzoni, D. Polli, and G. Cerullo, Rev. Sci. Instrum. **77**, 023103 (2006).

Manzoni09 "High-repetition-rate two-color pump–probe system directly pumped by a femtosecond ytterbium oscillator," C. Manzoni, R. Osellame, M.

Marangoni, M. Schultze, U. Morgner, and G. Cerullo, Opt. Lett. **34**, 620 (2009).

Marburger75 "Self-focusing: theory," J.H. Marburger, Prog. Quantum Electron. 4, **35** (1975).

Marceau10 "Femtosecond filament induced birefringence in argon and in air: Ultrafast refractive index change," C. Marceau, S. Ramakrishna, S. Genier, T. J. Wang, Y. Chen, F. Theberge, M. Chateauneuf, J. Dubois, T. Seideman, S. L. Chin, Opt. Commun. **283**, 2732 (2010).

Mayer13 "Sub-four-cycle laser pulses directly from a high-repetition-rate optical parametric chirped-pulse amplifier at 3.4 μm," B. W. Mayer, C. R. Phillips, L. Gallmann, M. M. Fejer, and U. Keller, Opt. Lett. **38**, 4265 (2013).

Mechain04 "Long range self-channeling of infrared laser pulses in air: a new propagation regime without ionization," G. Mechain, A. Couairon, Y.-B. Andre, C. D'Amico, M. Franco, B. Prade, B, S. Tzortzakis, A. Mysyrowicz, and R. Sauerbrey, Appl. Phys. B **79**, 379 (2004).

Mechain05 "Length of plasma filaments created in air by a multi terawatt femtosecond laser", G. Mechain, C. D'Amico, Y.-B. Andre, S. Tzortzakis, M. Franco, B. Prade, A. Mysyrowicz, A. Couairon, E. Salmon, and R. Sauerbrey, Opt. Commun. **247**, 171 (2005).

Megerle09 "Sub-50 fs broadband absorption spectroscopy with tunable excitation: putting the analysis of ultrafast molecular dynamics on solid ground," U. Megerle, I. Pugliesi, C. Schriever, C. F. Sailer, and E. Riedle, Appl. Phys. B **96**, 215 (2009).

Michelberger13 "Interferometric autocorrelation in the ultraviolet utilizing spontaneous parametric down-conversion inside an enhancement cavity," P. Michelberger, R. Krischek, W. Wieczorek, A. Ozawa, and H. Weinfurter, Opt. Lett. **37**, 1223 (2013).

Michelmann96 "Frequency resolved optical gating in the UV using the electronic Kerr effect," K. Michelmann, T. Feurer, R. Fernsler, and R. Sauerbrey, Appl. Phys. B **63**, 485 (1996).

Mintova04 "Photochemistry of 2-(2¢-Hydroxyphenyl)benzothiazole encapsulated in nanosized zeolites," S. Mintova, V. De Waele, M. Hölzl, U. Schmidhammer, B. Mihailova, E. Riedle, and T. Bein, J. Phys. Chem. A **108**, 10640 (2004).

Mokhtari87 "Ultrafast conformation equilibration in triphenyl methane dyes analyzed by time resolved induced photo absorption," A. Mokhtari, L. Fini, and J. Chesnoy, J. Chem. Phys. **87**, 3429 (1987).

Mokhtari90 "Subpicosecond fluorescence dynamics of dye molecules," A. Mokhtari, A. Chebira, and J. Chesnoy, J. Opt. Soc. Am. B **7**, 1551 (1990).

Moll03 "Self-similar optical wave collapse: observation of the Townes profile," K. D. Moll, A. L. Gaeta, G. Fibich, Phys. Rev. Lett. **90**, 203902 (2003).

Morgner99 "Sub-two-cycle pulses from a Kerr-lens mode-locked Ti:sapphire laser," U. Morgner, F. X. Kärtner, S. H. Cho, Y. Chen, H. A. Haus, J. G. Fujimoto, E. P. Ippen, V. Scheuer, G. Angelow, and T. Tschudi, Opt. Lett. **24**, 411 (1999).

Moses09 "Highly stable ultrabroadband mid-IR optical parametric chirped-pulse amplifier optimized for superfluorescence suppression," J. Moses, S. W. Huang, K. H. Hong, O. D. Mücke, E. L. Falcao-Filho, A. Benedick, F. O.

Ilday, A. Dergachev, J. A. Bolger, B. J. Eggleton, and F. X. Kärtner, Opt. Lett. **34**, 1639 (2009).

Moses12 "Fully efficient adiabatic frequency conversion of broadband Ti:sapphire oscillator pulses," J. Moses, H. Suchowski, and F. X. Kärtner, Opt. Lett. **37**, 1589 (2012).

Muecke09a "Scalable Yb-MOPA-driven carrier-envelope phasestable few-cycle parametric amplifier at 1.5 μm," O. D. Mücke, D. Sidorov, P. Dombi, A. Pugzlys, A. Baltuska, S. Alisauskas, V. Smilgevicius, J. Pocius, L. Giniunas, R. Danielius, and N. Forget, Opt. Lett. **34**, 118 (2009).

Muecke09b "Self-compression of millijoule 1.5 μm pulses," O. D. Mücke, S. Alisauskas, A. J. Verhoef, A. Pugzlys, A. Baltuska, V. Smilgevicius, J. Pocius, L. Giniunas, R. Danielius, and N. Forget Opt. Lett. **34**, 2498 (2009).

Muerk95 "Exciton and recombination processes in VAG crystals," V. Mürk and N. Yaroshevich, J. Phys. Condens. Matter **7**, 5857 (1995).

Myers95 "Quasi-phase-matched optical parametric oscillators in bulk periodically poled $LiNbO_3$," L. E. Myers, R. C. Eckardt, M. M. Fejer, R. L. Byer, W. R. Rosenberg, and J. W. Pierce, J. Opt. Soc. Am B **12**, 2102 (1995).

Nagura02 "Generation and characterization of ultrafast white-light continuum in condensed media," C. Nagura, A. Suda, H. Kawano, M. Obara, and K. Midorikawa, Appl. Opt. **41**, 3735 (2002).

Nabekawa03 "Broadband sum frequency mixing using noncollinear angularly dispersed geometry for indirect phase control of sub-20-femtosecond UV pulses," Y. Nabekawa and K. Midorikawa, Opt. Express **11**, 324 (2003).

Nagasawa99 "Solvent dependence of ultrafast ground state recovery of the triphenylmethane dyes, brilliant green and malachite green," Y. Nagasawa, Y. Ando, and T. Okada, Chem. Phys. Lett. **312**, 161 (1999).

Nagasawa02 "Ultrafast excited state deactivation of triphenylmethane dyes," Y. Nagasawa, Y. Ando, D. Kataoka, H. Matsuda, H. Miyasaka, and T. Okada, J. Phys. Chem. A **106**, 2024 (2002).

Nakayama11 "Ultrafast nonradiative decay of electronically excited states of malachite green: ab initio calculations," A. Nakayama and T. Taketsugu, J. Phys. Chem. A **115**, 8808 (2011).

Nebel91 "External frequency conversion of cw mode-locked Ti:Al_2O_3 laser radiation," A. Nebel and R. Beigang, Opt. Lett. **16**, 1729 (1991).

Nelson87 "Femtosecond time-resolved observation of coherent molecular vibrational motion," K. A. Nelson and L. R. Williams, Phys. Rev. Lett., 58, 745 (1987). Nibbering96 "Conical emission from self-guided femtosecond pulses in air," E. T. J. Nibbering, P. F. Curley, G. Grillon, B. S. Prade, M. A. Franco, F. Salin, A. Mysyrowicz, Opt. Lett. **21**, 62 (1996).

Nibbering04 "Ultrafast vibrational dynamics of hydrogen bonds in the condensed phase," E. T. J. Nibbering and T. Elsaesser, Chem. Rev. **104**, 1887 (2004).

Nikolov07 "Ultrabroadband continuum amplification in the near infrared using BiB_3O_6 nonlinear crystals pumped at 800 nm," I. Nikolov, A. Gaydardzhiev, I. Buchvarov, P. Tzankov, F. Noack, and V. Petrov, Opt. Lett. **32**, 3342 (2007).

Nillon14 "Two MHz tunable non collinear optical parametric amplifiers with pulse durations down to 6 fs," J. Nillon, O. Crégut. C. Bressler, and S. Haacke, Opt. Express **22**, 14964 (2014).

Nishioka93 "Single-shot UV autocorrelator that uses a two-photon-induced photo acoustic signal in water," H. Nishioka, M. Ishiguro, T. Kawasumi, K. I. Ueda, and H. Takuma, Opt. Lett. **18**, 45 (1993).

Noack99 "Laser-induced plasma formation in water at nanosecond to femtosecond time scales: calculation of thresholds, absorption coefficients, and energy density," J. Noack and A. Vogel, IEEE J. of Quantum. Electron. **35**, 1156 (1999).

Nomura12 "Phase-stable sub-cycle mid-infrared conical emission from filamentation in gases," Y. Nomura, H. Shirai, K. Ishii, N. Tsurumachi, A. Voronin, A. Zheltikov, and T. Fuji, Opt. Express 20, 24741 (2012).

Pellegrino82 "Features of the photochemically active state surface of azobezene," F. Pellegrino, A. Dagen, and R. R. Alfano, Chem. Phys. **67**, 1982 (1982).

Pelletier12 "Mid-infrared optical parametric amplifier based on a LGSe crystal and pumped at 1.6 μm," E. Pelletier, A. Sell, A. Leitenstorfer, and R. J. D. Miller, Opt. Express **20**, 27456 (2012).

Petrov95 "Tunable femtosecond optical parametric-amplifier in the midinfrared with narrow-band seeding," V. Petrov and F. Noack, J. Opt. Soc. Am. B **12**, 2214 (1995).

Petrov96 "Mid-infrared femtosecond optical parametric amplification in potassium niobate," V. Petrov and F. Noack, Opt. Lett. **21**, 1576 (1996).

Petrov97 "Seeded femtosecond optical parametric amplification in the mid-infrared spectral region above 3 μm," V. Petrov, F. Noack, R. Stolzenberger, Appl. Opt. **36**, 1164 (1997)

Petrov98 "Vacuum ultraviolet application of $Li_2B_4O_7$ crystals: Generation of 100 fs pulses down to 170 nm," V. Petrov, F. Rotermund, F. Noack, R. Komatsu, T. Sugawara, and S. Uda, J. Appl. Phys. **84**, 5887 (1998).

Petrov01 "Generation of high-power femtosecond light pulses at 1 kHz in the mid-infrared spectral range between 3 and 12 μm by second-order nonlinear processes in optical crystals," V. Petrov, F. Rotermund, F. Noack, J. Opt. A: Pure. Appl. Opt. 3, R1 (2001).

Petrov07 "High-power femtosecond optical parametric amplification at 1 kHz in BiB_3O_6 pumped at 800 nm," V. Petrov, F. Noack, P. Tzankov, M. Ghotbi, M. Ebrahim-Zadeh, I. Nikolov, I. Buchvarov, Opt. Exp. **15**, 556 (2007).

Piel06 "Sub-20 fs visible pulses with 750 nJ energy from a 100-kHz NOPA," J. Piel, E. Riedle, L. Gundlach, R. Ernstorfer, and R. Eichberger, Opt. Lett. 31, 1289 (2006).

Pilles14 "Mechanism of the decay of thymine triplets in DNA single strands," B. M. Pilles, D. B. Bucher, L. Liu, P. Clivio, P. Gilch, W. Zinth, and W. J. Schreier, J. Phys. Chem. Lett. **5**, 1616 (2014).

Polli07 "High-time-resolution pump-probe system with broadband detection for the study of time-domain vibrational dynamics," Rev. Sci. Instrum **78**, 10318 (2007).

Polli10 "Effective temporal resolution in pump-probe spectroscopy with strongly chirped pulses," D. Polli, D. Brida, S. Mukamel, G. Lanzani, and G. Cerullo, Phys. Rev. A **82**, 053809 (2010).

Plass92 "Surface Sum-Frequency Mixing for Auto- and Cross-Correlation of Ultrashort UV and IR Pulses," W. Plass, H. Rottke, W. Heuer, G. Eichhorn, and H. Zacharias, Appl. Phys. B **54**, 199 (1992).

Rairoux00 "Remote sensing of the atmosphere using ultrashort laser pulses," P. Rairoux, H. Schillinger, S. Niedermeier, M. Rodriguez, F. Ronneberger, R. Sauerbrey, B. Stein, D. Waite, C. Wedekind, H. Wille, L. Wöste, C. Ziener, Appl. Phys. B **71**, 573 (2000).

Ranka96 "Observation of pulse splitting in nonlinear dispersive media," J. K. Ranka, R. W. Schirmer, and A. L. Gaeta, Phys. Rev. Lett. **77**, 3783 (1996).

Ranka98 "Breakdown of the slowly varying envelope approximation in the self-focusing of femtosecond pulses," J. K. Ranka and A. L. Gaeta, Opt. Lett. **23**, 534 (1998).

Ranka00 "Visible continuum generation in air–silica microstructure optical fibers with anomalous dispersion at 800 nm," J. K. Ranka, R. S. Windeler, and A. J. Stentz, Opt. Lett. **25**, 25 (2000).

Reed94 "Widely tunable femtosecond optical parametric amplifier at 250 kHz with a Ti:sapphire regenerative amplifier," M. K. Reed, M. K. Steiner-Shepard, and D. K. Negus, Opt. Lett. **19**, 1855 (1994).

Reed95a "Microjoule-energy ultrafast optical parametric amplifiers," M. K. Reed, M. K. Steiner-Shepard, M. S. Armas, and D. K. Negus, J. Opt. Soc. Am B **12**, 2229 (1995).

Reed95b "30-fs pulses tunable across the visible with a 100-kHz Ti:sapphire regenerative amplifier," M. K. Reed, M. S. Armas, M. K. Steiner-Shepard, and D. K. Negus, Opt. Lett. **20**, 605 (1995).

Riedel13 "Long-term stabilization of high power optical parametric chirped-pulse amplifiers," R. Riedel, M. Schulz, M. J. Prandolini, A. Hage, H. Hoeppner, T. Gottschall, J. Limpert, M. Drescher, and F. Tavella, Opt. Express **21**, 28987 (2013).

Riedle00 "Generation of 10 to 50 fs pulses tunable through all of the visible and the NIR," E. Riedle, M. Beutter, S. Lochbrunner, J. Piel, S. Schenkl, S. Spörlein, and W. Zinth, Appl. Phys. B **71**, 457 (2000).

Rodriguez04 "Kilometer-range nonlinear propagation of femtosecond laser pulses," M. Rodriguez, R. Bourayou, G. Mejean, J. Kasparian, J. Yu, E. Salmon, A. Scholz, B. Stecklum, J. Eislöffel, U. Laux, A. P. Hatzes, R. Sauerbrey, L. Wöste, J.-P. Wolf, Phys. Rev. E **69**, 036607 (2004).

Rohwetter10 "Laser induced water condensation in air," P. Rohwetter, J. Kasparian, K. Stelmaszczyk, Z. Hao, S. Henin, N. Lascoux, W. M. Nakaema, Y. Petit, M. Queißer, R. Salame, E. Salmon, L. Wöste, and J. P. Wolf, Nat. Photon. **4**, 451 (2010).

Rosker86 "Femtosecond relaxation dynamics of large molecules," M. J. Rosker, F. W. Wise, and C. L. Tang, Phys. Rev. Lett. **57**, 321 (1986).

Ross97 "The prospects for ultrashort pulse duration and ultrahigh intensity using optical parametric chirped pulse amplifiers," I. N. Ross, P. Matousek, M. Towrie, A. J. Langley, and J. L. Collier, Opt. Commun. **144**, 125 (1997).

Rotermund99 "Femtosecond noncollinear parametric amplification in the mid-infrared," F. Rotermund, V. Petrov, and F. Noack, Opt. Com. **169**, 183 (1999).

Rothenberg92a "Pulse splitting during self-focusing in normally dispersive media," J. E. Rothenberg, Opt. Lett. **17**, 583 (1992).

Rothenberg92b "Space-time focusing: breakdown of the slowly varying envelope approximation in the self-focusing of femtosecond pulses," J. E. Rothenberg, Opt. Lett. **17**, 1340 (1992).

Russell03 "Photonic crystal fibers," P. St. J. Russell, Science **299**, 358 (2003).

Russell06 "Photonic-crystal fibers," P. St. J. Russell, J. Lightwave Technol. **24**, 4729 (2006).

Saeki07 "Stroboscopic picosecond pulse radiolysis using near-ultraviolet-enhanced femtosecond continuum generated by CaF_2," A. Saeki, T. Kozawa, K. Okamoto, and S. Tagawa, Jpn. J. Appl. Phys. **46**, 407 (2007).

Saliminia05 "Ultra-broad and coherent white light generation in silica glass by focused femtosecond pulses at 1.5 μm," A. Saliminia, S. L. Chin, and R. Vallee, Opt. Express **13**, 5731 (2005).

Scheller14 "Externally refuelled optical filaments," M. Scheller, M. S. Mills, M. A. Miri, W. Cheng, J. V. Moloney, M. Kolesik, P. Polynkin, and D. N. Christodoulides, Nature Photonics **8**, 297 (2014).

Schmidt10 "Compression of 1.8 μm laser pulses to sub two optical cycles with bulk material," B. E. Schmidt, P. Bejot, M. Giguere, A. D. Shiner, C. Trallero-Herrero, E. Bisson, J. Kasparian, J. P. Wolf, D. M. Villeneuve, J. C. Kieffer, P. B. Corkum, and F. Legare, Appl. Phys. Lett. **96**, 121109 (2010).

Schmidt11 "CEP stable 1.6 cycle laser pulses at 1.8 μm," B. E. Schmidt, A. D. Shiner, P. Lassonde, J. C. Kieffer, P. B. Corkum, D. M. Villeneuve, and F. Legare, Opt. Express **19**, 6858 (2011).

Schriever08 "Tunable pulses from below 300 to 970 nm with durations down to 14 fs based on a 2 MHz ytterbium-doped fiber system," C. Schriever, S. Lochbrunner, P. Krok, and E. Riedle, Opt. Lett. **33**, 192 (2008).

Schroeder04 "Visualization of the evolution of multiple filaments in methanol," H. Schroeder and S. L. Chin, Opt. Commun. **234**, 399 (2004).

Schroeder06 "Self-steepening is an abrupt process," H. Schroeder, S. A. Hosseini, Q. Luo, S. L. Chin, Opt. Commun, **266**, 302 (2006).

Schulz11 "Yb:YAG Innoslab amplifier: efficient high repetition rate subpicosecond pumping system for optical parametric chirped pulse amplification," M. Schulz, R. Riedel, A. Willner, T. Mans, C. Schnitzler, P. Russbueldt, J. Dolkemeyer, E. Seise, T. Gottschall, S. Hädrich, S. Duesterer, H. Schlarb, J. Feldhaus, J. Limpert, B. Faatz, A. Tünnermann, J. Rossbach, M. Drescher, and F. Tavella, Opt. Lett. **36**, 2456 (2011).

Schwarz12 "Active stabilization for optically synchronized optical parametric chirped pulse amplification," A. Schwarz, M. Ueffing, Y Deng, X. Gu, H. Fattahi, T. Metzger, M. Ossiander, F. Krausz, and R. Kienberger, Opt. Express **20**, 5557 (2012).

Sailer13a "A comprehensive microscopic picture of the benzhydryl radical and cation photo-generation and interconversion through electron transfer," C. F. Sailer, B. P. Fingerhut, S. Thallmair, C. Nolte, J. Ammer, H. Mayr, I. Pugliesi, R. de Vivie-Riedle, and E. Riedle, Chem. Phys. Chem. **14**, 1423 (2013).

Sailer13b "Photo-generation and reactions of benzhydryl cations and radicals: a complex sequence of mechanisms from femtoseconds to microseconds," C. F. Sailer and E. Riedle, Pure Appl. Chem. **85**, 1487 (2013).

Seifert94 ”Solid-state laser system for the generation of midinfrared femtosecond pulses tunable from 3.3 to 10 μm,” F. Seifert, V. Petrov, M. Woerner, Opt. Lett. **19**, 2009 (1994).

Shen75 “Self-focusing: experimental,” Y.R. Shen, Prog. Quantum Electron. **4**, 1 (1975).

Shen11 “Two-color deep-ultraviolet 40-fs pulses based on parametric amplification at 100 kHz,” H. Shen, S. Adachi, T. Horio, and T. Suzuki, Opt. Express **19**, 22637 (2011).

Shimizu67 “Frequency broadening in liquids by a short light pulse,” F. Shimizu, Phys. Rev. Lett. **19**, 1097 (1967).

Shirakawa98a “Noncollinearly phase-matched femtosecond optical parametric amplification with a 2000 cm^{-1} bandwidth,” A. Shirakawa and T. Kobayashi, Appl. Phys. Lett. **72**, 147 (1998).

Shirakawa98b “Pulse-front-matched optical parametric amplification for sub-10-fs pulse generation tunable in the visible and near infrared,” A. Shirakawa, I. Sakane, and T. Kobayashi, Opt. Lett. **23**, 1292 (1998).

Shirakawa99 “Sub-5-fs visible pulse generation by pulse-front-matched noncollinear optical parametric amplification,” A. Shirakawa, I. Sakane, M. Takasaka, T. Kobayashi, Appl. Phys Lett. **74**, 2268 (1999).

Silva12a “Multi-octave supercontinuum generation from mid-infrared filamentation in a bulk crystal,” F. Silva, D. R. Austin, A. Thai, M. Baudisch, M. Hemmer, D. Faccio, A. Couairon, and J. Biegert, Nature Commun. **3**, 807 (2012).

Silva12b “High-average-power, carrier-envelope phase-stable, few-cycle pulses at 2.1 μm from a collinear BiB_3O_6 optical parametric amplifier,” F. Silva, P. K. Bates, A. Esteban-Martin, M. Ebrahim-Zadeh, and J. Biegert, Opt. Lett. **37**, 933 (2012).

Smetanina12a “Femtosecond laser pulse filamentation under anomalous dispersion in fused silica. Part 1. Numerical investigation,” E. O. Smetanina, V. O. Kompanets, S. V. Chekalin, and V.P. Kandidov, Quantum. Elec. **42**, 913 (2012).

Smetanina12b “Femtosecond laser pulse filamentation under anomalous dispersion in fused silica. Part 2. Experiment and physical interpretation,” E. O. Smetanina, V. O. Kompanets, S. V. Chekalin, and V.P. Kandidov, Quantum. Elec. **42**, 920 (2012).

Smetanina13a “Anti-Stokes wing of femtosecond laser filament supercontinuum in fused silica,” E. O. Smetanina, V. O. Kompanets, S. V. Chekalin, A. E. Dormidonov, and V. P. Kandidov, Opt. Lett. **38**, 16 (2013).

Smetanina13b “Light bullets from near-IR filament in fused silica,” E. O. Smetanina, V. O. Kompanets, A. E. Dormidonov, S. V. Chekalin, and V. P .Kandidov, Laser Phys. Lett. **10**, 105401 (2013).

Stanislauskas14 “Table top TW-class OPCPA system driven by tandem femtosecond Yb:KGW and picosecond Nd:YAG lasers,” T. Stanislauskas, R. Budriunas, R. Antipenkov, A. Zaukevicius, J. Adamonis, A. Michailovas, L. Giniunas, R. Danielius, A. Piskarskas, and A. Varanavicius, Opt. Express **22**, 1865 (2014).

Steinmann06 “Generation of few-cycle pulses directly from a MHz-NOPA,” A. Steinmann, A. Killi, G. Palmer, T. Binhammer, and Uwe Morgner, Opt. Express **14**, 10627 (2006).

Stelmaszczyk04 "Long-distance remote laser-induced breakdown spectroscopy using filamentation in air," K. Stelmaszczyk, P. Rohwetter, G. Mejean, J. Yu, E. Salmon, J. Kasparian, R. Ackermann, J. P. Wolf, and L. Wöste, Appl. Phys. Lett. **85**, 3977 (2004).

Stolen78 "Self-phase-modulation in silica optical fibers," R. H. Stolen and C. Lin, Phys. Rev. A **17**, 1448 (1978).

Sun10 "Pulse duration dependent nonlinear propagation of a focused femtosecond laser pulse in fused silica, "Q. Sun, H. Asahi, Y. Nishijima, N. Murazawa, K. Ueno, and H. Misawa, Opt. Express **18**, 24495 (2010).

Takeushi09 "Coherent nuclear wavepacket motions in ultrafast excited-state intramolecular proton transfer: sub-30-fs resolved pump-probe absorption spectroscopy of 10-hydroxybenzo[h]quinoline in solution," S. Takeuchi and T. Tahara, J. Phys. Chem. A **109**, 10199 (2009).

Tanigawa11 "Optical parametric amplifier pumped at 266 nm toward ultrashort near-ultraviolet gigawatt pulses," T. Tanigawa, K. Yamane, N. Karasawa, and M. Yamashita, Jpn. J. Appl. Phys. **50**, 072701 (2011).

Tautz12 "Structural correlations in the generation of polaron pairs in low-bandgap polymers for photovoltaics," R. Tautz, E. Da Como, T. Limmer, J. Feldmann, H. J. Egelhaaf, E. von Hauff, V. Lemaur, D. Beljonne, S. Yilmaz, I. Dumsch, S. Allard, and U. Scherf, Nat. Commun. **3**, 970 (2012).

Teleki10 "Microscopic model for the higher-order nonlinearity in optical filaments," A. Teleki, E. M. Wright, and M. Kolesik, Phys. Rev. A **82**, 065801 (2010).

Trebino97 "Measuring ultrashort laser pulses in the time-frequency domain using frequency-resolved gating," R. Trebino, K. W. De Long, D. N. Fittinghoff, J. N. Sweetser, M. A. Krumbügel, B. A. Richman, and D. J. Kane, Rev. Sci. Instrum. **68**, 3277 (1997).

Thai11 "Sub-250-mrad, passively carrier–envelope-phase-stable mid-infrared OPCPA source at high repetition rate," A. Thai, M. Hemmer, P. K. Bates, O. Chalus, and J. Biegert, Opt. Lett. **36**, 3918 (2011).

Theberge06 "Tunable ultrashort laser pulses generated through filamentation in gases," F. Theberge, N. Aközbek, W. Liu, A. Becker, and S. L. Chin, Phys. Rev. Lett **97**, 023904 (2006).

Thomas12 "Generating few-cycle pulses for nanoscale photoemission easily with an erbium-doped fiber laser," S. Thomas, R. Holzwarth, and P. Hommelhoff, Opt. Express **20**, 13663 (2012).

Thomas13 "Probing of optical near-fields by electron rescattering on the 1 nm scale," S. Thomas, M. Krüger, M. Förster, M. Schenk, and P. Hommelhoff, Nano. Lett. **13**, 4790 (2013).

Trippenbach97 "Dynamics of short-pulse splitting in dispersive nonlinear media," M. Trippenbach and Y. B. Band, Phys. Rev. A **56**, 4242 (1997).

Tzankov02 "Broadband optical parametric amplification in the near UV-VIS," P. Tzankov, I. Buchvarov, and T. Fiebig, Opt. Commun. **203**, 107 (2002).

Tzankov06 "300 μJ noncollinear optical parametric amplifier in the visible at 1 kHz repetition rate," P. Tzankov, J. Zheng, M. Mero, D. Polli, C. Manzoni, and G. Cerullo, Opt. Lett. **31**, 3629 (2006).

Tzortzakis01 "Self-guided propagation of ultrashort IR pulses in fused silica," S. Tzortzakis, L. Sudrie, M. Franco, B. Prade, A. Mysyrowicz, and A. Couairon, Phys. Rev. Lett. **87**, 213902 (2001).

Tzortzakis06 "Long-range filamentary propagation of subpicosecond ultraviolet laser pulses in fused silica," S. Tzortzakis, D. G. Papazoglou, and I. Zergioti, Opt. Lett. **31**, 796 (2006).

Uryupina10 "Few-cycle optical pulse production from collimated femtosecond laser beam filamentation," D. Uryupina, M. Kurilova, A. Mazhorova, N. Panov, R. Volkov, S. Gorgutsa, O. Kosareva, A. Savelev, and S. L. Chin, J. Opt. Soc. Am. B **27**, 667 (2010).

Vardeni81 "Picosecond coherence coupling in the pump and probe technique," Z. Vardeny and J. Tauc, Opt. Commun. **39**, 396 (1981).

Vincotte04 "$\chi 5$ susceptibility stabilizes the propagation of ultrashort laser pulses in air," A. Vincotte and L. Berge, Phys. Rev. A **70**, 061802 (2004).

Vlasov89 "Three dimensional wave collapse in the nonlinear Schrödinger equation model," S. N. Vlasov, L. V. Piskunova, and V. I. Talanov, Sov. Phys. JETP **68**, 1125 (1989).

Vogel99 "Energy balance of optical breakdown in water at nanosecond to femtosecond time scales," A. Vogel, J. Noack, K. Nahen, D. Theisen, S. Busch, U. Parlitz, D. X. Hammer, G. D. Noojin, B. A. Rockwell, and R. Birngruber, Appl. Phys. B. **68**, 271 (1999).

Vozzi06 "High-energy, few-optical-cycle pulses at 1.5 μm with passive carrier-envelope phase stabilization," C. Vozzi, G. Cirmi, C. Manzoni, E. Benedetti, F. Calegari, G. Sansone, S. Stagira, O. Svelto, S. De Silvestri, M. Nisoli, and G. Cerullo, Opt. Express **14**, 10109 (2006).

Vozzi07 "Millijoule-level phase-stabilized few-optical-cycle infrared parametric source," C. Vozzi, F. Calegari, E. Benedetti, S. Gasilov, G. Sansone, G. Cerullo, M. Nisoli, S. De Silvestri, and S. Stagira, Opt. Lett. **32**, 2957 (2007).

Wan13 "High power 2 μm femtosecond fiber laser," P. Wan, L. M. Yang, and J. Liu, Opt. Express **21**, 21374 (2013).

Watanabe03 "Wavelength division with three-dimensional couplers fabricated by filamentation of femtosecond laser pulses," W. Watanabe, T. Asano, K. Yamada, K. Itoh, J. Nishii, Opt. Lett. **28**, 2491 (2003).

Werhahn11 "Dynamics of weak, bifurcated, and strong hydrogen bonds in lithium nitrate trihydrate," J. C. Werhahn, S. Pandelov, S. S. Xantheas, and H. Iglev, J. Phys. Chem. Lett. **2**, 1633 (2011).

Willhelm97 "Sub-20-fs pulses tunable across the visible from a blue-pumped single-pass noncollinear parametric converter," T. Wilhelm, J. Piel, and E. Riedle, Opt. Lett. **22**, 1494 (1997).

Wilson97 "Ultrafast rainbow: tunable ultrashort pulses from a solid-state kilohertz system," K. R. Wilson and V. V. Yakovlev, J. Opt. Soc. Am. B **14**, 444 (1997).

Wise02 "The hunt for light bullets – spatiotemporal solitons," F. Wise and P. Di Trapani, Opt. Phot. News **2**, 28 (2002).

Witte06 "A source of 2 terawatt, 2.7 cycle laser pulses based on noncollinear optical parametric chirped pulse amplification" S. Witte, R. T. Zinkstok, A. L. Wolf, W. Hogervorst, W. Ubachs, and K. S. E. Eikema, Opt. Express **14**, 8168 (2006).

Witte12 "Ultrafast optical parametric chirped-pulse amplification," S. Witte and K. S. E. Eikema, IEEE J. Sel. Top. Quant. Electron. **18**, 296 (2012).

Wouterson97 "Femtosecond mid-IR pump-probe spectroscopy of liquid water: evidence for a two-component structure," S. Woutersen, U. Emmerichs, and H. J. Bakker, Science **278**, 658 (1997).

Xing93 "Conical emission by four-photon parametric generation by using femtosecond laser pulses," Q. Xing, K. M. Yoo, and R. R. Alfano, Appl. Opt. **32**, 2087 (1993).

Yablonovitch72 "Avalanche ionization and the limiting diameter of filaments induced by light pulses in transparent media," E. Yablonovitch, N. Bloembergen, Phys. Rev. Lett. **29**, 907 (1972).

Zanni01 "Two-dimensional infrared spectroscopy: a promising new method for the time resolution of structures," M. T. Zanni and R. M. Hochstrasser, Curr. Opin. Struct. Biol. **11**, 516 (2001).

Zhao09 "Sub-15fs ultraviolet pulses generated by achromatic phase-matching sum-frequency mixing," B. Zhao, Y. Jiang, K. Sueda, N. Miyanaga, and T. Kobayashi, Opt. Express **17**, 17711 (2009).

Zhou10 "1 W average-power 100 MHz repetition-rate 259 nm femtosecond deep ultraviolet pulse generation from ytterbium fiber amplifier," X. Zhou, D. Yoshitomi, Y. Kobayashi, and K. Torizuka: Opt. Lett. **35**, 1713 (2010).

Ziegler98 "Tunable 50-fs pulse generation in the 250-310-nm ultraviolet range," L. D. Ziegler, J. Morais, Y. Zhou, S. Constantine, M. K. Reed, M. K. Steiner-Shepard, and D. Lommel, IEEE J. Quant. Elect. 34, 1758 (1998).

Zinth11 "The Long Journey to the laser and its rapid development after 1960," W. Zinth, A. Laubereau, and W. Kaiser, Eur. Phys. J. H 153, 181 (2011).

Ziolek04 "Some temporal and spectral properties of femtosecond supercontinuum important in pump–probe spectroscopy," M. Ziolek, R. Naskrecki, and J. Karolczak, Opt. Commun. **241**, 221 (2004).

Zozulya98 "Investigations of nonlinear femtosecond pulse propagation with the inclusion of Raman, shock, and third-order phase effects," A. A. Zozulya, S. A. Diddams, and T S. Clement, Phys. Rev. A **58**, 3303 (1998).

Part II

Appendix A0: Considerations on intensity calculations

The relation between full width half maximum (FWHM) and the beam radius w

During bulk continuum generation extremely high intensities occur. Most of the used pump pulses initially have a Gaussian shaped spatial and temporal intensity profile. Therefore, the proper determination of the peak intensity from measured parameter is not straight forward. When characterizing the pulses, often FWHM is measured to determine the pulse duration and its size. This value determines the diameter of the profile, where the intensity has dropped to 50%. A radically symmetric distribution is implicitly assumed. The more important measure for the electric field and hence the intensity is the beam radius w. At this radius, the electric field decreases to 1/e and hence the intensity to $1/e^2$ (13.7% level). The 13.7% level is in good agreement with the visual appearance of laser pulses. The correlation between both values for the spatial intensity profile in polar coordinates is evaluated.

$$E_0(r) \sim e^{-\left(\frac{r}{w}\right)^2}$$

$$I(r) = \frac{c\varepsilon_0 n}{2} \cdot \left| E_0(r)^2 \right| = I_{max} e^{-2\left(\frac{r}{w}\right)^2}$$

for $r_{50\%} = FWHM/2$

$$\frac{I}{I_{max}} = 0.5 = e^{-2\left(\frac{r_{50\%}}{w}\right)^2}$$

$$\ln 0.5 = -2\left(\frac{r_{50\%}}{w}\right)^2$$

$$w = r_{50\%} \cdot \sqrt{\frac{2}{\ln 2}}$$

$$w = FWHM \cdot \frac{1}{\sqrt{2 \ln 2}}$$

and as rule of thumb

$$w \approx FWHM \cdot 0.85$$

The peak intensity of Gaussian laser pulses

Since the intensity is not constant for Gaussian pulses in space and time, the use of the peak intensity (I_{peak}) is an adequate mean to describe the pulses. However, its calculation is not straight forward, if the total energy of the pulse and the FWHM in time and space have been measured. The full intensity of a Gaussian pulse in space and time is

$$I(r,t) = I_{peak} \cdot e^{\frac{-t^2}{\left(\frac{\tau_{FWHM}}{2\sqrt{\ln 2}}\right)^2} + -2\left(\frac{r}{w}\right)^2}$$

Integrating this expression over time and space leads to the pulse energy E

$$E = \int_{-\infty}^{+\infty}\int_{0}^{+\infty}\int_{0}^{2\pi} I_{peak} \cdot e^{\frac{-t^2}{\left(\frac{\tau_{FWHM}}{2\sqrt{\ln 2}}\right)^2} + \frac{-r^2}{\left(\sqrt{\frac{1}{2}}w\right)^2}} \cdot r \cdot \delta\theta\, \delta r\, \delta t$$

$$E = I_{peak} \times \int_{0}^{+\infty}\int_{0}^{2\pi} e^{\frac{-r^2}{\left(\sqrt{\frac{1}{2}}w\right)^2}} \cdot r \cdot \delta\theta\, \delta r \times \int_{-\infty}^{+\infty} e^{\frac{-t^2}{\left(\frac{\tau_{FWHM}}{2\sqrt{\ln 2}}\right)^2}} \delta t$$

$$E = I_{peak} \times 2\pi \times \left[-\frac{1}{4}w^2 \cdot e^{\frac{-r^2}{\left(\sqrt{\frac{1}{2}}w\right)^2}} \right]_0^{+\infty} \times \sqrt{\pi} \cdot \frac{\tau_{FWHM}}{2\sqrt{\ln 2}}$$

$$E = I_{peak} \cdot 2\pi \cdot \frac{1}{4}w^2 \cdot \sqrt{\pi} \cdot \frac{\tau_{FWHM}}{2\sqrt{\ln 2}}$$

$$E = I_{peak} \cdot w^2\pi \cdot \tau_{FWHM} \cdot \frac{\sqrt{\pi}}{4\sqrt{\ln 2}}$$

$$I_{peak} = \frac{E}{\tau_{FWHM} \cdot \pi w^2} \times \frac{4\sqrt{\ln 2}}{\sqrt{\pi}} = \frac{E}{\tau_{FWHM} \cdot w^2} \times \frac{4\sqrt{\ln 2}}{\pi^{3/2}}$$

When using the beam diameter, FWHM the peak intensity is

$$I_{peak} = \frac{E}{\tau_{FWHM} \cdot FWHM^2} \times \frac{8(\ln 2)^{3/2}}{\pi^{3/2}} = \frac{E}{\tau_{FWHM} \cdot FWHM^2} \cdot 0.829...$$

Since many considerations do not take into account the Gaussian distributions explicitly, an effective intensity I_{eff} can be considered [A15]:

$$I_{eff} = \frac{E}{\tau_{FWHM} \cdot \left(\frac{FWHM}{2} \right)^2 \pi}$$

The pulse is described as a disc in the transversal directions and a flat-top of temporal length τ_{FWHM} and according longitudinal length. It follows that

$$I_{eff} = \frac{\sqrt{\pi}}{2(\ln 2)^{3/2}} \cdot I_{peak} \approx 1.536 \cdot I_{peak}$$

$$I_{peak} \approx 0.651 \cdot I_{eff}$$

The simplification strongly overestimates the intensity. This is of considerable importance for the calculations of the gain in parametric amplifiers. In this thesis, all intensities are peak intensities since this is the only unambiguous value.

Appendix A1

Femtosecond continuum generation in bulk laser host materials with sub-μJ pump pulses

M. Bradler, P. Baum, and E. Riedle

Appl. Phys. B **97**, 561 - 574 (2009)

Reprinted with kind permission from Springer Publishing

Appl Phys B (2009) 97: 561–574
DOI 10.1007/s00340-009-3699-1

Applied Physics B
Lasers and Optics

Femtosecond continuum generation in bulk laser host materials with sub-μJ pump pulses

M. Bradler · P. Baum · E. Riedle

Received: 24 April 2009 / Revised version: 3 August 2009 / Published online: 21 August 2009
© Springer-Verlag 2009

Abstract We report a comprehensive investigation of femtosecond continuum generation in single crystals of several common laser host materials. The absolute spectral energy density, pulse-to-pulse stability, pump threshold, and beam profile are studied in dependence on the focusing conditions, crystal thickness, pump pulse energy, and pump wavelength (775–1600 nm). Continuum generation is shown at repetition rates of up to 80 MHz and for pump pulse durations of up to 350 fs. In yttrium aluminum garnet (YAG), yttrium vanadate (YVO_4), gadolinium vanadate ($GdVO_4$), and potassium-gadolinium tungstate (KGW) thresholds below 50 nJ, plateau-like visible and infrared spectra, and higher infrared photon flux as compared to conventional materials like sapphire are found. We discuss the particular advantages of these materials for application in parametric amplification, femtosecond spectroscopy, and carrier-envelope phase stabilization.

PACS 42.25.Dd · 42.65.Jx · 42.65.Ky · 42.65.Re

M. Bradler (✉) · P. Baum · E. Riedle
Lehrstuhl für BioMolekulare Optik,
Ludwig-Maximilians-Universität München, Oettingenstraße 67,
80538 Munich, Germany
e-mail: Maximilian.Bradler@physik.lmu.de
Fax: +49-89-21809202

P. Baum
e-mail: peter.baum@lmu.de
Fax: +49-89-21809202

E. Riedle
e-mail: riedle@physik.lmu.de
Fax: +49-89-21809202

1 Introduction

When an ultrashort laser pulse is focused into an optically nonlinear transparent medium, conditions can be found to achieve extreme spectral broadening [1–3]. Many media have been found suitable for continuum generation (also called supercontinuum or white-light generation) and the multitude of investigations is comprehensively summarized in [4]. The concurrent process of filamentation is excellently documented in two recent reviews [5, 6].

For picosecond pulses, long monomode fibers are suitable since they allow for a large integral nonlinearity and the inherent dispersion is comparable to the pulse length. For extremely high intensities as rendered by focused mJ level femtosecond pulses, even gases offer enough nonlinearity [7]. To guide the optical pulse for distances far larger than typical Rayleigh lengths, hollow fiber waveguides are successfully used [8] and the resulting spectral broadening is sufficient for compression of the output to well below 5 fs [9]. Similar spectral broadening and compression has also been demonstrated if filamentation in a gas cell is used and thereby the complexity of input coupling into the hollow fiber is avoided [10].

Photonic crystal fibers with their freely selectable zero dispersion point can produce extremely wide spectra from nJ pump pulses of tens of femtosecond duration. These continua initially were the basis of the celebrated frequency comb [11, 12] before octave spanning lasers became readily available. However, for longer pulses and other unfavorable conditions the output pulses show imperfect coherence, energy fluctuations, and highly structured spectral energy densities [13–15].

Bulk materials of a few millimeters of thickness have been shown to render continua with a very broad and smooth spectrum, high temporal and spatial coherence, and very

high stability [16–18]. With respect to gases, bulk materials require less input energy but also yield less output. The extreme pulse to pulse energy stability and the high amount of coherence nevertheless render bulk continua a most valuable source of broadband radiation for spectroscopy and laser technology. Because of these favorable properties, continua from bulk materials have replaced the continua generated in liquids. The latter typically show an exponential decrease of the spectral intensity with increasing distance to the pump wavelength [19].

Brodeur and Chin have studied the obtainable width of the continuum in a variety of bulk materials [20, 21]. In particular, they concentrated towards the short wavelength side and provided a convincing model of the important role of the band gap for the continuum width. Of all the materials that render a spectrum with significant contributions in the UV, only CaF_2 has been found to be useable in routine applications [22–24]. Even at low repetition rates in the kHz regime the disk has to be moved to avoid accumulative damage [25, 26]. Rotation leads to a depolarization [27] and therefore a purely translation motion is to be preferred [28]. If UV output is not required, a much more favorable and commonly used bulk material for continuum generation is sapphire [16, 17, 29, 30]. It is widely used for seeding optical parametric amplifiers [31–34], for pump-supercontinuum probe experiments [35–39], and more advanced transient spectroscopy [40, 41], for carrier-envelope-stabilization [42], and other emerging applications.

Despite this widespread use of femtosecond continua from bulk materials, only limited studies exist on alternative materials, which could well outperform sapphire in selected aspects and the optimum operational conditions [43, 44]. Triggered by two recent reports that briefly mentioned alternative materials [45, 46], we studied continuum generation in several promising bulk materials and present investigations of the spectral energy density, pulse-to-pulse stability, pump energy thresholds, and continuum beam profiles in dependence on the focusing conditions, crystal thickness, pump pulse energy, and pump wavelength.

Single crystals of yttrium aluminum garnet (YAG), yttrium vanadate (YVO_4), gadolinium vanadate ($GdVO_4$), and potassium-gadolinium tungstate (KGW) were obtained commercially. These materials are common laser host crystals and were chosen here because of their high damage threshold and good crystalline quality [47–56]. They differ strongly in the nonlinear indexes of refraction [57–59], and we thus expect large variations in the continuum generation. All crystals except YAG with its cubic crystalline structure were cut oriented along the optical axis to avoid birefringence. They were undoped, not coated, and used at room temperature. All experiments were performed with clean single filaments and none of the investigated crystals showed damage after many days of operation at the reported input parameters.

2 Measurements and experimental results

Typical spectra of continua generated in bulk materials are shown in Figs. 1b and 1c. They extend from the blue end of the visible spectrum well into the infrared, spanning about two octaves. To the short wavelength side a broad and flat plateau is seen that is the attractive feature of continua generated in bulk materials. Both the continua from gases and from microstructured fibers have a much more modulated spectrum and this spectral modulation transfers to pronounced satellites in the temporal domain.

Contrary to the situation found for microstructured fiber supercontinuum generation [60], in most reported studies on bulk materials no absolute calibration of the spectral energy density can be found. For any selected wavelength the spectral energy density is, however, directly proportional to the number of photons per spectral interval and pulse. The number of photons is crucially important for seeding of optical parametric amplifiers and for the shot noise limit in measurements utilizing the continuum. We therefore devised a

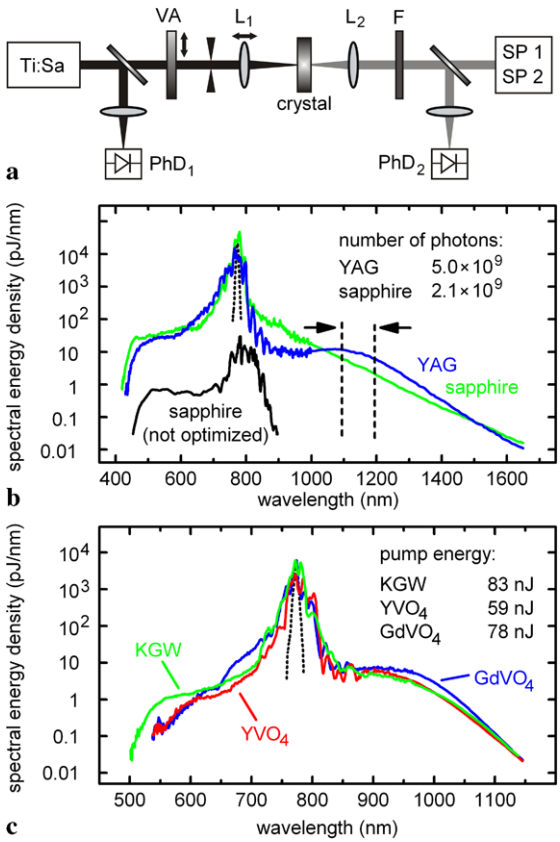

Fig. 1 (**a**) Setup for the quantitative analysis of the continuum generation by 775 nm pulses (*dotted black lines* in (**b**) and (**c**), not to scale). (**b**) Black: femtosecond continuum from 3 mm sapphire with conventional pumping conditions [31] (not to scale, shifted for clarity). *Green*: 3 mm sapphire with the optimizations described in the text. *Blue*: 4 mm YAG with improved photon density in the infrared region. (**c**) Continua generated in KGW (*green*), YVO_4 (*red*) and $GdVO_4$ (blue) crystals (all 4 mm)

simple scheme how to calibrate the spectral energy density and used this setup for all the studies reported in this work. In addition, one finds that only rarely the infrared part of the continuum is reported. Since the long wavelength part of the continuum is, however, of great practical interest, we also covered this part with the same care.

2.1 Measurement of absolute spectral energy densities

In most of the experiments reported in this work continuum generation was initiated by pump pulses from a Ti:sapphire regenerative amplifier, which delivers pulses of 150 fs duration at a center wavelength of 775 nm with a repetition rate of 1 kHz in a collimated beam with a diameter of 5 mm (CPA 2001; Clark MXR, Inc.). The setup is shown in Fig. 1a. Pulses with energies in the range of 50 to 1000 nJ—adjusted by a variable density attenuator (VA)—were focused with a lens (L1) into the respective crystal to start continuum generation. An iris just in front of the lens was used to crop the outer parts of the beam profile, in order to adjust the effective beam diameter at the lens, and thus the numerical aperture of the arrangement. The importance of the numerical aperture for continuum generation has been emphasized in a recent investigation [61]. The white-light is than collimated with a 30 mm lens (L2).

For coverage of the full spectral range from the blue to the near infrared, two different spectrographs were required. For 200 to 1100 nm we used a grating-based spectrograph with a silicon CCD detector (SP1, HR 2000+; Ocean Optics, Inc.[1]), for 900 to 1700 nm a grating-based spectrograph with a thermo-electrically cooled InGaAs detector array was applied (SP2, NIR 256 Standard InGaAs Array; Control Development, Inc. (see footnote 1)). The spectral sensitivity of both spectrographs, including the fiber for input coupling, was calibrated by recording the spectra of a black-body radiation source at a temperature of 1800 K (HL-2000-CAL; Ocean Optics, Inc. (see footnote 1)).

The total energy of the continuum pulses was measured by a power meter (FieldMax II TO, Coherent, with the thermal sensor head PS10Q (see footnote 1)). Because of the power meter's large sensitive area of ∼80 mm^2, no focusing was necessary to collect and record all spatial components. In principle, this already allows to scale the measured spectra to absolute power densities. However, this procedure is not very accurate for the weak parts of the continuum where much less than 1% of the total energy is contained. We therefore selected the two weak regions (<700 nm and >850 nm) with short- and long-pass filters (Calflex-X; LINOS Photonics GmbH, and RG850; Schott AG; F in Fig. 1a (see footnote 1)) and focused each on a large active area integrating photodiode module (PDI-400-UV; Becker&Hickel GmbH; PhD1 in Fig. 1a (see footnote 1)). To avoid saturation, calibrated neutral density filter were sometimes used to attenuate the pulses. The photodiode was calibrated relative to the power meter with well-defined pump pulses at 775 nm and by taking the photodiode's wavelength-dependent response into account. The pulse-to-pulse stability of the pump and the different spectral parts of the supercontinuum were also measured with the photodiodes PhD_1 and PhD_2. This procedure then allowed to precisely scale the measured weak parts of the continuum spectra to absolute units of pJ/nm. We estimate that the absolute spectral energy densities are accurate to about 10%.

2.2 Spectral energy densities of investigated materials

An overview of the continua of the investigated materials is depicted in Figs. 1b and 1c and they are compared to the standard material sapphire. The spectrum of the pump pulses at 775 nm (not to scale) is plotted as dotted black line. The solid black trace shows the spectrum of a typical single-filament continuum from a 3 mm sapphire plate, like it is used for noncollinear parametric amplifiers [31]. This spectrum was not absolutely calibrated and is offset in the figure for clarity. As in many experiments [16, 17], a 30 mm lens was used for focusing into the sapphire plate. One can clearly see the typical features that make continua from bulk materials so attractive for numerous applications: The spectrum is very smooth and extends from below 500 nm up to the near infrared. A plateau of almost constant energy extends throughout the visible from ∼500 to 700 nm. In the infrared part, however, the spectral energy density decreases exponentially (−10 dB/100 nm).

With the optimizations for the focusing conditions that we report in Sect. 2.5, it was possible to dramatically increase the visible and infrared output from the same sapphire plate (green curve). The infrared side of the pump still shows an exponential decay, but its cutoff is significantly extended (only −5 dB/100 nm decrease). The energy density in the visible is increased to about 30 pJ/nm, somewhat higher than the value of 10 pJ/nm reported by others [34].

For comparison, the blue trace in Fig. 1b depicts the spectrum of a continuum generated in 4 mm of YAG. Only 415 nJ of pump energy were used to generate this spectrum. In the visible, the spectral characteristics are very similar, but, surprisingly, the YAG continuum exhibits also a plateau in the region from 800 to 1200 nm. Such a plateau is of high interest for applications, not only because of the improved energy density, but also for use in broadband spectroscopy (see Sect. 3.3). In the range from 1100 to 1200 nm,

[1] Mention of vendor names and model numbers is for technical communication purposes only and does not necessarily imply recommendation of these units, nor does it imply that comparable units from another vendor would be any less suitable for this application.

the number of photons (5.0×10^9 per pulse) is significantly higher than the one generated from the sapphire continuum (2.1×10^9 per pulse). Note that both continua were optimized for stable and intense visible and infrared output. Like in the sapphire continuum, the spectrum also decreases exponentially towards the infrared edge but later and with an increased energy density. The high infrared power makes YAG a very promising material for seeding of parametric amplifiers and for spectroscopic use.

Figure 1c shows continua from the other investigated materials, KGW (green), YVO_4 (red), and $GdVO_4$ (blue), again in comparison to the pump spectrum (dotted black, not to scale). All crystals had a length of 4 mm. Of these materials, only KGW shows a pronounced plateau in the visible region but all show one in the infrared. Notably, the pump power required to obtain stable single-filaments from these materials is more than one order of magnitude lower as needed for sapphire or YAG. This makes these materials highly attractive for continuum generation with high repetition rate lasers of lower single-pulse energy, such as long-cavity oscillators [62] or cavity-dumped lasers [63]. They will allow to extend the spectral coverage, to shorten the pulse duration to the few-fs regime, or use these lasers in broadband spectroscopy. Of the low-threshold materials shown in Fig. 1c, KGW is most suited for visible output, $GdVO_4$ for infrared coverage, and YVO_4 for the lowest required pump power. Already 39 nJ are sufficient to start continuum generation, only 59 nJ pump pulses are needed for optimized spectral extent.

The observed blue edge of the continuum, the transmission cutoff and the derived band gap are summarized for all crystals in Table 1. As previously documented [21], the amount of anti-Stokes broadening as given by the photon energy difference between the blue edge and the pump increases monotonically with the band gap. Contrary to the older report we do, however, find clear continuum generation to the short wavelength side even for those three crystals that have a band gap of significantly less than three times the pump photon energy (KGW, $GdVO_4$, YVO_4).

2.3 Pump energy threshold and dependence

Continuum generation in bulk media is a highly nonlinear process, which is closely linked to self-focusing and filamentation [21, 64]. To understand the material dependence of the threshold for continuum generation, we consider the required power to initiate self-focusing of the incoming pump pulses. Self-focusing leads to a largely increased intensity that can reinforce various nonlinear processes like self-steepening, formation of a shock wave, filamentation, and self-phase modulation. In particular the filamentation results in a largely increased length of the nonlinear interaction. Filamentation is a balance between positive nonlinear contribution to the refractive index and a negative contribution from multiphoton-induced ionization. From a delicate combination of all nonlinear processes efficient continuum generation results. Experimentally the connection between self-focusing and continuum generation can be seen by bare eye. As the pump energy is increased a dramatic change of the output divergence from the crystal is seen at the same level as the appearance of white-light.

For a continuous Gaussian beam, the characteristic power P_{SF} for self-focusing is given by [65, 66]

$$P_{SF} \approx \frac{0.15\lambda_0^2}{n_0 n_2} \tag{1}$$

with the center wavelength λ_0 and the linear and nonlinear refractive index n_0 and n_2. For convenience the values reported in the literature for the various crystals are summarized in Table 1. Note that P_{SF} is a power and does not, within the applied approximations, depend on the details of the focusing conditions or intensity [65]. A minimum intensity, however, is required to have significant self-focusing happening within a given crystal thickness. Experimentally this intensity is reached by sufficiently tight focusing of the pump. The expected critical power is plotted as dotted line in Fig. 2 in dependence on the materials' characteristic indices of refraction [57–59]. The measured values for the minimum power that is required to just start continuum generation are plotted as squares. The good agreement shows that

Table 1 Summary of relevant properties of the crystals used for continuum generation. For reference CaF_2 is included since it produces the continuum reaching the furthest into the UV

	CaF_2	Sapphire	YAG	KGW	$GdVO_4$	YVO_4
n_0	1.4278[a]	1.7555[a]	1.815[a]	2.01[b]	1.972[c]	1.96[b]
$n_2[10^{-16}\ cm^2/W]$	1.24[d]	3.1[e]	6.9[f]	10[b]	15	15[b]
Continuum cut off [nm]	280	440	470	500	550	550
Transmission cut off [nm]	135[a]	190[a]	210[a]	315	345	345
Deduced band gap [eV]	9.2	6.5	5.9	3.9	3.6	3.6

[a] [47],[b] [59], [c] [53], [d] [54], [e] [57], [f] [58], all other values determined in this work

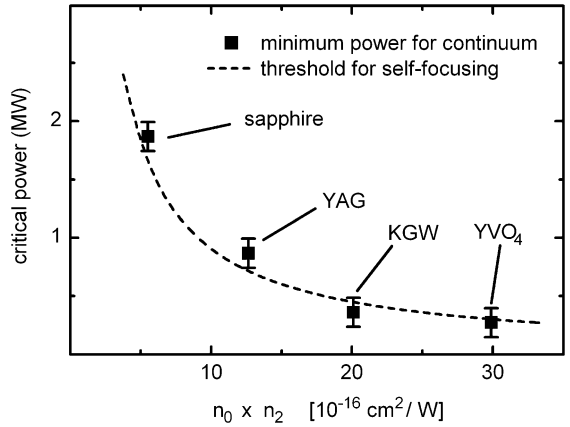

Fig. 2 Measured threshold power for continuum generation (*squares*) and calculated critical power for self-focusing (*dotted line*) for the investigated crystals

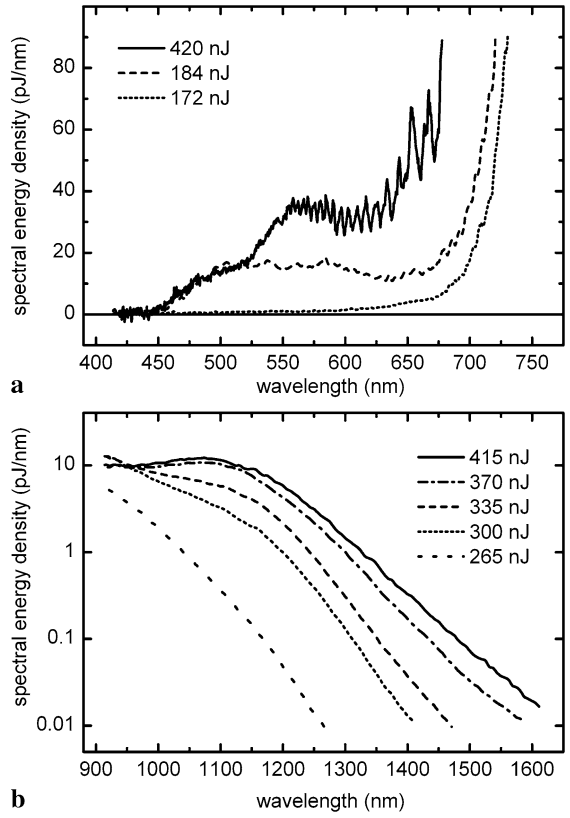

Fig. 3 Continuum spectra generated in 4 mm YAG for increasing pump pulse energies. (**a**) Visible part of the spectrum (linear scale); (**b**) infrared part of the spectrum (logarithmic scale)

self-focusing is indeed the initial step of continuum generation in bulk media, and explains why significantly lower thresholds for the pump pulse energy as compared to sapphire are sufficient for the newly investigated materials.

For pump energies slightly above the threshold a stable continuum is obtained. To characterize the pump energy dependence of the continuum output, we performed measurements with a 4 mm-long YAG crystal. YAG was chosen because of its high infrared output. Figure 3 shows the changes in the output, when the pump pulse energy is gradually increased while keeping all other settings identical. The visible part of the spectrum is shown in Fig. 3a. At a pump pulse energy of 172 nJ (dotted line) almost no spectral broadening is observed. A slight increase to a pump energy of 184 nJ (dashed line) results already in continuum generation and the appearance of a pronounced plateau in the visible. For pump energies up to 415 nJ, this part of the spectrum stays quite similar. At pump pulse energies of 420 nJ (solid line) and above pronounced spectral wiggles show up that are reminiscent of the spectral modulations typically found in fibers due to of self-phase modulation [67]. However, the observed spacing decreases with increasing distance from the pump, contrary to the reported situation in fibers. As an alternative explanation one might therefore look at possible refocusing of the filament [68] and continuum generation at two distinct locations within the crystal. These continua could be temporally separated at the crystal output and lead to spectral beating. At pump pulse energies of larger than 450 nJ the single filament breaks up and instable, speckle-like, and colorful patterns are observed, which are believed to be the result of interference between transversally neighboring filaments.

The corresponding behavior at the infrared side of the pump wavelength is depicted in Fig. 3b. Starting from pump pulse energies of 265 nJ, spectral broadening also sets in the infrared, initially as an exponentially decreasing spectral energy density (dotted line). With increasing pump energy, the infrared output increases significantly and a plateau-like spectrum starts to develop at 300 nJ. At pump energies of 420 nJ and above significant spectral modulation is also seen on the infrared side of the pump. Multifilament breakup occurs at pump energies greater than 450 nJ. The appearance of a spectral plateau in the infrared region has not been reported for conventional materials such as sapphire but is clearly evident here, as well as in KGW, YVO_4, and $GdVO_4$ (see Fig. 1c).

The threshold behavior and pump energy dependence of the continuum generation in YAG is shown in Fig. 4. We plotted the integrated pulse energy of the visible part of the continuum (450–600 nm, open circles) and the integrated infrared part of the continuum (850–1600 nm, squares) for different pump pulse energies. In the visible, the threshold at ∼160 nJ is very pronounced and the continuum energy stays largely constant up to the filament breakup above 420 nJ. In contrast, the infrared part of the continuum increases in energy continuously until breakup. Although the two plateaus on the two spectral sides of the pump wavelength seem to have similar characteristics, they differ in their power dependence. Gaeta predicted such a differing behavior and connected it to the generation of the visible part with the shock

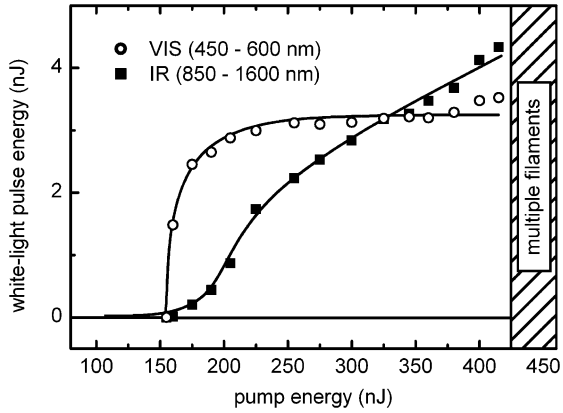

Fig. 4 Integrated visible (*circles*) and infrared (*squares*) energy content of continua generated in 4 mm YAG for increasing pump pulse energy

wave at the trailing edge of the splitting pulse and the infrared part to the leading edge [64].

2.4 Filament size and continuum divergence

To gain some insight into the nonlinear pulse propagation inside the crystal and the dimension of the filament, we performed some auxiliary measurements. For YAG the white-light expands to a $1/e^2$ diameter (intensity) of about 2 mm at 50 mm distance from the crystal output surface. From this value we can estimate the effective diameter of the filament to 20 µm. We find a variation of this value between 18 and 25 µm depending on the exact focusing condition and the detection wavelength. For sapphire we find values between 14 and 20 µm. All values are lower limits because of the assumption of diffraction limited propagation. A value of 8 µm was reported for a similar, yet not in-depth described measurement for sapphire pumped by 100 kHz 800 nm pulses [17].

In extensive investigations Chin and coworkers performed two types of measurements to characterize the filament formation and propagation. In a first type of measurement they weakly focused pump pulses with 1.1 times the self-focusing threshold into thick samples and positioned the resulting focus in the vicinity of the output surface [21]. The emerging light was then imaged onto a detector with a magnification of 29.2. Filament diameters of close to 10 µm were observed for all materials with continuum output. To understand this large difference to our values, we performed a closely related measurement and indeed found about 10 µm diameter at 550 nm increasing toward the red. We therefore have to look for an explanation that can reconcile these differences.

The primary aim of all the optimization presented in this work is the generation of a most useful continuum. We therefore typically work at twice the threshold and focus roughly onto the front surface. As demonstrated in the second series of measurements of Chin and coworkers, this positions the first focus early in the sample and a filament of 0.5 to 1 mm length develops [68]. After this length the beam expands but less than predicted by diffraction. Eventually it refocuses at sufficient pump energy. With the help of an autocollimation telescope which images the beam inside the crystal from a side view we observe that the filamentation sets in close to the output surface at the threshold and moves nearer to the front surface under typical operational conditions. Such a situation was also documented in transversal imaging experiments in fused silica that were supported by extensive simulations [69]. Our observation of a decreasing brightness in the latter part of the crystal indicates that no refocusing occurs but a slight widening of the channel. The free space propagation would then be determined from this larger diameter at the output surface. The continuum generation is most likely localized to the beginning of the filament [21, 64]. Indeed we and others [23] have repeatedly observed that the dispersion of the continuum amounts to significant propagation within the crystal.

We want to emphasize that the actual diameter of the filament is of primary interest for the elucidation of the filamentation and continuum generation mechanisms. For the spectroscopic use and as seed for parametric amplifiers mainly the divergence is important as it determines the proper design of the beam guiding optics.

2.5 Focusing conditions and crystal thickness

In order to investigate the influence of the focusing conditions on the obtained continua, we varied the focal length of the focusing lens for continuum generation in a 4 mm long YAG crystal. For all investigated focal lengths, we iteratively optimized the pump energy, adjusted the effective beam diameter with the iris and varied the location of the focus, in order to achieve optimum output of all spectral parts of the continuum. Figure 5a shows the result of different focal lengths. For $f = 30$, 50, and 80 mm, pump pulse energies of 345, 360, and 415 nJ were found to be optimal. The amount of generated white-light increases with the focal length.

According to a previous investigation, the numerical aperture (NA) is the decisive geometric parameter for continuum generation [61]. To a good approximation we find that the optimum input NA is equal to the NA of the emerging continuum. In the approximation of a Gaussian beam profile, it should not matter whether a small or large focal length is used as long as the NA is preserved by suitable adjustment of the beam diameter and by keeping the total pump energy constant. Also no change in the generated continuum should result for equal pump energy and NA. Experimentally we find significant deviations from this expectation.

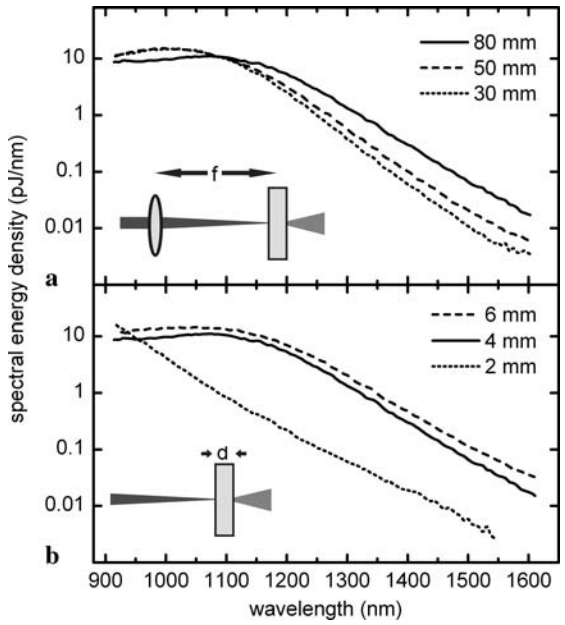

Fig. 5 (**a**) Infrared part of the continuum spectrum from 4 mm YAG for different focal lengths f. (**b**) Infrared part of continua generated in 2 (*dotted line*), 4 (*solid line*), and 6 mm (*dashed line*) YAG crystals

We believe that this discrepancy is due to the hard aperturing by the iris. The first diffraction ring has a phase shift of π and will likely interfere with the central Airy disk at the focus inside the crystal. The details of this interaction will depend on the aperture size and the resulting angles and as a consequence could well lead to the observed behavior. The envisioned scenario is similar to the demonstrated stabilization of single optical filaments in gases by the use of a circular phase mask [70]. Interestingly we do not find a changed threshold for filamentation and also not for the breakup into multifilaments.

From a practical point of view the experimental findings give a guideline for the design of an optimized continuum generator. If spectral components far from the pump are needed, a long focal length lens and more input energy have to be used. If little pump energy is available, a short focal length should be employed.

After self-focusing and filament formation, the beam travels as a narrow channel for several millimeters within the crystal. To investigate the influence of this propagation on the obtained spectra, we studied YAG crystals of different length. For each crystal we reoptimized the pump pulse energy for maximum output in the infrared region of the spectrum. Figure 5b shows the results: For an increasing crystal length of 2 (dotted line), 4 (solid line), and 6 mm (dashed line), the spectrum shows largely increasing energy density in the infrared spectral region. The necessary pump pulse energy for best possible output decreases from 510 nJ for 2 mm, over 415 nJ for 4 mm, to 380 nJ for the 6 mm long crystal. These observations clearly indicate that the nonlinear propagation of the spectrally broadened pulse adds to the spectral energy density even so all spectral components are already generated early on. A plateau is only possible to obtain for crystal lengths larger than 2 mm but lengths of 4 or 6 mm do not yield significantly different output. A threshold of the minimum propagation distance to enter the regime of plateau-like spectra is therefore evident. For YAG, a crystal length on the order of 4 mm seems to be a good choice, as a compromise between a stable and intense plateau-like output spectrum and best-possible reduction of the chirp (dispersion) that is the result of the propagation within the crystal.

2.6 Beam profile

Single-filament continua show, by eye, smooth and circular beam profiles. The generation process, however, involves highly nonlinear propagation in a very narrow filament. It is therefore essential to investigate the spatio-spectral focusing behavior when imaging the continuum towards an experiment.

To account for the large divergence of the white-light that is the result of the narrow filament, we used a lens system, consisting of an $f = 30$ mm and an $f = 300$ mm lens, to image the continuum from a YAG crystal towards a focus at about 300 mm distance with a tenfold magnification (see Fig. 6a). A spectrally narrow part around 675 nm was selected with an interference filter. A CCD camera (DMK 21F04; The Imaging Source Europe GmbH (see footnote 1)) was used to record the beam profile for different points along the beam direction. Figure 6b shows the radial beam profiles for different distances from the focusing lens. Before the focus, the beam consists of a central part with an almost Gaussian shape, surrounded by a halo (see left inset in Fig. 6b; 15 mm diameter at the $f = 30$ mm lens). This beam profile is always obtained with sufficient high pump energy. It does not depend on the profile of the pump pulse focused into the YAG crystal. For demonstration, we blocked the right half of the pump beam at constant energy and found that the white-light still emerged round and homogeneous including the halo.

The appearance of the ring around the main beam [71, 72] is correlated with the existence of strong infrared components in the beam center and is absent for low pump pulse energies. Even with the bare eye a reddish ring can be seen. At a distance of 280 to 330 mm from the focusing lens some radial structures appear which result from the interference between the main beam and the ring. A similar interference pattern has also been reported for filamentation in air [73]. In addition, the beam profile shows some azimuthal asymmetry, which is closely related to the generation of the halo. However, at a distance slightly behind the theoretical focus at 300 mm, the beam profile becomes smooth and narrow,

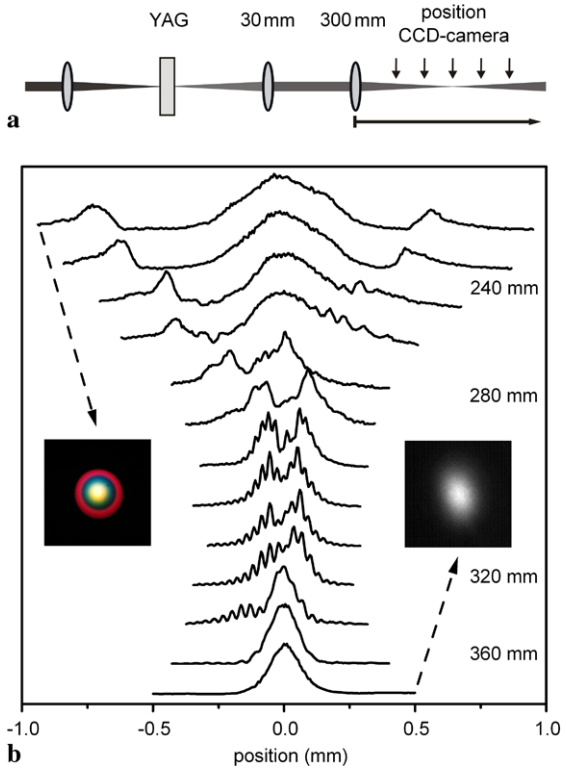

Fig. 6 Beam profile of continuum pulses from 4 mm YAG measured along the propagation axis in the vicinity of the focus. (**a**) Setup for analysis. (**b**) Radial beam profile of a 5 nm wide spectral part around 675 nm at various distances from the $f = 300$ mm focusing lens. The insets show the characteristic shapes before (*left*) and shortly after (*right*) the focus

with a diameter of ∼200 µm (see right inset). The infrared part of the continuum shows a very similar behavior but less energy is contained in the halo as compared to the central part. The clean beam waist at a few mm behind the theoretical focal position is well suited for experimental applications.

By blocking away the halo, no significant energy loss in the different spectral parts were observed, whereas the beam profile before, in and after the focus has a Gaussian shape for all spectral parts. To the best of our knowledge this beneficial effect of suppressing the reddish halo has not been discussed in the literature. It would be interesting to investigate the influence on the beam quality of white-light seeded optical parametric amplifiers. Both in our own work [29, 31] and in early reports [17, 18] it was discussed that operation of the amplifier behind the pump and white-light focus appears to improve the performance.

2.7 Stability and spectral fluctuations

Stability and pulse-to-pulse fluctuations are one of the central aspects in the choice of continuum sources for applications. Especially for broadband spectroscopy or in optical parametric amplification, the quality of the probe or seed continuum directly determines the overall stability of the arrangement. We therefore investigated the pulse-to-pulse fluctuations of a continuum from a YAG crystal by recording the energy for each single pulse in the 1 kHz train. To obtain correlations between different spectral parts and also the pump, we simultaneously employed three photodiode modules.

Figure 7a shows typical results: The black trace depicts the normalized pulse energy fluctuations $E_k/\bar{E}$ of the pump pulses k for 4500 consecutive shots. The energy fluctuations of the visible (450–700 nm) and infrared (850–1100 nm) parts of the continuum are shown in green and orange. A clear correlation is evidenced by synchronous behavior of all traces. The fluctuations of the visible parts of 1.1% (RMS) are very similar to the noise of the pump pulses of 0.9% (RMS). The fluctuations of the infrared part amount to 1.3% (RMS).

Figures 7b and 7c show density plots of the noise correlation (binned into a 75 × 75 histogram) between the pump pulse energy and the visible or infrared continuum parts. The presence of tilted ellipses is the result of the mentioned correlation. The tilts of only slightly above one show that energy fluctuations in the pump pulses are not significantly amplified during continuum generation. This demonstrates that the outcome of the large spectral broadening in YAG quite deterministically depends on the pump conditions and no statistical processes are involved.

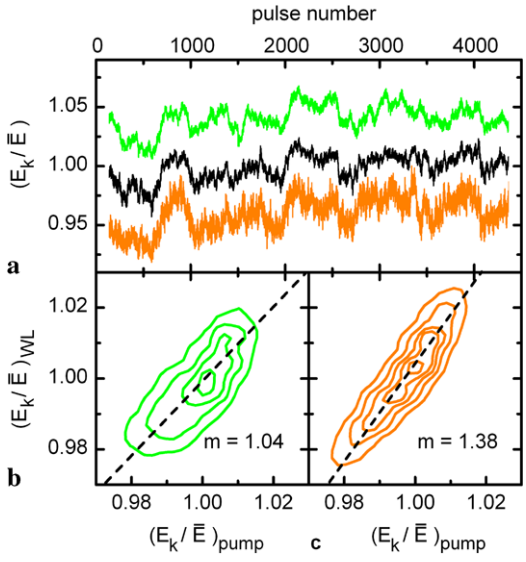

Fig. 7 Correlation between pump pulse energy and continuum output. (**a**) Normalized pulse energies of the pump pulses (*black*), of the visible part of the continuum (*green*, 450–700 nm) and of the infrared region (*orange*, 850–1600 nm). (**b**) and (**c**) Correlation between the pump energy fluctuation and the continuum energy in the visible (*green*) and infrared (*orange*) part of the spectrum

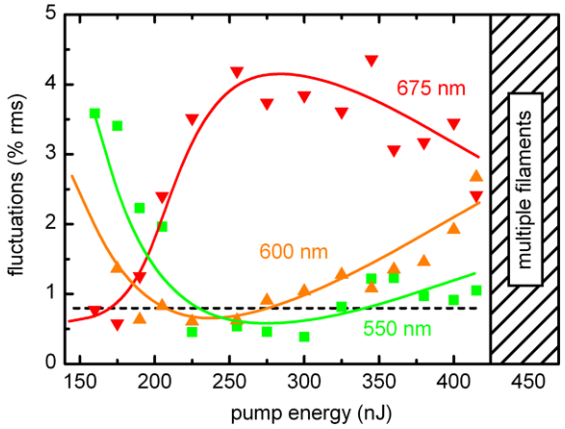

Fig. 8 Fluctuations of selected spectral components of a continuum generated in a 4 mm YAG crystal in dependence on the pump pulse energy. 675 nm: inverted *red triangles*, 600 nm: *orange triangles*, 550 nm: *green squares*. The *colored solid lines* are guides to the eye. The *dashed line* shows the fluctuations of the pump

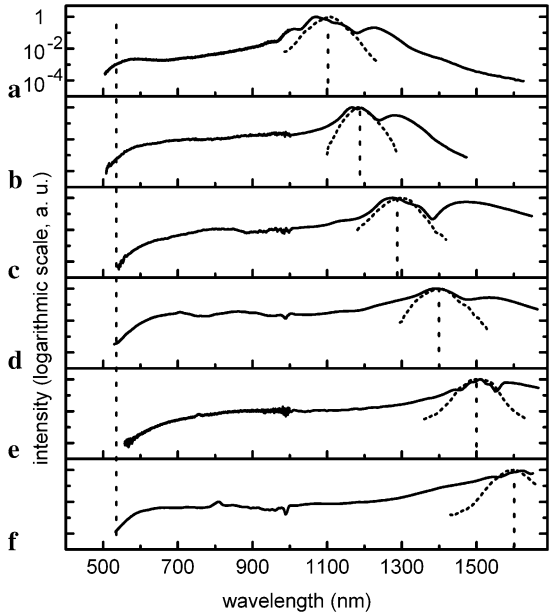

Fig. 9 Continua generated in a 4 mm YAG crystal (*solid lines*) with different pump spectra (*dotted lines*). The visible part of all continua reaches down to almost the same wavelength (530 nm, *dashed line*). The spectrum in (**f**) smoothly covers about 1.5 optical octaves

To understand the influence of the pump conditions on the spectral distribution of the noise, we measured the fluctuations for narrow spectral ranges at around 550, 600, and 675 nm selected by interference filters. Figure 8 shows the fluctuations as function of the average pump pulse energy. The best pump pulse energy can be found for each of the investigated wavelengths. The green and orange traces have minima at around 250 nJ, but the red part of the continuum at around 675 nm runs most stable at lower pump pulse energies of about 175 nJ. The higher the wavelength is, the lower the ideal pump pulse energy becomes. Remarkably, the narrow spectral ranges can have even lower fluctuations than the pump pulses, which is a consequence of the pronounced threshold and saturation behavior of the visible part of the continuum (compare to Fig. 4). Such low fluctuations can be most advantageous for applications, in particular since they do not require a decrease of the spectral energy density in the visible.

2.8 Variation of the pump wavelength

Whether white-light generation is possible in a crystal depends strongly on the pump wavelength. It was argued that no white-light generation is possible when the energy of the pump photons exceeds one third of the band gap of the crystal because multiphoton excitation from the valence to the conduction band restricts self-focusing [21]. To test this concept and to investigate the effect on the supercontinuum if the energy of the pump photons is reduced, we tuned the pump to shorter and longer wavelengths.

The pump pulses in this experiment were provided by a noncollinear optical parametric amplifier (NOPA) [31, 32] pumped by the 775 nm pulses. For pulses at 387 and 500 nm we were not able to see any white-light generated in YAG. This matches the expectation, since the reported band gap of YAG is 6.5 eV [74] and a lower limit for the continuum generation of 570 nm results.

For longer wavelengths we took special care that only the infrared beam and no residual 775 nm light were focused onto the white-light crystal. This was achieved with a filter (RG850; Schott AG (see footnote 1)) after the first stage of the NOPA. The NOPA was tuned from 1100 to 1600 nm. No pulse compression was applied and the pulse duration was below 100 fs throughout this range. The pump energy used for the continuum generation was ∼1 μJ at all wavelengths and an $f = 30$ mm lens was used to focus into a 4 mm long YAG crystal with a numerical aperture of about 0.08.

Figure 9 shows the resulting continua (black curve) for the variation of the pump wavelength (dotted curves). For all pump wavelengths the spectra display a blue edge at about 520 nm very similarly to pumping at 775 nm. All spectra show a pronounced plateau and have comparable energy densities. It is interesting to note that tuning the pump wavelength to the infrared can result in much broader spectra than typically obtained with Ti:sapphire lasers. The spectrum of Fig. 9f has a width of about 1.5 optical octaves and the spectral region below 1500 nm has a Fourier limit of around 3 fs, corresponding to a sub-cycle pulse.

Besides the possible use for the synthesis of optical waveforms, such a spectrum has also a strong potential for spectroscopic applications, because most of the visible and a good part of the near infrared are covered very smoothly. While the region around the 775 nm pump is not properly

covered with a Ti:sapphire pumped continuum due to the large spectral oscillations and varying spectral phase, the use of the NIR operated NOPA as pump renders a useful continuum that reaches well into the infrared to 1500 nm while still overlapping with the 280 to 700 nm continuum from CaF_2 used in our broadband transient spectrometer [28].

It should be noted that the IR-pumped continua do not display any significant dip in the middle of the spectrum. Such a behavior has been seen many times in the literature and limits the use of the NIR continuum. As can be seen from Fig. 9, the proper generation and characterization of the continuum avoids this problem.

2.9 Phase coherence within the continuum

The optical phase characteristics of continuum pulses are of high interest for the generation of pulses with stable carrier-envelope phase [33], for heterodyne detection in microscopy [75], for phase-sensitive spectroscopy [76] or for the use in f–$2f$ interferometers. Several experiments have resulted in strong evidence for phase preservation from the pump pulses to the continuum [15, 77]. Two separately generated continua can effectively interfere [78, 79], and separate colors within the visible part of a continuum were shown to have a stable phase with respect to each other [80].

A remaining question is whether the infrared part of the continuum is also phase-locked to the visible part. A step like change in the group delay of 250 fs was reported at the pump wavelength in a continuum generated in sapphire [30]. This corresponds to about an 185 π phase jump! In the region of the pump (775 nm) the spectrum is highly structured, presumably due to self-phase modulation and pulse splitting [81]. It is generally accepted that this major fraction of the light possesses a complicated spectral phase and is therefore not used in most applications.

To investigate the phase relation between the two parts, we split a continuum generated in YAG into the visible and the infrared part with a dichroic mirror (see Fig. 10a). The infrared part is parametrically amplified at around 1100 nm with phase preservation [79], and used for generating a new continuum, which is phase-locked to the first one [78, 79]. This continuum extends again into the visible region (compare Fig. 9a) and is brought to interference with the visible part of the original continuum. The phase of the resulting pattern provides information about possible fluctuations between the infrared and visible phases of the primary continuum.

For recording the expected interference we use a spatial interference arrangement [82] and record the 2D patterns for selected single shots at 30 Hz by a CCD camera (DMK F2104, The Imaging Source Europe GmbH (see footnote 1)). The spectral sensitivity was restricted to a region around 600 nm with a narrow band-pass filter. To obtain spatial interference fringes, a different divergence was chosen

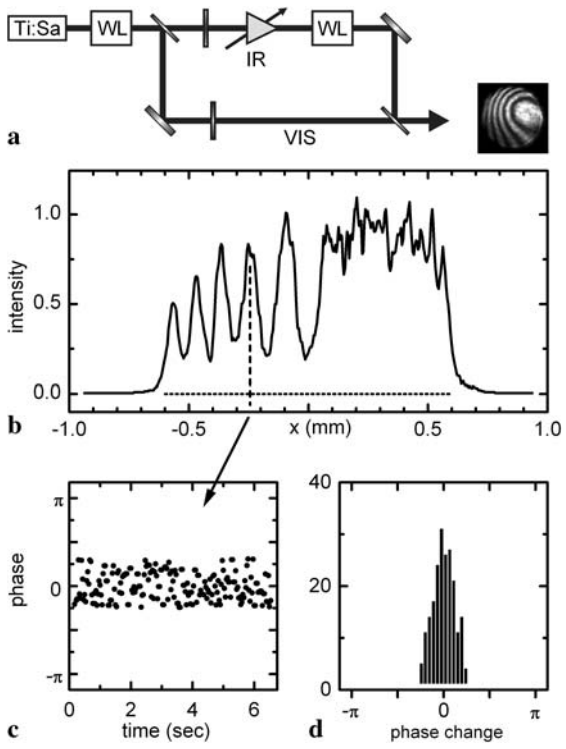

Fig. 10 Phase coherence between the visible and infrared part of a continuum. (**a**) Setup for the interference measurement (for details see text). (**b**) Cut through the spatial interference pattern. (**c**) Relative phase between the visible and the infrared part of the continuum for several seconds (averaged at 30 Hz). *Inset*: histogram of the phase changes

for the two continua. Figure 10b shows a radial cut through a typical interferogram (see inset).

The phase of each interferogram is evaluated by Fourier transformation [82] and gives direct information about the variation of the relative phase between the infrared and the visible part of the continuum for the recorded laser shot. Figs. 10c and 10d depict the results: For a set of 200 laser pulses within about 6 s we measure an effective fluctuation of 500 mrad (RMS). The setup was not environmentally isolated or protected from the laboratory acoustics. We therefore believe that the major part of the noise is due to technical contributions. We take the measurement as direct evidence that the phase of the infrared part and the phase of the visible part of the continuum from bulk YAG are locked and have very similar fluctuations. It is therefore indeed safe to use such a continuum in an f–$2f$ interferometer for the determination of carrier-envelope-phase (CEP) fluctuations.

3 Applications and perspectives

3.1 Weak pump pulses, high repetition rates and long pulse durations

The laser system used in this investigation is a Ti:sapphire regenerative amplifier, which provides 150 fs pulses, cen-

Table 2 Performance of the various crystals for continuum generation pumped by the output of different femtosecond lasers. The repetition rate, center wavelength, pulse duration and available output pulse energy are given in the second column. In each box to the right, the first line gives the pump energy for optimum operation, the second line the achieved spectral range

Laser system		Sapphire	YAG	KGW	YVO_4	$GdVO_4$
CPA 2001	1 kHz, 775 nm	900 nJ	420 nJ	83 nJ	59 nJ	78 nJ
	150 fs, 1 mJ	420–1600 nm	480–2800 nm	500–1150 nm	550–1150 nm	550–1200 nm
RegA 9050	100 kHz, 800 nm	Works	200 nJ	95 nJ	Not tested	Not tested
	60 fs, 6 μJ	[16]	480–1600 nm	550–1300 nm		
XL 500	5.1 MHz, 800 nm	400 nJ	230 nJ	Instable	50 nJ	75 nJ
	50 fs, 500 nJ	450–1100 nm	450–1100 nm	white-light	550–1000 nm	550–1050 nm
Home built [83]	80 MHz, 650–1000 nm	Detectable	Detectable	10 nJ	Detectable	Detectable
	7 fs, 16 nJ	broadening	broadening	600–1100 nm	broadening	broadening
JenLas® D2.fs	100 kHz, 1025 nm	Instable	500 nJ	140 nJ	200 nJ	220 nJ
	350 fs, 40 μJ	white-light	480–1400 nm	500–1400 nm	600–1600 nm	600–1300 nm

tered at 775 nm with a repetition rate of 1 kHz. However, the present tendency in laser development goes to longer central wavelengths as determined by Nd or Yb based amplifiers, higher repetition rates and often longer pulse durations. Therefore we tested continuum generation in the various crystals with four additional laser systems: Two 800 nm Ti:sapphire lasers which provide 60 fs pulses at a repetition rate of 100 kHz (RegA; Coherent Inc.) and 50 fs pulses at 5.1 MHz (FEMTOSOURCE scientific XL 500; Femtolasers GmbH), an Yb:KYW laser (JenLas®D2.fs; Jenoptik GmbH) which produces 350 fs long pulses centered at 1025 nm with 100 kHz repetition rate and finally a home-built 80 MHz system delivering 7 fs pulses with up to 16 nJ at 80 MHz [83].

The results of these tests are summarized in Table 2. The pulse energy given for each combination of laser and crystal is the value that provided the best continuum in terms of spectral coverage, stability, and beam profile. A considerably lower threshold was found in all cases. All lasers systems allowed a long-term stable broad continuum (see second line) with homogeneous round beam profile for at least one crystal. The visible part of selected spectra is shown in Fig. 11. For the comparison of the different curves it is essential that we determined absolute values of the spectral energy density (see Sect. 2.1).

From Table 2 it is apparent that the material dependence of the threshold and the optimum pump energy is found for all lasers. So for the higher repetition rate systems with their inherently lower single pulse output sapphire will not be the best choice. YAG already lowers the needed energy sufficiently that it should prove useful for many applications. The comparison also shows that for Ti:sapphire systems with comparable center wavelength, a shorter pulse leads to a lower continuum pump energy. This is obtained, however, at the cost of a smaller spectral energy density (see Fig. 11). On the other hand, as the pulse length increases for the Yb:KYW laser, more pump pulse energy is needed.

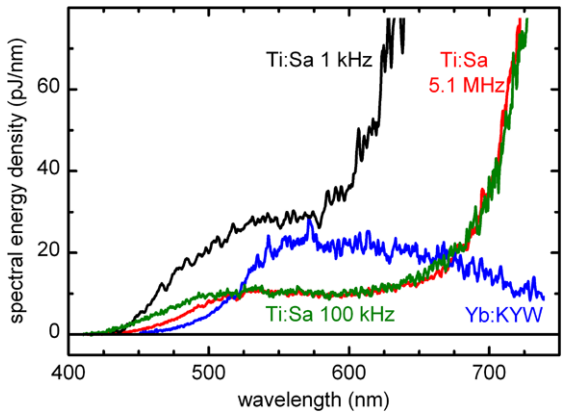

Fig. 11 Visible part of continua generated in 4 mm YAG by laser systems with differing pump wavelength, pulse length and repetition rate. Black (*upper curve*): Ti:sapphire at 775 nm, 150 fs, 1 kHz; *green* (*upper middle*): Ti:sapphire at 800 nm, 60 fs, 100 kHz; *red* (*lower middle*): Ti:sapphire at 800 nm, 50 fs, 5.1 MHz; *blue* (*lower right*): Yb:KYW 1025 nm, 350 fs, 100 kHz

The comparison of the 100 kHz and the 5.1 MHz Ti:sapphire system shows that the spectral broadening and even the energy density are quite independent of the repetition rate as long as a stable continuum can be generated. If the average power becomes too high, the continuum will only light up briefly and then cease again, often with permanent damage to the crystal. In recent work we showed that this can be avoided to some degree by rapid motion of the crystal [84]. This increased complexity can, however, be avoided by the change of crystal type, as demonstrated by the successful continuum generation in YAG with the 350 fs pulses at 1025 nm. Despite this longer pump wavelength, still most of the visible is covered.

The use of a 100 kHz pump laser for continuum generation in bulk materials has long been documented [16] and MHz operation has recently been shown [84]. This work adds the regime of long cavity oscillators operating at 5 MHz. To further push the limit, we investigated white-light generation with a home-built 80 MHz system delivering 7 fs pulses at 80 MHz and up to 16 nJ pulse energy. Significant additional broadening of the already broad pulse spectrum was observed in a 4 mm KGW crystal. Because of the extremely low input energy of 10 nJ per pulse available at the crystal extremely tight focusing down to 2 μm was used. Owing to this spectral broadening the Fourier limit of the pulses is reduced from 6.4 to 5.1 fs. In addition the beam profile improved. The spectral broadening is due to white-light generation and not only to self-phase modulation, as can be judged from the white round disk that emerged with a larger divergence than the pump beam.

3.2 Seed light for optical parametric amplification

With the improved infrared output of YAG as compared to sapphire, this material seems ideally suited for the generation of intense ultrashort pulses in the near infrared by parametric amplification. As a first application, we replaced the 3 mm long sapphire crystal in a standard NOPA [29, 31, 32] with a 4 mm long YAG crystal and changed the focal length to 80 mm. The improved seed intensity resulted in an increase of the quantum efficiency to up to 40% and infrared NOPA output pulse energies of 4–9 μJ were obtained in the region of 1000–1600 nm from 250 μJ pump at 775 nm. This is about twice the reported values [29]. In addition, we were able to directly amplify pulses at center wavelengths of up to 2800 nm with energies of 100 to 3000 nJ. The spectra of all infrared pulses were broad enough to support sub-50-fs pulse duration.

We can estimate the number of available seed photons at 2600 nm from the measurement shown in Fig. 5. At 1600 nm the continuum still amounts to an energy density of 20 fJ/nm or 1.6×10^5 photons/nm. The roll-off is about 5 dB/100 nm in the monitored region and we extrapolate this behavior. As a result we guess 400 photons at 2600 nm center wavelength for a typical bandwidth of 250 nm needed for a 50 fs pulse. This corresponds to a shot noise on the order of 1/20 and is sufficient for seeding the NOPA.

In a second application we built a two-stage “hybrid” OPA system pumped by the 100 kHz Ti:sapphire laser (RegA, Coherent Inc.). A first amplification stage is pumped by the second harmonic of the RegA at 400 nm and the infrared idler output is further amplified in a second stage by 800-nm pump pulses. With YAG used for the continuum generation, we were able to fully cover the NIR and MIR from 900 nm to 5 μm. The extension of this concept to other pump systems should be straightforward and renders exciting new sources of tunable UV, visible, and IR pulses.

3.3 Broadband probe light for transient spectroscopy

A widespread use of continua is in tunable pump/supercontinuum probe experiments (PSCP) [35]. With sapphire the range of 450 to 720 nm is accessible for such a transient femtosecond spectrometer and CaF_2 widens the range to below 300 nm [28]. The region around the pump wavelength is, however, inaccessible due to the large intensity modulations and complicated time structure. Toward the IR the typical sapphire continuum falls off exponentially and the achievable sensitivity and dynamic range is highly limited.

As shown in Sect. 2.8 the pump wavelength has practically no influence on the visible part of the continuum (see Fig. 9) and an octave spanning plateau-like continuum can be generated which is well suited for PSCP due to the flat spectrum, good beam profile and high stability. A pump at 1600 nm will increase the detection range out to 1500 nm while still maintaining a good overlap with the UV/visible recording. Extending the upper wavelength limit of the spectrometer to 1500 nm corresponds to the possible detection of excited states at just 0.8 eV. Even for 800 nm pumping, with YAG a plateau-like spectral density is available in the NIR and can directly be used.

The white-light generated in the bulk media is much more stable than the output of microstructured fibers and yields a flat spectrum. In addition, the typical 3 nJ integrated energy in the visible (see Fig. 4) is already comparable to the input into the fiber and therefore higher than the energy available from the fiber output for the spectroscopic application. A high number of photons per spectral interval is found to be of uttermost importance for a low shot noise limit and the full use of the dynamic range of available line detectors.

4 Conclusions and perspectives

The results reported here on continuum generation in bulk materials have implication to several areas of current and future research. In order to understand the broadening process, our results should contribute to finding advanced numerical models for the continuum generation process that take into account the material properties. The connection between the nonlinear index of refraction and the threshold for continuum generation (see Fig. 2) provides indication of the involved physics and, from a practical perspective, provides the design criteria for finding suitable novel crystal materials for even further improved performance.

For the pursuit of generating photon pulses of highest intensity and shortest duration by amplification in lasers or parametric processes [85–87], the bandwidth of the seed pulses, their coherence, and good stability are decisive for success. We believe that continua from crystalline materials are a valuable alternative to many of the concepts used so far

for spectral broadening of the seed pulses in state-of-the-art optical parametric chirped-pulse amplification schemes, because only nJ-level energies are required and the spectrum can coherently cover the visible to infrared region simultaneously without significant spectral modulation. A continuum from sapphire was indeed used in a recently reported optical parametric chirped amplifier [88]. Lately it was even shows that mJ pump pulses can be used for continuum generation in fused silica and this might pave the way to further improved seed levels [89].

Spectroscopic access to molecular dynamics and processes in condensed matter physics requires an as high as possible repetition rate of the laser system to acquire good statistics, but, on the other hand, the sample under investigation must have enough time to cool back to the initial state or to be exchanged for fresh substance each time. These constraints result in experimental repetition rates in the range of 1 kHz to 1 MHz to be ideal. Our results show that continuum generation in bulk materials works well with a large variety of such laser sources at different wavelengths and for pulse durations from 7 to at least 350 fs.

The spectrum shown in Fig. 1b has a Fourier limit of 3.9 fs. With ∼10 pJ/nm of energy density in the plateau region, the total pulse energy amounts to ∼5 nJ; these pulses can be generated for example at 5 MHz repetition rate or more, where phase stabilization of lasers is straightforward as compared to amplified sources. With proper compression, which was for example reported from 450 to 800 nm with Brewster-angled chirped mirrors [90], this results in a very simple source of stabilized few-cycle pulses at average powers of up to 25 mW. These possibilities open up the route towards studying the effects of the carrier-envelope phase of few-cycle pulses to materials and molecular transitions with highest stability and sensitivity.

Our main use for advanced materials for continuum generation is in the contexts of tunable pulse generation by parametric amplification and in broadband spectroscopy, as outlined earlier in the text. In both fields, application of the findings reported here has already resulted in valuable improvements; further reports will provide more details.

Acknowledgements We are grateful to C. Homann, K. Peeper, A.C. Böck, C. Schriever, and A. Ozawa for valuable experimental help and fruitful discussions. We thank P. Hommelhoff, T. Udem, as well as the company Jenoptik for access to their laser systems. The work was supported by the DFG-Cluster of Excellence: Munich-Centre for Advanced Photonics, the SFB 749 (Dynamics and Intermediates of Molecular Transformations), and by the Austrian Science Fund within the Special Research Program F16 (Advanced Light Sources).

References

1. R.R. Alfano, S.L. Shapiro, Phys. Rev. Lett. **24**, 584 (1970)
2. R.R. Alfano, S.L. Shapiro, Phys. Rev. Lett. **24**, 592 (1970)
3. R.L. Fork, C.V. Shank, C. Hirlimann, R. Yen, W.J. Tomlinson, Opt. Lett. **8**, 1 (1983)
4. R.R. Alfano, *The Supercontinuum Laser Source* (Springer, Berlin, 2006)
5. A. Couairon, A. Mysyrowicz, Phys. Rep. **441**, 47 (2007)
6. L. Bergé, S. Skupin, R. Nuter, J. Kasparian, J.-P. Wolf, Rep. Prog. Phys. **70**, 1633 (2007)
7. P.B. Corkum, C. Rolland, T. Srinivasan-Rao, Phys. Rev. Lett. **57**, 2268 (1986)
8. M. Nisoli, S. De Silvestri, O. Svelto, Appl. Phys. Lett. **68**, 2793 (1996)
9. M. Nisoli, S. De Silvestri, O. Svelto, R. Szipöcs, K. Ferencz, Ch. Spielmann, S. Sartania, F. Krausz, Opt. Lett. **22**, 522 (1997)
10. A. Guandalini, P. Eckle, M. Anscombe, P. Schlup, J. Biegert, U. Keller, J. Phys. B **39**, S257 (2006)
11. D.J. Jones, S.A. Diddams, J.K. Ranka, A. Stentz, R.S. Windeler, J.L. Hall, S.T. Cundiff, Science **288**, 635 (2000)
12. R. Holzwarth, Th. Udem, T.W. Hänsch, J.C. Knight, W.J. Wadsworth, P.St.J. Russell, Phys. Rev. Lett. **85**, 2264 (2000)
13. J.K. Ranka, R.S. Windeler, A.J. Stentz, Opt. Lett. **25**, 25 (2000)
14. J.M. Dudley, L. Provino, N. Grossard, H. Maillotte, R.S. Windeler, B.J. Eggleton, S. Coen, J. Opt. Soc. Am. B **19**, 765 (2002)
15. J.M. Dudley, G. Genty, S. Coen, Rev. Mod. Phys. **78**, 1135 (2006)
16. M.K. Reed, M.K. Steiner-Shepard, D.K. Negus, Opt. Lett. **19**, 1855 (1994)
17. M.K. Reed, M.K. Steiner-Shepard, M.S. Armas, D.K. Negus, J. Opt. Soc. Am. B **12**, 2229 (1995)
18. M.K. Reed, M.S. Armas, M.K. Steiner-Shepard, D.K. Negus, Opt. Lett. **20**, 605 (1995)
19. M. Wittmann, A. Penzkofer, Opt. Commun. **126**, 308 (1996)
20. A. Brodeur, S.L. Chin, Phys. Rev. Lett. **80**, 4406 (1998)
21. A. Brodeur, S.L. Chin, J. Opt. Soc. Am. B **16**, 637 (1999)
22. N.P. Ernsting, S.A. Kovalenko, T. Senyushkina, J. Saam, V. Farztdinov, J. Phys. Chem. A **105**, 3443 (2001)
23. R. Huber, H. Satzger, W. Zinth, J. Wachtveitl, Opt. Commun. **194**, 443 (2001)
24. P. Tzankov, I. Buchvarov, T. Fiebig, Opt. Commun. **203**, 107 (2002)
25. M. Raytchev, E. Pandurski, I. Buchvarov, C. Modrakowski, T. Fiebig, J. Phys. Chem. A **107**, 4592 (2003)
26. S. Laimgruber, H. Schachenmayr, B. Schmidt, W. Zinth, P. Gilch, Appl. Phys. B **85**, 557 (2006)
27. I. Buchvarov, A. Trifonov, T. Fiebig, Opt. Lett. **32**, 1539 (2007)
28. U. Megerle, I. Pugliesi, C. Schriever, C.F. Sailer, E. Riedle, Appl. Phys. B **96**, 215 (2009)
29. T. Wilhelm, J. Piel, E. Riedle, Opt. Lett. **22**, 1494 (1997)
30. G. Cerullo, M. Nisoli, S. De Silvestri, Appl. Phys. Lett. **71**, 3616 (1997)
31. E. Riedle, M. Beutter, S. Lochbrunner, J. Piel, S. Schenkl, S. Spörlein, W. Zinth, Appl. Phys. B **71**, 457 (2000)
32. J. Piel, M. Beutter, E. Riedle, Opt. Lett. **25**, 180 (2000)
33. A. Baltuška, T. Fuji, T. Kobayashi, Phys. Rev. Lett. **88**, 133901 (2002)
34. G. Cerullo, S. De Silvestri, Rev. Sci. Instrum. **74**, 1 (2003)
35. S.A. Kovalenko, A.L. Dobryakov, J. Ruthmann, N.P. Ernsting, Phys. Rev. A **59**, 2369 (1999)
36. T. Bizjak, J. Karpiuk, S. Lochbrunner, E. Riedle, J. Phys. Chem. A **108**, 10763 (2004)
37. B. Schmidt, C. Sobotta, S. Malkmus, S. Laimgruber, M. Braun, W. Zinth, P. Gilch, J. Phys. Chem. A **108**, 4399 (2004)
38. A.V. Zamyatin, A.V. Soldatova, M.A.J. Rodgers, Inorg. Chim. Acta **360**, 857 (2007)
39. J. Savolainen, D.v.d. Linden, N. Dijkhuizen, J.L. Herek, J. Photochem. Photobiol. A **196**, 99 (2008)
40. D.W. McCamant, P. Kukura, S. Yoon, R.A. Mathies, Rev. Sci. Instrum. **75**, 4971 (2004)

41. M.J. Klopf, P. Norris, Appl. Surf. Sci. **253**, 6305 (2007)
42. A. Baltuška, Th. Udem, M. Uiberacker, M. Hentschel, E. Goulielmakis, Ch. Gohle, R. Holzwarth, V.S. Yakovlev, A. Scrinzi, T.W. Hänsch, F. Krausz, Nature **421**, 611 (2003)
43. C. Nagura, A. Suda, H. Kawano, M. Obara, K. Midorikawa, Appl. Opt. **41**, 3735 (2002)
44. A.K. Dharmadhikari, F.A. Rajgara, D. Mathur, Appl. Phys. B **80**, 61 (2005)
45. I. Nikolov, A. Gaydardzhiev, I. Buchvarov, P. Tzankov, F. Noack, V. Petrov, Opt. Lett. **32**, 3342 (2007)
46. G. Cirmi, C. Manzoni, D. Brida, S. De Silvestri, G. Cerullo, J. Opt. Soc. Am. B **25**, B62 (2008)
47. M. Bass (ed.), *Handbook of Optics, Vol. II* (McGraw–Hill, New York, 1995)
48. J.R. O'Connor, Appl. Phys. Lett. **9**, 407 (1966)
49. A. Ikesue, T. Kinoshita, K. Kamata, K. Yoshida, J. Am. Ceram. Soc. **78**, 1033 (1995)
50. K. Shimamura, S. Uda, V.V. Kochurikhin, T. Taniuchi, T. Fukuda, Jpn. J. Appl. Phys. **35**, 1832 (1996)
51. I.V. Mochalov, Opt. Eng. **36**, 1660 (1997)
52. M.C. Pujol, M. Rico, C. Zaldo, R. Solé, V. Nikolov, X. Solans, M. Aguiló, F. Díaz, Appl. Phys. B **68**, 187 (1999)
53. H. Zhang, X. Meng, J. Liu, L. Zhu, C. Wang, Z. Shao, J. Wang, Y. Liu, J. Cryst. Growth **216**, 367 (2000)
54. D. Milam, M.J. Weber, A.J. Glass, Appl. Phys. Lett. **31**, 822 (1977)
55. H.-D. Jiang, H.-J. Zhang, J.-Y. Wang, H.-R. Xia, X.-B. Hu, B. Teng, C.-Q. Zhang, Opt. Commun. **198**, 447 (2001)
56. J. Lu, K.-I. Ueda, H. Yagi, T. Yanagitani, Y. Akiyama, A.A. Kaminskii, J. Alloys Compd. **341**, 220 (2002)
57. A. Major, F. Yoshino, I. Nikolakakos, J.S. Aitchison, P.W.E. Smith, Opt. Lett. **29**, 602 (2004)
58. W. Koechner, *Solid-State Laser Engineering* (Springer, Berlin, 2006)
59. A.G. Selivanov, I.A. Denisov, N.V. Kuleshov, K.V. Yumashev, Appl. Phys. B **83**, 61 (2006)
60. B.A. Cumberland, J.C. Travers, S.V. Popov, J.R. Taylor, Opt. Express **16**, 5954 (2008)
61. J.B. Ashcom, R.R. Gattass, C.B. Shaffer, E. Mazur, J. Opt. Soc. Am. B **23**, 2317 (2006)
62. S. Naumov, A. Fernandez, R. Graf, P. Dombi, F. Krausz, A. Apolonski, New J. Phys. **7**, 216 (2005)
63. R. Huber, F. Adler, A. Leitenstorfer, M. Beutter, P. Baum, E. Riedle, Opt. Lett. **28**, 2118 (2003)
64. A.L. Gaeta, Phys. Rev. Lett. **84**, 3582 (2000)
65. J.H. Marburger, Prog. Quantum Electron. **4**, 35 (1975)
66. Y.R. Shen, Prog. Quantum Electron. **4**, 1 (1975)
67. A.M. Weiner, J.P. Heritage, R.H. Stolen, J. Opt. Soc. Am. B **5**, 364 (1988)
68. W. Liu, S.L. Chin, O. Kosareva, I.S. Golubtsov, V.P. Kandidov, Opt. Commun. **225**, 193 (2003)
69. S. Tzortzakis, L. Sudrie, M. Franco, B. Prade, A. Mysyrowicz, A. Couairon, L. Bergé, Phys. Rev. Lett. **87**, 213902 (2001)
70. T. Pfeifer, L. Gallmann, M.J. Abel, D.M. Neumark, S.R. Leone, Opt. Lett. **31**, 2326 (2006)
71. Q. Xing, K.M. Yoo, R.R. Alfano, Appl. Opt. **32**, 2087 (1993)
72. G.G. Luther, A.C. Newell, J.V. Moloney, E.M. Wright, Opt. Lett. **19**, 789 (1994)
73. S.L. Chin, S. Petit, W. Liu, A. Iwasaki, M.-C. Nadeau, V.P. Kandidov, O.G. Kosareva, K.Yu. Adrianov, Opt. Commun. **210**, 329 (2002)
74. G.A. Slack, D.W. Oliver, R.M. Chrenko, S. Roberts, Phys. Rev. **177**, 1308 (1969)
75. M. Greve, B. Bodermann, H.R. Telle, P. Baum, E. Riedle, Appl. Phys. B **81**, 875 (2005)
76. D. Marion, K. Wüthrich, Biochem. Biophys. Res. Commun. **113**, 967 (1983)
77. C.P. Hauri, W. Kornelis, F.W. Helbing, A. Heinrich, A. Couairon, A. Mysyrowicz, J. Biegert, U. Keller, Appl. Phys. B **79**, 673 (2004)
78. M. Bellini, T.W. Hänsch, Opt. Lett. **25**, 1049 (2000)
79. P. Baum, S. Lochbrunner, J. Piel, E. Riedle, Opt. Lett. **28**, 185 (2003)
80. P. Baum, E. Riedle, M. Greve, H.R. Telle, Opt. Lett. **30**, 2028 (2005)
81. J.E. Rothenberg, Opt. Lett. **17**, 583 (1992)
82. P. Baum, S. Lochbrunner, E. Riedle, Appl. Phys. B **77**, 129 (2003)
83. A. Ozawa, W. Schneider, T.W. Hänsch, T. Udem, P. Hommelhoff, New J. Phys. (in print)
84. C. Schriever, S. Lochbrunner, P. Krok, E. Riedle, Opt. Lett. **33**, 192 (2008)
85. O.V. Chekhlov, J.L. Collier, I.N. Ross, P.K. Bates, M. Notley, C. Hernandez-Gomez, W. Shaikh, C.N. Danson, D. Neely, P. Matousek, S. Hancock, L. Cardoso, Opt. Lett. **31**, 3665 (2006)
86. F. ., A. Tavella, F. Marcinkevičius, Krausz. Opt. Express **14**, 12822 (2006)
87. J.A. Fülöp, Zs. Major, A. Henig, S. Kruber, R. Weingartner, T. Clausnitzer, E.-B. Kley, A. Tünnermann, V. Pervak, A. Apolonski, J. Osterhoff, R. Hörlein, F. Krausz, S. Karsch, New J. Phys. **9**, 438 (2007)
88. P. Tzankov, J. Zheng, M. Mero, D. Polli, C. Manzoni, G. Cerullo, Opt. Lett. **31**, 3629 (2006)
89. K. Stelmaszczyk, P. Rohwetter, Y. Petit, M. Fechner, J. Kasparian, J.-P. Wolf, L. Wöste, Phys. Rev. A **79**, 053856 (2009)
90. P. Baum, M. Breuer, E. Riedle, G. Steinmeyer, Opt. Lett. **31**, 2220 (2006)

Appendix A2

Widely Tunable Infrared Pulse Generation up to 5 µm with Novel Optical Parametric Amplifiers at 100 kHz Repetition Rate

M. Bradler, E. Riedle, and C. Homann

Ultrafast Phenomena XVII
M. Chergui, D. Jonas, E. Riedle, R.W. Schoenlein, A. Taylor, eds.
(Oxford University Press, Inc., New York 2011), 733 - 735

Reprinted with kind permission from Oxford University Press, Inc.

Widely Tunable Infrared Pulse Generation up to 5 µm with Novel Optical Parametric Amplifiers at 100 kHz Repetition Rate

Maximilian Bradler, Eberhard Riedle, Christian Homann

LS fuer BioMolekulare Optik, LMU Munich, Germany
E mail: Maximilian.Bradler@physik.lmu.de

INTRODUCTION. Ultrashort tunable mid-infrared pulses are useful tools for numerous applications such as time-resolved vibrational spectroscopy, high field science, or the analysis of superconductors. To increase the quality of complex spectroscopic experiments, short measurement times with high averaging is needed. Therefore laser systems with high repetition rate are on the advance and spreading quickly. However, the reduced energy of these systems requires novel and optimized concepts to generate the mid-infrared pulses. Difference frequency generation with high repetition rates is challenging, so that low efficiencies, narrow spectra and limited tunability are not unusual.

FEMTOSECOND MID-INFRARED PULSE GENERATION WITH STRONG PREAMPLIFICATION OF THE SEED. Here we present a 100 kHz optical parametric amplifier (OPA) system for mid-infrared fs pulse generation in $LiNbO_3$ with gap free tunability from 1 to 5 µm. Due to the fact that for longer wavelengths no white-light seed is available, the idler of an OPA pumped at the fundamental wavelength (1ω) of the pump system (IR amplifier in figure 1) has to be used instead of directly amplified light. However, for idler wavelengths above 4 µm and therefore signal wavelengths close to the pump the phasematching conditions for the amplifier crystal cannot be well fulfilled and the gain factor is decreasing dramatically. To generate highly energetic mid-infrared pulses even with low gain factors we pre-amplify the white-light seed in a first collinear OPA stage (Pre-amplifier in figure 1) pumped by the second harmonic (2ω) and with BBO as nonlinear crystal. The second harmonic pumping allows broad phasematching and high gain factors, because the desired signal wavelengths are now close to degeneracy. This concept is shown in figure 1.

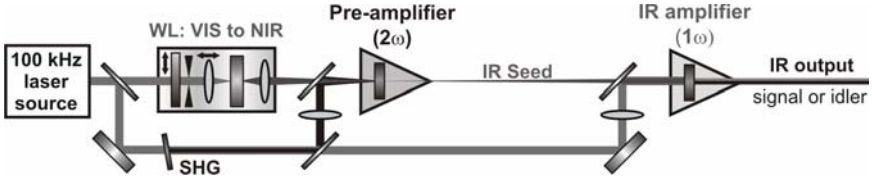

Fig. 1. Pre and main amplifier for efficient and fully tunable infrared pulse generation at high repetition rate

Due to the collinear setup the idler of the pre-amplifier can be used as seed of the IR amplifier without any optics for color recombination. This avoids the

need to cope with the exponential decrease of the white-light on the Stokes side of the pump and the intense and flat plateau on the Anti-Stokes side can be used instead. This increases the energy of the pre-amplified light (IR seed in figure 1) by a factor of two to three. Generating highly energetic midinfrared pulses with the concept of strong pre-amplification in a first 2ω pumped stage and only modest amplification in a second 1ω pumped stage allows even the use of nonlinear crystals with low damage thresholds like $LiIO_3$.

Typically pulses of a second harmonic pumped collinear amplifier like in the present pre-amplifier yield relatively narrow spectra and only support Fourier limits above 50 fs. However, when raising the pump energy in the pre-amplifier, we observe strong spectral broadening. The pulses are fully compressible with Fourier limits down to 11 fs and a measured pulse duration of only 13.8 fs (see fig. 2 for a test with a kHz Ti:sapphire system).

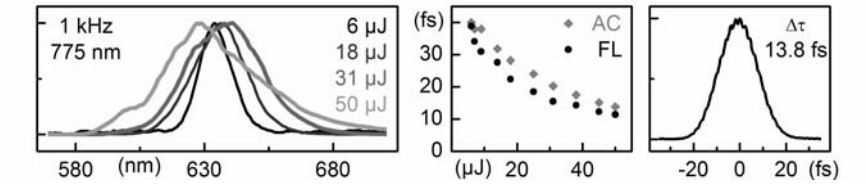

Fig. 2. Spectral broadening when raising the pump energy during collinear optical parametric amplification

ADAPTABILITY OF THE PRE-AMPLIFICATION CONCEPT TO VARIOUS LASER SYSTEMS. To show the adaptability of this concept, we used several laser systems with central wavelengths from 775 to 1025 nm and pulse durations from 50 to 300 fs. One realization uses a commercially available ytterbium-based diode-pumped solid state laser system (JenLas® D2.fs, JenOptik AG) as primary pump source. It delivers 40 µJ output pulses with 300 fs duration at 1025 nm and at a repetition rate of 100 kHz. For the seed generation we split off pulses with an energy of 1.5 µJ and focus them into a 4 mm thick YAG plate. The use of YAG allows the generation of a stable single white-light filament in spite of the relatively long pump pulses [1]. The main part of the pump pulses is frequency doubled in a 0.8 mm thick BBO crystal, cut at 23.5°, with a very high conversion efficiency of more than 60%.

The seed and pump pulses are collinearly combined with a dichroic filter and each focused with a lens (f = 400 mm) towards a 2 mm thick type I BBO crystal, cut at 24.5°, where they are spatially and temporally overlapped. Again, we observe a strong dependence of the spectral bandwidth of the amplified pulses on the pump pulse intensity. When varying the pump intensity from 80 to 160 GW/cm^2 by changing the pulse energy, we can increase the bandwidth of a pulse centered at 780 nm from 32 to 91 nm. We observe no significant deterioration of the beam profile or pulse-to-pulse stability when increasing the pump intensity. The pulses can be compressed to a measured duration of 13.6 fs, nearly their Fourier-Limit of 13.5 fs, by a simple fused silica prism sequence. In this way we achieve pulses with a Fourier-limit of sub-20 fs in a broad tuning range between 630 nm and 930 nm even in the collinear geometry. This geometry additionally allows us to make full use of the idler pulses in the range of 1140 to 2750 nm without any spatial chirp and with spectra supporting

likewise around 20 fs pulse duration. The calculated idler energies are in the range of 1 µJ, much higher than when we try to amplify the NIR part of our supercontinuum seed directly for the wavelength region above 1400 nm, because of the exponential decrease of the white-light in this wavelength region.

In a second amplification stage we now use the idler of the first stage as seed light and the fundamental light remaining after frequency doubling at 1025 nm as pump light. We combine both pulses with a dichroic mirror collinearly and focus them towards a 1.5 mm thick type I $LiNbO_3$ crystal, cut at 45°. Again the collinear geometry allows us to use the idler of the amplification process, which now is in the spectral region between 2.4 and 4.3 µm. The spectra support a Fourier-limited duration of 25 fs at 2.4 µm and 150 fs at 4.3 µm. Combining all outputs of the two-stage system, this means an extremely wide tuning range from the visible to the mid-infrared (see Fig. 3).

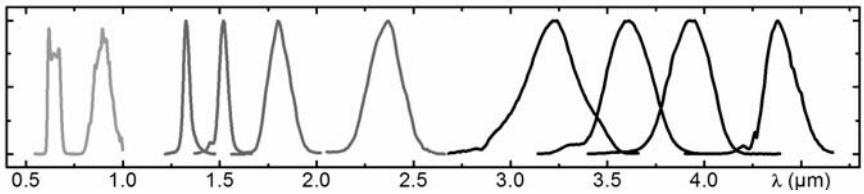

Fig. 3. Output spectra of our OPA system showing the extreme tunability from 630 nm to 4.3 µm

Matching of the beam diameter and wave front curvature is a challenge in multi-stage OPAs with identical pump wavelength. The twofold switch in "signal" wavelength totally eliminates this problem. The initial visible seed is discarded between the two amplifiers and equally the intermediate near infrared radiation at the output. No adverse interferences can therefore happen.

Above approximately 3 µm, we find that the bandwidth of the output spectra is limited by the phasematching properties of $LiNbO_3$ and is smaller than the bandwidth of the seed spectra. Therefore part of the seed light is not used and we loose conversion efficiency and output energy. When we now insert suitable amounts of dispersive material in our supercontinuum seed before the first amplification stage (e.g. BK7, SF57), we can tune the spectral bandwidth of the amplified pulses in the first stage and match it to the phase-matching properties of our amplifying crystal in the second stage. In that way we gain up to a factor of 2.6 in output energy, resulting for example in 750 nJ at 3.6 µm, or 75 mW at the 100 kHz rate of the system.

We also implemented our concept of strong pre-amplification in a first 2ω pumped stage and only minor amplification in a second 1ω pumped stage with a 100 kHz Ti:Sa regenerative amplifier system (RegA 9050, Coherent), that delivers pulses centered around 810 nm with a duration of 60 fs and an energy of only 6.3 µJ. We show tunability from 970 nm up to 5 µm with output energies of around 250 nJ at 1050 nm and 20 nJ at 5 µm. This demonstrates that our presented concept of mid-infrared generation is also feasible with lowest pump energies and with varying pump wavelengths.

1 M. Bradler, P. Baum, and E. Riedle, in Appl. Phys. B **97**, 561, 2009.

Appendix A3

Continuum Generation in Laser Host Materials towards Table-Top OPCPA

M. Bradler, P. Baum, and E. Riedle

Ultrafast Phenomena XVII
M. Chergui, D. Jonas, E. Riedle, R.W. Schoenlein, A. Taylor, eds.
(Oxford University Press, Inc., New York 2011), 712 - 714

Reprinted with kind permission from Oxford University Press, Inc.

Continuum Generation in Laser Host Materials towards Table-Top OPCPA

Maximilian Bradler, Peter Baum, and Eberhard Riedle

LS fuer BioMolekulare Optik, LMU, Munich, Germany
E mail: maximilian.bradler @physik.uni muenchen.de

INTRODUCTION. Super-continuum generation is one of the most fascinating phenomena in ultrafast nonlinear optics. Because of octave wide spectral broadening, wavelength regions not supported by the available laser media become accessible. Especially continuum generation in solids renders smooth, flat and gap free spectra with a high amount of coherence and compressibility down to below 5 fs, and pulse-to-pulse and long term stability. This favors them as a most valuable primary source for broadband radiation in laser technology and spectroscopy [1].

CONTINUUM GENERATION IN BULK MATERIALS FROM THE FEMTO- TO THE PICOSECOND REGIME. To achieve stable continuum generation even with ps pulses the material dependent threshold energy for white-light generation has to be low enough to avoid crystal damage. This threshold for continuum generation closely matches the critical power for self-focusing because the dramatic increase of intensity during self-focusing triggers further nonlinear processes in the crystal. The critical power for self-focusing depends inversely on the linear and nonlinear refractive index. To avoid local damage to the sample, a superior crystalline quality and high damage threshold are necessary. Therefore we focused our search for materials with improved continuum generation properties on novel laser-host materials so that one can benefit from the newest developments in the field. We find indeed that none of the tested crystals shows damage after weeks of use if operated with a standard amplified Ti:sapphire system. With a systematic search among the crystals with high refractive indices, YAG, KGW, $GdVO_4$, YVO_4, Sc_2O_3, Lu_2O_3, and Y_2O_3 were found as suitable candidates for white-light generation with longer pulses. We could actually decrease the energy for white-light generation and increase the pulse duration by up to a magnitude compared to the established continuum generation in sapphire. This is summarized in table 1, which shows the refractive indices and energy thresholds for continuum generation in some of the mentioned crystals. The more established CaF_2 and sapphire are shown as reference.

Table 1. Refractive indices and threshold energy for continuum generation of selected crystals

crystal type	CaF_2	Al_2O_3	YAG	Y_2O_3	KGW	$GdVO_4$	YVO_4
n_0	1.43	1.76	1.82	1.92	2.01	1.97	1.96
n_2 [$10^{-16}cm^2/W$]	1.24	3.1	6.9	11.6	10	15	15
threshold [nJ]	900	280	130	100	54	41	39

Whereas continuum generation in sapphire is only practicable with a pump pulse duration up to 250 fs, upcoming white-light crystals such as YAG render continuum generation with 35 fs to at least 500 fs pump pulses. First evidence for ps continuum generation was found in YAG and KGW including some of the advantageous properties of fs white-light like flat and smooth plateau-like spectra with coverage of the entire visible range. But also infrared plateau-like spectra were observed during continuum generation in YAG crystals (see Figure 1).

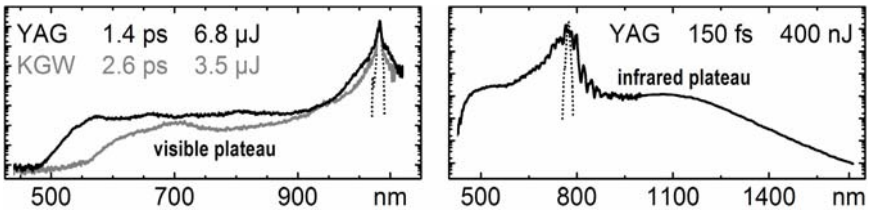

Fig. 1. Spectra of ps continuum generation in YAG and KGW covering nearly the entire visible (left) and demonstration of an infrared plateau (right).

APPLICATION AS SEED FOR OPCPA. Few-cycle light pulses with highest field intensities are of great interest for studying laser–matter interactions at extreme conditions such as the generation of mono energetic electron beams or intense single attosecond pulses from solid density plasmas. One very successful way to realize this is optical parametric chirped pulse amplification (OPCPA). Such systems are typically seeded by the output of Ti:sapphire oscillators and subsequently of hollow core fibers. However, it is not uncommon, that these continua show unfavorable properties such as structured spectra with intensities varying over magnitudes, low stability and imperfect coherence.

Continua generated in bulk materials on the other hand show smooth, flat spectra with high pulse-to-pulse stability, good beam quality and compressibility, and only a few µJ are necessary to generate such continua. The weak output compared to alternative seed sources can easily be compensated by multiple optical parametric amplification stages. Due to the principles of OPA subsequent stages can potentially amplify neighboring wavelength regions without phase jumps or loss of compressibility to achieve ultrabroad spectra and therewith few-cycle pulses simultaneously with multi-mJ pulse energies.

ROBUSTNESS OF CONTINUUM GENERATION AGAINST PUMP WAVELENGTH AND REPETITION RATE. Commercially available laser systems offer repetition rates from single Hz up to multi-MHz. We find that continuum generation in bulk materials is possible over the entire range. We compare similar laser systems, which only differ by the repetition rate and find no significant difference in the generated spectra. To further decrease the chance of local damage at high repetition rates because of the increased average power, the crystal plates can be rotated or moved. Since this concept is successfully used in pump-probe spectroscopy [2] and MHz-NOPA's, there are no major concerns about the adaptability for OPCPA systems. A further advantage of

these moving or rotating crystals is that local spots have enough time to recover from the high peak intensities during continuum generation.

To show that continuum generation is not limited to small regions of pump wavelength, we selected wavelengths ranging from 525 to 1600 nm and found that for all cases stable continuum generation occurs. The short wavelength cutoff of the continua remains nearly constant. This leads to octave-wide gap free continua with smooth and flat spectra when pumping with an infrared source. Combining the principles of OPA with the fact that the energy threshold is very low these infrared sources can easily be generated by laser systems with nearly every central wavelength. For OPCPA systems passive CEP stabilization should be used in this conversion.

In the case of calcium fluoride, we find a significantly shorter continuum edge when pumping with a short wavelength, which makes these spectra highly interesting for pump-probe spectroscopy. Even the spectra on the Stokes side of this continuum reach up to the near infrared wavelength region, again qualifying these continua as seed for optical amplifiers with special regard to the CEP stability of the idler.

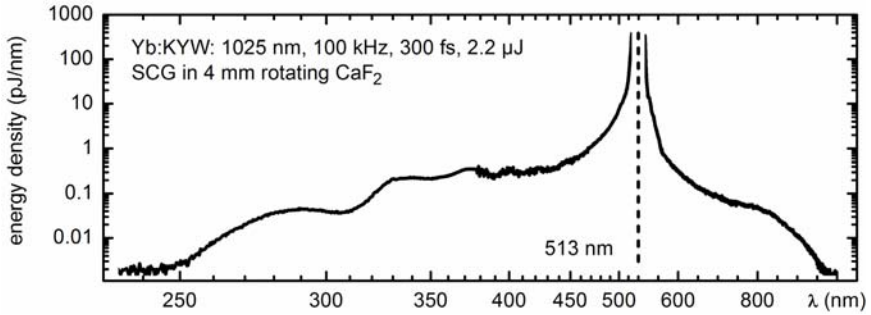

Fig. 2 Spectrum of continuum generated in a 4 mm rotating CaF_2 plate exceeding deep into the UV.

The field of super-continuum generation in bulk materials offers many rewarding opportunities for advanced laser applications and broadband femtosecond spectroscopy. With the systematic search for new crystals, continuum generation with ps pump is now within reach. This is confirmed by first successful experiments. The easy handling and the straight forward setup qualify continuum generation as good alternative broadband seed source for OPCPA systems, especially with regard to stability and synchronization issues.

1 M. Bradler, P. Baum, and E. Riedle, Appl. Phys. B **97**, 561, 2009.

2 U. Megerle, I. Pugliesi, C. Schriever, C.F. Sailer, and E. Riedle, Appl. Phys. B **96**, 215, 2009.

Appendix A4

Mid-IR femtosecond pulse generation on the microjoule level up to 5 µm at high repetition rates

M. Bradler, C. Homann, and E. Riedle

Opt. Lett. **36**, 4212 - 4214 (2011)

Reprinted with kind permission from the Optical Society of America (OSA)

Mid-IR femtosecond pulse generation on the microjoule level up to 5 μm at high repetition rates

Maximilian Bradler,* Christian Homann, and Eberhard Riedle

LS für BioMolekulare Optik, Ludwig Maximilians Universität München, Oettingenstrasse 67, 80538 Munich, Germany
**Corresponding author: maximilian.bradler@physik.lmu.de*

Received August 11, 2011; accepted September 7, 2011;
posted September 14, 2011 (Doc. ID 152672); published October 25, 2011

We show efficient generation of mid IR pulses tunable between 1 and 5 μm from 100 kHz class femtosecond systems. The concept can be applied to various sources, particularly based on Ti:sapphire and the newly evolving Yb^+ lasers. The mid IR pulses are generated as the idler of a collinear optical parametric amplifier pumped by the laser funda mental. The seed for this amplifier is the idler of a previous amplification stage pumped with the second harmonic and seeded with a visible continuum. This enhances the energy and allows us to influence the bandwidth of the final output. Pulses with microjoule energy and Fourier limits of 50 fs are achieved. © 2011 Optical Society of America

OCIS codes: 190.4970, 190.7110, 320.7130.

Femtosecond tunable mid-IR (MIR) pulses are a powerful tool to study ultrafast processes in physics, chemistry, and biology. Time resolved vibrational spectroscopy, carrier dynamics in monolayer graphene, high harmonic generation, and tunneling ionization are interesting research fields that benefit from studies with IR pulses. In most of these experiments weak signals slightly above the detection limit are measured. To achieve a good signal to noise ratio, high repetition rates are needed. Successful approaches generating tunable femtosecond MIR pulses at high repetition rates were already reported in the mid-90s [1–5]. They were based on optical parametric oscillators and amplifiers, as well as difference frequency generation (DFG). Current work extends these concepts by chirped pulse amplification [6,7] and the use of poled lithium niobate crystals [8,9]. A promising approach for higher efficiencies, especially for long wavelengths, is preamplification of the seed by the frequency doubled light [10–14]. However, the generation of ultrashort IR pulses at high repetition rates is still a challenging task. Up to now all approaches either have a complex setup, need synchronized lasers, show limited tunability, or have modest efficiencies or pulse energies.

In this Letter we present a novel concept for efficient and freely tunable MIR femtosecond pulse generation on the microjoule level with a compact setup based on a single laser source. No additional seed or pump lasers are needed, and pulses out to 5 μm are generated without an extra DFG stage. We solely use continuum generation and optical parametric amplification (OPA). Since these processes are not restricted to specific wavelengths, the concept can be applied to a variety of laser systems. Here we show the performance for a Ti:sapphire based system (RegA 9050; Coherent Inc.) that delivers 50 fs pulses at 800 nm with an energy of 5.7 μJ at 93 kHz repetition rate and for a Yb:KYW based system (Jenlas D2.fs; JENOPTIK Laser GmbH) delivering 300 fs pulses at 1025 nm with an energy of 40 μJ at 100 kHz.

Our concept is illustrated in Fig. 1(a). About 5% of the pump light is split off for supercontinuum generation (SCG) in YAG [15]; the main part is used for second harmonic generation (SHG). The SHG light pumps a first collinear OPA (pre-OPA) seeded by the visible part of the YAG continuum. The near-IR (NIR) idler of this pre-OPA is used to seed a second collinear amplifier (IR-OPA) pumped by the remaining fundamental light from the SHG. The collinear geometry in the IR-OPA allows use of the NIR signal and the MIR idler that is predicted to be passively carrier envelope phase stabilized [13,14]. Figure 1(b) shows the wavelength regions for the different stages: visible and NIR light in the pre-OPA (green), as well as NIR and MIR light in the IR-OPA (orange). Figure 1(c) shows spectra from the IR-OPA for the Ti:sapphire laser system and lithium niobate ($LiNbO_3$, orange) as an active medium. Spectra obtained with lithium iodate ($LiIO_3$) at 1 kHz are shown in black. The gray area indicates the absorption of air.

SHG pumped preamplification has two main advantages that are apparent when the desired MIR output is considered. Since there is no continuum seed available in the MIR, the IR-OPA has to be seeded in the NIR. For a wide MIR tunability, continuously tunable NIR light is needed. For the upcoming generation of pump lasers with high repetition rates and high average power, pulse

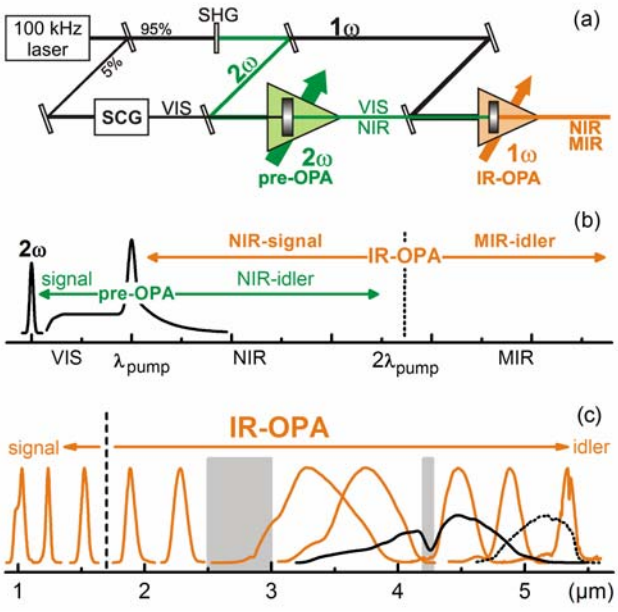

Fig. 1. (a) Scheme of the setup, (b) different wavelength re gions involved in the individual amplification stages, (c) typical MIR spectra when applying the concept to a Ti:sapphire system.

 © 2011 Optical Society of America

durations of 300 fs and longer are typical, and hence octave spanning spectra are only possible by continuum generation in solids [15]. Even these continua show an exponential dropoff on the red side of the pump and therefore only provide a weak NIR seed. However, they show smooth, flat, and gap free spectra in the visible that are well suited to seed an OPA. Therefore we amplify this part of the continuum in the pre-OPA, which is only possible with SHG pumping. The signal of this pre-OPA is in the visible, but the idler is in the desired NIR region and can seed the IR-OPA well.

The second advantage can be seen if the parametric gain G (ratio between signal and seed intensity) is considered as given by the following equation [4]:

$$G = \frac{1}{4}\exp\left(2 \cdot L \cdot \sqrt{\frac{8\pi^2 \cdot d_{\text{eff}}^2 \cdot I_p}{n_p \cdot n_s \cdot n_i \cdot \lambda_s \cdot \lambda_i \cdot \varepsilon_0 \cdot c_0}}\right). \quad (1)$$

I_p is the pump intensity, L the crystal length, d_{eff} the nonlinear coefficient, n_p, n_s, and n_i the refractive indices for pump, signal, and idler, respectively, λ_s and λ_i the signal and idler wavelengths, respectively, ε_0 the vacuum permittivity, and c_0 the speed of light. Bringing the picojoules per nanometer level of an NIR seed [15] over a 100 nm bandwidth to the desired microjoule level affords a gain of 10,000. Using only one amplification stage would necessitate pump intensities of 400 GW/cm^2 or more, even for $LiNbO_3$ with its high $d_{\text{eff}} = 4.04$ pm/V ($\lambda_s = 1.35$ μm, $\lambda_i = 4.2\,\mu$m, $L = 1$ mm effective [see Fig. 2(c)]; the refractive indices are about 2.3). Such high intensities are well in the continuum generation regime and close to the damage threshold. Therefore, multiple amplification stages are necessary (pre-OPA and IR-OPA). Because of the desired MIR output, the final amplifier must be pumped by the fundamental, and to ensure high output energies, it should be pumped with the main part of the available pump energy. In principle, SHG and fundamental pumping are possible in the pre-OPA, because only NIR seed light must be provided for the IR-OPA. Note that SHG pumping causes no loss of pump energy compared to fundamental pumping, because SHG efficiencies of up to 40% are achieved and the remaining fundamental light is used to pump the IR-OPA.

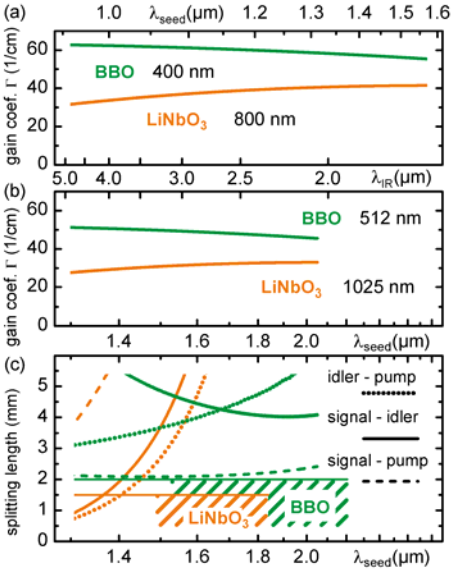

Fig. 2. Wavelength dependence of the gain coefficient in the pre OPA for (a) BBO pumped by 400 nm, $LiNbO_3$ pumped by 800 nm, and (b) BBO pumped by 512 nm, $LiNbO_3$ pumped by 1025 nm. The scale between (a) and (b) shows the final IR out put wavelength. (c) Pulse splitting length of the various wave combinations and crystals for the 1025 nm pump system.

To clarify the advantage of SHG pumping in the pre-OPA, we compare beta barium borate (BBO) pumped by the SHG with $LiNbO_3$ pumped by the fundamental at a pump intensity of 100 GW/cm^2. Fundamental pumping in BBO is not possible due to the idler absorption, and SHG pumping in $LiNbO_3$ causes two photon absorption. The wavelength dependence of the gain coefficient Γ [square root in Eq. (1)] is shown in Fig. 2(a) for a Ti:sapphire system and in 2(b) for a Yb^+ system. Throughout the NIR range (λ_{seed}) needed for MIR pulses out to 5 μm [see scale between Figs. 2(a) and 2(b)], Γ is much larger for the SHG pumped BBO than for the fundamental pumped $LiNbO_3$. The main reason for a higher gain coefficient for SHG pumping is the reduced product of signal and idler wavelength. The higher nonlinear coefficient of $LiNbO_3$ is cancelled by the lower refractive index of BBO. The pulse splitting lengths that limit the useful crystal length are given in Fig. 2(c) for the 1025 nm system. For the BBO crystal all lengths are above the 2 mm length used; for $LiNbO_3$ the range of λ_{seed} needed for MIR pulses in the interesting range of 3.5 to 5 μm results in significantly shorter splitting lengths. This would lead to a reduced amplification, since the gain in the small signal limit depends exponentially on this effective length. These two issues allow gain factors of 1000 in an SHG pumped pre-OPA even with moderate pump intensities, so that only a modest gain of around 10 is necessary for the IR-OPA, again achievable with intensities far below continuum generation or crystal damage. Thus SHG pumped preamplification allows high IR output with pump intensities below 100 GW/cm^2.

As amplifier material for the IR-OPA, we use $LiNbO_3$ because of its high d_{eff} in the MIR, where BBO is not transparent, and the high damage threshold. Since our concept demands only moderate pump intensities, even the use of $LiIO_3$ with its low damage threshold [12,13] was possible [see Fig. 1(c)]. The spectral width of close to 2 μm is due to the favorable acceptance bandwidth of $LiIO_3$ beyond 3 μm. The concept will also work for other typical IR crystals like potassium niobate ($KNbO_3$) or potassium titanyl phosphate (KTP) [16].

A potential challenge is that the seed for the IR-OPA is the idler of the pre-OPA and not a flat continuum. The bandwidth of this idler can easily be larger than the bandwidth supported by the IR-OPA. This means that not all NIR photons contribute to the IR amplification. To use all seed photons, the NIR bandwidth must be matched to the IR-OPA. This is done by chirping the visible seed continuum in the pre-OPA by inserting glass. Now the temporal overlap between seed and pump limits the bandwidth of the pre-OPA, and the bandwidth of the amplified signal (and hence the idler) can be controlled. We find no significant loss of NIR energy due to the seed chirp. Idler spectra of the pre-OPA when using different glasses in the visible seed are shown in Fig. 3(a) for the Yb:KYW pump. The gray area shows the bandwidth

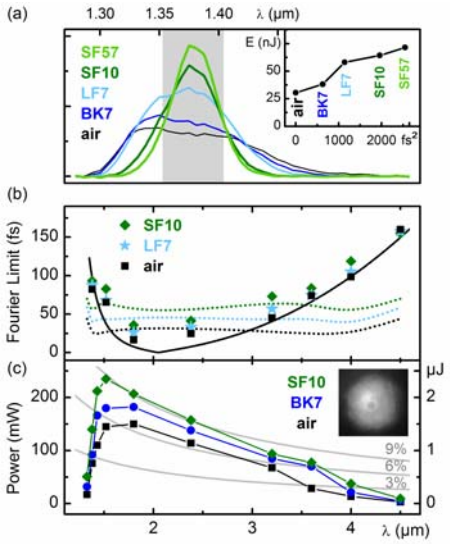

Fig. 3. (a) Idler spectra of 512 nm pumped pre OPA with chirped seed continuum. Gray area: bandwidth supported by IR OPA; inset: energy contained in this area. (b) Fourier limits (symbols) for IR OPA. Black curve: acceptance bandwidth for $LiNbO_3$; dotted curves: bandwidths of seed pulses. (c) Output power of MIR pulses with overall efficiencies.

supported in the IR-OPA for a 1.5 mm thick $LiNbO_3$ crystal. The inset shows the energy of the pre-OPA contained in this bandwidth. If the idler is narrower than this bandwidth, the MIR output inherits the bandwidth of the NIR seed. Nevertheless, the energy of the MIR output does not suffer, because all seed photons are amplified.

Figure 3(b) shows the Fourier limits and 3(c) the average output power of the MIR pulses for the chirped visible seed. Limits below 50 fs can be achieved over a wide tuning range with a power above 200 mW in the maximum and 50 mW at 4 μm. The maximum output energy with the shortest possible Fourier limit is reached if the bandwidth of the idler of the pre-OPA [dotted curves in Fig. 3(b)] matches the bandwidth supported by amplification in $LiNbO_3$ [black curve in Fig. 3(b)]. In this configuration the output energy increased by a factor of up to 2.6 with a constant Fourier limit.

With the Ti:sapphire system pulses from 1 to 5 μm with energy up to 420 nJ at 1.1 μm and 110 nJ at 3.4 μm with a Fourier limit of 27 fs are demonstrated. At 3.4 μm this corresponds to an overall energy conversion efficiency of 2.0%, i.e., up to 8.2% of the 800 nm photons are converted to IR photons. To show the energy scalability of our concept, we apply it to a 1 kHz Ti:sapphire system (CPA 2001; Clark MXR Inc.) that provides 150 fs pulses at 775 nm. Pulses of 250 μJ are used to operate the OPA. Again pulses tunable from 1 to 5 μm with energies of up to 8 μJ at 3.5 μm with measured pulse durations down to 38 fs are obtained. The low repetition rate allows us to measure the shot to shot stability. Typical values vary from 1% to 2% rms for the entire range. An IR beam profile was recorded [see inset of Fig. 3(c)].

In summary, we have shown ultrafast femtosecond MIR pulse generation at 100 kHz repetition rates based on continuum generation and optical parametric amplification. The compact setup with a footprint of below 1 m^2 operating with a single turn-key pump laser allows stable and reliable day to day operation. The wide tunability from one to 5 μm is only limited by the available amplifier material. Essential is the strong preamplifier pumped by the frequency doubled laser output, which allows use of the flat plateau of the visible continuum, matches the bandwidth to the IR-OPA, and enables high IR output with a modest gain in the IR-OPA pumped by the remaining fundamental. Our method will hopefully help to simplify actual approaches and benefit a new field of spectroscopic experiments due to the wide tuning range and the adjustable bandwidth.

We thank M. Breuer, C. Elsner, M. Betz, and D. J. Nesbitt for pilot investigations, the Deutsche Forschungsgemeinschaft (DFG) through the Cluster of Excellence: Munich-Centre for Advanced Photonics for financial support, and Horiba Jobin Yvon GmbH and JENOPTIK Laser GmbH for technical assistance.

References

1. A. Lohner, P. Kruck, and W. W. Rühle, Appl. Phys. B **59**, 211 (1994).
2. U. Emmerichs, H. J. Bakker, and H. Kurz, Opt. Commun. **111**, 497 (1994).
3. G. R. Holtom, R. A. Crowell, and X. S. Xie, J. Opt. Soc. Am. B **12**, 1723 (1995).
4. M. K. Reed, M. K. Steiner Shepard, M. S. Armas, and D. K. Negus, J. Opt. Soc. Am. B **12**, 2229 (1995).
5. B. Golubovic and M. K. Reed, Opt. Lett. **23**, 1760 (1998).
6. C. Erny, L. Gallmann, and U. Keller, Appl. Phys. B **96**, 257 (2009).
7. O. Chalus, P. K. Bates, M. Smolarski, and J. Biegert, Opt. Express **17**, 3587 (2009).
8. C. Manzoni, R. Osellame, M. Marangoni, M. Schultze, U. Morgner, and G. Cerullo, Opt. Lett. **34**, 620 (2009).
9. C. Heese, L. Gallmann, U. Keller, C. R. Phillips, and M. M. Fejer, Opt. Lett. **35**, 2340 (2010).
10. G. M. Gale, M. Cavallari, T. J. Driscoll, and F. Hache, Opt. Commun. **119**, 159 (1995).
11. G. M. Gale, G. Gallot, F. Hache, and R. Sander, Opt. Lett. **22**, 1253 (1997).
12. V. Petrov, F. Rotermund, and F. Noack, J. Opt. A **3**, R1 (2001).
13. D. Brida, C. Manzoni, G. Cirmi, M. Marangoni, S. De Silvestri, and G. Cerullo, Opt. Express **15**, 15035 (2007).
14. O. D. Mücke, D. Sidorov, P. Dombi, A. Pugzlys, A. Baltuska, S. Alisauskas, V. Smilgevicius, J. Pocius, L. Giniunas, R. Danielius, and N. Forget, Opt. Lett. **34**, 118 (2009).
15. M. Bradler, P. Baum, and E. Riedle, Appl. Phys. B **97**, 561 (2009).
16. C. J. Fecko, J. J. Loparo, and A. Tokmakoff, Opt. Commun. **241**, 521 (2004).

Appendix A5

Carrier-envelope phase stable sub-two-cycle pulses tunable around 1.8 μm at 100 kHz

C. Homann, M. Bradler, M. Förster, P. Hommelhoff, and E. Riedle

Opt. Lett. **37**, 1673 - 1675 (2012)

Reprinted with kind permission from the Optical Society of America (OSA)

Carrier-envelope phase stable sub-two-cycle pulses tunable around 1.8 μm at 100 kHz

Christian Homann,[1,*] Maximilian Bradler,[1] Michael Förster,[2] Peter Hommelhoff,[2] and Eberhard Riedle[1]

[1]*Lehrstuhl für BioMolekulare Optik, Ludwig Maximilians Universität München, Oettingenstrasse 67, 80538 Munich, Germany*

[2]*Ultrafast Quantum Optics Group, MPI für Quantenoptik, Hans Kopfermann Strasse 1, 85748 Garching, Germany*

**Corresponding author: christian.homann@physik.lmu.de*

Received November 24, 2011; revised February 13, 2012; accepted February 23, 2012;
posted February 23, 2012 (Doc. ID 158713); published May 10, 2012

We present a simple and efficient concept for the generation of ultrashort infrared pulses with passively stabilized carrier envelope phase at 100 kHz repetition rate. The central wavelength is tunable between 1.6 and 2.0 μm with pulse durations between 8.2 and 12.8 fs, corresponding to a sub two cycle duration over the whole tuning range. Pulse energies of up to 145 nJ are achieved. As a first application we measure the high nonlinearity of multiphoton photoemission from a nanoscale metal tip. © 2012 Optical Society of America

OCIS codes: 190.4970, 320.5520, 320.7110, 120.5050.

The generation of few-cycle light pulses with stable carrier-envelope phase (CEP) at wavelengths around 2 μm is still a challenging task [1–8], recently highlighted by a comprehensive review [9]. High-power pulses at these wavelengths are of great interest to extend the cutoff of high-order harmonic generation toward the water window [8]. Also, in the CEP-sensitive emission of electrons from metal nanostructures, where pulse energies of only 240 pJ at 800 nm sufficed to generate electrons with kinetic energies of up to 13 eV, the use of longer wavelengths is expected to greatly enhance electron energies and to give further insight into the interplay between multiphoton and tunneling ionization [10]. Investigations along these lines, which require high repetition rates, motivated us to develop a tunable few-cycle source.

Because sufficiently broadband laser materials for the generation of few-cycle pulses around 2 μm are still in their early stages of development, all concepts to generate such pulses rely on parametric processes, such as difference-frequency generation (DFG) or optical parametric (chirped pulse) amplification [OP(CP)A]. At repetition rates up to 1 kHz the generation of CEP-stable sub-two-cycle pulses for wavelengths up to 1.8 μm has been successfully demonstrated [5,6]. However, at higher repetition rates only significantly longer pulses with 6 to 7 optical cycles have been shown to date [4,11,12], although spectra with Fourier limits in the 20 fs regime have been achieved [13]. The difficulty in transferring the concepts used at 1 kHz to higher rates originates from the high pulse energies needed. To achieve the required spectral width, various approaches are combined with spectral broadening in hollow-core fibers, either for broadening the seed [2,3] or the final output [5,6], which necessitates pulse energies of several 100 μJ. Implementations without additional spectral broadening, e.g., by DFG of two noncollinear optical parametric amplifier (NOPA) outputs [1] depended on 200 μJ of pump pulse energy at 800 nm, not readily available at 100 kHz. Especially when only moderate pulse energies are needed for the experiment, the generation of hundreds of μJ of pump pulse energy at 100 kHz is unreasonable and might jeopardize future system miniaturization and integration.

In this Letter we present an efficient and simple scheme for the generation of CEP-stable pulses with a duration around 10 fs and energies on the order of 100 nJ at a repetition rate of 100 kHz. The pulses are tunable from 1.6 to 2.0 μm while maintaining a sub-two-cycle duration. To the best of our knowledge this constitutes the shortest pulse durations in this wavelength range for repetition rates above 1 kHz, combined with excellent tunability.

Our concept is based on broadband DFG between the short visible output of a NOPA and the narrow-band pump laser. A schematic of the setup is depicted in Fig. 1. A commercial Yb:KYW based pump laser (Jenlas D2.fs; JENOPTIK Laser GmbH) delivers ~300 fs pulses at 1025 nm with an energy of 40 μJ at 100 kHz repetition rate. For the current setup, 32 μJ of the pulse energy are used. Approximately 5% are split off for SCG in a 4 mm thick YAG crystal producing the seed for the NOPA [14]. The remaining part of the pump pulse is frequency doubled in a 0.8 mm thick BBO crystal cut at 23.5° with an efficiency of about 30%. Due to the small beam size of the pump laser ($1/e^2$ radius of 880 μm), no focusing was needed. The seed and the pump are both focused into a 3 mm thick BBO crystal cut at 20° with an external noncollinearity angle of 3.3°. The amplified spectrum can be tuned in central wavelength between 650 and 700 nm while maintaining a Fourier limit below 10 fs and energies around 2 μJ per pulse. After collimation with a spherical mirror, the output pulses are compressed to sub-20-fs duration using a sequence of fused silica prisms.

The 1025 nm light remaining after frequency doubling is rotated in polarization by 90° with a half-wave plate, and transmitted through a pair of wedges (10°, BK7),

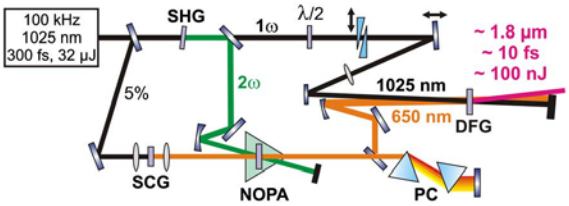

Fig. 1. (Color online) Setup; SHG, second harmonic genera tion; $\lambda/2$, half wave plate; SCG, supercontinuum generation; NOPA, noncollinear optical parametric amplifier; PC, prism compressor; DFG, difference frequency generation.

 © 2012 Optical Society of America

used for controlling the CEP of the 1.8 μm output. It is then focused into a 0.8 mm thick BBO crystal cut at 23.5° together with the compressed NOPA output to perform type-I DFG to the infrared (IR). This crystal thickness is much less than that typically used for an OPA stage and therefore allows a largely increased acceptance bandwidth and minimizes dispersion and group velocity mismatch. The beam radii ($1/e^2$ value) were 120 μm for the 1025 nm beam and 70 μm for the NOPA output for ease of alignment. To avoid the need for dichroic optics, the two beams are combined under a small angle, which is kept as small as possible (~0.9°) to limit the resulting spatial chirp of the IR pulse to below the divergence of 1°.

The spectrum of the IR output can be tuned in a considerable wavelength range by changing the NOPA spectrum and readjusting the phase-matching angle of the DFG and the time delay between the NOPA output and the 1025 nm pulses (Fig. 2, top row). The deconvolved pulse durations, obtained from autocorrelation measurements, lie between 8.2 and 12.7 fs, corresponding to only 1.5 to 1.9 optical cycles (Fig. 2, bottom row). Pulse energies of up to 145 nJ are achieved, however with slightly longer pulses (11.7 fs at 1.6 μm central wavelength). For the shortest pulse durations pulse energies of 40 nJ are achieved, corresponding to 4 mW of average power.

After frequency doubling, the temporal shape and the spectro-spatial phase of the remaining 1025 nm pulses are distorted from the original near-Gaussian, leading to a temporal double peak structure. Varying the delay between the relatively long 1025 nm pulses and the much shorter NOPA output results in two maxima in the IR energy. Interestingly, the shortest pulses are achieved when the NOPA pulses interact with the outer wings of the 1025 nm pulses. This also leads to smooth IR spectra without strong modulations, whereas spectral dips can occur when the NOPA output is overlapped with the distorted part of the 1025 nm pulse.

To substantiate the autocorrelation measurements we performed second-harmonic-generation frequency-resolved optical gating (SHG-FROG). As can be seen in Fig. 3, the measured and retrieved FROG traces show excellent agreement. The spectrum calculated from the frequency doubled spectrum fits the original spectrum measured with the monochromator almost exactly. To be able to compare the spectra, all spectrometers used were intensity calibrated with a black body lamp. The evaluation shows that in this case the IR pulses had some residual chirp resulting in a pulse duration of 13.4 fs.

The compression of the IR pulses is solely adjusted by the chirp of the NOPA output and thus the prism compressor in the visible. The shortest IR pulses are achieved when the NOPA pulses are also nearly optimally compressed. This scheme even allows compensating for material dispersion in the IR, introduced by, e.g., an entrance window to a vacuum chamber. For example, a pulse centered at 1.8 μm with a duration of 14.6 fs is negatively chirped by a 5 mm thick calcium fluoride window to 21.7 fs. By positively chirping the visible pulse through insertion of the second prism of the compressor deeper into the beam and readjusting the temporal overlap with the 1025 nm pulse, the IR pulse is recompressed to 16.1 fs. In principle, a nearly arbitrary pulse shaping of the IR pulse is possible by shaping the visible pulse in its Fourier plane at the end mirror of the compressor by, e.g., a deformable mirror or phase or intensity masks [15].

The NOPA output inherits the CEP fluctuations of the supercontinuum seed and hence of the 1025 nm pump. Since the NOPA output is subsequently difference frequency mixed with the 1025 nm light, the IR output is expected to be CEP stable [1,9]. To verify this, we set up an f-2f interferometer [12,16]. In our scheme, the phase-matching angle chosen for broadband DFG is close to that for frequency doubling of the 1.8 μm pulses, which leads to some weak 0.9 μm output. This light was separated from the main IR output by a dichroic mirror and rotated in polarization by 90°. The IR pulses were transmitted through a silicium filter and focused with a reflective microscope objective into a highly nonlinear fiber to broaden their spectrum. The broadened pulses and the frequency doubled light were then collinearly recombined by a metallic beam splitter and focused into a spectrometer with a time delay of ~400 fs. For proper

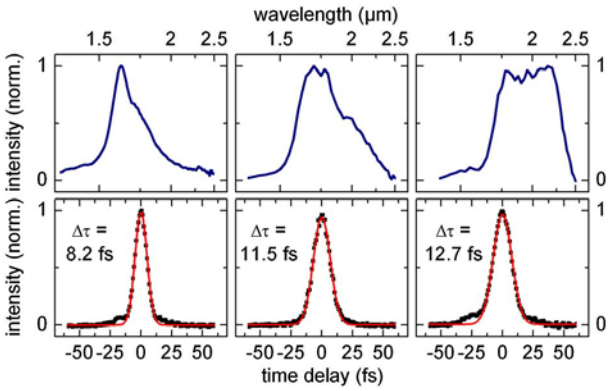

Fig. 2. (Color online) Spectra and corresponding autocorrelation measurements showing the wavelength tunability of our concept while maintaining a sub two cycle pulse duration ($\Delta\tau$: deconvolved FWHM Gaussian pulse duration).

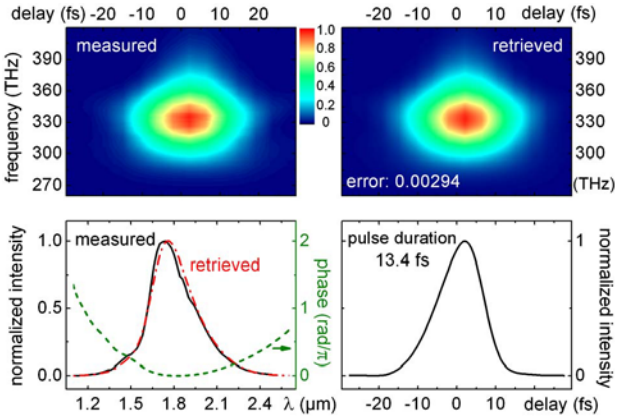

Fig. 3. (Color online) SHG FROG measurement of the IR output pulse. The measured and retrieved FROG trace show excellent agreement, as do the directly measured spectrum around 1.8 μm and the calculated spectrum from the SH spectrum (dashed dotted curve). The spectral phase (dashed curve) indicates some residual chirp. Bottom right: Retrieved intensity in the time domain.

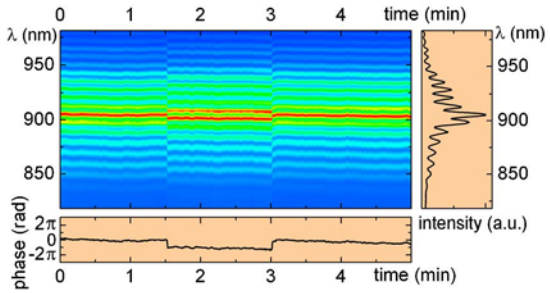

Fig. 4. (Color online) f 2f interference measurement. The right panel shows the spectrum of a single scan, the lower panel the evaluated phase. After 1.5 min. a CEP shift of π is induced by moving a wedge, which is reversed after 3 min.

alignment of the NOPA continuum generation, we observe a high contrast interference pattern that directly shows the CEP stability of the IR pulses. When integrating over 1 ms and acquiring 500 consecutive spectra (i.e., 0.5 s acquisition time), we measure phase fluctuations of only 78.5 mrad rms. Fig. 4 shows a measurement over 5 min (averaged over 100 ms). After 1.5 min we induce a CEP change of π by translating one of the wedges in the 1025 nm beam in front of the DFG stage (see Fig. 1) by approximately 6 μm. After 3 min the wedge is moved back. This clearly shows that we have full control of the CEP and can compensate for the observed slow drift. For the slower fluctuations (0.1 to 5 Hz) we find a value of 135 mrad rms.

As a first experimental application of our new source, we tightly focused pulses centered at ~2.0 μm and with durations of ~20 fs onto a nanoscale tungsten tip, with the laser polarization parallel to the tip-pointing direction. This leads to photoemission of electrons from the tip, which we accelerate by an electric dc field toward a microchannel plate (MCP) detector. Fig. 5 shows the count rate on the MCP screen as function of the incident pulse energy in a double-logarithmic plot. The fitted slope of 3.8 is close to the expected value for multiphoton photoemission, when the reduction of the work function due to the applied dc field (1.9 GV/m at the tip) is taken into account [10].

In summary, we have demonstrated the generation of CEP-stable sub-two-cycle pulses with tunable central wavelength from 1.6 to 2.0 μm and energies in the range of 100 nJ at 100 kHz repetition rate. The necessary spectral bandwidth is efficiently achieved by DFG in a mixing crystal much thinner than used in typical OPAs. The compression is achieved by just a simple prism compressor in the intermediate NOPA output. The principle is not limited to the sub-2-μm range, but can be readily extended far into the IR. The new setup is a highly attractive source for numerous applications, such as the study of electron emission from nanoscale metal tips, as demonstrated with the first experimental data. The photoemission from the metal tip shows that already extremely weak pulses are sufficient for this interesting regime of nonlinear optics.

Our concept is also an interesting seed source for high power applications. It allows omitting the Ti:Sa oscillator/amplifier with subsequent intra-pulse DFG [3], which has to be synchronized to the pump laser. Additionally, it

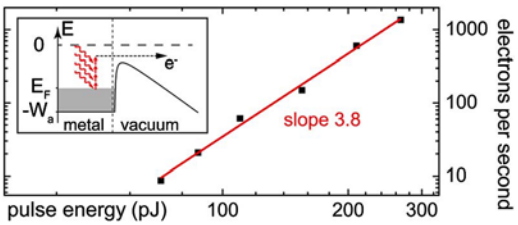

Fig. 5. (Color online) Current as function of the pulse energy focused onto a tungsten tip. Inset: schematic of the multiphoton photoemission process: E_F, Fermi energy; W_a, work function.

would provide much more seed energy than the reported few picojoules [7] to nanojoules, which will lead to a drastic improvement in pulse contrast. The remaining challenge will be to either generate a stable supercontinuum from the typical picosecond pump pulses or to boost the Jenlas D2.fs output pulses to the millijoule regime.

We thank M. Schenk and M. Krüger for experimental support with the electron measurement, and the DFG-Cluster of Excellence: Munich-Centre for Advanced Photonics for financial support.

References

1. C. Manzoni, G. Cerullo, and S. De Silvestri, Opt. Lett. **29**, 2668 (2004).
2. C. Vozzi, G. Cirmi, C. Manzoni, E. Benedetti, F. Calegari, G. Sansone, S. Stagira, O. Svelto, S. De Silvestri, M. Nisoli, and G. Cerullo, Opt. Express **14**, 10109 (2006).
3. X. Gu, G. Marcus, Y. Deng, T. Metzger, C. Teisset, N. Ishii, T. Fuji, A. Baltuska, R. Butkus, V. Pervak, H. Ishizuki, T. Taira, T. Kobayashi, R. Kienberger, and F. Krausz, Opt. Express **17**, 62 (2009).
4. O. D. Mücke, D. Sidorov, P. Dombi, A. Pugžlys, A. Baltuška, S. Ališauskas, V. Smilgevicius, J. Pocius, L. Giniunas, R. Danielius, and N. Forget, Opt. Lett. **34**, 118 (2009).
5. C. Li, D. Wang, L. Song, J. Liu, P. Liu, C. Xu, Y. Leng, R. Li, and Z. Xu, Opt. Express **19**, 6783 (2011).
6. B. E. Schmidt, A. D. Shiner, P. Lassonde, J. C. Kieffer, P. B. Corkum, D. M. Villeneuve, and F. Légaré, Opt. Express **19**, 6858 (2011).
7. K. H. Hong, S. W. Huang, J. Moses, X. Fu, C. J. Lai, G. Cirmi, A. Sell, E. Granados, P. Keathley, and F. X. Kärtner, Opt. Express **19**, 15538 (2011).
8. M. C. Chen, P. Arpin, T. Popmintchev, M. Gerrity, B. Zhang, M. Seaberg, D. Popmintchev, M. M. Murnane, and H. C. Kapteyn, Phys. Rev. Lett. **105**, 173901 (2010).
9. G. Cerullo, A. Baltuska, O. D. Mücke, and C. Vozzi, Laser Photon. Rev. **5**, 323 (2011).
10. M. Krüger, M. Schenk, and P. Hommelhoff, Nature **78**, 475 (2011).
11. C. Heese, L. Gallmann, U. Keller, C. R. Phillips, and M. M. Fejer, Opt. Lett. **35**, 2340 (2010).
12. A. Thai, M. Hemmer, P. K. Bates, O. Chalus, and J. Biegert, Opt. Lett. **36**, 3918 (2011).
13. M. Bradler, C. Homann, and E. Riedle, Opt. Lett. **36**, 4212 (2011).
14. M. Bradler, P. Baum, and E. Riedle, Appl. Phys. B **97**, 561 (2009).
15. T. Witte, D. Zeidler, D. Proch, K. L. Kompa, and M. Motzkus, Opt. Lett. **27**, 131 (2002).
16. M. Kakehata, H. Takada, Y. Kobayashi, K. Torizuka, Y. Fujihara, T. Homma, and H. Takahashi, Opt. Lett. **26**, 1436 (2001).

Appendix A6

Ultrafast photo-induced charge transfer unveiled by two-dimensional electronic spectroscopy

O. Brixner, V. Lukes, T. Mancal, J. Hauer, F. Milota, M. Fischer, I. Pugliesi, M. Bradler, W. Schmid, E. Riedle, H. F. Kauffmann, and N. Christensson

J. Chem. Phys. **136**, 204503 (2012)

Reprinted with kind permission from AIP Publishing

Ultrafast photo-induced charge transfer unveiled by two-dimensional electronic spectroscopy

Oliver Bixner,[1] Vladimír Lukeš,[2] Tomáš Mančal,[3] Jürgen Hauer,[1] Franz Milota,[1] Michael Fischer,[4] Igor Pugliesi,[5] Maximilian Bradler,[5] Walther Schmid,[4] Eberhard Riedle,[5] Harald F. Kauffmann,[1,6,a)] and Niklas Christensson[1]
[1]*Faculty of Physics, University of Vienna, Strudlhofgasse 4, 1090 Vienna, Austria*
[2]*Department of Chemical Physics, Slovak Technical University, Radlinského 9, 81237 Bratislava, Slovakia*
[3]*Institute of Physics, Faculty of Mathematics and Physics, Charles University, Ke Karlovu 5, Prague 121 16, Czech Republic*
[4]*Department of Organic Chemistry, University of Vienna, Währinger Straße 38, 1090 Vienna, Austria*
[5]*Lehrstuhl für BioMolekulare Optik, Ludwig-Maximilians-University, Oettingenstrasse 67, 80538 Munich, Germany*
[6]*Ultrafast Dynamics Group, Faculty of Physics, Vienna University of Technology, Wiedner Hauptstrasse 8 - 10, 1040 Vienna, Austria*

(Received 9 March 2012; accepted 5 May 2012; published online 24 May 2012)

The interaction of exciton and charge transfer (CT) states plays a central role in photo-induced CT processes in chemistry, biology, and physics. In this work, we use a combination of two-dimensional electronic spectroscopy (2D-ES), pump-probe measurements, and quantum chemistry to investigate the ultrafast CT dynamics in a lutetium bisphthalocyanine dimer in different oxidation states. It is found that in the anionic form, the combination of strong CT-exciton interaction and electronic asymmetry induced by a counter-ion enables CT between the two macrocycles of the complex on a 30 fs timescale. Following optical excitation, a chain of electron and hole transfer steps gives rise to characteristic cross-peak dynamics in the electronic 2D spectra, and we monitor how the excited state charge density ultimately localizes on the macrocycle closest to the counter-ion within 100 fs. A comparison with the dynamics in the radical species further elucidates how CT states modulate the electronic structure and tune fs-reaction dynamics. Our experiments demonstrate the unique capability of 2D-ES in combination with other methods to decipher ultrafast CT dynamics. © *2012 American Institute of Physics*. [http://dx.doi.org/10.1063/1.4720492]

I. INTRODUCTION

Charge transfer (CT) is a ubiquitous process in nature representing the initial step in many chemical reactions and bioenergetic pathways.[1] Photo-induced CT is intimately related to harnessing and conversion of radiative energy in photovoltaics,[2–4] photosynthesis,[5–7] and catalysis.[8] CT states, representing an excitation in a molecular aggregate where the electron and hole are located on different chromophores, are characterized by low transition dipole moments and strong sensitivity to environmental perturbations.[9,10] Due to their low transition dipole moments, CT states participate in photo-induced reactions via the interaction with optically allowed (bright) states. If the interaction with the CT states is weak, the resonance interaction between locally excited (LE) states leads to excited states which are delocalized over the chromophores in the aggregate (exciton states). For a more pronounced CT interaction, the mixing of excitonic and CT states leads to (delocalized) eigenstates exhibiting various degrees of charge separation. After photo-excitation, interaction with the nuclear degrees of freedom enables relaxation within the manifold of excited states, ultimately leading to population of the CT states.

The influence of the CT states on the electronic structure depends on the relative magnitude of resonance-coupling (Coulombic interaction between LE states) and CT-coupling (between LE and CT states, depending on the wave function overlap[11]). This elementary interplay can be studied in model systems where the different couplings can be controlled via the inter-pigment distance, and where the energies of the CT states can be altered electrochemically. One such class of molecules is bisphthalocyanines, which comprise two macrocyclic phthalocyanine moieties held together at a fixed distance by a rare earth cation.[12,13] The close proximity of the two rings (2.8 Å for lutetium) gives rise to delocalized charge distributions and results in strong CT coupling due to significant wavefunction overlap.[14] The resulting high degree of charge carrier mobility readily explains their semiconductivity[15,16] and electrochromic behavior.[17,18]

In its electronic ground state, lutetium bisphthalocyanine ($[LuPc_2]$) is a stable radical ($[LuPc_2]^{\bullet}$) with an intermediate oxidation state of -1.5 on each ring.[19] $[LuPc_2]^{\bullet}$ cannot stabilize inter-ring CT states, and the electronic structure can be understood via resonance interaction between the LE states. The electronic structure will be similar to that of a H-type dimer, which gives rise to a single transition in the linear absorption spectrum (Fig. 1). On the other hand, the anion ($[LuPc_2]^{-}$) exhibits CT states in the same energy range as the

a)Electronic mail: harald.f.kauffmann@univie.ac.at.

 © 2012 American Institute of Physics

Downloaded 19 Jun 2012 to 129.187.254.47. Redistribution subject to AIP license or copyright; see http://jcp.aip.org/about/rights and permissions

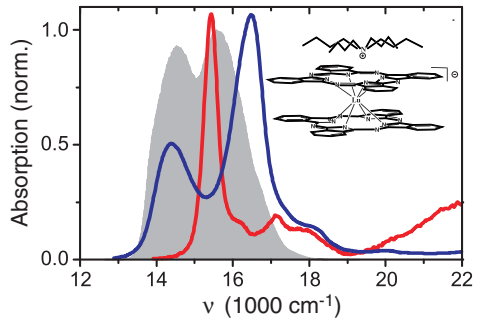

FIG. 1. Linear absorption of $[LuPc_2]^-TBA^+$ in benzonitrile (blue line) and $[LuPc_2]^\bullet$ in toluene (red line) shown together with the pulse spectrum used in the 2D experiments (grey). The inset shows the structure of $[LuPc_2]^-$ and the position of the TBA^+ counter-ion.

LE states.[14] The additional CT coupling drastically changes the electronic structure and gives rise to two bands in the linear absorption spectrum (Fig. 1). Therefore, the comparison of $[LuPc_2]$ in different oxidation states provides a perfect opportunity to pinpoint the influence of the CT states on the electronic structure and dynamics.

The structural and electronic similarities favor $[LuPc_2]^-$ as a biomimetic model system for studies of the special pair in the photosynthetic reaction center (RC).[5] However, for isolated $[LuPc_2]^-$, the CT states representing forward and backward CT between the rings are energetically degenerate, and the electronic structure can be described by charge resonance states.[14] The presence of an environmental asymmetry breaks the energetic degeneracy of the CT states, lowering the energy of the CT state on one side of the complex and enables a net transfer of charge after photo-excitation. In the RC, such asymmetry arises from differences in the electronic couplings among pigments due to slightly different spacings between the cofactor units,[20] distinct dielectric environments due to intra-protein electric fields,[21–23] and different hydrogen bonding pattern around the central units.[24] In other redox systems, the asymmetry may be provided by counter-ions. The formation of ion associates can have profound influence on the electronic structure and the path of chemical reactions.[25–27] For weak CT coupling (non-adiabatic CT), the role of the counter-ion has been studied, and it has been shown that the counter-ion can actively or passively control the rate of CT depending on the strength of association.[26–29]

Conventionally, CT has been studied in systems where the CT coupling is larger than the resonance coupling, implying that CT proceeds without interference from energy transfer processes. However, in systems like the natural RCs or in novel architectures for artificial light harvesting, the two couplings can be of equal magnitude and both energy transfer and CT will take place simultaneously. The interplay of resonance- and CT-coupling in these systems tunes the excited state evolution and the dynamics of the charge separation and energy transfer processes. Such excited state dynamics gives rise to complicated spectral signatures, making a detailed investigation of the underlying mechanisms with conventional techniques difficult. In this work we employ two-dimensional-(2D) and ultra-broadband pump-probe-spectroscopy to disentangle the excited state dynamics in a metal bridged dimer ($[LuPc_2]$), where the resonance- and CT-couplings are of equal magnitude. The influence of CT states and CT coupling on the excited state structure and dynamics is further studied via electrochemical tuning of the CT state energies. In addition, we investigate how specific details of ion-pairing enable ultrafast charge transfer across the complex. The combination of various approaches, both theoretical (quantum chemistry and density matrix propagation) and experimental (absorption, pump-probe, and 2D spectroscopy), gives a detailed picture of the ultrafast CT dynamics.

II. EXPERIMENTAL METHODS

Lutetium(III)bisphthalocyanine-tetrabutyl-ammonium salt ($[LuPc_2]^-TBA^+$) and its radical form $[LuPc_2]^\bullet$ were synthesized via a base catalyzed cyclotetramerization reaction of phthalonitrile with lutetiumacetate in the bulk-phase at elevated temperature. The synthesis was carried out using known procedures from the literature.[13,30] Both the synthetic preparation and the characterization of the complex are described in detail in the supporting material.[31]

The setup and methodology used for the 2D experiments has been described in detail previously.[32] In the experiments reported here, a home built non-collinear optical parametric amplifier (NOPA) operated at 200 kHz repetition rate generated pulses centered at 15 000 cm^{-1} with a bandwidth of 2500 cm^{-1} FWHM (Fig. 1). The FWHM of the intensity autocorrelation was 13 fs (9.2 fs pulse duration), while the corresponding width assuming a flat phase over the pulse spectrum was 10 fs. Two phase stable pulse pairs were generated by diffracting the NOPA pulses through a transmission grating. In the 2D experiment, the delay between the first two pulses, t_1, was scanned with interferometric accuracy, while the delay between the second and third interaction, t_2, was held constant. The signal radiated in the phasematching direction was overlapped with the local oscillator (LO), and the signal field was recovered by spectral interferometry. The 2D spectrum as a function of υ_1 and υ_3 was obtained by Fourier transforming over t_1 and addition of rephasing and non-rephasing signal contributions. The absolute phase of each 2D spectrum was determined by adjusting the LO delay and phase to optimize the overlap of the projection of the real part of the 2D spectrum with the spectrally resolved pump-probe signal.[31] $[LuPc_2]^-TBA^+$ dissolved in benzonitrile was used in a wire-guided flow jet giving a film thickness of 230 μm. The structure and linear absorption spectrum of $[LuPc_2]^-TBA^+$ are shown in Fig. 1 together with the NOPA spectrum used in the experiments.

Broadband pump-probe measurements were carried out in a setup described in detail previously.[33] To extend the probe range to the near-infrared (NIR) region, a home built optical parametric amplifier (OPA) operating at 8300 cm^{-1} was used to generate white-light from 9000–25 000 cm^{-1}.[4,34] To cover the bands in the UV region (25 000–32 000 cm^{-1}), white-light was generated by focusing the output from the Ti:Sapphire laser into a CaF_2 plate.[33] Pump pulses of ~40 fs duration were used to selectively excite the two bands at 14 200 and 16 200 cm^{-1} giving a time resolution of 50 fs.

Downloaded 19 Jun 2012 to 129.187.254.47. Redistribution subject to AIP license or copyright; see http://jcp.aip.org/about/rights and permissions

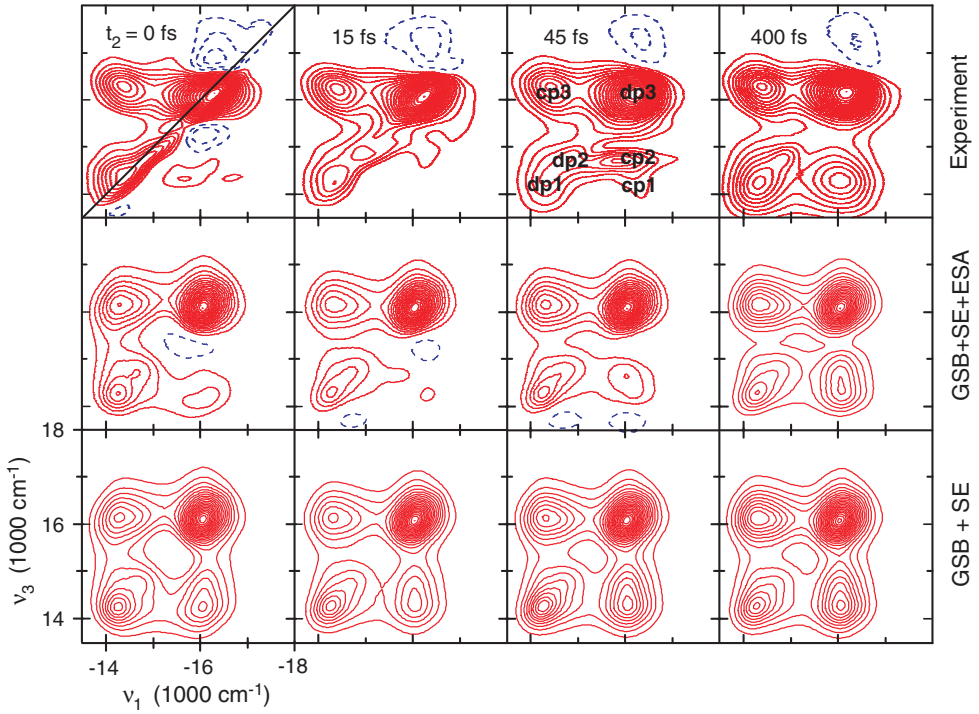

FIG. 2. 2D spectra of $[LuPc_2]^-TBA^+$ at different waiting times (t_2) indicated in the figure. The top row shows the experimental results, while the middle and bottom rows show the simulated total spectra and ground state bleach (GSB) plus stimulated emission (SE) contributions, respectively. All spectra have been normalized to the maximum of the total signal, and contour lines are drawn in 5% increments starting at 5%. Positive signal contributions (GSB + SE) are shown in red while negative (ESA) are shown in blue dash. The points used for the kinetics in Fig. 3 are shown for $t_2 = 45$ fs.

III. RESULTS

A. Experimental results

The interplay of exciton and CT states and their influence on the excited state dynamics in $[LuPc_2]^-$ have been studied previously with pump-probe and two-color photon echo-spectroscopy.[35,36] The pump-probe measurements revealed that the transient spectra were independent of which of the two bands was pumped, indicating rapid relaxation in the excited state. To resolve the excited state dynamics we turned to 2D spectroscopy.[37] By correlating the optical coherence evolution between the first and third time interval in a four-wave mixing sequence, 2D spectroscopy maps the system dynamics onto two dimensions, thereby minimizing spectral congestion, and provides a very detailed picture of the system's evolution.[38]

Figure 2 shows the real part of the 2D spectrum of $[LuPc_2]^-TBA^+$ in benzonitrile for $t_2 = 0$, 15, 45, and 400 fs. The waiting time t_2 denotes the delay between the first and the second pulse pairs, and corresponds to the probe delay in a pump-probe experiment. All spectra have been normalized to their respective maxima, and contour lines are drawn in 5% increments. In Fig. 2, positive signals correspond to stimulated emission (SE) and ground state bleach (GSB), while excited state absorption (ESA) results in negative signals. The 2D spectrum at $t_2 = 15$ fs (outside pulse overlap) shows two diagonal peaks corresponding to the two bands in the linear absorption spectrum. A closer inspection of the low energy diagonal peak reveals that it is more accurately described as two separate peaks at $\upsilon_3 = 14\,200$ and $14\,800$ cm^{-1}, respectively. Above the high energy diagonal peak we observe small amounts of ESA (blue dashed lines). In addition to the diagonal peaks and ESA contributions, one cross-peak at υ_1, $\upsilon_3 = 14\,200$, $16\,200$ cm^{-1} is clearly visible. This cross-peak shows that the transitions responsible for the main bands in the linear absorption spectrum share a common ground state. Surprisingly, there is no corresponding cross-peak below the diagonal. For longer t_2 we find that the cross-peak below the diagonal recovers. However, the recovery of the cross-peak is not uniform. The 2D spectrum at $t_2 = 45$ fs shows that the cross-peak at $\upsilon_3 = 14\,800$ cm^{-1} grows much faster than the one at $14\,200$ cm^{-1}. For longer t_2, the cross-peak below the diagonal becomes more symmetric, but its amplitude remains weaker than the amplitude of the opposite cross-peak for all t_2.

The 2D spectra in Fig. 2 do not provide an accurate picture of the dynamics in the system because of the normalization. The variation of the amplitudes of the different peaks as a function of t_2 provides information on population dynamics of the system which cannot be obtained from the normalized spectra. To analyze the kinetics, we show in Fig. 3 the time evolution of the volume of a 30×30 cm^{-1} box for the diagonal peaks at $14\,200$ (dp1), $14\,800$ (dp2), and $16\,200$ cm^{-1} (dp3), and the cross-peaks υ_1, $\upsilon_3 = 16\,200$, $14\,200$ cm^{-1} (cp1); υ_1, $\upsilon_3 = 16\,200$, $14\,800$ cm^{-1} (cp2); and υ_1, $\upsilon_3 = 14\,200$, $16\,200$ cm^{-1} (cp3). The positions of these points are also shown in Fig. 2 for $t_2 = 45$ fs. The kinetics of the diagonal peaks display a fast decay to about 50% of the value at $t_2 = 0$. The amplitude of dp3 decays on a 30 fs timescale, while dp1 and dp2 show an

Downloaded 19 Jun 2012 to 129.187.254.47. Redistribution subject to AIP license or copyright; see http://jcp.aip.org/about/rights and permissions

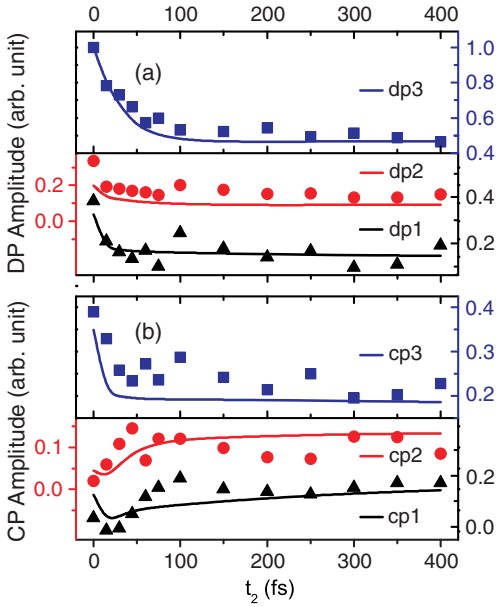

FIG. 3. Kinetics of the different points in the 2D spectra indicated in Fig. 2. (a) Diagonal peak kinetics for dp1 (black triangles), dp2 (red circles), and dp3 (blue squares, upper panel) together with the simulations (solid lines in the same color). The different curves have their own y-axis as indicated by the colors. (b) Cross-peak kinetics for cp1 (black triangles), cp2 (red circles), and cp3 (blue squares, upper panel) together with the simulated curves (solid lines).

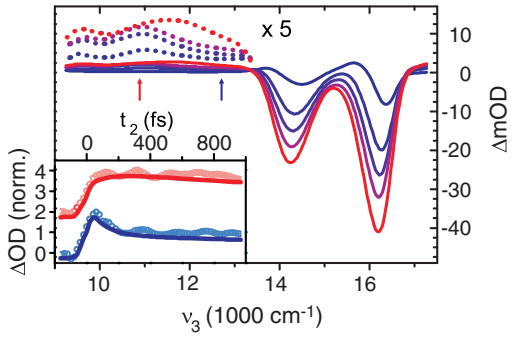

FIG. 4. Pump-probe spectra of $[LuPc_2]^-TBA^+$ in benzonitrile with a focus on the NIR region for t_2 = 0.1, 0.6, 1.5, 3, and 10 ps (from red to blue). The inset shows the (normalized) kinetics at the frequencies indicated by the arrows in the main figure, i.e., at 10 870 cm^{-1} (red circles) and 12 500 cm^{-1} (blue circles). The solid lines are the corresponding fits. In pump-probe spectroscopy, the standard sign convention (i.e., ΔOD) is opposite to that in 2D, e.g., ESA gives rise to positive signal contributions.

almost constant amplitude outside pulse overlap ($t_2 \geq 15$ fs). The cross-peaks exhibit more complicated behavior. While cp3 behaves qualitatively in the same way as dp3, the cross-peaks below the diagonal show distinct dynamics. The amplitude of cp2 rises on a 20 fs timescale followed by a quick decay. After about 50 fs, the rise is complete and the signal shows a slow oscillation around a stationary value. The amplitude of cp1 shows a delayed rise, reaching its peak value after about 100 fs. After reaching their final values, cp1 and cp2 both oscillate with a frequency of 160 cm^{-1}. The same modulation is found in pump-probe,[35] two-color photon echo.[36] We can assign this mode, based on our quantum chemical calculations, to a modulation of the Lu-N distance.[31]

The appearance of the 2D spectrum for $t_2 \geq 30$ fs deviates from what we expect for a coupled dimer, insofar as it does not display a characteristic four peak pattern.[39] The absence of a cross-peak below the diagonal gives rise to a pronounced asymmetry of the spectra. This effect clearly remains outside pulse overlap, but diminishes as the population relaxes from the upper band (decay of dp3). This points to ESA from the upper band as the origin of the cancellation of the cross-peak below the diagonal. As the ESA signal decays, the underlying GSB contribution becomes visible. Such relaxation should give rise to a SE signal in the region of the cross-peak below the diagonal (relaxation cross-peak). For this reason, we expect this cross-peak to be stronger than the corresponding one above the diagonal (cp3) when relaxation from the upper band has been completed. However, we find that the cross-peak below the diagonal remains weaker for all t_2. This observation could in principle be explained by loss of the SE signal due to relaxation to a state outside the spectral window or into a state with low transition dipole moment. However, we see no indication of such relaxation in the kinetics of either dp1+dp2 or cp1+cp2. If the population remains in the lower band, the positive SE signal could be hidden by a negative ESA signal overlapping with the positive GSB of the low energy band. While this would explain the 2D kinetics, it cannot explain the reported lack of fluorescence from the low energy band.[35]

It thus becomes apparent that the 2D experiment, despite the 4500 cm^{-1} probe range, is not able to follow all relaxation processes in the system and cannot provide on its own the basis for a complete relaxation model. To be able to probe the response of (possible) low energy states in the NIR which are not covered in our 2D experiment, we turned to broadband pump-probe spectroscopy. Figure 4 shows the pump-probe spectra in the NIR region for a few selected delays. At t_2 = 100 fs, a broad ESA signal covers the entire region from 9000 to 13 000 cm^{-1}. For longer t_2, the ESA around 12 500 cm^{-1} (blue arrow) seems to decay significantly faster than the ESA below 11 000 cm^{-1} (red arrow). The single wavelength fits shown in the inset reveal that the ESA at 10 870 cm^{-1} decays with a 3.8 ps exponential component, which is equal to the lifetime of the lowest excited state obtained from a global fit.[31] On the other hand, the signal at 12 500 cm^{-1} shows an additional 70–100 fs decay component. The kinetics in this spectral region reflects the sum of ESA and SE contributions. The additional fast decay of the signal at 12 500 cm^{-1} can thus be interpreted as the delayed rise of SE from an almost dark state with a transition in the NIR region as discussed above. The SE signal at 12 500 cm^{-1} is about 20 times weaker (∼1 compared to 20 mOD) than the main GSB peak at 14 200 cm^{-1}. The low transition dipole moment of this transition readily explains the lack of fluorescence in this system. Based on the 1/20 ratio of the transition strength of the "dark state" and the GSB togehter with the 3.8 ps lifetime, we estimate a fluorescence quantum yield in the 10^{-5} range. This is beyond the detection sensitivity of our and previous experiments.[35]

The discussion of 2D and pump-probe spectra above provides a rough overview of electronic structure and ultrafast

Downloaded 19 Jun 2012 to 129.187.254.47. Redistribution subject to AIP license or copyright; see http://jcp.aip.org/about/rights and permissions

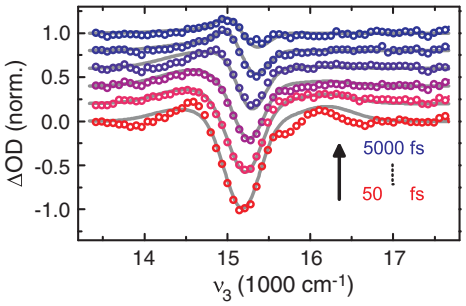

FIG. 5. Pump-probe spectra of $[LuPc_2]^\bullet$ in toluene for $t_2 = 0.05$, 0.2, 0.5, 1, 3, and 5 ps (from bottom to top). The spectra have been shifted for ease of viewing. Solid lines are fitted results based on a model discussed in the text. Negative signals correspond to SE/GSB in accordance with the convention in pump-probe.

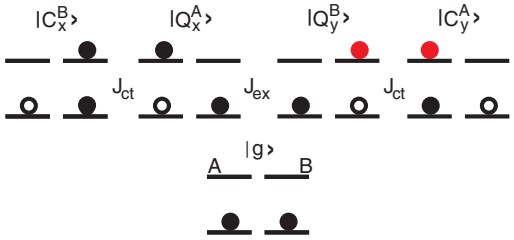

FIG. 6. Diagrams illustrating selected singly excited states contributing to the model. The full set of states is obtained by permutations of A → B. Solid circles represent electrons, hollow circles represent holes. Black and red color refer to excitation of x- and y-orbital, respectively. The couplings between the states are indicated by J_{ex} and J_{ct}.

dynamics in $[LuPc_2]^-TBA^+$. The states initially prepared by pumping the upper band decay to the low energy bright band on a 30 fs timescale. The presence of two diagonal peaks and the distinct relaxation dynamics associated with cp1 and cp2 point to two separate electronic states in this band (Fig. 3). The population of these two states flows on a 100 fs timescale into an almost dark state with a transition in the NIR range (Fig. 4).

To elucidate the influence of the CT states on the electronic structure in $[LuPc_2]$, we carried out pump-probe experiments on $[LuPc_2]^\bullet$. Figure 5 shows pump-probe spectra at selected delays together with the fit based on a kinetic model including the upper (optically allowed) exciton state, the lower (optically forbidden) exciton state, and a hot ground state. From the fit we conclude that the upper exciton level decays to the lower one with a 400 fs time-constant. From this level, there is an ESA transition to a doubly excited state. This doubly excited state is shifted by -550 cm^{-1} as compared to twice the LE energy. The red-shifted ESA from the dark state leads to a seemingly faster decay of the signal on the red side of the spectrum as the population flows into the low energy exciton state. Finally, the lower exciton level decays into a hot ground state with a 2.5 ps time-constant, where subsequent cooling takes place on a timescale of 15 ps.

B. Electronic structure of $[LuPc_2]$

To be able to interpret the experimental results on $[LuPc_2]$ and specifically to elucidate the role of the CT states, it is necessary to develop a model of the electronic structure enabling simulations of the linear- and nonlinear-spectra. Such a representation is provided by the Frenkel exciton Hamiltonian with LE and CT states.[40] This model provides a descriptive picture of the interaction of optical excitations with CT states, which is useful for generalization and interpretation of the results. Furthermore, it allows us to include doubly excited states needed to account for ESA, which is extremely important for the interpretation of the 2D experiments.

As a starting point we include the Q_x- and Q_y-excitations on each monomer (A and B). $[LuPc_2]$ exhibits D_{4d} symmetry,[12] e.g., the two rings are twisted by 45° with respect to each other (Fig. 1). The transitions on the different monomers interact via resonance coupling, and due to the overlap of the wave functions, the excitations on the different rings are also coupled via electron transfer into the LUMO orbitals. This allows us to construct 4 distinguishable CT states. In our terminology, C_x^A is the state where the excited electron is transferred from the excited x- or y-orbital on monomer B to the excited x-orbital on monomer A. A subset of the states used to construct the basis states is shown in Fig. 6. Using the configuration diagrams we can write the Hamiltonian for the one-exciton manifold as

$$H_S = \begin{bmatrix} C_x^B & 0 & J_{ct} & J_{ct} & 0 & 0 & 0 & 0 \\ 0 & C_y^B & -J_{ct} & J_{ct} & 0 & 0 & 0 & 0 \\ J_{ct} & -J_{ct} & Q_x^A & 0 & -J_{ex} & J_{ex} & 0 & 0 \\ J_{ct} & J_{ct} & 0 & Q_y^A & J_{ex} & J_{ex} & 0 & 0 \\ 0 & 0 & -J_{ex} & J_{ex} & Q_y^B & 0 & J_{ct} & -J_{ct} \\ 0 & 0 & J_{ex} & J_{ex} & 0 & Q_x^B & J_{ct} & J_{ct} \\ 0 & 0 & 0 & 0 & J_{ct} & J_{ct} & C_y^A & 0 \\ 0 & 0 & 0 & 0 & -J_{ct} & J_{ct} & 0 & C_x^A \end{bmatrix}, \quad (1)$$

where J_{ex} is the resonance-coupling and J_{ct} is the CT-coupling.

Taking the rings as equivalent, $Q_x = Q_y$, and assuming that $C_x^A \geq Q_x^A$, the present model recovers the previously proposed electronic structure of $[LuPc_2]^-$.[14,41,42] In this model, the band at 14 200 cm^{-1} has predominant charge resonance character, while the band at 16 200 cm^{-1} has a dominant exciton character. In addition, this model predicts one dark transition in the NIR region.[14] This exciton model agrees very well with our time-dependent/density functional theory (TD/DFT) calculations on $[LuPc_2]^-$ discussed in Appendix A. These calculations yielded three doubly degenerate electronic states with vertical transition energies of 11 682, 15 848, and 18 657 cm^{-1}, and oscillator strengths of 0.00, 0.45, and 1.03, respectively.

Both the exciton model in the form discussed above and the direct TD/DFT calculations predict two bright states in the relevant spectral range, i.e., the two main absorption bands. However, none of the models are able to explain the double peak structure of the low energy band or the distinct dynamics of the cross-peaks below the diagonal in the 2D spectra. To find an explanation for these additional features found in the experiment, we investigated the role of the counter-ion (TBA^+) present in our experiments. NMR studies on a series of bisphthalocyanines have shown a considerable amount of

Downloaded 19 Jun 2012 to 129.187.254.47. Redistribution subject to AIP license or copyright; see http://jcp.aip.org/about/rights and permissions

TABLE I. Transition energies and oscillator strengths for the first 6 electronic states in $[LuPc_2]^-TBA^+$ at the BHLYP/SV(P) level of theory.

	ν (cm^{-1})	f	Orbitals
q_1	10 384	0.001	51% HOMO → [LUMO + 1], 48% HOMO → LUMO
q_2	10 449	0.003	51% HOMO → LUMO, 48% HOMO → [LUMO + 1]
q_3	15 625	0.150	86% HOMO → [LUMO + 2]
q_4	15 823	0.156	85% HOMO → [LUMO + 3]
q_5	17 986	0.504	85% [HOMO − 1] → LUMO
q_6	18 116	0.523	85% [HOMO − 1] → [LUMO + 1]

ion association in solution.[30,43] These experiments concluded that the counter-ion is situated on top of one of the Pc macrocycles as indicated in Fig. 1. This is similar to the arrangement in the crystal structure,[12] which we took as a starting point for the calculations of the optimized ground state geometries and vertical transition energies of the $[LuPc_2]^-TBA^+$ complex. The calculations show that the interaction with the counter-ion leads to a splitting of the doubly degenerate states found for $[LuPc_2]^-$, giving rise to 6 transitions in the relevant spectral range. The energies, oscillator strengths, and contributing orbitals for $[LuPc_2]^-TBA^+$ as derived from quantum chemistry are shown in Table I.

The association with the counter-ion leads to significant changes in the electronic structure of the complex and gives rise to additional allowed electronic transitions. To understand how these changes can be interpreted in terms of the energies and couplings between the states in the exciton model, Fig. 7 shows the optimized ground state geometry for $[LuPc_2]^-$ and $[LuPc_2]^-TBA^+$. For $[LuPc_2]^-$, the di-anionic rings (Pc^{2-}) display a symmetric off-planarity distortion due to electrostatic interaction with the central metal ion. In the presence of the counter-ion, the off-planarity distortion is decreased significantly along the axis in contact with the alkyl chains of the TBA^+ molecule. From an exciton model point of view, this implies that the excitation along this axis, here Q_x, on the ring closest to the counter-ion should be lowered in energy. Similarly, the state corresponding to CT into the same orbital should decrease in energy as well.

The simulations of the linear absorption spectra of $[LuPc_2]^\bullet$ and $[LuPc_2]^-TBA^+$ based on Eq. (1) are shown in Fig. 8(a). For $[LuPc_2]^-TBA^+$ we also show the stick-spectrum obtained after direct diagonalization of H_s. Denoting the ring closest to the (positive) counter-ion A, we find that lowering the energy of C_x^A (electron transfer towards the counter-ion) is able to mimic the general features of the electronic structure found in the quantum chemical calculations. For Fig. 8(a) we used $Q_x^A = Q_y^A = Q_x^B = Q_y^B = 13\,500$ cm^{-1}, $C_x^B = C_y^B = C_y^A = 15\,150$ cm^{-1}, $C_x^A = 11\,600$ cm^{-1}, $J_{ex} = 1395$ cm^{-1}, and $J_{ct} = 725.5$ cm^{-1}. Based on the quantum chemical calculations, we expect that the interaction with the counter-ion should lead to a decrease of the energy of Q_x^A as well. However, changing the energy of Q_x^A by -500 cm^{-1} only leads to minor changes in the linear absorption spectrum and we therefore kept all Q-transitions degenerate for the remainder of the paper. To avoid confusion with the states obtained from quantum chemistry, we will denote the states of the exciton model with e_n. States e_1, e_2, and e_3 are located in the NIR and have very low or zero transition dipole moments. States e_4 and e_5 are located in the low energy band seen in linear absorption and are separated by $\sim$500 cm^{-1} (Fig. 8(a)). This double peak structure in the low energy bright band is essential to reproduce the observations in the 2D spectrum. State e_6 is dark and is located in between the two bands, while states e_7 and e_8 are the origin of the upper band in linear absorption.

With the large number of states and couplings, a fit to the linear absorption spectrum is by no means unique. An important test of the validity of the model and the parameters is to apply the model derived for the $[LuPc_2]^-TBA^+$ to $[LuPc_2]^\bullet$. The radical itself is non-polar and can therefore not stabilize the CT states. We modeled the spectrum of $[LuPc_2]^\bullet$ by raising the energies of the CT states to a spectral position

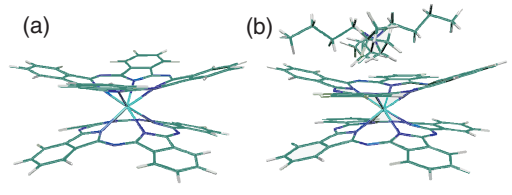

FIG. 7. Optimized ground state geometries at the BHLYP/SV(P) level of theory. (a) $[LuPc_2]^-$ and (b) $[LuPc_2]^-TBA^+$.

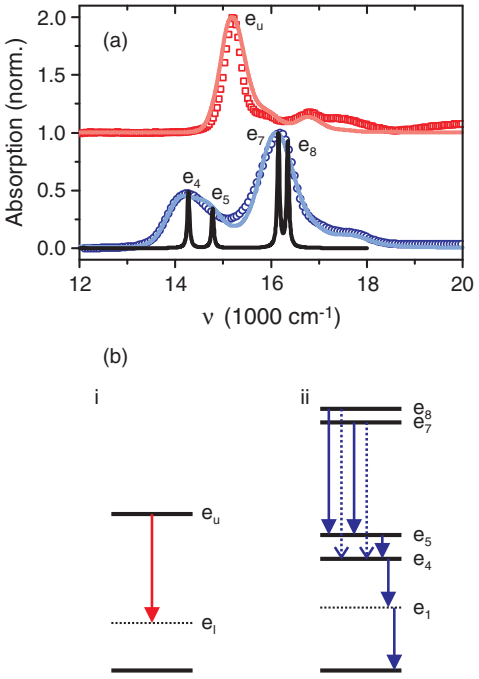

FIG. 8. (a) Linear absorption spectra of $[LuPc_2]^\bullet$ (red squares) and $[LuPc_2]^-TBA^+$(blue circles). The solid curves show the simulations based on the model discussed in the text. For $[LuPc_2]^-TBA^+$, the stick-spectrum using a single realization of disorder is also shown. The four peaks correspond to the transitions to the states e_4 (14 273 cm^{-1}), e_5 (14 778 cm^{-1}), e_7 (16 153 cm^{-1}), and e_8 (16 349 cm^{-1}) in the exciton model. (b) Energy level structure in the exciton model for $[LuPc_2]^\bullet$ (i) and $[LuPc_2]^-TBA^+$ (ii). Solid (dashed) lines correspond to states with large (small) transition dipole moment from the ground state. Solid (dashed) arrows indicate the major (minor) relaxation pathways discussed in the text.

Downloaded 19 Jun 2012 to 129.187.254.47. Redistribution subject to AIP license or copyright; see http://jcp.aip.org/about/rights and permissions

where their influence on the Q transitions is negligible. In addition, we used that the Q_x/Q_y-transitions are degenerate in the absence of the counter-ion. The successful prediction of the transition frequency, width of the main peak, and vibrational sideband for $[LuPc_2]^\bullet$ evident from Fig. 8(a) shows that we have correctly estimated the spectral densities, resonance coupling, and Q-transition energies in $[LuPc_2]$.

The quantum chemical calculations and the exciton model represent two different descriptions of the electronic structure of $[LuPc_2]$. The quantum chemical calculations adopt a supra-molecular perspective and include resonance- and CT-couplings between the two rings implicitly. The exciton model is based on distinguishable molecular excitations with free parameters (energies and couplings) and a minimum number of interactions. Using the language of the exciton model, the quantum chemical calculations include more states and couplings and will provide a more realistic molecular view. For instance, the quantum chemical calculations account for hole transfer and polarization of $[LuPc_2]^-TBA^+$ in the ground state, which is not included in the exciton model. However, the quantum chemical calculations do not provide insight into the dynamics of the system or provide any information about doubly excited states, and therefore the combination of both models is needed for the interpretation of the experimental results. The states of the two models cannot be linked one-to-one, but a comparison of the excited state manifolds[31] suggests that one can well connect the dynamics of states e_4, e_5 to q_3, q_4 and e_7, e_8 to q_5, q_6.

C. Excited state dynamics in $[LuPc_2]^-TBA^+$

The preceding paragraph outlined a realistic description of the electronic structure of $[LuPc_2]^-TBA^+$. To interpret the observed excited state dynamics we carried out simulations of the 2D spectra based on the CT-Hamiltonian (Eq. (1)) and time-dependent Redfield theory in the Markov approximation (see Appendix B). The simulated 2D spectra and kinetics are shown in the middle and bottom rows of Fig. 2 and in Fig. 3, respectively.

The simulations are in very good agreement with the experimental results, and reproduce the shape and evolution of the 2D spectra. At $t_2 = 0$, there is a clear asymmetry, where the cross-peak below the diagonal is significantly weaker than the one above the diagonal. It follows from the comparison of the total simulated signal with the GSB + SE contribution (Fig. 2) that the missing cross-peak is due to overlap of ESA from population in the upper band. The simulations also reproduce the double peak structure of the low energy band, and we can assign this feature to the eigenstates e_4 and e_5 of the Hamiltonian H_s. The splitting between dp1 and dp2 is close to the frequency of one of the vibrational modes found in the quantum chemical calculations (725 cm^{-1}).[31] If dp2 was a vibrational sideband to dp1, this mode would need to have a Huang-Rhys factor of the order of 1 to match the observed amplitude. This would give rise to a progression of peaks not seen in the experiments. Furthermore, within the Condon approximation, all vibrational transitions involving the same mode would have the same direction of the transition dipole moment and we would thus expect to see clear cross-peaks between them.[44] The lack of a cross-peak between dp1 and dp2 is readily reproduced in our model (Fig. 2). This can be understood from the perpendicular orientations of the transition dipole moments of e_4 and e_5, which suppress cross-peaks by a factor of three in an experiment with all parallel polarizations.[45]

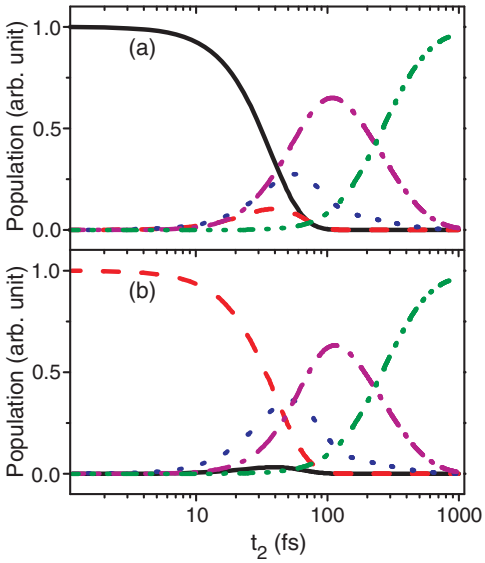

FIG. 9. Dynamics of e_8 (black solid), e_7 (red dash), e_5 (blue dot), e_4 (magenta dashed-dotted), and e_1 (olive dashed-dotted-dotted) after initial population of e_8 (a) and e_7 (b).

After excitation, coupling to the bath drives relaxation between energy levels in the one-exciton manifold leading to dynamics in the 2D spectrum. Figure 9 shows the simulated evolution of the populations after excitation of state e_7 and e_8 corresponding to the band at 16 200 cm^{-1}. The initially prepared states decay and populate state e_5 within 30 fs while the population of state e_4 rises somewhat slower. This is particularly obvious for initial excitation of state e_7 (Fig. 9(b)), where a clear separation of the rise of the population of e_4 and e_5 can be observed. By inspecting the relaxation rates, we can conclude that relaxation from $e_8 \rightarrow e_5$ and $e_7 \rightarrow e_5$ (Redfield rates[31] of 18 and 11 fs) is about 3 times faster than relaxation to state e_4 (64 and 75 fs). This indicates that the faster rise of cp2 can be traced to faster population relaxation into state e_5. To investigate if this relaxation path also leads to clear signatures in the 2D spectra, we show in Fig. 10 the simulated kinetics with and without the ESA contribution. Inspecting the kinetics, we find that the cross-peaks indeed show a fast rise reflecting SE after population transfer from the upper band, and cp2 rises somewhat faster than cp1. However, the SE contribution in cp2 does not acquire significant amplitude due to fast relaxation from state $e_5 \rightarrow e_4$. Although the ESA contribution strongly reshapes the kinetics in the 2D spectra, we can conclude that the dominating relaxation pathway from the upper band involves relaxation via state e_5 further on to e_4 (see Fig. 8(b)).

Turning to the diagonal peaks, we find that the SE signal decays on a 250 fs timescale. Interestingly, this decay is almost absent when the kinetics of the total signal is evaluated

Downloaded 19 Jun 2012 to 129.187.254.47. Redistribution subject to AIP license or copyright; see http://jcp.aip.org/about/rights and permissions

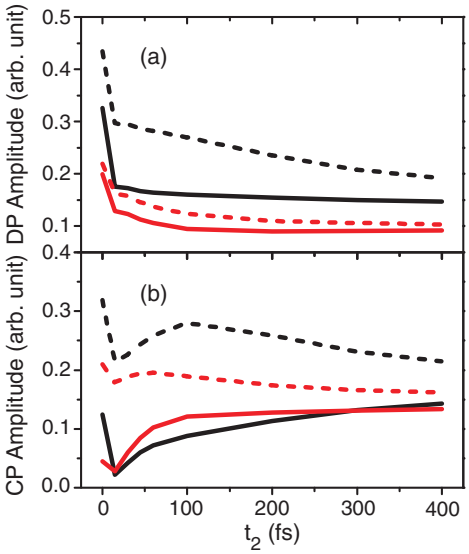

FIG. 10. Kinetics of the simulated 2D spectra with (solid) and without (dashed) ESA contribution. (a) dp1 (black) and dp2 (red). (b) cp1 (black) and cp2 (red).

(Fig. 10(b)). This implies that the ESA contribution has a similar magnitude as the SE contribution, and that they both decay as the population flows out of e_4 and e_5. This matches the observations of the experiments, where the low energy diagonal peak shows little dynamics even though it is clear from the pump-probe measurements that the dark states in the bottom of the manifold of excited states get populated on a 100 fs timescale.

The changes in the shape of the cross-peak below the diagonal during relaxation from the upper to the lower band could provide valuable information on the relaxation pathways. The experimental 2D spectrum at $t_2 = 45$ fs (Fig. 2) shows that cp2 has its maximum at lower υ_1 as compared to cp1. The simplest interpretation of this effect is that e_5 gets populated from e_7 while e_4 gets populated from e_8. The kinetics shown in Fig. 9 shows that e_7 preferentially populates e_4 and thus gives some support for such a conclusion. However, inspecting the simulated spectra in Fig. 2, we can conclude that the inclusion of ESA is essential to reproduce the temporal evolution of the shape of the cross-peaks. The negative ellipticity of the cross-peaks (an elongation along the anti-diagonal) remains after relaxation, but is only reproduced when the ESA contribution is included in the simulations. The shape of the cross-peaks is thus not related to anti-correlated diagonal disorder[46] (site energies) or off-diagonal disorder (coupling disorder), but result from the overlap of the different signal contributions.

IV. DISCUSSION

A. Role of charge transfer states in [LuPc$_2$]

The ability to alter the CT state energies in [LuPc$_2$] electrochemically gives a good opportunity to study the influence of CT states on the electronic structure and dynamics in a coupled system. In this respect, it is instructive to compare [LuPc$_2$]$^-$ to [LuPc$_2$]$^\bullet$ and for a moment neglect the influence of the counter-ion. It is already clear from Fig. 1 that the presence of the CT states in [LuPc$_2$]$^-$ dramatically changes the excited state structure giving rise to new transitions and a redistribution of the oscillator strength. Comparing the evolution of the upper state(s) in [LuPc$_2$]$^\bullet$ and [LuPc$_2$]$^-$ illustrates that there is a strong impact on the dynamics as well: the lifetime decreases from 400 to 30 fs in the presence of the CT states. The results summarized in Fig. 8(a) show that our model can interpolate between [LuPc$_2$]$^-$ and [LuPc$_2$]$^\bullet$ by just shifting the energy of the CT states, and this allows us to pinpoint the mechanism for the slower dynamics in [LuPc$_2$]$^\bullet$. Our model shows that the energetic splitting between the upper and lower band is significantly larger in [LuPc$_2$]$^\bullet$ ($\sim$2800 cm^{-1}) as compared to [LuPc$_2$]$^-$ ($\sim$2000 cm^{-1}). We find that the fast rates in [LuPc$_2$]$^-$ can only be reproduced when we include vibrational (intra-molecular) modes in the bath. From this we conclude that the 1600 cm^{-1} mode responsible for the vibrational sideband in [LuPc$_2$] plays a central role in the relaxation processes. To fully explain the rates in the experiments we need to account for the influence of the counter-ion. The association with the counter-ion splits the degenerate energy levels and opens up additional relaxation pathways in the appropriate energy range ($\sim$1600 cm^{-1}). Turning to [LuPc$_2$]$^\bullet$, we find that the energy gap is too large for relaxation via the high frequency vibrational mode. Relaxation must thus proceed via the (weak) high energy wing of the Brownian oscillator spectral density used to describe the overdamped bath modes. The difference in the relaxation rates between [LuPc$_2$]$^-$ and [LuPc$_2$]$^\bullet$ is thus not related to the enhanced coupling to the bath of the CT states, but determined by the differences in the energy level structure of the two systems. We note that the speedup of relaxation in the presence of CT states depends on the details of the relaxation mechanism and the spectral densities. In the presence of high frequency vibrational modes, the larger system-bath coupling of the CT states may not necessarily lead to a significant increase in the relaxation rates as was shown recently in a simulation study of the photosystem II reaction center.[40]

From the geometrical structure and linear optical properties, [LuPc$_2$]$^-$ seems to be a highly suitable candidate for investigations of fundamental processes such as electronic coherence dynamics, dephasing, and population relaxation. Such studies would be valuable for a better understanding of the more complicated dynamics observed in protein pigment complexes.[47–49] However, the 2D spectra of [LuPc$_2$]$^-$TBA$^+$ show distinct differences to the dimer models in the literature.[39,46,50–55] These differences cannot be explained by a rapid damping of the electronic coherences due to stronger system-bath coupling of the CT states. Rather, our analysis shows that including vibrational modes as well as employing a proper model for the two-exciton manifold is needed in order to understand the spectra and dynamics. The properties of the states in the two-exciton manifold responsible for ESA cannot be deduced from available quantum chemical calculation with the needed precision, and therefore we need to resort to the exciton model. Perhaps the most prominent observation in the present experiments is the absence of a cross-peak below the diagonal at short population times (or

Downloaded 19 Jun 2012 to 129.187.254.47. Redistribution subject to AIP license or copyright; see http://jcp.aip.org/about/rights and permissions

lack of SE in pump-probe). While this requires a special structure of the two-exciton manifold, the same effect can show up in any coupled system. In fact, such cancelation happens readily in the exciton model when the two LEs have unequal transition dipole moments. The absence of the cross-peak should thus not be seen as a direct effect of the CT states, but illustrates the importance of the two-exciton manifold and ESA for a proper interpretation of the spectra and dynamics. This might seem surprising because the 2D spectra are dominated by positive signal contributions (Fig. 2). However, ESA reshapes the peaks and strongly affects the observed kinetics (Fig. 10). We note that our simple model for the two-exciton band can account for the cancelation of the cross-peak below the diagonal as well as the absence of decay dynamics in the low energy band. To reach this agreement we need to shift the two-exciton band by $-1000\ \mathrm{cm}^{-1}$ from the values estimated from the Frenkel exciton model. A similar redshift of the two-exciton manifold can be observed in $[LuPc_2]^{\bullet}$ ($-550\ \mathrm{cm}^{-1}$), indicating that electron correlation effects[56] are significant in this system even in the absence of the CT states. Inspecting the (full) pump-probe spectrum, one finds a very broad ESA covering the entire visible spectral range.[31] In order to reproduce the ESA spectrum in the visible spectral range, we would need to include more (high energy) configurations to the two-exciton Hamiltonian. The interaction of these high energy configurations with the ones included in our model could further contribute to the red-shift of the ESA observed in the experiments.

The current experiments and analysis highlight the importance of the two-exciton manifold for the interpretation of time-resolved spectroscopy of processes which take place exclusively in the one-exciton manifold. In one-dimensional techniques, like pump-probe or transient grating, the presence of ESA may easily be overlooked leading to erroneous interpretation of the dynamics. In this respect, the combination of single- and double-quantum 2D spectroscopy is most useful to elucidate the role of ESA and the associated signal contributions.[57,58]

The pronounced influence of ESA in $[LuPc_2]$ makes in-depth analysis of the 2D spectra without numerical modeling difficult. Such simulations require a simple Hamiltonian mimicking the electronic structure of the system. There are many models which could fit the linear spectrum and give rise to a suppressed cross-peak below the diagonal which grows as t_2 increases, e.g., the simple exciton model with unequal transition dipole moments of the two LEs or the isolated $[LuPc_2]^-$ model discussed above. However, none of these models is able to reproduce the dynamics in the cross-peak below the diagonal, or the double peak structure of the low energy band. By linking the exciton model to quantum chemical calculations, it is clear that precisely these features are signatures of special interactions, and that they provide important information on the dynamics in the system.

B. Excited state charge transfer in $[LuPc_2]^-TBA^+$

The association of $[LuPc_2]^-$ with the TBA^+ counter-ion provides a natural explanation for the observation of the double peak structure in the low energy band in the 2D spectra (Fig. 2). The formation of such ion-pairs has strong impact on the character of the excited states. The (positive) charge of the counter-ion serves to stabilize states representing CT towards the counter-ion. This gives rise to an asymmetry in the energies of the CT states, and as a result, the electronic eigenstates in $[LuPc_2]^-TBA^+$ will reflect varying degrees of charge separation. Relaxation between the different energy levels thus represents a net redistribution of electron and hole densities between the two rings, which can be followed by the evolution of the cross-peaks in the 2D spectra. By combining the analysis of the cross-peak dynamics within the exciton model with the results of the quantum chemical calculations, it becomes possible to obtain a molecular view of the CT dynamics.

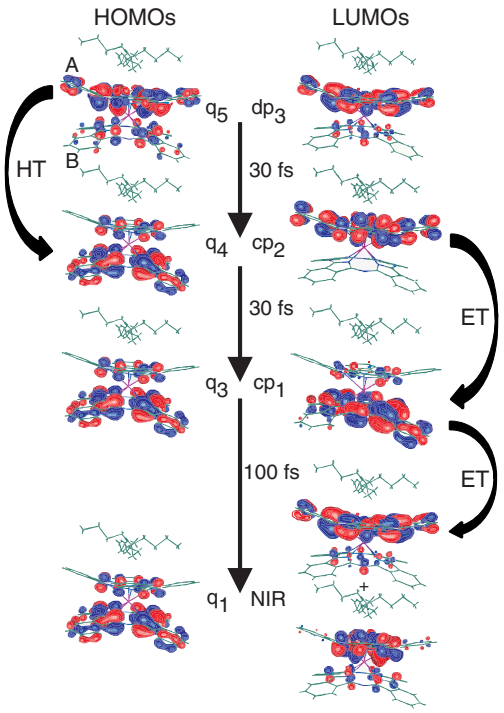

FIG. 11. Dominant orbitals involved in selected transitions for $[LuPc_2]^-TBA^+$ using TD-BHLYP/SV(P). The legend to the left refers to the number of the state in Table I, and the legend to the right to the features assigned in Fig. 2. The timescales are obtained from the analysis of the kinetics of the 2D spectra. The curved arrows indicate the different electron (ET) and hole-transfer (HT) processes taking place after excitation of the upper band in $[LuPc_2]^-TBA^+$.

Figure 11 shows the orbitals for the different bright transitions with labels indicating the states and the corresponding features in the spectrum in Fig. 2. In addition, curved arrows are used to indicate the CT processes connecting the different states. An excitation of the high energy band (dp3) populates an excited state with most of the charge density located on the side of the counter-ion (ring A). The system first relaxes via hole transfer (CT in the HOMO orbital) to ring B in 30 fs. This process is revealed via the faster rise of cp2 in the 2D spectrum. Further relaxation requires electron transfer (CT in the LUMO orbital) to ring B, and we find that this process also takes place on a 30 fs timescale. The system then goes to a stable (on ps timescale) charge separated state with a transition in the NIR. For this state, the excited state charge density

Downloaded 19 Jun 2012 to 129.187.254.47. Redistribution subject to AIP license or copyright; see http://jcp.aip.org/about/rights and permissions

is located on the ring closest to the counter-ion. Our pump-probe measurements reveal that populating the dark states in the NIR takes only about 100 fs. The combination of CT states and asymmetric interaction with the counter-ion thus opens up a relaxation pathway which very rapidly localizes the charge on one side of the complex. At first glance, one may assume that the counter-ion lowers the energy of both C_x^A and C_y^A and stabilizes the charge in both orbitals on the side of the counter-ion. However, it is clear from both the quantum chemical calculations as well as the exciton model that the molecular details of the interaction between $[LuPc_2]^-$ and the counter-ion need to be considered. The counter-ion induces different distortions of the molecular structure along the x- and y-coordinates, and this also affects the energies of the CT states representing CT into the corresponding orbitals on the macrocycle closest of the counter-ion. This selectivity is clearly manifested in the orbitals shown in Fig. 11, and shows that a detailed understanding of the ultrafast dynamics requires careful consideration of the interactions in the ion-pair.

$[LuPc_2]^-TBA^+$ has many similarities to the so called special pair in the bacterial reaction center. The special pair is a dimer of bacteriochlorophylls coupled to CT states with higher transition energy than the fundamental excitations.[9] However, because of different orientation of the transition dipoles, the lowest excited state (often named P^-) carries most of the oscillator strength. Charge separation in the special pair takes place after direct excitation or energy transfer to P^-. Numerous works have concluded that P^- corresponds to a state with most of the charge density located on the M-side of the special pair. This localization of the charge density has been explained by specific interactions, such as hydrogen bonds,[24,59] asymmetric interaction with the protein,[21,23] or a special arrangement and interaction of the reaction center pigments.[20,59–61] In the language of the exciton model, all these mechanisms serve to lower the CT states on one side of the complex in a similar way as the counter-ion in our case. Our results show that the presence of an asymmetric interaction facilitates relaxation to the bottom of the band, where the charge is localized on one side of the complex. In the special pair, the relaxation time between the upper and lower exciton band has been measured to be 65 fs.[62] The localization of the charge density on the M side of the special pair is thought to be important for the directionality of electron transfer in the bacterial reaction center, since the M side has a better overlap with the accessory bacteriochlorophyll on the L branch.[61] Our experiments show that this type of charge localization can be mimicked by our model system, and followed in real time with 2D spectroscopy. The combination of 2D spectroscopy and theoretical analysis including density matrix propagation and quantum chemical calculations thus offers new possibilities to disentangle the complicated CT dynamics observed in the photosystem II reaction center.[63,64]

V. CONCLUSIONS

In this work we have investigated the electronic structure and excited state dynamics in a bis-phthalocyanine dimer ($[LuPc_2]^-$) where the resonance- and CT-coupling are of the same magnitude. To selectively investigate the effects from the resonance coupling, we have exploited the possibility to "turn off" the CT coupling by oxidation of the complex ($[LuPc_2]^\bullet$). Based on linear absorption, 2D spectroscopy, and pump-probe measurements, we have shown that the mixing of exciton and CT states in $[LuPc_2]^-$ leads to significant changes of the electronic structure and a tenfold speedup of the excited state dynamics as compared to the excitonic $[LuPc_2]^\bullet$. The speedup of the dynamics in $[LuPc_2]^-$ can be qualitatively understood from the changes in the energy level spacing due to the presence of CT states in combination with quasi-resonances between the energy gaps and high frequency vibrational modes. However, a detailed analysis of the 2D spectra has shown that the interaction of $[LuPc_2]^-$ with its TBA^+ counter-ion needs to be considered to account for all peaks and their evolution. Using quantum chemical calculations, we have demonstrated that the specific details of the interaction in the ion-pair determines the electronic structure of $[LuPc_2]^-TBA^+$. The interaction with the counter-ion stabilizes CT states corresponding to CT into specific orbitals on the macrocycle closest to the counter-ion. The subsequent imbalance in energy of the CT states results in an electronic structure where the different excited states represent varying degrees of charge separation. Relaxation in the excited state of the complex thus proceeds via electron- and hole-transfer processes, which give rise to distinct cross-peak dynamics in the 2D spectra. The analysis of the cross-peak dynamics, together with quantum chemical calculations, demonstrate the ability of 2D electronic spectroscopy to provide a detailed molecular view on these transient CT processes.

ACKNOWLEDGMENTS

This work was supported by the Austrian Science Foundation (FWF), Project Nos. P223311 and F016-18 (SFB ADLIS), Österreichischer Austauschdienst (OeAD, WTZ CZ07/2011), and the Deutsche Forschungsgemeinschaft through the DFG-Cluster of Excellence Munich-Centre for Advanced Photonics. V.L. thanks for the opportunity to use the computer facilities at the University of Vienna (Schrödinger Cluster) and at the Institute of Theoretical Chemistry, University of Vienna. T.M. acknowledges support by the Czech Science Foundation (GACR) through Grant No. 205/10/0989 and by the Ministry of Education, Youth, and Sports of the Czech Republic through Grant No. KONTAKT ME899 and the Research Plan No. MSM0021620835. N.C. acknowledges support from the Wenner-Gren foundation.

APPENDIX A: QUANTUM CHEMICAL CALCULATIONS

The BHLYP[65]) functional was applied in DFT and TD/DFT[66]) calculations of optimal electronic ground state and lowest singlet excited-state geometries. This functional combines Becke's half-and-half exchange functional with the LYP correlation functional proposed by Lee, Yang, and Parr. Among the tested functionals (PBE,[67] B3LYP,[68] and BHLYP[65]), the overall best results were obtained using BHLYP, which can be explained by the larger amount of exact exchange.[69] The optical transitions were calculated

Downloaded 19 Jun 2012 to 129.187.254.47. Redistribution subject to AIP license or copyright; see http://jcp.aip.org/about/rights and permissions

using TD/DFT on the basis of the optimized geometries. We employed the split valence basis sets def-SV(P) (for N, C, H, and O atoms) and def-ecp for lutetium[70] from the TURBOMOLE library. Herein, valence orbitals were calculated in a double-zeta basis and augmented with higher angular momentum polarization functions to account for the nonplanarity of the macrocycles. All quantum chemical calculations were performed with the TURBOMOLE 5.7 package.[71]

APPENDIX B: SIMULATIONS OF EXCITED STATE DYNAMICS AND NONLINEAR SPECTRA

Excited state dynamics were simulated by applying time-dependent Redfield theory to the diagonalized Frenkel exciton Hamiltonian of the system.[11] Altogether eight singly excited electronic states were considered in the [$LuPc_2$] dimer. In addition to the local Q_x/Q_y-excitations on each Pc ring, CT states corresponding to electron transfer from the excited state orbital on one macrocycle to the excited state orbital on the other ring were considered. The CT states were modeled as excited states with zero transition dipole moment from the electronic ground state and increased reorganization energy (with respect to the LE states).[9,10] The sign of the resonance coupling matrix elements, J_{ex}, was determined from the structure. For the coupling between CT and LE states, J_{ct}, we chose the signs of the matrix elements so that the Hamiltonian was invariant under rotation of the rings. The magnitudes of J_{ex} and J_{ct} were fitted to the linear absorption spectrum. Linear and nonlinear spectra were calculated by a standard semiclassical response function theory.[72] For calculation of nonlinear spectra we constructed response functions corresponding to GSB, SE, and ESA in the Markov approximation,[73] i.e., neglecting correlations between the systems time evolution at different intervals of the response functions. Orientational average was directly taken into account for each response function.[45] To describe line shapes and kinetics of the peaks, the dissipative population and coherence dynamics have to be calculated for the electronic states of the molecule. Dissipation was included via an analytical form of the time-dependent Redfield equation, invoking the secular approximation.[31] For the calculation of the nonlinear spectra, the two-exciton manifold responsible for the ESA contributions needs to be included. As a first approximation we included the 28 states which can be constructed by simultaneous excitation of two single exciton transitions (doubly excited states). This is a straightforward generalization of the usual Frenkel exciton model to the case of CT states. However, electron correlation effects,[56] or inclusion of doubly excited monomeric states[74] can shift the energy of the two-exciton manifold. To account for these effects, not included in our model, we adjusted the energy of the two-exciton band to obtain the best agreement between simulation and experiment. A more rigorous treatment of the two-exciton CT band would have to account for various special properties of the combined doubly excited states, e.g., the fact that some double CT configurations result in normal double exciton states.[40] For calculation of the dephasing in the ESA part of the signal, the depopulation rates of the doubly excited states are required. Here we assumed that the depopulation rates are equal in the one- and two-exciton manifolds.

The coupling of the electronic transitions to the bath, described by the spectral density, determines both the line shapes and the population relaxation rates. Each transition was coupled to 3 vibrational modes with frequencies of 160, 725, and 1600 cm^{-1} and Huang-Rhys factors of $S = 0.3$, 0.4, and 0.3, respectively. Additionally, one over-damped Brownian oscillator with reorganization energy of 80 cm^{-1} and a decay rate of 100 fs^{-1} was used. For the CT states, we increased the coupling to the over-damped mode by a factor of 1.3. The vibrational modes are needed in order to reproduce the vibrational sideband in linear absorption as well as the fast rates found for $[LuPc_2]^-$. In all calculations of optical spectra, we explicitly averaged the signals over 1000 configurations where the transition energies were randomly sampled from a Gaussian distribution with a FWHM of 300 cm^{-1}.

[1] R. A. Marcus and N. Sutin, Biochim. Biophys. **811**, 265 (1985).
[2] C. Deibel, T. Strobel, and V. Dyakonov, Adv. Mater. **22**, 4097 (2010).
[3] J. R. Durrant and T. M. Clarke, Chem. Rev. **110**, 6736 (2010).
[4] D. Herrmann, S. Niesar, C. Scharsich, A. Köhler, M. Stutzmann, and E. Riedle, J. Am. Chem. Soc. **133**, 18220 (2011).
[5] R. E. Blankenship, *Molecular Mechanisms of Photosynthesis* (Wiley-Blackwell, 2002).
[6] S. R. Meech, A. J. Hoff, and D. A. Wiersma, Proc. Natl. Acad. Sci. U.S.A. **83**, 9464 (1986).
[7] V. I. Novoderezhkin, J. P. Dekker, and R. van Grondelle, Biophys. J. **93**, 1293 (2007).
[8] A. Bauer, F. Westkämper, S. Grimme, and T. Bach, Nature (London) **436**, 1139 (2005).
[9] T. Renger, Phys. Rev. Lett. **93**, 188101 (2004).
[10] T. Mančal, L. Valkunas, and G. R. Fleming, Chem. Phys. Lett. **432**, 301 (2006).
[11] V. May and O. Kühn, *Charge and Energy Transfer Dynamics in Molecular Systems* (Wiley-VCH, Berlin, 2000).
[12] N. Koike, H. Uekusa, Y. Ohashi, C. Harnoode, F. Kitamura, T. Ohsaka, and K. Tokuda, Inorg. Chem. **35**, 5798 (1996).
[13] M. Moussavi, A. D. Cian, J. Fischer, and R. Weiss, J. Opt. Soc. Am. B **27**, 1287 (1988).
[14] N. Ishikawa, O. Ohno, Y. Kaizu, and H. Kobayashi, J. Phys. Chem. **96**, 8832 (1992).
[15] M. Bouvet and J. Simon, Chem. Phys. Lett. **172**, 299 (1990).
[16] M. Maitrot, G. Guillaud, B. Boudjema, J.-J. André, H. Strzelecka, J. Simon, and R. Even, Chem. Phys. Lett **133**, 59 (1987).
[17] K. M. Kadish, T. Nakanishi, A. Gürek, V. Ahsen, and I. Yilmaz, J. Phys. Chem. B **105**, 9817 (2001).
[18] M. M. Nicholson, Ind. Eng. Chem. Prod. Res. Dev. **21**, 261 (1982).
[19] G. Ostendorp and H. Homborg, Z. Anorg. Allg. Chem. **622**, 1222 (1996).
[20] D. Kolbasov and A. Scherz, J. Phys. Chem B **104**, 1802 (2000).
[21] M. R. Gunner, A. Nicholls, and B. Honig, J. Phys. Chem. **104**, 4277 (1996).
[22] M. Wakeham and M. Jones, Biochem. Soc. Trans. **33**, 851 (2005).
[23] M. A. Steffen, K. Lao, and S. G. Boxer, Science **264**, 810 (1994).
[24] L. J. Moore, H. Zhou, and S. G. Boxer, Biochemistry **38**, 11949 (1999).
[25] A. Cembran, F. Bernardi, M. Olivucci, and M. Garavelli, Proc. Natl. Acad. Sci. U.S.A. **102**, 6255 (2005).
[26] E. V. Vakarin, M. F. Holovko, and P. Piotrowiak, Chem. Phys. Lett. **363**, 7 (2002).
[27] R. A. Marcus, J. Phys. Chem. B **102**, 10071 (1998).
[28] P. Piotrowiak, Inorg. Chim. Acta **225**, 269 (1994).
[29] P. Piotrowiak and J. R. Miller, J. Phys. Chem. **97**, 13052 (1993).
[30] H. Konami, M. Hatano, and A. Tajiri, Chem. Phys. Lett. **160**, 163 (1989).
[31] See supplementary material at http://dx.doi.org/10.1063/1.4720492 for details of the synthesis, phasing of the 2D spectra to pump-probe, vibrational modes obtained from the quantum chemical calculations, a comparison of the transitions obtained from quantum chemistry and the exciton model, a discussion of the time dependent Redfield equation, and broadband pump-probe spectra of the anion.
[32] F. Milota, J. Sperling, A. Nemeth, and H. F. Kauffmann, Chem. Phys. **357**, 45 (2009).
[33] U. Megerle, I. Pugliesi, C. Schriever, C. F. Sailer, and E. Riedle, Appl. Phys. B **96**, 215 (2009).

Downloaded 19 Jun 2012 to 129.187.254.47. Redistribution subject to AIP license or copyright; see http://jcp.aip.org/about/rights and permissions

[34]M. Bradler, P. Baum, and E. Riedle, Appl. Phys. B **97**, 561 (2009).
[35]B. S. Prall, D. Y. Parkinson, N. Ishikawa, and G. R. Fleming, J. Phys. Chem. A **109**, 10870 (2005).
[36]B. S. Prall, D. Y. Parkinson, G. R. Fleming, M. Yang, and N. Ishikawa, J. Chem. Phys. **120**, 2537 (2004).
[37]D. M. Jonas, Annu. Rev. Phys. Chem. **54**, 425 (2003).
[38]M. Cho, Chem. Rev. **108**, 1331 (2008).
[39]P. Kjellberg and T. Pullerits, J. Chem. Phys. **124**, 24106 (2006).
[40]D. Abramavicius and S. Mukamel, J. Phys. Chem. **133**, 184501 (2010).
[41]N. Ishikawa, J. Porphyr. Phthalocyanines **5**, 87 (2001).
[42]R. Rousseau, R. Aroca, and M. Rodríguez-Méndez, J. Mol. Struct. **356**, 49 (1995).
[43]M. S. Haghighi, G. Peters, and H. Homborg, Z. Anorg. Allg. Chem. **620**, 1285 (1994).
[44]N. Christensson, F. Milota, J. Hauer, J. Sperling, O. Bixner, A. Nemeth, and H. F. Kauffmann, J. Phys. Chem. B **115**, 5383 (2011).
[45]R. M. Hochstrasser, Chem. Phys. **266**, 273 (2001).
[46]A. V. Pisliakov, T. Mančal, and G. R. Fleming, J. Chem. Phys. **124**, 234504 (2006).
[47]J. M. Womick and A. M. Moran, J. Phys. Chem. B **113**, 15771 (2009).
[48]D. Zigmantas, E. L. Reed, T. Mancal, T. B. A. T. Gardiner, R. J. Cogdell, and G. R. Fleming, Proc. Natl. Acad. Sci. U.S.A. **103**, 12672 (2006).
[49]D. B. Turner, K. E. Wilk, P. M. G. Curmi, and G. D. Scholes, J. Phys. Chem. Lett. **15**, 1904 (2011).
[50]D. Egorova, M. F. Gelin, and W. Domcke, J. Chem. Phys. **126**, 074314 (2007).
[51]D. V. Voronine, D. Abramavicius, and S. Mukamel, J. Chem. Phys. **125**, 224504 (2006).
[52]D. Abramavicius, V. Butkus, J. Bujokas, and L. Valkunas, Chem. Phys. **372**, 22 (2010).
[53]J. Yuen-Zhou and A. Aspuru-Guzik, J. Chem. Phys. **134**, 134505 (2011).
[54]M. Cho and G. R. Fleming, J. Chem. Phys. **123**, 114506 (2005).
[55]L. Chen, R. Zheng, Q. Shi, and Y. Yan, J. Chem. Phys. **132**, 024505 (2010).
[56]K. Raghavachari and J. B. Anderson, J. Phys. Chem. **100**, 12960 (1996).
[57]A. Nemeth, F. Milota, T. Mančal, T. Pullerits, J. Sperling, J. Hauer, H. F. Kauffmann, and N. Christensson, J. Chem. Phys. **133**, 094505 (2010).
[58]N. Christensson, F. Milota, A. Nemeth, I. Pugliesi, E. Riedle, J. Sperling, T. Pullerits, H. F. Kauffmann, and J. Hauer, J. Phys. Chem. Lett. **1**, 3366 (2010).
[59]W. W. Parson and A. Warshel, J. Am. Chem. Soc. **109**, 6152 (1987).
[60]P. O. J. Scherer and S. F. Fischer, Chem. Phys. **131**, 115 (1989).
[61]Y. Ren, W. Ke, Y. Li, L. Feng, J. Wan, and X. Xu, J. Phys. Chem. B **113**, 10055 (2009).
[62]D. C. Arnett, C. C. Moser, P. L. Dutton, and N. F. Scherer, J. Phys. Chem. B **103**, 2014 (1999).
[63]J. Myers, K. Lewis, F. Fuller, P. Tekavac, C. Yocum, and J. Ogilvie, J. Phys. Chem. Lett. **1**, 2774 (2010).
[64]K. L. M. Lewis and J. P. Ogilvie, J. Phys. Chem. Lett. **3**, 503 (2012).
[65]A. D. Becke, J. Chem. Phys. **98**, 1372 (1993).
[66]R. Bauernschmitt, M. Häser, O. Treutler, and R. Ahlrichs, Chem. Phys. Lett. **264**, 573 (1997).
[67]J. P. Perdew, K. Burke, and M. Ernzerhof, Phys. Rev. Lett. **77**, 3865 (1996).
[68]A. D. Becke, J. Chem. Phys. **98**, 5648 (1993).
[69]A. Dreuw and M. Head-Gordon, J. Am. Chem. Soc. **126**, 4007 (2004).
[70]T. H. Dunning and P. J. Hay, *Methods of Electronic Structure Theory* (Plenum, New York, 1977).
[71]R. Ahlrichs, M. Bär, M. Häser, H. Horn, and C. Kölmel, Chem. Phys. Lett. **162**, 165 (1989).
[72]S. Mukamel, *Principles of Nonlinear Optical Spectroscopy* (Oxford University Press, New York, 1995).
[73]W. M. Zhang, T. Meier, V. Chernyak, and S. Mukamel, J. Chem. Phys. **108**, 7763 (1998).
[74]T. Pullerits, M. Chachisvilis, and V. Sundström, J. Phys. Chem. **100**, 10787 (1996).

Downloaded 19 Jun 2012 to 129.187.254.47. Redistribution subject to AIP license or copyright; see http://jcp.aip.org/about/rights and permissions

Appendix A7

Electronic transient spectroscopy from the deep UV to the NIR: unambiguous disentanglement of complex processes

E. Riedle, M. Bradler, M. Wenninger, C. F. Sailer, and I. Pugliesi

Faraday Disc. **163**, 139 - 158 (2013)

Reprinted with kind permission from the Royal Society of Chemistry (RSC)

Faraday Discussions

RSC Publishing

Cite this: *Faraday Discuss.*, 2013, **163**, 139

PAPER

Electronic transient spectroscopy from the deep UV to the NIR: unambiguous disentanglement of complex processes

Eberhard Riedle, Maximilian Bradler, Matthias Wenninger, Christian F. Sailer and Igor Pugliesi

Received 5th February 2013, Accepted 11th February 2013
DOI: 10.1039/c3fd00010a

Complex multi-stage relaxation and reaction pathways after the optical excitation of molecules makes the disentanglement of the underlying mechanisms challenging. We present four examples that a new transient spectrometer with excitation fully tunable from the deep UV to the IR and 225 to 1700 nm probing allows for an analysis with greatly reduced ambiguity. The temporal resolution of about 50 fs allows us to resolve all relevant processes. For each example there is a new twist in the sequence of relaxation steps that had previously been overlooked. In malachite green it appears that the importance of the phenyl twisting has been overemphasized and rather a charge transfer state should be considered. In TINUVIN-P the predicted twisting as the driving motion for the ultrafast IC is confirmed and leads to a resolution of the earlier puzzle that the sub-5 ps regime shows kinetics deviating from a pure cooling process despite the sub-ps proton transfer cycle. For the bond cleavage of Ph_2CH–Cl and Ph_2CH–Br the degree of electron transfer within the radical pair can now be determined quantitatively and leads to a profound understanding of the long term cation yield. For the first time coherent wavepacket motion in the photoproducts is reported. Last but not least the measurement of the GSB recovery in the deep UV allows for the surprising result, that even after S_2 excitation of cyclopentenones the triplet states are reached with near unity probability within a few picoseconds.

1 Introduction

Optical spectroscopy in a wide range of varieties is a prime source of microscopic information on molecular systems and processes. Simple continuous wave ultraviolet visible (UV/vis) absorption allows the identification of the energies of excited electronic states and infrared (IR) measurements render typical vibra tional modes that are used to identify the associated motives in the molecule. The

Lehrstuhl für BioMolekulare Optik, Ludwig-Maximilians-Universität München, Oettingenstr. 67, 80538 München, Germany. E-mail: Riedle@physik.uni-muenchen.de; Fax: (+49)089-2180-9202; Tel: (+49)089-2180-9210

two regimes are complementary in many ways and the skilful choice or combi nation is often needed.

Modern time resolved versions of UV/vis and IR spectroscopy permit the observation of the temporal evolution of the system with well below 100 fs precision. Particularly in the UV/vis practically all relevant processes can now be resolved. The interpretation of the raw measurements does, however, require the identification of unambiguous signatures of the reaction intermediates and the eventual products. This is by far not trivial, as only the spectrum of the reactants is typically well known and possibly that of the product, if it can be isolated in sufficient quantity and purity. Any short lived intermediates can only be characterized by the transient measurement itself and so there is often a "chicken and egg" dilemma that a model of the reaction is needed to assign the observed spectral signatures and these would be of great help to develop the model.

As the structural motives that determine the vibrational frequencies are quite localized, *e.g.*, N H or C C stretches or specific bending motions in the finger print region, at least first guesses for the assignment are readily made. However, this also means that only moderate changes result in many regions of the IR spectrum due to the chemical transformation. Identifying the significant ones and isolating them from solvent signals can then become quite challenging. The electronic bands do change quite largely on the contrary, both in position and in strength. The problem there is the large homogenous and inhomogeneous width of each electronic transition. Sometimes even the decision of what is a separate electronic band or just a vibronic structure can become difficult.

Many of the seminal experiments in femtochemistry were done with fixed frequency pulses[1] and this in retrospect required a fair amount of chemical intuition for the analysis. Broadband transient measurements have, however, been developed continuously and the change from liquid based continuum generation to crystal based continua has allowed an ever widening application. Due to the intrinsically broad spectrum of a femtosecond IR pulse relative to the typical 15 cm $^{-1}$ width of vibrational transitions somewhat of an overview was originally easier to gain in this spectral range.[2] The coverage of a wide spectral range requires tuning the probe pulse repeatedly and performing the time scan at each setting. This is where UV/vis transient spectroscopy has an intrinsic advantage, as extremely broad continua are now available[3,4] and can be combined with detectors of a thousand or more pixels.

In this contribution we want to demonstrate the potential of a cutting edge broadband UV/vis/NIR transient spectrometer that will be briefly described in Sec. 2. We then present and discuss measurements on four sample systems ranging from ultrafast nonradiative decay, excited state proton transfer, and bond cleavage to ultrafast intersystem crossing. For all systems we find surprising new details that had been overlooked by the earlier investigations with limited spectral coverage. We thus can demonstrate that transient electronic spectroscopy is now becoming extremely powerful and the redundancy of information obtained in the measure ments gives an unambiguous and clear picture of the complex dynamics. Combined with high level computations the energy flow in molecules after absorption of a photon and leading eventually to photochemistry can be traced most reliably.

 This journal is © The Royal Society of Chemistry 2013

2 Ultra-broadband transient spectroscopy with 50 fs resolution

The transient spectrometer used for our measurements relies on a fully tunable pump source and a broadband continuum for wavelength selective probing. The general setup has been described in detail[4] and is based on a kHz Ti:sapphire amplifier (CPA2001; Clark MXR, Inc.). The pump pulses are derived from a blue pumped noncollinear optical parametric amplifier (NOPA) frequency doubled in a BBO crystal with typically 100 μm thickness. The visible NOPA pulses are over compressed in a fused silica prism compressor to precompensate for all dispersing elements after the doubling stage. With various mixing strategies and a possible intermediate continuum stage the range from 189 nm to 5 μm can be covered without any gaps.[5,6] The pump pulse lengths can be adjusted to 30 fs or below from the deep UV to 1200 nm and are only slightly longer at longer wavelengths.

In the original setup we used a 775 nm pumped single filament super continuum that spans from 290 to 720 nm as the probe. Such a wide continuum is generated in a selected 5 mm CaF_2 plate that is translated in a circular fashion to avoid optically induced damage. The plate is carefully oriented to avoid depo larization of the continuum.[7,8] The broadband probe light is dispersed in a fused silica prism and detected with a multichannel detector. The continuum chirp is corrected in the data postprocessing. The pump probe delay up to 2 ns is adjusted with the help of a computer controlled delay line accurate to better than 10 fs. The overall temporal resolution is as good as 50 fs, mainly limited by residual group velocity mismatch between pump and probe in the 120 μm solu tion sample. Transient spectrometers with parameters similar or close to ours are in use in a number of laboratories around the world.[9–12]

To access an even wider probe spectral range we alternatively pump the CaF_2 based continuum generation by the frequency doubled or tripled Ti:sapphire

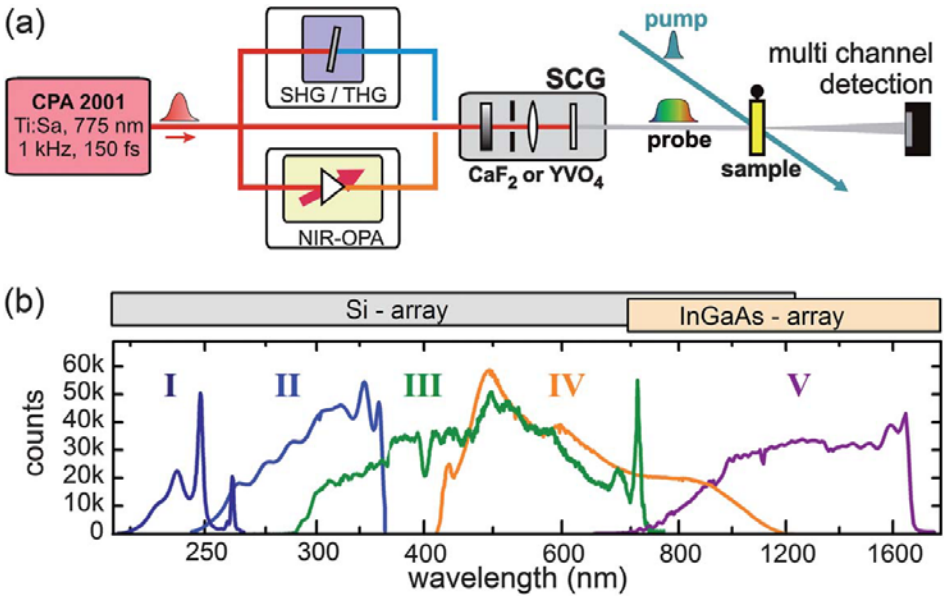

Fig. 1 (a) Scheme of the supercontinuum generation with various harmonics of the Ti:sapphire amplifier or the output of a NIR OPA. (b) Spectra of the continua as seen on the spectroscopic multi-channel detector.

output (see Fig. 1(a)). We find that significantly less pump energy is needed at these shorter wavelengths (387 and 258 nm) and therefore no damage is found even in prolonged operation. The resulting spectra are shown in Fig. 1(b). They span from close to the pump wavelengths down to 245 and 225 nm. The long wavelength cut off is given by the dielectric filter used to suppress the high spectral power near the pump wavelength. Optimized filters with a smooth roll off could add some more spectral range in this vicinity to the probe pulse.

To access the near infrared (NIR) probe range we use a single stage collinear optical parametric amplifier (OPA) to generate a red shifted continuum.[3] With the OPA signal at 1200 nm and the CaF_2 plate the useful continuum spans from 420 to 1100 nm. In this range the silicon based CCD or diode array can still be used. For the 750 to 1700 nm range we use the idler at 2100 nm to generate the continuum in a 4 mm YVO_4 crystal. As detector an InGaAs based 256 pixel detector (Series 2000CV2 camera with uncooled Hamamatsu G9203 256D detector; Ent wicklungsbüro Stresing) was used.

All continua are single filament and can therefore be well collimated and focused into the sample cell. Their spectra are summarized in Fig. 1(b). They overlap sufficiently and in total span from 225 nm to 1.7 μm. Typically two or three of the ranges are needed to cover the region of interest for a particular molecule. They are measured sequentially and then stitched together in the postprocessing to render the comprehensive manifold of transient spectra for all desired delay times.

3 Selection of sample molecules and processes

The development of the transient spectrometer described above has been moti vated by our various investigations of ultrafast molecular and chemical dynamics. These range from photophysical process, *via* excited state electron and proton transfer to complex chemical reaction sequences. For this discussion we have chosen four examples that serve to demonstrate the newly available capabilities from the application point of view.

The first decision that has to be made in an ultrafast molecular experiment is the choice of the pump wavelength, λ_{pump}. As we have ultrashort pulses at all possibly needed wavelengths to our disposal, we choose λ_{pump} purely according to the energy level structure of the molecule. We strongly believe that this enhances the value of the results as we do not have to worry about some initial electronic relaxation that is inevitably connected to some vibrational excitation. As shortly discussed above, such a choice of pump wavelength is always possible with the existing nonlinear pulse generation schemes.

The choice of λ_{pump} can be made quite readily by inspecting the linear absorption spectrum of the sample. The spectra of the four substances are shown in Fig. 2. For 2,3,4,5 tetramethyl 2 cyclopentenone (TMCPO) in cyclohexane there is an extremely weak $S_1 \leftarrow S_0$ transition around 320 nm and a quite strong $S_2 \leftarrow S_0$ transition below 250 nm. We excite TMCPO at 228 nm to specifically investigate the relaxation from the S_2 state. Diphenylmethylbromide (Ph_2CH Br) can be excited through the weak benzoic absorption at 270 nm. In 2 (2′ hydroxy 5′ methylphenyl) benzotriazole (commercial name TINUVIN P) ultrafast excited state intramolecular proton transfer (ESIPT) can be triggered by π π^* absorption at 350 nm. The cationic dye malachite green (4 [(4 dimethylaminophenyl)phenyl methyl]

 This journal is © The Royal Society of Chemistry 2013

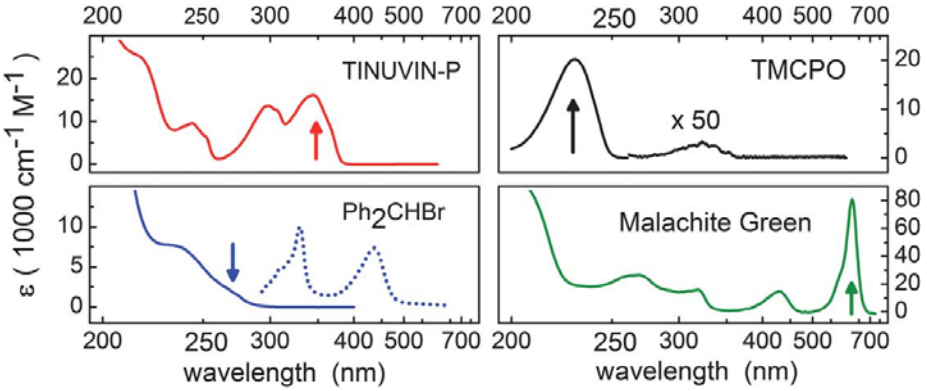

Fig. 2 Absorption spectra of the molecules studied in this work. TMCPO: 2,3,4,5-tetramethyl-2-cyclopentenone. In the panel for Ph_2CHBr also the spectra of the benzhydryl radical and cation are shown (dotted line). The arrows indicate the pump wavelength.

N,*N* dimethylaniline; MG) is known to laser spectroscopists as it made the first real femtosecond laser system, the colliding pulse mode locked laser (CPM) possible due to its saturability at the 620 nm emission wavelength of Rhodamine 6G. In the present report we reinvestigate the ultrafast dynamics after 620 nm excitation.

4 Putting the analysis of the ultrafast dynamics in malachite green on a sound basis

Malachite green (MG, see Fig. 3(a)) is a cationic triarylmethane dye that absorbs strongly in the visible region. Since this absorption overlaps perfectly with the output of the CPM laser it is actually used as a saturable absorber in this device it was one of the first molecules investigated for its ultrafast dynamics. The early studies concentrated on the ground state bleach (GSB) recovery. Rather complex kinetics with a main time constant of 2.1 ps in methanol and a strong solvent dependence were found.[13,14] The solvent dependence is attributed to the viscosity of the solvent and it is postulated that an intermediate state S_x is reached after

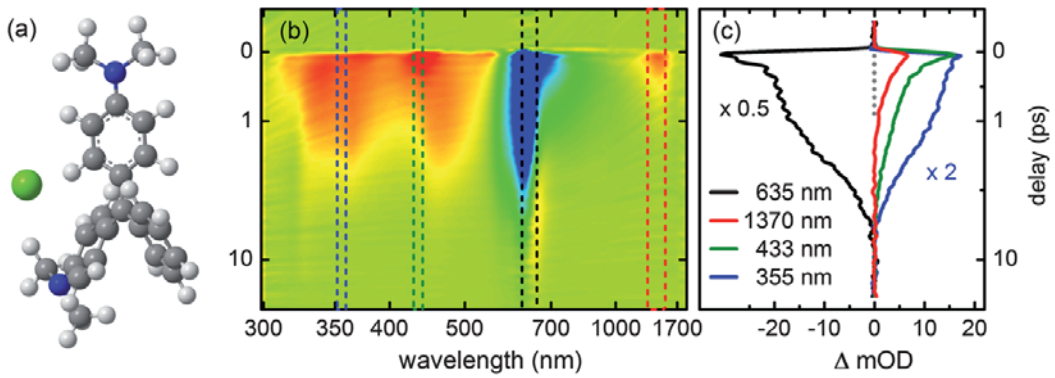

Fig. 3 Transient spectroscopy of malachite green dissolved in ethanol. (a) Structure of the dye. (b) Manifold of transient spectra. Red colours indicate an increase in absorption, blue colours a decrease. The wavelength scale is roughly reciprocal to pronounce different energetic parts equally. The time scale is linear in the range of 1 to +1 ps and logarithmic beyond. (c) Selected kinetic traces at the maximum of the NIR absorption of the LE state (1420 nm), the broad excited state absorption in the UV (350 nm) and the GSB (620 nm).

excitation through torsion of the phenyl rings.[14–19] After relaxation from the S_x state to the ground state the geometrical relaxation and cooling of the hot S_0 is thought to complete the cycle.

We investigated the dynamics of MG in ethanol after 620 nm pumping and utilizing the probe ranges III and V to cover the range from 300 to 1700 nm. The resulting manifold of the transient spectra is shown in Fig. 3(b). A pump probe cross correlation of 35 fs in the NIR and slightly longer in the UV is reached and matches the resolution of previous one [14,20] or two colour pump probe[15] and fluorescence up conversion[18] measurements.

The strongest feature in the transient spectrum is the region of negative optical density around 635 nm (blue colours; Fig. 3(b))), where GSB and stimulated emission (SE) overlap. This is also the spectral region where most of the inves tigations were performed. In addition, the whole range from 300 nm to the GSB region and the NIR displays strong excited state absorption (ESA). A preliminary global fit analysis shows a 100 fs component with an increase of signal in the SE region and a decrease in the GSB region. This can be interpreted as the inertial motion of the optically prepared wavepacket away from the Franck Condon point towards the equilibrium geometry of the excited electronic state S_1 that leads to a time dependent red shift of the SE. Such an extremely fast dynamics was already reported previously.[14,20]

A second decay component of about 440 fs has major peaks in the decay associated spectrum (DADS) at 433 nm (with 33 nm width) and at 1400 nm (430 nm width). These peaks can be readily assigned to the ESA following S_1 excitation and leading to the S_2 and S_4 excited electronic states. In the absorption spectrum, transitions to these two states are found at the matching positions of 428 and 255 nm (compared in Table 1). A third spectral feature with a positive amplitude in the DADS is found to be nearly coinciding with the $S_1 \leftarrow S_0$ absorption band, but is significantly different in shape. If this feature was due to a change in the GSB, it would indicate an increase in GSB with time. There is no argument known to us that would predict such a change in the hundreds of fs range. Therefore we have to assign this feature to the $S_3 \leftarrow S_1$ transient absorption (ESA). Finally a decrease in SE with a 440 fs time constant is found that reaches from 635 nm to 1100 nm. This matches the spontaneous emission spectrum within the limitation that certainly the stimulated emission in the sub ps range does not originate from a thermalized S_1 vibronic distribution. In summary, this means that the strong transient signal around the usual 620 nm pump

Table 1 Absorption energies for the $S_n \leftarrow S_0$ and $S_n \leftarrow S_1$ transitions obtained from the cw spectrum of MG together with the $S_n \leftarrow S_1$ transitions energies (widths in brackets) extracted from the transient absorption (TA) of MG. The time constants are obtained from single wavelength fits. "d" signals where the time constant cannot be determined due to spectral overlap, "a" signals no amplitude for the associated time constant

	λ (nm) $S_n \leftarrow S_0$	λ (nm) $S_n \leftarrow S_1$	λ (nm) TA exp	τ_1 (ps)	τ_2 (ps)	τ_3 (ps)
S_1	622			0.10	0.44	2.2
S_2	428	1372	1400 (430)	a	0.44	a
S_3	315	638	~635	d	d	d
S_4	255	432	433 (33)	a	0.33	1.7
ESA			355	a	a	2.0

 This journal is © The Royal Society of Chemistry 2013

wavelength of most investigations is the sum of GSB, SE and ESA. It follows that the undiscussed averaging over the spectral width of the pump/probe pulse will not lead to any unambiguous interpretation of the dynamics of MG.

To display the transient absorption at selected times more clearly, we extracted the spectrum of absorption change (black lines in Fig. 4) from the complete manifold shown in Fig. 3(b). We then added a constant fraction of the ground state absorption spectrum (grey line in all panels of Fig. 4) to obtain the momentary spectrum (blue lines) of the sub ensemble of molecules that was initially excited. The rapid decay of the 1400 and 433 nm peaks is clearly seen, as are the changes in the 635 nm region. At 1 ps, there is a broad absorption beyond the ground state absorption remaining that decays with about 2 ps. At 2 ps the 622 and 428 nm bands are the only remaining signals. The 622 nm $S_1 \leftarrow S_0$ absorption band has, however, not yet fully recovered. It is interesting to notice that the shape of the 622 nm band does not significantly change during the relaxation processes. This is surprising in view of the generally accepted interpretation that large amplitude torsional motions of the phenyl rings dominate the dynamics. We cannot rationalize how such motions do not lead to changes in the 622 nm band of more than the 3% upper limit we can deduce as maximum spectral change compared to the full GSB signal.

Kinetic traces at selected wavelengths are shown in Fig. 3(c). The fitted exponential decay constants are shown in Table 1. At 1400 nm we explicitly probe the S_1 population through the $S_2 \leftarrow S_1$ ESA. We find a relaxation time of 440 fs in good agreement with fluorescence measurements.[21] It should be noted that the largely increased probe range of our experiment allows for this unambiguous determination of the S_1 lifetime by transient spectroscopy alone. At 433 nm there is an overlap between the specific $S_4 \leftarrow S_1$ ESA and the very broad ESA that lasts into the ps range. The decay curve can be fitted with a first 330 fs exponential contribution that again signals the S_1 decay and a further 1.7 ps components. At 355 nm there is no ground state absorption and we do not have to expect any GSB. At this wavelength we can therefore exclusively probe the intermediate state S_x that the S_1 state relaxes to with the 440 fs time constant. The 2.0 ps decay is within experimental accuracy identical to the 1.7 ps component already found at 432 nm.

For the GSB recovery we need a 100 fs, a 440 fs and a 2.2 ps time constant. The first two most likely just result from the overlapping SE and ESA components. The

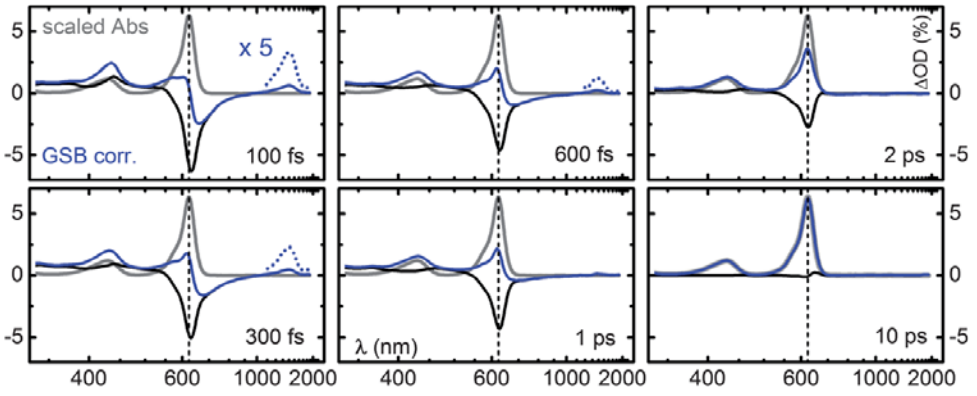

Fig. 4 Selected transient spectra at the indicated pump–probe delays (black lines). For visualization of the underlying changes in malachite green dissolved in ethanol, an equal amount of absorption spectrum is added to each transient spectrum (blue lines). In this way the recovery to the absorption spectrum (grey line) of the sub-ensemble excited by the pump pulse can be recognized.

slightly longer 2.2 ps recovery time of the GSB as compared to the S_x decay is quite reasonable in view of cooling processes. Temporal signal oscillations of about 226 cm ^{1} that can be attributed to a symmetric carbon phenyl stretch vibration[14,22,23] are only found in the region from 605 to 635 nm. This must mean that a ground state wavepacket prepared by resonant stimulated Raman scattering is observed.

The extremely wide probe range of our measurements and the detailed anal ysis leads to the following conclusions. After S_1 excitation MG relaxes to a state S_x that neither fluoresces below 900 nm nor carries any oscillator strength to the known higher electronic states. Instead a nearly 2 eV broad ESA band decaying with a time constant very close to the GSB recovery is found. This all points to a charge transfer (CT) character of the S_x state. Indeed, recent high level calcula tions predict such a character already for the S_1 state[24] and for the related molecule crystal violet a relaxation mechanism involving charge redistribution has been proposed.[25,26] We suggest that the initially excited (local excited) state has an electronic character more similar to the ground state. This property would explain the very strong $S_1 \leftarrow S_0$ absorption. The often discussed torsion of the phenyl rings starts after the initial 100 fs geometric relaxation and leads to a simultaneous change in the electronic character towards a CT state on the half ps time scale. Charge recombination then takes about 2 ps to repopulate the S_0 state with little optical signature from the "reverse" torsion of the phenyl rings.

From an extensive search of the literature it does not become clear, why repeatedly claims were made that the polarity of the solvent does not influence the dynamics of MG. It was always the viscosity that has been considered. If one, however, considers a series of alcohols with increasing size, not only the viscosity increases but also the polarity decreases. Future work should investigate this point by the reanalysis of existing data and solvent dependent transient spec troscopy. The solvation times of alcohols that are much longer than the ps times in the decay of excited MG are no intrinsic hindrance, as already a partial solvation can lead to efficient CT.[27] Given the capabilities demonstrated in this section, a final decision on the MG relaxation mechanisms should readily be possible.

5 An overlooked twisting isomerization in the proton transfer cycle of TINUVIN-P

TINUVIN P is one of the best studied ESIPT systems.[28–31] After a 60 80 fs proton transfer the keto type molecule relaxes to the electronic ground state with a 120 150 fs time constant. In the excited keto state a pronounced wavepacket motion is observed.[31] As the internal conversion (IC) was assumed to happen in the closed keto form originating from the optically excited enol form, the subsequent 600 fs decay found at probe wavelengths in the visible region was assigned to the proton back transfer.[29,30] In the enol form a 180° twist around the central bond between the phenyl and the benzotriazole ring regenerates an identical conforma tion and a possible "isomerization" cannot be detected spectroscopically. In the keto type form the same twist transfers TINUVIN P from the closed form with the intramolecular hydrogen bond to the open form.[32]

The ultrafast proton transfer cycle leaves the TINUVIN P in a highly vibra tionally excited state. This is seen as a positive transient absorption below the $S_1 \leftarrow S_0$ absorption edge at 367 nm and a decrease in absorption at shorter

 This journal is © The Royal Society of Chemistry 2013

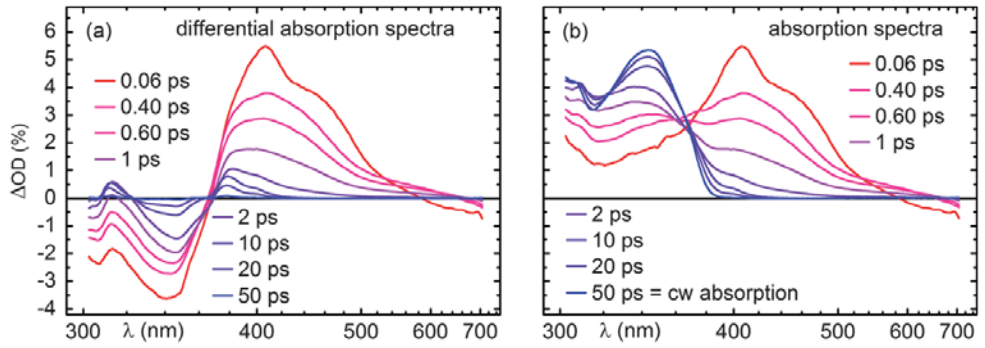

Fig. 5 (a) Transient absorption changes at selected delay times for TINUVIN-P in cyclohexane excited at 355 nm. (b) Absorption spectrum of the sub-ensemble excited by the pump pulse.

wavelengths.[33,34] For times from 5 ps onward the relaxation of this transmission change can be well modelled with a cooling process. However, it was already realized in the earlier investigations that the cooling picture was not sufficient to explain the spectral evolution in the first few picoseconds.

With our broadband spectrometer we investigated the dynamics of TINUVIN P in cyclohexane. The differential absorption spectra shown in Fig. 5(a) display a rich variety of kinetics in the first 50 ps. To allow for an easier discussion of the under lying dynamics, we added a suitable fixed fraction of the ground state spectrum to all traces. The resulting time dependent absorption spectrum of the sub ensemble excited by the pump pulse (see Fig. 5(b)) is used to discuss the observations.

At 60 fs after the excitation depletion of the ground state absorption is clearly seen below 367 nm. In the blue spectral region a strong transient absorption is found that initially displays some vibronic structure. This initial absorption must be due to ESA from the enol or keto excited state. The absorption extends into the UV and overlaps with the ground state absorption. A weaker structure between 500 and 600 nm that develops with some delay is assigned to the closed keto ground state in accordance with ref. 30. Beyond 600 nm stimulated emission is found. The SE decays very rapidly and therefore can be assigned to the excited keto type state.

Kinetic traces at selected wavelengths are shown in Fig. 6. For clarity the traces are shown on an expanded scale in part (a,c) and over the full relevant range of 30 ps in part (b,d). At 684 nm we find a delay/increase of the SE with about 80 fs and a decay with 154 fs. Within the experimental precision this ESIPT and IC behaviour matches the previous reports.[29,30] At 551 nm we find a 144 fs increase of the signal and a 588 fs decay. Therefore we can confirm that in the 500 to 600 nm region the suggested proton back transfer is observed and takes 600 fs.

At exactly the vibrationless 0 0 transition of the optically pumped $S_1 \leftarrow S_0$ band (367 nm) we find an isosbestic point in the sub ensemble spectra (Fig. 5(b)) at times beyond some ps. This is in close agreement with the earlier reports[33,34] and we can safely assign the decrease of absorption around 400 nm and the increase in the range around 350 nm to vibrational cooling. The spectral evolution of a cooling process does not render simple exponential decays with a wavelength independent decay time. Still, the value of 13 ps found at 344 nm near the band maximum gives a characteristic time constant of the cooling process. A very detailed resonance Raman study finds mode specific behaviour with time constants in the same range.[35,36] The traces at 362 and 375 nm, energetically

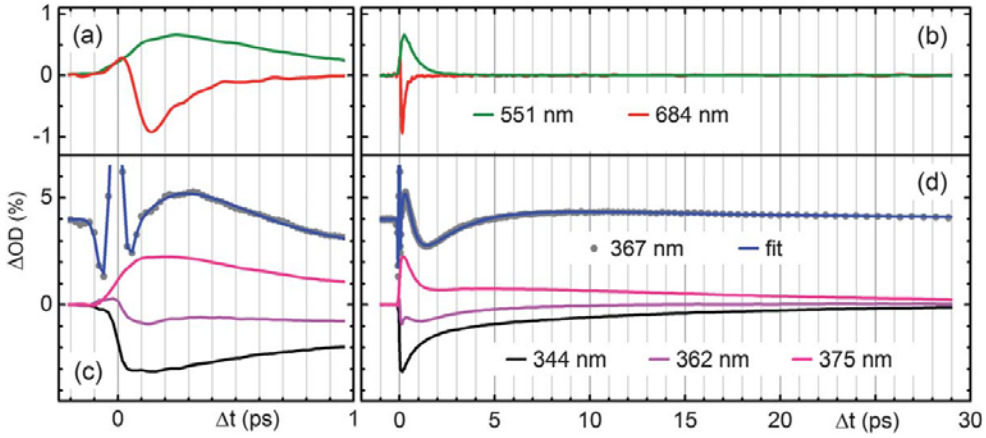

Fig. 6 Selected kinetic traces at the spectral positions, where the various conformers and relaxation processes of TINUVIN-P can be best differentiated. (a) and (c) show the traces within the first picosecond, while (b) and (d) show the range up to 30 ps. For clarity the coherent artefact due to the solvent cyclohexane has been subtracted from the traces except at 367 nm. The trace for 367 nm is multiplied by a factor of 4 and shifted upward.

slightly above and below the 0 0 transition consequently display quite compli cated kinetics as many opposing effects contribute to the optical signal.

At exactly 367 nm the cooling does not influence the optical signal and the kinetics at this wavelength can therefore report the pure population evolution of the enol electronic ground state. We still have to assume that none of the other states involved in the full ESIPT and relaxation cycle contributes to the signal. Since the ESIPT itself proceeds in below 100 fs, the IC in 150 fs and the back transfer from the closed keto type form in 600 fs, this is a fairly safe assumption after about 1 ps. Inspection of the 367 nm trace (Fig. 6(c,d); grey filled circles for the experimental values and blue line for a multi exponential fit) shows indeed an 80 fs decrease, a 150 fs increase and a 410 fs decrease. The vibrational cooling is seen as a very weak 15 ps decrease of the signal back to zero. Clearly there is another 2.2 ps contribution that was not seen in earlier work. In a global fit this time constant can be found as a prominent decay within most of the GSB range and the range around 450 nm. However, single wavelength fits show a systematic variation of the time constant due to the cooling and the overlap with the ESA.

To assign this 2.2 ps relaxation constant we return to the red region of the spectrum. The width of the spontaneous emission spectrum of the closed keto type form of TINUVIN P is known[31] and it is also established that the ground state closed keto type form shows a mirror image to the fluorescence spectrum with a 0 0 transition at 625 nm.[30] Assuming a similar width and strength for emission and the absorption bands, only the region down to about 500 nm in the transient absorption spectrum can be assigned to the closed keto type form. What is left to explain is the strong absorption in the range 380 to 500 nm and the 2.2 ps time constant.

It has been calculated, that the IC of the excited closed keto type form proceeds *via* a conical intersection that involves a twisting around the central bond and a pyramidization.[32] A similar prediction backed up by experimental evidence was also made for the related 2 (2′ hydroxyphenyl)benzothiazole (HBT).[37] As a result of the twisting motion necessary for the extremely fast IC, parts of the molecules do not relax to the closed keto type form but to the open keto type form. This is

 This journal is © The Royal Society of Chemistry 2013

directly corroborated by transient IR spectroscopy[38] and in line with early indi cations.[29,39] In view of all the evidence we assign the 2.2 ps time constant in TINUVIN P to the back isomerization of the open to the closed keto type form that is then followed by an even faster back transfer of the proton to lead to vibra tionally excited enol molecules. These are subsequently cooled by the solvent in 10 to 20 ps. The majority of the strong transient absorption in the blue is consequently assigned to the open form.

These additional species populated with the 150 fs IC can readily explain the difficulties discussed previously to model the cooling kinetics at times before 5 ps.[34] It is not yet clear what this means for the interpretation of the resonance Raman studies.[35,36] In summary, the relaxation cycle in UV excited TINUVIN P, that takes as little as some ten picoseconds for completion, involves forward ESIPT (τ 80 fs), a branching in the IC to the closed and open keto type form (τ 150 fs), a back twisting (τ 2.2 ps), back proton transfer (τ 600 fs) and finally cooling (τ 15 ps). One might ask oneself whether such a complex sequence is a rare exception or a more general occurrence. The ring opening of 1,3 cyclohexadiene comes to mind with the subsequent multi step relaxation to the lowest energy tZt conformer. In this system also highly complicated kinetics were reported.[40]

6 The generation and interconversion of benzhydryl radicals and cations by photolysis of diphenylmethylbromide

After UV excitation diarylmethylhalides undergo homolysis to the pair of a benzhydryl radical and halogen radical or heterolysis to the benzhydryl cation and the halogen anion. The overwhelming majority of investigations on this process and the subsequent interconversion between radical and ion pairs were per formed without transient spectroscopy which renders spectra of the reactive intermediates, but rather by *a priori* chosen pump and probe pulse wavelengths. In addition, very intricate analysis with multiple exponential rates and a highly complex interpretation was deduced from these fixed colour recordings.[41] Last but not least, only ps resolution was employed, even though it had been shown that the initial processes proceed on the sub ps time scale.[42]

We utilized 30 fs pulses at the first maximum of the absorption spectrum (270 nm; see Fig. 1) to excite either diphenylmethylchloride (Ph_2CH Cl) or diphe nylmethylbromide (Ph_2CH Br). As the strong absorption features of the photo lytic products Ph_2CH^+ and $Ph_2CH^\bullet$ are well separated from the absorption of the precursors, we can use the range III of our continuum generation for a full process analysis. The spectrum of $Ph_2CH^\bullet$ at 330 nm and the one of Ph_2CH^+ at 430 nm are shown as dotted lines in Fig. 1.

The manifold of transient spectra for Ph_2CH Br in acetonitrile at various pump probe delays is shown in Fig. 7(a). It can be readily seen that the radical signal appears very early after the optical excitation and decreases in the ps range. The cation signal increases more slowly and then also decreases later. The kinetic traces shown in Fig. 7(b) give a more detailed view. They show the integrated signal over the full bands. The optical signal can be considered to be proportional to the species population within good approximation. The step in the rise of $Ph_2CH^\bullet$ (blue line) at about 50% amplitude happens at 100 fs. In agreement with

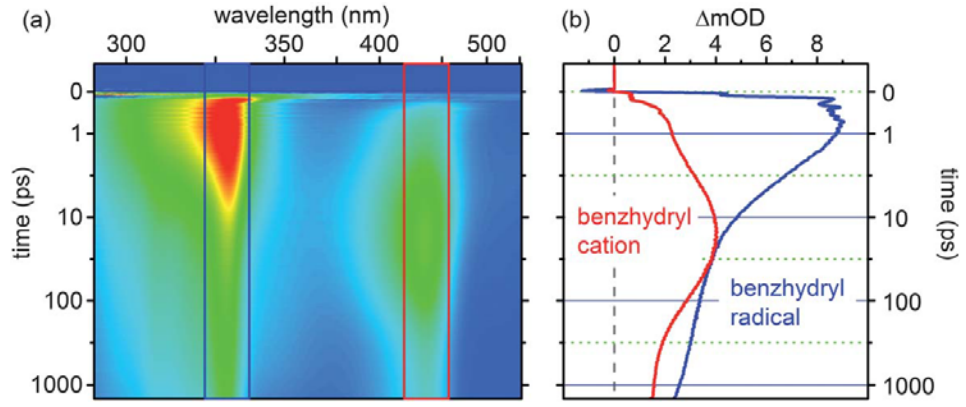

Fig. 7 (a) Transient spectra after 270 nm excitation of diphenylmethylbromide in acetonitrile. Red colour indicates a large transient absorption, green an intermediate one and blue colours little. (b) Signal for the resulting benzhydryl radical (blue line) and benzhydryl cation (red line) integrated over the respective band.

the observation for Ph_2CH Cl, where we observe such a step at 80 fs,[43] we assign this to the delayed generation of the radical. The excited state wavepacket propagates from the Franck Condon region to a first conical intersection that leads part of the wavepacket to the radical product. The remainder of the wavepacket stays on the excited potential hypersurface and reaches a second conical intersection leading to the cation product. This takes a total time of 125 fs in Ph_2CH Cl and 200 fs in Ph_2CH Br (see step in the red line). This means that the cation does not appear until this later time. No more radical and cation population is generated at later times. The slight increase in the optical signals is rather due to an increase in transition strength due to solvation and planarization of the products.[44]

A close inspection of the product signal curves and the full set of transient spectra show significant modulations up to about 2 ps. The frequency is about 300 cm^{-1} for the radical and 350 cm^{-1} for the cation. To analyze these modulations, we compare the signal at the blue side of the radical absorption to that at the red side (see Fig. 8(a)). Clearly a π phase shift is seen that proves that the modulation is due to a vibronic wavepacket. In addition, we determined the position of the maximum of the radical and cation absorption for each delay.[45,46] The resulting temporal dependence of the peak position shows the already mentioned ps relaxation due to solvation and planarization and also the oscillations. This confirms the interpretation as a vibronic wavepacket. An analysis of the normal modes of the radical and cation suggests that these wavepackets correspond to a symmetric stretch motion of the phenyl rings relative to the central carbon. This is very similar to the situation in MG (see above). However, in the photolysis of Ph_2CH Br the wavepacket motion is in the photochemical products. The bond cleavage proceeds so fast that an impulsive excitation of the vibrational motion occurs. The stabilization of the radical and the cation leads to an increased electron density in the vicinity of the central carbon. Such an increase in electron density leads in turn to an impulsive shortening of the bonds and the suggested vibrational motion.

In the time up to about 10 ps the radical population decreases while the population of the cation increases. This is due to electron transfer between closely spaced benzhydryl and bromine radicals leading to the ion pair. We find that a

 This journal is © The Royal Society of Chemistry 2013

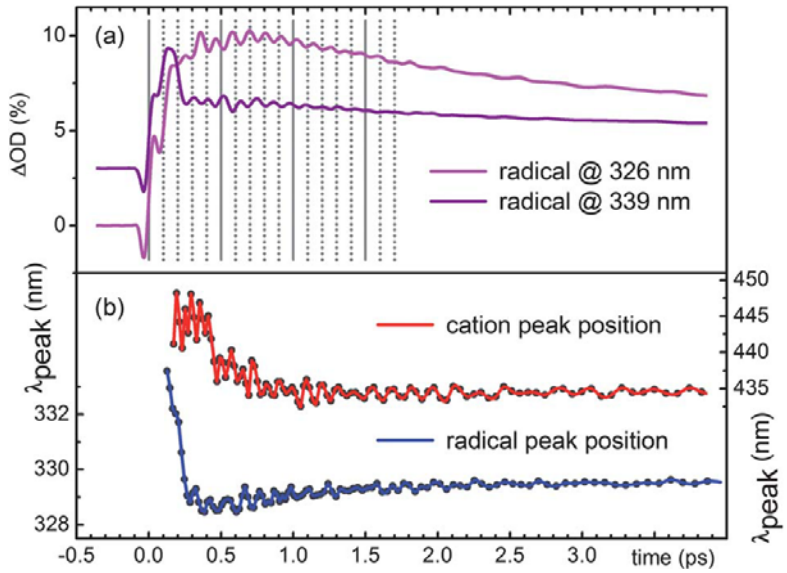

Fig. 8 (a) Transient absorption changes after 270 nm excitation of Ph_2CH–Br on the low wavelength (326 nm) and high wavelength (339 nm) edge of the radical product band. (b) Temporal dependence of the peak position of the benzhydryl radical (blue curve) and cation (red curve) band.

stretched exponential describes this process best, just as in our recent analysis of Ph_2CH Cl.[46] The only difference is that for the chloride system an 11 ps time constant was found for this process compared to the shorter time constant of 2.1 ps in the bromide system. The decay of the radical population and the increase of the cation population with the identical temporal behaviour is direct proof of the interconversion by electron transfer. This finding is in contrast to the conclusions drawn from ps experiments on Ph_2CH Br.[47,48] Clearly the very fast termination of the electron transfer in the bromide system did not allow the correct interpreta tion in the earlier experiments with 20 ps resolution. The electron transfer is stopped by the depletion of closely spaced radical pairs.[46]

After the end of the electron transfer the remaining radical pairs separate by diffusion to give a stable population of free radicals. The ion pairs stick together for a longer time due to the Coulomb attraction. Therefore they can effectively undergo recombination and the reduced population of free ions eventually evolves (94 ps time for Ph_2CH Br and 138 ps for Ph_2CH Cl).

The complete set of transient data cannot be modelled anymore with the usual kinetic scheme of well defined species like contact pairs, solvent separated pairs and free species. Instead we developed a combined model of Marcus type electron transfer and Smoluchowski diffusion.[46] We have to assume an initial radical and cation pair distance distribution that extends far beyond the contact distance considered explicitly in earlier work.[41,42,47,48] The various processes are treated as distance dependent. The time dependent populations can then be deduced by integration over the full radial distribution for each delay time. The time dependent rates result from the convolution of the distributions with the distance dependent rates.[46]

The observation of the full range of optical signals connected with the photolysis of diarylmethylhalides with 50 fs temporal resolution renders many hitherto covered details on the dynamics. Hypotheses that have been carried on for decades can now finally be scrutinized. The investigation of complex and multistep chemical process is now possible in a most direct fashion. Together

with high level theoretical considerations the influence of conical intersections[49] and the microscopic arrangement can be investigated quantitatively. Since the breadth of optical signals renders a high degree of redundancy and cross checks, the ambiguity of many theories will be put to a serious test.

7 Direct determination of the triplet yield after S_2 excitation

One of the little mentioned understandings in ultrafast molecular dynamics seems to be that the rates connecting the originally excited state to the series of product states or chemical species are evaluated, presented and discussed, while the efficiencies and possible branching ratios are much less often put into the focus of the investigation. This stems from the fact that the yields of transient species are much less direct to determine compared to final product yields. For a hypothetical photochemical process leading from a precursor A to a stable product B the yield can readily be determined, as well established chemical means can be used to determine the product quantum yield. With modern illu mination sources like high power LEDs this is extremely simple.[50] As a by product one finds out which fraction returns to the reactant and effectively just undergoes a photophysical nonradiative relaxation.

For transient species or states the situation is much more difficult. Even if a time resolved measurement is available and able to uniquely identify the tran sient species as exemplified in the sections above one can still not rely on the Beer Lambert law as the molar absorption coefficient ε of the species is generally not known. So only the product of ε and concentration can be determined. For the benzhydrylbromide photolysis discussed in Sec. 6 one can chemically stabilize the cation and actually measure the value of ε. If in addition the fluence of the pump pulses at the sample position and all other relevant geometric parameters are determined, quantitative transient spectroscopy results that actually determines the time dependent yield of all species absolutely.[46]

More frequently other methods have been employed to determine the yield of intermediate species, particularly triplet states. Triplets are of special interest to chemistry as they are long lived compared to singlet states and therefore can allow for diffusion controlled photo initiated bimolecular processes like the ones found in photocatalysis[51] and photo initiated organic synthesis. One method uses triplet triplet energy transfer to a system with a known triplet absorption coeffi cient and the measurement of the resulting quencher triplet by spectral photometry can be used. However this procedure requires very careful calibration and a certain degree of assumptions. The oxygen production by triplet sensitized photooxidation of 1,3 diphenylisobenzofuran is an example of actually producing a physically measurable specific product that should be proportional in amount to the amount of triplet molecules produced over a selected period.[52] Another spectroscopic method that requires many assumptions and checks is the measurements of the ESR spectrum that specifically can report the triplet concentration.[53] To decouple the triplet yield and the triplet absorption cross section, Van Stryland and coworkers have introduced a very elaborate double pump method that relies on the partial saturation of transitions. This approach still has limitations given mainly by the molecular energy level structure.[54] The most direct method is the determination of the ground state bleach recovery. This

 This journal is © The Royal Society of Chemistry 2013

method relies on the ability to separate the time scales of the decay of the initially excited singlet and the resulting triplet in the GSB signal. This has been demonstrated by various single colour probe transient absorption measurements in the visible region.[55–57]

A more general application of the GSB recovery has so far been hampered by two issues. First, many systems of interest have their first strong absorption far in the UV. Second, a measurement at just one GSB wavelength still leaves the uncertainty that a superimposed ESA falsifies the interpretation. Both issues can now be solved with our extended probing range reaching as low as 225 nm. This is certainly sufficient to reach the strong absorption bands of almost any substance of chemical interest. By recording a full transient spectrum, the shape of the known ground state absorption spectrum can be used to unambiguously disen tangle GSB and ESA or product contributions.

For an experimental demonstration we chose 2,3,4,5 tetramethyl 2 cyclo pentenone (TMCPO) in cyclohexane. As seen from the absorption spectrum dis played in Fig. 2, there is a very weak $S_1 \leftarrow S_0$ absorption around 320 nm and a strong $S_2 \leftarrow S_0$ absorption centred at 229 nm. The assignment of the spectrum and the qualitative picture of the dynamics are made in analogy to the closely related acrolein.[58] We pump the S_2 state with 228 nm pulses of sub 60 fs duration. The transient spectra are measured with the three continuum ranges I III (Fig. 1(b)). They display very broad structures (see Fig. 9(a)) and it becomes clear that such a wide probe range is needed for a clear interpretation. The spectrum at 0.15 ps pump probe delay is dominated by the S_2 state through its ESA and possibly direct stimulated emission. The TMCPO relaxes to the S_1 state with a time constant of 0.25 ps, a quite reasonable time for an IC mediated by a conical intersection. Subsequently the molecule relaxes to the triplet manifold within 4 ps. This is quite fast and the underlying mechanisms are presently under study (compare the scheme in Fig. 9(b)).

To determine the S_1 and triplet yield, we evaluate kinetic traces at probe wavelengths that allow for a straightforward interpretation. A full analysis shows that a kinetic scheme purely based on population transfer cannot describe the observed dynamics. A more complex model incorporating solvation and vibra tional relaxation has to be considered. At 400 nm we can see predominantly the S_2

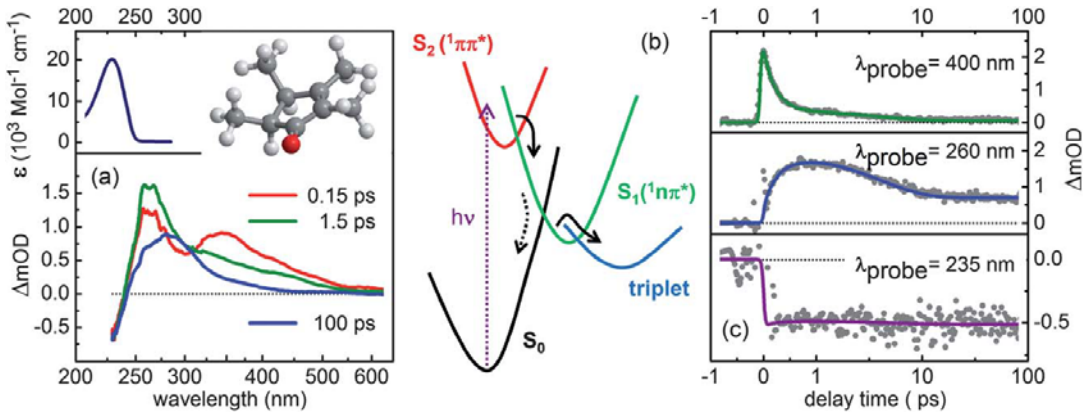

Fig. 9 (a) Selected transient spectra after 227 nm excitation of TMCPO in cyclohexane. The spectra were recorded in three parts and stitched afterwards. (b) Reaction scheme after S_2 excitation. (c) Selected kinetic traces monitoring mainly the S_2 population (400 nm), the S_1 population (260 nm) and the GSB (235 nm).

state relaxation with a 0.25 ps exponential decay. At 260 nm the signal reports the S_1 build up and decay with 0.25 and 4 ps. Finally, at 235 nm the lack of any GSB recovery can be directly seen. Within the present experimental uncertainty given by signal fluctuations and the coherent contributions from the solvent and cell windows, we see no recovery of the GSB. This means that the whole S_2 population initially generated by optical excitation transfers to the triplet. We can compare this to the previously reported triplet yield of the parent molecule cyclopentenone of also near unity.[59] While an ultrafast intersystem crossing (ISC) proceeding with such a high yield is not unreasonable when the vibrationless S_1 state is excited, the finding of a unity yield after S_2 excitation is surprising. The vibrational excess energy released in the $S_2 \rightarrow S_1$ relaxation would easily suffice for IC to the electronic ground state as reported for acrolein.[58] High level quantum chemical calculations do indeed show a low lying conical intersection between the S_1 and the S_0 state. The fact that this process is highly inefficient while the ISC is highly efficient indicates that kinetic factors determine the dynamics and the branching ratio. That the triplet is accessed with near unity yield can be deduced from the transient spectra without any necessary assumptions as the GSB acts as an easily interpretable internal standard. The measurement is also corroborated by further recordings of TMCPO and 3 methyl 2 cyclopentenone in acetonitrile that also show near unity triplet quantum yield after S_2 excitation.

8 Summary and conclusions

The four molecules investigated in this work all display complex multi stage relaxation after optical excitation. This has in the past lead to investigations with partially contradicting interpretations and conclusions. The extremely broadband probe investigations now possible with about 50 fs temporal resolution render a detailed picture that allows an interpretation with unprecedented unambiguity. For each example a new twist in the story of the relaxation results that had been overlooked. In malachite green it appears that the importance of the phenyl twisting has been overemphasized and rather a charge transfer state should be considered. In TINUVIN P the predicted twisting as the driving motion for the ultrafast IC is confirmed and leads to a resolution of the earlier puzzle that the sub 5 ps regime shows kinetics deviating from a pure cooling process. For the bond cleavage of Ph_2CH Cl and Ph_2CH Br the degree of electron transfer within the radical pair can now be determined quantitatively. The earlier single wavelengths measurements with ps resolution lead to strongly contradicting conclusions. For the first time coherent wavepacket motion in the photoproducts is reported. Last but not least the measurement of the GSB recovery in the deep UV allows for the surprising result, that even after S_2 excitation of cyclopentenones the triplet states are reached with near unity probability within a few picoseconds.

All these investigations were purely based on UV/vis/NIR transient spectroscopy. As similar problems have been tackled in the past with transient IR spectroscopy, we would like to ask ourselves how the two methods with state of the art setups[4,10–12,60–62] compare. For the comparison a figure of merit is helpful. A sensible figure of merit seems to be the ratio of the broadest spectral probe range available to the smallest width found in the spectrum. In the IR vibrational transitions in solution are about 15 cm^{-1} wide and the whole spectrum covers about 3000 cm^{-1}. This gives a factor of 200. The spectral width in the electronic

 This journal is © The Royal Society of Chemistry 2013

spectrum is at least as wide as the homogeneous broadening determined by the pure electronic dephasing on the time scale of tens of fs. This converts to a linewidth of 200 cm^{-1}. Our experimental setup can cover close to 40 000 cm^{-1} probe range and again a factor of 200 results. This means that transient electronic spectroscopy has finally caught up with transient IR spectroscopy with respect to detection width.

In both kinds of spectroscopies one has to identify the relevant spectral regions where the intermediates can be most unambiguously identified and tracked. The continua used in our setup (compare Fig. 1(b)) cover huge ranges and together with the highly resolving UV/vis/NIR detector arrays a first overview can be gained from a single time scan measurement requiring one or two hours. The temporal resolution is typically 50 to 100 fs, somewhat superior to the IR. Most importantly we find that the extension to the NIR allows for a qualitative new feature. We can always probe to the red of the GSB and SE region where only ESA or product bands can be located. Identifying the "last transition" in the NIR then allows to obtain the kinetics of the single species. This is nicely seen in the MG transient peak at 1400 nm assigned to the $S_2 \leftarrow S_1$ transition. Once the kinetics of this species are deduced from the measurement, the full associated spectral components can be extracted and used to decompose the set of transient spectra. In a second step the next to last transition is tackled and so on leading to a complete picture of photoinduced dynamics, however complex it might be.

The quantitative determination of transition strengths is readily possible by comparison with the intrinsic standard of the GSB of known strength. This is then often helpful to determine the electronic character of the intermediate species by comparison to quantum chemical calculations. What our setup also provides is sufficient spectral reproducibility and resolution to allow the observation of shifts as small as 0.1 nm or 10 cm^{-1}. These can be identified with solvation, ion or radical pairing,[46] and cooling. The temporal evolution of the shifts gives extra information on the dynamics.

It is also interesting to compare the ultra broadband TA spectroscopy with fs fluorescence spectroscopy (fs FS) as it can be measured with up conversion[63,64] or Kerr gating.[65] The reason that much effort is put into developing techniques of fs FS is that the fluorescence is a very clean signature of the electronically excited molecule. There is no superposition in the signal by ESA or GSB as typically seen in TA spectroscopy with a limited detection range. As demonstrated in the examples of this work, ultra broadband TA spectroscopy can fulfil the same condition by choosing the right spectral range, typically to the red of the GSB and stimulated emission. The well separated ESA transitions seen in this low energy part of the spectrum are also clean reporters of excited state dynamics. The great advantage is that the transient ESA signal can be measured with sub 50 fs temporal resolution, only reached by extremely well optimized fs FS experiments.[64] Contrary to fs FS, where an improvement in temporal resolution leads to a largely decreased signal strength and long averaging times, the TA spectroscopy can be performed quite quickly. We therefore expect that particularly transient NIR detection will be able to rival fs Fs without the need for a dedicated setup.

Last but not least we want to address the detection and identification of vibronic coherences. In many one colour pump probe measurements much debate is needed to find out whether the observed modulations in the TA signal are due to vibrational wavepackets in the electronic ground state or to vibronic

wavepackets in an excited state. The first are a nice confirmation of our understanding of ultrafast experiments and the underlying molecular level structure, but they do not reveal much information beyond that already known from Raman spectroscopy and resonance Raman spectroscopy. Only the latter render real new information on the structure of the excited molecule and the course of reactions. We were able to report earlier that in ESIPT those modes contribute to the wavepacket signature that are intimately connected with the proton transfer by shortening of the donor acceptor distance.[66] Now we even find that in the bond cleavage discussed in Sec. 6 the photoproducts display long lasting vibrational coherences. This can only be understood if the whole cleavage process proceeds coherently. It gives great hope that coherent control, *e.g.*, by double pulses or shaped pulses, can be used to control the branching ratio between homolysis and heterolysis and the yield of individual products. Also incoherent control by time delayed pulses of largely differing wavelengths might be feasible as the electron transfer, the recombination and the diffusional separation are understood in detail.

The newly available experimental capabilities should be able to revitalize the use of electronic spectroscopy for the elucidation and quantitative analysis of complex molecular and chemical processes. Unlike the typical use of UV/vis spectroscopy for stable species or just processes in the ms range, our strategy comes with 50 fs temporal resolution. As a consequence, even the shortest lived intermediates can be looked for. Unlike the earlier fs experiments the ultra broadband detection allows the full range of spectroscopic knowledge to be utilized. We therefore think that the best is still to come for electronic spectroscopy and we look forward to a bright, visible future.

Acknowledgements

We thank P. Lang and Oliver Schalk for experimental help, and R. de Vivie Riedle, S. Thallmair and T. Tahara for stimulating discussions. Financial support of this work by the Deutsche Forschungsgemeinschaft through the SFB 749, the GRK 1626, and the excellence cluster 'Munich Center for Advanced Photonics' (MAP) is gratefully acknowledged.

References

1 A. H. Zewail, *Angew. Chem., Int. Ed.*, 2000, **39**, 2586.
2 P. Hamm, S. Wiemann, M. Zurek and W. Zinth, *Opt. Lett.*, 1994, **19**, 1642.
3 M. Bradler, P. Baum and E. Riedle, *Appl. Phys. B: Lasers Opt.*, 2009, **97**, 561.
4 U. Megerle, I. Pugliesi, C. Schriever, C. F. Sailer and E. Riedle, *Appl. Phys. B: Lasers Opt.*, 2009, **96**, 215.
5 M. Bradler, C. Homann and E. Riedle, *Opt. Lett.*, 2011, **36**, 4212.
6 C. Homann, P. Lang and E. Riedle, *J. Opt. Soc. Am. B*, 2012, **29**, 2765.
7 P. J. M. Johnson, V. I. Prokhorenko and R. J. D. Miller, *Opt. Express*, 2009, **17**, 21488.
8 I. Buchvarov, A. Trifonov and T. Fiebig, *Opt. Lett.*, 2007, **32**, 1539.
9 R. Huber, T. Köhler, M. O. Lenz, E. Bamberg, R. Kalmbach, M. Engelhard and J. Wachtveitl, *Biochemistry*, 2005, **44**, 1800.
10 A. N. Tarnovsky, W. Gawelda, M. Johnson, C. Bressler and M. Chergui, *J. Phys. Chem. B*, 2006, **110**, 26497.
11 T. A. Zeidan, Q. Wang, T. Fiebig and F. D. Lewis, *J. Am. Chem. Soc.*, 2007, **129**, 9848.
12 A. L. Dobryakov, S. A. Kovalenko, A. Weigel, J. L. Pérez-Lustres, J. Lange, A. Müller and N. P. Ernsting, *Rev. Sci. Instrum.*, 2010, **81**, 113106.
13 E. P. Ippen, C. V. Shank and A. Bergman, *Chem. Phys. Lett.*, 1976, **38**, 611.
14 Y. Nagasawa, Y. Ando and T. Okada, *Chem. Phys. Lett.*, 1999, **312**, 161.

 This journal is © The Royal Society of Chemistry 2013

15 Y. Nagasawa, Y. Ando, D. Kataoka, H. Matsuda, H. Miyasaka and T. Okada, *J. Phys. Chem. A*, 2002, **106**, 2024.
16 D. Ben-Amotz and C. B. Harris, *J. Chem. Phys.*, 1987, **86**, 4856.
17 M. D. Hirsch and H. Mahr, *Chem. Phys. Lett.*, 1979, **60**, 299.
18 A. Mokhtari, L. Fini and J. Chesnoy, *J. Chem. Phys.*, 1987, **87**, 3429; A. Mokhtari, A. Chebira and J. Chesnoy, *J. Opt. Soc. Am. B*, 1990, **8**, 1551.
19 F. Pellegrino, A. Dagen and R. R. Alfano, *Chem. Phys.*, 1982, **67**, 1982.
20 P. Sen, S. Yamaguchi and T. Tahara, *Faraday Discuss.*, 2010, **145**, 411.
21 N. H. Gottfried, B. Roither and P. O. J. Scherer, *Opt. Commun.*, 1997, **143**, 261.
22 M. J. Rosker, F. W. Wise and C. L. Tang, *Phys. Rev. Lett.*, 1986, **57**, 321.
23 K. A. Nelson and L. R. Williams, *Phys. Rev. Lett.*, 1987, **58**, 745.
24 A. Nakayama and T. Taketsugu, *J. Phys. Chem. A*, 2011, **115**, 8808.
25 M. M. Martin, E. Breheret, F. Nesa and Y. H. Meyer, *Chem. Phys.*, 1989, **130**, 279.
26 Z. R. Grabowski, K. Rotkiewicz and W. Rettig, *Chem. Rev.*, 2003, **103**, 3899.
27 U. Schmidhammer, U. Megerle, S. Lochbrunner, E. Riedle and J. Karpiuk, *J. Phys. Chem. A*, 2008, **112**, 8487.
28 S. R. Flom and P. F. Barbara, *Chem. Phys. Lett.*, 1983, **94**, 488.
29 M. Wiechmann, H. Port, W. Frey, F. Lärmer and T. Elsässer, *J. Phys. Chem.*, 1991, **95**, 1918.
30 C. Chudoba, S. Lutgen, T. Jentzsch, E. Riedle, M. Woerner and T. Elsaesser, *Chem. Phys. Lett.*, 1995, **240**, 35.
31 C. Chudoba, E. Riedle, M. Pfeiffer and T. Elsaesser, *Chem. Phys. Lett.*, 1996, **263**, 622.
32 A. L. Sobolewski, W. Domcke and C. Hättig, *J. Phys. Chem. A*, 2006, **110**, 6301.
33 W. Frey and T. Elsaesser, *Chem. Phys. Lett.*, 1992, **189**, 565.
34 K. Lenz, M. Pfeiffer, A. Lau and T. Elsaesser, *Chem. Phys. Lett.*, 1994, **229**, 340.
35 V. Kozich and W. Werncke, *J. Mol. Struct.*, 2005, **735**, 145.
36 V. Kozich, J. Dreyer and W. Werncke, *Chem. Phys. Lett.*, 2004, **399**, 484.
37 M. Barbatti, A. J. A. Aquino, H. Lischka, C. Schriever, S. Lochbrunner and E. Riedle, *Phys. Chem. Chem. Phys.*, 2009, **11**, 664.
38 O. F. Mohammed, S. Luber, V. S. Batista and E. T. J. Nibbering, *J. Phys. Chem. A*, 2011, **115**, 7550.
39 P. F. Barbara, L. E. Brus and P. M. Rentzepis, *J. Am. Chem. Soc.*, 1980, **102**, 5631.
40 S. Lochbrunner, W. Fuss, W. E. Schmid and K.-L. Kompa, *J. Phys. Chem. A*, 1998, **102**, 9334.
41 K. S. Peters, *Chem. Rev.*, 2007, **107**, 859.
42 M. Lipson, A. A. Deniz and K. S. Peters, *Chem. Phys. Lett.*, 1998, **288**, 781.
43 C. F. Sailer, N. Krebs, B. P. Fingerhut, R. de Vivie-Riedle, E. Riedle, *Phys. Rev. Lett.*, submitted for publication.
44 B. P. Fingerhut, C. F. Sailer, J. Ammer, E. Riedle and R. de Vivie-Riedle, *J. Phys. Chem. A*, 2012, **116**, 11064.
45 C. F. Sailer, R. B. Singh, J. Ammer, E. Riedle and I. Pugliesi, *Chem. Phys. Lett.*, 2011, **512**, 60.
46 C. F. Sailer, B. P. Fingerhut, S. Thallmair, C. Nolte, J. Ammer, H. Mayr, I. Pugliesi, R. de Vivie-Riedle and E. Riedle, *ChemPhysChem*, 2013 (in print).
47 J. Dreyer and K. S. Peters, *J. Phys. Chem.*, 1996, **100**, 15156.
48 J. Dreyer, M. Lipson and K. S. Peters, *J. Phys. Chem.*, 1996, **100**, 15162.
49 B. P. Fingerhut, D. Geppert and R. de Vivie-Riedle, *Chem. Phys.*, 2008, **343**, 329.
50 U. Megerle, R. Lechner, B. König and E. Riedle, *Photochem. Photobiol. Sci.*, 2010, **9**, 1400.
51 M. Wenninger and E. Riedle, in *Chemical Photocatalysis*, ed. B. König, DeGryuter, Berlin, 2013.
52 M. R. Detty and P. B. Merkel, *J. Am. Chem. Soc.*, 1990, **112**, 3845.
53 M. Guéron, J. Eisinger and R. G. Shulman, *Mol. Phys.*, 2006, **14**, 116.
54 D. Peceli, S. Webster, D. A. Fishman, C. M. Cirloganu, H. Hu, O. V. Przhonska, V. V. Kurdyukov, Y. L. Slominsky, A. I. Tolmachev, A. D. Kachkovski, R. R. Dasari, S. Barlow, S. R. Marder, D. J. Hagan and E. W. Van Stryland, *J. Phys. Chem. A*, 2012, **116**, 4833.
55 H. E. Lessing, A. von Jena and M. Reichert, *Chem. Phys. Lett.*, 1976, **42**, 218.
56 S. M. King, C. Rothe, D. Dai and A. P. Monkman, *J. Chem. Phys.*, 2006, **124**, 234903.
57 B. Lament, J. Karpiuk and J. Waluk, *Photochem. Photobiol. Sci.*, 2003, **2**, 267.
58 A. M. D. Lee, J. D. Coe, S. Ullrich, M.-L. Ho, S.-J. Lee, B.-M. Cheng, M. Z. Zgierski, I.-C. Chen, T. J. Martinez and A. Stolow, *J. Phys. Chem. A*, 2007, **111**, 11948.
59 R. Bonneau, *J. Am. Chem. Soc.*, 1980, **102**, 3816.
60 E. T. J. Nibbering and T. Elsaesser, *Chem. Rev.*, 2004, **104**, 1887.
61 E. T. J. Nibbering, H. Fidder and E. Pines, *Annu. Rev. Phys. Chem.*, 2005, **56**, 337.

62 M. L. Groot, L. J. G. W. van Wilderen and M. Di Donato, *Photochem. Photobiol. Sci.*, 2007, **6**, 501.
63 X.-X. Zhang, C. Würth, L. Zhao, U. Resch-Genger, N. P. Ernsting and M. Sajadi, *Rev. Sci. Instrum.*, 2011, **82**, 063108.
64 C. H. Kim and T. Joo, *Opt. Express*, 2008, **16**, 20742.
65 B. Schmidt, S. Laimgruber, W. Zinth and P. Gilch, *Appl. Phys. B: Lasers Opt.*, 2003, **76**, 809.
66 S. Lochbrunner, A. J. Wurzer and E. Riedle, *J. Phys. Chem. A*, 2003, **107**, 10580.

 This journal is © The Royal Society of Chemistry 2013

Appendix A8

Internal Conversion vs. Intersystem Crossing –
What Drives the Dynamics of Cyclic α,β-Enones?

O. Schalk, P. Lang, M. S. Schuurman, G. Wu, M. Bradler, E. Riedle, and A. Stolow

Proceedings of the XVIIIth International Conference on Ultrafast Phenomena, Lausanne, Switzerland. EPJ Web of Conferences **41**, 05029 (2013)

Reprinted with kind permission from Oxford University Press, Inc.

EPJ Web of Conferences **41**, 05029 (2013)
DOI: 10.1051/epjconf/20134105029
© Owned by the authors, published by EDP Sciences, 2013

Internal Conversion vs. Intersystem Crossing – What Drives the Dynamics of Cyclic α,β-Enones?

O. Schalk[1,2], P. Lang[1], M. S. Schuurman[2], G. Wu[2], M. Bradler[1], E. Riedle[1], A. Stolow[2]

[1]Lehrstuhl für BioMolekulare Optik, LMU München, Oettingenstraße 67, D-80538 Munich,
[2]National Research Council of Canada, Sussex Drive 100, Ottawa, Ontario K1A 0R6,

Abstract. The origin of ultrafast intersystem crossing and its competitiveness with singlet pathways was studied in cyclic α,β-enones by transient absorption, time-resolved photoelectron spectroscopy and *ab initio* calculations.

1 The role of triplet state dynamics

Intersystem crossing (ISC) in photoexcited organic molecules is often thought of as an inherently slow process. Especially in molecules with fast singlet channels as those governed by conical intersection (CoIns), triplet state formation is rarely seen. For example, the dynamics in butadiene (CH_2 CH-CH CH_2) takes place within 100 fs after light absorption [1]. However, there exist examples where this is not the case as, e.g., for α,β-enones [2,3]. In acrolein (CH_2 CH-CH O) a CH_2-group of butadiene is replaced by an oxygen and triplet state formation can be observed although both butadiene and acrolein dynamics are governed by ethylene-type CoIns which are localized only at one side of the molecule [2]. So the question arises as to why such a small change in the molecular structure causes completely different dynamics. To address this issue, we used time-resolved photoelectron spectroscopy (TRPES) and transient absorption (TA) in cyclohexane, acetonitrile and methanol as solvent to discern the initial dynamics of cyclic α,β-enones. Here, we focus on our results on 2,3,4,5-tetramethyl-2-cyclopentenone (TMCPO) and compare them with the less methylated derivatives 2-cyclopentenone (CPO) and 3 methyl-2-cyclopentenone (3MeCPO).

2 Absorption Spectrum and Potential Energy Surfaces

The absorption spectrum of TMCPO is typical for many α,β-enones. It has a bright $^1\pi\pi^*$-state around 220 nm and a weakly absorbing $^1n\pi^*$-state on its red flank (see Fig. 1a). The significant spectral shifts correlate with the dipole moments of the states which increases for the $^1\pi\pi^*$-state and decreases for the $^1n\pi^*$-state with respect to the ground state. The shape of the $^1n\pi^*$-band shows that the lifetime of this state might be significantly reduced in methanol as a solvent.

A sketch of the relevant potential energy surfaces is shown in Fig. 1b. Upon excitation to the bright $^1\pi\pi^*$-state, the molecules relax to the lower lying $^1n\pi^*$-state from where they can return to the ground state by one of multiple CoIns (see examples for CPO in Fig. 1c) or progress to the triplet manifold where various pathways are possible [3]. Our calculations show that direct access to the CoIns is hindered by a large energy gap to the energetic minimum of S_1 (more than 1 eV at the

This is an Open Access article distributed under the terms of the Creative Commons Attribution License 2.0, which permits unrestricted use, distribution, and reproduction in any medium, provided the original work is properly cited.

3s2p1d ANO/MR-SOCI level) but that the $^3\pi\pi^*$-state is energetically close favoring ISC through a spin-orbit coupling of 30-50 cm^{-1} on the whole $^1n\pi^*$-manifold.

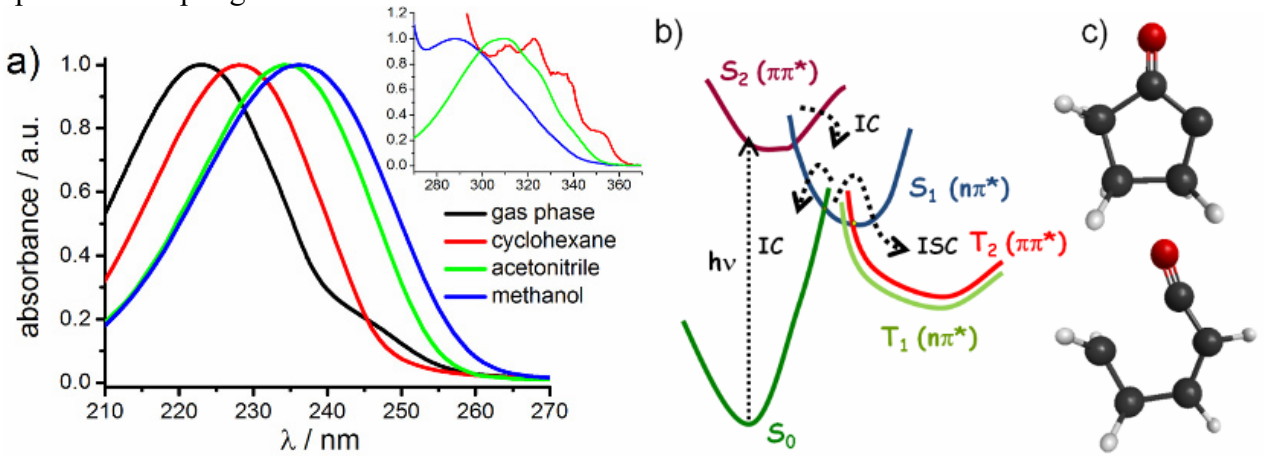

Fig. 1. a) Absorption spectrum of TMCPO b) Sketch of the potential energy surfaces c) Lowest lying conical intersections between S_1 and S_0 at 3s2p1d ANO/MR-SOCI for 2-cyclopentenone (CPO).

3 Experimental results

The photoelectron spectrum of TMCPO excited to the $^1\pi\pi^*$-state at 216 nm and probed at 267 nm is shown in Figure 2. The $^1\pi\pi^*$-state is seen by the band at low photoelectron kinetic energy and relaxes to the $^1n\pi^*$-state within roughly 150 fs. It is shifted in time toward lower photoelectron kinetic energy due to large amplitude motions caused by the CoIn between the $^1\pi\pi^*$- and the $^1n\pi^*$-state being strongly deformed out-of-plane (a similar motion has been observed before in TRPES [3]). The $^1n\pi^*$-state is seen in the two photon probe region at higher photoelectron kinetic energy and decays itself within 2.8 ps. These decay times are much shorter in CPO and 3-methyl-CPO (ca. 100 fs for $^1\pi\pi^{**}$-state and 1.15 and 1.4 ps for the $^1n\pi^*$-state, respectively). A residual spectrum which is similar for all investigated molecules stays constant for at least 250 ps.

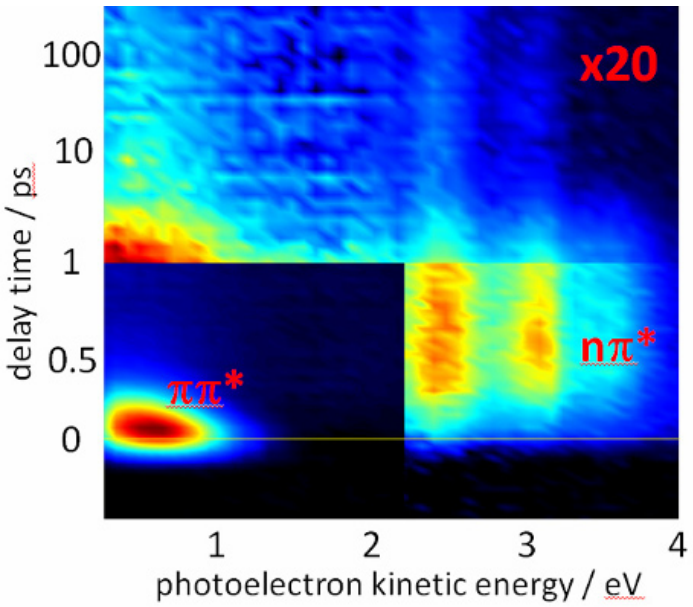

Fig. 2. a) Photoelectron spectrum of TMCPO excited at 216 nm and probed at 267 nm.

The TA spectrum following excitation of TMCPO in acetonitrile at 228 nm is depicted in Figure 3. Besides the coherent artifact around time zero, one sees three processes, one on the 200 fs timescale originating from the $^1\pi\pi^*$-state relaxation, one on the ps timescale ($^1n\pi^*$-state) and a residual spectrum peaking around 280 nm which can be assigned to the triplet states in agreement with [4]. When comparing the time constants for the $^1n\pi^*$-decay, one sees no big changes between the solvents and the gas phase (between 3 and 4 ps). This is different for CPO and 3MeCPO where the gas phase dynamics are more than a factor of 3 faster than those in the liquid phase. Between 230 and 240 nm, we see a strong ground state bleach. On the timescale of the experiment, we do not observe a change in optical density which means that no population has returned to the ground state and hence, intersystem crossing seems to be the predominant relaxation channel.

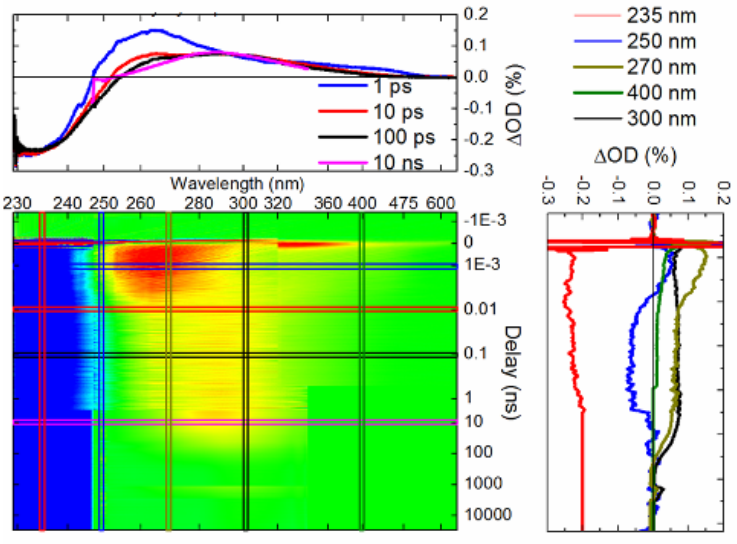

Fig. 3. Transient absorption spectrum of TMCPO in acetonitrile excited at 227 nm measured with different white light continua and pump sources (see [5]).

4 Discussion

Considering the similarity of the transient spectra of the investigated molecules (both TRPES and TA), we conclude that the main reaction pathway is via ISC which is governed by the presence of a $^{1}n\pi^{*}$-state and the energetically close lying $^{3}\pi\pi^{*}$ acceptor state. If internal conversion (IC) were dominant, we would expect the ground state bleach to recover on a ps time scale. Similar time constants in the different solvents indicate that ISC does not depend on polarity and that the relative energetic position of the states only plays a minor role, although relative shifts of the $^{1}n\pi^{*}$-band indicate that the singlet dynamics might differ. This behavior can be explained with the large 1 eV barrier between the CoIns with the ground state and the $^{1}n\pi^{*}$-state minimum. The CoIn can be accessed after conversion to the $^{1}n\pi^{*}$-state. However, as time progresses, the $^{1}n\pi^{*}$-state minimum is reached and the CoIn lies energetically too high to play a significant role. Therefore, IC might play a role in the gas phase where a faster time constant for the $n\pi^{*}$-state is observed and where vibrational motions are less dampened than in liquid phase. In solvent, however, we almost exclusively observe ISC.

5 Outlook

Exact calculations of the solvent dependent energetic position of the states as well as *ab initio* dynamics calculation will reveal more information about these systems. In addition, further experiments on differently substituted molecules and wavelength dependent pump pulses will allow deciphering the role of specific motions on the dynamics. The final goal is to understand the conditions for ISC in molecules which, in principle, would also allow fast IC-processes and to predict when a molecule can be supposed to predominantly react via its singlet or its triplet manifold.

References

1. W. Fuß, W. E. Schmid, S. A. Trushin, Chem. Phys. Lett. **342**, 91 (2001)
2. A. M. D. Lee, J. D. Coe, S. Ullrich, M.-L. Ho, S.-J. Lee, B.-M. Cheng, M. Z. Zgierski, I.-C. Chen, T. J. Martinez, A. Stolow, J. Phys. Chem. A **111**, 11948 (2007)
3. O. Schalk, A. E. Boguslavskiy, A. Stolow, M. S. Schuurman, J. Am. Chem. Soc. **135**, 16451 (2011)
4. I. Schuster, D. A. Dunn, G. E. Heibel, P. B. Brown, J. M. Rao, J. Woning, R. Bonneau, J. Am. Chem. Soc. **113**, 6245 (1991)
5. U. Mergele, I. Pugliesi, C. Schriever, C. F. Sailer, E. Riedle, Appl. Phys. B **96**, 215 (2009)

Appendix A9

Continuum generation in bulk materials from the deep UV to the infrared with pump pulse durations over the entire femtosecond regime

M. Bradler and E. Riedle

Proceedings of the XVIIIth International Conference on Ultrafast Phenomena, Lausanne, Switzerland. EPJ Web of Conferences **41**, 10011 (2013)

Reprinted with kind permission from Oxford University Press, Inc.

EPJ Web of Conferences **41**, 10011 (2013)
DOI: 10.1051/epjconf/20134110011
© Owned by the authors, published by EDP Sciences, 2013

Continuum generation in bulk materials from the deep UV to the infrared with pump pulse durations over the entire femtosecond regime

M. Bradler[1] and E. Riedle[1]

[1]LS für BioMolekulare Optik, Ludwig-Maximilians-Universität München, Oettingenstraße 67, 80538 München, Germany

Abstract. We demonstrate continuum generation with pulses from the long femtosecond up to the picosecond regime. To understand the mechanism involved in this process we study the influence of the spectral width and the chirp of the pump pulses. We further investigate the threshold for stable continuum generation with smooth, plateau-like spectra from the deep ultraviolet to the infrared. We visualize the processes of the generation and study filament parameter such as length, diameter and observe multiple filamentation. This visualization allows us to determine and understand the temporal jitter of newly generated frequencies.

1 Influence of pump pulse duration on continuum generation in bulk

When ultrashort intense laser pulses are focused in bulk materials, one of the most fascinating phenomena in ultrafast nonlinear optics can occur: supercontinuum generation. The octave wide spectral broadening gives access to wavelength regions not supported by available laser systems. These continua render smooth, flat and gap free spectra with a high amount of coherence, compressibility, and high stability on all time scales [1]. This favors them as a most valuable source for broadband radiation in laser technology and spectroscopy [2]. Continuum generation works well with a pump pulse duration below 150 fs, even with extremely short few cycle pulses. However, it fails with longer pulses in common crystals like sapphire owing to avalanche ionization. Nevertheless continuum generation with longer pulse duration would be of great interest for many applications. It would be particularly advantageous for strong pump lasers of optical parametric chirped pulse amplifiers which have pulse durations in the picosecond regime.

In this contribution we show first proof of ps continuum generation in laser crystals retaining the advantageous properties of fs continua like flat and smooth plateau-like spectra over the entire visible range (see figure 1 (a)). To understand the role of the pulse duration on continuum generation, experiments on the influence of the spectral width and chirp were performed. For this purpose we generate picosecond pulses from a Ti:Sappire system (Clark MXR, CPA 2001, 775 nm, 150 fs): One time by narrowing the spectrum and one time by up-chirping the pulse with the entire spectrum by transmission through glass. With sufficient pump energy new spectral components can occur for these pulses during propagation in crystals. The stability at selected wavelengths serves as criterion for continuum generation. Figure 1 shows the pump energy for stable continuum generation in sapphire, YAG and KGW, when chirping (b) and spectral narrowing (c) the pump pulse.

This is an Open Access article distributed under the terms of the Creative Commons Attribution License 2.0, which permits unrestricted use, distribution, and reproduction in any medium, provided the original work is properly cited.

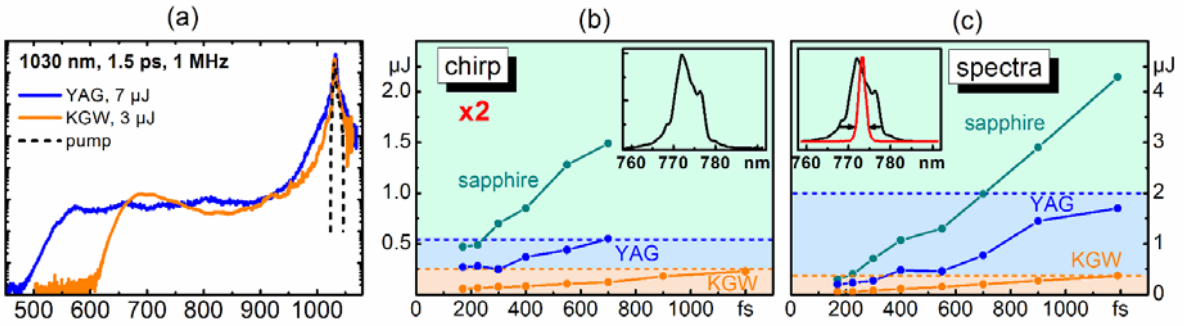

Fig. 1. Continuum generation in selected crystals with picosecond pulses (a), chirped (b) and spectrally narrowed (c) femtosecond pulses.

Further studies indicate that especially for longer pulses the spectral width is a limiting factor, because long pulses compress towards the Fourier limits during the propagation in the first few mm of the crystal due to self-steepening. If the spectral width is low, self-phase modulation has to first broaden the pulse to reduce the Fourier limit and than self-steepening can shorten the pulses. This configuration needs more energy and show a stronger broadening, as confirmed by the experiment. In upcoming experiments we will analyze the chirp of the newly generated frequencies and the temporal behavior of the pump region during filamentation.

2 Continuum generation with pump wavelengths from the UV to the IR

Nonlinear processes like optical parametric amplification, second harmonic generation, and sum or difference frequency generation allow the generation of energetic pulses from the deep UV to the infrared [3] largely independent from the original laser wavelength. However, these pulses often have a limited spectral bandwidth originating from the necessary phase-matching of the nonlinear processes. The generation of broadband spectra around these new frequencies is a challenging task and often requires high energies. Continuum generation in bulk materials on the other hand only needs µJ energies and therefore spectral broadening is possible. The choice of the crystals additionally allows to reduce the necessary energy or to increase the spectral width. To show that continuum generation is not only limited to small regions around the pump wavelength, we show continua generated with frequency doubled Ti:sapphire and Yb:KYW lasers, the original wavelength, and infrared pulses from an optical parametric amplifier. Figure 2 shows selected continua covering the ultraviolet, visible and infrared. The pump wavelength is blocked with filters, so that only the newly generated frequencies are shown.

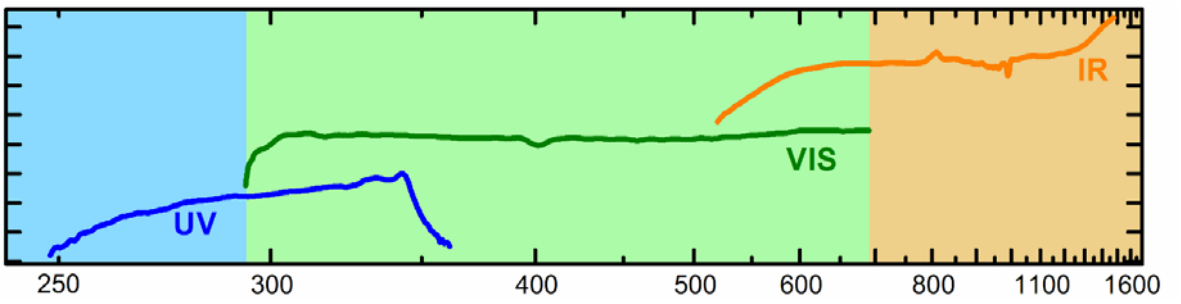

Fig. 2. Continuum generation with pump wavelengths from the UV to the IR (400, 800 and 1600 nm).

All these continua show a smooth, gap free and wide spectrum with a proper beam profile and a high stability. This favors them for the use in femtosecond pump probe spectroscopy. The spectral overlapping allows combining the results from different continua. The short wavelength continuum

cut-off remains constant if the pump wavelength is increasing. This allows octave-wide gap free flat continua when pumping with an infrared source. Combining the principles of optical parametric amplification (OPA) with the fact that the energy threshold is low, these infrared sources can easily be generated by nearly any laser systems. For OPCPA systems passive carrier-envelope phase (CEP) stabilization can be obtained in this conversion.

3 Visual observation of continuum generation in YAG

During filamentation and continuum generation many nonlinear processes take place like self-focusing, self-steepening, self-phase modulation, or multi-photon excitation. In Yttrium aluminum garnet (YAG) not only the continuum can be observed as beam profile along the propagation axis, but also the filament channel is clearly visible from the side. This is presumably due to the recombination of the electrons from the conduction to the valence band. By imaging the visible filament on a camera we can investigate the position and length of the filament. The filament length of up to 2 mm is independent of the incidental numerical aperture and can therewith be significantly larger than the Rayleigh length. This is due to the balance between self-focusing and plasma defocusing which overcomes the natural divergence. Also filamentation starts closer to the entrance surface of the crystal, if the input energy is increased. This is due to the stronger self-focusing, what leads to a shorter self-focal distance.

From the side view of the filamentation also the temporal jitter of the newly generated frequencies can be analyzed and optimized to 0.5 fs/nJ. The jitter comes from the fluctuation of the filament position which originates from the energy fluctuations of the pump. This is for example important for passively CEP stabilized pulses from an OPA [4]. If the energy for continuum generation is increased and exceeds twice the threshold for continuum generation we observe a second filament arising. These filaments line up on the propagation axis and show spatial and spectral interference. Figure 3 shows this spatial (a) and spectral (b) interference, and the side view of two filaments in a YAG crystal (c).

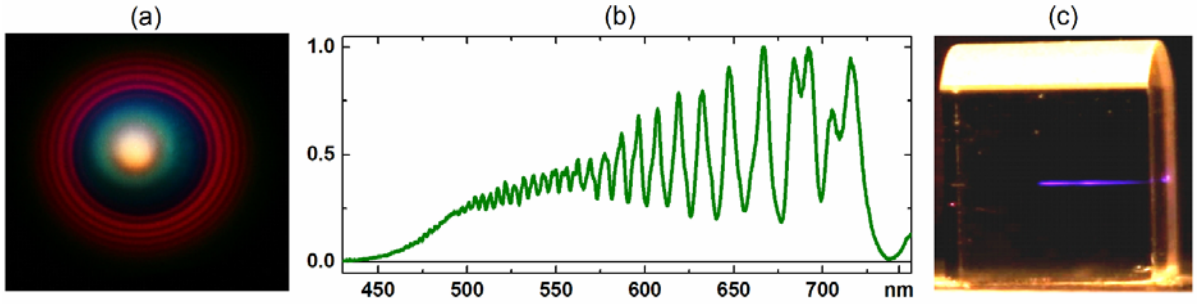

Fig. 3. Spatial (a) and spectral (b) interference and side view (c) of two filaments in YAG

The field of continuum generation in bulk materials is still under investigation and offers many rewarding opportunities for advanced laser applications and broadband spectroscopy. Continuum generation with multi-ps pump pulses is within reach, as confirmed by our first successful experiments. The ease of handling and the very compact setup qualify continuum generation as excellent alternative broadband source for many applications.

References

1. M. Bradler, P. Baum, E. Riedle, Appl. Phys. B **97**, 561 (2009)
2. U. Megerle, I. Pugliesi, C. Schriever, C.F. Sailer, E. Riedle, Appl. Phys. B **96**, 215 231 (2009)
3. M. Bradler, C. Homann, E. Riedle, Opt. Lett. **36**, 4212 (2011)
4. C. Homann, M. Bradler, E. Riedle, Opt. Lett. **37**, 1673 (2012)

Appendix A10

Generation of sub-two-cycle pulses tunable around 1.8 µm with passively stabilized carrier-envelope phase at 100 kHz repetition rate

C. Homann, M. Bradler, M. Förster, P. Hommelhoff, and E. Riedle

Proceedings of the XVIIIth International Conference on Ultrafast Phenomena, Lausanne, Switzerland. EPJ Web of Conferences **41**, 10012 (2013)

Reprinted with kind permission from Oxford University Press, Inc.

EPJ Web of Conferences **41**, 10012 (2013)
DOI: 10.1051/epjconf/20134110012
© Owned by the authors, published by EDP Sciences, 2013

Generation of sub-two-cycle pulses tunable around 1.8 µm with passively stabilized carrier-envelope phase at 100 kHz repetition rate

C. Homann[1], M. Bradler[1], M. Förster[2], P. Hommelhoff[2], and E. Riedle[1]

[1]LS für BioMolekulare Optik, Ludwig-Maximilians-Universität, 80538 München, Germany
[2]Ultrafast Quantum Optics Group, MPI für Quantenoptik, 85748 Garching, Germany

Abstract. We present an efficient concept for generating carrier-envelope phase stable pulses tunable between 1.6 and 2.0 µm with durations down to 8.2 fs based on nonlinear frequency conversion. As a first application we measure the high nonlinearity of multiphoton photoemission from a nanoscale metal tip.

1 Sub-two-cycle pulses by OPA and DFG at 100 kHz

The generation of few-cycle light pulses with stable carrier-envelope phase (CEP) at wavelengths around 2 µm is still a challenging but worthwhile task [1]. High-power pulses at these wavelengths are of interest because they allow extending the cutoff of high-order harmonic generation towards the water window. But also in the CEP-sensitive emission of electrons from metal nanostructures, where pulse energies of only 240 pJ at 800 nm sufficed to generate electrons with kinetic energies of up to 13 eV, the use of longer wavelengths is expected to greatly enhance electron energies and to give further insight into the interplay between multiphoton and tunneling ionization [2]. For investigations along these lines, CEP stable sub-two-cycle pulses with high repetition rates are a promising tool.

Here we present an efficient and simple scheme for the generation of such pulses with a duration around 10 fs and energies on the order of 100 nJ at a repetition rate of 100 kHz [3]. The pulses are tunable in the range from 1.6 to 2.0 µm while maintaining a sub-two-cycle duration (see Fig. 1). To the best of our knowledge this constitutes the shortest pulse durations in this wavelength range for repetition rates above 1 kHz, combined with excellent tunability.

Our concept is based on supercontinuum generation (SCG) in bulk material followed by noncollinear optical parametric amplification for the generation of a broadband visible spectrum, and subsequent broadband difference frequency generation (DFG) with the narrow-band pump laser to generate the passively CEP stabilized output around 1.8 µm. A commercial Yb:KYW based pump laser (Jenlas® D2.fs; JENOPTIK Laser GmbH) delivers ~ 300 fs pulses at 1025 nm with an energy of 40 µJ at 100 kHz repetition rate. Approximately 5 % of the used 32 µJ are split off for SCG in a 4 mm thick YAG crystal, producing the seed for the NOPA. The remainder of the pump pulse is frequency-doubled in a BBO crystal with an efficiency of about 30 %. The continuum seed is then noncollinearly amplified by the 512 nm pump pulses in a 3 mm thick BBO crystal. The amplified spectrum can be tuned in central wavelength between 650 nm and 700 nm while maintaining a Fourier limit below 10 fs and energies around 2 µJ per pulse. After collimation with a spherical mirror the output pulses are compressed using fused silica prisms.

This is an Open Access article distributed under the terms of the Creative Commons Attribution License 2.0, which permits unrestricted use, distribution, and reproduction in any medium, provided the original work is properly cited.

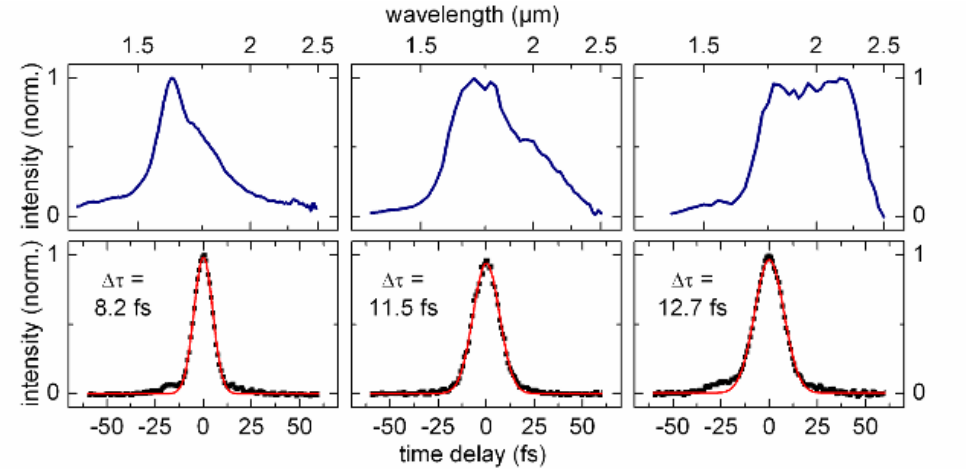

Fig. 1. Spectra and corresponding autocorrelation measurements showing the wavelength tunability of our concept while maintaining a sub-two-cycle pulse duration (Δτ: deconvolved FWHM Gaussian pulse duration).

The 1025 nm light remaining after frequency doubling is rotated in polarization by 90°. It is then focused into a 0.8 mm thick BBO crystal together with the compressed NOPA output to perform type-I DFG to the infrared. This crystal thickness is much less than typically used for an OPA stage and therefore allows a largely increased acceptance bandwidth. To avoid the need for dichroic optics, the two beams are combined under a small angle, which is kept as small as possible (~ 0.9°) to limit the associated spatial chirp of the infrared pulse. For the chosen angle the angular dispersion between the spectral components at 1.6 μm and 2.2 μm of the output pulse is 0.55° and therewith less than the natural divergence of ~ 1°.

The spectrum of the infrared output can be tuned in a considerable wavelength range by changing the NOPA spectrum and readjusting the phase-matching angle of the DFG and the time delay between the NOPA output and the 1025 nm pulses (see Fig. 1). The deconvoluted pulse durations, obtained from autocorrelation measurements, lie between 8.2 fs and 12.7 fs, corresponding to only 1.5 to 1.9 optical cycles. Pulse energies of up to 145 nJ are achieved, however with slightly longer pulses (11.7 fs at 1.6 μm central wavelength). For the shortest pulse durations pulse energies of 40 nJ are achieved.

The compression of the infrared pulses is solely adjusted by the chirp of the NOPA output and thus the prism compressor in the visible. The shortest IR pulses are achieved when the NOPA pulses are also nearly optimally compressed. This scheme even allows compensating for material dispersion in the infrared, introduced by, e.g., an entrance window to a vacuum chamber.

2 Stability and control of the carrier-envelope phase

The NOPA output inherits the CEP fluctuations of the supercontinuum seed and hence of the 1025 nm pump. Since the NOPA output is subsequently difference frequency mixed with the 1025 nm light, the infrared output is expected to be CEP stable [1]. To verify this, we set up an f-2f interferometer. To achieve the necessary bandwidth, we coupled the infrared pulses into a highly nonlinear fiber. The broadened spectrum and the frequency-doubled light were then focused into a spectrometer with a time delay of ~ 400 fs. For proper alignment of the continuum generation, we observe high contrast interferences that directly show the CEP stability of the IR pulses. When integrating over 1 ms and acquiring 500 consecutive spectra (i.e. 0.5 s acquisition time), we measure phase fluctuations of only 78.5 mrad rms. Fig. 2 shows a measurement over 5 minutes (averaged over 100 ms). After 1.5 minutes we induce a CEP change of π by translating one of a pair of wedges located in the 1025 nm beam before the DFG stage. After 3 minutes the wedge is moved back. This clearly shows that we have full control of the CEP and can compensate for the observed slow drift. For the slower fluctuations (0.1 Hz to 5 Hz) we find a value of 135 mrad rms.

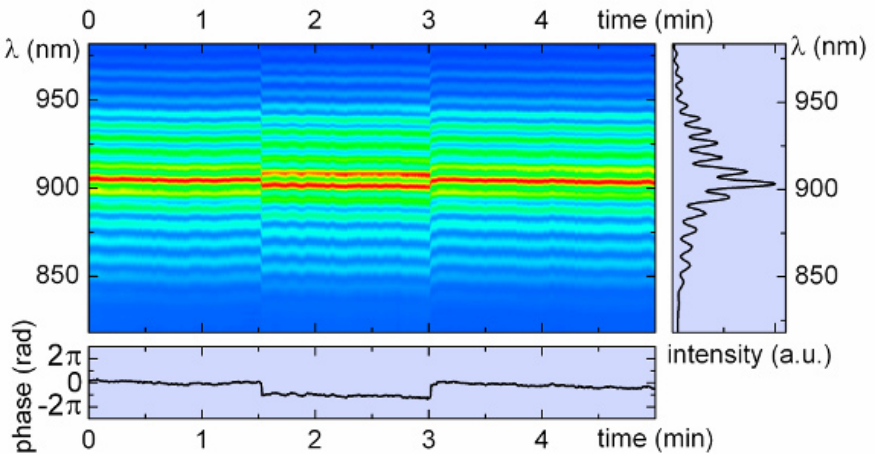

Fig. 2. f-2f interference measurement over 5 min. The right panel shows the spectrum of a single scan, the lower panel the evaluated phase. After 1.5 min. a CEP shift of π is induced by moving a wedge, which is reversed after 3 min.

3 Electron emission from nanoscale metal tips and outlook

As first experimental application of our new source, we tightly focus the IR pulses onto a nanoscale tungsten tip, with the laser polarization parallel to the tip-pointing direction (see Fig. 3(a)). This leads to photoemission of electrons from the tip, which we accelerate by an electric dc field towards a microchannel plate (MCP) detector. When measuring the electron current I on the MCP screen as a function of the incident pulse energy E, we find a $I \propto E^{3.8}$ dependence, indicating dominating multiphoton photoemission in this pulse energy range (see Fig. 3(b),(c) and [2]). The next step will be the measurement of the energy spectrum of the emitted electrons, which is expected to have a clear dependence on the CEP of the IR pulses.

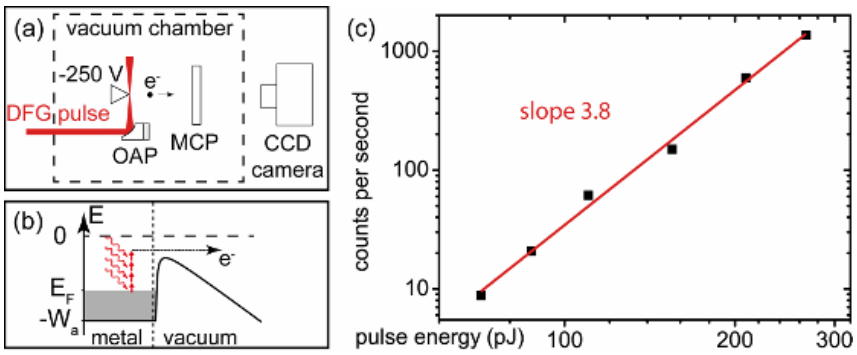

Fig. 3. (a) Schematic of the setup for the photoemission of electrons from a nanoscale metal tip. (b) Schematic of the multiphoton photoemission step. (c) Measured electron counts per second on the MCP as function of the laser pulse energy in a double logarithmic plot with a linear fit.

Our concept is also an interesting seed source for high power applications. It provides much more seed energy than the nowadays used few pJ to nJ, which will lead to a drastic improvement in pulse contrast. The combination of SCG, preamplification in the visible and subsequent DFG is furthermore expected to provide few-cycle pulses throughout a large part of the IR when used with different crystals.

References

1. G. Cerullo, A. Baltuska, O.D. Mücke, and C. Vozzi, Laser Photon. Rev. **5**, 323 (2011).
2. M. Krüger, M. Schenk, and P. Hommelhoff, Nature **78**, 475 (2011).
3. C. Homann, M. Bradler, M. Förster, P. Hommelhoff, and E. Riedle, Opt. Lett. **37**, 1673 (2012).

Appendix A11

Broadband difference frequency mixing between visible and near-infrared pulses for few-cycle pulse generation with stable carrier-envelope phase

M. Bradler, C. Homann, and E. Riedle

Appl. Phys. B **113**, 19 - 25 (2013)

Reprinted with kind permission from Springer Publishing

Appl. Phys. B (2013) 113:19 25
DOI 10.1007/s00340 013 5432 3

Applied Physics B
Lasers and Optics

Broadband difference frequency mixing between visible and near-infrared pulses for few-cycle pulse generation with stable carrier-envelope phase

Maximilian Bradler · Christian Homann · Eberhard Riedle

Published online: 6 April 2013
© Springer Verlag Berlin Heidelberg 2013

Abstract Difference frequency generation between broadband visible noncollinear optical parametric amplifier (NOPA) pulses and the fundamental pump laser pulses allows the generation of ultrashort infrared pulses with passively stabilized carrier-envelope phase. A simple prism compressor for the visible NOPA pulses is sufficient to generate few-cycle pulses in the infrared and no additional compression is needed. We theoretically investigate the concept, explain the principles, and demonstrate it for high repetition rate, long pulse durations, and various wavelengths by applying it to a Ti:sapphire and an Yb:KYW-based laser systems. For the latter sub-15 fs phase stable pulses around 1.8 μm with an energy of 100 nJ are obtained at 100 kHz repetition rate.

1 Introduction

Infrared light pulses are a very helpful tool to reveal elementary ultrafast processes in biology, chemistry, medicine, and physics. Especially vibrational absorption bands of molecules are located in the infrared and give an insight into the inner life of complex systems. Also many applications of strong-field physics like high harmonic generation, attosecond science or tunneling ionization benefit from ultrashort infrared pulses. Besides the wavelength also the carrier-envelope phase and peak intensity can play an essential role in such experiments. Therefore, often phase stable few-cycle pulses with highest intensities are needed. Many experiments also demand high repetition rates, because this allows detecting even weak signals and dramatically decreases the measuring time. Laser systems with high repetition rates and high pulse energies in the sub picosecond regime become readily available. Therefore, it is of considerable interest to develop simple and reliable concepts for the generation of ultrashort infrared pulses.

Sufficiently broadband laser materials for the direct generation of infrared few-cycle pulses are still in their early steps of development and therefore alternative concepts must be applied. A very successful approach is optical parametric amplification [1 12], often with chirped pulses [13 19] as recently reviewed in [20]. Also filamentation and hollow core fibers are additionally used for spectral broadening and compression [21 28]. Other techniques to produce shortest infrared pulses are parametric generation [29], difference frequency generation [30], and single mode fibers [31, 32]. Most recently sub-10 fs pulses with a spectrum ranging from 2 to 10 μm were achieved as conical emission from a filament created with 800 and 400 nm light [33]. Generating few-cycle pulses is always challenging independently from the wavelength region. Especially working in the infrared is demanding and requires well-suited equipment.

In this paper, we focus on a very recent approach [11, 34, 35] to generate few-cycle pulses in the infrared and study it in more detail. It is based on difference frequency generation between the very broadband visible pulses generated in a noncollinear optical parametric amplifier (NOPA) and the narrowband pump laser pulses in a thin nonlinear crystal. We first explain in general the setup and discuss the single stages. Then we theoretically investigate the key principles of the concept and why it is working so well. After this we describe the experimental realization in full detail, characterize infrared sub-two-cycle pulses from

M. Bradler (✉) · C. Homann · E. Riedle
Lehrstuhl für BioMolekulare Optik,
Ludwig Maximilians Universität (LMU),
Oettingenstraße 67, 80538 München, Germany
e mail: Maximilian.Bradler@physik.uni muenchen.de

an Yb:KYW-based system and show the potential for different laser wavelengths and mixing crystals.

2 General setup and results

Our concept is shown in Fig. 1a and based on difference frequency generation (DFG) between the narrowband laser pulses and a visible whitelight seeded NOPA pumped by the second harmonic of the laser light and compressed with just a prism compressor.

In the beginning, a small part of the laser light is used to generate a broadband visible whitelight seed for the NOPA. Here we use continuum generation in bulk, because it works over the entire femtosecond regime Bradler and Riedle (unpublished data) and so even laser systems with pulse durations up to picoseconds are suited for this concept. A big advantage of the concept is that no infrared seed must be provided and one can benefit from the well established visible whitelight generation and its favorable properties [36] such as smooth, flat, gap-free spectrum and superior beam quality. But also other visible light sources like fiber-based continua might be suited as seed light for the amplifier. The visible broadband whitelight seed is amplified in a NOPA pumped by the second harmonic of the laser light and compressed in a conventional prism compressor of two Brewster angled fused silica prisms. These pulses are difference frequency mixed with the remaining fundamental laser light, which is not frequency doubled. To perform DFG the polarization of the fundamental laser light is rotated by 90°. Since continuum generation, optical parametric amplification, and compression only add a constant phase term, the relative phase between the visible and the laser light is constant and the difference frequency generation delivers phase stable pulses even if the carrier-envelope phase of the laser system is not stable [20]. Two wedges in the path of the laser light allow controlling the final carrier-envelope phase. Note that the infrared pulses do not have to be further compressed. The prism compressor for the visible NOPA can precompensate the phase of the infrared pulses so that nearly transform-limited pulses are generated. Even further optical elements in the pathway like filters, entrance windows or lenses can be compensated, so that few-cycle possible pulses are still available at the experimental site.

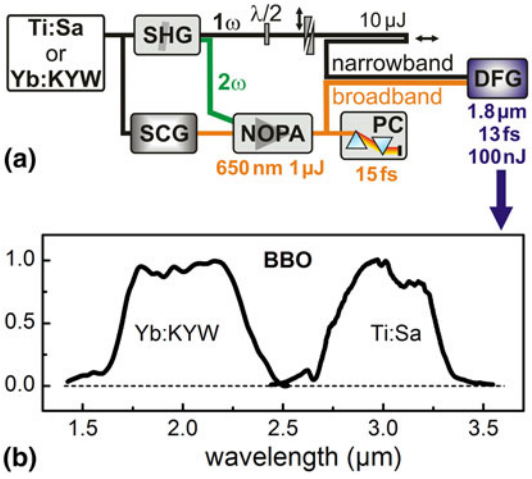

Fig. 1 **a** Broadband visible pulses from a whitelight (SCG) seeded NOPA pumped by second harmonic (2ω, SHG) are compressed with a prism compressor (PC) and frequency mixed with the narrowband laser pulses (1ω). A half wave plate ($\lambda/2$) rotates the polarization of the laser pulses to perform type I DFG and movable wedges allow controlling the phase of the final infrared output. **b** Two typical DFG spectra for Ti:sapphire and Yb:KYW as pump source and BBO as mixing crystal

To demonstrate the concept we used two laser systems: a commercial Yb:KYW-based pump laser (Jenlas D2.fs; JENOPTIK Laser GmbH) which delivers 300 fs pulses at 1025 nm with an energy of 40 µJ at 100 kHz repetition rate and a Ti:sapphire-based laser system (CPA2001; Clark MXR) delivering 150 fs pulses at 775 nm with an energy of 1 mJ at 1 kHz. The carrier-envelope phase of both systems is not stable. Infrared few-cycle pulses which are produced with each system are shown in Fig. 1b when using beta-barium-borate (BBO) as mixing crystal in the DFG. This section should only briefly describe the basic setup. A more complete and accurate description is given in section IV.

3 Broadband difference frequency generation

To understand how such broadband pulses in the infrared can be generated with difference frequency generation one has to consider the group velocities of the participating wavelengths. The difference frequency generation is performed in a nearly collinear geometry. All shown calculations are performed for exact collinearity, as the used angle of less than 1° does not significantly alter the phase matching or the group velocities. For the difference frequency generation we use type-I polarization, i.e., the visible pulses are extraordinarily polarized (e) and the laser and infrared light ordinarily (o). The small angle of $<1°$ between the visible pulse and the laser light is used to allow for spatial separation between the generated infrared and the input light. This avoids all dichroic optics.

The focusing of both input pulses is performed individually. This allows full control of the intensity, beam waist, and divergence of both pulses and therefore angular phase-matching limitations can be avoided. For selected nonlinear mixing crystals wavelength combinations can be found such that the group velocity of the visible pulses matches the group velocity of the final infrared pulses. All

Table 1 Wavelength combinations for extremely broadband DFG between visible NOPA pulses and narrowband pulses at 800 and 1025 nm in BBO, $LiNbO_3$, and $LiIO_3$

Mixing wavelength	800 nm (o)			1025 nm (o)		
	VIS (e) (nm)	IR (o) (μm)	Θ (°)	VIS (e) (nm)	IR (o) (μm)	Θ (°)
BBO	606	2.5	20.4	696	2.2	20.0
$LiNbO_3$	677	4.4	45.1	796	3.4	44.3
$LiIO_3$	693	5.2	20.1	820	4.1	19.8

A collinear mixing geometry is assumed

relevant data such as phase-matching angles, group velocities, and acceptance bandwidth are obtained with the program SNLO [37]. These wavelength combinations and the cut angle for the crystals are shown in Table 1 for BBO, lithium niobate ($LiNbO_3$) and lithium iodate ($LiIO_3$) when mixing with 800 or 1025 nm pulses. In addition, the polarization of the individual pulses is given. Infrared pulses from 2 to 5 μm can therewith be generated. The necessary visible pulses range from 600 to 800 nm.

The equal group velocities of visible and infrared pulses result in a very broad acceptance bandwidth and allow transferring a large bandwidth from the visible to the infrared, even for crystal lengths of up to 1 mm. This is illustrated in Fig. 2, which shows typical spectra for visible, laser, and infrared pulses using an 800 μm BBO crystal.

Since the narrowband laser pulses have significantly longer pulse duration, the group velocity mismatch between the laser wavelength and the visible or infrared wavelength is not relevant. The laser light field is present the entire time. Therefore the visible, the infrared and the fundamental laser pulses can interact over the entire crystal length.

The pulse duration of the infrared output directly after the difference frequency generation is nearly transform limited. This is due to the dispersion properties of the mixing crystals. For a better understanding we demonstrate this for Gaussian pulses and an 800 μm BBO as mixing crystal in Fig. 3.

The visible pulses centered at 675 nm have a Fourier limit of 10 fs [38], but they are chirped due to the imperfect compression in the prism compressor and show some residual spectral phase (black dotted line in Fig. 3a). The actual pulse duration is measured to 14 fs. In addition, the propagation in BBO adds spectral phase (orange dashed line in Fig. 3a). After 50 % of propagation in the BBO the pulse length is 17.5 fs. When these chirped visible pulses are difference frequency mixed with narrowband transform-limited laser pulses the resulting infrared pulses centered at 2000 nm will have nearly the same spectral phase (orange dashed line in Fig 3b) [39, 40]. Now an advantageous property of BBO becomes relevant. The zero dispersion wavelength lies between the visible and the

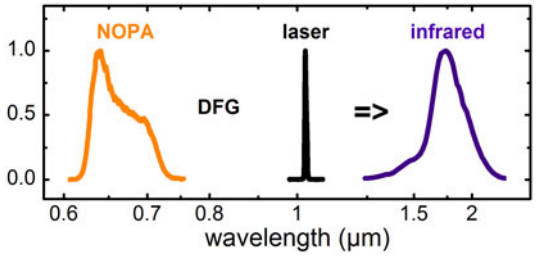

Fig. 2 Broadband visible pulses (*orange*) are difference frequency mixed with the narrowband laser pulses (*black*) resulting in broad band, infrared pulses (*violet*)

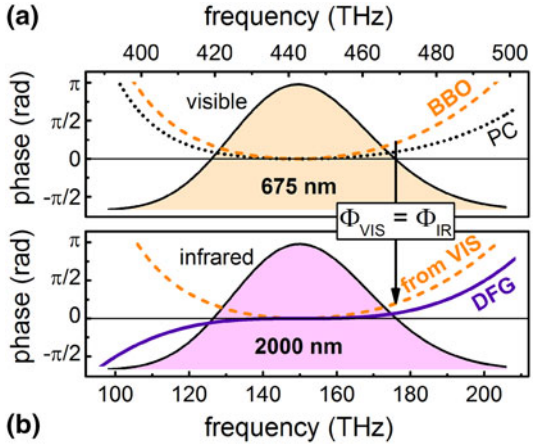

Fig. 3 **a** Spectrum (*light orange*) and spectral phase of visible pulses after the prism compressor (PC) (*black dotted*) and propagation through 400 μm BBO (*orange dashed*); **b** the infrared pulses (*magenta*) inherit the spectral phase of the visible pulses during DFG (*orange dashed*) and self compress due to the remaining propagation in BBO and become nearly transform limited (*violet solid*)

infrared wavelength. This means the infrared pulses are in the anomalous dispersion regime and self-compress during the remaining propagation in BBO, which leads to nearly transform-limited pulses in the infrared (violet line in Fig 3b). The pulse duration of the infrared pulses shown in Fig. 3b is 11.8 fs. Since the infrared pulses are generated over the entire crystal length, we decided to use half of the

crystal lengths as effective propagation lengths for both the visible and the infrared pulses. But also for the other constellations such as earlier or later infrared generation in the crystal the pulses remain short. Note that there is no additional pulse lengthening of the infrared pulses caused by separation between visible and infrared pulses because of the equal group velocities. And since chirped visible pulses are needed for the DFG it is sufficient to work with a simple prism compressor. Even additional chirp from later propagation in crystals, lenses, or entrance windows can be pre-compensated with the visible prism compressor, so that few-cycle pulses arrive at the sample. Residual higher order chirp will only weakly increase the pulse duration beyond the Fourier limit.

Another more fundamental aspect is that the duration of one optical cycle is much longer in the infrared than in the visible. Therefore it is sufficient to generate five to six cycle pulses in the visible for sub-two-cycle pulses in the infrared because only the bandwidth and pulse duration are transferred to the infrared but not the number of cycles. A 13 fs pulse in the visible corresponds to a six cycle pulse, whereas a 13 fs pulse around 2 μm corresponds to a sub-two cycle pulse. This strongly facilitates the generation and compression of the visible pulses. No few-cycle pulses must be generated in the visible and moderate demands are placed on the compression. No further compression with chirped mirrors or gratings or pulse shortening techniques like filamentation must be applied, not in the visible nor in the infrared.

Besides the choice of the material also the crystal length is important in difference frequency generation. Normally the length is a compromise between the efficiency and the attainable bandwidth and limits both. Particularly in an OPA that aims at a large amplification factor a rather long crystal with its reduced acceptance bandwidth is needed. In our case, the immense bandwidth due to negligible group velocity mismatch allows using crystals with lengths up to 1 mm, which is long if compared to mixing crystals for few-cycle visible pulses. This allows an enhanced efficiency. In our case, we transfer up to 22 % of the photons from the visible to the infrared (see section IV). An even longer crystal length will not increase this efficiency significantly due to saturation effects and back conversion which leads to distortion of the infrared beam. In addition, the pulse lengthening becomes more relevant for longer crystals. However, crystal lengths below 1 mm are still short compared to crystals used in amplifier systems and unwanted effects like self-phase modulation, self-focusing, parametric superfluorescence background, crystal damage or pulse lengthening can be avoided. It should also be noted that the NOPA amplifies the nJ level SCG seed into the μJ regime and therefore no further amplification is needed for the broadband NIR generation. If one starts directly in the NIR, the required long crystal for the initial amplification seriously limits the bandwidth which can only be partly compensated by the use of periodically poled crystals [18, 41].

4 Full characterization of infrared few-cycle pulses

To demonstrate the concept we fully characterize sub-two-cycle pulses generated with the Yb:KYW-based system. For this purpose we use 32 μJ pulses at 100 kHz with a pulse duration of 300 fs and a central wavelength of 1025 nm. Five percent are split off for continuum generation in a 4-mm thick YAG plate serving as seed for the visible NOPA [36]. The remaining 95 % are frequency doubled in an 800 μm thick BBO crystal cut at 23.5° with an efficiency of about 30 %. Due to the small beam size of the laser ($1/e^2$ radius of 0.9 mm), focusing is not necessary. Seed and the SHG pump are focused into a 3-mm thick BBO crystal cut at 20° with an external noncollinearity angle of 3.3°. The amplified spectrum is tunable in central wavelength from 650 to 700 nm while maintaining a Fourier limit below 10 fs. Typical pulse energies are around 1.5 μJ per pulse. After collimation with a spherical mirror, the output pulses are compressed to well below 15 fs using a sequence of fused silica prisms with an apex angle of 68.7°. Please note that the time-bandwidth product of 0.66 for the visible pulses is sufficient for short infrared pulses.

The 1025 nm light which is not frequency doubled is rotated in polarization by 90° with a half-wave plate to perform type-I DFG and transmitted through a pair of wedges (10°, BK7) which are used to control the carrier-envelope phase of the infrared output. The laser light (10 μJ) and the compressed NOPA output (1.2 μJ) are then focused into a 0.8-mm thick BBO crystal cut at 23.5° to perform type-I DFG. The beam radii ($1/e^2$ value) were 120 μm for the 1025 nm beam and 90 μm for the NOPA output for ease of alignment and to ensure total overlap. The intensity of the laser pulses was 100 GW/cm^2 and the intensity of the visible pulse was 250 GW/cm^2. To avoid the need for dichroic optics, the two beams are combined under a small angle, which is kept below 1°. The resulting spatial chirp of the infrared pulse is below the divergence of also 1°. The energy of the infrared pulses was 100 nJ. This means that 22 % of the visible photons are transferred to the infrared (100 nJ * 1.8 μm/(1.2 μJ * 680 nm) = 0.22).

A typical 1.8-μm pulse was fully characterized with second-harmonic-generation frequency resolved optical gating (SHG-FROG) [42]. For the retrieval of the spectral phase and the temporal intensity profile the software "FROG 3.0" was used [43]. The spectrum of the sub-two-cycle pulse is shown in Fig. 4a (black line). The spectrum

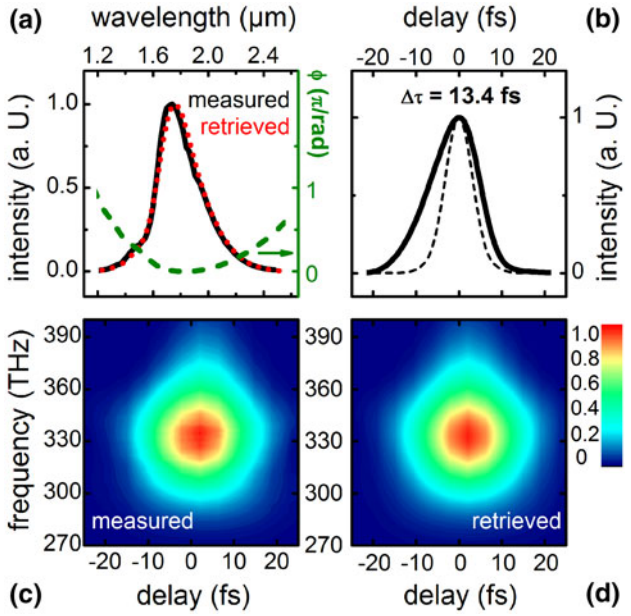

Fig. 4 **a** Measured (*black line*) and retrieved (*red dotted line*) spectrum including spectral phase (*green dashed line*); **b** temporal intensity profile (*black line*) and Fourier limit (*black dashed line*); **c** measured; **d** retrieved FROG traces of a carrier envelope phase stable, sub two cycle infrared pulse

retrieved from the FROG measurement (red dotted line) matches the experimental one perfectly. There is a small remaining spectral phase (green dashed line) that indicates a small amount of residual second and higher order phase. The reconstructed temporal intensity profile (black line in Fig. 4b) renders a pulse duration of 13.4 fs. The slight asymmetry is due to the remaining higher order phase. A time-bandwidth product of 0.55 results that is fairly close to the Fourier limit (dashed line in Fig. 4b). Figure 4c, d show the measured and retrieved FROG traces and their excellent agreement.

Finally, the carrier-envelope phase of the infrared pulses is checked with an f-2f interferometer. In our case, the phase-matching angle for broadband DFG is close to that for frequency doubling of the 1.8 μm pulses. This leads to some frequency doubled light directly from the mixing crystal. This light is extracted with dichroic mirrors and its polarization rotated by 90°. The remaining infrared few-cycle pulses are focused with a microscope objective into a highly nonlinear fiber to broaden their spectrum down to 500 nm. The broadened pulses and the frequency doubled light are then collinearly recombined and temporarily delayed by 400 fs. The resulting stable interference pattern is shown in Fig. 5 and directly shows the carrier-envelope phase stability of the infrared pulses. Only a proper alignment of the continuum generation ensures highest phase stability.

When integrating over 1 ms and acquiring 500 consecutive samples of these "1 ms" spectra, we measure a phase

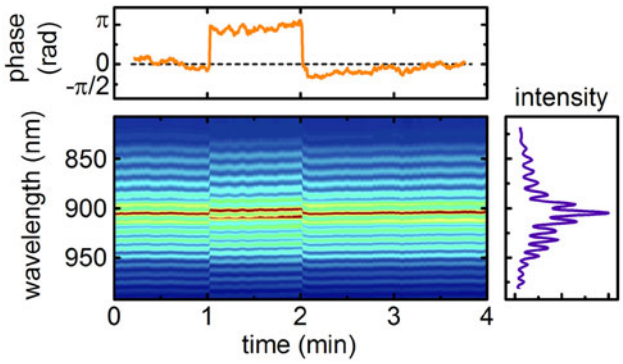

Fig. 5 Interference pattern of an f to 2f interferometer to show carrier envelope phase stability of an infrared sub two cycle pulse over 4 min (with induced phase change after 1 and 2 min)

stability of 80 mrad rms. To check the long time stability we integrated over 100 ms and measured over 5 min. This measurement is shown in Fig. 5. A slight spectral drift of the interference pattern in Fig. 5 can be observed which likely is due to a laser output power drift and intensity-phase coupling [44] and small environmental changes. The two BK7 wedges allow fully controlling the carrier-envelope phase and set the phase to the desired value at the experiment. We induced a carrier-envelope phase change of $+\pi$ after 1 and $-\pi$ after 2 min by moving the two BK7 wedges. The slow drift seen in Fig. 5 is compensated in spectroscopic measurements by actively controlling the two BK7 wedges. For the remaining fluctuations in the bandwidth from 0.1 to 5 Hz we find a residual phase noise of 150 mrad.

For the Ti:sapphire-based system typical NOPA pulses [38] at 600 nm were compressed down to 15 fs and difference frequency mixed with the 775-nm laser light also in an 800 μm thick BBO cut at 20°. Figure 1b shows the generated pulses centered at 3 μm. The energies, beam radii and most importantly the intensities are comparable to the values described for the Yb:KYW-based system above. For Ti:sapphire systems, this concept also works well for few-cycle phase stable pulse generation around 2 μm as was recently demonstrated [34].

5 Summary and outlook

We have presented the generation of carrier-envelope phase stable few-cycle pulses in the infrared. We discussed the relevant theoretical background and simulations that should allow others to adopt the concept to their specific pump laser and needs. The necessary spectral bandwidth is generated in a continuum seeded noncollinear optical parametric amplifier in the visible. This bandwidth can then be transferred to the infrared by broadband difference

frequency generation. This approach avoids broadening techniques in the infrared which can become experimentally challenging. For the common mixing crystals, different wavelength combinations can be found so that the group velocity mismatch between visible and infrared pulses becomes negligible and nearly the full bandwidth of the visible pulses can be transferred to the infrared. Since only a modest pump intensity and a small parametric gain are needed in this second stage, a rather thin crystal without severe limitation of the acceptance bandwidth can be used. For a classical infrared OPA, a much thicker crystal has to be used and spectral gain narrowing likely limits the bandwidth further.

The use of very thin mixing crystals is also most advantageous for the generation of tunable deep UV pulses with 30 fs pulse length [45]. Just as in the present situation of infrared generation, a good efficiency is already assured by the intrinsic high intensity of the femtosecond pulses and does not have to be achieved by a thick crystal. In the present setup, the obtained infrared energies are limited since the visible amplification and the difference frequency generation are nonlinear processes that should not be driven to efficiencies much beyond 20 % to avoid pulse deterioration. The infrared light is, however, ideally suited as seed light for further amplification pumped by the laser fundamental if higher pulse energies are needed. Fortunately for all obtainable infrared wavelengths in Table 1, broadband optical parametric amplification is possible when using BBO, $LiNbO_3$, or $LiIO_3$ and taking the different types of amplification, i.e., choices of polarization directions, into account [8, 35].

The infrared pulses are already compressed in the mixing crystal due to the anomalous dispersion and any chirp further downstream can be well compensated with the prism compressor for the visible pulses. No further compression in the infrared must be applied and few-cycle pulses with a stable and controllable carrier-envelope phase are directly available after the difference frequency generation. The residual phase drifts are slow enough that they can be actively compensated. It is sufficient to generate and compress only several cycle pulses in the visible, because difference frequency generation inherits the short visible pulse duration and due to the longer wavelengths this results in few-cycle pulses in the infrared. Since the visible and laser pulses have a constant phase relationship the infrared pulses have a stable carrier-envelope phase independently from the phase fluctuation of the laser. This is all obtained in a comparatively simple setup which is easily aligned and passively stable. It only consists of continuum generation, a noncollinear amplifier, a prism compressor, and a final difference frequency generation stage. All participating pulses are in the range accessible by bare eye or viewer cards, except the very final output.

This easily manageable setup is a highly attractive source for numerous applications in the infrared wavelength region such as electron emission from metal tips [11, 46], as seed source for high power applications or in advanced amplifier chains [34, 35]. For some infrared mixing crystals two-photon absorption of the NOPA input has to be taken into account. Since we limit the input intensity as far as possible, this usually is not a serious concern. Another important point is that this setup is suited for a wide range of laser systems. The most critical point might be thought to be the continuum generation. We were, however, able to recently demonstrate that bulk continuum generation is possible up to at least a pulse duration of 1 ps and only requires energies in the μJ regime. Therefore, we are sure that the presented concept works well for even longer pulse duration, high repetition rates, and different wavelengths.

Acknowledgments We thank the group of P. Hommelhoff for access to their laser system and supplying us with experimental equipment, and the DFG Cluster of Excellence: Munich Centre for Advanced Photonics for financial support.

References

1. R.A. Kaindl, M. Wurm, K. Reimann, P. Hamm, A.M. Weiner, M. Woerner, J. Opt. Soc. Am. B **17**, 2086 (2000)
2. G. Cirmi, D. Brida, C. Manzoni, M. Marangoni, S. De Silvestri, G. Cerullo, Opt. Lett. **32**, 2396 (2007)
3. G. Cirmi, C. Manzoni, D. Brida, S. De Silvestri, G. Cerullo, J. Opt. Soc. Am. B **25**, B62 (2008)
4. D. Brida, M. Marangoni, C. Manzoni, S. De Silvestri, G. Cerullo, Opt. Lett. **32**, 2901 (2008)
5. D. Brida, G. Cirmi, C. Manzoni, S. Bonora, P. Villoresi, S. De Silvestri, G. Cerullo, Opt. Lett. **33**, 741 (2008)
6. J. Moses, S. W. Huang, K. H. Hong, O.D. Muecke, E.L. Falcao Filho, A. Benedick, F.Ö. Ilday, A. Dergachev, J.A. Bolger, B.J. Eggleton, F.X. Kärtner, Opt. Lett. **34**, 1639 (2009)
7. D. Brida, C. Manzoni, G. Cirmi, M. Marangoni, S. Bonora, P. Villoresi, S. De Silvestri, G. Cerullo, J. Opt. **12**, 013001 (2010)
8. M. Bradler, C. Homann, E. Riedle, Opt. Lett. **36**, 4212 (2011)
9. K. H. Hong, S. W. Huang, J. Moses, X. Fu, C. J. Lai, G. Cirmi, A. Sell, E. Granados, P. Keathley, F.X. Kärtner, Opt. Express **19**, 15538 (2011)
10. C. Li, D. Wang, L. Song, J. Liu, P. Liu, C. Xu, Y. Leng, R. Li, Z. Xu, Opt. Express **19**, 6783 (2011)
11. C. Homann, M. Bradler, M. Förster, P. Hommelhoff, E. Riedle, Opt. Lett. **37**, 1673 (2012)
12. F. Silva, P.K. Bates, A. Esteban Martin, M. Ebrahim Zadeh, J. Biegert, Opt. Lett. **37**, 933 (2012)
13. T. Fuji, N. Ishii, C.Y. Teisset, X. Gu, Th Metzger, A. Baltuska, N. Forget, D. Kaplan, A. Galvanauskas, F. Krausz, Opt. Lett. **31**, 1103 (2006)
14. X. Gu, G. Marcus, Y. Deng, T. Metzger, C. Teisset, N. Ishii, T. Fuji, A. Baltuska, R. Butkus, V. Pervak, H. Ishizuki, T. Taira, T. Kobayashi, R. Kienberger, F. Krausz, Opt. Express **17**, 62 (2009)
15. O. Chalus, P.K. Bates, M. Smolarski, J. Biegert, Opt. Express **17**, 3587 (2009)
16. O. Chalus, A. Thai, P.K. Bates, J. Biegert, Opt. Lett. **35**, 3204 (2010)

17. G. Andriukaitis, T. Balciunas, S. Alisauskas, A. Pugzlys, A. Baltuska, T. Popmintchev, M. C. Chen, M.M. Murnane, H.C. Kapteyn, Opt. Lett. **32**, 2755 (2011)
18. A. Thai, M. Hemmer, P.K. Bates, O. Chalus, J. Biegert, Opt. Lett. **36**, 3918 (2011)
19. J. Biegert, P.K. Bates, O. Chalus, IEEE J. Sel. Top. Quantum Electron **18**, 531 (2012)
20. G. Cerullo, A. Baltuska, O.D. Muecke, C. Vozzi, Laser Photon. Rev. **5**, 323 (2011)
21. C. Manzoni, C. Vozzi, E. Benedetti, G. Sansone, S. Stagira, O. Svelto, S. De Silvestri, M. Nisoli, G. Cerullo, Opt. Lett. **31**, 963 (2006)
22. C. Vozzi, G. Cirmi, C. Manzoni, E. Benedetti, F. Calegari, G. Sansone, S. Stagira, O. Svelto, S. De Silvestri, M. Nisoli, G. Cerullo, Opt. Express **14**, 10109 (2006)
23. C. Vozzi, F. Calegari, E. Benedetti, S. Gasilov, G. Sansone, G. Cerullo, M. Nisoli, S. De Silvestri, S. Stagira, Opt. Lett. **32**, 2957 (2007)
24. C.I. Blaga, K.D. Schultz, J. Cryan, R. Chirla, P. Colosimo, G. Doumy, A.M. March, C. Roedig, E. Sistrunk, J. Tate, J. Wheeler, L.F. DiMauro, Opt. Lett. **32**, 868 (2007)
25. O.D. Mücke, S. Alisauskas, A.J. Verhoef, A. Pugzlys, A. Baltuska, V. Smilgevicius, J. Pocius, L. Giniunas, R. Danielius, N. Forget Opt. Lett. **34**, 2498 (2009)
26. M. Giguere, B.E. Schmidt, A.D. Shiner, M. A. Houle, H.C. Bandulet, G. Tempea, D.M. Villeneuve, J. C. Kieffer, F. Legare, Opt. Lett. **34**, 1894 (2009)
27. B.E. Schmidt, P. Bejot, M. Giguere, A.D. Shiner, C. Trallero Herrero, E. Bisson, J. Kasparian, J. P. Wolf, D.M. Villeneuve, J. C. Kieffer, P.B. Corkum, F. Legare, Appl. Phys. Lett. **96**, 121109 (2010)
28. B.E. Schmidt, A.D. Shiner, P. Lassonde, J.C. Kieffer, P.B. Corkum, D.M. Villeneuve, F. Legare, Opt. Express **19**, 6858 (2011)
29. C. Heese, L. Gallmann, U. Keller, C.R. Phillips, M.M. Fejer, Opt. Lett. **35**, 2340 (2010)
30. C. Manzoni, G. Cerullo, S. De Silvestri, Opt. Lett. **29**, 2668 (2004)
31. E.A. Anashkina, A.V. Andrianov, S.V. Muravyev, A.V. Kim, Opt. Express **19**, 20141 (2011)
32. S. Thomas, R. Holzwarth, P. Hommelhoff, Opt. Express **20**, 13663 (2012)
33. Y. Nomura, H. Shirai, K. Ishii, N. Tsurumachi, A. Voronin, A. Zheltikov, T. Fuji, Opt. Express **20**, 24741 (2012)
34. J. Darginavicius, N. Garejev, A. Dubietis, Opt. Lett. **37**, 4805 (2012)
35. J. Darginavicius, G. Tamosauskas, A. Piskarskas, G. Valiulis, A. Dubietis, Appl. Phys. B **108**, 1 (2012)
36. M. Bradler, P. Baum, E. Riedle, Appl. Phys. B **97**, 561 (2009)
37. SNLO nonlinear optics code, available from A.V. Smith, AS Photonics, Albuquerque, NM, (2013), "http://www.as photonics.com" and references given therein to the crystal properties
38. E. Riedle, M. Beutter, S. Lochbrunner, J. Piel, S. Schenkl, S. Spörlein, W. Zinth, Appl. Phys. B **71**, 457 (2013)
39. C. Schriever, S. Lochbrunner, E. Riedle, Opt. Lett. **31**, 543 (2006)
40. I. Walmsley, L. Waxer, C. Dorrer, Rev. Sci. Instrum. **72**, 1 (2001)
41. O. Chalus, P.K. Bates, J. Biegert, Opt. Express **16**, 21297 (2008)
42. R. Trebino, K.W. De Long, D.N. Fittinghoff, J.N. Sweetser, M.A. Krumbügel, B.A. Richman, D.J. Kane, Rev. Sci. Instrum. **68**, 3277 (1997)
43. R. Trebino, "FROG 3.0", Femtosoft Technologies, (1999). http://www.femtosoft.biz/frog/frog.php
44. P. Baum, S. Lochbrunner, J. Piel, E. Riedle, Opt. Lett. **28**, 185 (2003)
45. C. Homann, P. Lang, E. Riedle, J. Opt. Soc. Am. B **29**, 2765 (2012)
46. M. Krüger, M. Schenk, P. Hommelhoff, Nature **78**, 475 (2011)

Appendix A12

Ultrafast Dynamics of meso-Tetraphenylmetalloporphyrins: The Role of Dark States

Y. Liang, M. Bradler, M. Klinger, O. Schalk, M. C. Balaban, T. S. Balaban, E. Riedle, and A. N. Unterreiner

Chem. Plus. Chem. **78**, 1244 - 1251 (2013)

Reprinted with kind permission from John Wiley and Sons Publishing

DOI: 10.1002/cplu.201300143

Ultrafast Dynamics of *meso*-Tetraphenylmetalloporphyrins: The Role of Dark States

Yu Liang,[a] Maximilian Bradler,[b] Melanie Klinger,[a] Oliver Schalk,[b, c] Mihaela Carmen Balaban,[d, e] Teodor Silviu Balaban,[d, e] Eberhard Riedle,[b] and Andreas-Neil Unterreiner*[a]

Studying the relaxation pathways of porphyrins and related structures upon light absorption is crucial to understand the fundamental processes of light harvesting in biosystems and many applications. Herein, we show by means of transient absorption studies, following Q- and Soret-band excitation, and ab initio calculations on *meso*-tetraphenylporphyrinato magnesium(II) (MgTPP) and *meso*-tetraphenylporphyrinato cadmium(II) (CdTPP) that electronic relaxation following Soret-band excitation of porphyrins with a heavy central atom is mediated by a hitherto disregarded dark state. This accounts for an increased rate of internal conversion. The dark state originates from an orbital localized at the central nitrogen atoms and its energy continuously decreases along the series from magnesium to zinc to cadmium to below 2.75 eV for CdTPP dissolved in tetrahydrofuran. Furthermore, we are able to directly trace fast intersystem crossing in the cadmium derivative, which takes place within (110 ± 20) ps.

Introduction

Cyclic tetrapyrroles and their derivatives are ubiquitous natural pigments and play an important role in nature. For example, hemoglobin in heme proteins is responsible for oxygen transport in blood, whereas chlorophyll in plant cells is part of the light-harvesting system that regulates photosynthesis. Its functionality can be tuned by several factors, such as the C N skeleton, which can be saturated to a certain degree; the surroundings, for example, a protein environment; and the central metal atom. In recent years, porphyrin derivatives were investigated for different purposes, such as light-harvesting complexes in solar cells,[1] photodynamic therapy in medicine,[2] and electronic devices.[3] Consequently, there is much interest in the optical properties and photophysical behavior of porphyrins.[4–7] To better understand these properties, model systems such as metal *meso*-tetraphenylporphyrins (MTPP, M = Mg, Cd) were chosen for investigation.[8]

A simplified molecular structure is presented in Figure 1. Its symmetry is supposed to be close to D_{4h}. However, in the minimum energy geometry, the four peripheral phenyl rings are known to be twisted by 65–70° with respect to the porphyrin skeleton;[10–13] this lowers the symmetry to C_{2v}. In coordinating solvents, magnesium atoms in chlorophylls or porphyrins become five- or even sixfold coordinated, which reduces the symmetry further. The electronic structure of porphyrins in the free-base or metal-coordinated forms is largely characterized by their absorption and fluorescence spectra.[14–18] For metals with closed d shells, the absorption spectra consist of an intense band at $\lambda \approx 420$ nm in the blue/ultraviolet spectral region (characteristic of the Soret band, also called the B band) with a blueshifted shoulder assigned to another close-lying

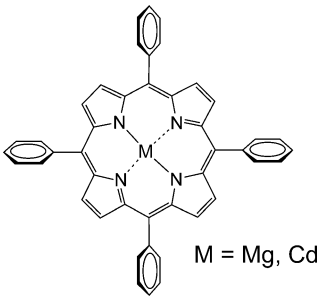

Figure 1. Molecular structure of *meso* tetraphenylporphyrinato metal(II) complexes. In addition to the four fold coordinated species implied, M·THF and THF·M·THF can also be present.[9]

[a] Dr. Y. Liang, Dr. M. Klinger, Dr. A. N. Unterreiner
Institute for Physical Chemistry and Center for Functional Nanostructures
Karlsruhe Institute of Technology (KIT)
Fritz Haber Weg 2, 76131 Karlsruhe (Germany)
E mail: andreas.unterreiner@kit.edu

[b] M. Bradler, Dr. O. Schalk, Prof. Dr. E. Riedle
Lehrstuhl für BioMolekulare Optik
Ludwig Maximilians Universität
Oettingenstraße 67, 80538 München (Germany)

[c] Dr. O. Schalk
Stockholm University, AlbaNova University Center
Roslagstullsbacken 21, 106 91 Stockholm (Sweden)

[d] M. C. Balaban, Prof. Dr. T. S. Balaban
Institute for Nanotechnology and Center for Functional Nanostructures
Karlsruhe Institute of Technology (KIT) (Germany)

[e] M. C. Balaban, Prof. Dr. T. S. Balaban
Present address:
Aix Marseille Université, CNRS, iSm2 UMR 7313
13397 Marseille (France)

Supporting information for this article is available on the WWW under http://dx.doi.org/10.1002/cplu.201300143.

WILEY ONLINE LIBRARY © 2013 Wiley-VCH Verlag GmbH & Co. KGaA, Weinheim

state.[19] Two weaker absorption maxima in the visible region between $\lambda = 550$ and 650 nm are assigned to the Q bands. The next higher-lying state in MgTPP is at $\lambda \approx 360$ nm. The fifth and more prominent absorption band lies at $\lambda \approx 320$ nm and is called the N band.[20] All of these bands have E_u symmetry and are assigned to $\pi\pi^*$ transitions. These can be qualitatively explained by means of the well-established Gouterman four-orbital model[21–23] or, more convincingly, by the molecular orbital (MO) interpretation of Baerends et al.[24] In the context of this paper, this interpretation is sufficient. However, higher states are better described by more advanced models, for example, those from Solheim et al.[25] or Peralta et al.[26] In the MO interpretation, the electronic structure is explained by the interaction of the four pyrrole rings ($(Py)_4^{2-}$ cage) with CH methine bridges. For a metalloporphyrin, this leads to several e_g orbitals and non-degenerate ungerade states. The Q and Soret bands arise from excitation between the two highest occupied orbitals, which have a_{1u} and a_{2u} symmetry and a pair of e_g orbitals (LUMO). The higher $\pi\pi^*$ transitions in the UV region are mainly from lower lying ungerade states to the LUMO. The fluorescence spectrum exhibits a small Stokes shift. In addition to emission from the Q band, one also observes fluorescence from the Soret band.[27,28]

Photophysical properties of many diamagnetic metalloporphyrin derivatives, such as ZnTPP, MgTPP and CdTPP (TPP = tetraphenylporphyrinato), have been studied after excitation to the Soret band. Fluorescence up-conversion experiments of Zewail and co-workers showed that, for ZnTPP in benzene, the fluorescence lifetime of the Soret band was measurably longer than the rise time of the Q-band fluorescence and was interpreted by the presence of an additional state close to the Soret band.[29] These findings could not be confirmed by other groups;[28,30–34] however, a small fraction of excited ZnTPP molecules was found to bypass the Q band.[4,35] In MgTPP, the efficiency of S_2–S_1 relaxation was close to unity, whereas it is decreased to 70% in CdTPP.[30] As possible explanations for this behavior, reaction paths through dark gerade states and the triplet-manifold[30–33,35–37] were proposed. Evidence for the existence of dark states has been given by time-dependent (TD) DFT calculations[38–41] and by direct access upon Q-band excitation and near-infrared (NIR) probe in tetratolyl derivatives (*meso*-tetra-*para*-tolyl-*21H,23H*-porphyrin (TTP-H_2) and ZnTTP).[42] Most recently, Hopkins and co-workers examined the transient absorption spectra of ZnTPP in the NIR region.[43] They assigned the NIR bands to transitions from the Q band to gerade-symmetry dark states. The role these states might play in the relaxation pathway of (metallo)porphyrins upon Soret excitation necessitates additional information about their origin, for example, from a complete set of experimental data in the series 2H, Mg, Zn, Cd. Hence, we studied transient absorption of MgTPP and CdTPP dissolved in tetrahydrofuran (THF) upon excitation to the Q and the Soret band and scanned the probe wavelength with various white lights covering the region between $\lambda = 290$ and 1660 nm. These experiments allowed dark states to be located up to the N band and also a comparison of transient spectra upon Q and Soret band excitation; thus it is possible to decipher pathways the molecule may take upon Soret excitation. Additionally, TDDFT calculations were performed on several TPP derivatives. Based upon experimental findings and calculations, a model for the relaxation pathway of these molecules upon Soret excitation is presented and sheds light on apparent inconsistencies presented in the literature to date.

Results and Discussion

Steady-state absorption and emission spectra

Steady-state absorption and emission spectra of MgTPP and CdTPP in THF are shown in Figure 2. In the absorption spectrum, the maxima of the Soret bands ($2E_u$ symmetry) were found at $\lambda = 429$ nm (2.89 eV) for MgTPP and $\lambda = 431$ nm (2.87 eV) for CdTPP with a small shoulder on their blue sides at

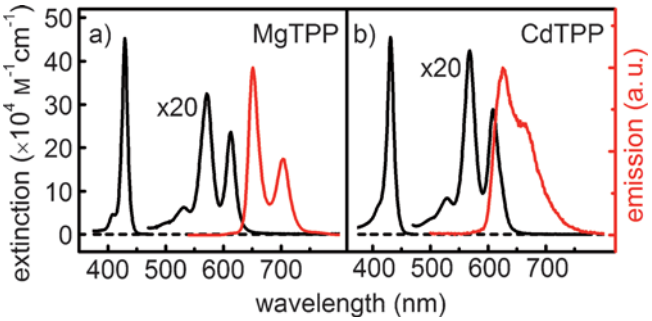

Figure 2. Steady state absorption and emission spectra of (a) MgTPP and (b) CdTPP in THF at room temperature; emission spectra were excited at $\lambda = 431$ nm for CdTPP and $\lambda = 429$ nm for MgTPP.

$\lambda = 409$ nm (3.03 eV) for MgTPP and $\lambda = 411$ nm (3.02 eV) for CdTPP. These shoulders are assigned to the higher lying $3E_u$ state. The peaks of the Q band ($1E_u$ symmetry) were observed at $\lambda = 613$ (610) nm for the Q(0,0) band and $\lambda = 571$ (569) nm for the Q(1,0) band, along with a smaller shoulder at 530 (529) nm for MgTPP (CdTPP). The Q-band absorptions can be understood in terms of vibrational progressions with an energy splitting of about 1170 cm^{-1}.[44] The $S_1 \rightarrow S_0$ emission spectra of both porphyrins are mirror images of the corresponding absorption spectrum. The emission band originating from the first excited state Q(0,0) has a maximum at $\lambda = 617$ nm for MgTPP and $\lambda = 626$ nm for CdTPP. The second, weaker band corresponding to the Q(1,0) transition was observed at $\lambda = 671$ nm for MgTPP and $\lambda = 665$ nm for CdTPP. The emission spectra show Stokes shifts of roughly 120 cm^{-1} for MgTPP and 434 cm^{-1} for CdTPP. The fluorescence yield of CdTPP is much lower than that of MgTPP; this was attributed to fast intersystem crossing (ISC) in CdTPP in previous experiments.[45]

TDDFT calculations

To study the absorption spectrum of the one-color forbidden gerade states, we performed TDDFT calculations on MgTPP and CdTPP using the GAMESS package[46,47] and compared

© 2013 Wiley-VCH Verlag GmbH & Co. KGaA, Weinheim

Table 1. Electronic energy levels [eV] of MgTPP, ZnTPP, CdTPP, and TPP H_2, as calculated with different DFT functionals in the 6 31G* basis set. Geometries were calculated at the B3LYP/6 31G* level with C_{2v} symmetry.

	MgTPP				ZnTPP				CdTPP				TPP H_2			
	B3LYP	BP86	M05 2X	OPBE	B3LYP	BP86	M05 2X	OPBE	B3LYP	BP86	M05 2X	OPBE	B3LYP	BP86	M05 2X	OPBE
Q state	2.232	2.1	2.299	2.112	2.293	2.14	2.364	2.155	2.278	2.082	2.4	2.116	2.136	2.081	2.17	2.034
													2.281	2.136	2.381	2.153
B state	3.225	3.018	3.416	3.04	3.337	3.055	3.456	3.078	3.312	3.07	3.493	3.095	3.146	3.095	3.382	3.121
													3.265	3.133	3.462	3.158
3^1E_u state	3.625	3.08	4.28	3.116	3.688	3.151	4.225	3.18	3.668	3.134	4.36	3.163				
3^1B_{2u} state													3.553	2.855	4.111	2.872
3^1B_{3u} state													3.563	2.898	4.395	2.913
1 "$e_g \otimes e_g$"	3.617	3.122	4.198	3.146	3.61	3.112	4.194	3.139	3.533	3.047	4.133	3.076	3.74	3.126	4.665	3.154
2 "$e_g \otimes e_g$"	3.666	3.13	4.249	3.129	3.656	3.142	4.261	3.169	3.576	3.07	4.202	3.099	3.867	3.255	4.537	3.264
$d_{x^2\ y^2}$ state	4.471	4.452	4.489	4.447	3.169	2.398		2.492	2.969	2.332	3.86	2.4	3.306	2.842	3.849	2.853
													3.475	2.879	4.307	2.889

them with ZnTPP, TPP-H_2, and MgP (magnesium porphyrin without any substituents).[24,38] Ground-state geometries were calculated at the B3LYP/6-31G* level under the restriction of both D_{4h} and C_{2v} symmetry. Symmetry labels are given based on D_{4h} (D_{2d} in the case of TPP-H_2) in agreement with Solheim et al.[25] Singlet excitation energies for C_{2v} symmetry were calculated at the B3LYP/6-31G* level and compared with various functionals (BP86, OPBE, and M05-2X) using the same basis set. B3LYP results and a comparison of the different methods are shown in Table 1, and geometries are given in the Supporting Information.

There is a long history of interpreting the excited states of porphyrins (see the Introduction). Herein, we use the MO interpretation of Baerends et al.[24] to address a few points: Comparing MgP and MgTPP, one important feature is the energetic difference between equivalent states (about 0.15–0.3 eV). The phenyl group at the methine bridge of MgTPP allows slightly better stabilization than the C H bond of MgP, which is governed partly by the hyperconjugation effect caused by tilting of the phenyl group; thus reducing the interaction between the bridges and the $(Py)_4^{2-}$ cage. This lowers the $5e_g$ state and raises the $4e_g$ state. As a consequence, the gap between the (nearly) unaffected $4a_{2u}$ and $1a_{1u}$ states (HOMO and HOMO 1, the orbital numbering is adopted from MgP) and the $5e_g$ state (LUMO) decreases, leading to a redshift in the absorption spectrum. The differences in the theoretical values for the Q and Soret band ($1E_u$ and $2E_u$) between MgP and MgTPP of 0.16 and 0.28 V, respectively, are in good agreement with the experimental values of 0.11 and 0.23 eV, respectively (see Ref. [48] for a discussion of the spectrum of MgP). The excited states of the TPP derivatives investigated are not very sensitive with respect to the central metal ion (Mg, Zn, and Cd): they all have no open d shells, the same charge, and similar radii, although Cd^{2+} is about 20 pm larger[49] and even small changes in the radius might lead to serious distortions of the ring (see below). The excited-state manifold consists of a set of E_u states that represent the visible absorption spectrum and a variety of different gerade states. The E_u states of the B3LYP calculations are approximately 0.2 eV higher in energy than the experimental values, but seem to be better represented by both the BP86 and OPBE-functionals (see Ref. [50] for cold gas-phase spectra of ZnTPP and TPP-H_2 in He). The description of the gerade states turns out to be more challenging. These consist of 4 states, following an $e_g \rightarrow e_g$ excitation between 3.6 and 3.9 eV (B3LYP) that cannot be assigned to a certain symmetry, because $e_g \otimes e_g = a_{1g} \otimes a_{2g} \otimes b_{1g} \otimes b_{2g}$ (a_1 and a_2 have C_{2v} symmetry) and a B_{2g} state following HOMO to LUMO+1 excitation at around 4.0 eV. The $e_g \rightarrow e_g$ states are significantly reduced by 0.5 eV in energy when using BP86 and OPBE, which brings them close to the Soret excitation. The crucial difference between the molecules with different central metal atoms, however, is an E_g state that results from excitation from a b_{1g} orbital to the LUMO. This orbital is localized at the central nitrogen atoms of the porphyrin skeleton and interacts with an unoccupied $d_{x^2-y^2}$ orbital at the central metal (see Figure S1 in the Supporting Information). In MgTPP, the d manifolds are empty and at B3LYP/6-31G* level the state is located at 4.46 eV, which is on the blue side of the Soret band. In ZnTPP, however, the orbital becomes significantly destabilized owing to interaction of the larger $4d_{x^2-y^2}$ orbital, compared with the $3d_{x^2-y^2}$ orbital in MgTPP, which causes poorer overlap with the N cage. This lowers the gap to the LUMO and reduces the excitation energy to 3.17 eV, which places this state between the Q and Soret bands. This effect is even more pronounced in CdTPP, in which the excitation energy drops to 2.96 eV concomitantly with an increase in the ion radius (see Table 1). The energy of the state significantly varies with the functional. For BP86 and OPBE, it is placed only 0.3–0.35 eV above the Q band for CdTPP and ZnTPP. A comparison of these results with experimental results and a comment on the applicability of DFT for calculations of this type is given in the next section. The most significant difference between the metalated porphyrins and TPP-H_2 is the reduction of the symmetry to D_{2h}. This reduction leads to a splitting not only of the Q band (Q_x and Q_y), but also of the E_g transition centered at the nitrogen atoms. The latter state turns into B_{1g} and A_g states, which are separated by 0.2 eV.

Transients of MgTPP

To discuss the role of the dark states and the existence of the "unknown channel" in CdTPP, we first address the features of

© 2013 Wiley-VCH Verlag GmbH & Co. KGaA, Weinheim

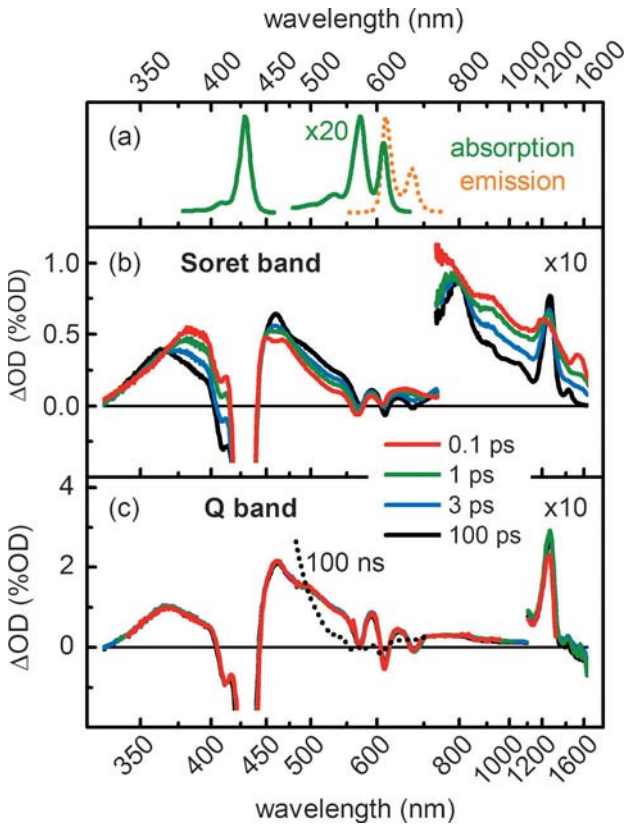

Figure 3. a) Absorption and emission spectra of MgTPP, (b) transient spectra after excitation of the Soret band at $\lambda = 425$ nm, and (c) transient spectra after excitation of the Q band at $\lambda = 620$ nm. For clarity, the early time spec tra in (c) are clipped in the display to indicate that all four show spectra are identical within experimental precision.

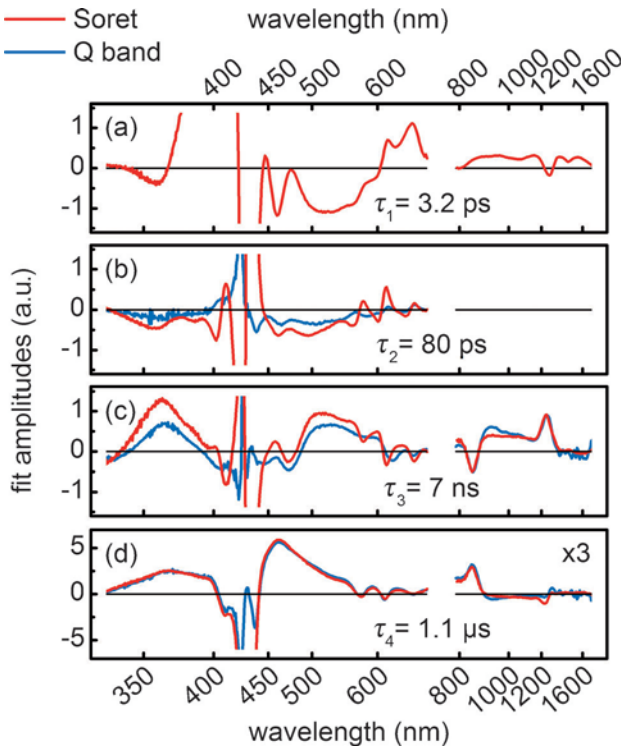

Figure 4. DADS for MgTPP upon excitation of the Q(0,0) (blue) and Soret (red) bands.

the transient spectra of MgTPP, which act as a reference, but are interesting in themselves. Transient spectra at delay times of 0.1, 1, 3, and 100 ps, ranging between $\lambda = 320$ and 1700 nm, are shown in Figure 3 for excitation to the Soret band at $\lambda = 425$ nm (Figure 3 b) and excitation to the Q band at $\lambda = 620$ nm (Figure 3 c). The data can be fitted with a global fitting routine to a sum of exponential functions, as given by Equation (1):

$$S_i(t,\lambda) = \sum\nolimits_i a_i(\lambda) \exp\left(\frac{t}{\tau_i}\right) \otimes g(t,\lambda) \qquad (1)$$

in which τ_i are the exponential decay constants, $\alpha_i(\lambda)$ are the decay-associated difference spectra (DADS), and $g(t,\lambda)$ is the experimental response function, including the chirp (see Ref. [51]). The DADS for MgTPP are shown in Figure 4 and consist of three (four) components for Q-band (Soret-band) excitation. The spectra predominantly exhibit excited-state absorption (ESA) with contributions from ground-state bleaching (GSB) in the Soret- and Q-band regions and stimulated emission (SE) in the region between $\lambda = 600$ and 700 nm. Upon Soret excitation, the appearance of the SE band is delayed by $\tau_1 = 3.2$ ps, so we can assign the first time constant to internal conversion from the Soret to the Q band, in agreement with previous reports.[30,35] The third component of 7 ns was obtained with our ns-setup, with which we only probed the visible region, and which can be assigned to ISC,[45] while recovery of the ground state takes place within more than 1 μs. For the last two time constants, the DADS are almost identical and signify that relaxation from the Soret to Q band upon excitation at $\lambda = 425$ nm takes place with (almost) unity quantum yield; this is in agreement with analysis from the Steer group.[30] The second time constant cannot unambiguously be assigned to an electronic relaxation and its amplitude is largest in the vicinity of strong modulations of the transient spectrum, that is, close to the regions where GSB and SE can be observed. This is an indication that we observe a shift of the bands which would represent a vibrational relaxation of the molecules. This can be confirmed when analyzing the shift of the band maxima. An exemplary shift of the Q(1,0) GSB for Q- and Soret-band excitation and details of the analysis is given in Figure S2 in the Supporting Information. These shifts confirm that cooling of porphyrins is a complex process, which takes place on at least two timescales (1–3 ps and >10 ps). Hence, the time constant obtained by the global fitting routine probably has no significant meaning. Accordingly, Brixner and co-workers[34] assigned a time interval ranging between 10 and 100 ps to vibrational relaxation of the Q band of ZnTPP in ethanol.

The spectral shape of the ESA signal is the test case to judge the dynamics of MgTPP. The dominant band in the IR (after relaxation to the Q band) region has a maximum at $\lambda \approx 1280$ nm (0.97 eV), and a minor maximum can be found at $\lambda \approx 1430$ nm (0.86 eV). When summing up the energies from the Q(0,0) band (2.02 eV) and the ESA maxima, one realizes

© 2013 Wiley-VCH Verlag GmbH & Co. KGaA, Weinheim

that the total energy for the major peak is 2.99 eV, which is exactly the excitation energy of the $3E_u$ band, whereas the energy of the side peak (2.88 eV) corresponds to the energy of the Soret band (see also Figure S3). Because it is known that there are no dark gerade states below the Soret band in MgTPP (see the TDDFT calculations section), this essentially shows that the oscillator strength between the Q and Soret bands is significantly decreased with respect to the $3E_u$ band. On the other hand, ESA on the blue side of the $3E_u$ band is relatively structureless, which is in agreement with the UV/Vis spectrum that also has no marked maximum on the blue side of the Soret/$3E_u$ band. In conclusion, there is no evidence for ESA to a gerade state in the MgTPP data. The similarities of a strong ESA signal between $\lambda = 1250$ and 1300 nm in MgTPP, ZnTPP, and CdTPP furthermore show that these bands cannot be addressed to a dark state in the other porphyrins, in contrast to the analysis of Hopkins et al. who only considered zinc–porphyrins.[43] As a final result, according to the literature values,[52] we state that the triplet splitting (T_1 and T_3) in MgTPP is 1.44 eV ($\lambda = 860$ nm), as shown by the DADS in Figure 4 and the complete transient spectra in Figure S4 in the Supporting Information.

Transients of CdTPP

Transient spectra of CdTPP following excitation at $\lambda = 425$ (Soret band) and 620 nm (Q band) are shown in Figure 5 and their DADS are presented in Figure 6 together with the DADS from the data following excitation of the Q(1,0) band at $\lambda = 569$ nm. The spectra bear some resemblance to the spectra of MgTPP. The GSB and SE structure in the regions of the Soret- and the Q-band excitations show similar behavior and the ESA structures are alike. As expected, there are a few well-known deviations: Opposite to MgTPP, the Q band is reached within 230 fs upon Soret excitation and ISC proceeds within 120 ps instead of 7 ns, which is mainly caused by the strong spin-orbit coupling (heavy-atom effect)[45] of the central cadmium atom. These findings agree nicely with results in the literature.[30] In the following, we discuss 1) the dynamics upon Soret excitation and compare them with the findings in MgTPP and 2) the spectrum of the gerade states of CdTPP.

In a previous study, the energy gap law was taken as an indication that part of the population (30%) generated by Soret-band excitation was bypassing the Q band.[30] There are several alternative pathways available: 1) depopulation directly to the ground state, 2) ISC from the Soret band to the triplet manifold, and 3) internal conversion to the "dark" $1E_g$ state. However, inspection of the DADS for excitation to the Q and Soret bands reveals that the spectra are identical within two percent, in addition to the existence of the 230 fs component in the case of Soret excitation. Moreover, no spectral features appear in the transient spectrum between $\lambda = 290$ and 1660 nm, which could be caused by probing either the triplet state or the $1E_u$ state. In addition, the dynamics cannot be caused by direct repopulation of the ground state because this should be seen in the GSB spectrum at $\lambda = 569$ nm. Bleaching, however, does not seem to change significantly within the first few ps.

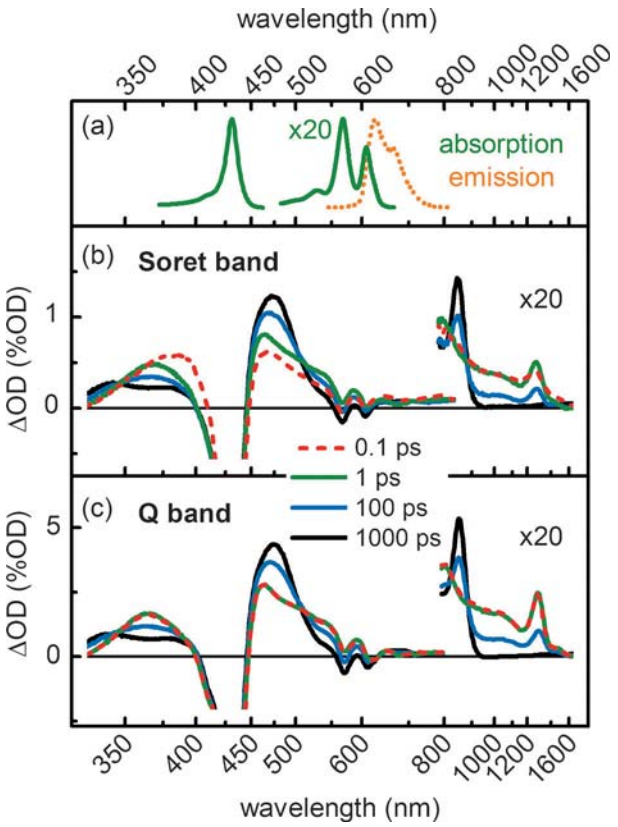

Figure 5. a) Absorption and emission spectra of CdTPP, (b) transient spectra after excitation of the Soret band at $\lambda = 425$ nm, and (c) transient spectra after excitation of the Q band at $\lambda = 620$ nm. For clarity, the 0.1 ps spectrum is indicated by a dashed line to signal that it is identical to the 1 ps spec trum after Q band excitation within experimental precision and different for Soret band excitation.

Hence, the only remaining explanation of the spectra is quantitative (100±2)% population of the Q band within 230 fs. Because direct internal conversion would be in disagreement with the energy gap law applied in the work of Steer and coworkers,[30] it is likely that internal conversion between the Soret and Q bands is mediated by a close-lying state. If this is the case, the only candidate would be the dark E_g state (see below).

To confirm the existence of this E_g state, we first analyzed the spectral structure of the dynamics upon Q-band excitation of CdTPP. As explained above, the ESA spectrum of MgTPP upon probing the Q band was dominated by features caused by u to u transitions and the close similarity of the spectra taken from MgTPP and CdTPP indicate that the contributions from gerade states are minor. As in MgTPP, a strong band at $\lambda \approx 1280$ nm shows access of the $3E_u$ state and the peak at $\lambda \approx 1450$ nm indicates the Soret band. Because no state was found in the transient spectrum up to $\lambda = 1660$ nm, we performed single-color non-collinear optical parametric amplifier–optical parametric amplifier (NOPA-OPA) experiments with probe wavelengths up to $\lambda = 1750$ nm (see Figure 7). For probe wavelengths of $\lambda = 1280$ and 1500 nm, the recorded transients agree with the respective slices from our transient spectra. For $\lambda = 1660$ nm, the spectrum shows no signal and

© 2013 Wiley-VCH Verlag GmbH & Co. KGaA, Weinheim

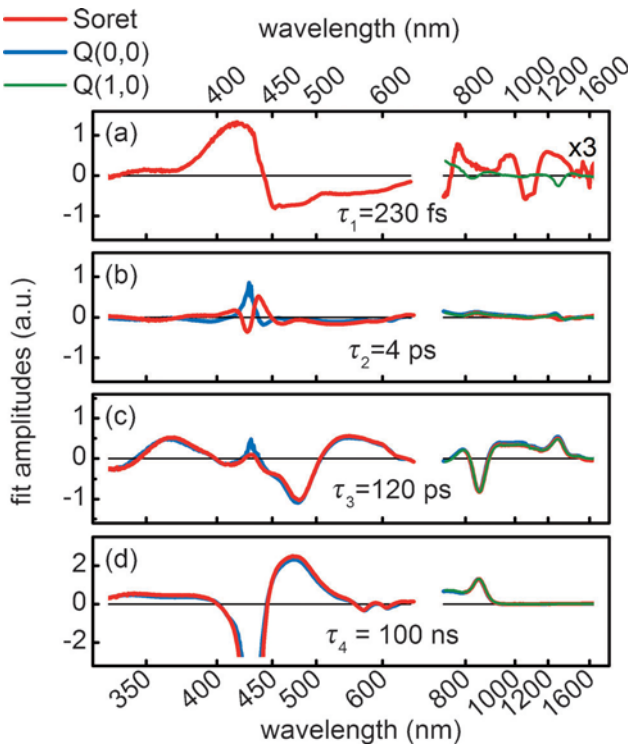

Figure 6. DADS for CdTPP upon excitation at the Q(0,0) (blue), Q(1,0) (green, only IR), and Soret (red) bands.

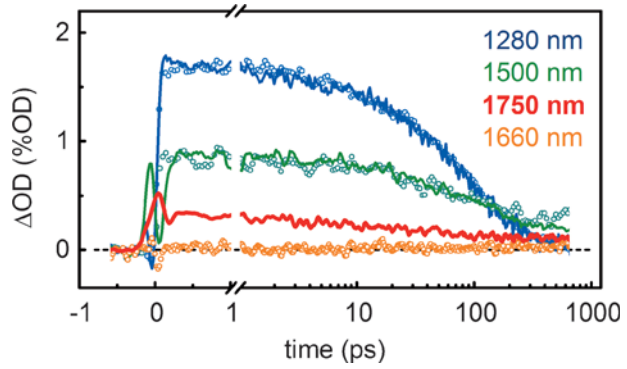

Figure 7. Single color pump probe experiments of CdTPP with a pump wavelength of $\lambda = 620$ nm and selected probe wavelengths. The open circles represent data taken from the transient spectrum with probe wavelengths of $\lambda = 1280$, 1550, and 1660 nm. The solid lines show NOPA OPA measure ments with probe wavelengths at $\lambda = 1280$, 1500, and 1750 nm.

we see an increased signal at $\lambda = 1750$ nm, which can be assigned to a rising band. Owing to missing alternatives, this band must be assigned to the dark $1E_g$ state, especially when comparing it to the distinctively weaker signal in MgTPP. The total energy of this state then results to about (2.75 ± 0.1) eV. Its small oscillator strength might be taken as an indication that the gerade states do not possess high oscillator strengths, even for [1+1] excitation. As a final result, we state that the triplet splitting in CdTPP is 1.47 eV ($\lambda = 846$ nm), as shown by the DADS in Figure 6 and the complete transient spectra in Figure S4 in the Supporting Information.

Conclusion

We performed pump–probe investigations of the Soret and Q bands of MgTPP and CdTPP in THF to decipher the dependence of the relaxation pathways and the excited-state manifolds from the central metal ion for closed d-shell atoms. The relaxation dynamics were monitored by measuring transient absorption spectra in the visible and NIR spectral regimes and the results were backed by ab initio calculations. Upon Soret excitation, the dynamics of CdTPP were significantly faster than for the other complexes, which depended on a dark E_g state. This state was located at the central N_4 cage and mediated the transition between the Soret and Q bands and took place with $(100 \pm 2)\%$ quantum yield. In MgTPP and ZnTPP the E_g state was higher in energy. This caused the internal conversion in CdTPP an order of magnitude faster than that in MgTPP for which relaxation required 3.2 ps. In summary, the light-induced reaction dynamics of porphyrins all proceeded along the same pathway and the only major modification between the different central metal ions were the lifetimes of the singlet and triplet states caused by the dark E_g state and different spin-orbit couplings.

Further investigations into different porphyrins include transition-metal atoms with open d shells and the dependence of the dynamics of the porphyrin cage.

Experimental Section

Sample preparation

5,10,15,20-Tetraphenylporphyrinato magnesium(II): The purified free-base *meso*-tetraphenylporphyrin was magnesiated by using the method optimized by Lindsey and Woodford[53] with a tenfold excess of magnesium dibromide diethyl etherate (413 mg, 1.62 mmol) in dry dichloromethane (8 mL) in the presence of triethylamine (0.45 mL) under an argon atmosphere. UV/Vis spectroscopy showed that metalation was completed within 15 min at room temperature. The reaction mixture was diluted with dichloromethane (25 mL) and washed twice (2×25 mL) with an aqueous solution of sodium hydrogen carbonate and then with distilled water. Column chromatography on neutral alumina eluted with dichloromethane containing 0.1% triethylamine afforded the magnesium triethylamine adduct (65 mg). A second chromatography step on alumina, which was eluted with pure dichloromethane freshly distilled from calcium hydride, gave after evaporation of the solvent a plum-colored powder, which was sublimed in vacuum (10^{-3} mbar) by heating to over 180 °C.

5,10,15,20-Tetraphenylporphyrinato cadmium(II): A solution of 5,10,15,20-tetraphenyl-porphyrin free of the corresponding chlorin (0.1 g, 0.16 mmol) in anhydrous DMF (10 mL) was degassed under nitrogen. Cadmium acetate monohydrate (Aldrich) was dehydrated by heating at 110 °C for 5 h under vacuum (<1 mbar). The anhydrous cadmium acetate (0.375 g, 1.6 mmol) was added to the violet solution of the porphyrin and heated at 120 °C for 1 h under an argon atmosphere. The solution changed color to pine green. The reaction mixture was extracted into dichloromethane (50 mL) and washed with water (2×50 mL). The organic layer was evaporated to afford, after drying overnight in vacuum, lavender green crystals CdTPP (0.1 g, 87.5%).

© 2013 Wiley-VCH Verlag GmbH & Co. KGaA, Weinheim

MgTPP and CdTPP were checked for impurities by ^{1}H NMR and UV/Vis absorption spectroscopy. The CdTPP spectra in anhydrous toluene and THF showed only a very small bathochromic shift of the two Q bands from λ 568 to 573 nm and from λ 609 to 615 nm, respectively, which we assigned to a solvatochromic effect (see Figure S5). For MgTPP, especially in THF, five-coordinated species should be prevalent, in addition to the six-coordinated one.[13] A four-coordinated Mg species within porphyrins and (bacterio)-chlorophylls has never been encountered experimentally in crystal structures owing to them being unstable and coordinatively unsaturated. Either solvent or even adventitious water molecules are spontaneously tightly bound, whereas in a protein environment, various polar amino acid residues function as apical ligands to the Mg atom.[9] However, upon vertical excitation with a rather large laser pulse width, the excited species are assumed to be of D_{4h} symmetry. Future experimental and theoretical studies will address this issue.

Experimental methods

Steady-state absorption spectra of MgTPP and CdTPP in THF were recorded by using a Varian Cary5E spectrophotometer and fluorescence spectra were recorded by using a Cary Eclipse fluorescence spectrophotometer.

For UV to visible and IR time-resolved pump probe spectroscopy, we used a commercial 1 kHz Ti:sapphire-based laser system (CPA 2001; Clark-MXR), which generated pulses with a center wavelength of λ 778 nm, a full-width at half maximum (FWHM) of 170 fs pulses, and an output energy of 1 mJ. The pump was generated in a two-stage NOPA system and subsequently compressed with a pair of fused silica prisms down to 20 fs, which corresponded to a time bandwidth product of 0.84. The excitation wavelength for both MgTPP and CdTPP was λ 620 nm. The spectral width was 35 nm. To ensure the same properties for the probe pulse during the experiment, we delayed the pump pulse with a commercial translation stage (M-531.PD; Physik Instrumente Inc.) and checked that the spatial overlap and size of the pump stayed constant when moving the delay stage.

For the UV and visible probe light, we generated a continuum in a moving 5 mm CaF_2 plate with the pump laser. A thin filter was used to block the region around the pump wavelength. To generate an IR probe continuum, we used the idler of a white-light-seeded λ 778 nm pumped collinear OPA centered at 2.1 μm. Focusing this idler onto a YVO_4 crystal allowed the generation of a continuum down to λ 550 nm.[54] The broadened 2.1 μm pump was cut off with a dielectric filter with an edge at λ 1650 nm.

For both continua, pump and probe were focused onto the sample under a small external angle of 4°. To minimize anisotropy effects, the polarization of the pump pulse was set at a magic angle with respect to the probe pulse by using an achromatic $\lambda/2$ wave plate. An additional polarizer after the sample minimized pump stray light. The probe beam was completely located within the excitation area of the pump pulse in the sample and its diameter was half of the pump beam ($1/e^2$ radius for intensity of pump w_0 135 μm). The probe beam was spectrally dispersed and imaged onto a line array. For the UV to visible continuum, we used a fused silica prism to disperse the colors and imaged it onto a photodiode array (NMOS; S3902-512Q; Hamamatsu Inc.). The IR white light was dispersed with a SF10 prism and then focused on an InGaAs array. This allowed stepwise probing from λ 290 to 1660 nm. More details on the basic setup are given in Ref. [51] and the infrared extension will be discussed in a forthcoming publication.[55] Additionally NOPA-OPA measurements with λ 620 nm pumping and probing at λ 1280, 1550, and 1750 nm were performed. Therefore, we directly used the light from the collinear IR OPA as the probe light without any further IR continuum generation.

MgTPP and CdTPP were measured in a 1 mm cuvette from Hellma, as well as in a flowthrough cell. The optical density for MgTPP was 0.2, the pump energy was 800 nJ, and the pump intensity was 6.0×10^{10} W cm^{-2}. For CdTPP, the optical density was 0.3, the pump energy was 200 nJ, and the pump intensity was 2.0×10^{10} W cm^{-2}. All experiments were performed at room temperature.

Acknowledgements

This study was funded by the Deutsche Forschungsgemeinschaft (DFG), the State Baden-Württemberg and the Karlsruhe Institute of Technology (KIT) through the Center for Functional Nanostructures (CFN, projects C3.2 and C3.5). O.S. is thankful for financial support from the Humboldt-Foundation and the Wenner-Gren Foundation. M.B., O.S., and E.R. are furthermore grateful to be supported by the DFG Cluster of Excellence: Munich Centre for Advanced Photonics.

Keywords: dark states · density functional calculations · femtosecond spectroscopy · porphyrinoids

[1] a) H. Shinmori, T. Kajiwara, A. Osuka, *Tetrahedron Lett.* **2001**, *42*, 3617; b) A. Kay, R. Humphry, M. Grätzel, *J. Phys. Chem.* **1994**, *98*, 952; c) D. Wu, Z. Shen, Z. Xue, M. You, *Chin. J. Inorg. Chem.* **2007**, *23*, 1.
[2] a) E. D. Sternberg, D. Dolphin, C. Brückner, *Tetrahedron* **1998**, *54*, 4151; b) X. Chen, C. M. Drain, *Drug Des. Rev. Online* **2004**, *1*, 215; c) M. P. Donzello, C. Ercolani, P. A. M. P. Stuzhin, *Coord. Chem. Rev.* **2006**, *250*, 1530; d) V. Gottumukkala, R. J. Luguya, F. R. Fronczeck, M. G. H. Vicente, *Bioorg. Med. Chem.* **2005**, *13*, 1633.
[3] a) C. A. Mirkin, M. A. Ratner, *Annu. Rev. Phys. Chem.* **1992**, *43*, 719; b) M. J. Gunter, M. R. Johnston, *J. Chem. Soc. Chem. Commun.* **1992**, 1163; c) K. Sienicki in *Molecular Electronics and Molecular Electronic Devices, Vol. 3*, CRC Press, Boca Raton, **1994**.
[4] J. Karolczak, D. Kowalska, A. Lukaszewicz, A. Maciejewski, R. P. Steer, *J. Phys. Chem. A* **2004**, *108*, 4570.
[5] H. Z. Yu, J. S. Baskin, B. Steiger, C. Z. Wan, F. C. Anson, A. H. Zewail, *Chem. Phys. Lett.* **1998**, *293*, 1.
[6] R. E. Haddad, S. Gazeau, J. Pécaut, J. C. Marchon, C. J. Medforth, J. A. Shelnutt, *J. Am. Chem. Soc.* **2003**, *125*, 1253.
[7] A. Marcelli, P. Foggi, L. Moroni, C. Gellini, P. R. Salvi, *J. Phys. Chem. A* **2008**, *112*, 1864.
[8] a) L. Luo, C. H. Chang, Y. C. Chen, T. K. Wu, E. W. G. Diau, *J. Phys. Chem. B* **2007**, *111*, 7656; b) A. Gadalla, J. B. Beaufrand, M. Bowen, S. Boukari, E. Beaurepaire, O. Crégut, M. Gallart, B. Hönerlage, P. Gilliot, *J. Phys. Chem. C* **2010**, *114*, 17854; c) R. Kumble, S. Palese, V. S. Y. Lin, M. J. Therien, R. M. Hochstrasser, *J. Am. Chem. Soc.* **1998**, *120*, 11489.
[9] T. S. Balaban, P. Braun, C. Hättig, A. Hellweg, J. Kem, W. Saenger, A. Zouni, *Biochim. Biophys. Acta Bioenergetics* **2009**, *1787*, 1254.
[10] A. Hazell, *Acta. Crystallogr. Sect. C* **1986**, *42*, 296.
[11] A. Hazell, *Acta. Crystallogr. Sect. C* **1984**, *40*, 751.
[12] J. L. Hoard in *Porphyrins and Metalloporphyrins* (Eds.: K. M. Smith), Elsevier, Amsterdam, **1975**, pp. 317.
[13] O. Schalk, Y. Liang, A. N. Unterreiner, *Z. Phys. Chem. (Muenchen Ger.)* **2013**, *227*, 35.
[14] M. Gouterman in *The Porphyrins, Vol. 3* (Eds.: D. H. Dolpin), Academic Press, New York, **1978**, pp. 1.
[15] K. Kalyanasundaram, *Photochemistry of Polypyridine and Porphyrin Complexes*, Academic Press, London, **1992**.

© 2013 Wiley-VCH Verlag GmbH & Co. KGaA, Weinheim

[16] V. V. Apanasovich, E. G. Novikov, N. N. Yatskov, R. B. M. Koehorst, T. J. Schaafsma, A. van Hoek, *J. Appl. Spectrosc.* **1999**, *66*, 613.
[17] S. F. Shkirman, K. N. Solov'ev, T. F. Kachura, S. A. Arabei, E. D. Skakovskii, *J. Appl. Spectrosc.* **1999**, *66*, 68.
[18] I. T. Oliver, W. A. Rawlinson, *Biochem. J.* **1955**, *61*, 641.
[19] L. Edwards, D. H. Dolpin, M. Gouterman, *J. Mol. Spectrosc.* **1971**, *38*, 16.
[20] L. Edwards, D. H. Dolpin, M. Gouterman, *J. Mol. Spectrosc.* **1970**, *35*, 90.
[21] M. Gouterman, *J. Chem. Phys.* **1959**, *30*, 1139.
[22] M. Gouterman, *J. Mol. Spectrosc.* **1961**, *6*, 138.
[23] C. Weiss, H. Kobayashi, M. Gouterman, *J. Mol. Spectrosc.* **1965**, *16*, 415.
[24] E. J. Baerends, G. Ricciardi, A. Rosa, S. J. A. van Gisbergen, *Coord. Chem. Rev.* **2002**, *230*, 5.
[25] H. Solheim, K. Ruud, S. Coriani, P. Norman, *J. Phys. Chem. A* **2008**, *112*, 9615.
[26] G. A. Peralta, M. Seth, T. Ziegler, *Inorg. Chem.* **2007**, *46*, 9111.
[27] H. Chosrowjan, S. Tanigichi, T. Okada, S. Takagi, K. Tokumaru, *Chem. Phys. Lett.* **1995**, *242*, 644.
[28] G. G. Gurzadyan, T. H. Tran Thi, T. Gustavsson, *J. Chem. Phys.* **1998**, *108*, 385.
[29] H. Z. Yu, J. S. Baskin, A. H. Zewail, *J. Phys. Chem. A* **2002**, *106*, 9845.
[30] U. Tripathy, D. Kowalska, X. Liu, S. Velate, R. P. Steer, *J. Phys. Chem. A* **2008**, *112*, 5824.
[31] X. Liu, U. Tripathy, S. V. Bhosale, S. J. Langford, R. P. Steer, *J. Phys. Chem. A* **2008**, *112*, 8986.
[32] S. Sorgues, L. Poisson, K. Raffael, L. Krim, B. Soep, N. Shafizadeh, *J. Chem. Phys.* **2006**, *124*, 114302.
[33] N. Mataga, Y. Shibata, H. Chosrowjan, N. Yoshida, A. Osuka, *J. Phys. Chem. B* **2000**, *104*, 4001.
[34] M. Kullmann, A. Hipke, P. Nuernberger, T. Bruhn, D. C. G. Götz, M. Sekita, D. M. Guldi, G. Bringmann, T. Brixner, *Phys. Chem. Chem. Phys.* **2012**, *14*, 8038.
[35] A. Lukaszewicz, J. Karolczak, D. Kowalska, A. Maciejewski, M. Ziolek, R. P. Steer, *Chem. Phys.* **2007**, *331*, 359.
[36] S. Velate, X. Liu, R. P. Steer, *Chem. Phys. Lett.* **2006**, *427*, 295.
[37] J. S. Baskin, H. Z. Yu, A. H. Zewail, *J. Phys. Chem. A* **2002**, *106*, 9837.
[38] X. Liu, E. K. L. Yeow, S. Velate, R. P. Steer, *Phys. Chem. Chem. Phys.* **2006**, *8*, 1298.
[39] G. Niranjian, V. Marat, J. Lasse, K. Karol, *J. Phys. Chem. A* **2009**, *113*, 6041.
[40] Z. L. Cai, M. J. Crossley, J. R. Reimers, R. Kobayashi, R. D. Amos, *J. Phys. Chem. B* **2006**, *110*, 15624.
[41] R. Kobayashi, R. D. Amos, *Chem. Phys. Lett.* **2006**, *420*, 106.
[42] O. Schalk, H. Brands, T. S. Balaban, A. N. Unterreiner, *J. Phys. Chem. A* **2008**, *112*, 1719.
[43] D. B. Moravec, B. M. Lovaasen, M. D. Hopkins, *J. Photochem. Photobiol. A* **2013**, *254*, 20.
[44] M. Gouterman, F. P. Schwarz, P. D. Smith, *J. Chem. Phys.* **1973**, *59*, 676.
[45] A. Harriman, *J. Chem. Soc. Faraday Trans. 2* **1981**, *77*, 1281.
[46] M. W. Schmidt, K. K. Baldridge, J. A. Boatz, S. T. Elbert, M. S. Gordon, J. H. Jensen, S. Koseki, N. Matsunaga, K. A. Nguyen, S. J. Su, T. L. Windus, M. Duquis, J. A. Montgomery, *J. Comput. Chem.* **1993**, *14*, 1347.
[47] M. S. Gordon, M. W. Schmidt in *Theory and Applications of Computation al Chemistry, the First Forty Years* (Eds.: C. E. Dykstra, G. Frenking, K. S. Kim, G. E. Scuseria), Elsevier, Amsterdam **2005**, pp. 1167.
[48] D. Sundholm, *Chem. Phys. Lett.* **2000**, *317*, 392.
[49] R. D. Shannon, C. T. Prewitt, *Acta Crystallogr. Sect. B* **1969**, *25*, 925.
[50] U. Even, J. Magen, J. Jortner, J. Friedman, H. Levaon, *J. Chem. Phys.* **1982**, *77*, 4374.
[51] U. Megerle, I. Pugliesi, C. Schriever, C. F. Sailer, E. Riedle, *Appl. Phys. B* **2009**, *96*, 215.
[52] D. Sundholm, *Phys. Chem. Chem. Phys.* **2000**, *2*, 2275.
[53] J. S. Lindsey, J. N. Woodford, *Inorg. Chem.* **1995**, *34*, 1063.
[54] M. Bradler, P. Baum, E. Riedle, *Appl. Phys. B* **2009**, *97*, 561.
[55] E. Riedle, M. Bradler, M. Wenninger, C. F. Sailer, I. Pugliesi. *Faraday Disc.*, **2013**, DOI: 10.1039/C3FD00010A.

Received: April 19, 2013
Published online on July 5, 2013

© 2013 Wiley-VCH Verlag GmbH & Co. KGaA, Weinheim

Appendix A13

A novel setup for femtosecond pump-repump-probe IR spectroscopy with few cycle CEP stable pulses

M. Bradler, J. C. Werhahn, D. Hutzler, S. Fuhrmann, R. Heider, E. Riedle, H. Iglev, and R. Kienberger

Opt. Express **21**, 20145 - 20158 (2013)

Reprinted with kind permission from the Optical Society of America (OSA)

A novel setup for femtosecond pump-repump-probe IR spectroscopy with few cycle CEP stable pulses

Maximilian Bradler,[2] Jasper C. Werhahn,[1] Daniel Hutzler,[1] Simon Fuhrmann,[1]Rupert Heider,[1] Eberhard Riedle,[2,*] Hristo Iglev,[1] and Reinhard Kienberger[1]

[1]*Physik-Department E11, Technische Universität München, James-Franck-Str. 1,85748 Garching, Germany*
[2]*Lehrstuhl für BioMolekulare Optik, Ludwig-Maximilians-Universität, Oettingenstraße 67,80538 Munich, Germany*
[*]*Eberhard.Riedle@Physik.uni-muenchen.de*

Abstract: We present a three-color mid-IR setup for vibrational pump-repump-probe experiments with a temporal resolution well below 100 fs and a freely selectable spectral resolution of 20 to 360 cm^{-1} for the pump and repump. The usable probe range without optical realignment is 900 cm^{-1}. The experimental design employed is greatly simplified compared to the widely used setups, highly robust and includes a novel means for generation of tunable few-cycle pulses with stable carrier-envelope phase. A Ti:sapphire pump system operating with 1 kHz and a modest 150 fs pulse duration supplies the total pump energy of just 0.6 mJ. The good signal-to-noise ratio of the setup allows the determination of spectrally resolved transient probe changes smaller than $6 \cdot 10^{-5}$ OD at 130 time delays in just 45 minutes. The performance of the spectrometer is demonstrated with transient IR spectra and decay curves of HDO molecules in lithium nitrate trihydrate and ice and a first all MIR pump-repump-probe measurement.

© 2013 Optical Society of America

OCIS codes: (300.6190) Spectrometers; (300.6340) Spectroscopy, infrared; (300.6500) Spectroscopy, time-resolved; (300.6530) Spectroscopy, ultrafast; (320.7110) Ultrafast nonlinear optics; (320.7150) Ultrafast spectroscopy.

References and links

1. H. Graener, G. Seifert, and A. Laubereau, "New spectroscopy of water using tunable picosecond pulses in the infrared," Phys. Rev. Lett. **66**(16), 2092 2095 (1991).
2. S. Woutersen, U. Emmerichs, and H. J. Bakker, "Femtosecond mid-IR pump-probe spectroscopy of liquid water: evidence for a two-component structure," Science **278**(5338), 658 660 (1997).
3. M. T. Zanni and R. M. Hochstrasser, "Two-dimensional infrared spectroscopy: a promising new method for the time resolution of structures," Curr. Opin. Struct. Biol. **11**(5), 516 522 (2001).
4. M. Khalil, N. Demirdöven, and A. Tokmakoff, "Coherent 2D IR spectroscopy: molecular structure and dynamics in solution," J. Phys. Chem. A **107**(27), 5258 5279 (2003).
5. E. T. J. Nibbering and T. Elsaesser, "Ultrafast vibrational dynamics of hydrogen bonds in the condensed phase," Chem. Rev. **104**(4), 1887 1914 (2004).
6. D. Kraemer, M. L. Cowan, A. Paarmann, N. Huse, E. T. J. Nibbering, T. Elsaesser, and R. J. D. Miller, "Temperature dependence of the two-dimensional infrared spectrum of liquid H_2O," Proc. Natl. Acad. Sci. U.S.A. **105**(2), 437 442 (2008).
7. H. J. Bakker and J. L. Skinner, "Vibrational spectroscopy as a probe of structure and dynamics in liquid water," Chem. Rev. **110**(3), 1498 1517 (2010).
8. J. C. Werhahn, S. Pandelov, S. S. Xantheas, and H. Iglev, "Dynamics of weak, bifurcated, and strong hydrogen bonds in lithium nitrate trihydrate," J. Phys. Chem. Lett. **2**(13), 1633 1638 (2011).
9. P. Hamm, S. Wiemann, M. Zurek, and W. Zinth, "Highly sensitive multichannel spectrometer for subpicosecond spectroscopy in the midinfrared," Opt. Lett. **19**(20), 1642 1644 (1994).
10. J. L. Bingaman, C. L. Kohnhorst, G. A. Van Meter, B. A. McElroy, E. A. Rakowski, B. W. Caplins, T. A. Gutowski, C. J. Stromberg, C. E. Webster, and E. J. Heilweil, "Time-resolved vibrational spectroscopy of [FeFe]-hydrogenase model compounds," J. Phys. Chem. A **116**(27), 7261 7271 (2012).

#191026 - $15.00 USD Received 23 May 2013; revised 26 Jul 2013; accepted 27 Jul 2013; published 20 Aug 2013

11. P. M. Donaldson, H. Strzalka, and P. Hamm, "High sensitivity transient infrared spectroscopy: a UV/visible transient grating spectrometer with a heterodyne detected infrared probe," Opt. Express **20**(12), 12761 12770 (2012).
12. R. A. Kaindl, M. Wurm, K. Reimann, P. Hamm, A. W. Weiner, and M. Woerner, "Generation, shaping, and characterization of intense femtosecond pulses tunable from 3 to 20 μm," J. Opt. Soc. Am. B **17**(12), 2086 2094 (2000).
13. N. Demirdöven, M. Khalil, O. Golonzka, and A. Tokmakoff, "Dispersion compensation with optical materials for compression of intense sub-100-fs mid-infrared pulses," Opt. Lett. **27**(6), 433 435 (2002).
14. J. B. Asbury, T. Steinel, and M. D. Fayer, "Vibrational echo correlation spectroscopy probes of hydrogen bond dynamics in water and methanol," J. Lumin. **107**(1-4), 271 286 (2004).
15. H. S. Chung, M. Khalil, A. W. Smith, and A. Tokmakoff, "Transient two-dimensional IR spectrometer for probing nanosecond temperature-jump kinetics," Rev. Sci. Instrum. **78**(6), 063101 (2007).
16. S. Park, K. Kwak, and M. D. Fayer, "Ultrafast 2D-IR vibrational echo spectroscopy: a probe of molecular dynamics," Laser Phys. Lett. **4**(10), 704 718 (2007).
17. S. H. Shim and M. T. Zanni, "How to turn your pump-probe instrument into a multidimensional spectrometer: 2D IR and Vis spectroscopies via pulse shaping," Phys. Chem. Chem. Phys. **11**(5), 748 761 (2009).
18. K. C. Jones, Z. Ganim, C. S. Peng, and A. Tokmakoff, "Transient two-dimensional spectroscopy with linear absorption corrections applied to temperature-jump two-dimensional infrared," J. Opt. Soc. Am. B **29**(1), 118 129 (2012).
19. D. R. Skoff, J. E. Laaser, S. S. Mukherjee, C. T. Middleton, and M. T. Zanni, "Simplified and economical 2D IR spectrometer design using a dual acousto-optic modulator," Chem. Phys. in press., doi:10.1016/j.chemphys.2012.08.019.
20. D. Eisenberg and W. Kauzmann, *The Structure and Properties of Water* (Oxford University, 1969).
21. F. Franks, *Water: A Comprehensive Treatise* (Plenum Press, 1972).
22. Y. Tanimura and S. Mukamel, "2-dimensional femtosecond vibrational spectroscopy of liquids," J. Chem. Phys. **99**(12), 9496 9511 (1993).
23. M. Bradler, C. Homann, and E. Riedle, "Mid-IR femtosecond pulse generation on the microjoule level up to 5 μm at high repetition rates," Opt. Lett. **36**(21), 4212 4214 (2011).
24. M. Bradler, P. Baum, and E. Riedle, "Femtosecond continuum generation in bulk laser host materials with sub-μJ pump pulses," Appl. Phys. B **97**(3), 561 574 (2009).
25. J. Piel, M. Beutter, and E. Riedle, "20-50-fs pulses tunable across the near infrared from a blue-pumped noncollinear parametric amplifier," Opt. Lett. **25**(3), 180 182 (2000).
26. I. Hartl and W. Zinth, "A novel spectrometer system for the investigation of vibrational energy relaxation with sub-picosecond time resolution," Opt. Commun. **160**(1 3), 184 190 (1999).
27. V. Petrov, F. Rotermund, and F. Noack, "Generation of high-power femtosecond light pulses at 1 kHz in the mid-infrared spectral range between 3 and 12 μm by second-order nonlinear processes in optical crystals," J. Opt. A, Pure Appl. Opt. **3**(3), R1 R19 (2001).
28. D. Brida, C. Manzoni, G. Cirmi, M. Marangoni, S. De Silvestri, and G. Cerullo, "Generation of broadband mid-infrared pulses from an optical parametric amplifier," Opt. Express **15**(23), 15035 15040 (2007).
29. W. E. White, F. G. Patterson, R. L. Combs, D. F. Price, and R. L. Shepherd, "Compensation of higher-order frequency-dependent phase terms in chirped-pulse amplification systems," Opt. Lett. **18**(16), 1343 1345 (1993).
30. R. Trebino, K. W. De Long, D. N. Fittinghoff, J. N. Sweetser, M. A. Krumbügel, B. A. Richman, and D. J. Kane, "Measuring ultrashort laser pulses in the time-frequency domain using frequency-resolved gating," Rev. Sci. Instrum. **68**(9), 3277 3295 (1997).
31. A. Baltuska, M. Überacker, E. Goulielmakis, R. Kienberger, V. S. Yakovlev, T. Udem, T. W. Hänsch, and F. Krausz, "Phase-controlled amplification of few-cycle laser pulses," IEEE J Sel. Top. Quantum Electron. **9**(4), 972 989 (2003).
32. G. Cerullo, A. Baltuska, O. D. Mücke, and C. Vozzi, "Few-optical-cycle light pulses with passive carrier-envelope phase stabilization," Laser Photonics Rev. **5**(3), 323 351 (2011).
33. S. Pandelov, B. M. Pilles, J. C. Werhahn, and H. Iglev, "Time-resolved dynamics of the OH stretching vibration in aqueous NaCl hydrate," J. Phys. Chem. A **113**(38), 10184 10188 (2009).
34. H. Graener, G. Seifert, and A. Laubereau, "Vibrational and reorientational dynamics of water molecules in liquid matrices," Chem. Phys. **175**(1), 193 204 (1993).
35. H. J. Bakker, J. J. Gilijamse, and A. J. Lock, "Energy transfer in single hydrogen-bonded water molecules," ChemPhysChem **6**(6), 1146 1156 (2005).
36. S. Woutersen, U. Emmerichs, H. K. Nienhuys, and H. J. Bakker, "Anomalous temperature dependence of vibrational lifetimes in water and ice," Phys. Rev. Lett. **81**(5), 1106 1109 (1998).
37. H. Iglev, M. Schmeisser, K. Simeonidis, A. Thaller, and A. Laubereau, "Ultrafast superheating and melting of bulk ice," Nature **439**(7073), 183 186 (2006).
38. C. Schriever, S. Lochbrunner, E. Riedle, and D. J. Nesbitt, "Ultrasensitive ultraviolet-visible 20 fs absorption spectroscopy of low vapor pressure molecules in the gas phase," Rev. Sci. Instrum. **79**(1), 013107 (2008).
39. U. Megerle, I. Pugliesi, C. Schriever, C. F. Sailer, and E. Riedle, "Sub-50 fs broadband absorption spectroscopy with tunable excitation: Putting the analysis of ultrafast molecular dynamics on solid ground," Appl. Phys. B **96**(2-3), 215 231 (2009).

#191026 - $15.00 USD Received 23 May 2013; revised 26 Jul 2013; accepted 27 Jul 2013; published 20 Aug 2013
(C) 2013 OSA

40. M. S. Lynch, K. M. Slenkamp, M. Cheng, and M. Khalil, "Coherent fifth-order visible-infrared spectroscopies: ultrafast nonequilibrium vibrational dynamics in solution," J. Phys. Chem. A **116**(26), 7023 7032 (2012).
41. M. L. Groot, L. J. G. W. van Wilderen, and M. Di Donato, "Time-resolved methods in biophysics. 5. Femtosecond time-resolved and dispersed infrared spectroscopy on proteins," Photochem. Photobiol. Sci. **6**(5), 501 507 (2007).
42. P. Hamm, R. A. Kaindl, and J. Stenger, "Noise suppression in femtosecond mid-infrared light sources," Opt. Lett. **25**(24), 1798 1800 (2000).
43. Y. Deng, A. Schwarz, H. Fattahi, M. Ueffing, X. Gu, M. Ossiander, T. Metzger, V. Pervak, H. Ishizuki, T. Taira, T. Kobayashi, G. Marcus, F. Krausz, R. Kienberger, and N. Karpowicz, "Carrier-envelope-phase-stable, 1.2 mJ, 1.5 cycle laser pulses at 2.1 μm," Opt. Lett. **37**(23), 4973 4975 (2012).

1. Introduction

Infrared pump-probe and two dimensional spectroscopy are very powerful tools to elucidate the complex ultrafast dynamics of an abundance of condensed systems [1 4]. For hydrogen bonded systems, high-lying stretching vibrations of the hydrogen bond donors can be utilized as local probe of the chemical environment of the donor group [1,5 8]. Despite the fact, that ultrafast infrared pump probe spectroscopy is used in many different disciplines including biology and chemistry, detailed descriptions of the setups remain scarce [5,9 11]. Modern developments in two dimensional IR spectroscopy and photon echo techniques are much better documented [12 19]. The intention of this paper is to demonstrate new sources of femtosecond pulses with a greatly simplified concept and a wide variability of output parameters. They are combined to a new three-color spectrometer with very flexible operating parameters. We include detailed insight into the construction of the spectrometer, which we hope will prove useful particularly for newcomers to the field.

With the advent of ever shorter laser pulses, the time resolution of pump-probe setups evolved from several picoseconds down into the 100 fs regime, allowing the resolution of increasingly fast dynamics. Important information on the chemical nature of the vicinity of the probed molecule lies in the spectral position of the vibration under consideration. It is for example commonly agreed on, that an increased red shift in the position of an OH stretching vibration correlates with an increased strength of the corresponding hydrogen bond [20,21]. This means that complementary information can be obtained with long pulses with a narrow spectrum, as compared to the information gained from investigations with extremely short pulses that lack high spectral resolution. More advanced techniques like photon echo spectroscopy partially circumvent this problem, but the interpretation of the obtained data is quite demanding and has to rely heavily on simulations, where the physical result depends on the applied theoretical model [6,22]. Pump-probe spectroscopy still yields the most quantitative and direct information.

With pump-repump-probe spectroscopy, higher lying vibrational levels can be reached via successive excitation. These high-lying states are a very convenient probe of the shape of the potential of the hydrogen bond under consideration. Experimental data on the shape of the H bond potential in different chemical environments are in turn very valuable information for theory to accomplish a better modeling of this still poorly understood interaction. It could furthermore open a pathway towards optically induced chemical reactions like proton transfer, which has not yet been achieved with infrared pulses.

We present first results obtained with a newly developed optical setup that allows mid-IR pump-repump-probe spectroscopy with a time resolution significantly shorter than 100 fs. The infrared pulses are generated via a recently demonstrated hybrid NOPA layout [23]. In order to achieve a selective excitation of the vibrational modes under investigation, the pump pulses are tunable in the range from 2,000 to 10,000 cm^{-1}, and their spectral widths are controlled by a spectral grating selector. The pulses generated in this way have a spectral bandwidth between 20 and 360 cm^{-1} and pulse durations between 50 and 850 fs, with typical pulse energies of 3 μJ. The probe pulses are shorter than 50 fs (FWHM up to 450 cm^{-1}), yielding few-cycle mid-IR pulses with unprecedented spectral width. The Fourier limit for these pulses is below 30 fs.

#191026 - $15.00 USD Received 23 May 2013; revised 26 Jul 2013; accepted 27 Jul 2013; published 20 Aug 2013
(C) 2013 OSA

This paper is organized as follows: In Section 2 we will present the experimental setup and briefly discuss the layout of the used optical parametric amplifiers and grating selectors. Section 3 presents a full characterization of the employed pulses, including their spectral and temporal phase and we will demonstrate that all our pulses have a stable carrier envelope phase (CEP). Section 4 shows first measurements with the new setup, where we significantly improve recently published measurements on OH stretching vibration lifetimes of HDO molecules in lithium nitrate trihydrate [8]. Section 5 concludes with a detailed classification and comparison to existing state of the art spectrometers.

2. Experimental setup

The basic layout of our setup is illustrated in Fig. 1(a). As source we use a Ti:sapphire based laser system (CPA 2010; Clark MXR) which delivers 779 nm pulses at 1 kHz repetition rate with a pulse duration of 150 fs and a pulse energy of 900 μJ. For the current setup we use 600 μJ. The remaining pulse energy is used for diagnostics and further experiments.

To generate the infrared pump pulses we use a hybrid pumping technique [23] which allows the generation of femtosecond pulses tunable from 1 to over 5 μm at the μJ level. The idea of the amplifier is shown in Fig. 1(b). A near-infrared continuum is generated in a 4 mm YAG plate (SCG) [24] and amplified in a noncollinear optical parametric amplifier (pre-NOPA) pumped by 60 μJ of the second harmonic of the laser light [25]. As amplifier crystal we use a 2 mm thick BBO crystal (type I, 32° cutting angle). Pulses on the μJ level which are tunable between 900 nm and 1.6 μm are generated in this pre-amplifier. Here, the noncollinearity is only used to geometrically separate the pump and idler pulses. In this work we denominate the light which is amplified with the term "signal light", and with the term "idler light" the light which is newly generated, independent from their wavelengths.

The near-infrared pulses are then further amplified in a collinear amplifier (IR-OPA) pumped by the 120 μJ of the fundamental laser light left over in the second harmonic generation (SHG). Here we use a 1.5 mm thick $LiNbO_3$ crystal (type I, cut at 45°) as amplifier material. The idler pulses which are produced during this amplification process spectrally range between 1.6 to 5.0 μm (2,000 to 6,250 cm^{-1}) and typically have pulse energies of several μJ. The full details and advantages of this concept have been presented recently [23]. The blue pumped pre-amplification drastically increases the MIR output energy especially at the spectral limits of the main amplifier. The high output can be reached with moderate pump intensities in the IR-OPA that allow the use of nonlinear crystals like $LiIO_3$ which were previously considered critical for fs OPA-operation due to the low damage threshold [26 28]. The amplifier is operated completely collinear to avoid any spatial chirp of the idler pulses. A good method to experimentally realize the collinearity is to minimize the spatial separation between signal and pump light. Since the pump, signal, and idler pulses propagate in the same direction dichroic optics are used to separate the 779 nm light (HR 800 nm, HT 1 - 5 μm) and filters (germanium or silicon plates) to separate the signal pulses. Due to the high refractive index of germanium and silicon an anti-reflection coating is needed. It should be mentioned that germanium plates have a drastically decreased infrared transmission if they are illuminated by high intensity 800 nm light and therefore these filters should be placed in the unfocussed beams or after the separation of the 800 nm light. If the signal pulses are intended to be used for the experiment to cover the range from 1.0 to 1.6 μm (6,250 - 10,000 cm^{-1}) a slight noncollinearity in the IR-OPA already leads to spatial separation from the pump and idler pulses and for the signal pulses no spatial chirp will occur. For all measurements shown in this paper we use the idler pulses and all IR-OPAs are operated in the collinear geometry.

In some experiments an energetically selective excitation of the sample is required. A spectral selector [29] whose setup is shown in Fig. 1(d) allows decreasing the spectral bandwidth of the pump pulses down to 20 cm^{-1}. A gold coated grating (3 cm x 3 cm, Horiba Scientific GmbH) with a blaze wavelength of 3 μm and 100 lines/mm disperses the infrared light. A f = 100 mm calcium fluoride (CaF_2) lens is used to focus the light onto the end mirror

#191026 - $15.00 USD Received 23 May 2013; revised 26 Jul 2013; accepted 27 Jul 2013; published 20 Aug 2013
(C) 2013 OSA

which reflects the light back to the entrance of the selector. By changing the width of the slit in front of the end mirror the spectral width of the pump pulses can be adjusted continuously down to 20 cm^{-1}. To separate the input and output pulses at the exit of the selector a slight vertical shift is introduced by the end mirror. To maintain collimation for the transverse plane of the pump pulses at the exit and zero dispersion, the distance between lens and grating must be equal to the focal length [29]. For the sagittal plane the distance between lens and end mirror must be the focal length. The energy of the pump pulses also decreases proportionally to the narrower bandwidth. The throughput of the selector is around 85% for the full bandwidth.

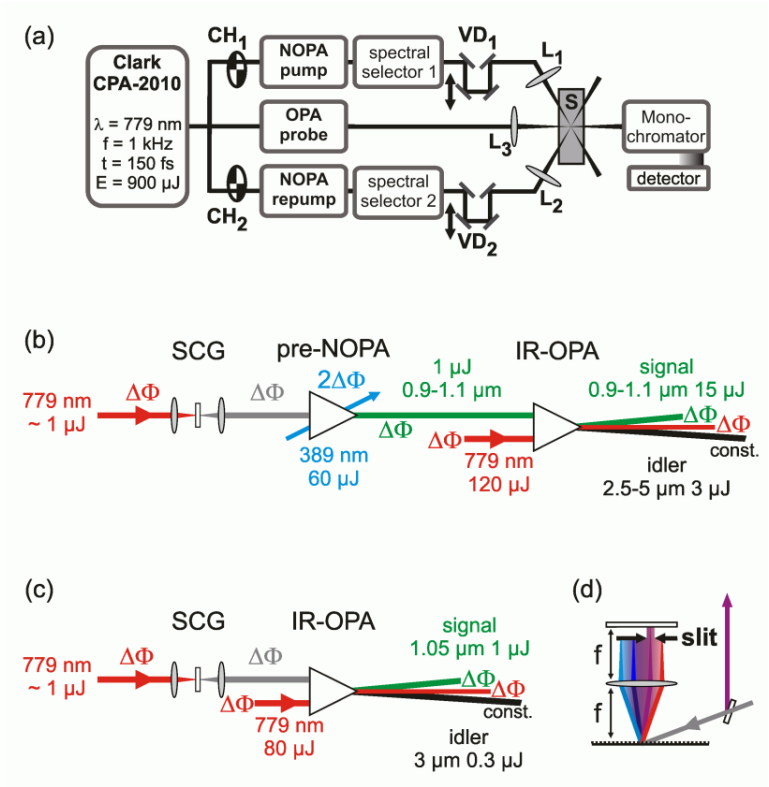

Fig. 1. (a) Schematic representation of the mid-IR pump-repump-probe setup. CH_1 and CH_2 denote chopper wheels, VD_1 and VD_2 are variable delay lines, L are lenses, and S represents the sample. (b) Setup of the hybrid NOPA used to generate the pump and repump pulses including the order of the phase fluctuations (n·ΔΦ). (c) Setup of the probe OPA for the generation of the broadband probe pulses including phase fluctuations. (d) Layout of the *4f* grating spectral selector. To avoid any spatial chirp all infrared OPAs are operated collinearly. The different pulses are shown with a slight angular separation in the figure for a better visualization.

The infrared pump pulses are sent over a motorized linear stage (M-521.DD; Physik Instrumente GmbH; variable delay VD_1 in Fig. 1) to set the delay time between pump and probe light. A hollow retroreflector with gold mirrors (50.8 mm clear aperture, 1 arcsec precision; Edmund Optics Inc.) ensures highest reflectivity and with proper alignment no spatial deviation is found when moving the delay stage over its full range of 200 mm corresponding to 1.33 ns. A mechanical chopper (CH_1) synchronized to the laser is used to obtain alternatingly a pumped and not pumped sample for measuring the transmission changes. The setup for the repump pulses is completely identical to the setup of the pump including the amplifier, spectral selector, chopper (CH_2), and variable delay (VD_2).To obtain adequate probe pulses we generate an infrared continuum in a 4 mm thick YAG plate and amplify the spectral region around 1.1 µm

#191026 - $15.00 USD Received 23 May 2013; revised 26 Jul 2013; accepted 27 Jul 2013; published 20 Aug 2013
(C) 2013 OSA

in a single stage collinear OPA pumped by 80 µJ pulses at 779 nm. The setup is shown in Fig. 1(c). Type I amplification in a 2 mm thick $LiNbO_3$ crystal cut at 45° allows the generation of extremely broadband pulses around 3 µm. The pulse energy of 300 nJ allows a good signal-to-noise ratio. The broad bandwidth and the favorable dispersion properties of silicon or germanium at 3 µm can be used to compress the pulses down to the few-cycle limit. A full characterization of the pump and probe pulses will be presented in the next section. The easy wavelength tuning of the single stage OPA even allows expanding the probe range from 1 to over 5 µm in a stepwise manner. For the shorter wavelengths a BBO crystal can be used. Figures 1(b) and 1(c) additionally show the phase fluctuations of the different pulses which will be discussed in Section 3.

For polarization resolved experiments, it is important to have control over the respective polarizations of all pulses. This is achieved by broadband half-wave plates and polarizers (Thorlabs, nanoparticle linear film polarizer, 1.5 - 5 µm) for all beams. Pump, repump and probe beams are focused into the sample chamber which can be controlled in temperature and pressure. The pump beams are focused with f = 100 mm ZnSe lenses (L_1, L_2), the probe with a 75 mm ZnSe lens (L_3). The advantage of the ZnSe lenses compared to reflective optics is that small angles of only 10° between pump and probe beams can be experimentally realized and that no astigmatism occurs. Additionally, the high refractive index leads to less strongly curved lenses and hence reduced aberrations and an improved beam profile in the focus. The high losses due to the high refractive index can be partially compensated by anti-reflection coatings. The probe pulse is finally coupled into a spectrometer (Chromex 250is) which is set up in a Czerny-Turner configuration. The infrared light is focused into the 200 µm entrance slit via a parabolic mirror with an effective focal length of 50 mm. After an internal collimation in the spectrometer a grating with 300 lines/mm and a blaze wavelength of 4 µm is used to disperse the probe light. At the exit of the spectrometer a nitrogen cooled multichannel infrared HgCdTe detector (IR-3216; Infrared systems development Inc.) is used which offers 32 neighboring pixels with 500 µm width and 2000 µm height. The spectral resolution for one pixel is about 5 cm^{-1} (equal to 5 nm at 3 µm) which enables to cover a wavelength range of around 150 nm at once. The broadband probe pulses cover up to 1,000 nm spectral width which can be covered in a stepwise manner, simply by turning the internal grating of the spectrometer. This means that for capturing the full probe wavelength range no adjustments of the infrared amplifier have to be made. Only the grating in the spectrometer has to be adjusted to change the probe range.

The complete tunability of pump and repump in central wavelength, spectral width, and delay time allows, in combination with the extremely short and broadband probe pulses, pump-repump experiments which can reveal molecular dynamics up to the nanosecond scale with sub-100 fs time resolution and over the spectral region from 1 to 5 µm.

3. Pulse characterization

To perform ultrafast infrared pump-repump-probe experiments adequate infrared pulses must be provided. The probe pulses should cover a wide wavelength range and the pump pulses should be tunable in wavelength and spectral width for a selective excitation of the investigated systems. Our setup described in the previous section allows for the generation of such pulses. Figure 2 shows spectra of the broadband probe pulses (red) with a full width at half maximum (FWHM) of 450 nm (more than 400 cm^{-1}). The width at the 10% level is 900 nm (900 cm^{-1}) and can be employed for transient probing. The Fourier limit (calculated for zero spectral phase) of these pulses is 30 fs which corresponds to just three cycles in the mid-IR. Additionally, spectra of pump pulses with different degrees of spectral confinement (15 100 nm, black and blue lines) are shown in Fig. 2. The spectral width of the pump pulses can be tuned between 20 and 360 cm^{-1}.

The use of few-cycle mid-IR pulses as probe light will significantly improve the temporal resolution. To determine the pulse duration and spectral and temporal phase of our pulses we performed frequency resolved optical gating measurements based on second harmonic

#191026 - $15.00 USD Received 23 May 2013; revised 26 Jul 2013; accepted 27 Jul 2013; published 20 Aug 2013
(C) 2013 OSA

generation (SHG-FROG) for both the pump and the probe light [30]. To be able to perform the SHG-FROG and to set up the *f 2f* interferometer (to show the CEP stability, see below) with available nonlinear crystals, we slightly had to readjust the pump and probe pulses, but the obtained results can be readily transferred to the pulses used in the pump-probe spectroscopy.

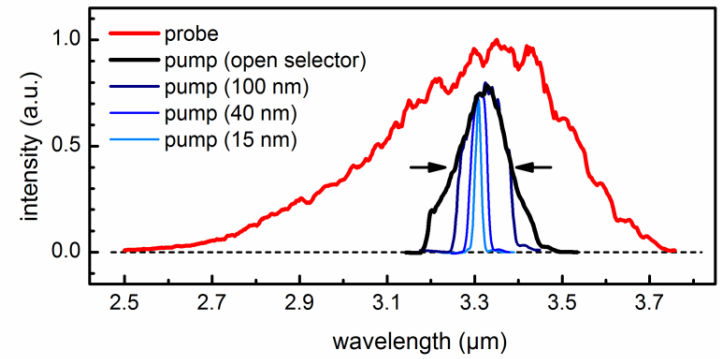

Fig. 2. Spectra of pump pulses with different spectral widths (black and blue). A typical probe pulse spectrum is shown for comparison (red).

Figure 3(a) shows the spectrum and the spectral phase of the probe pulses. The SHG-FROG measurement of the probe pulses yields a pulse duration of 45 fs which is shown in Fig. 3(b). At a central wavelength of 3.15 μm this corresponds to 4.5-cycle pulses. We used germanium plates with different thicknesses to compress the pulses and a 500 μm plate was found to be optimum [13]. The flat phase shows that this straight forward compression is sufficient and no extensive compression schemes must be applied. This is due to the fact that the second and third order chirp accumulated in the visible and near-infrared is flipped because of the use of the idler and then can be compensated by passing through transparent infrared material which has analog dispersion properties as the material in the visible and near-infrared. This increases the energy available at the sample and the stability of the setup. The time-bandwidth product for the probe pulses is 0.55, showing their excellent compression.

The spectrum and spectral phase of typical pump pulses measured without passing the spectral selector are shown in Fig. 3(c). The almost flat spectral and temporal phase (see Fig. 3(d)) shows that the pulses are close to the Fourier limit of 40 fs. The pulse duration of the pump pulse is 51 fs and the time-bandwidth product is 0.52. There is a slight post pedestal which is on the 5% level and also only contains 5% of the pulse energy. When reducing the spectral width with the spectral selector the time-bandwidth product remains nearly the same leading to an increased pulse duration of up to 850 fs for a spectral width of 20 cm^{-1}.

Another pulse property of high interest is the carrier envelope phase (CEP) [31]. In commonly used setups the infrared pulses are generated via difference frequency mixing between signal and idler from a collinear infrared amplifier. Since the pump laser for this infrared amplifier typically does not have a stable CEP, it is not manageable to obtain equal phase fluctuations of signal and idler pulses. Thus, the infrared output of the difference frequency mixing does not have a stable CEP. Since pump and probe pulses in these setups have pulse durations which lead to many cycles of the electric field this is usually of no concern. Nevertheless, if theses pulses would be few cycle pulses, the phase fluctuations would lead to strong variations in the strength of the maximum electric field. And this can affect the experimental response of the investigated system although the nominal pulse energy shows very low fluctuations from pulse to pulse. Therefore a stable CEP is desired when operating with few cycle pulses to ensure a reproducible answer of the studied molecules.

#191026 - $15.00 USD Received 23 May 2013; revised 26 Jul 2013; accepted 27 Jul 2013; published 20 Aug 2013
(C) 2013 OSA

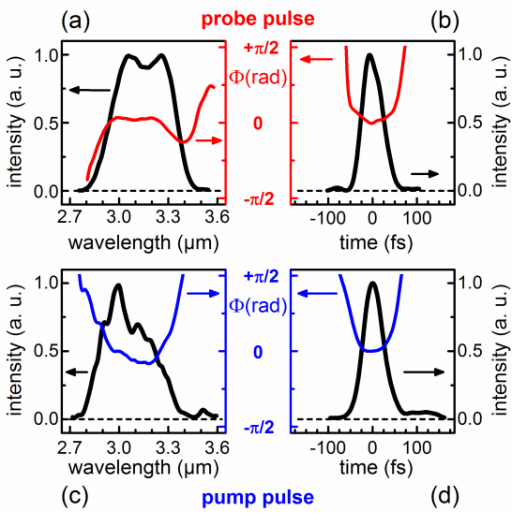

Fig. 3. Spectral intensity with corresponding spectral phase for typical probe (a) and pump (c) pulses. Temporal intensity profile and respective phase of the probe (b) and the pump (d) pulses obtained from SHG-FROG measurements.

In our setup the pump and probe pulses are few cycle pulses and have a stable CEP. This is ensured by the pulse generation setup, although our Ti:sapphire based laser system does not have a stable CEP. In Figs. 1(b) and 1(c) the order of the phase fluctuations for all participating pulses is indicated. The probe pulses are the idler output of a collinear infrared OPA. The seed for this amplifier is generated with the laser light by continuum generation in bulk which does not alter the phase fluctuations and therefore the seed has the same phase fluctuations as the laser light ($\Delta\Phi$). Since the amplifier is also pumped by the laser light with its phase fluctuations of $\Delta\Phi$, the idler pulses have a constant CEP [32]. This is due to the fact that the idler pulses inherit the relative phase difference between signal and pump pulses (besides a constant phase term).

The situation is more complex for the generation of the pump pulses due to the pre-amplifier. There the seed light is a bulk continuum generated with the laser light and therefore it has again the same fluctuations as the laser light ($\Delta\Phi$). The pre-amplifier is pumped by the second harmonic light which has twice the fluctuations of the laser light ($2\Delta\Phi$). This means that the signal pulses of the pre-amplifier have the same phase fluctuations as the seed light and hence the laser light ($\Delta\Phi$) because parametric amplification only adds a constant phase term and does not alter the fluctuations. Furthermore, the idler pulses have the same phase fluctuations ($\Delta\Phi$) because they inherit the phase difference between signal and pump phase fluctuations besides some constant phase terms ($2\Delta\Phi - \Delta\Phi = \Delta\Phi$). The infrared amplifier is pumped by the laser light ($\Delta\Phi$) and since the seed light for this infrared amplifier has the same phase fluctuations ($\Delta\Phi$) the idler pulses are again CEP stable.

To prove the phase stability we set up an *f 2f* interferometer [31] and measured the CEP for both pulses. The setup for the interferometer is shown in Fig. 4(b). We first generate a super continuum in a 4 mm YAG with either the probe or the pump pulses. These continua range down to 500 nm. We frequency double the 1,000 to 2,000 nm part in a thin BBO crystal (SHG) and overlap it with the 500 to 1,000 nm part. The interference pattern is recorded with a fiber coupled spectrometer (HR2000 + ; Ocean Optics). Since the frequency doubled light and the original continuum have different phase fluctuations ($2\Delta\Phi$ and $\Delta\Phi$) a stable interference pattern will only appear if there are vanishing phase fluctuations. This means that the infrared pulses have a stable CEP. Figure 4(a) shows interference patterns between 500 and 900 nm for the pump pulses over three hours. The Fourier transform of the individual spectra enables the

#191026 - $15.00 USD Received 23 May 2013; revised 26 Jul 2013; accepted 27 Jul 2013; published 20 Aug 2013
(C) 2013 OSA

readout of the spectral phase of the pump pulses. The resulting carrier envelope phase of the pump pulses are shown in Fig. 4(d) for the first 90 min (blue line). To show the tunability of the CEP we inserted a 4 mm ZnSe plate after 10 min, removed it after 20 min, and reinserted it after 30 min (light blue line). The standard deviation of the CEP fluctuations is 67 mrad.

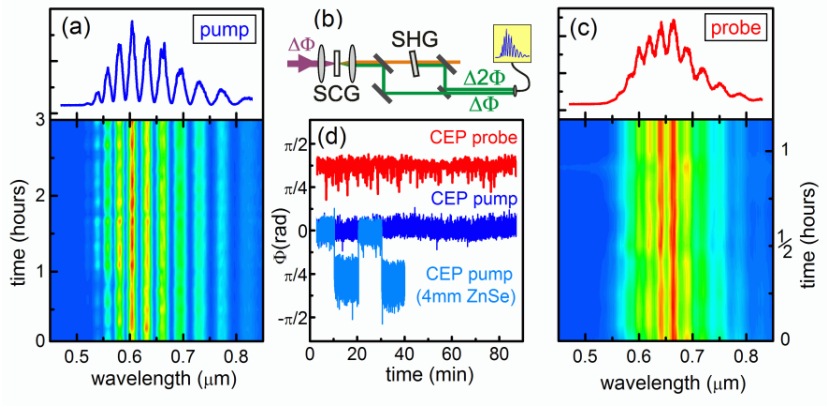

Fig. 4. Spectrum of the long time stable interference pattern from the *f-2f* interferometer obtained with the pump (a) and probe (c) pulses. (b) Setup of the continuum generation and second harmonic based *f-2f* interferometer. (d) Temporal evolution of the CEP of the pump (blue) and probe (red) pulses over 90 min. To demonstrate the CEP control we inserted, removed, and reinserted a 4 mm ZnSe plate after 10, 20, and 30 min (light blue).

Figure 4(c) shows the interference pattern obtained from the probe pulses which was measured over 1.2 hours. The corresponding phase is shown in Fig. 4(d) (red line). For clarity we shifted the CEP of the probe pulse upward. The standard deviation of the CEP of the probe pulses is 97 mrad. The intensity fluctuations of the interference pattern which can be observed in Fig. 4(c) are due to the continuum generation. The energy of the probe pulses is just above the threshold for proper and stable continuum generation. However, long time laser power drifts will lead to temporally unstable white light which explains the observed intensity fluctuations.

Summarizing, we have shown that broadband probe pulses and bandwidth and wavelength tunable pump pulses can be generated on the multi-100 nJ or even μJ level with our simplified setup. The pulse duration of both pulses is very close to the Fourier limit. The utilization of few-cycle IR pump and probe pulses significantly improves the time resolution. Also the carrier envelope phase of both pulses is stable. This ensures the same electric field for all measurement points. After the full characterization of the infrared (re-)pump and probe pulses we next show the potential of the setup by investigating the ultrafast dynamics of isotopically diluted lithium nitrate trihydrate and ice.

4. Validation of the temporal resolution, high sensitivity and the repump capability in $LiNO_3$•(HDO + $2D_2O$) and ice

Aqueous salt hydrates serve as a promising model system for confined water molecules in a very well-defined geometrical arrangement [8,33]. In this study we document our improved measurements of isotopically diluted (5 *M* HDO in D_2O) aqueous lithium nitrate trihydrate. The polarization resolved FTIR spectra in Fig. 5(a) show three different features arising from three different kinds of H bonds, a strong (3385 cm^{-1}), a weak (3536 cm^{-1}) and a bifurcated one (3475 cm^{-1}), leading to parallel and perpendicular signals. This behavior is due to the crystal structure of $LiNO_3$x(HDO + $2D_2O$) with all of its OH groups lying in two mutually normal planes [8]. We performed time resolved measurements at 220 K with the new spectrometer. Figure 5(b) shows the transient change in optical density, measured at various delays after pumping of the OH group engaged in the weak H bond. For short times the ground state is

#191026 - $15.00 USD Received 23 May 2013; revised 26 Jul 2013; accepted 27 Jul 2013; published 20 Aug 2013
(C) 2013 OSA

depleted by the pump pulse, leading to the ground state bleaching (GSB) at 3536 cm^{-1}. Due to the anharmonicity of the OH stretching mode an excited state absorption (ESA) is observed at 3325 cm^{-1}. Both features decay within the first 10 ps. The spectral lineaments remaining after 15 ps are assigned to transient heating of the sample. By fitting Lorentzian distributions to the transient data we achieve a FWHM of 62 ± 10 cm^{-1} for the ESA which is significantly larger than that of the GSB (20 ± 10 cm^{-1}). The analysis of the spectra corresponding to strong and bifurcated H bond shows widths of 125 ± 10 cm^{-1} and 110 ± 10 cm^{-1} for the ESAs (centered at 3140 cm^{-1} and 3260 cm^{-1}) and 30 ± 10 cm^{-1} and 80 ± 10 cm^{-1} for the GSBs [8].

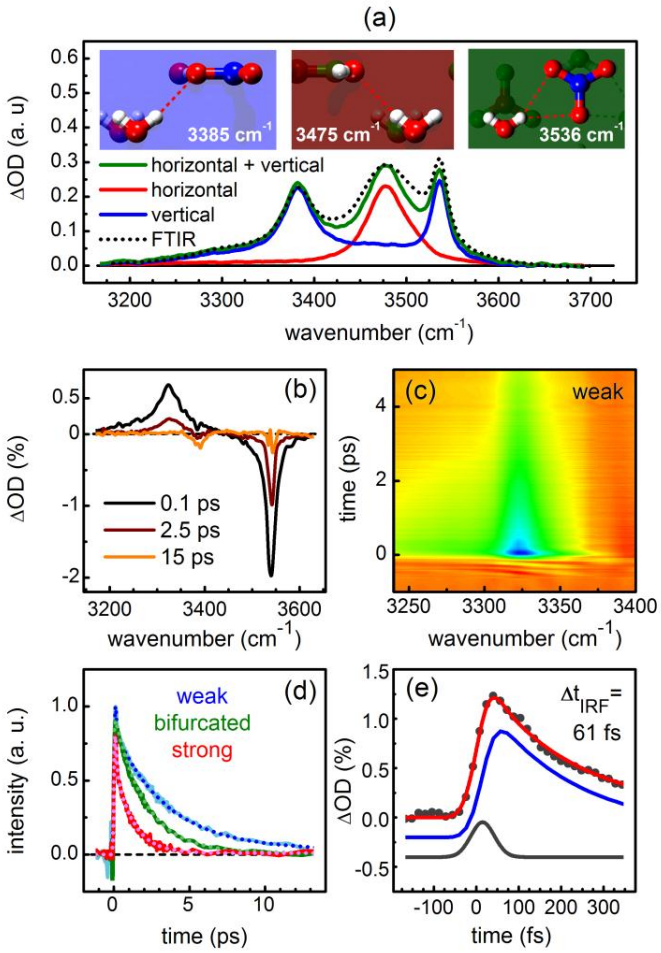

Fig. 5. (a) FTIR spectra of the OH stretching region of the sample. It can be seen how the three resonances are polarization separated due to the orthorhombic structure of the crystal. The corresponding H bonds are depicted in the insets above the spectrum. (b) Transient spectra after excitation of the OH group engaged in the weak H bond. The delay times between pump and probe are 0.1 ps (black), 2.5 ps (brown), and 15 ps (orange). (c) Transient measurement of the weak OH stretching resonance for one detector position. (d) Transient signal of the maximum of the excited state absorption of the weak (blue), bifurcated (green), and strong (red) OH stretching resonances in $LiNO_3$ × (HDO + $2D_2O$) including fits. (e) Transient signal over the first few hundred femtoseconds of an ice sample to demonstrate the ultrafast instrumental response function of 61 fs.

Figure 5(d) shows the temporal evolution of the ESA after excitation of the three individual OH stretching vibrations at the center wavelength of the associated GSB. After a short time of

#191026 - $15.00 USD Received 23 May 2013; revised 26 Jul 2013; accepted 27 Jul 2013; published 20 Aug 2013
(C) 2013 OSA

about 0.3 ps all three signals start to decay exponentially. The fast dynamics observed around delay time zero may be influenced by coherent artifacts that become more significant in the blue shifted part of the ESA approaching the excitation wavelength of the pump beam. The extracted lifetimes for strong, bifurcated and weak H bond are 1.1 ± 0.1 ps, 1.9 ± 0.2 ps and 3.4 ± 0.3 ps. It is noteworthy that the lifetime, just like the strength of the observed H bonds, correlates not only with the red shift of the respective OH stretching, but also with the magnitude of their anharmonicity, indicated by the spectral shift between GSB and ESA. The lifetimes in $LiNO_3$x(HDO + $2D_2O$) are considerably faster than those of isolated HDO monomers that are on the order of 6.8 ps [33 35] and exceed those measured in isotopically diluted ice Ih of about 380 fs [36]. To show the spectral coverage of the 32 pixel detection, Fig. 5(c) presents the transient measurement from 3240 to 3400 cm^{-1} of the weak OH stretching resonance. The entire transient spectrum shown in Fig. 5(b) is obtained by adding the transient measurements from other spectral regions. For this purpose no optical alignment is needed. Just the internal grating of the detection setup has to be rotated.

A first estimation of the temporal resolution is obtained from the FROG measurements of the pump and probe pulses. The FWHM of the convolution between both pulses is 72 fs. Although a possible resolution of 72 fs is already quite competitive, it has to be considered that pump and probe pulses were slightly optimized to perform the FROG and CEP measurements. A better method to determine the temporal resolution of our new spectrometer is the analysis of the transient signals. This is superior to a pure optical determination by cross correlation in a nonlinear crystal as it incorporates not only the pulse durations, but also any possible broadening mechanisms in the interaction region. Furthermore it measures the instrumental response function directly at the sample position. In addition, no restraints as continuum generation for the CEP measurements must be regarded.

The instrumental response function was determined by the increase of the ESA (at 2920 cm^{-1}) in pure H_2O ice excited in the maximum of the OH stretching mode at 3300 cm^{-1}. As shown in Fig. 5(e), we find a time resolution of 61 fs. To fit the experimental trace (dark grey solid circles, red curve for the fit) we included a coherent artifact (grey curve) in addition to the exponentially decaying molecular response (blue curve). The coherent artifact steepens the initial rise and slightly shifts the apparent time zero. If we do not include the artifact in the fit, an even better time resolution would be concluded. The future full analysis will clarify this situation. We can, however, be sure from both the pulse convolution and the spectroscopic measurement that the new spectrometer has a temporal resolution far better than 100 fs.

Extracting the pulse durations from the cross correlation represented by the increase of the measured signal yields time bandwidth products of 0.6 ± 0.1, which are in good accordance with the FROG measurements shown in Section 3. The setup allows to determine transmission changes with just a strength of $1.5 \cdot 10^{-4}$ for short measurement times which corresponds to $6 \cdot 10^{-5}$ OD. The extracted lifetimes are in good agreement with our former measurements that rendered lifetimes of 1.2 ± 0.3 ps, 1.7 ± 0.3 ps and 2.2 ± 0.3 ps for the strong, bifurcated and weak H bond [8]. The deviation of about 1 ps for the weak bond is believed to be a result of an improved fit procedure which explicitly considers the coherent artifact. The artifact is most distinctive in the signal from the OH group engaged in the weak H bond because of the smaller red shift of the ESA. On the other hand the observation in the new recording may be due to the improved signal-to-noise ratio. The extremely high temporal resolution and excellent sensitivity of the setup should be noted. The employed pump pulse energy was just 1 μJ, to avoid artifacts due to excessive heating of the sample. Even this comparatively low excitation energy already results in about 10% excitation of the sample. The signal-to-noise ratio of the measurements is extremely satisfactory. The probe pulses have energies on the order of 100 nJ.

To prove the repump capability of our setup, we performed pump-repump-probe measurements in a 5M HDO in H_2O sample at a temperature of 230 K. The sample thickness was 10 μm, the absorption spectrum of the sample is shown in the lower right hand part of Fig. 6 (black curve, note differing scaling). Due to the low concentration of OD oscillators as

#191026 - $15.00 USD Received 23 May 2013; revised 26 Jul 2013; accepted 27 Jul 2013; published 20 Aug 2013
(C) 2013 OSA

compared to the OH oscillators, the OD stretch band at 2440 cm^{-1} is much weaker than the OH stretch at 3250 cm^{-1}. When we raise the temperature of the sample by 20 K a shifted spectrum is found [37]. The difference between the two spectra is shown as dotted blue line. Since the deposition of energy into one of the high lying stretching modes yields a heating of the sample after the relaxation of the high frequency modes, this difference spectrum represents the transient response at long delay times [37]. Thus, we expect a build-up of the GSB with the instrumental response function, and a subsequent relaxation to a constant signal value, which depends on the probed spectral position and can be deduced from the stationary difference spectrum.

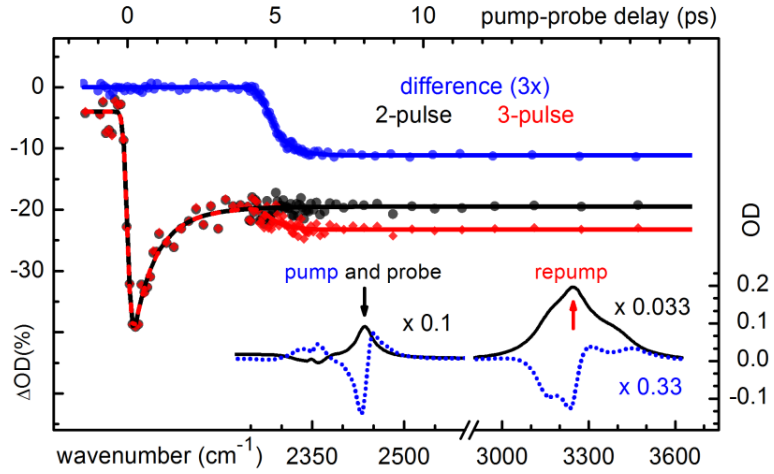

Fig. 6. Transient 2-pulse (black), 3-pulse (blue) and difference signal (red) measured at 2440 cm^{-1} (OD stretching mode) in a 5M HDO in H_2O sample at 230 K. The solid lines are fits according to a simple exponential model as guide to the eye. The symbols represent the raw data. The delay between pump and repump pulse is set to 4.5 ps. At this time the pump-repump-probe curve shows an additional signal due to further heating induced by the repump pulse absorbed by the OH stretching modes. The inset shows the absorption spectrum of the sample (black, note differing scaling factors) and the difference spectrum obtained by heating the sample by 20 K (blue dotted). The spectral position of pump, repump and probe pulse at the OD and OH stretch band are shown as black and red arrows.

For the pump-repump-probe measurements the pump and probe beams were tuned in resonance with the fundamental OD stretching vibration at 2440 cm^{-1} (4100 nm). The repump beam was set to 3250 cm^{-1} (3075 nm), corresponding to the equivalent excitation in the OH regime. The black curve in Fig. 6 shows the pump induced signal. It consists of a ground state bleaching of the OD stretching vibration around zero delay time (sub-100 fs rise). The aforementioned long-term signal is due to a spectral shift of the OD stretching band caused by heating of the sample [37]. An effective signal decay of 1.1 ps is determined from the measurement and sets a lower limit for the heating time. The initial change of optical density is 35%, a very large value for MIR experiments. This shows that the 3 µJ pump energy together with the 100 µm focal diameter in the sample is well sufficient for any transient measurements on water or ice. At 4.5 ps after the pump pulse the repump pulse is applied. The excitation of the OH oscillators is not immediately visible in the OD stretching region, but results in an additional heating of the sample with a new rise time of 0.5 ps, in which the high-lying vibrations located on individual water molecules relax to low lying thermal modes including many molecules. This manifests itself as a clearly visible additional signal in the OD stretching vibration region and can only be observed in 3-pulse experiments.

#191026 - $15.00 USD Received 23 May 2013; revised 26 Jul 2013; accepted 27 Jul 2013; published 20 Aug 2013
(C) 2013 OSA

The blue curve shows the pure repump-induced effect as a difference between the 3- and 2-pulse signal transients. The 3.5% signal increase at 4.5 ps is recorded with excellent signal-to-noise ratio. This is in striking difference to the pure signals with and without repump. From earlier work we know that the pulses of our Ti:sapphire pump system are highly correlated, i.e. subsequent pulses are nearly identical in energy despite a sub-1% overall fluctuation [38]. The repump is blocked on every other shot and thereby the high degree of correlation is optimally used to reduce the fluctuations in the difference signal just as this is done in our broadband UV/Vis spectrometer [39].

Extended 3-pulse experiments are in progress to elucidate this combined action of OD and OH induced heating of ice. The first data presented here not only show the possibility to perform three-color experiments with excellent signal-to-noise. They also demonstrate that the high spectral tunability of the setup in combination with well engineered samples facilitates the interpretation of the data. In this way the influence of overlapping pump-probe signals on top of the pump-repump-probe signal [40] can be minimized.

5. Summary and conclusions

In summary, we have presented a detailed description of a novel setup for IR pump-repump-probe spectroscopy with few-cycle, carrier-envelope phase stable pulses. A Ti:sapphire pump system operating with 1 kHz and a modest 150 fs pulse duration supplies the total pump energy of just 0.6 mJ. The pump and repump pulses are tunable in the range from 2,000 to 10,000 cm^{-1}. The range from 6,250 cm^{-1} downward is covered by the idler of the IR-OPA, the higher energy range by the signal. This enables investigations on a broad variety of vibrations (e.g., OH, NH, CH stretching modes and overtones) important for a plethora of biological and chemical systems. Pump and repump spectral widths are controlled by grating selectors. The pulses generated in this way have a spectral bandwidth between 20 and 360 cm^{-1} and are nearly Fourier limited with a time-bandwidth product of 0.55 ± 0.05. The probe pulses are shorter than 50 fs with an unprecedented spectral width of 450 cm^{-1} (FWHM). A first estimate of the ultrafast instrumental response function as short as 60 fs has been found. This is even shorter than the fastest vibrational dynamics like the relaxation of the OH stretching mode in ice Ih [17,19,41] and will allow the full temporal resolution of these processes.

The complete experimental system, delivering some of the shortest pulses applied for IR spectroscopy to date [12 14,42,43], allows to determine transient absorption changes smaller than 10^{-4} OD. This high sensitivity allows for measurements with extremely low pump intensities, to suppress artifacts due to strong temperature jumps [37]. The shot-to-shot stability of the presented setup is exceptionally high, allowing for high quality measurements with moderate measurement time. A typical time-resolved measurement like the one shown in Fig. 5(c) consists of about 130 time delays and takes around 45 minutes. The transient spectra presented in Fig. 5(b) were recorded by one selected pixel of the IR detector via turning the grating of the spectrometer and each was recorded in only 20 minutes. In the future we will implement and validate a procedure that uses all 32 pixels in parallel and should decrease the recording time by more than an order of magnitude.

With the available pump pulses, we have shown measurements with 8.5% of the molecules in the $LiNO_3$x($HDO + 2D_2O$) sample volume excited. For a thin ice sample even more than half of the OH stretch absorption is bleached. This allows the ready performance of pump-repump-probe measurements with large reasonable signal strength and excellent signal-to-noise. In combination with the extremely high time resolution, re-excitations within the short time window spanned by the lifetime of the initially excited vibrations are possible without temporal overlap of pump and repump pulses. Thus, we can avoid artifacts caused by the temporal overlap between pump and repump pulses. Excitations to higher lying levels will not only enable us to investigate the properties of higher lying vibrational states, but might also serve as a pathway to optically induced chemical reactions like proton transfer initiated by mid-IR pulses, which has not yet been achieved.

#191026 - $15.00 USD Received 23 May 2013; revised 26 Jul 2013; accepted 27 Jul 2013; published 20 Aug 2013
(C) 2013 OSA

The warming up of the system and the fine adjustment of the setup on a day-to-day basis only takes around two hours. The alignment of the invisible mid-IR pulses is greatly alleviated by the fact, that all IR-OPA stages are collinear. Thus, the visible components of the NOPA output can be employed as alignment guides. The low time consumption of both daily alignments and data recording makes the setup very suitable for the investigation of biological, short-lived samples, and enables high data output under routine operation. Finally, it is possible to tune the pump and repump pulses to the visible and UV via minor modifications of the NOPA layouts. This will allow us to carry out UV-pump-IR-probe experiments that can for example provide important information on the mechanisms of UV induced DNA damage or photosynthesis.

Acknowledgments

Financial support of this work by Deutsche Forschungsgemeinschaft through the excellence cluster 'Munich Center for Advanced Photonics' (MAP) and the SFB 749 is gratefully acknowledged.

#191026 - $15.00 USD Received 23 May 2013; revised 26 Jul 2013; accepted 27 Jul 2013; published 20 Aug 2013
(C) 2013 OSA

Appendix A14

A broad and tunable 250- to 430-nm source for microscopy and lifetime measurements by frequency doubling of a 78-MHz-picosecond white-light laser

M. Bradler, F. D. Nielsen, C. E. Eckert, and E. Riedle

Appl. Phys. B, published online, DOI 10.1007/s00340 014 5774 5 (2014)

Reprinted with kind permission from Springer Publishing

Appl. Phys. B
DOI 10.1007/s00340 014 5774 5

Applied Physics B
Lasers and Optics

A broad and tunable 250- to 430-nm source for microscopy and lifetime measurements by frequency doubling of a 78-MHz-picosecond white-light laser

Maximilian Bradler · Frederik D. Nielsen · Carl Elias Eckert · Eberhard Riedle

Received: 2 August 2013 / Accepted: 17 January 2014
© Springer Verlag Berlin Heidelberg 2014

Abstract Broadly tunable picosecond pulses in the UV for nonlinear microscopy and lifetime measurements are not yet readily available. Complex synchronously pumped optical parametric oscillators with subsequent frequency doubling are typically used. We show that direct second harmonic generation of a visible picosecond supercontinuum source at 78 MHz renders pulses easily tunable from 250 to 430 nm. We find that an unexpectedly large numerical aperture and the use of thick crystals increase the efficiency of the frequency doubling process dramatically. The observed spectral width and efficiency are nearly two orders of magnitude larger than predicted by conventional theory. With broadband achromatic doubling, a 130 nm wide spectrum is achieved. Pulse durations of 17 35 ps are found in the UV and an average power between 1 and 70 μW. This qualifies the setup for most UV-based microscopic investigations. As first application, the fluorescence lifetime of two differing conformations of 2-(2′-hydroxyphenyl) benzothiazole is measured.

1 High repetition rate sources of ultraviolet pulses

For many ambitious microscopic investigations involving chromophores absorbing in the ultraviolet (UV), reliable and readily tunable sources of UV pulses at high repetition rate are needed. Applications in chemistry and biology range from fluorescence lifetime imaging, total internal reflection fluorescence microscopy, stimulated Raman scattering, broadband spectroscopy, optical coherence tomography, nano photonics, and flow cytometry, to single molecule and bio-imaging. So far, only few possibilities have been found to generate the desired UV pulses. The simplest scheme uses a mode-locked Ti:sapphire laser that is then frequency tripled [1, 2]. As the Ti:sapphire laser only possesses a limited tunability, the tunability of the UV pulses is typically limited to the range from 250 to 300 nm. Even this performance comes at the price of a high-power green pump laser. When the Ti:sapphire laser is used to pump an optical parametric oscillator, full tunability is reached, however with an even higher system complexity. Still nonlinear frequency conversion is necessary to get to the UV [3]. Similarly, a near-infrared fiber laser can be frequency quadrupled in two consecutive stages [4].

Supercontinuum generation in microstructured fibers seems like the best suited method. It can readily generate a wide range of new frequencies covering the visible and near-infrared region [5 7]. It can be achieved with pulse durations over the entire femto- and picosecond regime, and also the input wavelength can vary over octaves. The favorable zero-dispersion properties of photonic crystal structures allow long fiber lengths and the highly efficient generation of new colors. As a consequence, even energies in the nJ regime out of MHz repetition rate oscillators are sufficient for the spectral broadening [8]. Nevertheless, the shortest observed wavelengths are just below 400 nm. Only for 30 fs pulses with 1 μJ energy from a low repetition rate Ti:sapphire amplifier pulses down to 200 nm have been reported with a gas-filled hollow-core fiber [9, 10]. High repetition rate UV light in the range from 250 to 300 nm as needed for the optical excitation of DNA bases has not been derived from either laboratory or

M. Bradler · C. E. Eckert · E. Riedle (✉)
Lehrstuhl für BioMolekulare Optik, Ludwig Maximilians Universität (LMU), Oettingenstraße 67, 80538 Munich, Germany
e mail: Riedle@physik.uni muenchen.de

F. D. Nielsen
NKT Photonics A/S, Blokken 84, 3460 Birkerød, Denmark

Published online: 15 February 2014

commercial white-light lasers in the MHz regime to the best of our knowledge. In particular, the attractive combination of a picosecond pump laser with a photonic fiber has not been utilized for UV generation.

It is not perspicuous why visible supercontinuum generation has not yet been combined with second harmonic generation (SHG). We can only speculate that the achievable SHG efficiency given by a simple estimate results in too low a value and makes this approach seem futile. In this study we show that tight focusing and the use of a crystal thickness well above the traditional acceptance bandwidth and angle actually renders a very useful level of UV light. We generate tunable as well as extremely broadband pulses from 430 down to 250 nm at repetition rates up to 78 MHz. We frequency double the visible and near-infrared output of a commercially available picosecond white-light laser in a 4-mm-thick beta-barium borate (BBO) crystal in a single-pass geometry. In addition, we also perform achromatically phase-matched SHG [11] to achieve pulses in the UV with more than 100 nm bandwidth. In combination with the high repetition rate, the available UV light is well suited either as pump or probe light. The simple setup allows an easy handling and offers a high robustness. To demonstrate this, we couple the new pulse source with a streak camera and measure the fluorescence lifetime of 2-(2′-hydroxyphenyl) benzothiazole (HBT).

2 Experimental setup and results

As pump source for the generation of tunable UV pulses we use a picosecond continuum source (EXR-15; NKT Photonics A/S) that delivers visible and infrared unpolarized light from 400 to 2400 nm and has an overall output power of 4 W. The high bandwidth is achieved by spectral broadening of a 5-ps pulse at 1064 nm in a nonlinear photonic crystal fiber. The repetition rate of the laser is stepwise tunable from 2 to 78 MHz. The newly generated colors have typical pulse durations of 50 ps. The blue end of the spectrum is delayed by 400 ps as compared to the red end (data measured with a streak camera, not shown). From the established mechanisms of supercontinuum generation in fibers, we have to conclude that the duration of each color is not further compressible [7]. We only use the visible and near-infrared part from 500 to 900 nm yielding 1.5 W of average power (see Fig. 1a). This corresponds to 20 nJ pulse energy over the whole spectrum and a typical spectral energy density of 20 50 pJ/nm. The peak power is about 50 W, quite low for nonlinear frequency conversion. By applying interference filters and black body lamps for calibration, we are able to determine the spectral power density in absolute units [12].

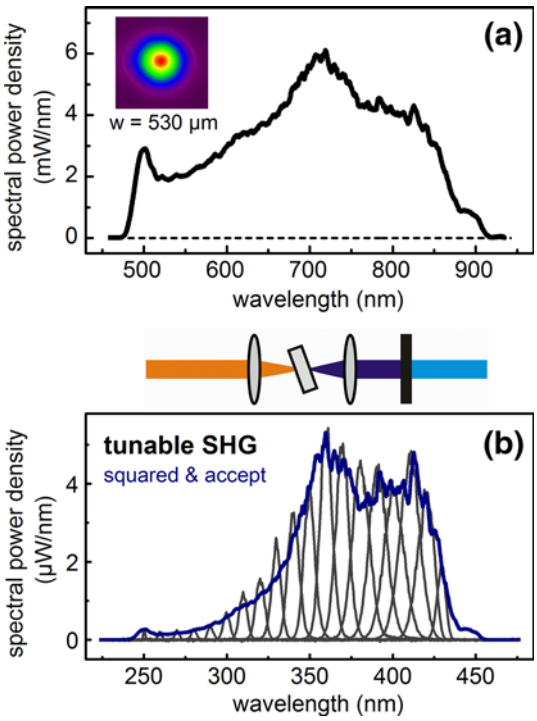

Fig. 1 **a** Spectral power density and beam profile of the visible part of the white light laser. **b** Spectra for tunable SHG with the single path scheme shown between the panels. The *blue curve* shows the spectrum of the continuum source when transferred to the UV considering the acceptance angle and bandwidth. For details of the calculation, see text

The white-light laser has an excellent beam profile (see inset in Fig. 1) with a beam radius of 530 µm (at 600 nm) after the collimator, a divergence of below 5 mrad, and an M^2 between 1.1 and 1.2 for the entire visible region. These properties and the high spatial coherence allow a good focusability close to the Gaussian limit. This is essential for our work as we have to achieve a sizable intensity despite the low peak power. Since the laser light is unpolarized, we use a polarizing beam splitter and therefore effectively 0.75 W of average power for frequency doubling. Since the nonlinear crystal can only utilize linearly polarized light, this splitting does not lower the conversion yield, but decreases the optical load on the crystal. The remaining half of the light can be used as broadband probe light or again for SHG.

Above Fig. 1b the setup for tunable SHG is shown. The laser light is focused with a short focal length lens (AR-coated achromat, $f = 30$ mm) to achieve a small focus and the necessary high intensity for efficient SHG. To further enhance the SHG efficiency, we use a 4-mm-thick type I BBO crystal cut at 32.5°. The used focal length and crystal length will be discussed in section 4. The generated UV light is collimated with a fused silica lens and highly reflecting dichroic mirrors. An α-BBO Glan-laser polarizer and a UG5 colored glass filters are used to separate the UV

from the fundamental light. Additionally dispersive elements like a prism or a grating can be used to further discriminate the UV from the remaining visible light.

The generated UV pulses are tunable from 430 down to 250 nm and have pulse energies up to 900 fJ corresponding to 70 μW average power. This corresponds to an efficiency of only 0.009 % if referring to the entire 1.5 W of the unpolarized white-light laser. The spectral width is found to decrease from 19 THz (11 nm) at 420 nm to 13 THz (3 nm) at 260 nm. Referred to the effectively used spectral region and considering the polarization, the effective efficiency is 0.26 %. Even the 900 fJ do not seem much for users accustomed to kilohertz femtosecond systems. Each pulse, however, still consists of 2×10^6 photons. Combining the high repetition rate of 78 MHz and the fact that even single photons can be readily detected, these pulse energies are well suited for many applications. At 250 nm the pulse energy is 13 fJ which is equal to 1 μW average power and still 16,000 photons per pulse. Already pulse energies as low as 1 aJ were found to saturate the optical transition in single-molecule measurements [13], and 500 photons were found to constitute a pi-pulse excitation [14]. Even though these experiments were performed in the visible, they show that the number of generated UV photons in our setup will be easily sufficient for many applications.

In Fig. 1b spectra for individual settings of the crystal tilt are shown. It is evident that the amount of UV energy generated decreases toward shorter wavelengths much more strongly than the pump spectral distribution. The blue curve in Fig. 1b shows a simulation of the UV power spectral density. We translate the wavelength scale from Fig. 1a to the UV according to the "frequency doubling" and square the spectral power due to the quadratic intensity dependence of SHG. In addition, the varying acceptance angle and bandwidth of the frequency-doubling process is explicitly taken into account. Both of them become smaller for shorter wavelengths and therefore allow less efficient doubling. All values are calculated with the module Q-Mix from the nonlinear optics program SNLO [15]. The SHG power was estimated with 2D-mix-SP also from SNLO [15]. For further details see section 3. Cross-terms can be neglected due to the strong chirp. When the blue curve is compared to the pulse energy generated for various UV wavelengths, a nearly perfect match is found. As a result we can be confident that the standard description of SHG is a good starting point to describe our observations.

The pulse-to-pulse fluctuations at 78 MHz are measured for the total output in the 500 850 nm region to 2.2 % rms. For a small spectral region around 700 nm we find a stability of 7.7 %. The lower fluctuations for the total output originate from the use of the 1064-nm pump source. Since the infrared light is shifted to other colors and there is no

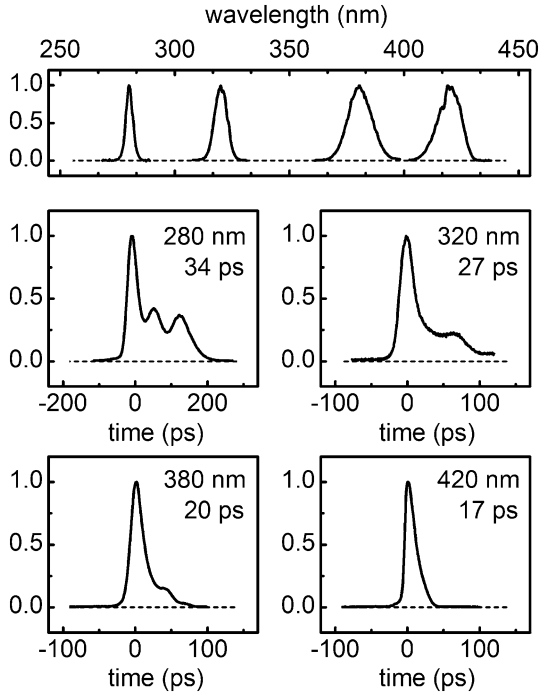

Fig. 2 Spectra of UV pulses at selected wavelengths and measured temporal intensity profiles

intensity-dependent loss in the fiber for the 2.2 % fluctuation, the shot-to-shot stability of the entire continuum is high. On the other side, the fluctuations for a small spectral region are much higher because the power spectra strongly vary from shot-to-shot due to the modulation instability effects observed for long pump pulses [7]. For the frequency doubled light at 350 nm, the single-shot fluctuations are determined to 13.5 %. Although these values seem high for users of standard mode-locked lasers, one has to bear in mind that the high repetition rate helps to obtain a much lower fluctuation for even small averaging times if the fluctuations are statistical. If for instance the averaging time is set to 1 ms at the full 78-MHz repetition rate, the fluctuation of the 350-nm light should decrease down to 0.05 % rms according to Poisson statistics. We indeed find this enhanced stability and can conclude that the fluctuations of the white-light laser are largely statistical. It should also be kept in mind that in applications like lifetime measurements moderate fluctuations do not play any role.

Besides the spectrum, energy, and stability of the UV source, we also measure the actual pulse duration with a streak camera (C5680; Hamamatsu Photonics). Pulse durations (FWHM) from 35 ps for shorter wavelengths (280 340 nm) to 17 ps for longer wavelengths (360 440 nm) are found (see Fig. 2).

This is in good agreement with the typical pulse shortening during the SHG process. At the shorter wavelengths

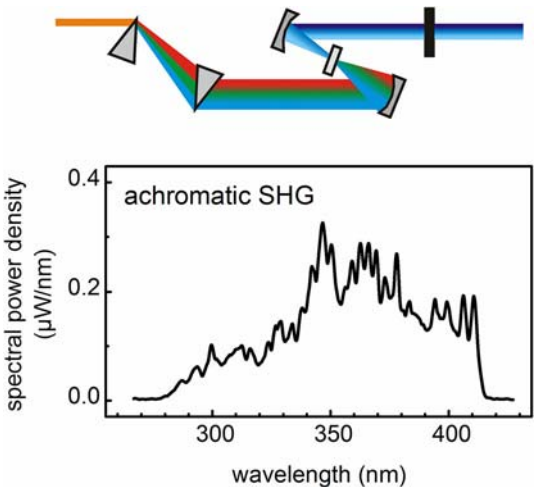

Fig. 3 Setup and spectrum for achromatic SHG

shoulders at later times are seen. These are already suggested in the corresponding visible spectral range. Future improvements in the white-light laser should be able to eliminate these afterpulses.

Figure 3 shows the setup for achromatic frequency doubling adapted from our previous femtosecond setup [11, 16]. First, the pulse is laterally dispersed with a pair of fused silica prisms (apex angle of 68.7°) with a tip distance of 150 cm. Then, the light is focused with an off-axis parabolic mirror onto a 4-mm-thick BBO crystal (type I, 32.5°). The mirror has a parent focal length of 35 mm and is designed for 45° deflection. An identical mirror is used to collimate the UV light, and the above-described methods were used to separate the UV and visible light.

The obtained spectrum is shown in Fig. 3 and has an integrated pulse energy of 380 fJ. This corresponds to an average power of 30 μW and roughly 500,000 photons per pulse. The extremely high bandwidth of 130 nm (10 % level) in combination with the MHz repetition rate favors such pulses as broadband continuum probe in the UV. In our previous work [16] we also show how to collimate the beam and manage the spatial dispersion. Again, we measured the pulse-to-pulse fluctuation. Since we frequency double nearly the entire spectrum that is more stable than parts at selected wavelengths, the achromatically doubled light is also more stable with 3.8 % rms at the single-shot level.

3 Modeling of the frequency conversion

The experimental results show that quite sizable amounts of UV light can be generated by single-pass SHG. For amplified femtosecond pulses at the μJ level such conversion is quite routine, and even for picosecond nJ pulses it has been reported quite early [2]. However, for a picosecond white-light source operating at tens of MHz, it has not been demonstrated. The question is whether this possibility has just so far been overlooked or whether expectations from standard SHG models fail for the optimized conditions used in our work.

To clarify these points, we perform simulations of the frequency doubling with the module 2D-mix-SP of SNLO [15]. The code uses established descriptions of $\chi^{(2)}$ three-wave mixing. To ensure the reliability of the obtained values under our experimental conditions, we first model the frequency doubling of a 1-kHz femtosecond Ti:sapphire system and find excellent agreement. For the investigated picosecond system, the extreme bandwidth of the white-light laser leads to a more complex situation. It is not appropriate to assume the entire pulse energy, since most wavelengths are certainly not frequency doubled. In addition, only half the average power shown in Fig. 1a is to be used due to the polarization selection. Within the plane-wave approximation, we can calculate the acceptance bandwidth for a selected crystal thickness. For 700-nm input wavelength and a 4-mm BBO crystal, this amounts to 0.8 THz (1.3 nm). As a result, the effective pulse energy of only 42 pJ in a roughly 50 ps pulse is available for conversion. The simulation predicts an UV pulse energy of only 1 fJ. Observed are 500 fJ.

At the same time we find an UV bandwidth of up to 22 nm at 350 nm compared to the predicted width of 0.5 nm. This excess by a factor of 40 hints at the relevant mechanism. When we use the much broader bandwidth that is necessary to generate the observed bandwidth in the UV, we obtain an effectively usable pulse energy of 1.7 nJ and predict an UV energy of 500 fJ. This value strikingly matches the experimental observation. The initial calculation assumes a 4-mm-thick crystal in the plane-wave approximation. The obviously too low acceptance bandwidth and efficiency are predicted. Since the SHG scales with the square of the intensity, a tight focus is used, and this leads to a focusing geometry that spans a much larger angle than the nominal acceptance angle for the 4-mm crystal. Therefore, wavelengths slightly off the nominal phase-matching condition can still be utilized for the SHG process. We believe that it is this effect that increases the UV bandwidth and the efficiency so drastically. A way too large SHG bandwidth in thick crystals has already been reported for single-pass SHG of femtosecond pulses [17]. To further study the hypothesis, we describe an investigation of the influence of the numerical aperture in the following section.

4 Influence of numerical aperture, crystal thickness, and spatial chirp

A major challenge in the nonlinear conversion of picosecond pulse trains of limited average power in the range of

1 W is the low peak power. This is particularly true for high repetition rate systems needed for applications like microscopy or single-molecule investigations. In our setup the peak power is only 260 W integrated over the whole spectrum. The most efficient method to achieve high enough intensities for nonlinear effects and hence SHG with such low peak powers is tight focusing. Therefore, we use an achromat with a very short focal length of 30 mm. Due to the M^2 value of 1.1 to 1.2 of the supercontinuum source, we are able to achieve a beam waist diameter of a few μm in the focus leading to a peak intensity of 2 GW/cm^2. This is still much less than the 50 GW/cm^2 used in femtosecond SHG. To achieve efficient SHG with such low intensities, long crystals are needed. Both of these conditions the long crystal and the high numerical aperture (NA) seem to be counterproductive for frequency doubling due to the resulting limited acceptance bandwidth and acceptance angle derived in the standard description of SHG. The full acceptance angle predicted for a 4-mm BBO crystal used at 700 nm is 1.2 mrad corresponding to an NA of just 0.6×10^{-3}. The typical numerical apertures (NA) used in our experiments are considerably higher and range from 12×10^{-3} to 150×10^{-3}.

Figure 4a shows SHG spectra centered at 350 nm for a variation in the NA. The different values for the numerical aperture were realized by enlarging the beam size at the achromat by propagation over a distance of a few meters. The dotted line shows the theoretically expected spectrum according to the acceptance bandwidth and angle of the 4-mm BBO crystal in the plane-wave approximation. Figure 4b shows the obtained average power and spectral width. The UV power maximizes at about NA $= 60 \times 10^{-3}$. For NA $= 150 \times 10^{-3}$ the obtained spectrum has a spectral width of 22 nm and is therewith 40 times broader than expected. It is interesting to note that the NA found to optimize the SHG yield and the resulting spectral width are larger by a factor of 100 and 40 than the predictions. This matches the observed increase in SHG yield over the plane-wave modeling. We interpret this as strong evidence that our picture described above, that the efficiency results from the utilization of a large spectral width, is correct.

The tight focusing and hence high numerical aperture already lead to partially achromatic phase-matched second harmonic generation [17]. The phase-matching angle for frequency doubling of 350 nm in BBO is 33.7°. The NA of 0.15 leads to an external range of input angles of 17° which corresponds to a variation over 10° inside the BBO due to refraction at the entrance surface. Since the crystal and the Rayleigh length have the same magnitude, the different transversal parts of the beam effectively see a different phase-matching angle. This allows other wavelengths beside 700 nm to be frequency doubled and enlarges the effective acceptance bandwidth. It should be noted that the plane phase front in the focus does not imply a uniform wave vector direction perpendicular to the phase front. The highly reduced transversal size necessitates a spread of the wave vector direction according to the uncertainty principle. The spread is just the spread that is generated by focusing the originally collimated beam.

The Rayleigh range (twice the Rayleigh length) and beam waist radius for the range of NA values shown in Fig. 4 are summarized in Table 1. Outside the Rayleigh range, the intensity and hence the SHG efficiency are strongly decreasing. As the NA is initially increased, the higher intensity increases the overall efficiency. Eventually, however, the effective interaction range decreases so strongly that the efficiency decreases again. The maximum of the efficiency is obtained at an NA of 0.060. From the NA we can also qualitatively deduce the obtained spectral shape of the UV light. As a rule of thumb, we see that the full width half maximum (FWHM) in nanometer is 150 times the numerical aperture. This directly follows from the larger range of phase-matching angles seen by the strongly focused beam.

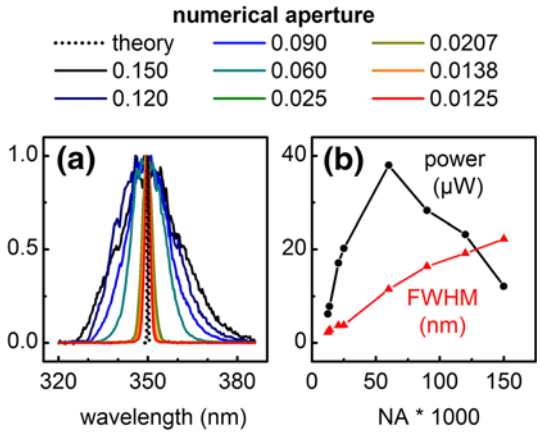

Fig. 4 **a** SHG spectra centered at 350 nm for varied numerical aperture (NA). The *dotted line* shows the expected spectrum (acceptance bandwidth) for a 4 mm BBO crystal in the plane wave approximation. **b** shows the obtained average power and spectral width of the UV light

Table 1 Beam waist radius w_0 and Rayleigh range (twice the Rayleigh length) for various numerical apertures (NA) used for frequency doubling

NA	w_0 (μm)	Rayleigh range (mm)
0.0125	17.8	2.85
0.0138	16.2	2.34
0.0207	10.8	1.04
0.025	8.9	0.71
0.06	3.7	0.12
0.09	2.5	0.06
0.12	1.9	0.03
0.15	1.5	0.02

Also the correct choice of the crystal length is crucial for efficient doubling. We tested a 1-, 2-, and 4-mm-thick BBO crystal under identical focusing conditions for frequency doubling. We obtained a nearly linear correlation of the efficiency to the crystal length while maintaining a constant spectral width of the UV light. An ever longer crystal did not improve the SHG efficiency because the intensity is getting too low for SHG near the borders of the long crystal. The 4-mm crystal length is close to the optimum, because when moving the crystal slightly back and forth from the optimum position, the SHG yield does not decrease. It is worthwhile to mention that the optimum position for the 4-mm BBO is not reached if the focus is in the middle of the crystal but slightly before the middle. The exponential dependence of the SHG on the crystal length is then optimally combined with the different intensity levels at the beginning, middle and end of the crystal.

Another important point that has to be mentioned is the beam profile and spatial chirp since partially achromatic frequency doubling is performed. Each spectral component is generated in a differing part of the beam. Therefore, the diverging beam has a pronounced spatial chirp. This is shown in Fig. 5. The gray lines show the spectrum for different parts of the beam. The spatial chirp occurs in the plane where the phase-matching angle is changing. In the orthogonal direction, no spatial chirp occurs. When focusing the diverging UV light and hence imaging the UV generation region, again an elliptical focus is obtained but without any spatial chirp (see Fig. 5b inset).

The remaining ellipticity is due to the spatial walk-off in the birefringent crystal. For larger spectral widths of the UV light also the ellipticity increases. To recollimate the UV beam properly and to obtain a round and spatial chirp-free focus, a setup similar to achromatic SHG with two CaF_2 prisms [16] has to be used.

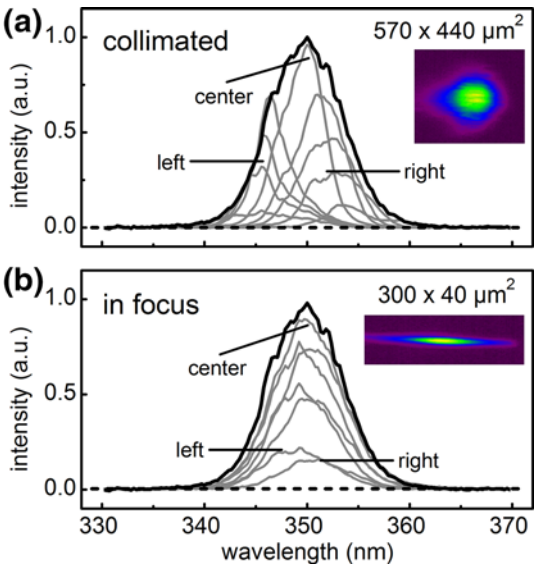

Fig. 5 Beam profile and spatial chirp of UV light for the collimated UV light (**a**) and in the focus (**b**)

5 Measurement of the fluorescence lifetime of HBT

As first application of the generated UV light, we measure the fluorescence lifetime of HBT. This molecule is of high interest since ultrafast photochemical processes such as proton transfer, coherent skeletal motion and internal conversion, and their interplay can be monitored [18 20].

To determine the fluorescence lifetime, we excite HBT at 330 nm and measure the fluorescence with a streak camera (C5680; Hamamatsu Photonics). No spectrograph is used to select a chosen range of emission wavelengths. Instead we use a combination of a WG345 and UG5 colored glass filter (Schott AG) to select a range from 345 to 400 nm and a GG475 filter to select emission longer than 475 nm. The emission of HBT after the ultrafast excited state proton transfer is found in the range from 470 to 600 nm [19]. The proton transfer is inhibited by substitution of the intramolecular hydrogen bond by a hydrogen bond to an ethanol molecule, and the emission is observed from 360 to 410 nm [20]. Since a mixture of both forms is present, dual fluorescence is observed. To determine the excited state lifetime of the two conformations, the emission decays in the two spectral ranges are measured.

The large number of photons from our setup and the high repetition rate allow a strong fluorescence signal and a good signal-to-noise ratio. We simply focused the 330-nm beam into a 1-mm cuvette containing the HBT solution and imaged the resulting emission onto the entrance slit of the streak camera with a $f = 50$ mm, 1″-diameter fused silica lens. We even had to significantly decrease the excitation power to not saturate the streak camera used in photon counting integration mode. Figure 6 shows the measured fluorescence decay around 500 nm (green solid line) and 380 nm (dark blue solid line). The two different signals are

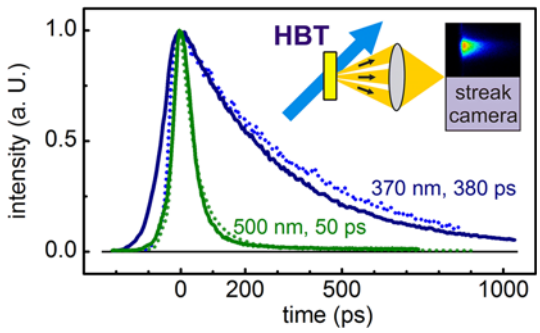

Fig. 6 Fluorescence lifetime of HBT in ethanol after excitation with 17 ps pulses at 350 nm

in excellent agreement with previous measurements (shown as dotted green line for 500 nm and dotted blue line for 370 nm) performed with selective femtosecond excitation at 1-kHz repetition rate.

The described example shows that the simple setup consisting just of the turn-key supercontinuum laser, a singlet lens, a doubling crystal, two more lenses and a cuvette for the "spectroscopy" and a streak camera allow determining picosecond dynamics of complex molecules. Each decay curve corresponds to only an averaging time of less than one minute. A variation in excitation wavelengths can be made by just tilting the doubling crystal.

6 Summary and concluding remarks

We have developed a tunable and broadband source of picosecond ultraviolet light at high repetition rates of up to 78 MHz. This is achieved with a commercially available supercontinuum laser and single-pass frequency doubling. Pulses from 430 down to 250 nm with average powers of up to 70 μW corresponding to two million photons per pulse are obtained. The conditions for optimum SHG were investigated and the proper crystal thickness and focusing geometry determined. The necessary tight focusing and hence high numerical aperture of 0.06 are far above the classical acceptance angle of the thick BBO crystal and lead to pseudo-achromatic phase matching. Pulses with spectral widths up to 30 nm are obtained from a setup consisting only of an achromatic lens and a crystal. The long crystal length of up to 4 mm does not limit the spectral width but increases the SHG efficiency and the average power of the UV light. The inescapable initial spatial chirp of SHG can be corrected either by focusing the light again onto a sample or by a proper setup with dispersive elements. Typical pulse durations of 17 to 35 ps are achieved in the UV. As first application, we measured the fluorescence lifetime of HBT to 380 and 50 ps with time-correlated single-photon counting. The longer time corresponds to the $S_1 \rightarrow S_0$ relaxation of the keto-type HBT, while the shorter to the relaxation of the intermolecularly hydrogen bonded enol-type HBT.

The remarkably simple setup with a single-pass doubling crystal allows fast and straightforward experiments. This favors the setup as unique tool for studying ultrafast processes with tunable and broadband UV light on the picosecond timescale with MHz repetition rates. In combination with well-established detection techniques like streak cameras or single-photon counting, even smallest signals can be resolved with a good signal-to-noise ratio. And since the setup only consists of one adjustable element the frequency doubling crystal it can easily be motorized to perform series of measurements in shortest time. If several UV sources are needed, one can use the two polarization components of the continuum source, separate wavelength regions, or reuse the not-yet-frequency-doubled light again. Due to the long pulses and hence low peak power and the resulting moderate SHG efficiency, the not-doubled light has nearly the same advantageous properties and power. Disturbing effects found for much shorter pulses such as self-focusing or back conversion are not present. The presented concept is not limited to the UV, and also infrared continuum sources can be transferred to the visible [21, 22]. Besides second harmonic generation, also sum or difference frequency mixing should be possible and therefore will further extend the accessible wavelength regions. This unique and easy manageable light source with high spatial coherence should allow many innovative experiments that so far have not been feasible. The system is ideally matched to microscopic techniques and single-molecule investigations.

Acknowledgments We are grateful to N. Krebs and I. Pugliesi for valuable experimental help and fruitful discussions. We thank S. Häuser and C. L. Thomsen from NKT photonics for access to their laser systems and cooperative experiments and T. Franzl from Hamamatsu Photonics for supplying the measurements with highly valuable equipment. The work is supported by the DFG Cluster of Excellence: Munich Centre for Advanced Photonics and the SFB 749.

References

1. R.J. Ellingson, C.L. Tang, Opt. Lett. **17**, 343 (1992)
2. A. Nebel, R. Beigang, Opt. Lett. **16**, 1729 (1991)
3. M. Ghotbi, A. Esteban Martin, M. Ebrahim Zadeh, Opt. Lett. **33**, 345 (2008)
4. X. Zhou, D. Yoshitomi, Y. Kobayashi, K. Torizuka, Opt. Lett. **35**, 1713 (2010)
5. P.J. St. Russell, Science **299**, 358 (2003)
6. P.J. St. Russell, J. Lightwave Technol. **24**, 4729 (2006)
7. J.M. Dudley, G. Genty, S. Coen, Rev. Mod. Phys. **78**, 1135 (2006)
8. T.A. Birks, W.J. Wadsworth, P.J. St. Russell, Opt. Lett. **25**, 1415 (2000)
9. N.Y. Joly, J. Nold, W. Chang, P. Hölzer, A. Nazarkin, G.K.L. Wong, F. Biancalana, P.J. St. Russell, Phys. Rev. Lett. **106**, 203901 (2011)
10. J.C. Travers, W. Chang, J. Nold, N.Y. Joly, P.J. St. Russell, J. Opt. Soc. Am. B **28**, A11 (2011)
11. P. Baum, S. Lochbrunner, E. Riedle, Opt. Lett. **29**, 1686 (2004)
12. M. Bradler, P. Baum, E. Riedle, Appl. Phys. B **97**, 561 (2009)
13. R. Hildner, D. Brinks, N.F. van Hulst, Nat. Phys. **7**, 172 (2010)
14. I. Gerhardt, G. Wrigge, G. Zumofen, J. Hwang, A. Renn, V. Sandoghdar, Phys. Rev. Lett. A **79**, 011402 (2009)
15. SNLO nonlinear optics code, available from A.V. Smith, AS Photonics, Albuquerque, NM, "http://www.as photonics.com"
16. P. Baum, S. Lochbrunner, E. Riedle, Appl. Phys. B **79**, 1027 (2004)
17. S.H. Ashworth, M. Joschko, M. Woerner, E. Riedle, T. Elsaesser, Opt. Lett. **20**, 2120 (1995)

18. M. Barbatti, A.J.A. Aquino, H. Lischka, C. Schriever, S. Lochbrunner, E. Riedle, Phys. Chem. Chem. Phys. **11**, 1406 (2009)
19. W. Frey, F. Lärmer, T. Elsaesser, J. Phys. Chem. **95**, 10391 (1991)
20. S. Mintova, V. De Waele, M. Hölzl, U. Schmidhammer, B. Mihailova, E. Riedle, T. Bein, J. Phys. Chem. A **108**, 10640 (2004)
21. F. Baronio, M. Conforti, C. De Angelis, M. Andreana, A. Tonello, V. Couderc, Laser Phys. Lett. **9**, 359 (2012)
22. F. Baronio, M. Conforti, C. De Angelis, M. Andreana, A. Tonello, V. Couderc, Opt. Fiber Technol. **18**, 283 (2012)

Appendix A15

Sub-20 fs μJ-energy pulses tunable down to the near-UV from a 1 MHz Yb-fiber laser system

M. Bradler and E. Riedle

Opt. Lett. **39**, 2588 – 2591 (2014)

Reprinted with kind permission from the Optical Society of America (OSA).

Sub-20 fs μJ-energy pulses tunable down to the near-UV from a 1 MHz Yb-fiber laser system

Maximilian Bradler and Eberhard Riedle*

Lehrstuhl für BioMolekulare Optik, Ludwig Maximilians Universität München, Oettingenstrasse 67, 80538 Munich, Germany
**Corresponding author: eberhard.riedle@physik.uni muenchen.de*

Received February 25, 2014; accepted March 24, 2014;
posted March 25, 2014 (Doc. ID 207206); published April 18, 2014

Optical parametric amplifiers render widely tunable ultrashort pulses, but for full spectral coverage, complex mixing schemes are needed. In particular, the blue and near UV part of the spectrum is not directly reached with the 800 nm pump from Ti:sapphire systems or the 1030 nm pump of Yb based lasers. We combine third harmonic pumping at 343 nm with seeding by a second harmonic (SH) pumped continuum to tune a noncollinear optical parametric amplifier down to 395 nm. Together with a SH pumped branch, the full range from 395 to 970 nm is covered with 20 fs pulse length or less. Pulse energies up to the μJ level with an average power of up to 200 mW at 200 kHz and 480 mW at 1 MHz are achieved. With additional frequency doubling, the full range down to 210 nm is reached without gap. Two photon absorption in the amplifier crystal is discussed as the critical issue in UV pumped systems. © 2014 Optical Society of America

OCIS codes: (190.2620) Harmonic generation and mixing; (190.4410) Nonlinear optics, parametric processes; (230.4480) Optical amplifiers; (320.7110) Ultrafast nonlinear optics.
http://dx.doi.org/10.1364/OL.39.002588

The generation of energetic ultrashort pulses at high repetition rates that are fully tunable in the ultraviolet (UV), visible, and near-IR (NIR) is still a challenging task. Many applications, such as transient spectroscopy, material processing, nonlinear imaging, diffraction of single electrons, high-harmonic generation, or resonant plasmonic field enhancement, benefit from such pulses. The high repetition rate ensures a good signal-to-noise ratio, enhances the total flux, and leads to reduced acquisition and measurement times. The tunability is needed to excite the samples resonantly and at the lowest possible flux to avoid rapid degradation. Such pulses can be generated by synchronously pumped optical parametric oscillators [1–4]. Modest pulse energies result from comparatively complex setups.

A broadly used technique to obtain high-energy pulses at sub-MHz repetition rates is optical parametric amplification of continuum seed light. It allows tunability in the visible [5–8] and shortest pulse durations [9]. Only a few reports are found on the extension to UV wavelengths [10–12]. The early developments were based on Ti:sapphire pump systems, and improvements like noncollinear phase-matching were pioneered with kHz systems [13]. The tuning range for a noncollinear optical parametric amplifier (NOPA) pumped by the second harmonic (SH) of a Ti:sapphire system ranges from 450 to 720 nm and from 860 nm into the NIR. The gap around the 800 nm pump is caused by the distorted seed light and can be filled by a two-stage NOPA with intermediate continuum generation [14]. Second harmonic generation (SHG) also renders a gap around 400 nm that is laborious to fill.

Recently, the development of femtosecond lasers has turned to Yb-based active media, because higher average powers are achievable with diode laser pumping. The consequences are a central wavelength around 1030 nm and pulse durations from hundreds of femtoseconds to picoseconds. Pumping a NOPA with the SH at 515 nm [7] and BBO as active material, the shortest output wavelength is 620 nm. With third harmonic (TH) pumping [8], 387 nm should be reachable, but this output was not yet demonstrated due to lack of suited seed light.

We now show with a Yb-based system at up to 1 MHz as pump that the sub-400 nm range can be reached if a SH pumped continuum is used as seed and combined with TH pumping at 343 nm [see Fig. 1(a)]. We generate fully tunable blue pulses with Fourier limits in the 10 fs range. Together with a SH pumped NOPA seeded by a fundamental pumped continuum, a tuning range from 395 to 950 nm and with just an additional SHG stage a gap free tuning range from 210 nm into the NIR results.

As pump source, we use a fiber amplifier (Tangerine fs; Amplitude Systems Inc.) that delivers 300 fs pulses at 1030 nm and 20 W output with high beam quality. We use pulse energies of 20 μJ at repetition rates between

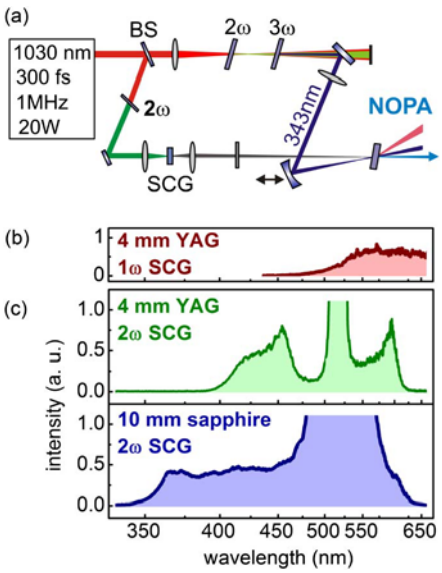

Fig. 1. (a) TH pumped NOPA seeded by the 2ω pumped continuum (SCG). (b) Continuum generated in a 4 mm YAG and 1030 nm pumping. (c) Continuum from a 4 mm YAG and a 10 mm sapphire plate with 515 nm pumping.

 © 2014 Optical Society of America

200 kHz and 1 MHz. Roughly 3 μJ are split off for continuum generation with a half-wave plate and a thin film polarizer (BS). With weak focusing of the remaining 1030 nm light ($f = 250$ mm at 2 mm beam diameter), 2 ω and 3 ω light can be generated efficiently by placing the SHG crystal (BBO type I, 23.0°, 700 μm) slightly before and the third harmonic generation (THG) crystal (BBO type II, 62.8°, 1.5 mm) slightly behind the focus [8]. The differing group velocities of the pulses during the generation are compensated by the proper choice of the crystal type and length. Dichroic mirrors separate the 343 nm TH pump light from the 515 nm SH and the fundamental. In the TH pumped NOPA, 3.5 μJ of UV light are used to amplify the seed pulses. The short pump wavelength allows amplification down to below 400 nm before idler absorption in the BBO crystal becomes relevant. Even at a 400 nm, very broadband phase matching is predicted.

To reach the near-UV and blue wavelengths, a suited seed light source must be provided. Bulk continuum generation with 1030 nm pulses only ranges down to slightly below 500 nm [7,15] [see Fig. 1(b)]. To utilize the potential blue tuning range, we generate a SH-pumped continuum [16–18] and use it as seed. The 3 μJ pulses are frequency doubled in a second, identical SHG crystal and 0.7 μJ green result. Spectra from a 4 mm YAG and 10 mm sapphire ($f = 50$ mm focusing) are shown in Fig. 1(c). A dielectric filter (B-51; Optics Balzers) is used to suppress the 515 nm pump light. A $f = 30$ mm fused silica lens recollimates the continuum and focuses it slightly before the amplifier crystal. The exact size at the BBO crystal has to be carefully adjusted to match it with the pump spot size for best use of the seed light.

The amplifier crystal in the TH pumped NOPA is a type I BBO crystal, cut at 32.5°, with 3 mm length. The noncollinear geometry in combination with the long pulse duration of 170 fs for the 343 nm pump light allows the generation of pulses with Fourier limits from 20 down to 10 fs [green line in Fig. 2(a)]. Tunable pulses from 395 to 640 nm [Fig. 2(b)] with energies of above 1 μJ in the maximum, but at least 0.5 μJ over the entire range, are obtained [black line in Fig. 2(a)]. If very clean pulses are needed around 515 nm, the 1030 nm pumped seed light should be used. For the tuning range, the noncollinearity angle has to be adjusted from 2° to 4.5° (internal) and the phase-matching angle from 28° to 37°. The choice of angle was guided by standard phase matching calculations and tweaked experimentally [8,13,14].

The 640 nm pulse is close to the degeneracy point and the needed noncollinearity is 3.0° (4.8° external). Operation close to degeneracy allows a large amplification bandwidth. Tuning toward the UV, the documented feature of the NOPA of a flat phase-matching behavior is found and large output bandwidths result. A particularly broadband pulse results near the inflection point at 550 nm. The Fourier limits start increasing at the blue edge due to the decreasing temporal overlap of the needed seed frequencies with the pump pulse [8]. At the shortest wavelengths, the chirp of the seed continuum is largest. In the present setup, the pump pulse is longer by 30% compared to our earlier work, and the SH pumped continuum seems to have less chirp than the 1030 nm pumped one. Both factors contribute to the much larger bandwidths seen now. The smaller chirp of the seed is thought to be due to the fact that, starting from 515 nm, we have to push less hard to reach the blue, and an effectively shorter distance is traveled by the new spectral components inside the crystal.

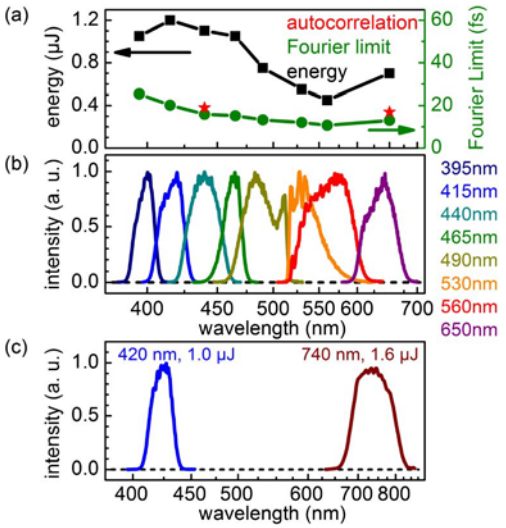

Fig. 2. (a) Pulse energy (black squares) and Fourier limit (green dots) of the UV and visible pulses. Red stars, measured sub 20 fs pulse duration. (b) Widely tunable pulses from the TH pumped amplifier. (c) Spectrum of simultaneously generated output from the 343 and 515 nm pumped NOPA stages.

The advantage of our scheme for TH pump generation is that enough SH light is produced and remains after THG to operate simultaneously a second SH pumped NOPA. We add a SH pumped amplification stage seeded with a fundamental pumped continuum and two independently tunable outputs result. Figure 2(c) shows an example of this dual output. Note the simultaneous output energy of 1.0 μJ in the blue and 1.6 μJ in the red.

A pair of Brewster angled fused silica prisms is used to compress the pulses to below 20 fs. Figure 3 shows the spectrum [(c) and (d)], the autocorrelation [(a) and (b)], and the predicted autocorrelation trace for transform limited pulses (dotted lines). The sub-20 fs pulse durations (Gaussian FWHM) correspond to a time bandwidth product of 0.73 each. More elaborate compression should render pulses close to 10 fs.

To show that the pulses are useful for spectroscopic applications, the pulse-to-pulse fluctuations were determined. The 1030 nm pump pulses have fluctuations of 2.9% rms, the SHG light 2.7%, the THG light 3.0%. The higher stability of the 2ω light is due to the starting saturation of the SHG process [8]. The output pulses of the NOPA fluctuate with 4.1% rms. This value seems slightly high, but the high repetition rate has to be taken into account. When averaging over 1 ms, the fluctuations between 1 ms bunches reduce to a measured value of 0.12% in good agreement with the predicted reduction following Poissonian statistics.

To demonstrate the superb output power at short wavelengths, Fig. 4(a) shows pulses at 445 nm with an average power of 480 mW. These pulses have sufficient energy (0.48 μJ) for further nonlinear processes like SHG. Figure 4(b) shows the spectrum of deep UV pulses at

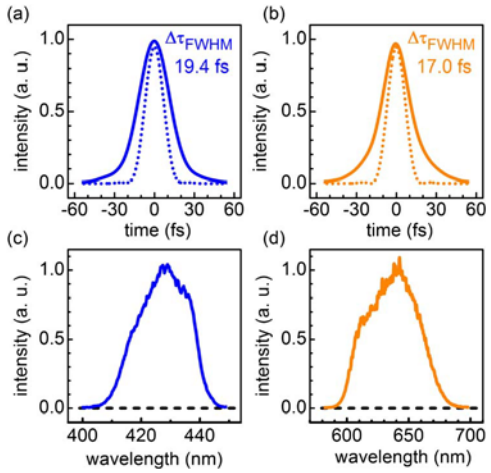

Fig. 3. Spectrum of 430 nm (c) and the 640 nm (d) pulses and autocorrelation traces (a) and (b) showing the compressibility to below 20 fs. The dotted line shows the predicted autocorrelation traces of transform limited pulses.

215 nm resulting from SHG of 430 nm pulses. A 30 μm type I BBO crystal cut at 55° is used. The SHG in combination with the wide tuning range of the NOPA allows covering a spectral range from the deep UV at 210 nm up to the NIR at 970 nm. The use of the 1030 nm pump system greatly simplifies the deep UV generation, as compared to a Ti:sapphire pump [19].

A critical issue when pumping with UV light is two-photon-absorption (TPA) in the amplifier crystal [20–22]. When operating at high repetition rates, a high thermal load on the amplifier crystal can result [23] that will decrease the amplification and lead to heat induced fracture. In 515 and 400 nm pumped systems, the main cause of heating is the residual linear absorption of the amplifier crystal and the idler absorption for the short wavelength edge of the tuning curve. It has also been suggested that TPA can lead not only to attenuation of the pump wave but also the generation of color centers with ms lifetimes that absorb at the pump and/or signal wavelength [24]. To limit the influence of these effects, the proper choice of pump intensity is essential. Figure 5(a) shows the TPA coefficient β of BBO [25–27]. The differing values at 264 nm are due to the various light polarizations and crystal cuts [28] used.

The reduced transmission due to TPA for a range of peak pump intensities is calculated from the analytic model for TPA for a 3 mm BBO crystal [29] [see lines in Fig. 5(b)]. It is in good agreement with the experimentally obtained value reported here (brown dot) and

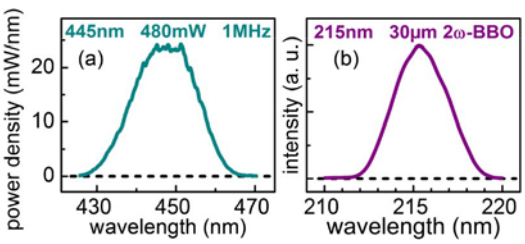

Fig. 4. (a) Spectrum of 445 nm pulses at 1 MHz with 480 mW average power. (b) SHG down to 215 nm in a 30 μm BBO crystal.

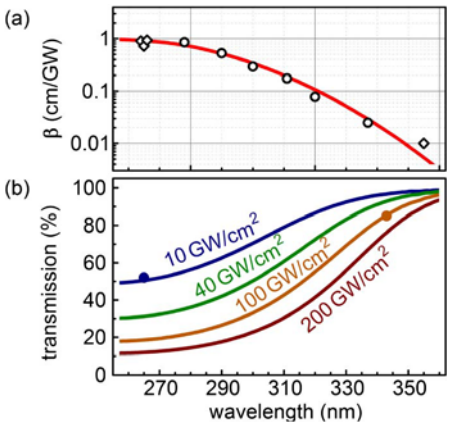

Fig. 5. (a) TPA coefficient β of BBO (circles from [27], diamonds from [25,26], [28]). (b) Transmission through a 3 mm BBO crystal for various peak pump intensities I_0.

from [28] (blue dot). For kHz Ti:sapphire-based NOPAs pumped with the SH, peak intensities of 200 GW/cm^2 are typically used. When applying such an intensity to 266 or 343 nm pumping, nearly complete TPA would occur and no useful amplification would be possible. For 266 nm pumping, TPA is so strong that already peak intensities of 4.8 GW/cm^2 lead to 75% absorption in a 12 mm BBO [20] or 50% at 24 GW/cm^2 in a 3 mm BBO [22]. For kHz systems, this is marginally acceptable, but for MHz repetition rates such a strong TPA not only decreases the pump intensity but also leads to a high thermal load. A significant thermal load in the crystal will lead to a dramatic increase of the local temperature [23,30], a change in the phase matching, and eventually the destruction of the crystal. Consequently, for high repetition rates the pump wavelength has to be increased to reduce TPA. The TH of Yb-based systems allows an optimal compromise between sufficiently high pump intensities and relatively weak TPA. For this wavelength peak intensities of up to 100 GW/cm^2 can be applied. Experimentally we observe about 15% TPA in the 3 mm NOPA crystal for this intensity.

It should be noted that we use the actual peak intensity I_0 of the pump pulse with spatial and temporal Gaussian profile. Frequently an effective intensity I_{eff} is used in the literature that is calculated from the ratio of pulse energy and FWHM circular area and duration. The two are connected by $I_0 = 0.65 \times I_{\text{eff}}$. This difference should also be kept in mind when the necessary pump intensity for a desired amplification is determined from published figures.

The TPA not only happens in the NOPA crystal but also in the THG crystal. When the repetition rate is raised from 200 kHz to 1 MHz, the amount of absorbed 343 nm light is accordingly increased. Experimentally we notice a loss of phase matching that needs a correction of the external tilt angle by 0.5°. An estimate shows that this is caused by an increase in the local temperature of 100 K, a value in the range reported in [23].

As shown in this work, the 343 nm are extremely well suited for amplification of ultrashort pulses down to below 400 nm. Therefore for MHz systems, 343 nm pumping is the ideal configuration to cover the full visible range. In addition, the group velocity mismatch between signal

and pump is only about 80 fs/mm as compared to a 266 nm pumped system with 340 fs/mm [22]. With the hundreds of fs pump pulse duration, amplifier crystals with a few millimeter length can be used before pump and signal lose temporal overlap. Even for the thick amplifier crystals, the noncollinear phase-matching ensures sufficiently broadband amplification for 10 fs pulses. Because of the exponential dependence of the output energy on the crystal length, lower pump intensities can be applied for the sub-10^4 amplification needed to boost the sub-nJ seed to the μJ level. To minimize the needed amplification and pump intensity, the size of the seed and the pump must be carefully matched. This is in contrast to the situation in kHz systems pumped by 400 nm, where saturation can be used to minimize the output fluctuations and a slightly too large seed diameter helps to clean up the beam profile.

In summary, we have described a NOPA pumped by the 343 nm TH pulses of a 20 W Yb-based fiber amplifier that delivers tunable pulses between 395 and 970 nm at up to 1 MHz repetition rate. The unprecedented tuning in the near-UV and blue is made possible by a seed continuum pumped by the second harmonic. Energies up to the μJ-level and durations below 20 fs are obtained throughout the tuning range of well above one octave when the THG pumped NOPA is amended by a second NOPA pumped with the remaining SHG. The parallel use of SH and TH light as pump allows the generation of two individually tunable pulses and favors this system as a light source for ultrafast time resolved two color pump-probe experiments at high repetition rates. The short pulse duration of the pulses leads to high peak powers and enables additional SHG. This extends the tuning range down to 210 nm. No spectral gap remains between 210 nm and the NIR. The combination of the Yb-based pump laser and the described NOPA setup thus renders for the first time a MHz-repetition rate instrument that can be tuned to any desired excitation wavelength in spectroscopic investigations.

It should be noted that the pump laser has a pulse duration of 300 fs. Because of the dramatic pulse shortening in the continuum seeded NOPA by more than a factor of 15, this is not even a limitation when few-cycle pulse are needed. Since continuum generation in solids is possible up to at least 1 ps pulse duration, laser systems with high repetition rates and pulse energies can be used as driving source for such an amplifier [31]. For the very broadest output pulses, the seed light can be amplified sequentially in a SH pumped amplifier and a TH pumped one [32,33].

We thank I. Thomann for initiating this project, C. Doiron and B. Baudisch for experimental help, and M. Drechsler and Amplitude Systemes for technical support. The Deutsche Forschungsgemeinschaft (DFG) is acknowledged for financial support through the Cluster of Excellence: Munich-Centre for Advanced Photonics.

References

1. R. J. Ellingson and C. L. Tang, Opt. Lett. **18**, 438 (1993).
2. L. E. Myers, R. C. Eckardt, M. M. Fejer, R. L. Byer, W. R. Bosenberg, and J. W. Pierce, J. Opt. Soc. Am. B **12**, 2102 (1995).
3. G. M. Gale, M. Cavallari, T. J. Driscoll, and F. Hache, Opt. Lett. **20**, 1562 (1995).
4. M. Ghotbi and M. Ebrahim Zadeh, Opt. Express **12**, 6002 (2004).
5. M. K. Reed, M. K. Steiner Shepard, M. S. Armas, and D. K. Negus, J. Opt. Soc. Am. B **12**, 2229 (1995).
6. J. Piel, E. Riedle, L. Gundlach, R. Ernstorfer, and R. Eichberger, Opt. Lett. **31**, 1289 (2006).
7. C. Schriever, S. Lochbrunner, P. Krok, and E. Riedle, Opt. Lett. **33**, 192 (2008).
8. C. Homann, C. Schriever, P. Baum, and E. Riedle, Opt. Express **16**, 5746 (2008).
9. M. Emons, A. Steinmann, T. Binhammer, G. Palmer, M. Schultze, and U. Morgner, Opt. Express **18**, 1191 (2010).
10. L. D. Ziegler, J. Morais, Y. Zhou, S. Constantine, M. K. Reed, M. K. Steiner Shepard, and D. Lommel, IEEE J. Quantum Electron. **34**, 1758 (1998).
11. L. Gundlach, R. Ernstorfer, E. Riedle, R. Eichberger, and F. Willig, Appl. Phys. B **80**, 727 (2005).
12. H. Shen, S. Adachi, T. Horio, and T. Suzuki, Opt. Express **19**, 22637 (2011).
13. G. Cerullo and S. De Silvestri, Rev. Sci. Instrum. **74**, 1 (2003).
14. E. Riedle, M. Beutter, S. Lochbrunner, J. Piel, S. Schenkl, S. Spörlein, and W. Zinth, Appl. Phys. B **71**, 457 (2000).
15. M. Bradler, P. Baum, and E. Riedle, Appl. Phys. B **97**, 561 (2009).
16. A. Baltuska, T. Fuji, and T. Kobayashi, Phys. Rev. Lett. **88**, 133901 (2002).
17. O. D. Mücke, D. Sidorov, P. Dombi, A. Pugzlys, A. Baltuska, S. Alisauskas, V. Smilgevicius, J. Pocius, L. Giniunas, R. Danielius, and N. Forget, Opt. Lett. **34**, 118 (2009).
18. G. Cerullo, A. Baltuska, O. D. Mücke, and C. Vozzi, Laser Photon. Rev. **5**, 323 (2011).
19. C. Homann, P. Lang, and E. Riedle, J. Opt. Soc. Am. B **29**, 2765 (2012).
20. K. Osvay, G. Kurdi, J. Klebniczki, M. Csatari, I. N. Ross, E. J. Divall, C. J. Hooker, and A. J. Langley, Appl. Phys. B **74**, S163 (2002).
21. P. Tzankov and T. Fiebig, Appl. Phys. Lett. **82**, 517 (2003).
22. T. Tanigawa, K. Yamane, N. Karasawa, and M. Yamashita, Jpn. J. Appl. Phys. **50**, 072701 (2011).
23. J. Rothhardt, S. Demmler, S. Hädrich, T. Peschel, J. Limpert, and A. Tünnermann, Opt. Lett. **38**, 763 (2013).
24. M. Takahashi, A. Osada, A. Dergachev, P. F. Moulton, M. Cadatal Raduban, T. Shimizu, and N. Sarukura, Jpn. J. Appl. Phys. **49**, 080211 (2010).
25. R. DeSalvo, A. A. Said, D. J. Hagan, E. W. van Stryland, and M. Sheik Bahae, IEEE J. Quantum Electron. **32**, 1324 (1996).
26. A. Dubietis, G. Tamosauskas, A. Varanavicius, and G. Valiulis, Appl. Opt. **39**, 2437 (2000).
27. C. Homann, N. Krebs, and E. Riedle, Appl. Phys. B **104**, 783 (2011).
28. L. I. Isaenko, A. Dragomir, J. G. McInerney, and D. N. Nikogosyan, Opt. Commun. **198**, 433 (2001).
29. P. Liu, L. Smith, H. Lotem, J. H. Bechtel, N. Bloembergen, and R. S. Hadav, Phys. Rev. B **17**, 4620 (1978).
30. M. J. Prandolini, R. Riedel, M. Schulz, A. Hage, H. Höppner, and F. Tavella, Opt. Express **22**, 1594 (2014).
31. M. Schulz, R. Riedel, A. Willner, T. Mans, C. Schnitzler, P. Russbueldt, J. Dolkemeyer, E. Seise, T. Gottschall, S. Hädrich, S. Duesterer, H. Schlarb, J. Feldhaus, J. Limpert, B. Faatz, A. Tünnermann, J. Rossbach, M. Drescher, and F. Tavella, Opt. Lett. **36**, 2456 (2011).
32. D. Herrmann, C. Homann, R. Tautz, M. Scharrer, P. St. J. Russell, F. Krausz, L. Veisz, and E. Riedle, Opt. Express **18**, 18752 (2010).
33. A. Harth, M. Schultze, T. Lang, T. Binhammer, S. Rausch, and U. Morgner, Opt. Express **20**, 3076 (2012).

Appendix A16

Temporal and spectral correlations in bulk continua and improved use in transient spectroscopy

M. Bradler and E. Riedle

J. Opt. Soc. Am. B **31**, 1465 (2014)

Reprinted with kind permission from the Optical Society of America (OSA)

Temporal and spectral correlations in bulk continua and improved use in transient spectroscopy

M. Bradler and E. Riedle*

Lehrstuhl für BioMolekulare Optik, Ludwig Maximilians Universität München, Oettingenstrasse 67, 80538 Munich, Germany
**Corresponding author: eberhard.riedle@physik.uni muenchen.de*

Received March 21, 2014; revised May 9, 2014; accepted May 11, 2014; posted May 12, 2014 (Doc. ID 208543); published June 5, 2014

Newly generated frequencies during bulk continuum generation with femtosecond pump pulses do not fluctuate statistically and show strong correlations in spectrum and time. When a femtosecond continuum is used as probe light for transient spectroscopic measurements, these correlations result in a seemingly low noise level but large scale pseudo structures that obscure the interpretation. We investigate the correlations for continua generated in YAG and calcium fluoride plates and incorporate the results into the design of our pump probe setup. The high degree of correlation to the next pulse is utilized through chopping of the pump and referencing between suc cessive laser shots. To suppress the adverse effect of the high degree of correlation to other wavelengths, we extend the detection by multichannel referencing with a second camera. The combination of both referencing schemes renders a precise spectral calibration unnecessary and increases the sensitivity of our spectrometer by a factor of 5 down to 20 μOD. This is already very close to the shot noise limit. To demonstrate the improvements, we present and discuss measurements on two different molecular solutions. © 2014 Optical Society of America

OCIS codes: (030.6600) Statistical optics; (120.4570) Optical design of instruments; (190.4360) Nonlinear optics, devices; (300.6500) Spectroscopy, time resolved; (320.7150) Ultrafast spectroscopy.
http://dx.doi.org/10.1364/JOSAB.31.001465

1. CONTINUUM GENERATION AND TRANSIENT PUMP–PROBE SPECTROSCOPY

A commonly used technique to study the dynamics of chemical or biological processes is time resolved transient pump probe spectroscopy with femtosecond pulses [1 7]. The comparison of the absorption of molecules in the excited and the ground state allows unraveling the inner life of the systems. A key role in these measurements is attributed to the probe pulses. The ideal probe pulse should cover a wide spectral range and be very stable to record even the weakest absorption changes of the investigated sample. Continuum generation in bulk material with femtosecond pulses [8 10] is a well established method to generate broadband probe light with low fluctuations. When just a single filament is uti lized, particularly stable conditions result.

In the last decade continua obtained from calcium fluoride turn out to fit the experimental needs very well [6 8,11 13]. They range down to 285 nm and have a spectral width of over one octave. The pulse to pulse fluctuations of the newly generated frequencies can be brought down to the same mag nitude as those of the laser system. However, they will never vanish because of the spectral, spatial, and energetic fluctua tions of the laser light and environmental instabilities. In addition, the dark current of the electronics and stray light contribute to the observed instabilities when imaging the light with a photoelectric detector. To improve the signal to noise ratio, the averaging time, the optical density of the sample, or the pump pulse energy applied to the spectroscopic sample could be increased. This is often not possible or sensible, because many samples are not available in the desired amounts and saturation of the pump transition has to be avoided. Increasing the pump power or averaging time can also lead to parasitic effects like photochemical reactions of the sample, degradation, or an increasing stray light contribution.

In addition, it has been observed that the fluctuations are not solely statistical, but the various spectral components show strong spectral and temporal intensity correlations. These are a result of the filamentation process and have been studied in bulk [7,14], gases [15,16], and fibers [17 21] to get a better understanding of the involved processes in continuum generation or of the sensitivity of transient spectrometers [7].

To demonstrate the challenge that can arise from such correlations in the probe light we turn to the typical algorithm used for the measurement of transient spectra in a multichan nel detection scheme [6]. The quantity of interest is the pump probe delay time Δt and probe wavelength λ dependent change in optical density $\Delta OD(\lambda, \Delta t)$:

$$\Delta OD(\lambda, \Delta t) = \log\left(\frac{S^*(\lambda, \Delta t)}{S_0(\lambda)}\right). \quad (1)$$

$S^*(\lambda, \Delta t)$ and $S_0(\lambda)$ are the transmitted probe light induced electronic signal through the excited and the unpumped sam ple. Ideally, two parallel measurements with identical replicas of the probe pulse should be made, one with and the other without pump. In the absence of a reference channel, a chop per alternately blocks and transmits the pump pulse so that subsequent continua are compared. Typically 500 of such single ratios are averaged to obtain a transient spectrum. Actually the ratio of the sample transmission $T^*(\lambda, \Delta t)/T_0$ is looked for. The spectral distribution of the continuum pulse

 © 2014 Optical Society of America

as seen in the optical setup is not explicitly measured in a single beam transient spectrometer. It is assumed that this spectrum is identical for the two consecutive laser shots 2 k and $2k+1$ and cancels out in the rationing in Eq. (1). Even if there are small variations, they are thought to average out quickly. Variations come from technical noise and the Poissonian photon fluctuations.

The black curve in Fig. 1(a) shows a typical transient spectrum from our setup [6] without sample and no applied pump pulse. We here use the notation S_{2k} and S_{2k+1} for the subsequent signals. The value of the ratios should be exactly 1.0 for all wavelengths. However, beside small local fluctuations (between neighboring wavelengths), we find large global deviations from unity, which range over several hundred nanometers. Such global deviations can easily be misinterpreted as molecular response if they are superimposed on an actual molecular spectrum. Figure 1(a) additionally shows the expected S_{2k}/S_{2k+1} spectrum (gray) if no spectral correlations would be present. To simulate this, random numbers close to 1.0 with a standard deviation according to the measured pulse to pulse stability are generated. The average of 500 such random numbers is shown for every wavelength in Fig. 1(a). The simulated spectrum shows a higher local noise level but no global structure.

To assess the observed noise level, we consider the shot noise limit of our experiment. The full well capacity of each detector pixel of the used charge coupled device (CCD) array (S7030 0906; Hamamatsu Inc.; electronics by Entwicklungsbüro Stresing) is 6×10^5 electrons. According to Poissonian statistics, the detected photon number varies as $\sqrt{N}$. A single observation utilizing 2/3 of the full well capacity can only be certain at best to $1/\sqrt{4\times10^5}=1.6\times10^{-3}$. Averaging over 500 samples and considering the $\sqrt{2}$ additional factor from the pairs of laser shots used, this uncertainty should decrease to 10×10^{-5} shot noise limited sensitivity. The high frequency noise of the experimental curve [black line in Fig. 1(a)] in the range from 350 to 550 nm is found to be 7×10^{-5}. This value is lower than the calculated shot noise despite all the extra technical noise. It can only be understood by a high degree of correlation in the continuum generation and therefore the measurement. Already the technical noise as represented by the simulated curve (gray) is indeed much higher than the apparent extremely low noise level.

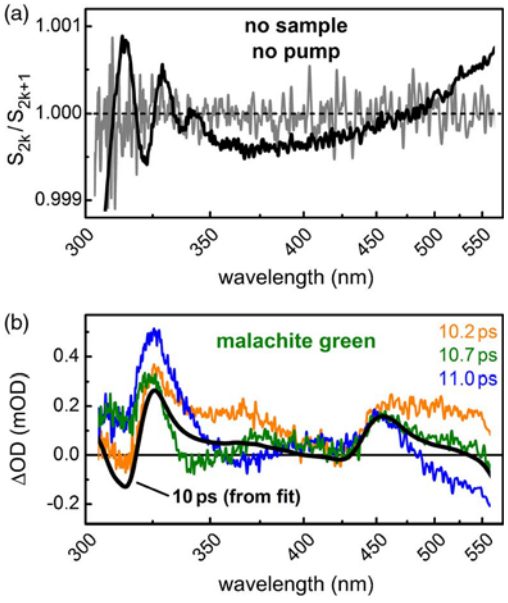

Fig. 1. (a) S_{2k}/S_{2k+1} spectrum of a test measurement (black, 500 pairs averaged) without a sample, obtained with a CaF_2 continuum and simulated spectrum for uncorrelated continuum pulses (gray). (b) Various transient absorption spectra of malachite green after S_2 excitation for time delays around 10 ps including the expected signal from the extrapolated fit (black).

To show that these large scale signatures influence the spectroscopic experiment, the well studied laser dye malachite green is used as the test sample. We excite it into the S_2 state by 350 nm pumping (for details see Section 5). For a time delay between 1 and 5 ps the transient signal is strong and can be fitted well. The data obtained from this fit allows extrapolating to the expected transient signal at a time delay of around 10 ps. Figure 1(b) shows this expected transient spectrum at 10 ps (black). In addition, various measured curves (spectra at 10.2, 10.7, and 11.0 ps) are shown. Beside small local fluctuations (between neighboring wavelengths), there are large global deviations from the expected transient signal, comparable in magnitude to the real spectral signatures. This can easily be misinterpreted as molecular response and attributed to not existing states or ultrafast processes. The actual decrease in signal should be only a few percent due to vibrational cooling on the 10 ps time scale, and no noticeable change in spectral structure.

To clarify the origin of the observed pseudo signals and to determine the proper way to avoid them, we study the spectral and temporal correlations of bulk continua. We find that multichannel referencing in combination with referencing to the subsequent continuum pulse nearly eliminates the spectral and temporal correlations. It fully reduces the unwanted global deviations and improves the sensitivity and fidelity of our spectrometer by a factor of 5 down to 20 μOD. The correlations between the different spectral parts of the continuum are eliminated by referencing to a second multichannel detector. The additional referencing to the subsequent pulse avoids the need to measure a highly precise spectral correction factor between the two detectors and eliminates correlations to later points in time.

2. SPECTRAL AND TEMPORAL CORRELATIONS OF BULK CONTINUA

A 1 kHz Ti:sapphire based laser system (CPA 2001; Clark MXR) that delivers 1 mJ pulses at 775 nm with a nominal duration of 150 fs is used as pump source. To study the spectral and temporal correlations the setup shown in Fig. 2(a) is used.

By focusing 1 μJ of the 775 nm light with a 10 cm lens onto a 4 mm YAG crystal or a 5 mm calcium fluoride (CaF_2) plate a broadband bulk continuum is generated [10]. Importantly, we ensure that a single filament is used and multi filamentation with a high degree of fluctuation is avoided. Spectral modulations close to the pump wavelength are avoided by working close to the threshold. A variable attenuator and an iris are used to optimize the beam quality, spectral shape, and stability of the continuum. To avoid the accumulation of color centers, the CaF_2 plate is moved in a circular pattern without changing the crystal orientation. The continuum is collimated with a

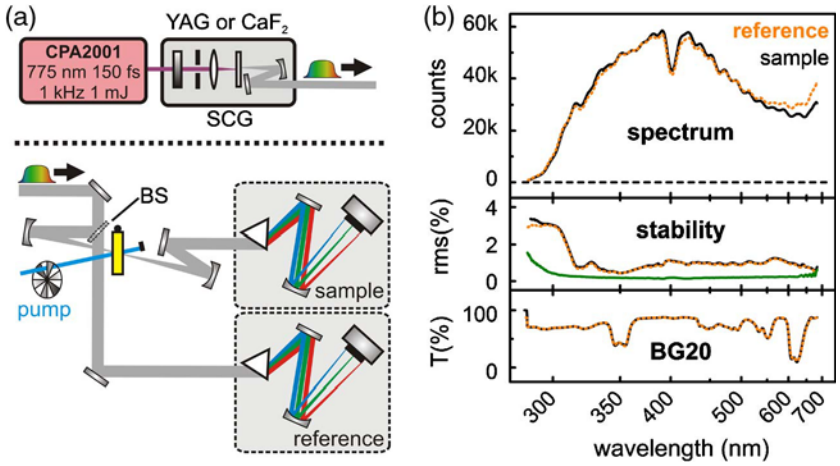

Fig. 2. (a) Single filament continuum generation in YAG and CaF_2 crystals and their use as probe light in a multichannel transient absorption spectrometer with two camera referencing. (b) shows the spectrum, stability, and transmission through a BG20 filter for both continuum halves (black and orange dotted).

slightly off axis spherical mirror (R = 200 mm) [6] and split in two roughly equal parts with a broadband beam splitter (BS). As beam splitter we use an Inconel coated fused silica plate with a nominal optical density of 0.5 transmission (NDUV505B; Thorlabs) that we find to reflect, absorb, and transmit about equal amounts. The reflected part is focused onto the sample with a spherical mirror (R = 500 mm) and recollimated afterward (R = 500 mm). The chosen number of reflections for the sample and reference beam ensures together with the focusing onto the sample that the lateral parts of the continuum are equally projected onto the two cameras.

Both continuum "halves" are dispersed with fused silica prisms with an apex angle of 68.7°, with horizontal polarization to minimize reflection losses. Finally, the dispersed light is focused with R = 600 mm spherical mirrors onto separate, identical CCDs. The spectrally resolved intensities of both continua at the cameras can be read out for every single pulse. This allows an operation at the full 1 kHz repetition rate. The detected spectrum for a CaF_2 continuum and the stability are shown in Fig. 2(b). To ensure that both continua are dispersed equally and to illuminate the corresponding pixels with the same spectral range we use optics with a highly structured transmission to adjust both spectrometers. The lower pattern of Fig. 2(b) shows the transmission of a BG20 colored glass filter (Schott) when monitored with both cameras. The transmission of such optics is excellently suited for the wavelength calibration [6]. Due to the single shot readout we are able to capture 1000 consecutive continuum spectra per second. Such a bunch of 1000 spectra is used to analyze the spectral and temporal correlations of the continuum.

At this point, we like to quantify the term correlation in accord with Ref. [7]. Due to the spectral dispersion of the continuum with the prism, each pixel of the camera is illuminated by a distinct small spectral part of the continuum. The employed beam geometry ensures that a quasi monochromatic part of the continuum is imaged to a spot smaller than the pixel size of 24 μm. The average dispersion of the polychromator projects a 38 cm^{-1} portion of the continuum onto each pixel, matching the observed 50 cm^{-1} spectral resolution [6]. The amount of light impinging on each bin is transferred to a 16 bit number (0 65,535 counts).

When considering 1000 consecutive continuum pulses, each pixel gives a series of 1000 counts. In the ideal case, all counts for one pixel should be equal. Due to the technical fluctuations of the continuum, the background noise and the Poissonian photon statistics, the values differ slightly. A good measure to describe the degree of fluctuations is the root mean square (rms) stability, which is defined as the ratio between the standard deviation (σ_X) and the mean (X) of a series of numbers (X). Here, X are the 1000 consecutive counts of a pixel. In this work, the correlation of the value of one pixel (and hence spectral part of the continuum) to another pixel is studied. The "other" pixel could be the neighboring pixel or a pixel at a completely different spectral position. A quantitative measure that describes the relation between two series of numbers is the Pearson product moment correlation coefficient $\gamma_{X,Y}$ [22 24]:

$$\gamma_{X,Y} = \frac{\mathrm{cov}(X,Y)}{\sigma_X \cdot \sigma_Y} = \frac{\sum_{i\ 1}^{n}(x_i - \overline{X}) \cdot (y_i - \overline{Y})}{\sqrt{\sum_{i\ 1}^{n}(x_i - \overline{X})^2} \cdot \sqrt{\sum_{i\ 1}^{n}(y_i - \overline{Y})^2}}. \quad (2)$$

X and Y are series of numbers (n = 1000 consecutive counts of two different pixels). The term $\mathrm{cov}(X,Y)$ is the covariance between series X and Y. σ_X and σ_Y are the standard deviations of X and Y, X and Y are their mean values, and x_i and y_i are the values for ith continuum pulse. The correlation coefficient indicates the degree of relation between the deviations from the mean for the single values. This means for strongly correlated series ($\gamma_{X,Y} \approx 1$) that if the ith value of one series (X) is above the average, most probably the ith value of the other series (Y) is also above the average. Strongly anticorrelated series ($\gamma_{X,Y} \approx -1$) mostly show the opposite deviation from the mean for the single values. Mathematically this is done by comparing the covariance between both series to the geometric mean of the single variances.

In addition to the relation of one wavelength part to another, we also investigate the correlation to later pulses. This means, how strong is the value of one pixel correlated to the value of the same pixel at a later time. The formula

is the same as above. X is still the series of 1000 consecutive counts for one pixel, Y is then the series of 1000 consecutive counts of the same pixel starting with a later pulse. To ensure that every single value has a later partner, actually 2000 con secutive continuum spectra are recorded and the correlation coefficient is formally calculated for the first 1000. For exam ple, when analyzing the temporal correlations to the 50th later pulse, shot 1 is compared to 51, shot 2 to 52, and so on until shot 1000 to 1050. The correlation between different pixels and hence different parts of the spectrum will be called *spectral correlations*, the correlation to later continuum pulses *temporal correlation*.

At first, continuum generation in a 4 mm thick YAG plate is considered. Figure 3 shows the spectral correlations between the newly generated visible and infrared frequencies as well as the fundamental wavelengths for two different pump energies of 300 nJ in (a), 600 nJ in (b). The strength of the correlation coefficient is indicated by the color scale and ranges from 1 to 1. The newly generated frequencies show high correlations for neighboring wavelengths. This can be attributed to the generation mechanism. The important self steepening and shock wave absorption [25] are abrupt processes and all col ors are generated in a very short time. This is thought to be the reason for the high correlations among the new frequencies.

The correlations between neighboring wavelengths in the pump region are also high, but the sign of the correlation coefficient is not predictable. The strong deformation of the input pulse in space and time due to the interacting non linear processes leads to the quasi random correlations in this spectral region. In addition, the two different pump energies show that the observed correlations for all wavelengths are not equal and strongly depend on the details of the generation. Even the correlations for continua with the same nominal pump energy taken at different times are not identical. This means that due to the complexity of the generation mecha nisms the exact correlation map cannot be predicted. In com bination with the highly structured spectrum and the low pulse to pulse stability, the light near the pump wavelengths is not suited as probe light and is therefore excluded in the further discussion. Only the newly generated frequencies will be investigated. Since the correlations are different for all

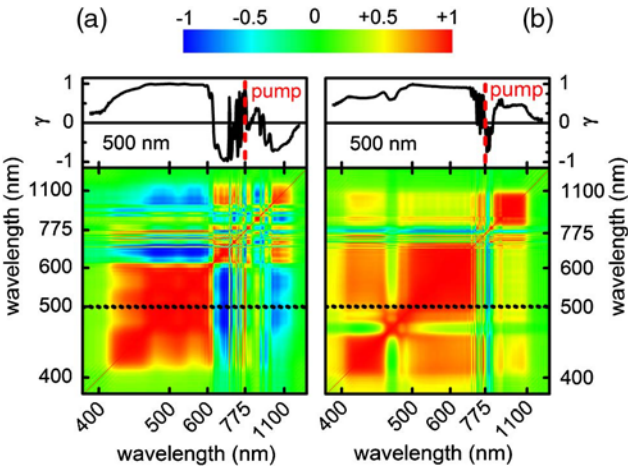

Fig. 3. Spectral correlations between various wavelengths of a con tinuum generated in a 4 mm YAG plate with (a) 300 nJ and (b) 600 nJ pump pulses for 1000 consecutive continua. The upper graph shows the correlation of the 500 nm part to other wavelengths.

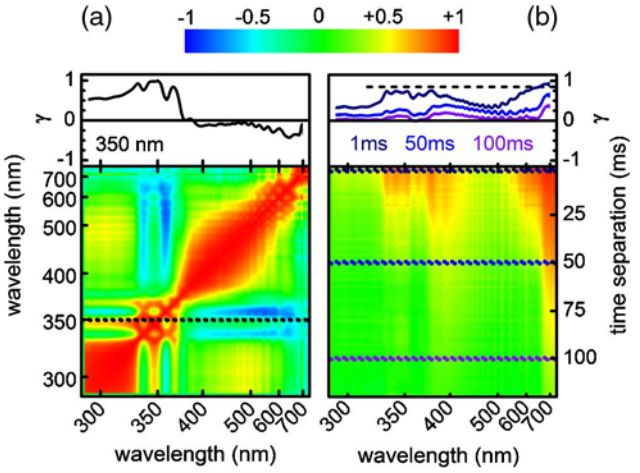

Fig. 4. (a) Spectral and (b) temporal correlations of continuum gen eration in CaF_2. The dashed line in the upper panel of (b) shows the correlation level (γ 0.93) of one laser pulse to the next [26].

generated continua it is not reasonable to study the specific appearance of one special correlation map. More interesting is the influence of these correlations on pump probe experi ments. Continua generated in YAG are rarely used in transient absorption spectroscopy. Therefore, we will focus on the continuum generation in CaF_2 and particularly the visible and ultraviolet wavelength range.

Figure 4 shows the spectral and temporal correlations of the newly generated frequencies of a continuum generated in a 5 mm CaF_2 plate [6]. The single wavelengths show strong correlations to other wavelengths in a not predictable shape just as for the YAG continuum.

In many transient spectrometers a chopper is used to compare the transmission changes between excited and equi librium samples. The chopper alternately blocks the pump light and therefore one hopes to benefit from the high corre lation between subsequent pulses [$\gamma = 0.93$, dashed black line in the upper graph of Fig. 4(b)] [26,27]. The dark blue curve in Fig. 4(b) (1 ms time separation) shows that the correlation of each single wavelength to the subsequent pulse is mostly not as high as the one for the laser pulse used for the continuum generation, but still on a reasonable level. For larger separa tion times this correlation decreases strongly. This implies that the highest correlation and therefore best experimental results are obtained, if subsequent continua are compared to obtain the desired transmission change.

Since every generated continuum shows a different corre lation map, the following investigations of the CaF_2 continua are all obtained from the same dataset. When studying refer encing schemes with only one camera, the data of the second camera are not considered. This ensures that the observed improvements are not due to accidentally better aligned continuum generation but due to the applied reference tech niques. We investigated several datasets and find the described improvements for all measured sets.

3. SPECTRAL AND TEMPORAL CORRELATION IN TRANSIENT ABSORPTION SPECTROSCOPY

In broadband pump probe experiments continua are used as probe light to determine the pump light induced transmission

change. To analyze the possible problems associated with the experimentally observed transmission changes, we compare the spectra of the two continuum pulses used for the determination. Only if there is an absorbing sample, sufficient pump light, and a reasonable temporal delay between pump and probe light, real transmission changes should occur. In this work, one of the main goals is to characterize our spectrometer and eliminate systematic errors and disturbing effects. Therefore, we perform test measurements without excitation and sample so that all ratios between the continuum spectra should be exactly unity. Only fluctuations and the detection noise lead to deviations from unity. Such measurements characterize the system and help avoid systematic errors.

In Section 1 we already showed and discussed a model measurement performed without sample and pump. The significant deviations from the expected unity signal display little local noise, but global structures. These are examples for possible systematic errors and have to be differentiated from real molecular signals. Only signals larger than a well determined confidence interval [7] are of use for the analysis of the molecular kinetics.

So far we have discussed the spectral and temporal correlations of the probe continuum. In the typical pump probe setup with pump chopping, actually the signal S and the reference S′ are derived from subsequent pulses. The raw correlations of the continuum are only of indirect importance, rather any correlations in the ratio S/S′ are seen in the spectrograms. We therefore switch from the correlations of the continuum itself to correlations of the ratios between subsequent pulses. Later we will also consider correlations between the sample branch and an additional reference branch.

The fact that neighboring wavelengths show high correlations independent from a molecular absorption is also true for the S/S′ spectra, as can be clearly seen from Fig. 5(a). In view of the rapid roll off of the temporal correlation for individual pixels [see Fig. 4(b)], this correlation found even for the ratios is somewhat surprising. The persistent correlations are the origin of the pseudo structures in the transient spectra. The value of the ratio at a selected wavelength does not average to the expected unity even with 500 samples. For totally uncorrelated neighbors, values would result that fluctuate statistically around unity with the probe wavelength and the apparent spectral "noise" would match the true sensitivity or fidelity. No apparent global structure should develop. That this is not the case is seen in Fig. 5(a), which shows the correlation between single wavelengths. Figure 6(a) shows the correlation of each wavelength of an S/S′ spectrum to later times obtained from a CaF_2 continuum.

The main problem is the high correlation between neighboring wavelengths of the S/S′ spectra. If the value at a certain wavelength is, e.g., above unity, then the values of the neighboring wavelengths are also above unity, independent of the true signal. Additionally, the correlation of the S/S′ spectra to later S/S′ spectra is not vanishing, although there is already a referencing to the next pulse. For the full 1000 ms significant correlations are remaining. This range corresponds to typical averaging times. Experimentally we find that there are a few dominant shapes for the S/S′ spectra which appear pseudo random in time.

To ensure that the observed correlations are only due to the continuum and not due to the detector, we perform a test measurement with a light emitting diode (LED) instead of the continuum probe. Especially the readout mechanisms of the CCD could be a reason for the observed correlations, in particular the binning of 58 vertical pixels and the stepwise transport of the charge in the CCD. Therefore, a LED is triggered so that it blinks in phase with the laser system and is positioned to illuminate the CCD homogeneously. To ensure that always the same amount of light is considered, additionally the emitted amount of light is monitored by a photodiode and used to normalize the measured data. We again display the ratios between subsequent LED flashes and evaluate the correlation between different pixels and separation times [see Figs. 5(d) and 6(d)]. This measurement proves that only the dark current and no additional systematic effects of the camera limit the

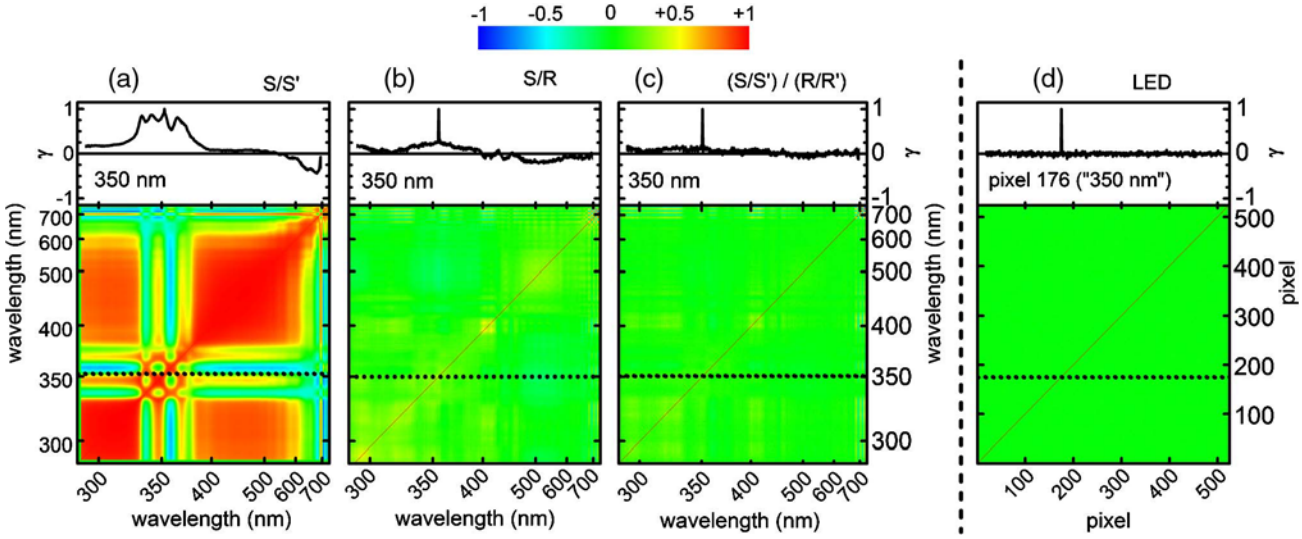

Fig. 5. Spectral correlations for a CaF_2 continuum (a) of S/S′ spectra (referencing to the subsequent pulses), (b) of S/R spectra for referencing to the reference camera, and (c) of (S/S′)/(R/R′) spectra for referencing to subsequent continuum spectra and a reference camera. (d) "Spectral" correlation between single pixels for homogeneous illumination with a pulsed LED. The values of −1 to +1 for the correlation coefficient are indicated in the color scale.

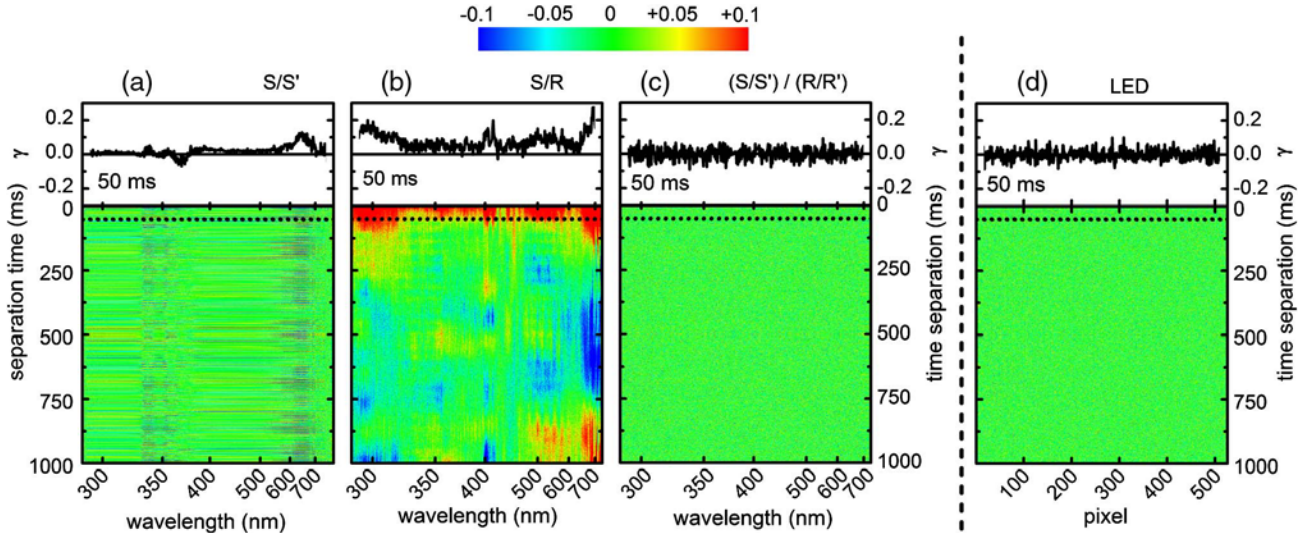

Fig. 6. Temporal correlations for (a) (c) a CaF_2 continuum and for (d) a pulsed LED. All details equivalent to Fig. 5. Note the expanded color scale.

detection sensitivity of the system. No spectral and temporal correlations are observed. The diagonal signal in Fig. 5(d) is the full correlation of the value of the pixel to itself.

4. MULTICHANNEL REFERENCING

The spectral correlations in the continuum and also in the ratio between subsequent pulses are strong and not predictable. In a first approach, one can accept the correlations, average over a small number of scans that are not correlated due to the many minutes of difference in recording time, and obtain spectra with a good sensitivity of 100 μOD with a simple setup [6]. However, an even better sensitivity and in particular a higher fidelity, i.e., the certainty that apparent spectral structures are indeed molecular signatures, is highly desirable. A method to enhance the sensitivity of the system is single shot referencing [7,28 32]. For this purpose a second identical CCD (reference camera) is installed and read out with the same technique as the first camera (sample camera). The continuum pulses are split in two parts and both parts are imaged in a similar manner onto the particular camera, as shown in Fig. 2(a). We choose to use no sample in the reference arm, others have opted to guide both the sample and the reference beam through the same sample at different positions [28,29,31]. Differences in strategy were also reported as to the use of one or two dispersing units and one detector with separate areas evaluated or two independent ones. We believe that these are only technical details that do not influence the present investigation of the spectral correlations. The common basis of the two camera referencing setups is the attempt to evaluate the change in optical density according to Eq. (1) in its original form. If the pumped and the unpumped signal are measured for the same laser shot, the true value of ΔOD should be obtained. No need for pump chopping is connected to this approach and the measurement time should be minimized.

The spectrum, stability, and transmission through a BG20 colored glass filter are shown in Fig. 2(b) for both arms. It can be seen that the continuum parts are dispersed and imaged very equally onto the two cameras. Due to the high correlations, we even find a small spectral mismatch to be insignificant for good referencing. The main advantage of the referencing to the second camera can be seen if the spectral correlations from sample to reference camera are considered (see Fig. 7, black dashed). They are compared to the spectral correlations between consecutive continuum pulses just on the sample camera (gray solid line).

The spectral correlation between the continuum pulses on the sample and the reference camera is nearly 100% for all wavelengths. This is in good agreement with the literature [7] and shows that the spectral correlation to the reference camera is dramatically higher for all wavelengths than the correlation to subsequent pulses. The measurement confirms the assumption that the reference arm is a suitable means to record the unpumped reference signal. Besides the matching transmission through filters, the high degree of the spectral correlations is a well suited method to find the optimum adjustment of both camera paths.

As discussed above, some correlations can lead to pseudo structures in the transient spectra. With the newly developed understanding of the correlations, we can develop and motivate the proper strategy to overcome this problem with the proper combination/selection of pump chopping and/or reference camera. In addition to the sample $S(\lambda)$, we denote $R(\lambda)$ as the electronic signal on the reference detector. The sample signal with pump is denoted as S^*, signals for subsequent

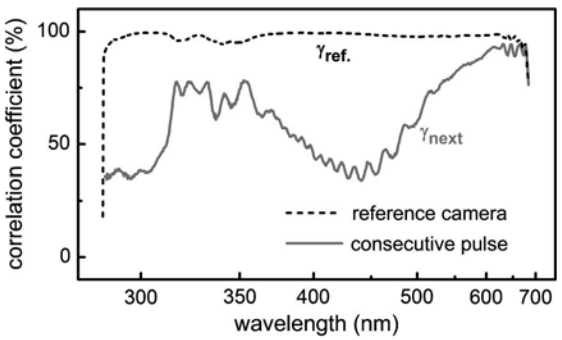

Fig. 7. Spectral correlations between the continuum "halves" on the sample and reference camera (black dashed) and between consecutive continuum pulses (gray).

pulses are S and S′. The notation for the reference is equivalent, except that there is no pumped reference. The spectral distribution of the incoming continuum is denoted by $I(\lambda)$. Due to the imperfect properties of the optics and a slightly differing wavelength dependent detector sensitivity, we have to introduce attenuation factors $A(\lambda)$. The molecular absorption is denoted by the transmission $T^*(\lambda, \Delta t)$ for the pumped sample and $T_0(\lambda)$ for the unpumped one. As we will restrict our explicit discussion to single wavelengths, the wavelength dependence is not explicitly indicated. This results in sample and reference signal equations for each laser shot i:

$$\begin{aligned} S_i^* &= T^*(\Delta t) \cdot A_S \cdot I_i \\ S_i &= T_0 \cdot A_S \cdot I_i \\ R_i &= T_0 \cdot A_R \cdot I_i. \end{aligned} \tag{3}$$

Statistical fluctuations and technical noise are neglected and it is assumed that they average out by a sufficient number of measurements. The change in optical density $\Delta OD(\lambda, \Delta t)$ is then given by

$$\begin{aligned} \Delta OD(\lambda, \Delta t) &= \log\left(\frac{T^*(\lambda, \Delta t)}{T_0(\lambda)}\right) \\ &= \log\left(\frac{T^*(\Delta t) A_S I_i}{T_0 A_S I_j} \cdot \frac{T_0 A_R I_j}{T_0 A_R I_i}\right) = \log\left(\frac{S_i^*}{S_j} \cdot \frac{R_j}{R_i}\right). \end{aligned} \tag{4}$$

An index $j = i$ signals that the same pulse is used as reference, while $j = i + 1$ signals a pair of subsequent pulses. The last equality immediately shows that all numerators and denominators can be associated with measured signals.

A. Pump Chopping and No Reference Camera

The case considered in Section 1 of pump chopping and no reference camera implies $j = i + 1$ and sets the right hand fraction in Eq. (4) (R_j/R_i) to unity. It is assumed that the spectral distributions of the consecutive continuum pulses are equal. This is a reasonable but not perfect assumption due to the finite temporal correlation according to Fig. 4(b). When the desired transmission change $T^*(\Delta t)/T_0$ is determined, the above documented issue with pseudo structures results. This is understood by the high degree of correlation seen in Fig. 5(a). Attempts to reference to further delayed pulses did not decrease the correlations significantly, but introduced other sources of noise.

B. Reference Camera and No Pump Chopping

The remaining differences in the continuum spectral distribution between subsequent pulses can be avoided by referencing the sample signal to the reference signal $(j = i)$. Then, S_j and R_j are effectively not measured. This is the commonly used spectral referencing discussed at the beginning of the section. The ratio A_S/A_R has to be determined in a proper calibration to obtain the correct transmission change. This can be done, e.g., by measuring S/R with a blocked pump pulse. To decrease the uncertainty of the calibration to less than the shot noise limit of the actual measurement, averaging for substantially longer than used for a single delay step is required. Also, any long time drift or Kerr and thermal lenses caused by the pump will not be accounted for properly. Besides these technical issues, the influence of the correlations has to be considered.

Figure 5(b) shows the spectral and Fig. 6(b) shows the temporal correlations of the S/R spectra, obtained without sample and pump pulse to focus purely on the continuum and detection aspects. The spectral map shows largely reduced correlations compared to the sample signal referencing to subsequent pulses [see Fig. 5(a)]. This should equally suppress the observation of pseudo structures, but a remaining level has to be expected. However, the temporal correlations increase significantly [compare Figs. 6(b) and 6(a)], not unexpectedly as the high correlation between subsequent pulses is not utilized. This is likely to cause problems with the kinetic analysis, e.g., if standard exponential behavior has to be differentiated from a stretched exponential due to a diffusive process. In addition, we expect a problem with the S/R referencing due to the dark current and the electronic background noise of both cameras. Since these counts are different for both cameras and for every averaging time, and cannot be corrected *in situ* or predicted, they limit the sensitivity of the measurement.

C. Reference Camera and Pump Chopping

The pseudostructures can be eliminated and the spectral calibration becomes obsolete, if pump chopping is combined with the use of two cameras. As already suggested from the last equality in Eq. (4), the ratio taken from the sample camera for two subsequent pulses S^*/S' should be divided by the ratio for the reference camera R/R'. At least theoretically this should directly render $T^*(\lambda, \Delta t)/T_0$ and therefore the transient change in optical density:

$$\Delta OD(\lambda, \Delta t) = \log\left(\frac{T^*(\lambda, \Delta t)}{T_0(\lambda)}\right) = \log\left(\frac{S^*}{S'} \Big/ \frac{R}{R'}\right). \tag{5}$$

This is equivalent to referencing the sample to the reference channel on each shot and rationing the results for subsequent pulses with and without pump. Equation (5) is identical to the procedure described by others [7,26,30,32]. Since subsequent pulses are compared, the differing attenuation factors A_S and A_R cancel and an explicit calibration is not needed. Also, the small but significant difference between the continuum distributions I and I′ is canceled out.

Figure 5(c) shows the spectral and Fig. 6(c) shows the temporal correlation map when this complete referencing is used in a measurement without pump and sample. No temporal correlations beyond the noise level can be observed and also the spectral correlations nearly vanish. Due to the excellent spectral resolution and imaging of our prism spectrometers (see Section 2), the spectral correlation already drops for the next neighbor to the broad socket level of about 0.1. Although the measurement time is not decreased compared to the more classic single camera/chopping method, the drastically reduced correlations eliminate the pseudo structures and lead to an increased spectroscopic sensitivity which will be discussed in Section 5. Compared to just S/R referencing, a nominal increase in laser pulses by a factor of 2 is needed. In practice the purely statistical noise is not the limiting factor and long averaging times are often used simply because the real limiting issue of the pseudo structures is not

appreciated. Averaging these out in a brute force approach leads to unnecessarily long measurement times.

5. IMPROVED SPECTROSCOPIC RESULTS

To demonstrate the improvement by the two camera/chopper referencing, transient spectra of the laser dye malachite green are measured. Malachite green is known to show an ultrafast decay of the excited state followed by vibrational cooling [33 36]. The pump light is centered at 350 nm, has a pulse energy of 150 nJ, and a duration of 50 fs. It is focused down to a beam diameter of 150 μm FWHM, resulting in a peak intensity of 11 GW/cm^2. To make a fair comparison between the standard one camera/chopper method used previously [6,36] and the two camera/chopper referencing, the same dataset for both measurements is used. The transient signal for a time delay between 1 and 5 ps is strong and can be fitted well. The data obtained from this global fit allows extrapolating the expected transient signal at a time delay around 10 ps. Figure 8 shows the expected transient spectrum (black) and selected measured curves for delay times of about 10 ps. Figure 8(a) shows the results obtained with the one camera method and Fig. 8(b) for the full two camera/chopper referencing.

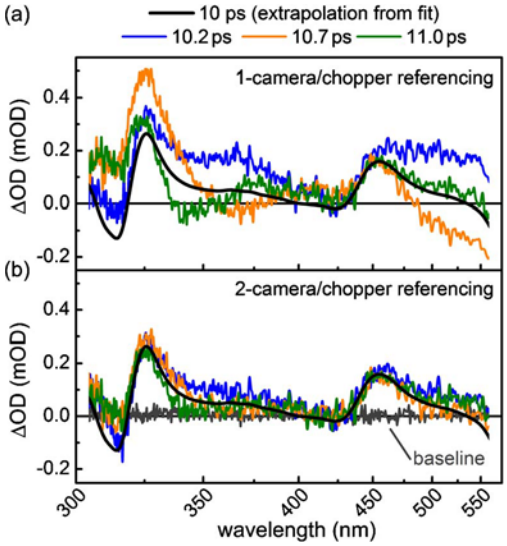

Fig. 8. Selected transient absorption spectra of malachite green measured (a) with the one camera/chopper method and (b) with the two camera/chopper referencing. The black line in both graphs is the transient spectrum obtained from the global fit at 10.6 ps. The gray curve in (b) is the transient spectrum without pumping (baseline).

For single measurements obtained with the one camera method [Fig. 8(a)] the molecular response signal is not clearly identified. Only for a sufficiently large number of transient spectra, the correct pump induced transmission change can possibly be determined. The main challenge is that the measured transient spectra are a superposition of the not predictable large scale pseudo structures and the real molecular signal. Both are on the same order of magnitude. From the expected transient signal obtained from the global fit (black) it is obvious that the correlation induced structures limit the sensitivity and not the low local fluctuations. In the case of two camera/chopper referencing [Fig. 8(b)], the pseudo structures vanish. Now mainly the small local fluctuations are limiting the sensitivity of the experiment and the observed spectra truly correspond to the molecular response.

To show that the improved sensitivity and avoidance of pseudo structures is indeed decisive, an additional experiment is performed. The transient signals of an artificial C nucleoside with benzophenone as chromophore (compound **1** in [37]) are measured. This compound is only weakly solvable in H_2O and the dynamics in H_2O could previously not be measured [37]. The sample is excited at 310 nm with an energy of 150 nJ. The pump is focused down to 70 μm FWHM corresponding to a peak intensity of 50 GW/cm^2 for the 50 fs pulses. The sample is contained in a 1 mm cuvette, leading to a largely reduced and wavelength dependent temporal resolution and a coherent artifact of some hundred femtosecond length. Altogether a weak but significant molecular response results. The transient spectra for simple pump chopping (a) and two camera/chopper referencing (b) are shown in Fig. 9.

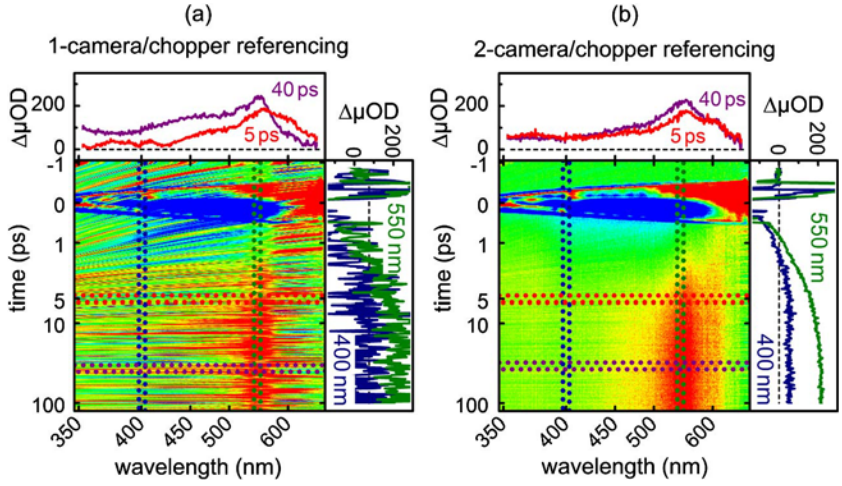

Fig. 9. Transient absorption spectra of compound **1** from [37] dissolved in H_2O with just (a) pump chopping and (b) two camera/chopper referencing. Note the logarithmic time scale starting at 1 ps.

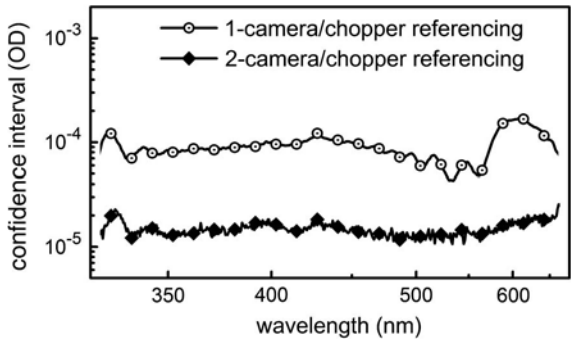

Fig. 10. Confidence interval for optical density achieved with the one and two camera/chopper referencing.

The main features of the ultrafast molecular response can be seen with the one camera method [Fig. 9(a)], but with very limited resolution. The slanted colored stripes are due to the chirp correction in the postprocessing [6]. With two camera/chopper referencing [Fig. 9(b)] the data are much clearer and show a good signal to noise ratio. The benzophenone excited state absorption from the S_1 state at about 580 nm changes to the persistent absorption from the T_1 state the system relaxes to in about 10 ps [37]. A fit to the 550 nm trace from Fig. 9(b) renders a first exponential time constant of 1.0 ps and a second one of 6.3 ps. Due to the 310 nm excitation, there is a first ultrafast $S_2 \rightarrow S_1$ relaxation [38], the intersystem crossing seems to be accelerated both by water as solvent and the S_2 excitation from the typical 10 ps [37,39].

Note that the transmission changes in Fig. 9 are in the range of 50 μOD. A quantitative measure that describes the observed improvement is the confidence interval [7]. It describes the minimum change of the optical density that can be assigned with certainty, and is shown in Fig. 10 for both methods.

The improvement due to the referencing is about a factor of 5 compared to the already highly competitive sensitivity of 100 μOD of our setup [6]. This enhancement is mainly due to the elimination of the impact of the spectral and temporal correlations. The nature of the residual fluctuations now seems to be purely statistical. Therefore, an increased averaging time could lead to the expected $1/\sqrt{N}$ reduction of the noise according to the Poissonian statistics. Compared to the example given in Section 1 with a resulting shot noise limit for $\Delta T/T$ of 10×10^{-5}, the number of averages was increased from 500 to 1000 and three scans were averaged. Together with the ln(10) factor needed to convert to ΔOD, we would predict a shot noise limit of 18 μOD. It might be fortuitous, but it seems like our spectrometer performs very close to the shot noise limit.

6. SUMMARY AND CONCLUSIONS

We have shown for continua generated in YAG and CaF_2 plates that the new wavelengths do not fluctuate statistically but show strong correlations among each other. This is mainly due to the generation mechanism, where all colors are generated within a very short temporal and spatial region because of the abrupt process of self steepening and shock wave formation. These correlations are not predictable and strongly depend on the parameters of the continuum generation like the energy of the individual laser pulse. Even for the same alignment two continua recorded at different times do not show the same correlations. The strong spectral and temporal correlations of the newly generated frequencies influence the obtained fluctuations of the transient spectra. Besides low local fluctuations, strong global deviations from the ideal unity value can be found in the spectra even when measuring without sample and pumping. These global deviations or pseudo structures are not random, but unfortunately not predictable and they overlap with the real molecular response. This limits the sensitivity and leads to erroneous interpretations when working with small transmission changes in the range of sub mOD. An increased averaging time, pump energy, or sample volume is often not possible or helpful.

To counteract this problem, possible and improved referencing methods are discussed and analyzed. First, referencing the continuum signal on the sample camera to the continuum signal on the reference camera is studied. In this case, the uncertainty and instability of the correction factor between sample and reference camera tend to decrease the sensitivity and quality of the measurement. The high correlation between the spectrum on the sample and reference camera is helpful to eliminate the spectral correlations. The missing referencing to the subsequent continuum pulses, however, increases the temporal correlations and limits the quality of the measurements. In the second referencing method, not the continuum spectra but the pumped/unpumped ratios from each camera are compared. In this case, no explicit determination of a spectral correction factor is needed. The high correlation of the single wavelengths from the sample to the reference camera is used to eliminate the strong correlation between neighboring wavelengths in the spectra. The additional referencing to the subsequent pulses provides the spectral correction factor intrinsically. Due to the combined referencing to the reference camera and the subsequent pulses, only the electronic noise and the photon statistics limit the quality of the results. The sensitivity is increased by a factor of 5 down to 20 μOD. This is very close to the shot noise limit.

In related work and discussions of the detection limit of broadband spectrometers that also use two camera/chopper referencing not a single filament continuum but a multifilament is used [32]. This results in as much as 10% fluctuation of the continuum at single wavelengths [7] that has to be averaged out subsequently. The multifilament continuum also seems to display a lower correlation to the subsequent pulse of only 0.5 [7] that reduces the improvement by the chopping. A high degree of correlation is recovered for ultrabroadband NOPA pulses and leads to 44 μOD sensitivity without a reference camera [5] and 25 μOD with a reference camera [7].

Our double referencing scheme has already been successfully used for the recording of two dimensional UV spectra [40]. Only through its use could reasonable averaging times be achieved with the 1 kHz laser system. An even higher sensitivity of 1 μOD could be achieved in a two color pump probe experiment [26]. Besides the higher stability and correlation to the consecutive pulse, the use of a photodiode based detector with a large effective full well capacity is essential for this performance. If the present CCDs were exchanged by diode arrays with their much larger full scale corresponding to around 10^8 detected photons, some of the attenuation needed now [6] could be traded for an even lower shot noise. A related effect is routinely reached by practitioners in transient spectroscopy, when neighboring wavelength signals or spectra for

nearly identical delay times are interpreted and fitted together. As a matter of fact, the technical quality of a global fit, incorporating all the hundreds of time steps and 500 wave length bins, will typically surpass the visual quality of transient spectroscopy by far. Often it is, however, the visual impres sion that leads to the specific fitting model, and this should be chosen without erroneous leads by signal correlations.

ACKNOWLEDGMENTS

We thank N. Krebs, I. Pugliesi, and R. Wilcken for experimen tal assistance and fruitful discussions. We are grateful to the DFG Cluster of Excellence: Munich Centre for Advanced Photonics and the SFB 749 for financial support.

REFERENCES

1. S. A. Kovalenko, A. L. Dobryakov, J. Ruthmann, and N. P. Ernsting, "Femtosecond spectroscopy of condensed phases with chirped supercontinuum probing," Phys. Rev. A **59**, 2369 2384 (1999).
2. P. A. van Hal, R. A. J. Janssen, G. Lanzani, G. Cerullo, M. Zavelani Rossi, and S. De Silvestri, "Full temporal resolution of the two step photoinduced energy electron transfer in a fullerene oligothiophene fullerene triad using sub 10 fs pump probe spectroscopy," Chem. Phys. Lett. **345**, 33 38 (2001).
3. C. Manzoni, D. Polli, and G. Cerullo, "Two color pump probe system broadly tunable over the visible and the near infrared with sub 30 fs temporal resolution," Rev. Sci. Instrum. **77**, 023103 (2006).
4. G. Cerullo, C. Manzoni, L. Lüer, and D. Polli, "Time resolved methods in biophysics. 4. Broadband pump probe spectroscopy system with sub 20 fs temporal resolution for the study of energy transfer processes in photosynthesis," Photochem. Photobiol. Sci. **6**, 135 144 (2007).
5. D. Polli, L. Lüer, and G. Cerullo, "High time resolution pump probe system with broadband detection for the study of time domain vibrational dynamics," Rev. Sci. Instrum. **78**, 103108 (2007).
6. U. Megerle, I. Pugliesi, C. Schriever, C. F. Sailer, and E. Riedle, "Sub 50 fs broadband absorption spectroscopy with tunable ex citation: putting the analysis of ultrafast molecular dynamics on solid ground," Appl. Phys. B **96**, 215 231 (2009).
7. A. L. Dobryakov, S. A. Kovalenko, A. Weigel, J. L. Pérez Lustres, J. Lange, A. Müller, and N. P. Ernsting, "Femtosecond pump/ supercontinuum probe spectroscopy: optimized setup and signal analysis for single shot spectral referencing," Rev. Sci. Instrum. **81**, 113106 (2010).
8. A. Brodeur and S. L. Chin, "Ultrafast white light continuum generation and self focusing in transparent condensed media," J. Opt. Soc. Am. B **16**, 637 650 (1999).
9. R. R. Alfano, *The Supercontinuum Laser Source*, 2nd ed. (Springer, 2006).
10. M. Bradler, P. Baum, and E. Riedle, "Femtosecond continuum generation in bulk laser host materials with sub μJ pump pulses," Appl. Phys. B **97**, 561 574 (2009).
11. R. Huber, H. Satzger, W. Zinth, and J. Wachtveitl, "Noncollinear optical parametric amplifier with output parameters improved by the application of a white light continuum generated in CaF_2," Opt. Commun. **194**, 443 448 (2001).
12. P. Tzankov, I. Buchvarov, and T. Fiebig, "Broadband optical parametric amplification in the near UV VIS," Opt. Commun. **203**, 107 113 (2002).
13. P. J. M. Johnson, V. I. Prokhorenko, and R. J. D. Miller, "Stable UV to IR supercontinuum generation in calcium fluoride with conserved circular polarization states," Opt. Express **17**, 21488 21496 (2009).
14. D. Majus and A. Dubietis, "Statistical properties of ultrafast supercontinuum generated by femtosecond Gaussian and Bessel beams: a comparative study," J. Opt. Soc. Am. B **30**, 994 999 (2013).
15. P. Bejot, J. Kasparian, N. Gisin, and J. P. Wolf, "Laser noise reduction in air," Appl. Phys. Lett. **88**, 251112 (2006).
16. P. Bejot, J. Kasparian, E. Salmon, R. Ackermann, and J. P. Wolf, "Spectral correlation and noise reduction in laser filaments," Appl. Phys. B **87**, 1 4 (2007).
17. S. Spälter, N. Korolkova, F. König, A. Sizmann, and G. Leuchs, "Observation of multimode quantum correlations in fiber optical solitons," Phys. Rev. Lett. **81**, 786 789 (1998).
18. J. K. Ranka, R. S. Windeler, and A. J. Stentz, "Visible continuum generation in air silica microstructure optical fibers with anomalous dispersion at 800 nm," Opt. Lett. **25**, 25 27 (2000).
19. T. Opatrny, "Mode structure and photon number correlations in squeezed quantum pulses," Phys. Rev. A **66**, 053813 (2002).
20. B. Wetzel, A. Stefani, L. Larger, P. A. Lacourt, J. M. Merolla, T. Sylvestre, A. Kudlinski, A. Mussot, G. Genty, F. Dias, and J. M. Dudley, "Real time full bandwidth measurement of spectral noise in supercontinuum generation," Sci. Rep. **2**, 882 (2010).
21. T. Godin, B. Wetzel, T. Sylvestre, L. Larger, A. Kudlinski, A. Mussot, A. B. Salem, M. Zghal, G. Genty, F. Dias, and J. M. Dudley, "Real time noise and wavelength correlations in octave spanning supercontinuum generation," Opt. Express **21**, 18452 18460 (2013).
22. K. Pearson, "Notes on the history of correlations," Biometrika **13**, 25 45 (1920).
23. J. L. Rodgers and W. A. Nicewander, "Thirteen ways to look at the correlation coefficient," Am. Stat. **42**, 59 66 (1988).
24. W. Mendenhall and T. Sincich, *Statistics for Engineering and the Sciences*, 3rd ed. (MacMillan, 1988).
25. A. L. Gaeta, "Catastrophic collapse of ultrashort pulses," Phys. Rev. Lett. **84**, 3582 3585 (2000).
26. C. Schriever, S. Lochbrunner, E. Riedle, and D. J. Nesbitt, "Ultrasensitive ultraviolet visible 20 fs absorption spectroscopy of low vapor pressure molecules in the gas phase," Rev. Sci. Instrum. **79**, 013107 (2008).
27. J. A. Moon, "Optimization of signal to noise ratios in pump probe spectroscopy," Rev. Sci. Instrum. **64**, 1775 1778 (1993).
28. G. Buntinx, R. Naskrecki, and O. Poizat, "Subpicosecond tran sient absorption analysis of the photophysics of 2,2' bipyridine and 4,4' bipyridine in solution," J. Phys. Chem. **100**, 19380 19388 (1996).
29. M. Seel, E. Wildermuth, and W. Zinth, "A multichannel detection system for application in ultra fast spectroscopy," Meas. Sci. Technol. **8**, 449 452 (1997).
30. N. P. Ernsting, S. A. Kovalenko, T. Senyushkina, J. Saam, and V. Farztdinov, "Wave packet assisted decomposition of femtosec ond transient ultraviolet visible absorption spectra: application to excited state intramolecular proton transfer in solution," J. Phys. Chem. A **105**, 3443 3453 (2001).
31. G. Duvanel, N. Banerji, and E. Vauthey, "Excited state dynamics of donor acceptor bridged systems containing a boron dipyrromethene chromophore: interplay between charge separation and reorientational motion," J. Phys. Chem. A **111**, 5361 5369 (2007).
32. B. Lang, S. Mosquera Vazquez, D. Lovy, P. Sherin, V. Markovic, and E. Vauthey, "Broadband ultraviolet visible transient absorp tion spectroscopy in the nanosecond to microsecond time domain with sub nanosecond time resolution," Rev. Sci. Instrum. **84**, 073107 (2013).
33. E. P. Ippen, C. V. Shank, and A. Bergman, "Picosecond recovery dynamics in malachite green," Chem. Phys. Lett. **38**, 611 614 (1976).
34. A. Mokhtari, L. Fini, and J. Chesnoy, "Ultrafast conformation equilibration in triphenyl methane dyes analyzed by time resolved induced photoabsorption," J. Chem. Phys. **87**, 3429 3435 (1987).
35. Y. Nagasawa, Y. Ando, D. Kataoka, H. Matsuda, H. Miyasaka, and T. Okada, "Ultrafast excited state deactivation of triphenylmeth ane dyes," J. Phys. Chem. A **106**, 2024 2035 (2002).
36. E. Riedle, M. Bradler, M. Wenninger, C. F. Sailer, and I. Pugliesi, "Electronic transient spectroscopy from the deep UV to the NIR: unambiguous disentanglement of complex processes," Faraday Discuss. **163**, 139 158 (2013).
37. T. Merz, M. Wenninger, M. Weinberger, E. Riedle, H. A. Wagenknecht, and M. Schütz, "Conformational control of benzo phenone sensitized charge transfer in dinucleotides," Phys. Chem. Chem. Phys. **15**, 18607 18619 (2013).

38. B. K. Shah, M. A. J. Rodgers, and D. C. Neckers, "The $S_2 \rightarrow S_1$ internal conversion of benzophenone and p iodobenzophe none," J. Phys. Chem. A **108**, 6087 6089 (2004).
39. S. Aloise, C. Ruckebusch, L. Blanchet, J. Rehault, G. Buntinx, and J. P. Huvenne, "The benzophenone $S_1(n, \pi^*) \rightarrow T_1(n, \pi^*)$ states intersystem crossing reinvestigated by ultrafast absorption spectroscopy and multivariate curve resolution," J. Phys. Chem. A **112**, 224 231 (2008).
40. N. Krebs, I. Pugliesi, J. Hauer, and E. Riedle, "Two dimensional Fourier transform spectroscopy in the ultraviolet with sub 20 fs pump pulses and 250 720 nm supercontinuum probe," New. J. Phys. **15**, 085016 (2013).

Appendix A17

Relaxation dynamics of the OH stretching overtones in isolated HDO molecules studied by IR pump-repump-probe spectroscopy

J. C. Werhahn, D. Hutzler, R. Heider, M. Bradler,
R. Kienberger, E. Riedle, and H. Iglev

to be submitted to Phys. Rev. Lett. (2014)

Relaxation dynamics of the OH stretching overtones in isolated HDO molecules studied by IR pump-repump-probe spectroscopy

Jasper C. Werhahn,[1] Daniel Hutzler,[1] Rupert Heider,[1] Maximilian Bradler,[2] Reinhard Kienberger,[1,*] Eberhard Riedle,[2] and Hristo Iglev[1]

[1]*Physik-Department, Technische Universität München, James-Franck-Strasse, D-85748 Garching, Germany*

[2]*Lehrstuhl für BioMolekulare Optik, Ludwig-Maximilians-Universität, Oettingenstraße 67, D-80538 Munich, Germany*

[*]*e-mail: reinhard.kienberger@tum.de*

Abstract: We present a novel method of IR pump-repump-probe spectroscopy, which enables for the first time to quantitatively investigate the relaxation dynamics of higher-lying vibrational states. The technique is used to study the OH stretching in $NaClO_4 \cdot HDO$ monohydrate. We observed a continuous decrease of the energy separation for the first four states, i.e. ν_{01} = 3575 cm^{-1}, ν_{12} = 3370 cm^{-1} and ν_{23} = 3171 cm^{-1}, respectively. The population lifetime of the first excited state is 7.2 ps, while the one of the second excited state is 1.4 ps. Information on the properties of the OH stretching overtones is valuable for a deeper understanding of the theoretical potentials, modelling the H bond interaction. This work also shows the potential of the technique for the precise study of complex vibrational relaxation pathways.

Water is an intriguing substance. Its presence is one of the pivotal prerequisites for life on this planet. Despite being remarkably simple in its chemical composition, the fundamental chemistry that gives rise to its unusual properties is astonishingly poorly understood. In order to elucidate the complex physical chemistry of water, scientists utilize various techniques to monitor the dynamics and properties of its H bond network on a molecular level and ultrashort timescales [1,2]. Pump-probe infrared (IR) spectroscopy is one of the most prominent tools to access this desired information [3-6]. Mostly, the transient response of the OH stretching vibration is probed to obtain indirect information on the dynamical evolution of the OH group's chemical vicinity. A variety of higher-order techniques, i.e. methods with more than two pulses have evolved in this field [7-11]. Photon echo and 3D-IR experiments for example have unraveled a plethora of novel information on the complicated dynamics of water and the intimate coupling between different vibrations [12-16]. Pump-repump-probe (PREP) spectroscopy on the other side has, to this day, focused on UV/VIS pump and repump, with varying probe wavelengths. With the help of this technique, the early dynamics of solvated electrons have for example been investigated [17-19]. The repump pulse was employed to manipulate the relaxation pathway of solvated electrons created by the pump pulse and shed new light on this highly complex process [18,19]. With our recently developed setup [20], we are now able to perform PREP spectroscopy with IR pump, repump, and probe with a time resolution of a few ten femtoseconds.

This mid-IR PREP technique can be used to selectively manipulate vibrational relaxation processes to access more detailed information on relaxation pathways. The present study, however, demonstrates another aspect of this spectroscopy, namely investigation of the properties of higher-lying vibrational states. Here we present, to the

best of our knowledge, the first purely vibrational PREP measurements in the mid-IR to access the overtones of the OH stretching mode. The pump pulse excites the OH v_{01}-transition of quasi-isolated HDO molecules in $NaClO_4$ monohydrate, while the repump is tuned to the first overtone of the OH stretch, v_{12}. The properties of the first and second excited state are recorded with a temporal resolution of 100 fs and spectral accuracy of 5 cm^{-1}. Information on these higher-lying vibrational states is expected to be valuable for a deeper understanding of the OH bond potential in condensed media, opening new data for modelling the H bond interaction in such systems, since new energetic regions of the underlying potentials can be investigated. The full characterization of the relaxation pathway underlines the potential of this novel technique.

The experimental setup used in the time-resolved measurements is described in full detail in [20] and should just be briefly mentioned here. The tunable mid–IR pulses acting as pump and repump are generated by two optical parametric amplifiers with pre-amplification in the visible [21]. They are both pumped by 300 µJ laser pulses at 778 nm with a pulse duration of 150 fs and a repetition rate of 1 kHz. The probe pulses are provided by a single-stage infrared amplifier. The used pulses are close to the Fourier limit and deliver a time resolution of sub-100 fs at pulse energies of several µJ for pump and repump [20]. The respective polarizations of all three pulses are the same in this study. In order to avoid spectral overlap between pump and repump pulses and to more precisely pump the OH-stretching transitions in the hydrate a 4*f* spectral selector allows decreasing their spectral bandwidths down to 20 (??) cm^{-1}. The time delay of pump and repump pulses with respect to the probe pulse can be set via two independent delay stages. The three pulses are focused onto the sample. The focal size of the probe pulse is ?? µm FWHM and therewith smaller than that of the pump and repump pulses (?? µm FWHM), so that only the central part of the interaction volume with maximum excitation is monitored. The probe pulse is finally coupled into a spectrometer and measured by a nitrogen cooled multichannel infrared HgCdTe detector. The spectral resolution of the system is about 5 cm^{-1}. The energy transmittance of the probing pulse is recorded for four different excitation conditions: $T_{11}(\nu)$ (pump and repump open), $T_{10}(\nu)$ (repump blocked), $T_{01}(\nu)$ (pump blocked), and $T_{00}(\nu)$ (pump and repump blocked). In this way the induced change of the optical density $\Delta OD_{ex}(\nu,t) = -\log(T_{ex}/T_{00})$ is determined for various excitation conditions (ex = 11, 10 or 01), probe frequencies ν, and delay times. In the following, t_{13} denotes the pump-probe delay time, t_{12} stands for pump-repump delay, and t_{23} is the repump-probe delay. The time-resolved data are measured for a sample temperature of 220 K.

The studied sample contains a saturated solution of $NaClO_4$ dissolved in 15 *M* HDO in D_2O. The solvent was prepared by isotopic exchange in a mixture of appropriate amounts of D_2O (> 99.9 atom% D) and tri-distilled H_2O. In the following discussion water always refers to a 15 M HDO/D_2O mixture. The hydrate crystals are grown by slowly cooling a salt solution between two CaF_2 windows in a cryostat at ambient pressure.

Steady state IR absorption spectra of the sample were obtained from a commercial VECTOR 22 Fourier-transform infrared spectrometer (FTIR, Bruker Optics) with a spectral resolution of 1 cm^{-1}.

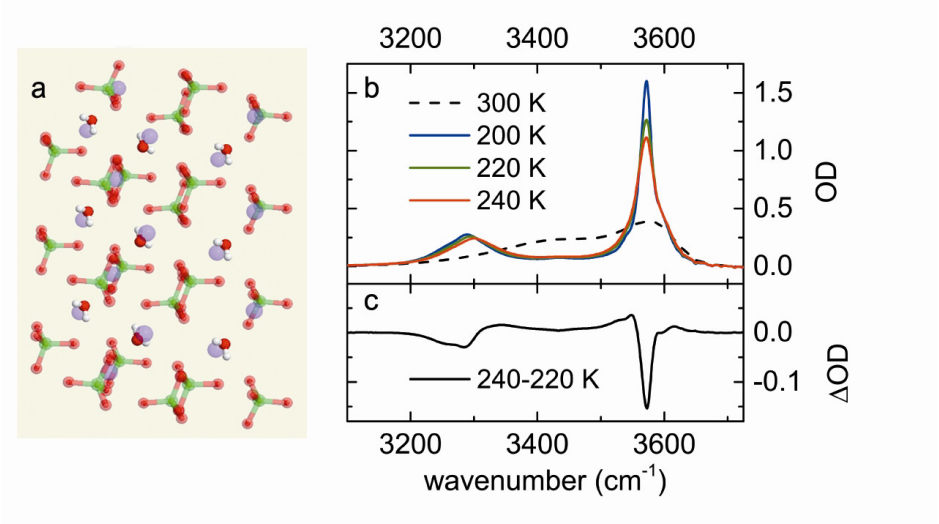

Fig. 1. a, Sketch of the crystal structure of $NaClO_4$ monohydrate (chlorine atoms are drawn green, sodium cations in purple, oxygen in red and hydrogen in white). **b**, FTIR absorption spectra of $NaClO_4$ in $HDO:D_2O$ measured at different temperatures for the liquid (300 K) and the solid phase. **c**, Absorption change measured by increasing the temperature of the sample from 220 to 240 K.

The crystal structure of $NaClO_4$ monohydrate has been determined from x-ray diffraction data [22]. The hydrate forms a monoclinic crystal structure, space group *C2/c*, which is schematically illustrated in Fig.1a. The water molecules are bound to the sodium cations with their lone pairs and the OH groups are always bound to two oxygen atoms of a perchlorate anion by very weak, bifurcated H bonds. The closest distance between two water molecules is 440 pm, they are distinctly separated from each other through the perchlorate anions. Therefore, this hydrate system gives us the possibility to investigate the characteristic dynamics of quasi-isolated water monomers.

Fig. 1b shows the FTIR spectra of the $NaClO_4$ – water sample at various temperatures. The spectrum measured in the liquid phase at 300 K (dashed line) exhibits a distinctive absorption increase at the high-energy wing of the OH stretching band and reaches it maximum at 3575 cm^{-1}. The high concentration of perchlorate anions, commonly known as structure breakers of H bonding network [23], is responsible for the deviation of the absorption spectrum of the liquid sample from pure water. Obviously, a significant part of the water molecules' OH groups has an extremely weak coupling to their environment. The position of this absorption peak does not change upon cooling and subsequent hydrate formation. The limited solubility of $NaClO_4$ leads to the formation of a polycrystalline structure, with spatially separated ice and hydrate crystal structures [24]. Accordingly, the spectra of the solid phase (below 240 K) show two clearly separated absorption peaks in the OH stretching region, corresponding to the sodium perchlorate monohydrate (3575 cm^{-1}) and ice (3297 cm^{-1}). The spectral width of the hydrate peak is 36 ± 5 cm^{-1} and that of the

ice band is 107 ± 5 cm^{-1}. Fig. 1b shows a significant rise of the amplitude of the hydrate peak for lower temperatures, while the ice band shows a lower amplitude increase accompanied by an almost linear spectral shift of the peak maximum. The thermal differential spectrum for a temperature jump of 20 K from 220 to 240 K, shown in Fig. 1c, indicates two conspicuous features due to heating of the ice and the hydrate phase, respectively.

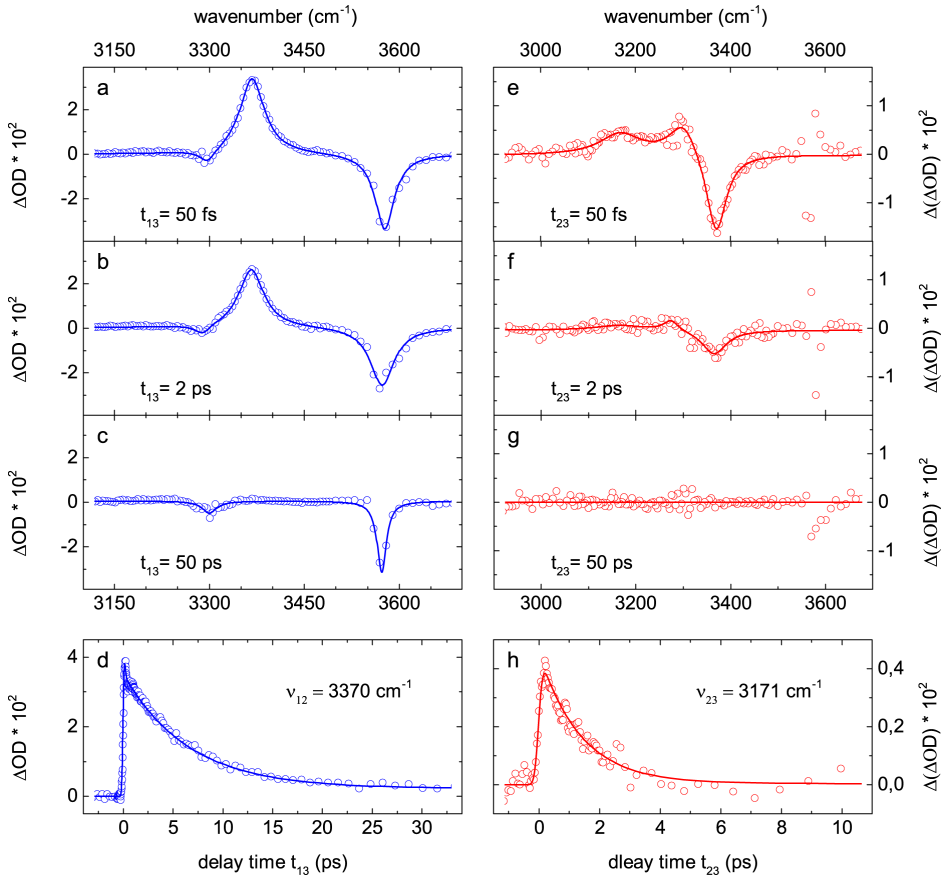

Fig. 2. a – c, Pump-probe spectra recorded after excitation of the hydrate peak at ν_{01} = 3575 cm^{-1} for three different pump-probe delay times t_{13}. The data show bleaching of the ν_{01}-transition and excited state absorption at ν_{12}. **d,** Signal transient measured at ν_{12} = 3370 cm^{-1}. **e – g**, Transient PREP spectra measured after pumping at ν_{01} and repumping at ν_{12}. The pump-repump delay time t_{12} is fixed at 750 fs, while the repump-probe delay time t_{23} is varied. **h**, PREP signal measured in the maximum of the repump-induced second excited state absorption at ν_{23} = 3171 cm^{-1}.. Measured data are shown as points and fits as solid lines.

The pump-probe data, $\Delta OD(\nu,t_{13}) = -\log(T_{10}/T_{00})$, measured after excitation in the maximum of the OH stretching band of the $NaClO_4$ monohydrate and blocked repump are presented in Figs. 2a – d. The transient spectra show that the optical excitation leads to a ground state bleaching (GSB) at 3575 ± 5 cm^{-1} and an excited state absorption (ESA_1) that is spectrally shifted to 3370 ± 5 cm^{-1} due to the anharmonicity of the OH stretching mode

(see Figs. 2a and b). The spectral width of the ESA_1 (FWHM of 48 ± 5 cm^{-1}) is significantly larger than that of GSB (39 ± 5 cm^{-1}). In contrast, the spectral width of the GSB is almost the same as the one determined by the FTIR measurements, which gives evidence for homogeneous broadening of the OH stretching vibration of the hydrate. The small feature at 3297 cm^{-1} can be ascribed to the spatially separated ice crystal structure in the sample that has been discussed above.

The absorption changes measured at 50 ps (see Fig. 2c) are assigned to a laser-induced transient heating of the sample. The qualitative agreement of the data to the thermal differential spectrum shown in Fig. 1c supports this assumption. However, the laser-induced temperature increase occurs at almost constant volume resulting in a simultaneous pressure increase [24,25] leading to the small disagreement between steady state and transient thermal differential spectra.

The relaxation dynamics of the quasi-isolated OH vibration is illustrated in Fig. 2d, where the temporal evolution of the absorption changes measured in the maximum of the ESA_1 is plotted vs. the pump-probe delay time t_{13}. The dynamics are dominated by a mono-exponential decay with an average time constant of 7.2 ± 0.5 ps. (The rapid signal change observed within the first 200 fs is treated as a coherent artifact and will not be further discussed here.) The extracted relaxation time is an order of magnitude larger than those reported for $HDO:D_2O$ ice [26]. Our earlier studies on $NaCl{\cdot}2HDO$ and $LiNO_3{\cdot}3HDO$ hydrates give evidence that the fast energy dissipation from the initially excited OH stretching vibration requires a strong coupling to appropriate accepting modes in the surrounding [24,27]. Here, the perchlorate anions supply the ClO stretching vibration with a frequency of 1100 cm^{-1} that in combination with the OD stretching mode (at roughly 2400 cm^{-1}) could be effectively accessed as a relaxation channel for the OH stretching. However, the weak coupling of the HDO molecule to the environment strongly decelerates the relaxation process. Our conclusions are in accordance with the results of Bakker et al. [28] for water monomers bound to acetone in the liquid phase. In this system, the OH vibration at 3530 cm^{-1} has a lifetime of 6.3 ± 0.3 ps, since the weak coupling between HDO and acetone hinders the fast relaxation via combination of the C=O stretching of acetone (around 1700 cm^{-1}) with the HOD bending or directly to the C=O overtone.

The properties of the higher overtones of the OH stretching vibration are studied using pump-repump-probe (PREP) spectroscopy. Here the pump pulse is resonant with v_{01}, while the repump pulse spectrally overlaps with the v_{12} transition. The peak intensities of both pulses are XX GW/cm² and therefore high enough to generate a measurable population of the first overtone, $n = 2$, of the OH stretching vibration. The probe pulse covers a broad spectral range in the mid-IR, but of particular interest will be the data for the second excited state absorption at v_{23} (ESA_2).

The probe absorption changes measured 800 fs after excitation at ν_{01} = 3575 cm^{-1} and secondary excitation 750 fs after the pump pulse (i.e. the repump is resonant with ν_{12} = 3368 cm^{-1} and t_{23} = 50 fs) are shown in green in Fig. 3a. The simultaneously measured pump-probe signal (repump blocked) is shown in blue for comparison. Note, that an excitation of the sample by the repump without a prior excitation by the pump induces only a very small (if any) effect in the hydrate due to the large spectral mismatch between repump and the ν_{01}-transition. However, the non-vanishing absorption of the ice fraction in the sample at the repump frequency leads to additional transient heating of the sample. In order to exclude this unused signal from the pump-repump-probe data (green points in Fig. 3a), the latter is calculated by comparison of the probe transmission after two pulse excitation (pump and repump) to the probe transmission after excitation with the repump only (pump is blocked), i.e. $\Delta OD_{PuRe}(\nu,t) = -\log(T_{11} / T_{01})$.

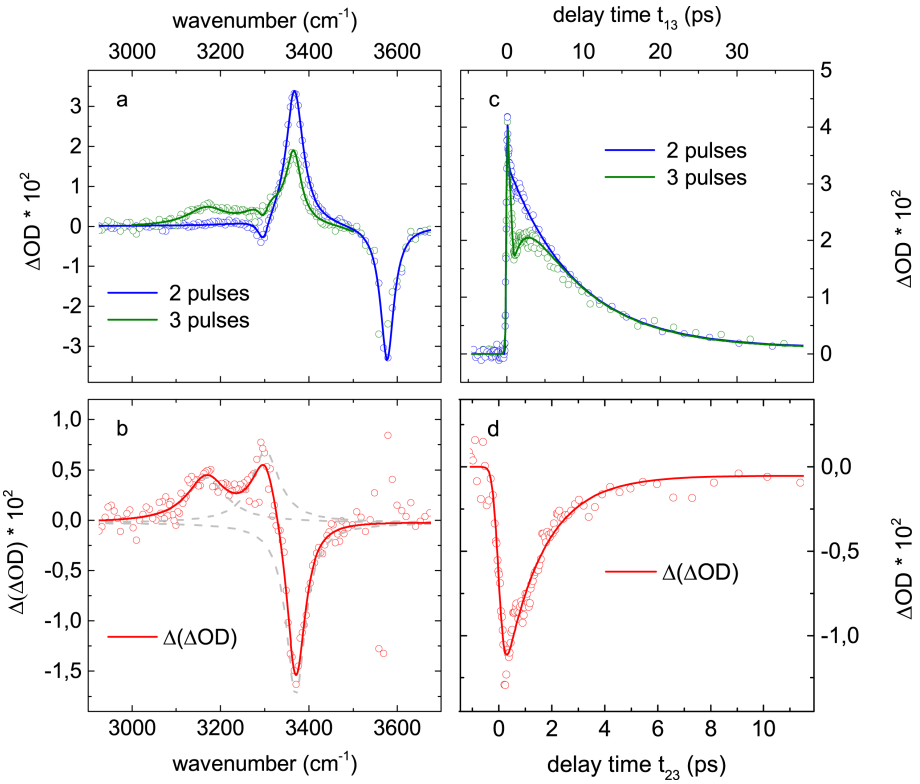

Fig. 3. Principle of vibrational PREP spectroscopy. **a**, Probe absorption changes measured after pumping at ν_{01} and repumping at ν_{12} in green. The pump-repump delay time is t_{12} = 750, while the repump-probe delay time is t_{23} = 50 fs. The according pump-probe signal is given in blue for comparison. **b**, Difference signal $\Delta(\Delta OD)$ between the 3- and 2-pulse data shown in a. The bleaching at ν_{12} = 3370 cm^{-1}, the absorption of the second excited state at ν_{23} = 3171 cm^{-1} and the contribution of the ice fraction at 3297 cm^{-1} are indicated by dashed lines. **c**, Absorption changes measured at ν_{12} as in a (green). The corresponding pump-probe signal is shown in blue. **d**, The difference between both curves in c represents the transient evolution of the repump-induced bleaching of the first excited state.

Both spectra in Fig. 3a show the ground state bleaching at ν_{01} and the first excited state absorption (ESA_1) at ν_{12}. The difference between green and blue data, $\Delta(\Delta OD) = -\log(T_{11} \cdot T_{00} / T_{01} \cdot T_{01})$, is the PREP signal (Fig. 3b). Three main features are observable in the PREP signal: a bleaching of the first excited state (at ν_{12}), a second excited state absorption (ESA_2) at ν_{23} = 3171 ± 5 cm^{-1}, and some additional absorption around the steady state absorption of the sample at 3297 and 3575 cm^{-1}. The last signal contribution is caused by overestimation of the probe absorption changes measured after excitations with the repump only and blocked pump pulse. Note that the lower sample transmission in the maximum of the ice and hydrate bands (see Fig. 1b) reduces the signal-to-noise ratio of the transient signals at these frequencies. This experimental artifact can be seen in the PREP signals measured at various delay times (see Figs. 2e – g) and should be improved in future three-pulse studies. The data in Fig. 3b are analyzed by Lorentzian distributions (see dashed lines) and the red solid line displays the resulting cumulative fit. The extracted spectral width of ESA_2 of 106 ± 30 cm^{-1} is a factor of two larger than that of the ESA_1. A quantitative understanding of the rapid increase of the spectral broadening requires additional experimental and theoretical investigations. The transient PREP spectra measured for different delay times t_{23} (see Figs. 2e – g) show that the signals due to absorption of the OH-stretching overtones decay within the first 10 ps. The long-term signal at t_{23} = 50 ps indicates some additional heating of the sample by the repump pulse [24].

Fig. 3c shows the probe absorption changes measured at ν_{12} = 3370 cm^{-1} after pumping at ν_{01} and secondary excitation at ν_{12} for fixed t_{12} = 750 fs and various repump-probe delay times t_{23} (green points). The corresponding pump-probe transient is depicted in blue. It can already be seen that the repumping of the first excited state depletes its population. The repump-induced signal decrease recovers within the next 5 ps so that the 2- and 3-pulse data coincide almost perfectly for probe delays longer than 10 ps. The PREP signal transient shown in Fig. 3d is the difference $\Delta(\Delta OD)$ between both data sets and illustrates the temporal evolution of the first excited state bleaching. Fig. 2h shows the transient dynamics of the second excited state measured under same excitation conditions. The probe absorption changes measured at 3171 cm^{-1}, as well as these shown in Fig. 3d, decay exponentially with an average time constant of 1.4 ± 0.2 ps. This is the lifetime of the second excited state. Note, that the equality of these two times, along with the fact, that the PREP signal in Fig. 3c recovers to the amplitude of the pump-probe signal after decay of the second excited state vibration give quantitative evidence, that the second excited state decays virtually exclusively to its first excited state, and no additional relaxation pathway is notable from the measured data. This shows, that vibrational PREP is not only capable of yielding quantitative lifetimes of higher-lying vibrational states, but can also unravel the relaxation pathway of these high-lying vibration via comparison to the analogous two pulse experiment.

Our pump-probe and PREP measurements reveal an energy gap ν_{01} = 3575 cm^{-1} for the first transition, ν_{12} = 3370 cm^{-1} for the second and ν_{23} = 3171 cm^{-1} for the third transition. As commonly known for an anharmonic potential, the distance between adjacent energy states decreases for higher energy states [1-4]. For quasi-isolated HDO molecules the frequency shift seems to remain constant or even to be slightly reduced for higher energy states ($\nu_{01} - \nu_{12}$ = 205 cm^{-1}, while $\nu_{12} - \nu_{23}$ = 199 cm^{-1}). This shift describing the velocity of the shrinking of the energetic distances between neighboring energy states can be regarded as a quantitative expression for the anharmonicity of the OH potential. Our data give evidence that the OH vibration in $NaClO_4 \cdot HDO$ can be approximated by a Morse-like potential. This potential has a constant anharmonicity and is used to describe isolated vibrations, as those of diatomic molecules in the gas phase [29]. This observation supports our assignment of the HDO molecules in $NaClO_4$ monohydrate as quasi-free.

We also observed a significant acceleration of the relaxation dynamics for higher overtones. Regarding the two lifetimes of the first (7.2 ps) and the second excited state (about 1.4 ps) we recognize a reduction of the lifetime by a factor of more than 5. The large acceleration factor cannot be explained only by the higher dipole matrix element for transitions between excited states [29], but indicates a stronger coupling of the OH stretching overtones with the low-frequency bath of the hydrate crystal. Measurements in various environments should yield novel information on the coupling mechanisms. Such knowledge is crucial for the better understanding of various chemical and biological processes in water initiated by irradiation with visible and near infrared light.

In conclusion, we have presented the first pump-repump-probe measurements with exclusively mid-IR pulses, to study the properties and relaxation pathways of higher-lying vibrational states. As an illustrative system, we have chosen HDO sodium perchlorate monohydrate, which contains well-isolated water monomers in a well-defined crystalline environment. The high degree of isolation from the surrounding manifests itself in the very long lifetime of the first excited state of the OH stretching vibration of 7.2 ps. The lifetime of the second excited state could for the first time be measured. It is 1.4 ps, and the analysis shows that it mainly relaxes back to the first excited state of the same vibration. This fact, together with the immense shortening of the lifetime with respect to the first excited state gives unambiguous and complete information on the relaxation pathway of this excited state, which can in turn be fruitful to the development of a theoretical description of the OH bond in condensed media.

An obvious application of our research is the obtainment of necessary parameters for a theoretical model capable of a profound and precise description of the H bond interaction. With our experimental data we are able to virtually scan the shape of the OH potential to high-lying energetic regions and provide this new information as additional input parameters to theoretical calculations and simulations. We have also demonstrated, that the frequency resolved probe measurements can help untangle the oftentimes complex

relaxation pathways of high-lying vibrational states. Furthermore, the PREP technique could enable an optical manipulation of the vibrational dynamics by the repump pulse, thus determining the importance of different relaxation pathways. This, as well as the mentioned development of meaningful theoretical models for a prominent bond as the OH bond, will be the subject of future investigations.

1. E. T. J. Nibbering, T. Elsaesser, *Chem. Rev.* **104**, 1887 (2004).

2. H. J. Bakker, J. L. Skinner, *Chem. Rev.* **110**, 1498 (2010).

3. R. Laenen, C. Rauscher, A. Laubereau, *Phys. Rev. Lett.* **80**, 2622 (1998)

4. S. Woutersen, U. Emmerichs, H. J. Bakker, *Science* **278**, 658 (1997).

5. G. M. Gale, G. Gallot, F. Hache, N. Lascoux, S. Bratos, J. C. Leicknam, *Phys. Rev. Lett.* **82**, 1068 (1999).

6. J. Linder, P. Vöhringer, M. S. Pshenichnikov, D. Cringus, D. A. Wiersma, M. Mostovoy, *Chem. Phys. Lett.* **421**, 329 (2006).

7. R. Torre, P. Bartolini, R. Righini, *Nature* **428**, 296 (2004).

8. M. Sovago, R. K. Campen, G. W. H. Wurpel, M. Muller, H. J. Bakker, M. Bonn, *Phys. Rev. Lett.* **100**, 173901 (2008).

9. J. Stenger, D. Madsen, P. Hamm, E. T. J. Nibbering, T. Elsaesser, *Phys. Rev. Lett.* **87**, 027401 (2001).

10. O. Golonzka, M. Khalil, N. Demirdoven, A. Tokmakoff, *Phys. Rev. Lett.* **86**, 2154 (2001).

11. J. Savolainen, S. Ahmed, P. Hamm, *Proc. Natl. Acad. Sci. U.S. A.* **110**, 20402 (2013).

12. C. J. Fecko, J. D. Eaves, J. J. Loparo, A. Tokmakoff, P. L. Geissler, *Science* **301**, 1698 (2003).

13. M. L. Cowan, B. D. Bruner, N. Huse, J. R. Dwyer, B. Chugh, E. T. J. Nibbering, T. Elsaesser, R. J. D. Miller, *Nature* **434**, 199 (2005).

14. J. B. Asbury, T. Steinel, K. Kwak, S. A. Corcelly, C. P. Lawrence, J. L. Skinner, M. D. Fayer, *J. Chem. Phys.* **121**, 12431 (2004).

15. S. Park, K. Kwak, M. D. Fayer, *Laser Phys. Lett.* **4**, 704 (2007).

16. S. Garrett-Roe, F. Perakis, F. Rao, P. Hamm, *J. Phys. Chem. B* **115**, 6976 (2011).

17. C. Silva, P. K. Walhout, K. Yokoyama, P. F. Barbara, *Phys. Rev. Lett.* **80**, 1086 (1998).

18. I. B. Martini, E. R. Barthel, B. J. Schwartz, *Science* **293**, 462 (2001).

19. H. Iglev, M. K. Fischer, A. Gliserin, A. Laubereau, *J. Am Chem. Soc*. **133**, 790 (2011).

20. M. Bradler, J. C. Werhahn, D. Hutzler, S. Fuhrmann, R. Heider, E. Riedle, H. Iglev, R. Kienberger, *Opt. Express* **21**, 20145 (2013).

21. M. Bradler, C. Homann, E. Riedle, *Opt. Lett.* **36**, 4212 (2011).

22. B. Berglund, J.O. Thomas, R. Tellgren, *Acta Cryst.* **B31**, 1842 (1975).

23. J. D. Worley, I. M. Klotz, *J. Chem. Phys.* **45**, 2868 (1966).

24. S. Pandelov, M. B. Pilles, J. C. Werhahn, H. Iglev, *J. Phys. Chem. A* **113**, 10184 (2009).

25. H. Iglev, Schmeisser, K. Simeonidis, A. Thaller, A. Laubereau, *Nature* **439**, 183 (2006).

26. S. Woutersen, U. Emmerichs, H. K. Nienhuys, H. J. Bakker, *Phys. Rev. Lett.* **81**, 1106 (1998).

27. J. C. Werhahn, S. Pandelov, S. S. Xanthes, H. Iglev, *J. Chem. Phys. Lett.* **2**, 1633 (2011).

28. H. J. Bakker, J. J. Gilijamse, A. J. Lock, *ChemPhysChem* **6**, 1146 (2005).

29. E. F. de Lima, J. E. M. Hornos, *J. Phys. B* **38**, 815 (2005).

Appendix A18

Small-scale filamentation and continuum generation in solids with femto-second pump sources from the ultraviolet to the infrared

M. Bradler, E. Wittmann, and E. Riedle

to be submitted to Opt. Express (2014)

Small-scale filamentation and continuum generation in solids with femtosecond pump sources from the ultraviolet to the infrared

Maximilian Bradler, Emanuel Wittmann, and Eberhard Riedle*

Lehrstuhl für BioMolekulare Optik, Ludwig-Maximilians-Universität (LMU), Oettingenstraße 67, 80538 München, Germany

** corresponding author:* Eberhard.Riedle@Physik.uni-muenchen.de

OCIS codes: (190.3270) Kerr effect; (190.4720) Optical nonlinearities of condensed matter; (190.7110) Ultrafast nonlinear optics; (260.5950) Self-focusing; (260.7120) Ultrafast phenomena; (320.2250) Femtosecond phenomena; (320.5390) Picosecond phenomena; (320.6629) Supercontinuum generation; (320.7110) Ultrafast nonlinear optics; (320.7120) Ultrafast phenomena;

Abstract

Bulk continuum generation is an excellent method to access new wavelength regimes. However, it is often assumed that it is only possible for a limited pump wavelength and pulse durations range. In this work we investigate continuum generation with pulse durations over the entire femtosecond regime and wavelengths from 258 nm to 2.2 µm. This allows octave spanning whitelight spectra. First evidences for picosecond continuum generation are shown. In addition, the influence of the spectral width and the chirp oft the pump pulse on continuum generation is studied. The phenomenon of multiple refocusing is regarded in more detail. Beside the direct observation of the filament channels, the spectral and spatial interference between single filaments is shown. From this, we can characterize phase fluctuations of the newly generated frequencies and by varying the crystal length the single steps of filamentation and continuum generation can be resolved.

1. Filamentation and continuum generation

One of the most spectacular phenomena in femtosecond nonlinear optics is filamentation. Highest intensities exceeding 10^{12} W/cm² can be conveyed over long distances in strong contrast to the natural Gaussian propagation and maintaining the advantageous properties such as superior beam quality and short pulse durations. The process of filamentation is intensely studied and reviewed, especially in weak nonlinear media such as gases or air [Bra95, Chi05, Ber07, Cou07, Chi10] and used for a wide range of applications [Dav96, Rai00, Kas03, Hau04, Ste04, Kas08, Roh10]. Filamentation also appears in highly nonlinear media like solids or liquids. Here, the process takes place on a much smaller scale. Whereas filaments in gases can last over several kilometers [Sau05, Rod04] filamentation in solids typically stops after several millimeter. This is due to the enhanced stopping mechanisms in condensed media and the limited energy contained inside a single filament. Filamentation often is accompanied by continuum generation. This is an excellent source for producing new frequencies beside the laser wavelength and its harmonic. Continuum generation was already observed in the early seventies [Alf70a, Alf70b, For83] and is still focus of many theoretical and experimental investigations [Bro99, Kan03, Alf09, Bra09]. A favorable property of bulk continuum generation is the low energy needed for filamentation inside crystals. The new generated colors show a high stability, strong coherence, good beam quality, easy compressibility and are well suited for further amplification or as probe light in spectroscopic applications. Due to the high nonlinearity in solids various processes occur and the interplay between them lead to the generation of new frequencies. Beside self-focusing, self-steepening, and self-phase-modulation, also pulse splitting [Rot92], the formation of optical shock waves [Gae00], intensity clamping [Liu02], four wave mixing [Xin93], Raman processes [Zoz98], and X-wave formation [Kol04, Fac06] are involved in continuum generation. There is still a discussion about the relevance of the single processes [Kol10, Tel10, Kos11, Kar13].

In this work, we experimentally study the influence of all important pump parameter on bulk continuum generation and characterize the generated filaments and continua. The input wavelength is varied from the ultraviolet (UV) to the infrared (IR), continuum generation with femto- to picoseconds pulses is demonstrated. We study the spatial and temporal chirp of the newly generated frequencies and show the influence of the pump fluctuations on the phase stability of the continua. Finally, single and multiple filamentation and refocusing are analyzed and a guide for best continuum generation for the specific applications is given.

2. Guidelines for continuum generation and setup

The processes of filamentation and continuum generation are very completely and comprehensively reviewed in [Cou07], [Alf09] and [Chi10] and the references within there. In this work, we focus on the experimental realization and the control of continuum generation. Since the Kerr effect plays a major role and self-focusing is the initial process the nonlinear refractive index is crucial for continuum generation. We want to give a guideline which should help to find the best suited crystal for the specific experiment. The following qualitative relations between several material and continuum properties can be deduced [Bra09].

- the higher the linear refractive index, the higher the nonlinear refractive index
- the higher the nonlinear refractive index, the lower the continuum threshold
- the higher the nonlinear refractive index, the longer the maximum pulse duration where continuum generation is still possible
- the higher the nonlinear refractive index, the redder the continuum cut-off

Especially laser crystals are well suited for continuum generation due to their superior crystalline quality, high damage threshold, good thermal properties, and wide availability.

The setup for continuum generation is shown in Fig. 1(a). As laser source a 1 kHz Ti:sapphire laser system is used (CPA2001; Clark MXR) which delivers 775 nm, 1 mJ, 150 fs pulses. Only a small fraction of 5 µJ is used for continuum generation. The pump energy is adjusted with a variable attenuator (VA) and the outer part of the beam is cropped by an iris. It has been experimentally observed that this has a stabilizing effect on continuum generation. An f = 100 mm lens is used to focus the light on the crystal to perform continuum generation. Filters and detection units are placed behind the continuum generation to measure the spectrum, beam profile, divergence, stability, spectral chirp, and polarization of the continuum. Continuum generation in calcium fluoride (CaF_2) and sapphire for various pump wavelengths is shown in Fig. 1(b).

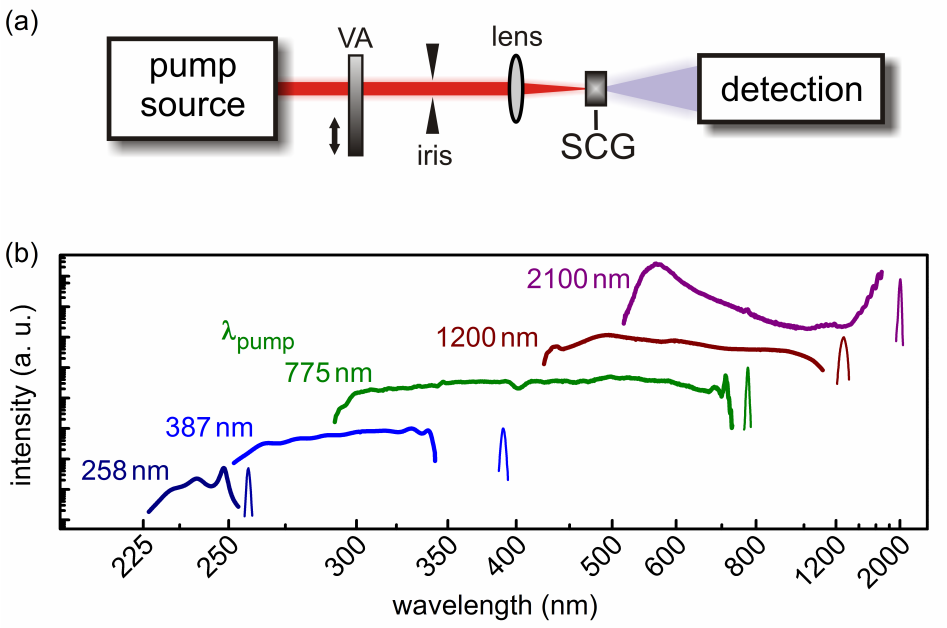

Fig. 1: (a) Setup for continuum generation (SCG), (b) continuum spectra from CaF_2 and sapphire (2100 nm) with pump wavelengths from 258 nm to 2.1 µm.

3. Pump wavelength from the UV to the IR

Most of the applications demand for specific wavelengths which are not directly available from the laser source or its harmonics. Continuum generation is a good method to gain access to new frequencies. Even if the desired wavelength region is not among the newly generated frequencies, further nonlinear processes like second harmonic generation, sum and difference frequency, or optical parametric amplification allow the generation of the wanted wavelength. Often a wide spectral range is needed at the new frequencies and continuum generation in solids is an easy and robust solution, only requiring some 100 nJ or a few µJ of pulse energy. The spectral shape of the continua generated at the new frequency shows a unique behavior due to its generation mechanisms [Gae00] and is nearly independent from the pump wavelength. On the short wavelength side a smooth, flat plateau is observed, which ranges down to the material specific continuum cut-off, where else on the long wavelength side an exponential decay occurs.

To show that continuum generation is not only possible with typical laser wavelengths 800 or 1000 nm, we generated light with various pump wavelengths by frequency doubling and tripling of the laser and optical parametric amplification. With this pump sources ranging from the UV to the IR, we perform continuum generation. Figure 1(b) shows these continua which

are generated in CaF_2 (258 to 1300 nm) and sapphire (2100 nm). The spectra are measured after the whitelight has passed a filter or mirror which blocks the fundamental region so that only the newly generated frequencies are obtained. All continua in Fig. 1(b) are successfully used in transient pump probe absorption spectroscopy [Rie13] which is a strong indicator for their excellent properties. The details on the generation of these continua are given in ref. [Rie13]. It is remarkable, that even with a pump wavelength of 258 nm, what corresponds to the 3rd harmonic of a Ti:sapphire or the 4th harmonic of Neodym or Ytterbium based laser system, continuum generation is possible in CaF_2, although this is below the typical continuum cut-off of 280 nm when pumping with 800 nm. This means that the continuum cut-off is only a rough estimation and slightly shifts with the pump wavelength. Continuum generation with harmonics is a good method to extend the continuum-cut off and is used in parametric amplifier or spectrometer [Bal02, Nag02, Joh09, Mue09, Cer11, Rie13].

Nevertheless, when increasing the pump wavelength the continuum cut-off only weakly increases and allows octave spanning spectra [Bra09, Etz12, Sil12, Dar13], what is interesting for the few-cycle regime or broadband detection. For example continuum generation in YAG crystals with infrared wavelengths was intensively studied [Sil12, Dar13] and continuum generation in a silicon plate with 2.1 µm is used in pump probe spectroscopy [Etz12]. We decided to use CaF_2 due to the short continuum cut-off and even continuum generation with ultraviolet wavelengths is possible. The energy threshold for continuum generation scales quadratically with the pump wavelength, because the first process is self-focusing which scales quadratically with the wavelength. Further, for the experimental realization of continua with longer wavelength, it has to be taken into account that the achievable beam waist radius increase for longer wavelength when using the same external focusing. If not enough pump energy can be provided, materials with a low continuum threshold can be utilized such as YVO_4 or KGW crystals [Bra09].

4. Chirp and spectrum of pump pulse

Beside the wavelength also the spectral distribution and the chirp of the pump pulses determine, whether continuum generation is possible or not. For longer pulses in the picosecond regime avalanche ionizations can stop continuum generation, because the freely generated electrons by multi-photon generation continuously seed the avalanche ionization and the damage threshold of a material can be exceeded if the pulse duration is too long. This scenario was simulated for YAG [Sch11] and it was shown that for 850 fs pulses proper contin-

uum generation is still possible and 1 ps is the typical limit. A very important issue is, that the temporal profile is changing during the propagation in the material. The pulse "duration" can become much lower due to self-phase modulation, self-steepening and pulse splitting than the initial one. This enables continuum generation even with picosecond pulses. This is especially the case when the Fourier limit of the pump pulses is shorter so that it does not prohibit the pulse shortening.

Table I summarizes the generation of continua in solids for long pump pulse durations observed up to now. Beside the needed energy for proper continuum, we also show the material used for continuum generation, the pump pulse duration including the Fourier limit. The plus or minus indicate the kind of chirp. Plus means that the reddish wavelengths come first.

TABLE I: Experimental realization of continuum generation for long pump pulse durations.

laser	λ_{pump}	material	pump energy	pulse duration	Fourier limit
JenOptik (JenLas D2.fs) [Bra09]	1025 nm	YAG	1.0 µJ	300 fs (+)	280 fs
Yb fiber osc. [Dob12]	1030 nm	KGW	1.6 µJ	1.6 ps (+)	300 fs
Yb rod-type fiber amp. [Emo10]	1030 nm	YAG	2.0 µJ	420 fs (+)	360 fs
Spirit; HighQ	1040 nm	YAG	7.2 µJ	1.0 ps (+)	400 fs
			6.8 µJ	1.4 ps (-)	
		KGW	3.5 µJ	2.6 ps (-)	
Yb:YAG Innoslab [Sch11]	1030 nm	YAG	10 µJ	0.85 ps (+)	560 fs
Yb:YAG thin disk laser [Met09]	1025 nm	YAG	10 µJ	0.9 ps (+)	770 fs

A typical spectrum of such continua can be seen in Fig. 2, where a continuum generated with 0.9 ps pump pulses in a 4 mm YAG plate (black) and one with 2.6 ps pump pulses in a 4 mm KGW (purple) is shown.

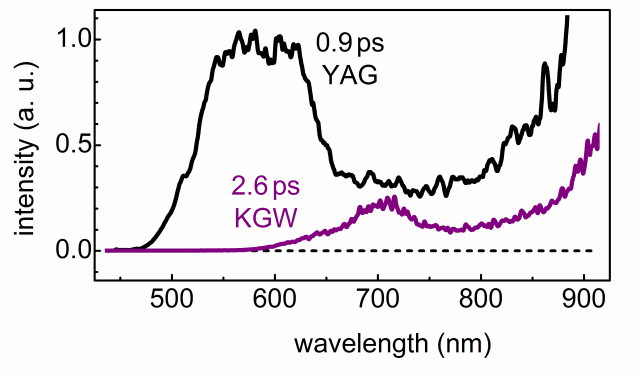

Fig. 2: Continuum generation with picosecond pump pulses in 4 mm YAG (black) and KGW (purple) plate.

To study the influence of the spectral width and the Fourier limit of the pump pulse on continuum generation we used the setup shown in Fig. 3(a). To perform continuum generation with longer pulses the pulse duration of the pulses is increased. One time this is done by putting glass into the beam path and one time by decreasing the spectral bandwidth. The latter was done in the Fourier plane of a prism compressor. The resulting pulse duration were measured with an autocorrelator.

At first, we want to study whether continuum generation is possible or not and focused the chirped and the spectrally narrowed 800 nm pulses onto 4 mm thick YAG, sapphire, and KGW plates. Since above a certain limit always some spectral broadening occurs we determine the stability and spectral distribution of the newly generated frequencies as criterion for continuum generation. Only if a smooth and gap free spectrum is obtained which extends to the typical continuum cut-off of the crystal and the pulse-to-pulse stability does not exceed 2% rms, this is seen as proper continuum generation. For best continuum generation the geometric conditions have been studied previously [Bra09] and we find that a f = 100 mm lens is well suited to generate intense continua. The laser beam has a radius of 2 mm ($1/e^2$ intensity level), an M^2 of 1.20 and a central wavelength of 775 nm. The beam waist radius in the focus and hence at the crystal entrance is 25 µm. With a pulse duration of 150 fs, this leads to a peak intensity of 640 GW/cm² per µJ pump energy.

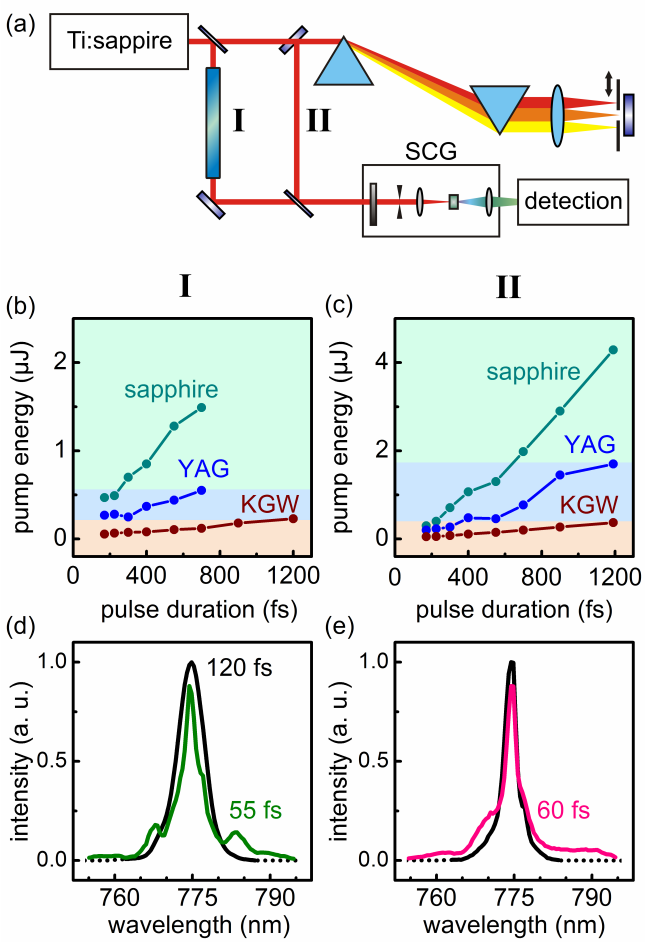

Fig. 3(a): (a) Setup for continuum generation with chirped (I) and spectrally narrowed (II) pump pulses. Pump energy for various pulse durations in sapphire, YAG, and KGW, when pumping with chirped (b) and spectrally narrowed (c) pulses. Spectrum before (black) and after (green and pink) continuum generation for chirped (d) and spectrally narrowed (e) pump pulses.

Figure 3 shows the necessary pump energy in dependence of the pulse duration for sapphire (green), YAG (blue), and KGW (brown) for chirped (b) and spectrally narrowed (c) pump pulses. In addition, the spectrum in the fundamental region before and after continuum generation is shown for both (chirped in (d), spectrally narrowed in (e)). For each crystal the ratio between pump energy and pulse duration is constant. This means that the required peak power and intensity is constant independently from the pulse duration. However, the needed pump energy can not be significantly reduced by changing the external focusing since the threshold for self-focusing depends on the peak power. Attempts to focus the laser light so tight that an intensity as inside a filament is already reached at the crystal entrance lead to destruction and permanent damage of the surface. For bulk continuum generation self-focusing is inevitable.

The energy for a given pulse duration is always higher for a spectrally narrowed than for a chirped pump pulse (typically a factor of 1.5). This is due to the fact that for chirped pulses self-steepening shortens the pulse down in the region of the Fourier limit and continuum generation is similar to the case of unchirped pulses. If the bandwidth of the pulses is spectrally narrower and hence have a longer Fourier limit, first self-phase-modulation has to broaden the spectrum to substantially perform pulse shortening. This leads to the enhanced needed pump energy. The fact that the Fourier limit after continuum generation is much more shortened in the case of spectrally narrowed pump pulses (factor of 5) than of chirped pulses (factor of 2) supports this concept. The Fourier limits after continuum generation of both are in the 50 fs regime and significantly lower than the initial one of 120 fs. We only rely on the region around the pump wavelength and exclude the newly generated frequencies in the Fourier limit calculations to purely analyze the effects of continuum generation on the pump pulses.

We further study the influence of the chirp and spectral width on the spectral distribution of the new frequencies. Pump pulses around 800 nm with different chirp and spectral widths are generated and used for continuum generation a 4 mm YAG plate. Figure 4(a) shows the generated spectra for a not chirped pump (black), a chirped pump with a pulse duration of 400 fs (green), and a spectrally narrowed pump (pink) with a duration of 400 fs. For all generated continua a similar spectral distribution is obtained. The region around the pump wavelength varies due to the spectral shaping and the different needed pump energies.

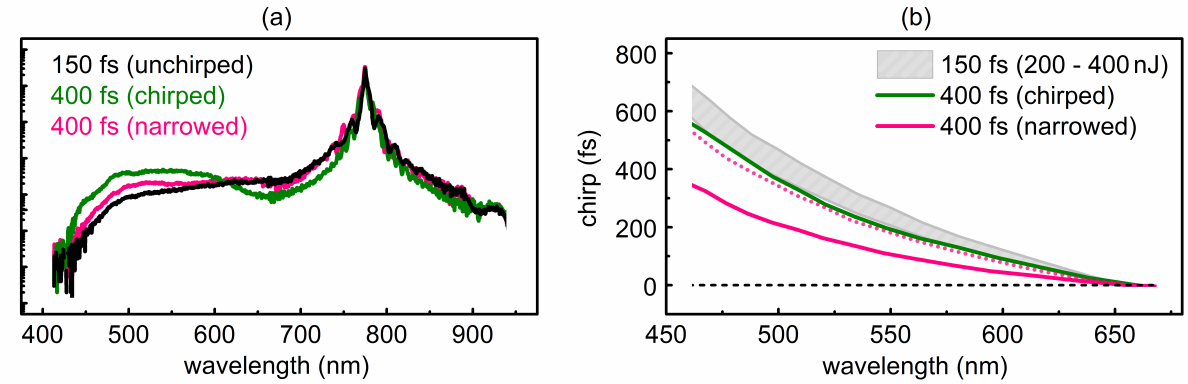

Fig. 4(a): Spectrum (a) and chirp (b) of continua generated in a 4 mm YAG plate with unchirped (black and grey area), chirped (green), and spectrally narrowed (pink) pump pulses with different pump energies for the latter in (b) (solid a dotted line).

The spectral distribution including the wavelength cut-off only depends on the material and not on the central wavelength, spectral width, pulse duration, or the intensity of the pump.

This is due to the generation mechanism. Self-steepening and the other nonlinear processes lead to shock waves and plasma formation and similar spectral distributions. Therefore we would also not expect a strongly varying chirp of the new frequencies. To proof this transient absorption measurements are performed [Meg09]. The continua are used as probe light and their chirp can be determined via two photon absorption. As pump light a 600 nm pulse with 30 fs pulse duration is used and as sample a 100 µm thin GGG plate. Only reflective optics are used to avoid chirp. The thin GGG plate does not remarkably increase the spectral chirp. For measurements at single wavelengths narrowband interference filters are used.

When generating the continuum with 150 fs pulses the pump energy was varied from slightly above the threshold up to closely below multiple refocusing (200 – 400 nJ). The chirp increases with higher pump energies (grey area in Fig. 4(b)) because self-focusing gets stronger and the filament is generated earlier in the crystal. According to the increased remaining pathway of the new wavelengths in the crystal and their different group velocities the chirp increases. We repeated the measurements for a chirped 400 fs pulse (green line). Beside the higher input energy the chirp is on a comparable level. The chirped pump pulses firstly self-compress and than continuum generation similar to the 150 fs pulses occurs. However some distance is needed for the self-compression and therefore the filament is generated at a later position in the crystal and the chirp tends to be weaker. For the spectrally narrowed 400 fs pulses (pink lines) the pulses first spectrally broaden, than self-compress, and finally continuum generation takes place. This needs even a longer part of the crystal and the obtained chirp is weakest because the continuum is generated very close to the exit surface. The pump energy is slightly above the threshold for the pink solid line in Fig. 4(b) (550 nJ) and close to multiple refocusing for the pink dotted line (1100 nJ).

From this measurements we can conclude that only the remaining pathway in the crystal is responsible for the resulting chirp. And indeed for the proper pump energy the chirp of the continua generated with unchirped, chirped, and spectrally narrowed pump pulses can become very similar (lower grey boarder, green line, dashed pink line in Fig. 4(b)). Then, the new frequencies are always generated at the same position inside the crystal and hence only the remaining pathway is responsible for the spectral chirp. Therefore, the amount of chirp reduces, when shorter crystal lengths are used [Cer97].

5. Single and multiple filamentation in solids

An interesting fact is that the filamentation channel is visible in YAG. During continuum generation in solids self-focusing is stopped by multiphoton excitation of electrons from the valence to the conduction band. Depending on the material the recombination radiation can be in the visible and therefore observable with the bare eyes. Figure 5(a) shows a photography of a 6 mm thick YAG plate, in which continuum generation takes place. The incident laser light propagates from left to right and is focused on the entrance surface (left) of the crystal. After the self-focal distance the laser intensity becomes so high that multi-photon absorption occurs. Due to self-trapped excitons and trapped excitons from anthracite Y^{3+} defects recombination occurs [Bab05]. The resulting luminescence is undirected and has spectral components in the visible (see Fig. 6(d), grey area). In the photography in Fig. 5(a) even multiple refocusing is observable. Figure 5(b) on the other side shows multifilamentation with many single filaments side by side in a fused silica glass block.

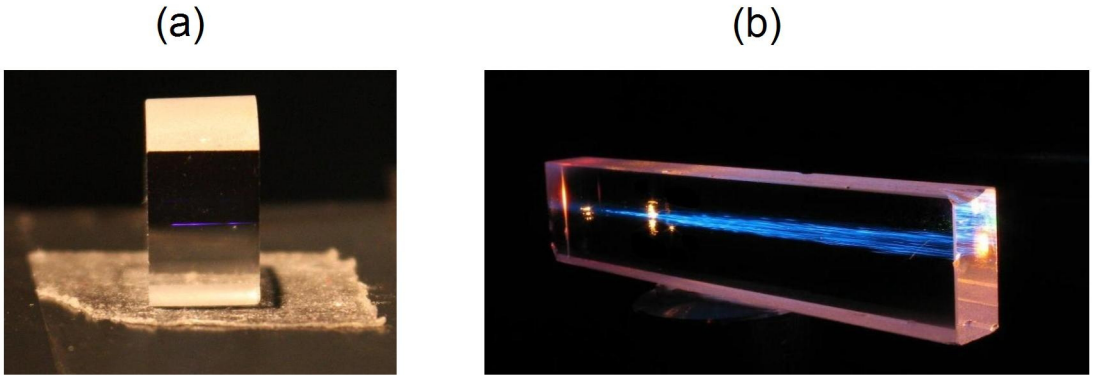

Fig. 5: (a) Photography of multiple refocusing in a 6 mm YAG crystal, (b) beam break up and multi-filamentation in a 10 cm fused silica block.

From this side view of the crystal the position and dimension of the filamentation channel can be determined. Observations from the side has been already used to study continuum generation in methanol [Sch04, Liu03]. To visualize the single colors laser dyes with absorption in the visible have been used. This can reveal the single steps during filamentation and continuum generation. To achieve the best image quality and highest spatial resolution for our side view we use a reflex camera (EOS 60D; Canon) and a five time enlarging objective (MP-E 65mm f/2.8 1-5x Macro Photo, Canon). We manually optimize the focus with linear micrometer translation stages and use a computer to control the camera. Note that we image an

object which is inside a high refractive transparent material. However, this only influences the depth in the material, but not the lateral size. To ensure this we take a picture of a micro objective (micro objective 200 in 2 mm; Qioptiq Inc.) in an empty and filled water basin and find no difference in the lateral size, only in the focusing depth. The micro objective is also used as scale and from this we can estimate a resolution of 0.85 µm per pixel. This is in good agreement with the calculated resolution from the pixel size and the enlargement factor (4.3 µm pixel size and 5:1 enlargement on sensor). Neutral density filters are used to calibrate the system and ensure a linear intensity scale. This allows directly measuring the dimensions of the filament channel inside a 6 mm YAG plate. Filaments have typical lengths of about 1.3 mm (see Fig. 6 (b)) and diameters of 8 µm (FWHM) (see Fig. 6 (b) and 6(c)). In addition, a recorded image is shown in Fig. 6 (a) and the spectrum of the recombination luminescence in Fig. 6(d). The grey area in Fig. 6(d) denotes the recombination spectrum for undoped YAG excited at 190 nm including its visible tail [Bab05].

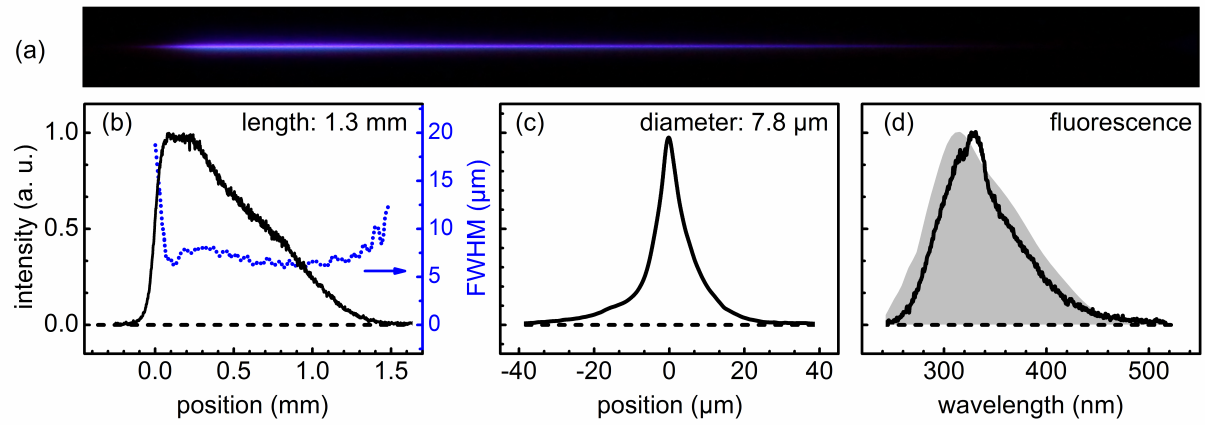

Fig. 6: Image (a) and profile of filament length (b) and diameter (c) and spectrum of the fluorescence (d) of filamentation in a 6 mm YAG plate. The blue curve in (b) additionally shows the beam diameter overt the filament.

The characteristic behavior of filamentation in gases of a long propagation distance and a small beam diameter are also observed for solids. For a beam diameter of 7.8 µm (FWHM) the Raleigh length would be 180 µm which is 7 times shorter than the observed filament length of 1.3 mm. The main differences between filamentation in gases and solids are the dimensions. Whereas filaments in gases have typically diameter of 100 µm and can range up to several kilometers, filamentation in solids have a 20 to 30 times smaller diameter and are much shorter.

To understand why the filament diameter is such small in solids the threshold and the stop-

ping mechanism of self-focusing hast to be considered. The high nonlinear refractive index of solids leads to threshold powers in the megawatt regime and is roughly three magnitudes lower compared to the typically needed gigawatt for self-focusing in gases [Cou07]. The stopping mechanism in solids is multiphoton absorption from the valence to the conduction band. And this requires intensities around 10^{12} W/cm² which is on the other side only one magnitude lower than typical intensities inside filaments in gases. The low self-focusing threshold combined with the high clamping intensity in solids leads to small diameters of filaments in solids in the µm regime. If the beam size is increased at the entrance surface of the solid smallest modulation instabilities of spatial modes will lead to a beam break up and multiple filaments side by side will occur [Cam74]. Each of these filaments has the properties and dimensions of one single filament. To illustrate this, Fig. 5(b) shows multiple filamentation when a 1 mJ, 150 fs, 775 nm pulse is propagating in a 10 cm fused silica block.

If the input beam size is kept small so that no beam break up occurs and the input energy is increased above twice the threshold, multiple refocusing occurs [Tal99, Liu03, Dha09]. Then, several filaments are generated along the propagation axis. Each has the same dimensions and properties. Due to the visible recombination radiation we are also able to directly observe multiple refocusing as shown in Fig. 5(a). The number of visible filaments correlates to the ratio between input power and threshold. This means, that only nearly twice of the threshold energy can be located in one filament in solids. Otherwise multiple refocusing, permanent damage, or break up of the beam occur. From Fig. 6(b) it can be seen that diameter of a filament in solids is always in the regime of several µm. Due to the high losses caused by multiphoton absorption also the length is limited to a few millimeter.

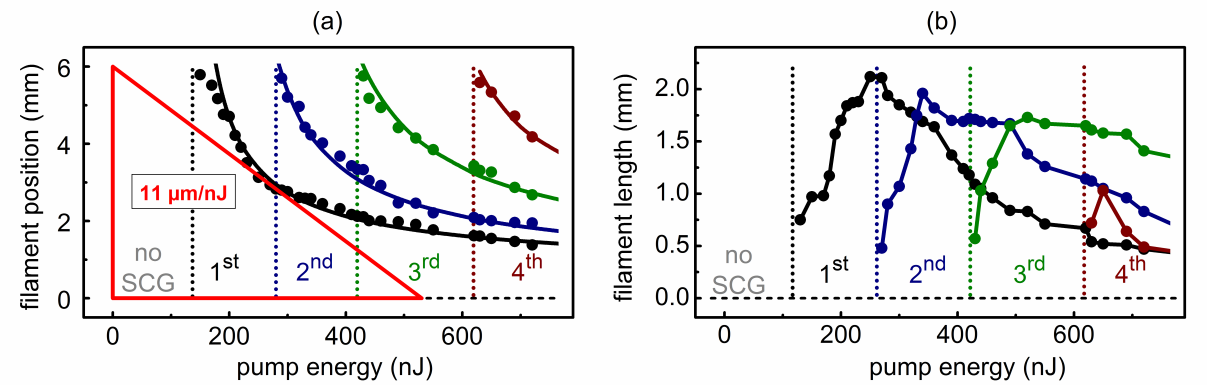

Fig. 7: Influence of pump energy on filament position (a) and length (b). Energy fluctuations lead to position and hence phase fluctuations of the new colors.

When increasing the pump energy the length of filament increases up to a maximum value of about 2 mm (see Fig. 7(b)). Interesting is that the filament length decreases if an additional filament appears. This could be due to the alternation of the surrounding photon bath which now has to feed more filaments.

The determination of the filament position in dependence of the input energy can be used to optimize the continuum generation. Figure 7(a) shows the position for the single filaments (circles) during multiple refocusing in dependence of the pump energy. For example at a pump energy of 500 nJ three filaments (2 mm, 2.5 mm, and 4 mm behind the front surface) were observed. The solids line show the theoretical self-focal distance, assuming one, two, three, or four times the self-focusing threshold as critical power. Since the energy of the laser is fluctuating also the positions of the filaments fluctuate, according to the slope of the tangent (red line in Fig. 7(a)). This means that for example for 280 nJ the position is varying 11 µm if the pump energy is varied 1 nJ.

This variation of the generation position results in temporal and hence phase fluctuations of the newly generated frequencies, because depending on the of the actual generation position the propagation pathways inside the crystal for fundamental and newly generated light are slightly different. And since both are propagating with different group velocities the traveling time and phase become different. The phase fluctuations in the dependence of the energy fluctuations ($\Delta\varphi/\Delta E$) can be written as

$$\frac{\Delta\varphi}{\Delta E} = \frac{2\pi c}{\lambda_{SCG}} \cdot \frac{\Delta t}{\Delta E} = \frac{2\pi c}{\lambda_{SCG}} \cdot \left| \frac{1}{v_{group}^{pump}} - \frac{1}{v_{group}^{SCG}} \right| \cdot \frac{\Delta z}{\Delta E} \tag{1}$$

λ_{SCG} is the considered continuum wavelength, c the speed of light, $\Delta t/\Delta E$ the time fluctuations in dependence of the energy fluctuations, ν_{group} the group velocity for pump and continuum wavelength, and $\Delta z/\Delta E$ the position variations in dependence of the energy fluctuations. The optimum condition with minimum temporal and phase jitter is reached, if strong energy fluctuations lead to weak position variations. This is the case for the smallest possible slopes of the tangent in Fig. 7(a). Note that for many applications only single filamentation is suited, because otherwise the interference between the filaments lead to unwanted instabilities. Therefore the optimum continuum generation is achieved, just before the multiple refocusing start. Here, this would be at 280 nJ and the position variations ($\Delta z/\Delta E$) are 11 µm/nJ. The resulting temporal jitter ($\Delta t/\Delta E$) of the newly generated light is 2.0 fs/nJ (for 500 nm). Assuming a energy fluctuation 0.2% rms of the pump this leads to 1 fs temporal jitter which is

equal to extremely high 3700 mrad. To reduce such high fluctuations shorter crystals can be used so that higher pump energies can be used but no multiple refocusing occur. Also helpful is the increase of the numerical aperture of the external focusing. We observe that for higher numerical apertures the position variations decreases. This is due to the fact that the higher numerical apertures leads to smaller beam waist radius and therefore to stronger self-focusing and self-focal distances with lower variations. With this two improvements, we were able to observe phase fluctuations of 100 mrad [Hom12]. There, we amplified a selected wavelength of a bulk continuum and difference frequency mixed the amplified light with the fundamental laser light to obtain carrier envelope phase stable few cycle infrared pulses. The main phase fluctuation of the infrared pulses originate from the continuum generation. For the best phase stability short crystals and pump energies close to multiple refocusing should be used.

Our goal is to find the optimum conditions for continuum generation. Therefore the correlation between beam profile, spectrum, and side view during multiple refocusing in a 6 mm YAG is studied. The input energy is continuously increased and simultaneously the spectrum, beam profile, and side view recorded. Figure 8 shows selected spectra and beam profiles for zero, one, two and three filaments. The fundamental light is blocked by a filter so that only the new spectral components are regarded.

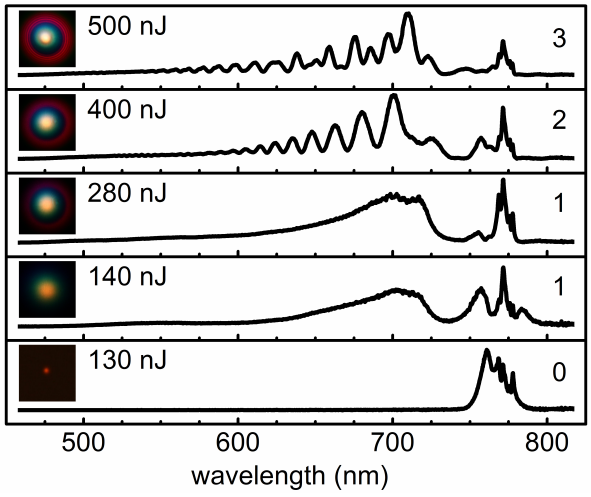

Fig. 8: Beam profile and spectrum of interfering filaments during multiple refocusing

Just below the threshold, a weak spectral broadening around the pump region due to self-phase modulation is observed. Between the onset on continuum generation and nearly twice the threshold a stable filament is built and continuum generation with all its advantageous properties occurs. Above twice the threshold, a second filament arises and a stable interfer-

ence pattern in the spectrum appears. The evaluation of these modulations allows determining the spatial and temporal distance between the filaments. The temporal discrepancy between the filaments originates from the fact that the fundamental light and the new frequencies have different propagation lengths in the crystal, if generated in the first or second filament. The calculated value confirm the observed distance between the two filaments obtained from the side view. When further increasing the input energy to above three times the threshold a third filament arises and the spectral interference becomes random. The beam profile on the other side shows a white central spot which is getting stepwise brighter with each additional filament. The conical emission [Lut94, Nib96, Kos97, Fac06] becomes stronger for higher input energies and show clear interference rings especially for more filaments, which show their spatial coherence. The high contrast and the extreme roundness of the interference pattern indicates that the filaments are located behind and not beside each other. These single steps of multiple refocusing are visualized in the attached video [Video01]. Please note that the energy threshold in the video for continuum is increased, because a 4 instead of 6 mm YAG plate is used and therefore higher energies are needed to built up the filaments within the shorter crystal length.

Another approach to increase the energy contained inside one filament is to use pump pulses which have initially a small beam size so that no self-focusing is needed and which contain this small beams size over a long distance. Bessel beams fulfill this conditions and can be generated by focusing with a small-angle axicon. When performing continuum generation with such beams, we do not observe one long filament which contains more power, but many single filaments behind each other. Nevertheless, the use of Bessel beams to generate continua is still under investigation [Dub07, Tra08, Maj13].

6. Variation of the crystal length

Although filamentation in solids happens on a smaller scale than in gases, it still lasts over millimeter distances. To study the single steps of continuum generation during filamentation we vary the crystal length and measure the influence on the newly generated frequencies. A YAG wedge is used which has a length of 2 mm at the one side and 4 mm at the other. The entrance surface of the wedge is kept perpendicular and hence the exit surface is hit under a small angle of 4.5°. This should have a negligible influence on continuum generation.

A f = 100 mm lens is used to focus the 775 nm, 150 fs, 500 nJ pulses on the entrance surface of the wedge. Interference filters at 500, 600, and 700 nm with a bandwidth of 10 nm are used to select small spectral parts of the continuum. These parts are focused on a photodiode to measure the energy of the continuum light in this spectral region.

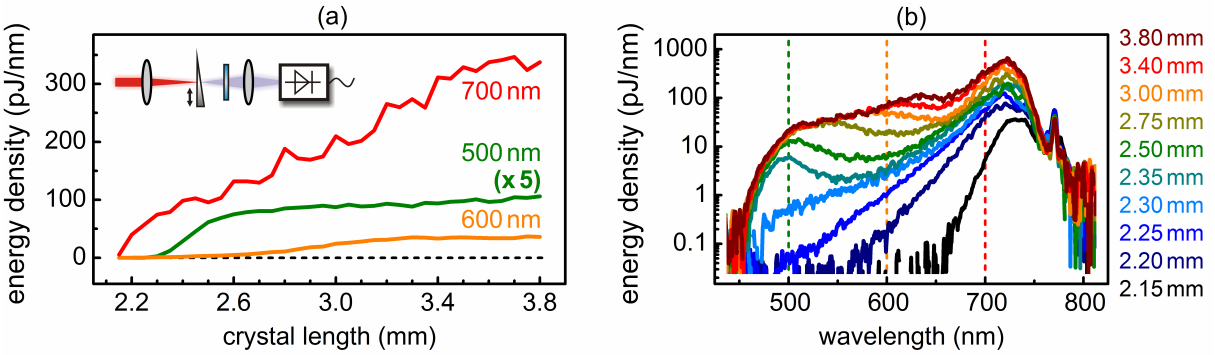

Fig. 9: (a) Amount of generated continuum around 500 (x5), 600, and 700 nm in a YAG wedge including setup and (b) spectra for various thicknesses.

Figure 9(a) shows that the amount of generated light at 500 nm is mostly generated in the beginning of the filament until 2.6 mm crystal length and then only slightly increases. For a better visualization the 500 nm curve is enlarged by a factor of 5. The amount of generated 600 nm light on the other side slowly grows until 3.2 mm crystal length and is then on a constant level. Whereas the 700 nm part continuously grows for an increasing crystal length. The different behavior for the single wavelength can be understood if the generation mechanisms are regarded. At the beginning at up to 2.30 mm crystal length only spectral broadening of the pump due to self-phase modulation occurs and no filamentation or other nonlinear processes which would lead to new frequencies. Within the next 50 µm an optical shock wave is formed and nearly the full amount for light at wavelengths close to the continuum cut-off is generated within this short section. The typical plateau-like structure [Gae00] and the white visual appearance shows up. The immediate arrival of the plateau is due to the fact that self-steepening is an abrupt process [Sch06] and can be seen if the spectra for 2.30 and 2.35 mm crystal length in Fig. 9(b) are compared. After this, self-phase modulation enhanced by multi-photon excitation is dominating the generation of new colors. It can be seen from the spectra in Fig. 9(b) that the shorter the continuum wavelength is the earlier the generation of the light at these wavelengths stops. For example for 500 nm no additional light is generated for crystal length above 2.75 mm. For 550 nm above 3.0 mm and for 600 nm above 3.40 mm crystal length no new light is generated. This indicates a reduced nonlinearity at the end of the fila-

ment. In addition, for lower wavelengths the group velocity is lower and the new colors can not follow the pump in its filamentation channel the entire filament length. From the made observation here, it could be possible that this is a necessary condition for continuum generation because the already generated light could act as seed. The experiment shows that the generation of the new frequencies during bulk filamentation is complex and different for every wavelength. It can be denoted that for an increasing filament length the amount of newly generated colors in general grows. This means when including Fig. 7(b) that the maximum amount of new frequencies is generated if the continuum generation is close to multiple refocusing due to the maximum filament length at this point. In addition, weak focusing and a long crystal length lead to the generation of long filaments and render the most new light, but also increase the chirp of the continuum. Therefore, it is depending on the specific application which external conditions and geometries should be chosen for best continuum generation.

7. Summary and conclusion

Many parameters influence continuum generation and determine, whether the generation of new frequencies is possible or not. Figure 10 gives an overview about two key parameters – the energy threshold and the maximum pulse duration – and set them in relation to the expected continuum cut-off.

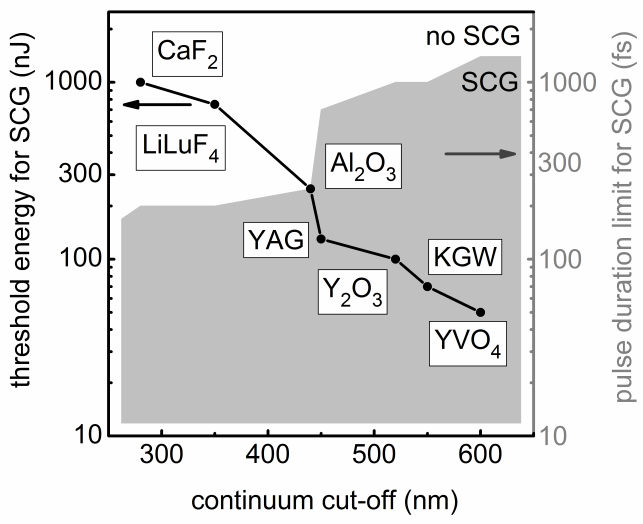

Fig. 10: Energy threshold for continuum generation (SCG) in various crystals and obtained continuum cut-off. The energy thresholds are shown for 775 nm, 150 fs pulses. The grey area shows the maximum pulse duration for continuum generation in dependence of the crystal.

Since self-focusing is the first process during continuum generation the threshold also depends on the pump wavelength and duration. In Fig. 10 the thresholds are shown for 775 nm and 150 fs. For longer pulses the energy increases linearly, so that the peak power remains constant. The threshold for self-focusing (and therefore continuum generation) scales quadratically with the pump wavelength. This means that for longer pump wavelengths more energy is needed. In addition, the intrinsically increasing beam waist radius for longer wavelengths has to be taken into account. To achieve continuum generation the peak intensity must be high enough so that the self-focal distance is smaller than the crystal length. To achieve such high intensities external focusing is needed. This also avoids multiple filamentation, a beam break up, or permanent damage. However, for a constant numerical aperture the beam waist radius increases linearly for longer wavelengths and hence the needed energy quadratically.

For a better understanding of Fig. 10 an example will be given. A system is considered where 1025 nm, 300 fs, 2 µJ pulses are available. First, the pulse duration limit has to be regarded (grey area in Fig. 10). Only YAG, Y_2O_3, KGW, and YVO_4 allow continuum generation which such long pulses. The next step is the necessary pulse energy. Since this laser system has not the same wavelength and pulse duration as the Ti:sapphire laser system here, the threshold has to be adapted. For the pulse duration the thresholds have to be increased by a factor of 2 (= 300 fs / 150 fs) and for the wavelength by a factor of 1.75 (= $(1025\ \text{nm})^2$ / $(775\ \text{nm})^2$). If the same focusing conditions as for 775 nm should be used, additionally a factor of 1.75 for the increased beam waist radius has to be added. The overall needed energy is increased therewith by a factor of 6. For YAG this means 900 nJ instead of 150 nJ. Depending on the desired continuum cut-off and remaining pulse energy, one can choose among the four mentioned crystals. A very remarkable material for bulk continuum generation which is shown in Fig. 10 is $LiLuF_4$ which is a newly developed laser host material [Cor07]. It allows continuum generation down to 350 nm in a static configuration and no moving of the crystal is necessary as typically needed for fluoride crystals to avoid color centers.

The correct choice of the material and its dimensions are important. The optimum material can be deduced from Fig. 10. The lateral size should not be a restriction since the active area has only a diameter of a few 10 µm. The desired length depends on the experimental needs. For a strong continuum or one with a low threshold long crystals are needed. For highest phase stability and a weak chirp short crystals are better suited. In all cases, the energy should

be close to multiple refocusing to reduce the fluctuations of the filament position and hence the phase of the newly generated fluctuation.

Filamentation and continuum generation in solids is an excellent method to generate new frequencies with a modest pump energy. Its favorable properties ideally favors them as seed or probe source in many applications such as parametric amplifier or transient spectrometer. Especially the wavelength independent continuum cut off in combination with long pump pulse durations renders such continua as broadband seed in chirped amplifier [Sch11, Rid13, Sta14]. Short pump wavelengths even allow extending the accessible range down to the deep UV and avoids complicated generation schemes if only modest energies are needed.

* *The energy values in the video refer to the position in front of the iris. The aperture was kept small so that the observed effects are emphasized for a clearer presentation. Nevertheless, the continua shown in the video are still fully suitable.*

Acknowledgments

We are grateful to U. Megerle and D. Herrmann, for valuable experimental help and fruitful discussions. We thank P. Hommelhoff, T. Udem, C. Fallnich, P. Baum as well as the companies JenOptik and HighQ for access to their laser systems. We are also thankful to the group of G. Huber for temporarily providing us with selected crystals. The work is supported by the DFG-Cluster of Excellence: Munich-Centre for Advanced Photonics, the SFB 749 (Dynamics and Intermediates of Molecular Transformations).

References

Alf70a R. R. Alfano, S. L. Shapiro, "Emission in the region 4000 to 7000 Å via four-photon coupling in glass," Phys. Rev. Lett. **24**, 584-587 (1970).

Alf70b R. R. Alfano, S. L. Shapiro, "Observation of self-phase modulation and small-scale filaments in crystal and glasses," Phys. Rev. Lett. **24**, 592-594 (1970).

Alf09 R.R. Alfano, *The supercontinuum laser source* (Springer, Berlin, 2006).

Bab05 V. Babin, K. Blazek, A. Krasnikov, K. Nejezchleb, M. Nikl, T. Savikhina, S. Zazubovich, "Luminescence of undoped LuAG and YAG crystals," Phys. Stat. Sol. **2**, 97-100 (2005).

Bal02 A. Baltuska, T. Fuji, and T. Kobayashi, "Controlling the carrier-envelope phase of ultrashort light pulses with optical parametric amplifiers," Phys. Rev. Lett. **88**, 133901 (2002).

Ber07 L. Bergé, S. Skupin, R. Nuter, J. Kasparian, J.-P. Wolf, "Ultrashort filaments of light in weakly ionized, optically transparent media," Rep. Prog. Phys. **70**, 1633-1713 (2007).

Bra95 A. Braun, G. Korn, X. Liu, D. Du, J. Squier, G. Mourou, "Self-channeling of high-peak-power femtosecond laser pulses in air," Opt. Lett. **20**, 73-75 (1995).

Bra09 M. Bradler, P. Baum, E. Riedle, "Femtosecond continuum generation in bulk laser host materials with sub-μJ pump pulses," Appl. Phys. B **97**, 561-574 (2009).

Bro99 A. Brodeur, S. L. Chin, "Ultrafast white-light continuum generation and self-focusing in transparent condensed media," J. Opt. Soc. Am. B **16**, 637-650 (1999).

Cam74 A. J. Campillo, S. L. Shapiro, B. R. Suydam, "Relationship of self-focusing to spatial instability modes," Appl. Phys. Lett. **24**, 178-180 (1974).

Cer97 G. Cerullo, M. Nisoli, S. De Silvestri, "Generation of 11 fs pulses tunable across the visible by optical parametric amplification," Appl. Phys. Lett **71**, 3616-3618 (1997).

Cer11 G. Cerullo, A. Baltuska, O. D. Mücke, and C. Vozzi, "Few-optical-cycle light pulses with passive carrier-envelope phase stabilization," Laser. Phot. Rev. **5**, 323-351 (2011).

Chi05 S. L. Chin, S. A. Hosseini, W. Liu, Q. Luo, F. Theberge, N. Aközbek, A. Becker, V. P. Kandidov, O. G. Kosareva, H. Schroeder, "The propagation of powerful femtosecond laser pulses in optical media: physics, applications, and new challenges," Can. J. of Phys. **83**, 863-905 (2005).

Chi10 S. L. Chin, *Femtosecond Laser Filamentation* (Springer New York, 2010)

Cor07 F. Cornacchia, A. Richter, E. Heumann, G. Huber, D. Parisi, M. Tonelli, "Visible laser emission of solid state pumped LiLuF4:Pr3+," Opt. Express **15**, 992-1002 (2007).

Cou07 A. Couairon, A. Mysyrowicz, "Femtosecond filamentation in transparent media," Phys. Rep. **441**, 47-189 (2007).

Dar13 J. Darginavicius, D. Majus, V. Junka, N. Garejev, G Valiulis, A. Couairon, and A. Dubietis, "Ultrabroadband supercontinuum and third-harmonic generation in bulk solids with two optical-cycle carrier-envelope phase-stable pulses at 2 μm," Opt. Express **21**, 25210-25220 (2013).

Dav96 K. M. Davis, K. Miura, N. Sugimoto, K. Hirao, "Writing waveguides in glass with a femtosecond laser," Opt. Lett **21**, 1729-1731 (1996).

Dha09 A. K. Dharmadhikari, J. A. Dharmadhikari, D. Mathur, "Visualization of focusing–refocusing cycles during filamentation in BaF_2," App. Phys. B **94**, 259-263 (2009).

Dob12 S. Dobner, C. Cleff, C. Fallnich, P. Groß, "Interferometric background reduction for femtosecond stimulated Raman scattering loss spectroscopy," J. Chem. Phys. **137**, 174201 (2012).

Dub07 A. Dubietis, P. Polesana, G. Valiulis, A. Stabinis, P. Di Trapani, A. Piskarskas, "Axial emission and spectral broadening in self-focusing of femtosecond Bessel beams," Opt. Express **15**, 4168-4175 (2007).

Emo10 M. Emons, A. Steinmann, T. Binhammer, G. Palmer, M. Schultze, U. Morgner, Opt. Express **18**, 1191-1196 (2010).

Etz12 F. Etzold, I. A. Howard, N. Forler, D. M. Cho, M. Meister, H. Mangold, J. Shu, M. R. Hansen, K. Müllen, F. Laquai, "The effect of solvent additives on morphology and excited-state dynamics in PCPDTBT:PCBM photovoltaic blends," J. Am. Chem. Soc. **134**, 10569-10583 (2012).

Fac06 D. Faccio, M. A. Porras, A. Dubietis, F. Bragheri, A. Couairon, P. Di Trapani, "Conical emission, pulse splitting, and X-wave parametric amplification in nonlinear dynamics of ultrashort light pulses," Phys. Rev. Lett. **96**, 19301 (2006).

For83 R. L. Fork, C. V. Shank, C. Hirlimann, R. Yen, W. J. Tomlinson, "Femtosecond white-light continuum pulses," Opt. Lett. **8**, 1-3 (1983).

Gae00 A. L. Gaeta, "Catastrophic collapse of ultrashort pulses", Phys. Rev. Lett. **84**, 3582-3585 (2000).

Hau04 C. P. Hauri, W. Kornelis, F. W. Helbing, A. Heinrich, A. Couairon, A. Mysyrowicz, J. Biegert, and U. Keller, "Generation of intense, carrier-envelope phase-locked few-cycle laser pulses through filamentation," Appl. Phys. B **79**, 673-677 (2004).

Hom12 C. Homann, M. Bradler, M. Förster, P. Hommelhoff, E. Riedle, "Carrier-envelope phase stable sub-two-cycle pulses tunable around 1.8 μm at 100 kHz," Opt. Lett. **37**, 1673-1675 (2012).

Joh09 P. J. M. Johnson, V. I. Prokhorenko, and R. J. D. Miller, "Stable UV to IR supercontinuum generation in calcium fluoride with conserved circular polarization states," Opt. Express **17**, 21488-21496 (2009).

Kan03 V. P. Kandidov, O. G. Kosareva, I. S. Golubtsov, W. Liu, A. Becker, N. Aközbek, C. M. Bowden, S. L. Chin, "Self-transformation of a powerful femtosecond laser pulse into a white-light laser pulse in bulk optical media (or supercontinuum generation)," Appl. Phys. B **77**, 149-165 (2003).

Kar13 T. M. Kardas, B. Ratajska-Gadomska, W. Gadomski, A. Lapini, and R. Righini, "The role of stimulated Raman scattering in supercontinuum generation in bulk diamond," Opt. Express **21**, 24201-24209 (2013).

Kas03 J. Kasparian, M. Rodriguez, G. Mejean, J. Yu, E. Salmon, H. Wille, R. Bourayou, S. Frey, Y.-B. Andre, A. Mysyrowicz, R. Sauerbrey, J.-P. Wolf, L. Wöste, "White-light filaments for atmospheric analysis," Science **301**, 61-64 (2003).

Kas08 J. Kasparian, J. P. Wolf, "Physics and applications of atmospheric nonlinear optics and filamentation," Opt. Express. **16**, 466-493 (2008).

Kol04 M. Kolesik, E. M. Wright, and J.V. Moloney, "Dynamic nonlinear X-waves for femtosecond pulse propagation in water," Phys. Rev. Lett. **92**, 253901 (2004).

Kol10 M. Kolesik, E. M. Wright, and J. V. Moloney, "Femtosecond filamentation in air and higher-order nonlinearities," Opt. Lett. **35**, 2550-2552 (2010).

Kos97 O. G. Kosareva, V. P. Kandidov, A. Brodeur, C. Y. Chien, S. L. Chin, "Conical emission from laser–plasma interactions in the filamentation of powerful ultrashort laser pulses in air," Opt. Lett. **22**, 1332-1334 (1997).

Kos11 O. Kosareva, J.-F. Daigle, N. Panov, T. Wang, S. Hosseini, S. Yuan, G. Roy, V. Makarov, and S. L. Chin, "Arrest of self-focusing collapse in femtosecond air filaments: higher order Kerr or plasma defocusing?," Opt. Lett. **36**, 1035-1037 (2011).

Liu02 W. Liu, S. Petit, A. Becker, N. Aközbek, C. M. Bowden, and S. L. Chin, "Intensity clamping of a femtosecond laser pulse in condensed matter," Opt. Commun **202**, 189-197 (2002).

Liu03 W. Liu, S. L. Chin, O. Kosareva, I. S. Golubtsov, V. P. Kandidov, "Multiple refocusing of a femtosecond laser pulse in a dispersive liquid (methanol)," Opt. Commun. **225**, 193-209 (2003).

Lut94 G. G. Luther, A. C. Newell, J. V. Moloney, E. M. Wright, "Short-pulse conical emission and spectral broadening in normally dispersive media," Opt. Lett. **19**, 789-791 (1994).

Maj13 D. Majus and A. Dubietis, "Statistical properties of ultrafast supercontinuum generated by femtosecond Gaussian and Bessel beams: a comparative study," J. Opt. Soc. Am. B **30**, 994-999 (2013).

Meg09 U. Megerle, I. Pugliesi, C. Schriever, C. F. Sailer, E. Riedle, "Sub-50 fs broadband absorption spectroscopy with tunable excitation: putting the analysis of ultrafast molecular dynamics on solid ground," Appl. Phys. B **96**, 215-231 (2009).

Met09 T. Metzger, A. Schwarz, C. Y. Teisset, D. Sutter, A. Killi, R. Kienberger, and F. Krausz, "High-repetition-rate picosecond pump laser based on a Yb:YAG disk amplifier for optical parametric amplification," Opt. Lett. **34**, 2123-2125 (2009).

Mue09 O. D. Mücke, D. Sidorov, P. Dombi, A. Pugzlys, A. Baltuska, S. Alisauskas, V. Smilgevicius, J. Pocius, L. Giniunas, R. Danielius, and N. Forget, "Scalable Yb-MOPA-driven carrier-envelope phasestable few-cycle parametric amplifier at 1.5 μm," Opt. Lett. **34**, 118-120 (2009).

Nag02 C. Nagura, A. Suda, H. Kawano, M. Obara, and K. Midorikawa, "Generation and characterization of ultrafast white-light continuum in condensed media," Appl. Opt. **41**, 3735-3742 (2002).

Nib96 E. T. J. Nibbering, P. F. Curley, G. Grillon, B. S. Prade, M. A. Franco, F. Salin, A. Mysyrowicz, "Conical emission from self-guided femtosecond pulses in air," Opt. Lett. **21**, 62-64 (1996).

Rai00 P. Rairoux, H. Schillinger, S. Niedermeier, M. Rodriguez, F. Ronneberger, R. Sauerbrey, B. Stein, D. Waite, C. Wedekind, H. Wille, L. Wöste, C. Ziener, "Remote sensing of the atmosphere using ultrashort laser pulses," Appl. Phys. B **71**, 573-580 (2000).

Rid13 R. Riedel, M. Schulz, M. J. Prandolini, A. Hage, H. Hoeppner, T. Gottschall, J. Limpert, M. Drescher, and F. Tavella, "Long-term stabilization of high power optical parametric chirped-pulse amplifiers," Opt. Express **21**, 28987-28999 (2013).

Rie13 E. Riedle, M. Bradler, M. Wenninger, C. F. Sailer, and Igor Pugliesi, "Electronic transient spectroscopy from the deep UV to the NIR: unambiguous disentanglement of complex processes," Faraday. Discuss. **163**, 139-158 (2013).

Rot92 J. E. Rothenberg, "Pulse splitting during self-focusing in normally dispersive media," Opt. Lett. **17**, 583-585 (1992).

Sch04 H. Schroeder and S. L. Chin, "Visualization of the evolution of multiple filaments in methanol," Opt. Commun. **234**, 399-406 (2004).

Sch06 H. Schroeder, S. A. Hosseini, Q. Luo, and S. L. Chin, "Self-steepening is an abrupt process," Opt. Commun, **266**, 302-306 (2006).

Sil12 F. Silva, D. R. Austin, A. Thai, M. Baudisch, M. Hemmer, D. Faccio, A. Couairon, and J. Biegert, "Multi-octave supercontinuum generation from mid-infrared filamentation in a bulk crystal," Nature Commun. **3**, 807 (2012).

Sta14 T. Stanislauskas, R. Budriunas, R. Antipenkov, A. Zaukevicius, J. Adamonis, A. Michailovas, L. Giniunas, R. Danielius, A. Piskarskas, and A. Varanavicius, "Table top TW-class OPCPA system driven by tandem femtosecond Yb:KGW and picosecond Nd:YAG lasers," Opt. Express **22**, 1865-1870 (2014).

Ste04 K. Stelmaszczyk, P. Rohwetter, G. Mejean, J. Yu, E. Salmon, J. Kasparian, R. Ackermann, J. P. Wolf, L. Wöste, "Long-distance remote laser-induced breakdown spectroscopy using filamentation in air," Appl. Phys. Lett. **85**, 3977-3979 (2004).

Tal99 A. Talebpour, S. Petit, S.L. Chin, "Re-focusing during the propagation of a focused femtosecond Ti:Sapphire laser pulse in air," Opt. Commun. **171**, 285-290 (1999).

Sch11 M. Schulz, R. Riedel, A. Willner, T. Mans, C. Schnitzler, P. Russbueldt, J. Dolke-meyer, E. Seise, T. Gottschall, S. Hädrich, S. Duesterer, H. Schlarb, J. Feldhaus, J. Limpert, B. Faatz, A. Tünnermann, J. Rossbach, M. Drescher, F. Tavella, "Yb:YAG Innoslab amplifier: efficient high repetition rate subpicosecond pumping system for optical parametric chirped pulse amplification," Opt. Lett. **36**, 2456-2458 (2011).

Sil12 F. Silva, D. R. Austin, A. Thai, M. Baudisch, M. Hemmer, D. Faccio, A. Couairon, J. Biegert, "Multi-octave supercontinuum generation from mid-infrared filamentation in a bulk crystal," Nature Commun. **3**, 807 (2012).

Tel10 A. Teleki, E. M. Wright, and M. Kolesik, "Microscopic model for the higher-order nonlinearity in optical filaments," Phys. Rev. A **82**, 065801 (2010).

Tra08 P. Polesana, M. Franco, A. Couairon, D. Faccio, P. Di Trapani, "Filamentation in Kerr media from pulsed Bessel beams," Phys. Rev. A **77**, 043814 (2008).

Roh10 P. Rohwetter, J. Kasparian, K. Stelmaszczyk, Z. Hao, S. Henin, N. Lascoux, W. M. Nakaema, Y. Petit, M. Queißer, R. Salame, E. Salmon, L. Wöste, J. P. Wolf, "Laser-induced water condensation in air," Nat. Photon. **4**, 451-456 (2010).

Xin93 Q. Xing, K. M. Yoo, and R. R. Alfano, "Conical emission by four-photon parametric generation by using femtosecond laser pulses," Appl. Opt. **32**, 2087-2089 (1993).

Zoz98 A. A. Zozulya, S. A. Diddams, and T S. Clement, "Investigations of nonlinear fem-tosecond pulse propagation with the inclusion of Raman, shock, and third-order phase effects," Phys. Rev. A **58**, 3303 (1998).

Appendix A19

Transient Spectroscopy covering three Octaves in Spectrum and 11 Orders of Magnitude in Time

M. Bradler, C. Sailer, N. Krebs, M. Wenninger, P. Lang, D. Herrmann, I. Pugliesi, and E. Riedle

to be submitted to Appl. Phys. B (2014)

Transient Spectroscopy covering three Octaves in Spectrum and 11 Orders of Magnitude in Time

Maximilian Bradler, Christian Sailer, Nils Krebs, Matthias Wenninger, Peter Lang, Daniel Herrmann, Igor Pugliesi, and Eberhard Riedle

Grill: Transport with fiber, NIR

Megerle: Ekspla

Homann: on sight UV AC, time zero, seed depolarization

Mikhailov: laser dyes

Lehrstuhl für BioMolekulare Optik, Ludwig-Maximilians-Universität (LMU), Oettingenstraße 67, 80538 München, Germany

Abstract

We give a full description of an extended transient pump probe spectrometer allowing to follow photochemical and photophysical processes from the ultraviolet to the infrared on a timescale from a few femtoseconds up to milliseconds. The layout is based on modules so that any spectral and temporal combination can be setup without great effort. We also describe additional key issues like calibration and straylight and show complete, in situ pulse characterization implemented in the setup.

The spectrometer is operated at 1 kHz and based on a commercial Ti:sapphire femtosecond laser and a Nd:YAG based nanosecond optical parametric oscillator. The pump is provided either by a optical parametric amplifier and optionally additional sum frequency generation or by the nanosecond oscillator and can be tuned from the deep UV to the infrared. Several whitelight continua are used as probe and allow an overall probe range from 230 nm to 1.7 μm. The continua are spectrally dispersed with a prism and detected with a silicon or InGaAs array operating at full 1 kHz. This allows either chopping the pump or referencing each pulse or even both. The latter significantly increase the sensitivity compared to the single approaches. The spectrometer allows a time resolution of sub-50 fs and a high detection sensitivity of better than $\Delta OD \quad 10^{-4}$.

I. Transient optical spectroscopy for molecular dynamics

The investigation of photophysical and photochemical processes is essential to gain insight in the molecular life and to understand the initial mechanisms in physics, chemistry, and biology. A very successful technique to uncover these elementary dynamics is transient absorption spectroscopy. First a short laser pulse is used to excite the molecules in an electronically upper state. Then a secondary light pulse determines the photo-induced transmission changes. This method allows tracing the spectral and temporal dynamics of the molecule. Typical durations of these ultrafast processes are in the femto- and picosecond regime. Nevertheless there are many systems which still show activity on longer time scale up to milliseconds. These time regimes are not less interesting since they contain the subsequent steps towards the final configuration. Also the wavelength range of the probe light is crucial for a proper analysis of the molecular sequence. Common pump probe setups cover the visible and a small part of the ultraviolet (UV) region. However, the extension of the probe light deeper in the UV and further into the infrared should help to get a more complete of the studied molecules. Organic solar cells, low bandgap polymers, DNA based molecules, light harvesting molecules are only a few examples of the manifold field of research. Especially the time extension up to milliseconds is a valuable alternative to the commercial laser flash systems.

In this paper we extend our well established pump probe setup [Meg09] to cover eleven magnitudes in time and three octaves in spectrum. Therefore we punctual added optical devices while maintaining the basic setup unchanged. This flexible approach allow adapting the setup to the molecular needs regardless to any experimental constraints. To cover new wavelength regime we use continuum generation with different fundamental wavelengths from the UV to the infrared. The huge time extension is realized by an additional pump laser which is electronically synchronized to the original femtosecond laser system. Not all measurements can be performed at the same time but there is always temporal and spectral overlap between all parts so that a the full picture can be constructed properly. Additionally we give useful improvements which can be easily implemented to raise the performance of existing setups. Figure I1 gives an overview over the entire time and wavelength regions achieved with our advanced transient pump probe setup and show how the single regions are realized. Wavelengths from down to 225 nm up to 1.6 μm can be achieved and time delays between pump and probe up to the millisecond regime are possible.

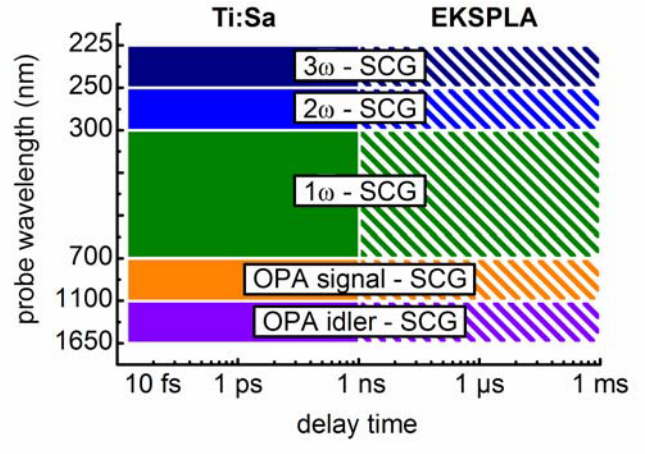

Fig I1: Temporal and spectral coverage of the extended transient spectroscopy setup consisting of a widely tunable pump, various probe continua, and a second synchronized laser system. All components are located within one experimental site.

Here the focus lies on day to day operation and optimization and not on unique and not repeatable measurements with days of alignment. Therefore we abdicate redundant elements and all optical devices are kept as simple and compact as possible. The open design also allows characterizing the pulses at all positions of the setup and give space for further extension and improvements. The aim is to generate an all-in-one setup with easy handling and outstanding performance.

II. Probe range extension down to 225 nm

In this section we will shortly repeat the basic setup and then give a detailed description of the experimental realization of the ultraviolet continuum and its experimental challenges and handling. Figure II1 shows the extended setup for transient time-resolved pump probe spectroscopy which covers wavelength regions starting from the deep UV up to the infrared. Delay times from few femtoseconds up to milliseconds can be measured. The laser source is a Ti:sapphire system (CPA 2001; Clark MXR Inc.) which delivers 1 mJ, 150 fs pulses at 775 nm with a repetition rate of 1 kHz. The pump pulses are generated in a continuum seeded noncollinear optical parametric amplifier (NOPA) and range from 450 720 nm. Subsequent second harmonic generation (2ω) allows extending the pump range down to 225 nm. The pulses are shortened with a prism compressor (PC) down to sub-30 fs pulse durations, sub-50 fs in the UV. The actual pulse duration at the sample can be in-situ characterized with a home built UV autocorrelator [Hom12]. As probe light we use a CaF_2 continuum which is

spectrally dispersed after the sample with a fused silica prism and then focused on a multi-channel detector. We focus around 2 µJ of the 775 nm light with a f 100 mm lens onto a 5 mm moving CaF_2 plate (157 nm, Korth Inc.) to generate the continuum. Thin dielectric mirrors are used to block the region around the pump wavelength (HR 800 nm, HT 280 720 nm) and to calibrate the wavelengths on the array (WG 320 nm, GG 475 nm, RG 695 nm, BG 20, and BG 36). The different delay time are realized by moving a motorized linear stage and the pump pulse is manually chopped to obtain the molecular transmission with and without excitation.

The powerful combination of continuum generation and frequency mixing allows the generation of widely tunable pump sources with sub-50 fs pulse durations for all wavelength regimes. This will be studied in more detail in section VI.D. But also the wavelength range for the probe light is important. Many experiments demand for ultraviolet probe light to follow the molecular dynamics. Continuum generation in fluorides with 800 nm pulses is well suited method to generate continua with spectra reaching down to 280 nm [Chi99]. Especially continua from calcium fluoride are well studied and optimized for the use in spectroscopy [Meg09, …]. However, if probe light even further in the UV is needed often optical parametric amplification in combination with sum frequency mixing and second harmonic generation is used. Nevertheless these pulses have a very limited bandwidth and only single color experiments can be performed which leads to extensive measurements series for obtaining frequency resolved signals [Loc98]. A more convenient method to obtain broadband spectra in the UV is to generate continua in calcium fluorides with the frequency doubled (2ω) and tripled (3ω) laser light.

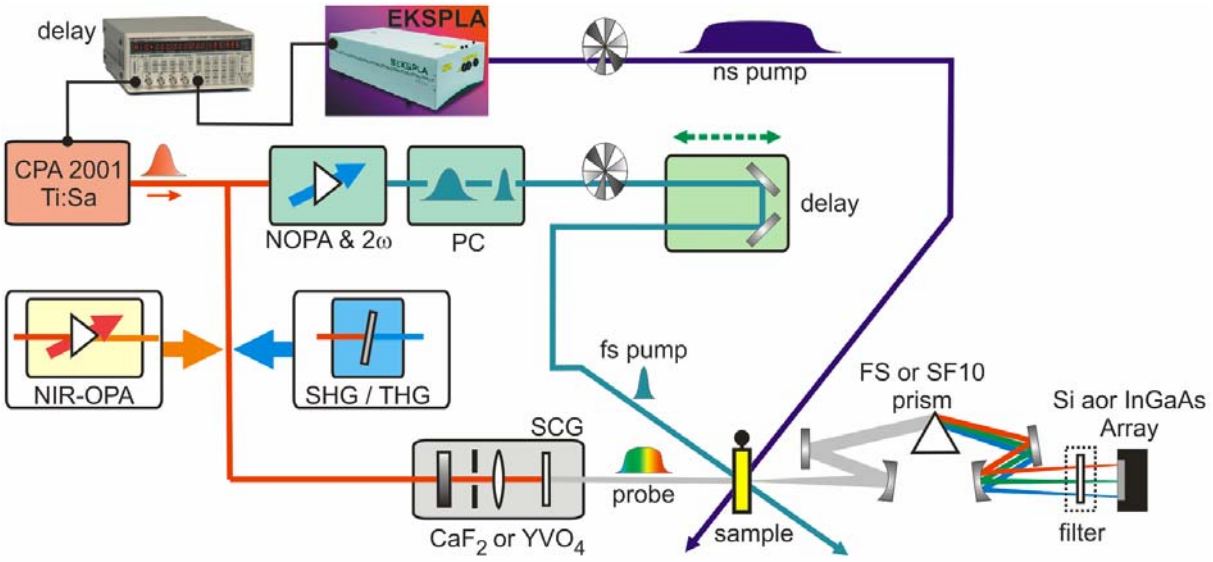

Fig. II1: Setup of the transient broadband spectrometer with ultraviolet and infrared wavelength extension and delay times up to milliseconds.

For the second harmonic generation we use a 700 µm thick type I BBO cut at 30°. To separate the 2w light from the remaining fundamental light two dichroic mirrors are used (2 x HR 400 nm, HT 800 nm, 45°). A λ/2 plate is used to adjust a horizontal polarization for the 2ω light to minimize the reflection losses at the following mirrors. Pulse energies of 400 nJ for the 2ω light at 387 nm are well suited to generate a continuum in a 5 mm moving CaF_2 plate (157 nm; Korth Inc.). For optimizing the continuum a variable attenuator and an iris to crop the outer part of the beam can be adjusted. The pulse duration of the 2ω light is 170 fs and comparable to the duration of the laser pulses. An external lens with 100 mm focal length is used to focus the 2ω light with an numerical aperture of 0.03 onto the fluoride plate. The continuum is collimated with a R -100 mm spherical aluminum mirror. To block the main part of the energy around 387 nm and only utilize the new generated frequencies we use a 500 µm thin dichroic filter (HR 360 nm, 0°). Note that the continuum generation can easily be overlooked with the bare eye on a business card. Continuum generation with 800 nm can be seen as a bright white spot although over 99% are still near 800 nm. This is due to the high sensitivity of our eyes for the visible wavelengths compared to the 800 nm. When generating a continuum with 400 nm the visible impression on a business card is still dominated by the fundamental light at 400 nm. Although when using a spectrometer the new frequencies are hardly detectable, because most of the light is contained near 400 nm and only 1% is in the wavelength region below. The usable spectrum of the 2ω continuum ranges from 245 to 355 nm and is shown in Figure II2 as blue curve. Additionally the shot to shot stability is given below and typically 2% rms. After passing through the sample the UV light is dispersed with a fused silica prism and focused with R 400 mm spherical aluminum mirror on a silicium array The latter is either a PDA sensor (NMOS; S3902-512Q; Hamamatsu) with 512 pixels, 50 × 500 µm each or a FFT sensor (S7030-0906; Hamamatsu) which is a two-dimensional CCD array of 524×58 pixels, 24×24 µm each. The analog to digital conversion is performed with two different electronic systems (2000 series; Entwicklungsbüro Stresing and photodiode array; tec5 AG). For the wavelength calibration we use thin dichroic mirrors (HR 226 nm (45°), HR 248 nm (0°), and HR 275 nm (45°)) and compare the transmission measured with the silicon array with the known cw transmission.

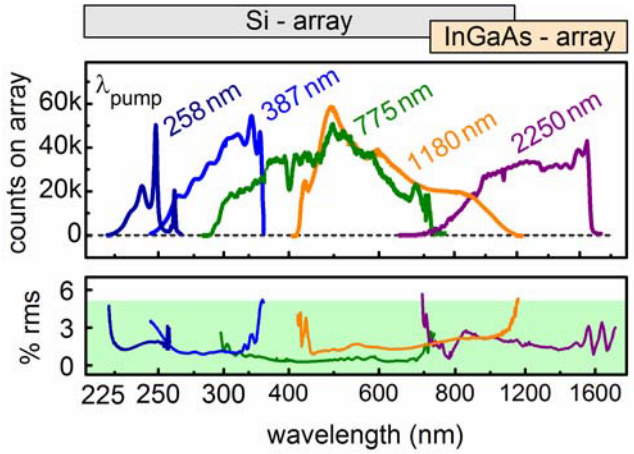

Fig. II2: Spectra and stability of various probe continua generated with different pump wavelengths.

To frequency triple the 775 nm light we use a simple but effective approach [Hom07]. The fundamental laser light is focused with a lens with a focal length of 250 mm. The second harmonic generation is performed 50 mm before the focus in a 300 µm thick BBO type I cut at 30°. Sum frequency mixing between fundamental and frequency doubled light is then performed in a 300 µm thick BBO type II cut at 62° at 120 mm behind the focus. This easy setup allows to avoid the preliminary separation and later combination between the 2ω and the laser light. At least 50 µJ of 775 nm light is needed for this setup. Pulses at 258 nm, with a duration of 170 fs, are generated. A λ/2 plate is used to set the polarization to horizontal. High reflecting mirrors (2 x HR 266 nm (45°), HT 400) separate the 3ω from the remaining 2ω and laser light. Energies of 200 nJ are sufficient to perform continuum generation in a 5 mm moving CaF_2 plate and still allow optimizations with an iris and a variable attenuator. We use again an external lens with 100 mm focal length for focusing (numerical aperture 0.03) and a spherical aluminum mirror for collimating the continuum. To block the 3ω light we use a dichroic filter (HR 275 nm (0°)). The new generated frequencies are again dispersed with a fused silica prism and focused with an R 400 mm spherical aluminum mirror on the CCD. To calibrate the wavelength we use three dichroic mirrors (HR 226 nm (45°), HR 248 nm (0°), and HR 275 nm (45°)). The spectrum of the 3ω continuum is ranges from 225 to 260 nm and is shown as dark blue curve in Figure II2 including the stability of roughly 2% rms.

At this point we want to point to the experimental challenge of handling the UV continua. Not only the wanted UV probe light is present, but also other remaining straylight which is much brighter for the bare eye and also the detection equipment such as beam cameras. To ensure the spatial overlap with the pump pinholes and interference filters are necessary to ensure that

the UV light is guided correctly through the setup. Here many techniques used in infrared spectroscopy can be applied. To demonstrate the potential of the system, we study 1,3-cyclohexadien after excitation at 250 nm. The transient signal is shown in Figure II3.

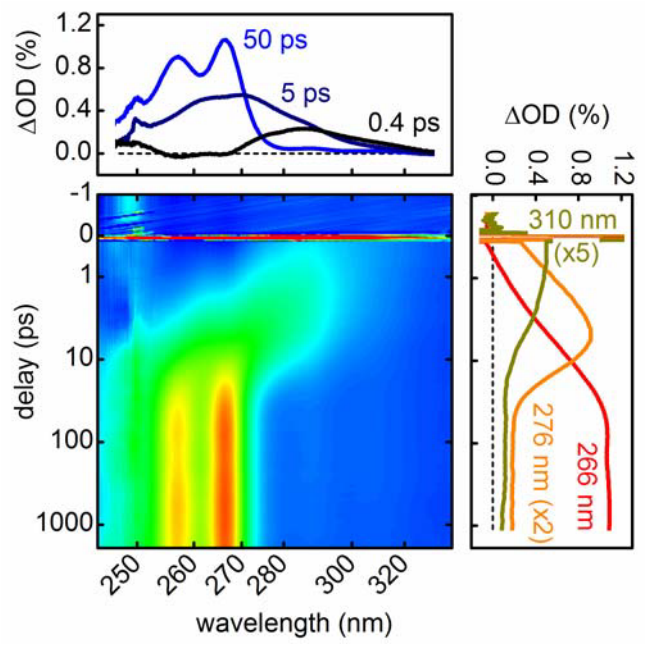

Fig. II3: Transient spectra of 1,3-cyclohexadien after 250 nm excitation.

This system was already investigated earlier [Loc98] with time-consuming NOPA-NOPA experiments. Here we could retrieve a more complete picture with only one measurements and achieved all at once a frequency and time resolved signal which nicely agree with the previously obtained results. One mature advantages when using continua as probe light is the direct comparability of the signal strength for different wavelengths since the same pump serves for all wavelengths and their comparable beam diameters.

III. Probe range extension up to 1700 nm

When probing in the visible wavelength region several molecular signals can overlap such as stimulated emission or excited state absorption. This means that at multiple wavelengths complex time dependant transition changes are observed which originate from contributions of the different processes. Especially for dynamics on comparable time scales with similar amplitudes it can be very challenging to uncover the real molecular behavior and complex multiple fit algorithm have to be applied. A very smart approach to clearly determine the dynamic of complex system is to firstly monitor at wavelengths where only one process is present and then stepwise characterize the entire transient signal. Typically these wavelength are located

at longer wavelengths. So beside the extended ultraviolet probe light also the an increased infrared probe range will contribute to complete the molecular picture. A very delicate method to perform these measurements is to use the fundamental wavelength of the region whitelight continuum. Beside the spectral instabilities, phase discontinuities, and high intensities, especially the distorted beam profile prohibits serious transient absorption experiments. To obtain a believable signal in this wavelength regime the wavelength with which the continuum should be generated has to be shifted to longer wavelength. A very advantageous properties of continuum generation in bulk is that the short wavelength continuum cut-off stays constant even when pumping with longer wavelength [Bra09]. This leads to octave spanning continua starting from the ultraviolet and covering the entire visible up to near infrared wavelength.

In the following paragraph we describe in detail how to generate such continua. At first we generated a infrared continuum by focusing 500 nJ of 775 nm light with a 100 mm lens onto a 4 mm YAG plate. The continuum is comprehensively described in [Bra09]. Then the continuum is amplified in a 3 mm BBO type I cut at 20° by 80 µJ of the 775 nm light in a collinear geometry. The central wavelength of the signal output of the amplifier is set to 1180 nm and has a pulse duration of 100 fs and an energy of 4 µJ. The pump light and the idler pulses which co-propagate with the signal pulses are blocked by filter and the use of dichroic mirrors for the 1180 nm light. The infrared light is then focused with a 50 mm lens and a numerical aperture of 0.04 onto a 5 mm moving CaF_2 plate. The generated continuum spans from 400 to 1100 nm (orange line figure II2) and is collimated with a 100 mm aluminum spherical mirror. To block the spectral parts near the 1180 nm pump light, we use a dichroic optic (HR 1200 nm, HT 400 1100 nm, 0°). The pulse to pulse fluctuation over the entire spectrum is in the range of 2 to 3% rms and are a little higher than the fluctuation of the infrared amplifier and its seed. After focusing the infrared probe light on the sample we collimate it sand disperses it with a 68.7° fused silica prism. The dispersed light is then focused with a R 500 mm mirror on a silicium array. For the wavelength calibration we use dichroic optics (HR 790 nm, 45°) and filters (BG 20 and BG 36).

As first application to demonstrate the potential of the infrared extension we study a donor-acceptor system. In this system the absorption band of acceptor and donor are spectrally very close and overlapping signals are obtained. We excite the molecule at 580 nm and used the extended infrared continuum as probe light. The transient spectrum for selected delay times is shown in figure III1. If only the visible continuum from 500 to 700 nm is considered no clear

temporal dynamics can be determined due to the strong overlap of the donor and acceptor dynamic. Only if the wavelength region between 800 and 900 nm (which is not available with the standard setup) is considered the contributions of donor and acceptor can be distinguished. The lower panel in figure III1 shows the decay associated spectra for donor and acceptor. If only the visible region is regarded it is obviously that determining the correct decay times is challenging and not automatically unique. The infrared extension allow monitoring the temporal behavior of donor and acceptor separately and uncovering the real molecular dynamic.

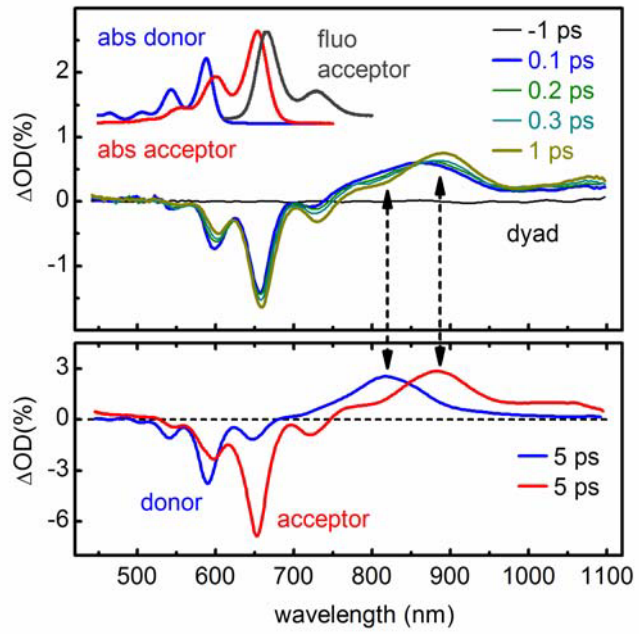

Fig. III1: Transient signal for donor acceptor system after 580 nm excitation for selected delay times. Additionally the absorption spectrum of the acceptor (red) and the donor (blue) and fluorescence spectrum of the acceptor (grey) are shown. The lower panel shows the decay associated spectra for donor and acceptor.

For several experiments for example at low bandgap polymers or organic solar cells, even this infrared wavelength extension is not sufficient and light even further in the infrared is needed. To extend the probe in these wavelength regime we still use the approach of an infrared pump which generate a continuum in a bulk material. Instead the signal output of the above described amplifier the idler pulses are used to generate a broadband continuum. The pulses have a central wavelength of 2250 nm, a pulse duration of 100 fs, and an energy of 2 µJ. Germanium plates are used to block the 775 nm pump light and the 1180 nm signal. The same geometry (50 mm lens, numerical aperture of 0.04) is used to generated a more than one octave spanning continuum from 700 to 1700 nm (violet line in figure II2). However, the thresh-

old for self-focusing and continuum generation scales quadratically with the wavelength [Bra09]. In our setup there is not enough energy available to generate a continuum in calcium fluoride. Therefore we generate the continuum in a 4 mm YVO_4, which has a high nonlinearity and therefore has a significantly lower threshold for self-focusing and continuum generation. The generated continuum is collimated with an R 100 mm spherical silver mirror. To block the wavelength region around the pump wavelength we used a dichroic optic (HR 1800 nm, 0°, HT 500 1700 nm). The new generated frequencies are dispersed with a SF 10 prism with an apex angle of 60° and then focused with an R 600 mm spherical silver mirror on an extended InGaAs array (G9203-256D; Hamamatsu Inc.). The array consists of 256 pixels with 50 µm widths and 500 µm height for each pixel. The array is sensitive from 650 to 2200 nm. Analog to digital conversion and electronic read-out are performed with a device from Stresing Entwicklungsbüro. The wavelength calibration is achieved by interference filter each 100 nm (FKB-IR-10 - IR bandpass filter kit (10 nm FWHM); Thorlabs Inc.). The stability of the new colors is in the region of 2 to 3 % rms for the entire wavelength region after proper alignment of the amplifier and whitelight generation.

As first example we investigated the well studied laser dye Malachit Green and excited it at 620 nm.

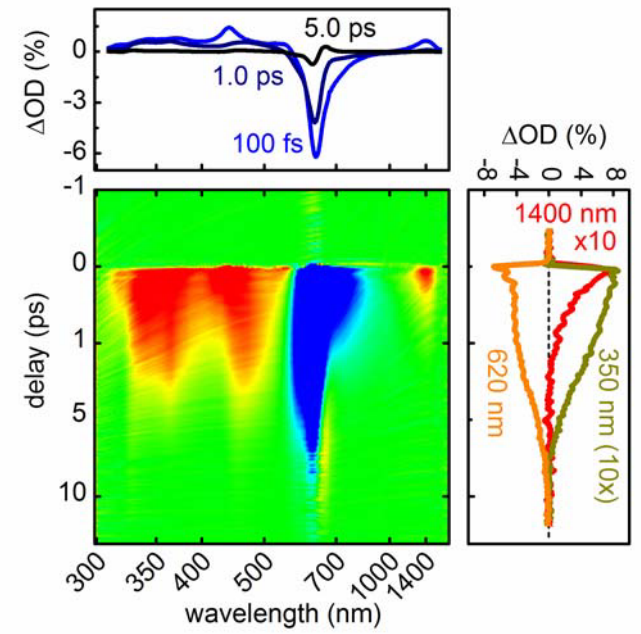

Fig III2: transient absorption spectra of malachite green from 300 to 1700 nm reveals hidden intermediate state

To further extend the probe range in the infrared continuum generation with infrared pulses is

still a well suited method if enough energy can be provided to exceed the threshold. Nevertheless in the infrared the favorable properties of b-barium-borate, lithium niobate and iodate crystals directly allow the generation of pulses with spectral widths of several hundreds or up to thousand nanometer. With optical parametric amplifiers such broadband pulses can be generated with energies on the μJ level. In ref [Bradler13] we use this method to introduce a novel setup for infrared pump-repump-probe measurements.

IV. Delay time expansion out to milliseconds

To comprehensively study chemical processes the extension to deeper UV and longer infrared wavelengths might not be sufficient. Many processes does not only consist of ultrafast components on the picosecond time scale but show a dynamical behavior on the nano- ore even microsecond scale. To fully characterize the inner life of such complexes the delay times between pump and probe pulses have to be tunable between few femtoseconds up to milliseconds. Relaxation to triplet states or intramolecular charge transfers are typical processes which take place on these time scales. The delay time between pump and probe pulses is often adjusted by a motorized linear stage which ether delay the pump or the probe pulses. A distance of 30 cm corresponds to 1 ns. However, when delay times of 10 ns or longer should be realized the delay distance would increase to 3 meter. Such large distances afford low spatial fluctuations of the laser system, exact alignment of the linear stage, and extremely well collimated beams. Even if this challenges are managed, the natural divergence and the changing pulse duration due to propagation in air (especially for ultraviolet pulses) complicates the setup and make reliable measurements nearly impossible.

A better approach to generate longer delay times is to synchronize a second laser system to the primary source and set the delay time electronically. Here we use a widely tunable laser system (NT242-SH/SFG; EKSPLA Inc.) which is based on a tunable optical parametric oscillator (OPO) with additional sum- and difference frequency mixing. This allows the generation of 3 6 ns pulses which are tunable between 210 and 2600 nm with pulse energies of several tens of μJ. The nanosecond oscillator is used as pump source, the continua from the femtosecond pulses are used as probe pulses. This combination allows to measure from the early nanosecond time scale up to milliseconds. The few nanoseconds allow to combine the measurements obtained solely from the femtosecond system and to cover 13 orders of magnitude in time. The jitter between the femto- and nanosecond laser systems is in the range of 10 ps. Due to the temporal resolution of a few nanoseconds this jitters does not significantly influ-

ence the signal. Due to the high energy of the nanosecond laser system several spatial filters and irises can be applied to obtain a round and homogenous beam profile in the overlap region.

To demonstrate the potential of the extended setup we analyze the temporal behavior of a MeOH-DPMS mixture after excitation with 370 nm pulses. The combined transient spectra of the anthracene are shown in Figure IV1 and show that after a few nanoseconds an electron is transferred from the anthracene to the surrounding DPMS.

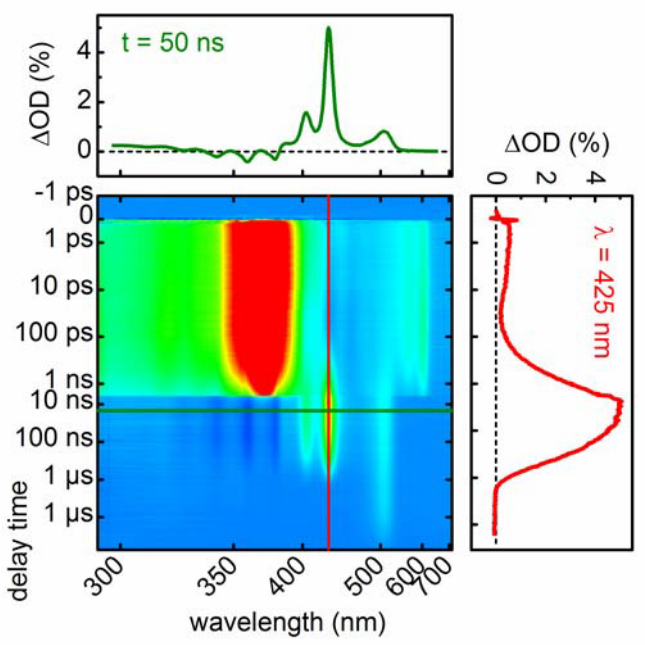

Fig. IV1: Transient spectra of an anthracene / MeOH-DPMS mixture after excitation with 370 nm pulses.

At delay times which are comparable to the laser repetition rate special care has be taken to avoid probing molecules excited by the previous pump pulses. For this purpose flow cells can be used. The overlap region of pump and probe pulses typically spans over 50 to 100 µm. With a repetition rate of 1 kHz this leads to a flow velocities of 10 cm per second in the cell.

V. Increase in fidelity by multi-channel referencing

An often used technique to improve the quality of the measurement in pump probe experiments is referencing. Here a second detector is used to retrieve the transient signal without pumping. This technique can be very advantageous but contains several challenges. Since a full description of the situation is out of the scope of this paper we discuss the referencing

method more detailed in a forthcoming publication. Here we only summarize the obtained results and show the conclusions for the application in pump probe experiments.

When dispersing the continuum with a prism on a camera one pixel only contains the information of very small spectral region. This information is represented by the amount of light which is imaged onto this pixel. The electronic readout transform this in a single number the counts on the detector. Without pumping the sample this number should be theoretically equal for each single laser shot. And hence the ratio between the counts of two subsequent continua (T/T_0) should be exactly 1.00 for all pixels without pump. Energy fluctuations of the continuum due to the spatial, spectral, and power fluctuations of the laser, environmental instabilities, the dark current of the detector, or inhomogeneities in the sample lead to deviations from 1.00 for these T/T_0. A value that represents how strong these deviations are is the rms which is defined as the ratio between the standard deviation and the mean of a serious of subsequent T/T_0. In this paper we always analyze 1000 subsequent T/T_0. A typical measured curve for the rms for each pixel is shown in Fig V1 (black curve). Usual values are around 1% rms. One property of the used laser system and the generated continua is that subsequent pulses are strongly correlated. This means for the experimental realization that only subsequent pulses should be used for T/T_0. Other averaging methods such as dividing the average of ten subsequent pulses with pump by the average of the next ten pulses without pump will lead to a lower stability and higher fluctuations.

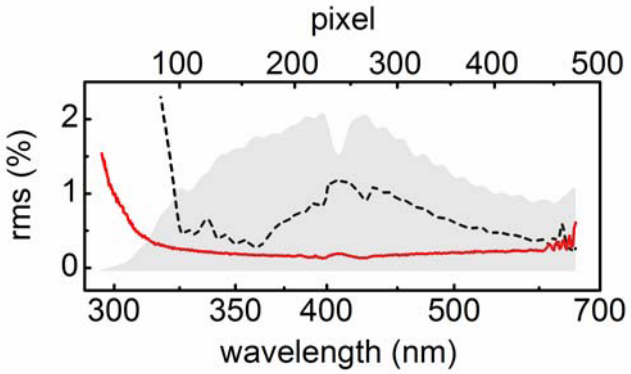

Fig. V1: wavelength depending stability of the continuum with (red dotted line) and without referencing (black). The grey are shows the spectrum of the continuum.

A important point is the type of fluctuation. Here the fluctuation of the continuum is not fully statistically and renders some features. A good way to analyze the fluctuations are zero measurements without pumping. We performed such zero measurements for our laser system. For

an ideal measurement the value of T/T_0 for one pixel should not be correlated to the T/T_0 of neighboring pixel so that every pixel only shows the behavior of the assigned wavelength region. Nevertheless when performing such a zero measurements we see extreme strong correlations of the T/T_0 to the neighboring pixel. Quantitatively the correlation can be expressed by the Pearson coefficient which is 1.0 for full correlation, -1.0 for full anticorrelation and 0.0 if there is no correlation. Figure V2 shows the correlation of the T/T_0 of selected pixels to their neighboring pixels. Only with referencing (ret dotted line) the correlation of the T/T_0 to the neighboring pixels disappears. A good indicator of the improvement with and without multi-channel referencing is the stability. Here we get an improvements of factor 5. The stability for each pixel (and wavelengths) is shown in Figure V1 (red dotted line).

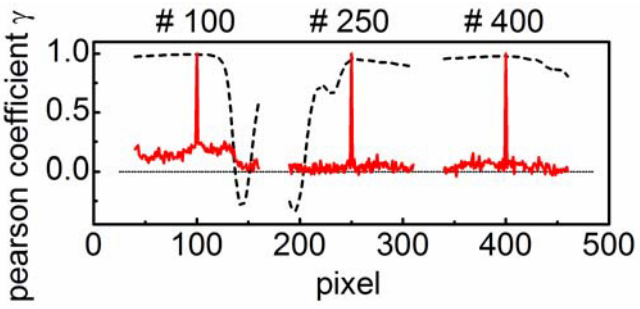

Fig. V2: correlation of T/T0 of selected pixel (100, 250, and 400) to the T/T_0 of their neighboring pixels with (red dotted line) and without referencing (black).

At this point two issues should be mentioned. Surprisingly it is not so important to disperse the continuum exactly equal on both cameras. A good way to optimize the alignment for both cameras are filters which are heavily structured. Then all minima, maxima, and sharp edges can be overlain. The second important issue is that beside the referencing to the second camera also the referencing to the subsequent laser pulse is needed. Due to the not perfect alignment, the different dark currents for both cameras, and environmental instabilities only referencing to the second camera will lead to strong deviations of the real signal. Only when referencing T/T_0 on both cameras the lowest deviations can be obtained. Figure V3 shows the experimental realization of the multi-channel referencing. Exactly the same geometry is used for the sample and the referencing arm to minimize the differences between both branches. The used mirror to split the continuum roughly reflects 50% of the whitelight and let the remaining 50% pass.

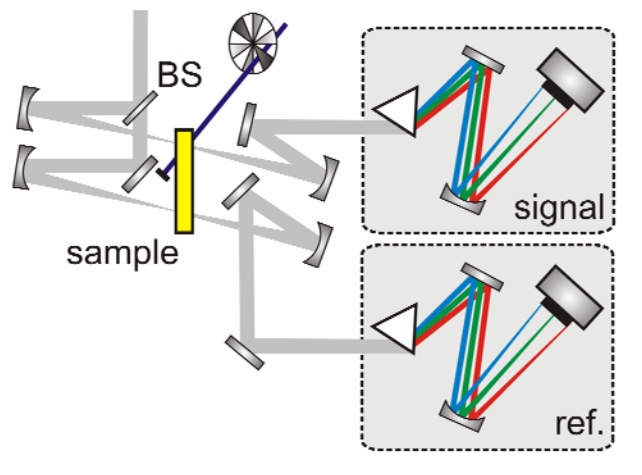

Fig V3: Setup for multi channel referencing. Both branches are geometrically equal. The beam splitter roughly divides the continuum in two equal parts.

To demonstrate that the improvement is not only cosmetically we analyzed an extreme weak signal. We studied a molecule pumped at 250 nm and excited with only 10 nJ. Figure V4 compares the transient signal obtained with (right) and without (left) referencing. For the case without referencing we just take the data measured with the signal camera. Although all features can be seen in both measurements the quality and signal to noise ratio is much better with referencing.

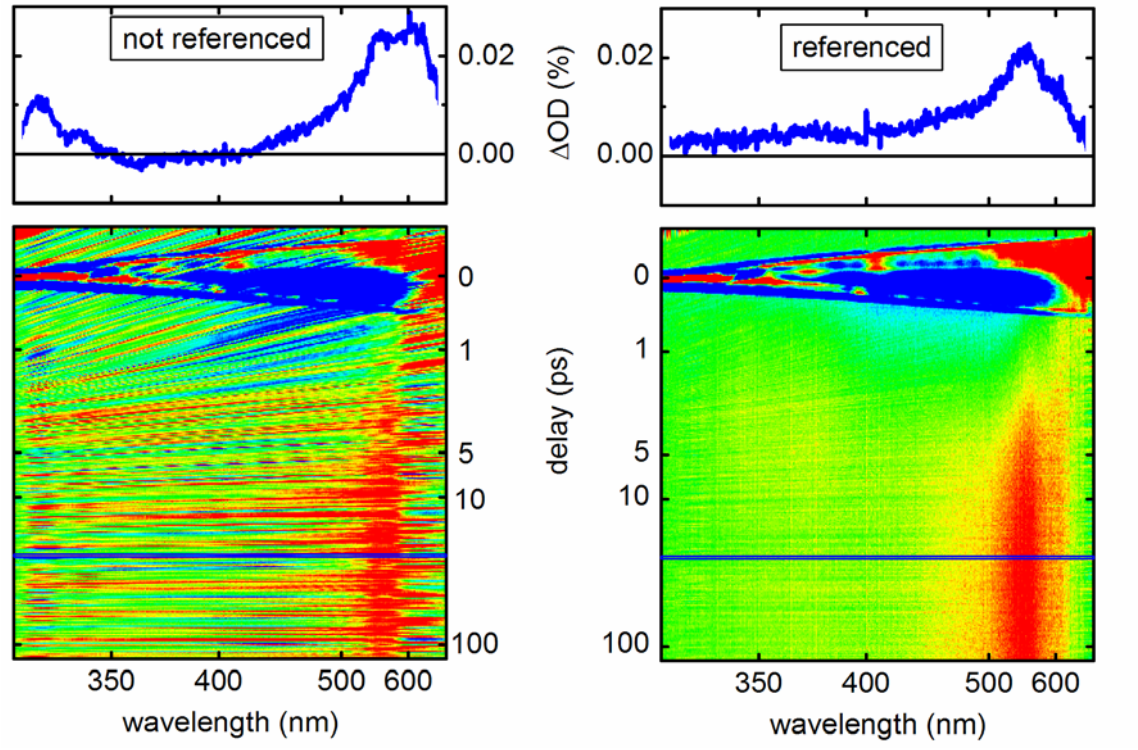

Fig. V4: typical measurement of weak transient absorption signals from bio molecules with and without referencing of T/T_0

The improved sensitivity of the setup when working with referencing allow reducing the average time, the optical density of the sample, and the pump pulse energies. All of these three issues can become necessary if rare samples with fast disaggregating times are studied. More details on this complex thematic are given in ref. [Bradler13].

VI. Useful details and improvements

Beside the basic elements such as optical amplifier to generate adequate pump pulses and broadband continua to cover a wide range of probe wavelengths also helpful tools and techniques are essential for proper and reliable measurements. In this section we will summarize the most important methods to perform high quality experiments.

A. Filtering, steering and spectral calibration of probe continua

Continuum generation in solids allows the generation of new frequencies, which are well suited for pump probe experiments. However, most of the energy of the whitelight is still in the fundamental region. Since this part of the beam has a different divergence, is very unstable, and show strong spectral modulations, it is not suited as probe light. Additionally the high intensity would lead to nonlinear processes in the sample what is not in the sense of noninvasive probe continuum and causes damage on the detection cameras. Therefore the fundamental region of the probe continuum has to be blocked. A spectral selector based on prisms or gratings is principally possible and can be advantageous, but in general it increases the complexity of the system needless. A proper solution are high reflecting mirrors which block the fundamental region and are highly transmitting for the well suited wavelengths. These filters are commercially available on demand and can be specified to the desired wavelength region. The colored areas in Figure VIA1 show the transmission of such filters. A small wavelength tuning of the transmission and blocking range can easily be achieved by tilting the mirrors. A very positive effect when using such mirrors is that the alignment of the continuum is much easier, especially for the UV continua. When generating a continuum with 800 nm or longer wavelengths the newly generated wavelengths only contains a small part of the energy but are much brighter for the eyes as the fundamental light. However, when generating the continuum with UV light the fundamental dominates the visible appearance of the continuum on a business card or beam camera. And since the fundamental beam profile is awful due to all the

nonlinear processes on could think that no proper continuum generation takes place although the newly generated wavelengths are well suited. This can be avoided if the beam profile is regarded behind such dielectric mirrors where only newly generated frequencies can pass. To be sure to only analyze the wanted short wavelength part of the continuum and not the accompanying long wavelength part the use of pinholes and filters is needed.

The short wavelength part spatially overlaps with the long wavelength part of the continuum. The latter dominates the appearance on a business card or on the beam camera. To follow the wanted short wavelength part wavelength selecting mirrors or filters have be used. Special care must be taken after dispersive elements to ensure that the entire non visible UV light is imaged onto the camera.

Another issue which is often not sufficient regarded is the steering of the probe to the experiments. Beside the reflectivity and number of the mirrors, it's also important that the mirrors do not destroy the phase and therefore the temporal resolution. Especially for aluminum or silver mirrors this is not self-evident for all wavelengths of the probe continuum. To check whether the used mirrors are suited or not we perform a pump probe measurement, with a 50 µm thin BBO plate as sample. In the probe arm we additionally add four mirrors and compare it to the measurement without mirrors. From this cross correlations the temporal resolution and the quality of the mirror can be obtained.

Up to now this section describes the proper guiding to the sample, but also the right treatment of the probe after the experiment is crucial for a successful measurement. The probe continuum after the sample contains all information about the molecular dynamics. To reveal them it must be spectrally dispersed and each wavelength must be analyzed independently. In ref. [Meg09] we compare the advantages and properties of different dispersions techniques and describe how to image a dispersed continuum onto the detection arrays best. We use a prism to disperse the continuum and a spherical mirror to image it on the single pixel. Therefore it is essential to know the exact position for every wavelength on the camera. This calibration can basically be calculated due to known dispersion and focal length, but since the experimental realization of the described setup allows uncertainties the calibration can be slightly wrong.

A better calibration can be achieved by measuring the throughput of substrates or filters with known transmission. Well suited for this applications are high reflecting mirrors because they show an obvious transmission minimum and strong oscillations nearby. Also a set of interference filter allow a good calibration. Important is that the substrates show a clear structure with

sharp edges, maxima or minima, so that the positions can easily be determined. Figure VIA1 shows different filters and mirrors for the presented probe continua. All filter are inserted under 0° to avoid wavelength shifts on the camera. For the different continua we use the following blocking and calibration filter, which are summarized in table 1.

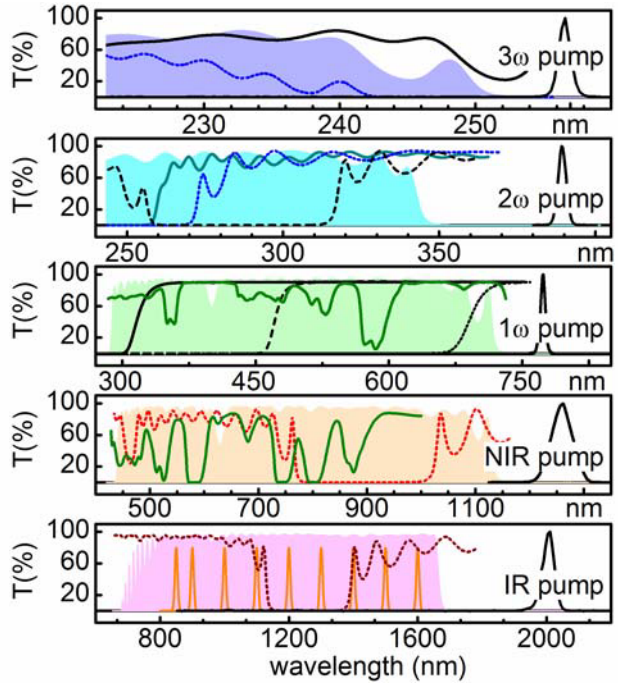

Fig VIA1: Spectral calibration with interference filter, color glasses and dielectric mirrors

We interpolate the transmission measured with the spectrometer to the known transmission. A commercial cw transmission spectrometer [] allows to exactly determine the transmission of any substrate.

B. Straylight reduction

The important information in transient absorption spectroscopy are the relative changes in transmission between pumped and not pumped system. Therefore it's crucial that no additional light, which is not influenced by the dynamic of the sample is detected, because this would alter the real signal height. Such straylight can be scattered pump light, the dark current of the camera, or just ambient light. To avoid that this falsify the experiment often the straylight is subtracted in the beginning or at the end of the measurement. Nevertheless conditions can change during long lasting measurement due to slight degeneration of the sample, accretion of molecules on the surfaces of the cuvettes, or long time fluctuations of the pump. This becomes especially important if the straylight has the same dimension as the probe continuum

on the detector and generally for low signals. Therefore we implemented a dynamic straylight subtraction. After a selectable number measurement points only the straylight is recorded. To not increase the measurement time significantly we typically choose 10 points, so that the overall time increases by around 10%. The dynamic straylight is interpolated to all time steps and than dynamically subtracted. Since this can not be done in situ, we separately save the pumped and not pumped system. This is possible due to the low repetition rate of the system and the full read out of the cameras. Fig VIB1 shows two transient absorption signals obtained from one dataset, once with a straylight correction only at the beginning (a) and once with a dynamic straylight correction (b).

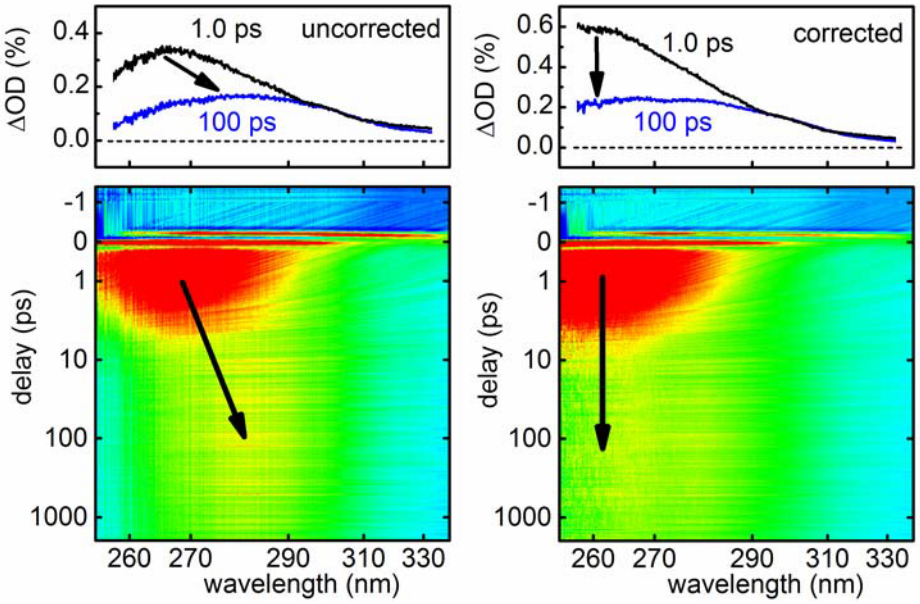

Fig VIB1: Comparison between transient absorption signal with static and dynamic straylight correction. Both transient spectra are obtained from the same data set.

The pump wavelength is 250 nm and its straylight increases during the measurement. In (a) this is not corrected dynamically and leads to an decreasing relative transmission change. This could be interpret as a shifting band and connected to chemical processes or temperature effects, although none of then are apparent.

C. Transport of nanosecond tunable pump by multimode fiber

Extending the temporal delay between pump and probe up to milliseconds often can reveal new photochemical and photophysical processes. The experimental implementation princi-

pally simple because of the electronically generated time delay. Nevertheless the steering of these pulses to the experiment can become challenging due to compact and complex setups and the not freely selectable position of the optical elements and lasers. One successful possibility to transfer optical pulses are large multimode fibers. Since the delay is generated electronically, even distances of several meters can easily be compensated. Typical needed length are commercially available and multimode fibers allow reasonable in- and throughput so that optical pulses can be guided to any positions on the table or even to neighboring laboratories. However, only nanosecond pulses are well suited due to the pulse lengthening of short pulses after propagation in such long fibers.

Typical fibers have a core diameter of 200 µm and consists of fiber glass. Powers of up 100 mW can be launched into the fiber without causing damage. Throughputs are measured to 30% and higher, depending on the wavelength and input beam parameter. We used optical fibers from fibers.

D. Pump optimization and insitu characterization

In the early times of spectroscopy the laser wavelength determines the usable wavelength, because only harmonics and the laser wavelength itself were available. However, this set of wavelengths only matches for selected molecules. To study the object of interest a fully tunable pump must be provided. Combining continuum generation, optical parametric amplification, and further nonlinear processes like sum or difference frequency allows the generation of pulses spanning from the deep-UV from below 200 nm up to the infrared up to above 5 µm. Figure VID1 shows selected pulses from this tuning range generated with modules of the NOPA family, which are also commercially available.

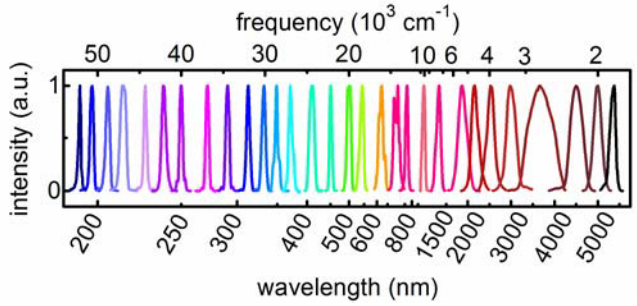

Fig. VID1: Tuning range of sub-50 fs pump pulses derived from the NOPA family

Beside providing the correct wavelength for the experiment also a well characterization of the

pump pulses is essential to determine the pump conditions. The important parameters are the spectrum, the energy, the size, the stability, and the pulse duration. Except the last point this parameter can be directly measured with the help of a spectrometer, powermeter, beam profiler, and diode. The only more complicated part is the pulse duration, especially when pumping in the ultraviolet region. Homann et al. presented a method based on two-photon absorption which allows to measure the pulse duration as it is at the samples position. Fig VIE1 shows the experimental implementation into our setup.

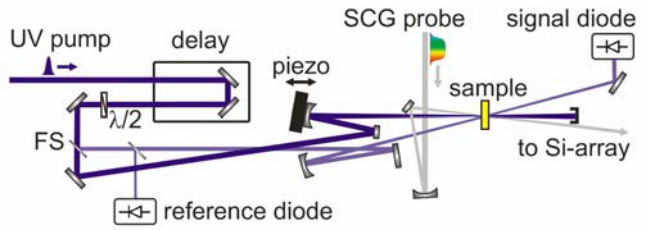

Fig. VIE1: schematic setup of two photon based autocorrelator for pulse duration measurement of UV pulses

By inserting a fused silica plate in the pump beam a weak copy of the pump is generated. This reflex will be temporally and spatially overlapped with the original pump at the sample position. This causes two-photon absorption, if selected materials are placed in the spatial overlap. By changing the time delay between the two pulses this two-photon absorption varies and this allows to determine the actual pulse duration at the samples position. Further details on the technique and the concrete setup can be found in [Ho11]. With all these data the pump conditions can be reconstructed.

E. Time zero and continuum chirp determination

Finding the temporal overlap between to femtosecond pulses can be extreme challenging. The first approach should always be a length measurement of pathways of probe and pump beam. This can be done just with a folding rule or measuring the time delay between both pulses with a photodiode. However this only allows to determine roughly the temporal overlap. A better way to find the exact time zero is to use laser dyes or other molecules with long living and strong signatures. The idea is based on having a strong signal if the probe comes after the pump and no signal otherwise, and iteratively finding the time zero. Fig VIE2 shows well suited dyes and molecules for different excitation wavelengths.

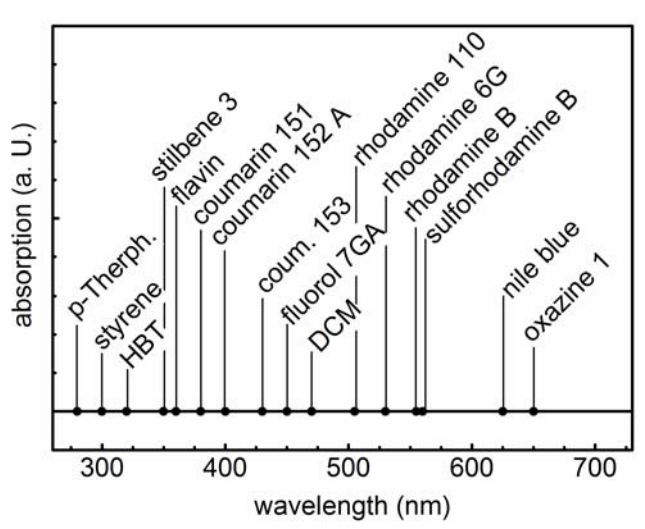

Fig. VIE2: various laser dyes for determination of time zero

All of the presented molecules can be used with ethanol as solution and in a 1 mm or a flow-through cell, so that the time zero directly can be determined.

VII. Summary and outlook

Tables

TABLE O: Overview about beam parameter for probe continuum generation

pump wavelength	beam parameter	equipment
257 nm (3ω)	200 nJ, 170 fs, NA 0.03	300 µm BBO type I (30°) for SHG 300 µm BBO type II (62.7°) for THF
387 nm (2ω)	400 nJ, 170 fs, NA 0.03	300 µm BBO type I (30°) for SHG
775 nm (1ω)	1.0 µJ, 170 fs, NA 0.03	
1180 nm (IR-OPA)	1.5 µJ, 80 fs, NA 0.06	signal of IR OPA
2100 nm (IR-OPA)	2.1 µJ, 80 fs, NA 0,06	idler of IR-OPA

TABLE I: Overview about blocking and calibration filter for probe continua

continuum pump	blocking filter	calibration filter
257 nm (3ω)	HR 275 nm (0°)	HR 226 nm (45°) HR 248 nm (0°) HR 275 nm (45°)
387 nm (2ω)	HR 360 nm (0°)	
775 nm (1ω)	HR 800 nm, HT 270 720 nm (0°)	WG 320 GG 475 RG 695 BG 20
1180 nm (IR-OPA)	HR 1200 nm, HT 400 1100 nm (0°)	HR 790 nm (45°) BG 20
2100 nm (IR-OPA)	HR 1800 nm, HT 500 1700 nm (0°)	interference filters all 100 nm HR 1200 nm (45°)

TABLE II: Solvent dependent absorption maxima of the investigated molecules.

laser dye	λ_{max}(nm)	OD_{max}(mOD)
p-Terphenyl	280	0.60
styrene	300	0.55
HBT	320	0.30
Stilbene 3	350	1.0*
Flavin	350	0.20
POPOP	360	0.75 *
Coumarin 151	380	1.3 *
Coumarin 152 A	400	2.1
Coumarin 153	430	1.8 *
Fluorol 7GA	450	1.3
DCM	470	1.6
Rhodamine 110	505	2.4 *
Rhodamine 6G	530	2.6
Rhodamine B	555	2.8 *
Sulforhodamine B	560	2.8 *
Nile Blue	625	7.5 *
Oxazine 1	650	9.0 *

References

Chi99 A. Brodeur, S. L. Chin, J. Opt. Soc. Am. B **16**, 637 (1999). "Ultrafast white-light continuum generation and self-focusing in transparent condensed media"

Loc98 S. Lochbrunner, W. Fuss, W. E. Schmid, K. L. Kompa, J. Phys. Chem. A **102**, 9334 (1998). "Electronic Relaxation and Ground-State Dynamics of 1,3-Cyclohexadiene and cis-Hexatriene in Ethanol"

Meg09 U. Megerle, I. Pugliesi, C. Schriever, C. F. Sailer, E. Riedle, Appl. Phys. B 96, 215 (2009). "Sub-50 fs broadband absorption spectroscopy with tunable excitation: putting the analysis of ultrafast molecular dynamics on solid ground"

Alf08 V. Kartazaev, R. R. Alfano, Opt. Commun. 281, 463 (2008).

Bra09 M. Bradler, P. Baum, E. Riedle, Appl. Phys. B **97**, 561 (2009).

Ern10 A. L. Dobryakov, S. A. Kovalenko, A. Weigel, J. L. Perez-Lustres, J. Lange, A. Müller, N. P. Ernsting, Rev. Sci. Instrum. **81**, 113106 (2010).

Ho11 C. Homann, N. Krebs, E. Riedle, Appl. Phys. B **104**, 783 (2011).

Kre10 N. Krebs, R. A. Probst, E. Riedle, Opt. Express **18**, 6164 (2010).

Appendix A20

Direct Generation of 7 fs Whitelight Pulses from Bulk Sapphire

E. Wittmann, M. Bradler, and E. Riedle

to be submitted to Optica (2014)

Direct Generation of 7 fs Whitelight Pulses from Bulk Sapphire

Emanuel Wittmann, Maximilian Bradler, and Eberhard Riedle

LS für BioMolekulare Optik, Ludwig-Maximilians-Universität München, Oettingenstr. 67 80538 München, Germany

E-Mail: e.wittmann@physik.uni-muenchen.de

Abstract: Generation of sub-10 fs continuum pulses without external compression is demonstrated. We investigate the propagation of the newly generated wavelengths and find that a short crystal in combination with an achromatic telescope leads to nearly chirp free continua

New insights into bulk Filamentation

Supercontinuum generation (SCG) in bulk material is a generally applicable method to broaden the spectrum of femtosecond laser pulses at various wavelengths. The Fourier limit for a possible compression of, e.g., an 800 nm pumped continuum from sapphire, amounts to about 4 fs. Yet, no results have been published which show that bulk continua have intrinsically such short pulse durations. This is in striking contrast to the situation in continua generated in gas-filled hollow core fibers or in gas filamentation. There compression to below 4 fs has been shown. In precise investigations of the continuum generation and propagation we now find that the inability to compress the continuum stems from the highly wavelength dependent effective generation locus and propagation. This knowledge gives us the chance for ideal control of the process and therefore the ability to generate sub 10 fs pulses without the use of any external compression scheme. This validates that the new frequencies generated during filamentation develop highly coherently.

Propagation properties of new frequencies and generation of sub-10-fs pulses during SCG

Two processes should be differentiated when the over-all appearance of continuum generation in a bulk material is considered. First, the spatial area or depth into the material where the new colors are developing has to be considered. Second, the propagation in the remaining material before exiting into free space has to be understood. That these issues are far from trivial is proven by the fact that a full collimation of a bulk continuum has not been reported and consequently the full temporal compression has not yet been achieved. In preliminary experiments we imaged the continuum from a 3 mm sapphire with a singlet lens and found that the blue part of the spectrum focuses earlier than the red part. In a semi-quantitative interpretation this could be attributed to the chromatic error. To circumvent this issue, we used a Schiefspiegler [1] that images all spectral components without chromatic error. We still found the blue

spectral components focused earlier. An explanation would be that during filamentation all colors are generated at once, but short wavelengths fall behind the filament channel because of their lower group velocity. Without guiding by the filament, they start to diverge. The wavelengths close to the pump follow the channel longer and diverge later, leading to the observed color dependent propagation.

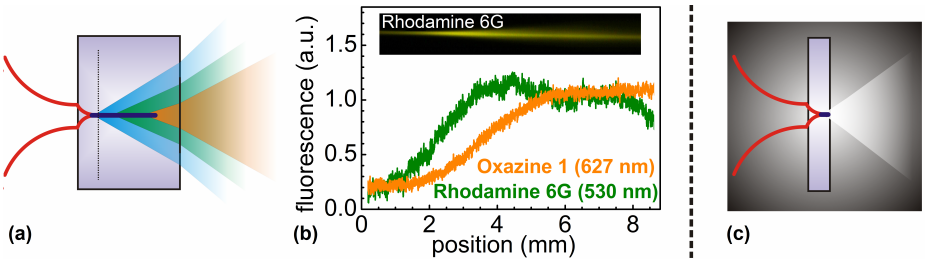

Fig 1 a) Scheme of bulk continuum generation and wavelength dependent beam propagation. b) Fluorescence of Rhodamine 6G (green) and Oxazine 1 (orange) to monitor the beam propagation during filamentation in ethanol. c) All colors diverge equally in a short crystal.

To verify this concept, a continuum is generated in ethanol and monitored from the side with a high resolution camera. To visualize the propagation of selected wavelength ranges we use a solvent (instead of sapphire) and Rhodamine 6G (absorbing around 530 nm) or Oxazine 1 (627 nm) were added separately. These laser dyes partly absorb the newly generated light and fluoresce so that the beam propagation can be monitored from the side. Fig 1 (b) shows the corresponding fluorescence signal and the side view from filamentation in ethanol with Rhodamine 6G (top). A strong signal is only found when the light has already broadened from the 8 µm filament and the dye absorption is not saturated as inside the channel. We find that different colors start to diverge at different positions in the solvent. Our proposed model is confirmed and we can explain the difficulty of properly imaging a continuum. To avoid the wavelength selective propagation, the continuum has to be generated at the very end of the crystal. The crystal should be terminated at the dashed line in Fig 1 (a) so that no spectral and local separation occurs and all colors start to diverge simultaneously as shown in Fig 1 (c). We find a short crystal length on the order of 1 mm suitable. This should lead to a chirp free continuum as the newly generated colors pass through no extra material, and all colors having the same spatial properties. With a 1 mm sapphire plate, we optimize the continuum generation onto the output face. A careful alignment still renders a continuum with little fluctuations. The pump source is a small fraction of the output of a Ti:sapphire amplifier (CPA 2001; Clark MXR) with a pulse duration of 170 fs and a central wavelength of 778 nm, focused with a f = 50 mm plano-convex lens. We obtain a continuum spanning down to 430 nm. For an anastigmatic and achromatic collimation or imaging of the generated continuum we use a reflective Schiefspiegler telescope [1], consisting of a suitable combination of a convex and a concave mirror. This allows us to measure the pulse duration of the newly generated frequencies with a SHG intensity autocorrelator without the loss of any frequencies due to aberrations. The main peak of the autocorrelation signal corresponds to a 7 fs continuum pulse.

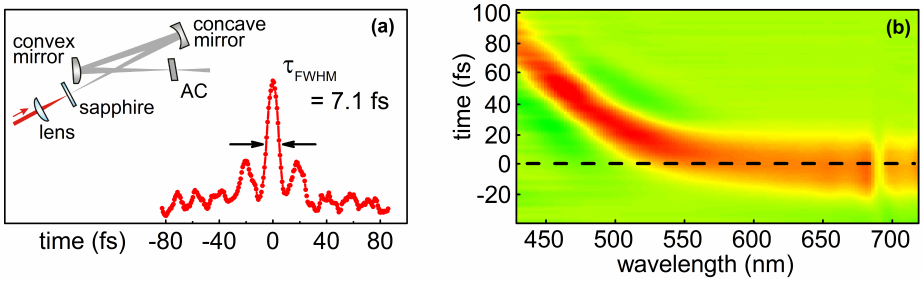

Fig 2 a) Schiefspiegler geometry for imaging the newly generated colors of a 1 mm sapphire continuum and autocorrelation trace demonstrating a 7 fs pulse. b) Transient absorption measurement in 200 µm GG400 to determine the chirp of the continuum generated in a 1 mm sapphire plate.

For a better insight into the spectrotemporal distribution of the continuum and to show that the autocorrelation signal does not correspond to a coherence spike [2] due to the complexity of the continuum pulse, the chirp of the sapphire continuum is determined with our transient spectrometer [3]. Fig 2 (b) shows the transient signal of the continuum generated in the 1 mm sapphire plate. With a 200 nJ, 25 fs pump pulse at 470 nm and the sapphire continuum as probe we measured the cross correlation via two-photon absorption in a 200 µm GG400 (Schott AG) substrate. Two-photon absorption of pump and probe only occurs for temporal overlap and allows determining the group delay for every wavelength. Since only reflective optics are used in the probe beam path, the signal represents the intrinsic spectral chirp of the continuum after propagation through just a short length of air. Fig 2 (b) shows that all spectral components from 500 to 700 nm coincide in time. The chirp for the short wavelength range mainly originates from the propagation in air. These chirped components of the pulse appear as broad and structured wings in the autocorrelation trace.

Conclusion & Outlook

It is possible to obtain sub-10 fs white light pulses directly from bulk filamentation. In the literature only a few examples for white light compression can be found, but until now the appropriate setup always is accompanied by huge complexity. By studying the propagation properties of the continuum we found a straightforward way to simplify the effort for generation of short continuum pulses. An elaborate apparatus can be replaced by a lens, a 1 mm sapphire plate and the adequate adjustment for the incident pulse energy. With the imaging by a Schiefspiegler also any chromatic aberrations as well as astigmatism can be avoided. Such pulses are highly interesting for broadband amplification, ultrafast 2D spectroscopy, or spectroscopic experiments.

[1] A. Kutter, Der Schiefspiegler: Ein Spiegelteleskop für hohe Bilddefinition (Weichhardt, 1953)
[2] Rick Trebino, Frequency-Resolved Optical Gating: The measurement of Ultrashort Laser Pulses, (Kluwer Academic Publishers, Boston / Dordrecht / London, 2000), Chap. 4
[3] U. Megerle, I. Pugliesi, C. Schriever, C.F. Sailer, E. Riedle, "Sub-50 fs broadband absorption spectroscopy with tunable excitation: putting the analysis of ultrafast molecular dynamics on solid ground", Appl. Phys. B 96, 215-231 (2009).

Appendix A21

Pushing the NOPA to New Frontiers: Output to below 400 nm, MHz Operation and ps Pump Duration

M. Bradler, L. Kasmi, P. Baum, and E. Riedle

to be submitted to book of proceedings for Ultrafast Phenomena XIX (2014)

Pushing the NOPA to New Frontiers: Output to below 400 nm, MHz Operation and ps Pump Duration

Maximilian Bradler[1], Lamia Kasmi[2], Peter Baum[2], and Eberhard Riedle[1]

[1] LS für BioMolekulare Optik, LMU München, Oettingenstr. 67 80538 München, Germany
[2] Ludwig-Maximilians-Universität München, Am Coulombwall 1, 85748 Garching, Germany

E-Mail: Riedle@physik.uni-muenchen.de

Abstract: Two sub-ps MHz range Yb-based lasers are used to pump NOPAs at 343 nm. A SHG driven supercontinuum allows tuning down to 395 nm. For a 1-ps pump, supercontinuum seeding is applicable, the pulses are compressed to the 20-fs regime with a potential for sub-10 fs.

Optical parametric amplifiers pumped by Yb-based lasers

For many years the generation of powerful ultrashort pulses was dominated by Ti:sapphire oscillators and amplifiers. Optical parametric amplifiers (OPA) were developed to provide full spectral tunability. The introduction of noncollinear phase matching (NOPA) and chirped parametric amplification (OPCPA) enables to generate some of the most intense, shortest and most widely tunable pulses available today. NOPAs were originally pumped by the SHG of kHz Ti:sapphire systems with a pulse duration around 100 fs. This allows efficient continuum generation to be used as seed light and provides a high intensity in the amplifier. Recently, the development of femtosecond lasers has turned to Yb-based active media, because higher average powers are achievable with diode laser pumping. The consequences are a central wavelength around 1030 nm and pulse durations not significantly below one picosecond. Pumping a NOPA with the SHG at 515 nm [1] and BBO as active material resulted in a shortest output wavelength of 600 nm. With THG pumping [2] 387 nm should be reachable, but was not yet demonstrated due to the lack of suited seed light. We now show in two setups employing newly available Yb-based systems at up to 1 MHz as pump that the sub-400 nm rang can be reached if a SHG-pumped continuum is used as seed. We generate tunable blue pulses with Fourier limits in the 10 fs range. With a 1 ps, 300 kHz pump system we generate a stable continuum and subsequently amplify major spectral parts into powerful pulses with the potential of sub-10 fs duration.

Fully utilizing the tuning possibility of a 343 nm pumped NOPA

In our first series of experiments we use a 20 W fiber-based system (Tangerine fs, Amplitude Systemes) delivering 1030 nm pulses with 20 µJ pulse energy and 300 fs pulse duration. The system is operated at 200 kHz for development and 1 MHz for full output. To generate 343 nm pump pulses (see Fig. 1 a) we frequency-triple the

major part of the pulses in a sequential arrangement of a type I doubling BBO and a type II BBO [2] to obtain 3 µJ UV pulses.

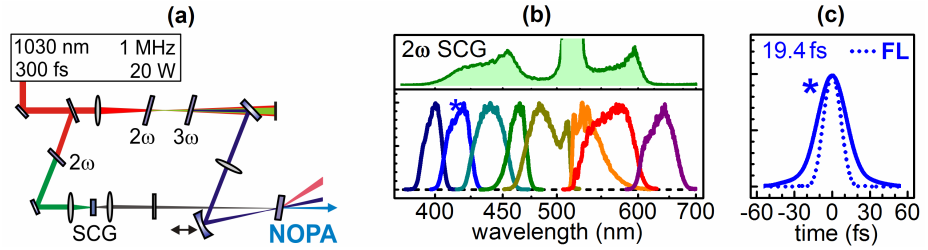

Fig 1 a) pumped by 343 nm pulses. b) Supercontinuum (SCG) generated by pumping with 515 nm pulses. Spectra of pulses tunable from 395 to 630 nm with Fourier limits below and close to 10 fs. c) Autocorrelation of 425 nm pulses.

For the seed light generation, part of the 1030 nm pump is frequency doubled in a 0.8 mm BBO crystal. The SHG pulses with an energy of 750 nJ are spectrally filtered with dielectric mirrors and focused onto a 4 mm thick YAG crystal [3]. The observed continuum (Fig. 1 b) contains spectral components well below 400 nm and with a thicker crystal down to 350 nm. The high-wavelength cutoff is above 650 nm. Significant parts of this extremely wide spectrum are amplified in a NOPA employing a 3 mm BBO crystal cut at 32.5°. Typical output spectra are shown in Fig. 1 b with Fourier limits between 10 and 20 fs for the entire range. The shortest central wavelength reached is 395 nm, limited by idler absorption at around 3 µm. When optimized for output power, the pulse energy exceeds 1 µJ, corresponding to a 40 % quantum efficiency in the nonlinear conversion of the pump light. The pulses are compressed with fused silica prisms. A typical autocorrelation at 425 nm is shown in Fig. 1 c, showing a sub-20 fs duration that is limited by higher-order chirp, but still highly competitive with alternative methods for generating tunable blue pulses at high repetition rate. We also frequency double the NOPA output and generate pulses down to 210 nm in a single additional conversion stage. The observed spectral width is only limited by the acceptance bandwidth of the BBO crystal, providing possible pulse durations of below 20 fs. Altogether, the system now provides fully tunable 10-20-fs pulses from the deep UV all the way up to 630 nm without any wavelength gaps. The additional range up to 950 nm can be reached with a NOPA pumped by the residual 515 nm light, which is already integrated in the actual amplifier layout.

Continuum-seeded NOPA with 1 ps 130 W pump pulses

The second pump system is a diode-pumped regenerative Yb:YAG disk amplifier based on a previous design [4], but operating at 50-300 kHz. The output power is up to 130 W at a central wavelength of 1032 nm and the pulses have 1 ps duration. The main challenge with these long pulses is the seed light generation. Here, we report on a stable supercontinuum generated with 7 µJ at 1032 nm in a 4 mm YAG crystal. This is the basis for the subsequent amplification in the NOPA, without resorting to external seed sources such as a synchronized Ti:sapphire oscillator. The continuum extends from below 500 nm up to the pump wavelength (Fig. 2 a). Using frequency-

tripled 6.7-µJ pulses for NOPA pumping, we are able to generate tunable pulses in the green spectral range with up to 1 µJ output energy and Fourier limits close to 10 fs (Fig. 2 c). At specific phase matching conditions, pulses with a Fourier limit of 6 fs can be obtained as a consequence of the long pump pulse length. With a compressor made of two SF10 prisms at less than 1 m of separation, the pulses were compressed to the 20 fs regime (Fig. 2 b). This represents a pulse shortening by a factor of 50.

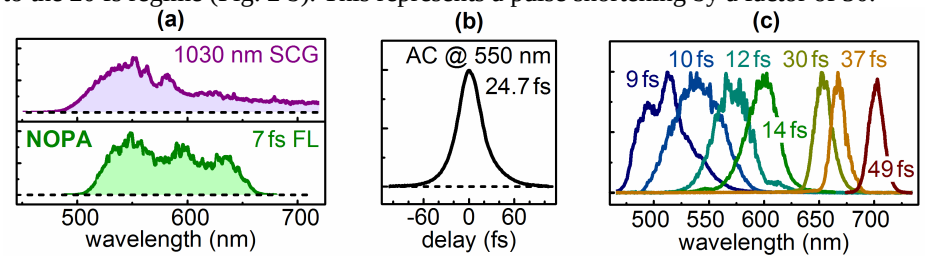

Fig 2 a) Continuum generated from 1-ps 1030 nm pulses and broadband NOPA output. b) Autocorrelation of 550 nm pulses. c) Tuning range of the 344-nm-pumped NOPA with Fourier limits.

In a first application, we produced narrow-band tunable pulses with a slit in the prism compressor and studied the performance of a femtosecond electron gun in dependence on the photoemission wavelength. We found that the two-photon photoemission regime with visible pulses reproduces earlier results with ultraviolet pulses [5]. The duration of the electron pulses decreases and the coherence increases as the photon energy approaches half of the work function. This result proves the applicability of a powerful picosecond laser at 50-300 kHz, which is powerful enough for providing tunable pump pulses for femtosecond electron diffraction and microscopy.

Towards new applications of wavelength-tunable MHz 10 fs pulses

The presented experimental results show that the presently evolving Yb-based ultrashort pulse sources operating at up to MHz repetition rate and with pulse durations close to 1 ps can be efficiently used to generate pulses tunable from 210 to 950 nm. Pulse durations below 20 fs are demonstrated and sub-10-fs capability is found. With both pump lasers, a supercontinuum generated in a YAG crystal is used as seed and avoids the need for elaborate temporal synchronization. Due to the high repetition rates, many new applications that need extensive scanning or a high degree of averaging together with a resonant excitation now become feasible.

[1] C. Schriever, S. Lochbrunner, P. Krok, and E. Riedle, Opt. Lett. **33**, 192-194 (2008).
[2] C. Homann, C. Schriever, P. Baum, and E. Riedle, Opt. Express **16**, 5746-5756 (2008).
[3] M. Bradler, P. Baum, and E. Riedle, Appl. Phys. B **97**, 561-574 (2009).
[4] T. Metzger, A. Schwarz, C. Y. Teisset, D. Sutter, A. Killi, R. Kienberger, and F. Krausz, Opt. Lett. **34**, 2123-2125 (2009).
[5] P. Baum, Chem. Phys. **423**, 55–61 (2013).

Appendix A22

Pulsed UV-light source

C. L. Thomsen, F. D. Nielsen, S. Hauser, E. Riedle, and M. Bradler

Danish patent application DK 2012 70597 A1

(19) DANMARK

(10) **DK 2012 70597 A1**

(12) PATENTANSØGNING

Patent- og
Varemærkestyrelsen

(51) Int.Cl.: ***G 02 F 1/35 (2006.01)***

(21) Ansøgningsnummer: **PA 2012 70597**

(22) Indleveringsdato: **2012-10-01**

(24) Løbedag: **2012-10-01**

(41) Alm. tilgængelig: **2013-08-15**

(71) Ansøger: **NKT PHOTONICS A/S, Blokken 84, 3460 Birkerød, Danmark**
Ludwig-Maximilians Universität München, Geschwister-Scholl-Platz 1, DE-80539 München, Tyskland

(72) Opfinder: **Carsten L. Thomsen, Ligustervænget 49, 2830 Virum, Danmark**
Frederik D. Nielsen, Sønder Boulevard 49 3. tv, 1720 København V, Danmark
Sascha Hauser, Obere Siedlung 21, Rechtenbach 97848, Tyskland
Eberhard Riedle, Moorackerweg 4, 80939 München, Tyskland
Maximillian Bradler, Adalbertstrasse 15, 80799 München, Tyskland

(74) Fuldmægtig: **Hegner & Partners A/S, Banemarksvej 50, 2605 Brøndby, Danmark**

(54) Benævnelse: **Pulsed UV-light source**

(56) Fremdragne publikationer:
US A1 2012/0099340 A1
US A1 2012/023631
US A1 2012/0049092
WO A2 2012/069612

(57) Sammendrag:
The invention relates to a tunable optical light source spanning the UV-range and possible also the visible and near-IR wavelengths. The tunable optical light source comprises, an input light source, a focusing element, a non-linear crystal arranged to convert the frequency of at least part of the output spectrum of said super continuum source, and a holding unit for said nonlinear crystal. The input light source is a super continuum light source with a spectral bandwidth of at least about 300 nm and the holding unit is adjustable for changing the frequency converted output wavelength of the non-linear crystal wfC such that the lowest obtainable output wavelength wuv of said tunable light source is ultraviolet.
The invention further relates to an illumination source and an optical measurement system.

Fortsættes ...

Fig. 6:

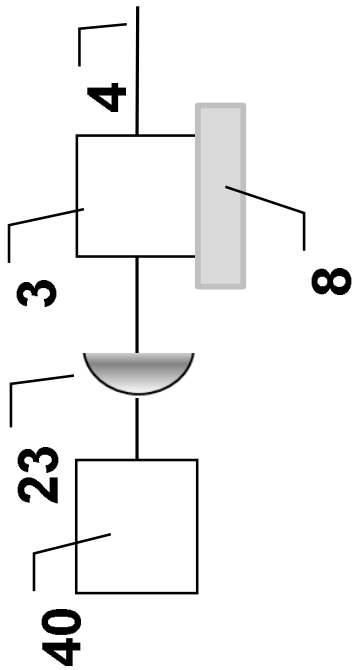

Pulsed UV-light source

TECHNICAL FIELD

The present invention relates to a tunable pulsed light source spanning the UV range and suitable for use in an illumination source and/or an optical measurement system. The invention also relates to an illumination source as well as an optical measurement system comprising such tunable pulsed light source.

BACKGROUND ART

Optical measurement systems are frequently used to analyze biological and chemical substances. In e.g. confocal microscopes a fluorophor is added to the substance under test. A laser light is used to excite the fluorophor, and when it subsequently decays radiatively a camera can detect its position.

Light is also used to study physical, chemical and biological reactions, which typically occur on a femtosecond (fs) to nanosecond (ns) scale. This is conventionally done by having a pump laser and a fs probe laser, which is slightly delayed compared to the pump laser.

In order to analyze many different samples and substances the optical measurement system should preferably contain several laser wavelengths. This can be achieved by combining multiple single line width lasers and/or having a tunable light source.

Applications within the field span light sources all the way from the UV (10-400 nm) through the visible (400-800 nm) to the near-IR region (800-2500 nm). E.g. to analyze spectra of gaseous benzene it is often preferred to measure spectra from 210 nm to 300 nm, whereas e.g. to analyse wheat it is normally preferred to span from 750 nm to 2500 nm.

The preferred choice of light source varies for different applications. Some examples are thermal sources or Ti:sapphire lasers for near-IR wavelengths,

and Ti:sapphire based non-collinearly phase matched optical parametric oscillators for visible and UV wavelengths. Within the last decade fiber-based systems have also been used to generate broad-band sources, examples include frequency combs spanning 530 nm to 2100 nm (e.g. FC1500-250-WG Optical Frequency Synthesizer from Menlo Systems) and super continuum (SC) sources spanning 400 nm to 2400 nm (e.g. SuperK EXR-15 from NKT Photonics A/S or WhiteLase SC400 from Fianium Ltd). Other examples include sub-nanosecond pulsed LEDs, such as e.g. the PLS series from PicoQuant, which have pulselengths down to 500 ps and can reach up to 80 µW output power in the visible range and around 1 µW in the UV. Here PicoQuant notes that 1 µW is still sufficient to use the source as an efficient fluorescence excitation source.

Another approach is to frequency double, triple or quadruple optical pulses to obtain shorter wavelengths. These processes are commonly referred to as second, third and fourth harmonic generation. For brevity, all these processes will in the following be described as frequency doubling, i.e. the term frequency doubling should be understood to include harmonic generation of any order.

Frequency doubling can be obtained by sending light pulses with a high intensity through a non-linear crystal. Inside the non-linear crystal some of the light photons combine to create light at the doubled frequency (and thus half the wavelength) whereas other parts of the light traverse the crystal without being doubled; see figure 1. Accordingly the output beam from the crystal will contain light at both the original frequency f1 and the doubled frequency 2f1.The amount of light at the different frequencies depends on the degree of phase matching between the photons at the fundamental and doubled frequency (i.e. f1 and 2f1). The phase matching again depends on the intensity, spectral content and angular dispersion of the incoming light, but also on the crystals material, length and how it is cut.

For un-dispersed incoming light, the path length inside the crystal where there is phase matching is inversely proportional to the bandwidth of the incoming light. Thus extremely short crystals have been used for frequency doubling broad band pulses, for example Szabo states that for frequency doubling a 50 fs beam at 496 nm the crystal length should be shorter than 0.07 mm if the light is un-dispersed (*Broadband frequency doubler for femtosecond pulse, G. Szabo and Z. Bor, Appl. Phys. B. 50, page 51-54, 1990, see first paragraph on page 51*).

Frequency doubling in short non-linear crystals is enabled by increasing the light intensity, since the degree of frequency doubling generally increases with the intensity of the incoming light. However, high intensity light will often lead to degradation of the crystal and hence limit its lifetime. This is in particular the case for conversion to wavelengths in the UV region.

For broad band sources, it has been shown that angularly dispersing the light before the non-linear crystal enables obtaining phase matching over a wider bandwidth. E.g. the prior mentioned reference by Szabo showed that dispersing the beam on a grating prior to the non-linear crystal enables doubling 10 fs pulses at 496 nm in a 1 mm long crystal, see fig. 2. For reference 10 fs pulses at 496 nm must have a bandwidth of at least 25 nm (Fourier transform limit).

The idea of dispersing the light before the crystal was experimentally demonstrated in a paper by Baum (*Tunable sub-10-fs ultraviolet pulses generated by achromatic frequency doubling, Peter Baum, Stefan Lochbrunner, Eberhard Rielde, Optics Letters, vol. 29, no.14, July 15, 2004, page 1686-1688*). Here a set of prisms between the laser and the doubling crystal are used to enhance the doubling bandwidth by a factor of 80 and obtain a tunable source from 275 – 375 nm with < 10 fs pulse length and a 360 µm thick BBO crystal, see figure 3.

A similar approach has furthermore been used to demonstrate a tunable source from 460 nm to 900 nm with < 50 fs pulse length (*Generation of 10 to*

50 fs pulses through all of the visible and the NIR, Appl. Phys. B, 457-465, 2000, E. Riedle, M. Beutter, S. Lochbrunner, J. Piel, S. Schenkl, S. Spörlein, W. Zinth).

Such a system is well suited for experiments requiring tunable very short fs pulses in the UV or visible range. However, it has a large cost, is complex to operate and requires highly skilled operators, and thus also has a large cost of ownership.

A lot of bio-optical applications require time resolved measurements but not necessarily on a short fs scale. Some examples include time resolved fluorescence, time correlation single photon counting, single molecule detection, intrinsic fluorescence, time resolved photoluminescence, UV polymerisation of resin, DNA sequencing, confocal microscope, FLIM, FRET, flow cytometry, cell-sorting, spectroscopy and food analysis.

Thus there is a commercial market for a low cost tunable light source spanning the UV-range with an output of at least 1 µW. The addressable market further increases if the tunability can be extended into the visible and/or near-IR wavelengths.

DISCLOSURE OF INVENTION

In view of the foregoing an object of the present invention is to provide a low cost tunable light source spanning the UV-range and possible also the visible and near-IR wavelengths.

This and other objects have been solved by the invention as defined in the claims and as described herein below.

It has been found that the invention and embodiments thereof have a number of additional advantages which will be clear to the skilled person from the following description.

The tunable pulsed light source of the invention comprises a super continuum light source with a pulse length of at least about 300 femtosecond and a non-linear crystal, which can be adjusted to enable tuning the output spectrum of the tunable source such that it comprises wavelengths in the UV range and simultaneously having an output of at least about 1 µW. The UV range is herein defined to be in the range from about 10 to about 400 nm.

In view of the prior art the traditional approaches for frequency doubling of broad band light sources are to use very short non-linear crystals and increase the intensity and peak power of the light incoming on said non-linear crystal and/or to disperse the light prior to reaching said non-linear crystal.

Fiber laser super continuum sources (super continuum sources where the amplifier chain is all-fiber) are very broad band, and compared to the cited prior art have low peak power. Hence heretofore the present invention it was expected that it would be very difficult to frequency double these light sources and accordingly that a useful output using such super continuum light source would be practically impossible to achieve.

Surprisingly, the inventors have discovered that it is possible to frequency double SC sources with a relatively simple and inexpensive frequency doubling set-up, and that the output spectral density can be in the order of µW, such as at least 1 µW, which is sufficient to detect the pulses and hence enabling use of such light source for a number of bio-optical measurements.

The tunable pulsed light source of the invention comprises

- an input light source;
- a focusing element;
- a non-linear crystal arranged to convert the frequency of at least part of the output spectrum of said super continuum source; and
- a holding unit for said non-linear crystal.

wherein the input light source is a super continuum light source.

The super continuum light source (in the following also referred to as a SC light source) has a spectral bandwidth of at least about 100 nm. The holding unit is adjustable such that it is suitable for changing the frequency converted output wavelength of the non-linear crystal w_{fc} to provide that the lowest obtainable output wavelength w_{UV} of the tunable light source is in the UV range.

Furthermore w_{fc} is defined as the central output wavelength of the frequency converted beam after the non-linear crystal at the given position, orientation and temperature of the crystal.

The lowest obtainable output wavelength w_{UV} of the tunable light source is defined as the lowest wavelength where it is possible to achieve an output power of at least about 1 µW.

Advantageously the non-linear crystal is arranged to convert the frequency of the SC source. This includes both non-linear crystals optimized for frequency doubling, sum frequency mixing and other non-linear conversions.

In one embodiment the lowest obtained output wavelength w_{UV} is less than 380 nm, such as less than 360 nm, such as less than 320 nm, such as less than 300 nm, such as less than 280 nm, such as less than 260 nm.

As mentioned in the background section, the central output wavelength of the frequency doubled beam w_{fc} is determined by the phase matching condition. Thus it depends on how the light enters, traverses and exits from the non-linear crystal and on the temperature of the crystal. Thus in one embodiment the adjustment of the non-linear crystal is performed by changing its position, orientation and/or temperature.

Surprisingly it was found that nearly any translation or rotation stage can be used for the non-linear crystal. Examples comprise Newport or Thorlabs standard mirror mounts, rotation stages and translation stages.

The efficiency of the frequency doubling inside the nonlinear crystal depends on the beam size. Hence, in one embodiment the holder unit is adjustable to position the non-linear crystal in the focus position of the light from the focus element.

In one embodiment the adjustment of the holder is computer controlled, so that the light source has a computer controlled output wavelength. In this embodiment the holder is advantageously in digital connection (with wire or wireless) with a computer which is programmed to adjust the holder to the desired position(s). Thereby the output wavelength w_{fc} can be controlled by the computer. The computer e.g. received feed back from the output light.

In one embodiment the holder unit is arranged to change the phase-matching angle and thereby the output wavelength w_{fc} without changing the distance to the focusing element.

However, it is known from literature that some non-linear crystals degrade with time due to the high intensity light impinging on them, see e.g. US 5,179,562. This degradation is typically very local and limited to the area where high intensity light impinges on the crystal. In one embodiment of the invention the holder of the non-linear crystal enables both adjusting the non-linear crystal to enable tuning the light source and moving the non-linear crystal with respect to the incoming beam so that it impinges on a new spot on the crystal, when the degradation of the currently used spot reaches a threshold value. An example for detecting the threshold value and moving the non-linear crystal is shown in patent application WO 2009/095022.

As prior noticed, SC sources have limited peak power. Typically the output from SC sources is either diverging or collimated with a spot size on the order of mm. In order to achieve high intensity on the non-linear crystal it has been found to be advantageous to include a focusing element before the non-linear crystal. Examples of such focusing elements comprise mirrors and/or lenses, and in one embodiment the focusing element is an achromat. In one embodiment the focusing element comprises several mirrors and/or lenses.

As will be clear to one skilled in the art, the focusing element can either be integrated in the SC source or it can be an external part relative to the SC source. Thus in one embodiment the focusing element is placed inside the SC source and in one embodiment the focusing element is placed outside the SC source.

If the non-linear crystal is placed in the focal point from the focusing element, then the beam size at the crystal is inversely proportional to the numerical aperture of the focusing element. Thus to achieve frequency doubling a minimum numerical aperture is required.

Advantageously the output from the focusing element has a numerical aperture of from about 0.001 to about 0.25.

In one embodiment the output from the focusing element has a numerical aperture of above 0.001, such as above 0.005, such as above 0.01, such as above 0.015, such as above 0.02.

In one embodiment the output beam from the focusing element has a numerical aperture which is below 0.25, such as below 0.2, such as below 0.15, such as below 0.1, such as below 0.08, such as below 0.06.

Furthermore it has been found that the optimal numerical aperture depends on the wavelength. Hence in one embodiment the light source comprises an adjustable NA of the output beam from the focusing element, such as an optical telescope positioned before the focusing element or a variable path length device.

In one embodiment the focal length of the focusing element is such as at least 9 mm, such as greater than 14 mm, such as greater than 19 mm, such as greater than 24 mm, such as greater than 29 mm.

For conversion to the ultraviolet it has found to be important using a non-linear crystal. Advantageously the non-linear crystal is suited for the converted wavelengths. Examples of suitable crystals are lithium triborate

(LiB3O5 = LBO), cesium lithium borate (CLBO, CsLiB6O10), β-barium borate (β-BaB2O4 = BBO, bismuth triborate (BiB3O6 = BIBO), cesium borate (CSB3O5 = CBO), Yttrium calcium oxyborate (YCOB), strontium beryllium borate (Sr2Be2B2O7 = SBBO) and K2Al2B2O7 (KAB).

In one embodiment the non-linear crystal is Type I cut, meaning that two photons having ordinary polarization with respect to the crystal will combine to form one photon with double the frequency and extraordinary polarization. It is noted that the maximal numerical aperture (NA) of the non-linear crystal depends on the crystal material, e.g. a BIBO crystal can obtain a larger NA than a BBO-crystal.

The crystal has a length defined as the length that the optical beam traverses inside said crystal when it is used for frequency doubling. Some companies as e.g. Eksma Optics denote this as the crystal thickness.

In one embodiment the length of the crystal is at least 0.5 mm, such as larger than or equal to 1 mm, larger than or equal to 1.5 mm, larger than or equal to 2 mm, larger than or equal 3 mm, larger than or equal to 4 mm, such as larger than or equal to 5 mm, such as larger than or equal to 6 mm, such as larger than or equal to 7 mm.

The focusing element provides a focal point and the light will from the focusing element traverse a focal length to the focal point.

Due to the focusing element, the light will diverge after having traversed its focal length. In one embodiment the focal point is inside or close to the non-linear crystal. The frequency doubled light after the non-linear crystal will in general be weak. In one embodiment the light source further comprises a collimating element receiving the beam from the non-linear crystal. Here collimating is defined in wide terms as an element that decreases the width of the beam e.g. over a typical working range used in a lab in order to enable measuring it. In one embodiment the collimating element is or comprises a

lens or mirror. In one embodiment the collimating element is a lens made of a material with high UV transmission.

Furthermore it might be advantageous including a wavelength filter after the non-linear crystal to remove light at unwanted wavelengths, e.g. the light which is not frequency doubled inside the non-linear crystal. Accordingly, in one embodiment the light source comprises a wavelength filter such as a bandpass filter or low pass filter, e.g. a filter that has high transmission for UV light and very low transmission for visible light. In one embodiment the wavelength filter is an optical glass filter, a low pass filter, a pass band filter and/or a dicroic mirror.

The simple frequency conversion scheme according to the invention has found to be able to frequency double light from substantially any SC source. However, the spectral output and tunability will depend on the specific architecture of SC source. Furthermore the thermal load on the non-linear crystal and the amount of light outside the UV range will depend on whether the SC source is filtered prior to entering the non-linear crystal. Accordingly, some preferred embodiments of the SC source will be described in the following.

In one embodiment the super continuum (SC) source comprises a pulsed master oscillator, one or more amplifiers and a non-linear fiber which transforms the input pulses into a broad band super continuum. In the following the repetition rate, pulse length and peak power after the SEED will be denoted f_{SEED}, t_{SEED} and P_{SEED}. The corresponding properties after the last amplifier will be denoted f_{MOPA}, t_{MOPA} and P_{MOPA}. Fig. 4 shows an example of such a SC source with two sets of amplifiers, each separated by an isolator. As will be clear to the skilled person a similar SC source could be built using either fewer or more amplifiers and isolators. SC sources can also be based on a Q-switch SEED laser, as e.g. the SuperK Compact from NKT Photonics A/S. Inside the non-linear fiber the super continuum spreads in time due to the chromatic dispersion of the non-linear fiber. As the chromatic dispersion is

wavelength dependent, different wavelength of light will in general be offset with respect to each other and will leave the non-linear fiber at a different time. Furthermore the pulse duration will vary as a function of the wavelength. As prior described the pulse length of the super continuum source t_{SC} is defined as the shortest pulse length of the SC source when measured over the visible range (400-800 nm). Furthermore t_{SC} will increase with the length of the non-linear fiber. This will decrease the intensity of the light impingent on the non-linear crystal and hence the efficiency of the frequency doubling. Accordingly, in one embodiment of the light source of the invention, the length of the non-linear fiber is less than 10 m, such as less than 5 m, such as less than 2 m, such as less than 1 m, such as less than 0.5 m.

In one embodiment the non-linear fiber is tapered along at least a length section along its longitudinal axis.

In one embodiment the SEED laser wavelength is between 1000 and 1100 nm.

In one embodiment of the invention the pulse length t_{uv} of the SC source t_{SC} is at least 500 fs, such as more than 1 ps, such as more than 2 ps, such as more than 5 ps, such as more than 8 ps, such as more than 10 ps, such as more than 15 ps, such as more than 25 ps.

In one embodiment of the invention the pulse length t_{uv} of the SC source t_{SC} is less than 100 ps, such as less than 50 ps, such as less than 25 ps, such as less than 15 ps, such as less than 10 ps, such as less than 8 ps, such as less than 5 ps, such as less than 2 ps, such as less than 1 ps.

Here t_{SC} is defined as the shortest pulse length of the SC source when measured over the visible range (400-800 nm) with a resolution of 1 nm. This pulse length can e.g. be measured on a streak camera.

In one embodiment of the invention the SC source furthermore comprises a pulse picker, which is placed between the SEED and the last amplifier before the non-linear fiber and is arranged to enable reducing the repetition rate to f_{MOPA} which is lower than or equal to f_{SEED}.

In one embodiment of the invention the repetition rate before the non-linear fiber f_{MOPA} is at least 500 kHz, such as more than 1 MHz, such as more than 5 MHz, such as more than 10 MHz, such as more than 40 MHz, such as more than 60 MHz.

In one embodiment of the invention the pulse length before the non-linear fiber t_{MOPA} is at least 300 fs, such as more than 500 fs, such as more than 1 ps, such as more than 2 ps, such as more than 5 ps, such as more than 8 ps, such as more than 10 ps, such as more than 15 ps, such as more than 25 ps, such as more than 50 ps, such as more than 100 ps.

In one embodiment of the invention the pulse length before the non-linear fiber t_{MOPA} is less than 1 ns, such as less than 500 ps, such as less than 100 ps, such as less than 50 ps, such as less than 25 ps, such as less than 15 ps, such as less than 10 ps, such as less than 8 ps, such as less than 5 ps, such as less than 2 ps, such as less than 1 ps.

In one embodiment of the invention the non-linear fiber is a micro-structured silica fiber such as e.g. the "SC-5.0-1040" or the "SC-5.0-1040-PM" fiber from NKT Photonics A/S, Denmark.

In one embodiment of the invention the non-linear fiber is tapered along its longitudinal axis to increase the amount of light below 450 nm and/or reduce the noise of the supercontinuum source and/or reduce the length of the non-linear fiber. An example of such a taper can be found in patent application WO2012028152.

In one embodiment the non-linear fiber is followed by a wavelength filter prior to entering the non-linear crystal. The wavelength filter removes the wavelength part of the supercontinuum spectrum, which does not contribute to frequency double light into the UV, but gives a thermal load on the non-linear crystal. In one embodiment the filter is an optical glass filter, a low pass filter, a pass band filter, a dicroic mirror, a low pass or a bandpass filter.

Furthermore frequency doubling only works for one polarization of light, whereas the other transverses the non-linear crystal nearly unaffected and furthermore may add undesired thermal load to it. In one embodiment of the invention there is a polarizing element between the SC source and the non-linear crystal. The polarizing element e.g be Glan-Taylor polarizing prisms (e.g. a Glan-Taylor alpha-BBO prism from Laser components), broad band polarization splitter cubes, polarizers or wire grits.

In one embodiment the output of the SC source is polarized. Here polarized is taken to mean that the polarization extinction ratio of the visible part of the super continuum is more than 10 dB. A polarized SC source can e.g. be obtained by using a polarization maintaining or polarizing non-linear fiber inside the SC source.

In general, the tunability of the light source increases with the width of the spectral region impinging on the crystal. Accordingly in one embodiment the spectral width of the light impinging on the non-linear crystal is broader than 100 nm, such as broader than 200 nm, such as broader than 300 nm, such as broader than 400 nm, such as broader than 500 nm. In one embodiment the spectral width is restricted to wavelength in the visible, i.e. such that a spectral width of more than 200 nm, preferably as a spectral width of more than 200 nm between 400 and 800 nm. In the context of the present text the spectral width is defined as the wavelength region where the output spectral power density is at least about 1 μW/nm.

As briefly mentioned, the light source of the present invention comprises advantageously a non-linear crystal optimized for sum frequency mixing. To achieve frequency conversion in such non-linear crystal requires that two beams are impinging on it. The frequency conversion will depend on phase matching between the two incoming beams and the frequency converted beam. An advantage of this approach is that the second beam can have a larger intensity than the SC beam and hence increase the efficiency of the frequency conversion. Preferable this second beam is extracted from the SC

source, at a position prior to the non-linear fiber and sent through a delay unit providing a variable delay stage so that it arrives at the non-linear crystal simultaneously with the output from the SC source. Furthermore the two beams might be recombined prior to the non-linear crystal, see fig. 15. Thus in one embodiment the non-linear crystal is optimized for sum frequency mixing between the output from the SC source and a second output extracted from the SC source prior to that the beam has traversed the non-linear filter. In one embodiment the second output from the SC source is amplified and/or sent through a variable delay stage and/or frequency doubled prior to reaching the non-linear crystal.

The addressable market for the light source increases if it is possible to extend the tunable output range from the UV and into the visible or even near-IR range. However, as the output of SC sources span these wavelengths this has found to be relatively easily achieved as will explained in the following.

In one embodiment of the invention, the output of the SC source is split before the light impinges on the non-linear crystal. A part of the light is sent through the non-linear crystal to achieve a tunable output pulse in the UV, as prior described. In one embodiment the remaining part of the light is sent through a tunable wavelength filter, which is adjustable to change the spectral output after the filter. Examples of such filters are acousto optical tunable filters (AOTF) or a combination of position dependent optical filters (such as e.g. Linear Variable Filters from the Danish company Delta). Such filters are commonly used for filtering existing SC sources, e.g. in the SuperK Varia and SuperK Select products from NKT Photonics, Denmark. In one embodiment the splitting is done in a polarization splitting element or a wavelength flattened coupler or splitter. An example of such a broadly tunable light source is shown in fig. 16. Optionally the two outputs (162, 6) can be recombined to the same beam path and/or a shutter can be included on either one of or both of the beams.

The invention also comprises an illumination source for time resolved measurements comprising a tunable optical light source as claimed and as described herein.

Advantageously the illumination source is configured for use in time resolved fluorescence and/or time correlation single photon counting.

In one embodiment the illumination source is configured for use in photoluminescence, DNA sequencing, single photon counting, single molecule detection, intrinsic fluorescence, time resolved photoluminescence, UV polymerisation of resin, DNA sequencing, confocal microscope, FLIM, FRET, flow cytometry, cell-sorting, spectroscopy and/or food analysis.

The invention also comprises an optical measurement system for time resolved measurements comprising a tunable optical light source as claimed and as described herein in combination with a streak camera, which is an instrument for measuring the variation in a pulse of light's intensity with time.

DETAILED DESCRIPTION OF THE INVENTION

Fig. 1 shows a schematic frequency doubling unit from prior art.

Fig. 2 shows a prior art demonstration of a broadband frequency doubler for broadband pulses, as published by Szabo.

Fig. 3 shows a prior art demonstration of a broadband frequency doubler for broadband pulses, as published by Baum.

Fig. 4 shows a prior art super continuum source.

Fig. 5 shows a prior art filtering system for a super continuum source.

Fig. 6 shows a tunable pulsed source according to the invention.

Fig. 7 shows a tunable pulsed source according to the invention. This embodiment is used to generate the experimental data shown in figs. 8 to 14.

Fig. 8 shows the power spectral density of a SC source 80 and after that the spectrum has been filtered in a low pass filter 81.

Fig. 9 shows the pulse arrival time as a function of wavelength from a SC source. The difference in arrival time between the light at 500 nm and the light at 800 nm is more than 600 ps.

Fig. 10 shows a collection of output spectra from a tunable pulsed source according to the invention.

Fig. 11 shows the spectral power output from a tunable pulsed source according to the invention for a crystal length of 2 mm 111 and 4 mm 112.

Fig. 12 shows the spectral output as a function of the NA at a central wavelength of 350 nm.

Fig. 13 shows the horizontal 131 and vertical beam radius 132 as a function of wavelength.

Fig. 14 shows the pulse duration of a tunable pulsed source as measured with a streak camera.

Fig. 15 shows a light source according to the invention, where the non-linear crystal 3 is optimized for sum frequency mixing.

Fig. 16 shows a very broad band light source according to the invention where the output extends into the visible range.

The figures are schematic and may be simplified for clarity. Throughout, the same reference numerals are used for identical or corresponding parts.

Further scope of applicability of the present invention will become apparent from the detailed description given hereinafter. However, it should be understood that the detailed description and specific examples, while indicating preferred embodiments of the invention, are given by way of illustration only, since various changes and modifications within the spirit and

scope of the invention will become apparent to those skilled in the art from this detailed description.

Fig. 1 shows a schematic frequency doubling unit from prior art. It consists of a laser light source 1 emitting light photons at a frequency of f1 2, a non-linear crystal 3 converting some of the light photons to the doubled frequency 2f1 and a wavelength filter 5 for separating the light at f1 and 2f1. To optimize the frequency doubling the non-linear crystal is mounted in a holder 8 which allows changing the position, orientation and/or temperature of the crystal.

Fig. 2 shows a prior art demonstration of a broadband frequency doubler, as published by Szabo. The input light is dispersed on a diffraction grating 21 and subsequently focused by a lens 23 to reach high intensity on the non-linear crystal 3. After the non-linear crystal another focusing element 24 and diffraction grating 22 are used to achieve the broadband frequency doubled output 6.

Fig. 3 shows a prior art demonstration of a broadband frequency doubler, as published by Baum. The input light is dispersed on a set of prisms 31 and 32 and subsequently focused by a lens 23 to reach high intensity on the non-linear crystal 3. After the non-linear crystal another focusing element and set of prisms 33 and 34 are used to achieve the broadband frequency doubled output 6.

Fig. 4 shows a prior art super continuum source 40. Light pulses are generated in a SEED laser 41 and amplified in two sets of amplifiers 43, 45, in between each stage there is an isolator 42, 44. After the last amplifier the light enters a non-linear fiber 46 to generate the super continuum output 47.

Fig. 5 shows a prior art filtering system for a super continuum source. The output from the super continuum light source 47 is sent through a wavelength splitter 51, which divides the output into a low wavelength and a

high wavelength part. Each of these spectra is subsequently sent through a tunable filter 52, 54.

Fig. 6 shows a tunable pulsed source according to the invention comprising a super continuum light source 40, a focusing element 23, a non-linear crystal 3, and a holder for the non-linear crystal 8. Ref no. 4 indicates the frequency doubled output.

Fig. 7 shows a tunable pulsed source according to the invention. In addition to the elements shown in fig. 6 it comprises a wavelength splitter (51), a polarizing element 71 arranged to receive the light prior to entering the non-linear crystal 3, a focusing element 23 and a wavelength filter 5 arranged to receive the light after it has traversed the non-linear crystal. All of these added features are optional for the invention. Ref no. 6 indicates the frequency doubled output.

The following text describes a number of experiments conducted with a pulsed source, as shown in figure 7. The SC source 40 is a SuperK EXR-15 from NKT Photonics. The SEED in the SC source has repetition rate f_{SEED} of 78 MHz, and a pulse length t_{SEED} of approximately 5 ps. The SC source was filtered in a low pass filter 51, which transmits light below approximately 900 nm. After the filter the spectral density of the SC source is more than 1 mW/nm from 500 nm to 900 nm. The power spectral density of the source 80 is shown in fig. 8, which also shows the power spectral density after the filter 81.

The pulse arrival time as a function of wavelength from a SC source was measured on a streak camera from Hamamatsu, and is shown on fig. 9. It is noted that the pulse arrives sooner for larger wavelengths, i.e. smaller arrival time on the figure. The difference in arrival time for light at 500 nm and a 900 nm is more than 600 ps, which is far longer than the pulse duration. Hence this prohibits doubling the entire spectrum simultaneously.

Thus in one embodiment the light source comprises a wavelength dependent time delay arranged to receive the light after the non-linear filter and before the non-linear crystal. In one embodiment the wavelength dependent filter has a delay which decreases with wavelength.

After the filter, the light was sent through a polarizing element (61) which was a set of Glan-Taylor α-BBO prisms from Laser Components. The focusing element 23 is an achromatic lens with a focal length of 25 mm from Thorlabs. The non-linear crystal 3 is a Type I cut BBO from Laser Components. Crystal lengths of 2 and 4 mm, and crystal cut angle of 32 degree and 45 degree were tested. The best crystal depends on the application as will be detailed later.

The collimating element 24 was a Fused silica lens with a focal length of 50 mm from Thorlabs. It was observed that a 30 mm lens also worked well for the application. It is noted that care should be taken when specifying the coating, e.g. the standard UV coating from Thorlabs ranges from 290 to 370 nm.

The subsequent wavelength filter 5 is intended to remove non-UV light. If not possible to get the desired contracts with a single filter then multiple filters can be used, examples include Schott UG5 (250 nm – 330 nm), Schott BG3 (300 nm – 350 nm) and Schott BG18 (350 nm – 600 nm). Here the wavelengths in brackets denote the region where the filter has large transmission.

A collection of output spectra were taken with a NA of the focusing lens of 0.06 and using a 4 mm Type I cut BBO crystal having a crystal angle of 32 degree. The NA was varied by letting the beam propagate different distances prior to reaching the focusing lens. It could also be varied by using a telescope prior to the lens.

Fig. 10 shows a collection of output spectra from the tunable pulsed source according to the invention. One example is the spectra 100 containing

wavelengths from roughly 305 nm to 315 nm with a central output wavelength w_{fc} of 310 nm. Other examples 101, 102 have central output wavelengths of around 360 nm and 410 nm.

It is observed that the spectral power density decreases for wavelengths below 300 nm. This is due to that the SuperK EXR-15 power density decreases below 600 nm and due to the low acceptance bandwidth and angle of the BBO crystal. Thus the power density in the low wavelength region could be increased by using a SC source with more power below 600 nm, such as e.g. SuperK EXW-12 from NKT Photonics and/or by using a crystal with a larger acceptance bandwidth.

The inventors have performed a number of calculations showing that to frequency double the spectral region between 700 to 900 nm a 4 mm thick BBO Type I cut at 32° is preferred. However, to double the spectral region from 500 and 700 nm a 4 mm thick BBO Type I cut at 45° would be the best.

Fig. 11 shows the spectral power output from a tunable pulsed source according to the invention for a crystal length of 2 mm 111 and 4 mm 112. The power at each wavelength is measured when the pulsed source is optimized for high output power at this particular wavelength.

Fig. 12 shows the spectral power density as a function of the NA for a central wavelength of 350 nm. The peak power 121 has a maximum with an NA of 0.025; a slightly broader spectrum 122 is obtained with a NA of 0.06. In general it is found the NA giving the maximum spectral density will vary with wavelength. Furthermore it is expected that it will be different for different types of crystals.

As mentioned, the set-up used for these experiments contain a focusing lens 24. Fig. 13 shows the horizontal 131 and vertical beam radius 132 as a function of wavelength.

The pulse length of the UV pulses was measured with a streak camera from Hamamatsu. It was observed that the pulse length decreased with

wavelength from 34 ps at 280 nm to 28 ps at 400 nm and 16 ps at 440 nm. Fig. 14 shows the streak camera measurements at 280 nm 141 and at 400 nm 142.

Fig. 15 shows a light source according to the invention, where the non-linear crystal 3 is optimized for sum frequency mixing. In this embodiment a second beam is extracted from the SC source, at a position prior to the non-linear fiber 150, it is redirected on beam manipulating elements 151, 153, and sent through a variable delay stage 152, and recombined with the output from the the SC source 154 so that the two beams arrive at the non-linear crystal at the same time as the output from the SC source.

Fig. 16 shows a very broad band light source according to the invention. It comprises two outputs. The first output origins from the non-linear crystal, and is similar to the configuration shown in fig. 7. The second output is split from the first before the light reaches the non-linear crystal in a polarization splitter 71. Subsequently it is redirected by a beam manipulating element 161 and optionally filtered in a tunable filter 52.

It should be emphasized that the term "comprises/comprising" when used herein is to be interpreted as an open term, i.e. it should be taken to specify the presence of specifically stated feature(s), such as element(s), unit(s), integer(s), step(s) component(s) and combination(s) thereof, but does not preclude the presence or addition of one or more other stated features.

All features of the inventions including ranges and preferred ranges can be combined in various ways within the scope of the invention, unless there are specific reasons for not to combine such features.

CLAIMS

1. A tunable optical light source comprising

   - an input light source;
   - a focusing element;
   - a non-linear crystal arranged to convert the frequency of at least part of the output spectrum of said super continuum source; and
   - a holding unit for said non-linear crystal,

wherein said input light source is a super continuum light source with a spectral bandwidth of at least about 300 nm and said holding unit is adjustable for changing the frequency converted output wavelength of said non-linear crystal w_{fc} to provide that the lowest obtainable output wavelength w_{UV} of said tunable light source is about 360 nm or less, preferably said input super continuum light source has a pulse length t_{sc} of at least about 300 fs.

2. The light source of claim 1 wherein the light source further comprising means for adjusting the NA of the output beam from said focusing element, such as an optical telescope positioned before said focusing element or a variable path length device.

3. The light source of any of the preceding claims further comprising a wavelength filter arranged to filter the light before it reaches said non-linear crystal and preferably a polarizing element arranged to polarize the light after is has traversed said non-linear crystal.

4. The light source of any of the preceding claims where said non-linear crystal is a Type I cut BBO crystal having a length of at least about 2 mm.

5. The light source of any of the preceding claims wherein said holder unit is adjustable for positioning said non-linear crystal in the focus position of the light from said focus element.

6. The light source of any of the preceding claims wherein the SC source comprises a non-linear fiber with a length of about 5 m or less.

7. An illumination source for time resolved measurements comprising a tunable optical light source as claimed in any of the proceeding claims, the illumination source is configured for use in time resolved fluorescence and/or time correlation single photon counting.

8. An illumination source according to claim 7 wherein the pulse length t_{UV} of said source is at least about 500 fs, such as at least about 1 ps, such as at least about 5 ps, such as at least about 10 ps, such as at least about 15 ps, such as at least about 25 ps.

9. An illumination source according to any of the claims 7-8 configured for use in photoluminescence, DNA sequencing, single photon counting, single molecule detection, intrinsic fluorescence, time resolved photoluminescence, UV polymerisation of resin, DNA sequencing, confocal microscope, FLIM, FRET, flow cytometry, cell-sorting, spectroscopy and/or food analysis.

10. An optical measurement system for time resolved measurements comprising a tunable optical light source or illumination source as claimed in any of the proceeding claims and a streak camera.

Fig. 1: prior art

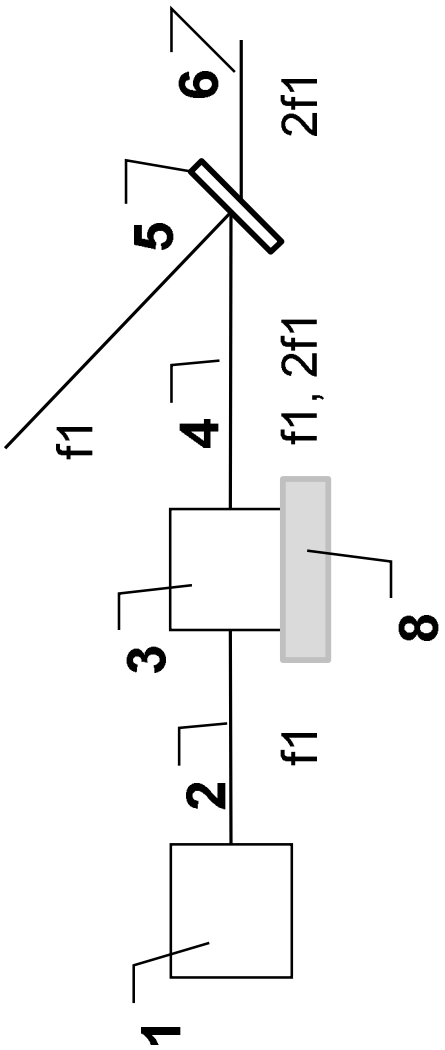

Fig. 2: Prior art from Szabo

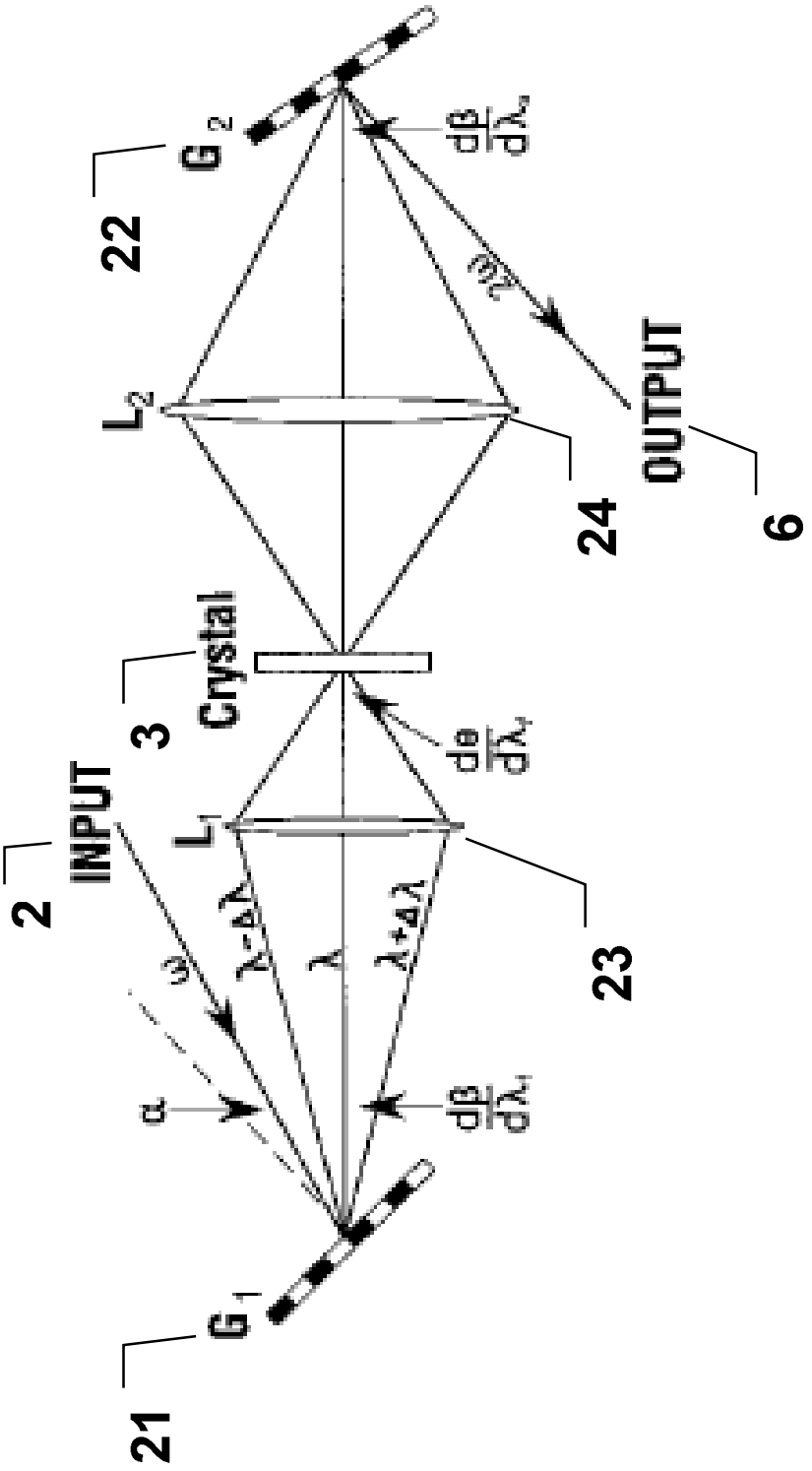

Fig. 3: Prior art from Baum

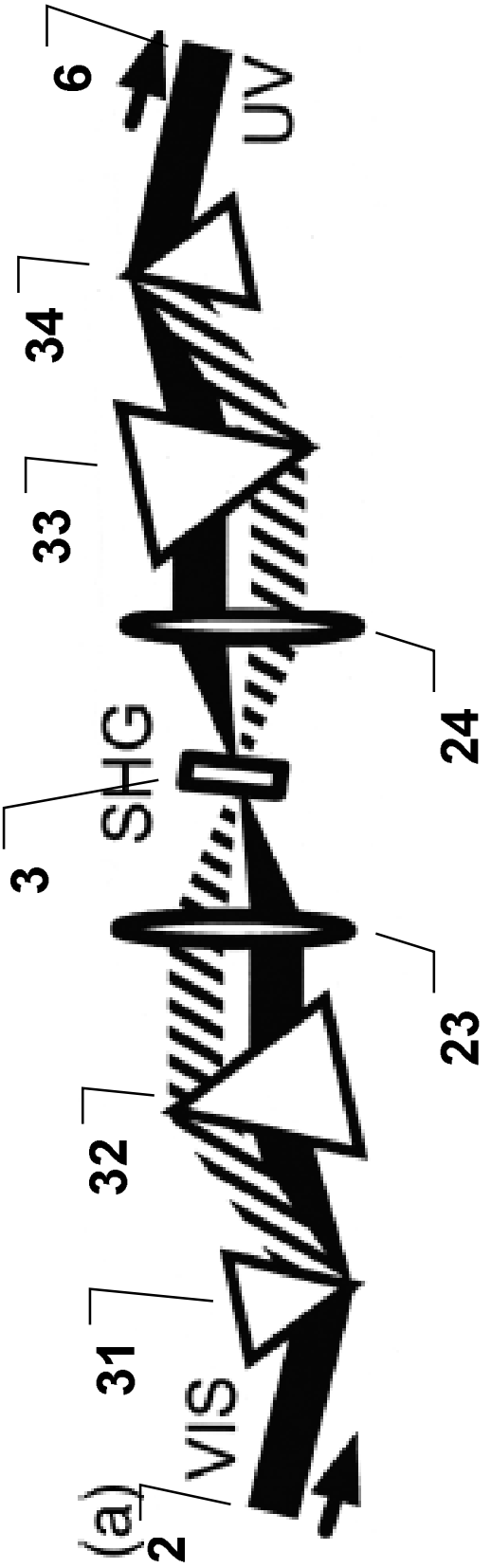

Fig. 4: Prior art SC source

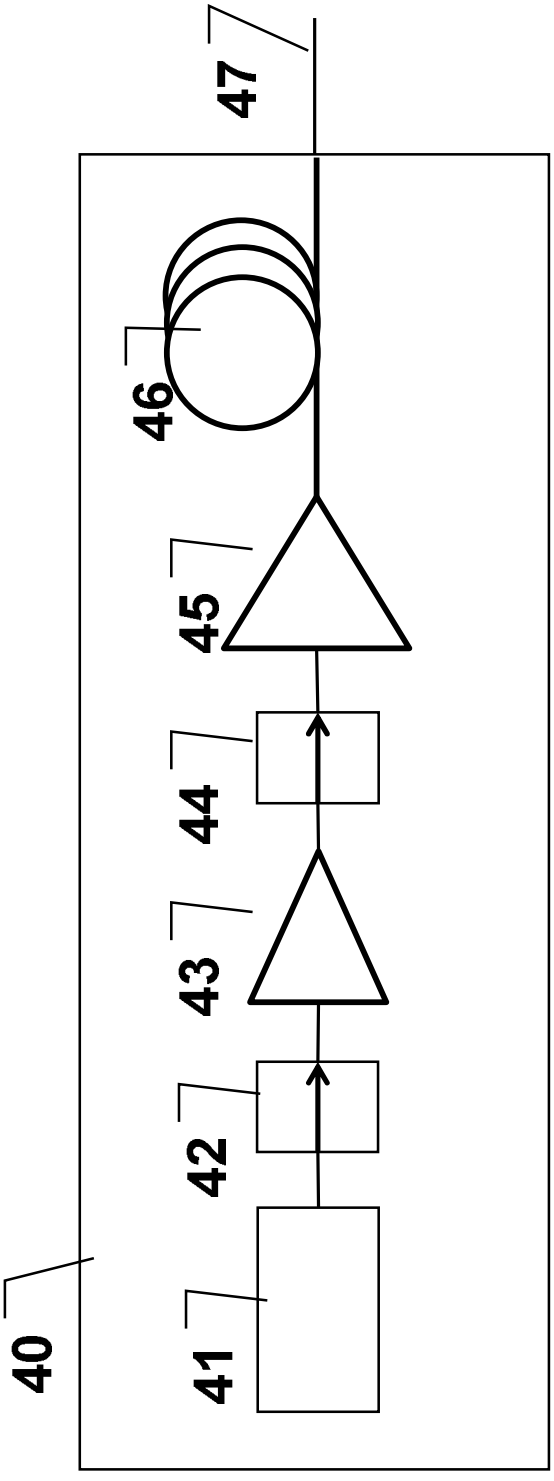

Fig. 5: Prior art

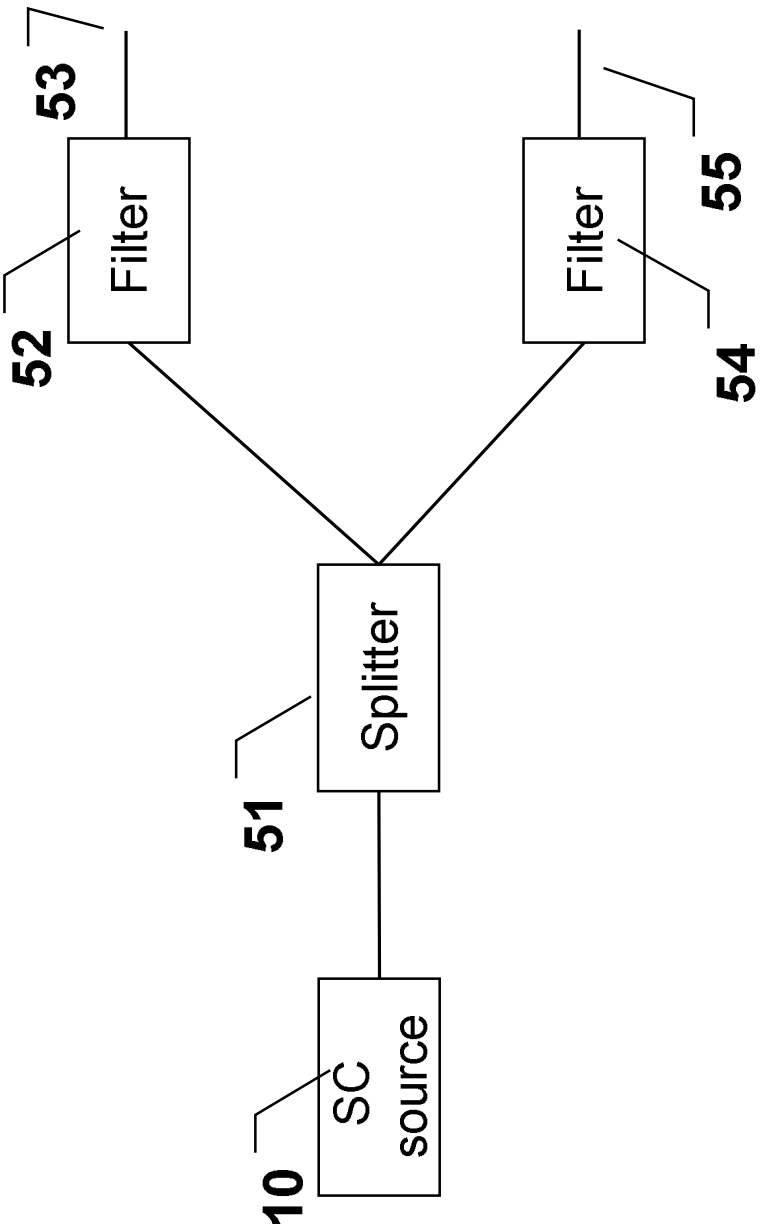

Fig. 6:

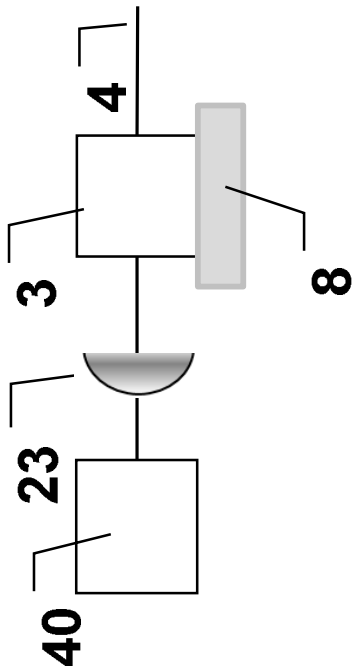

Fig. 7

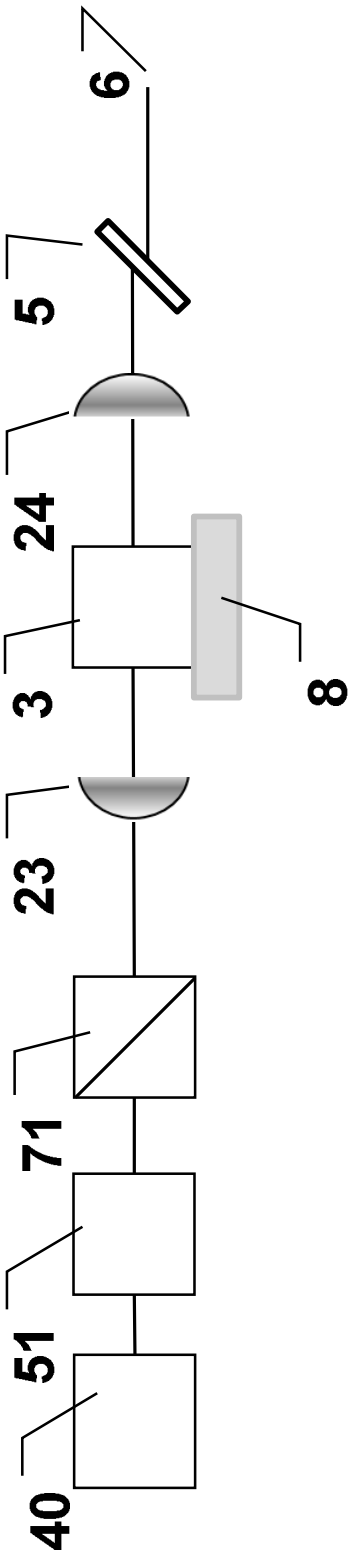

Fig. 8

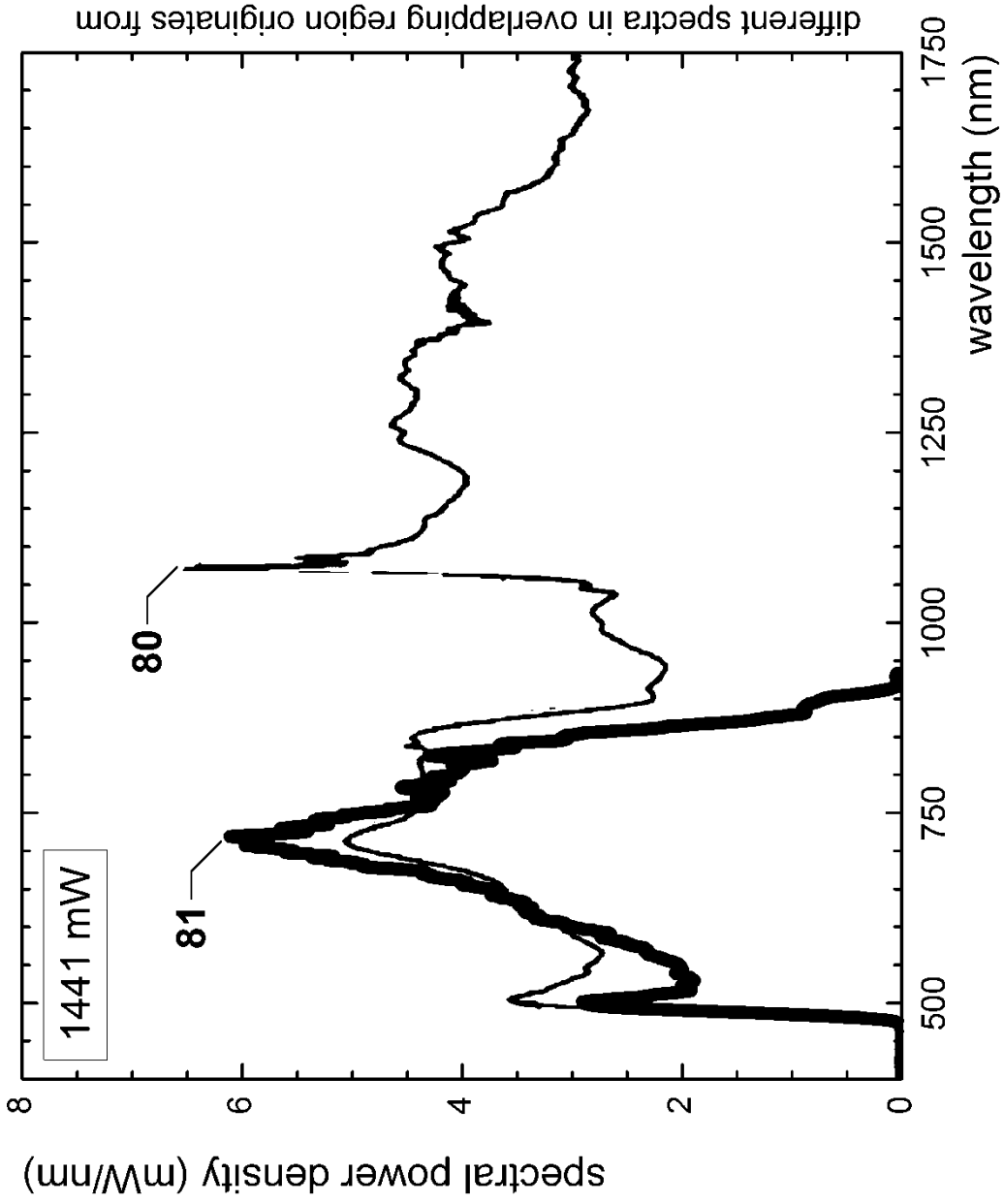
different spectra in overlapping region originates from
measuring 80 and 81 with a different spectrometer
spectral power density (mW/nm)
wavelength (nm)
1441 mW
80
81
0
2
4
6
8
500
750
1000
1250
1500
1750

Fig. 9

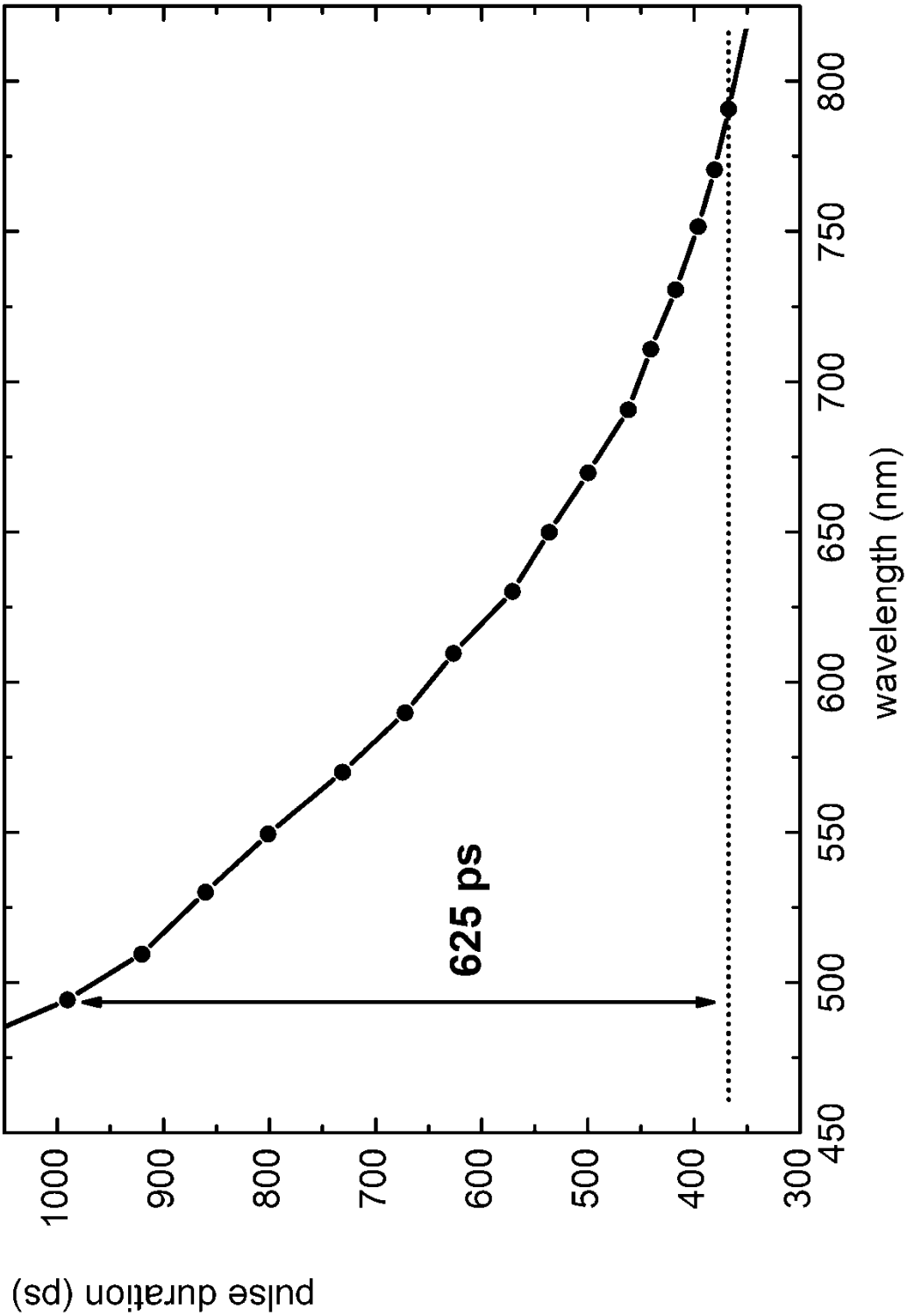
pulse duration (ps)
1000
900
800
700
600
500
400
300
450
500
550
600
650
700
750
800
wavelength (nm)
625 ps

Fig. 10

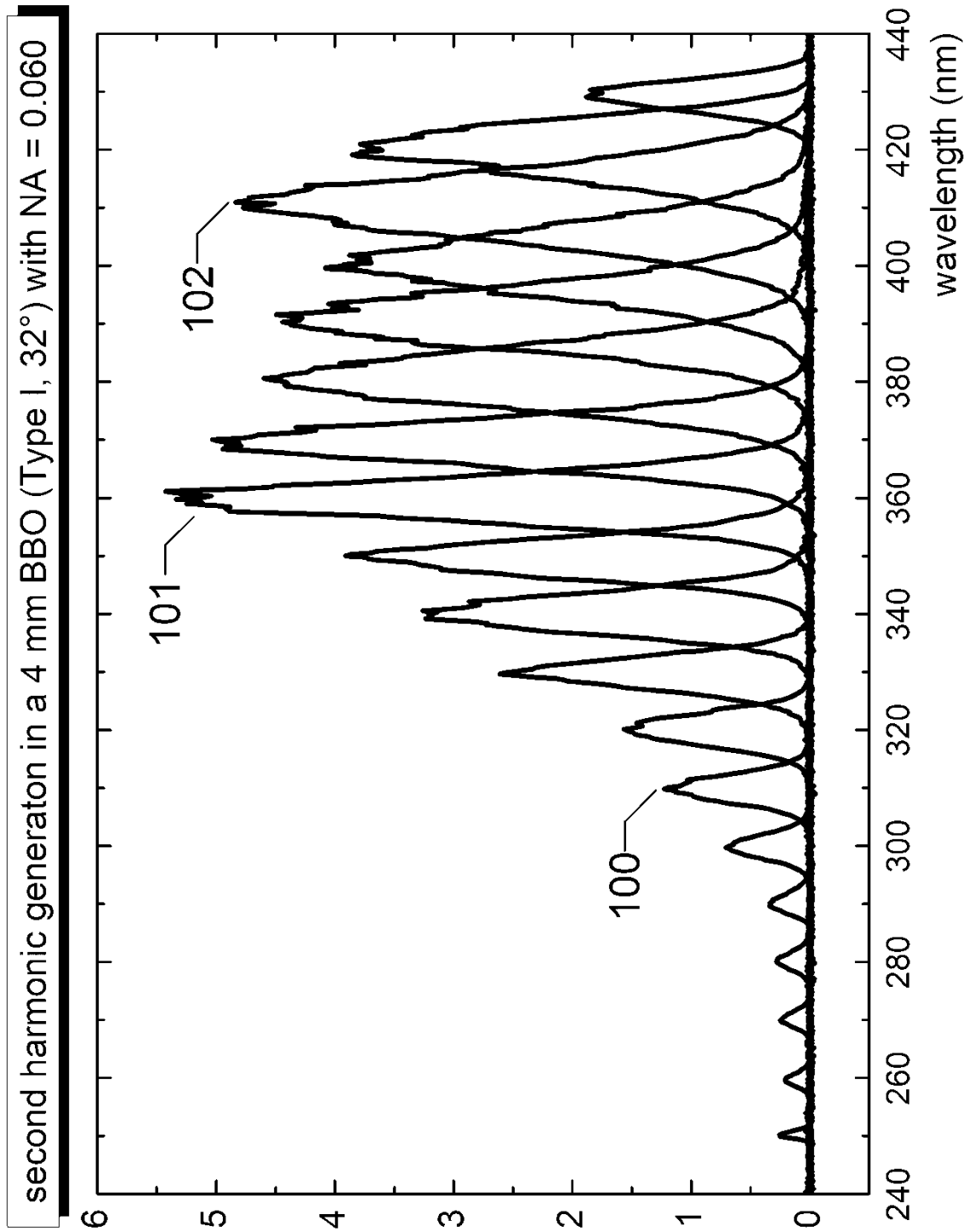
second harmonic generaton in a 4 mm BBO (Type I, 32°) with NA = 0.060
100
101
102
0
1
2
3
4
5
6
240
260
280
300
320
340
360
380
400
420
440
wavelength (nm)

Fig. 11

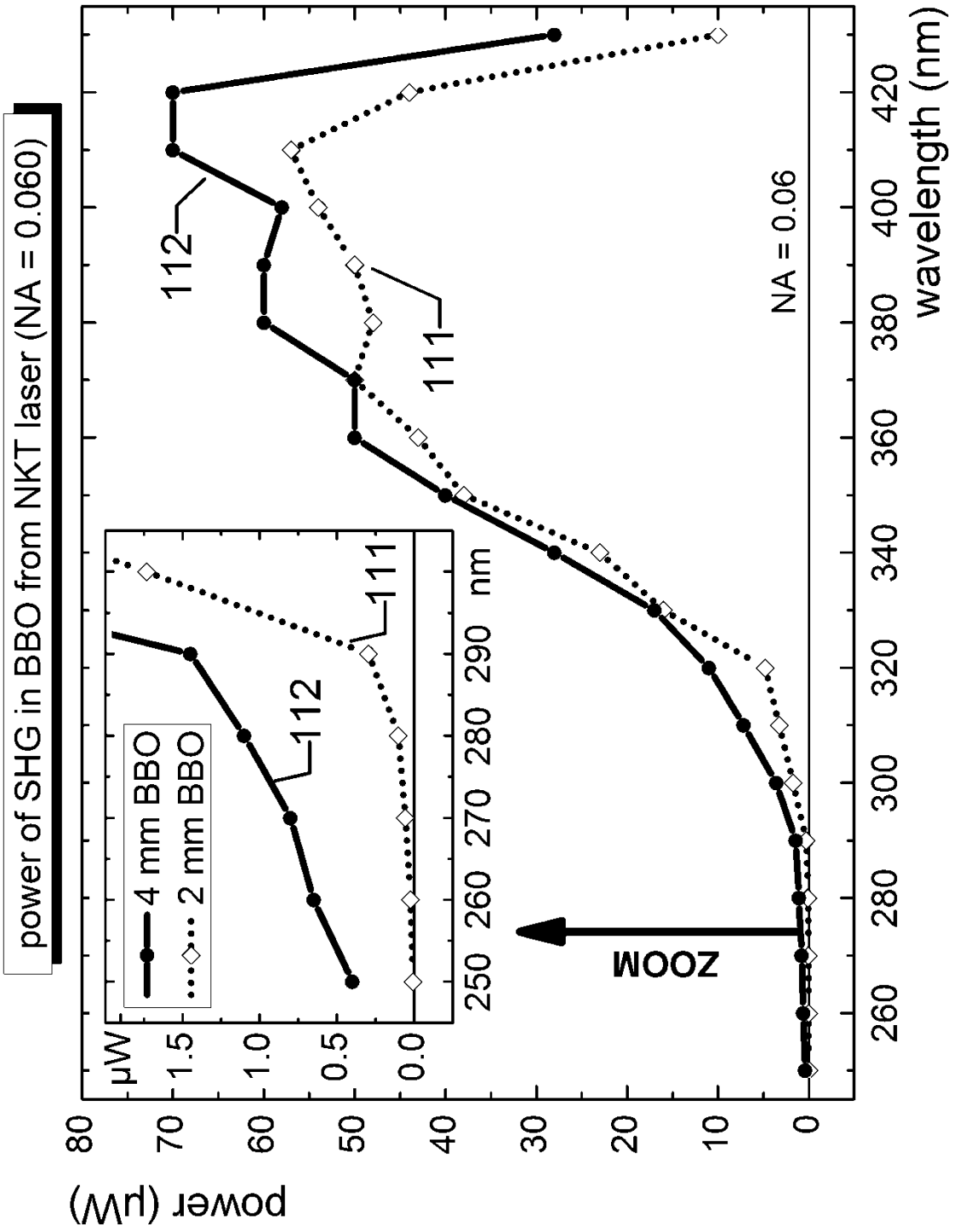
power of SHG in BBO from NKT laser (NA = 0.060)
power (µW)
wavelength (nm)
NA = 0.06
ZOOM
112
111
4 mm BBO
2 mm BBO
µW
nm

Fig. 12

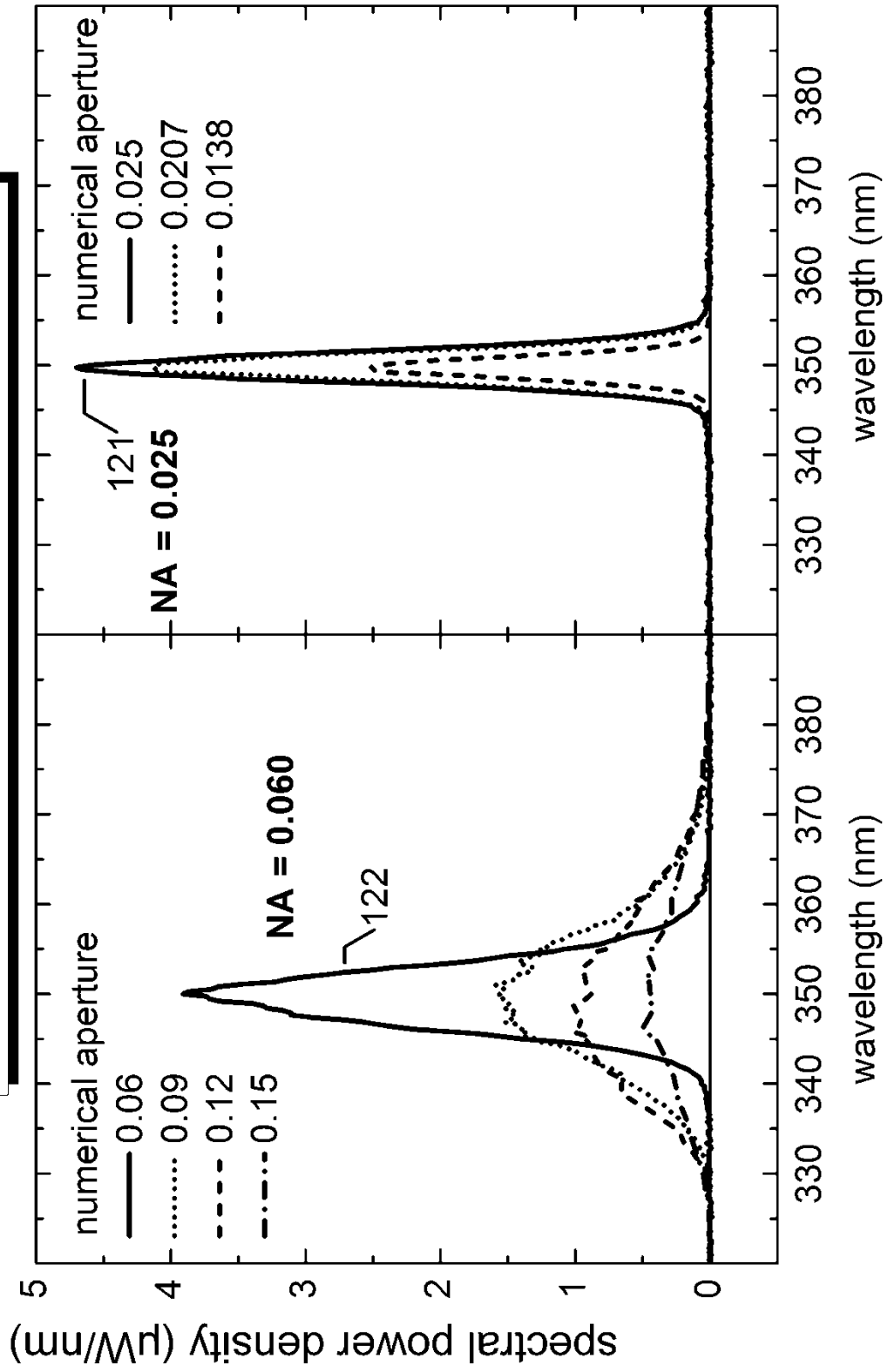
influence of numerical aperture (NA) on power density
numerical aperture
0.06
0.09
0.12
0.15
NA = 0.060
122
numerical aperture
0.025
0.0207
0.0138
121
NA = 0.025
spectral power density (µW/nm)
wavelength (nm)
wavelength (nm)

Fig. 13

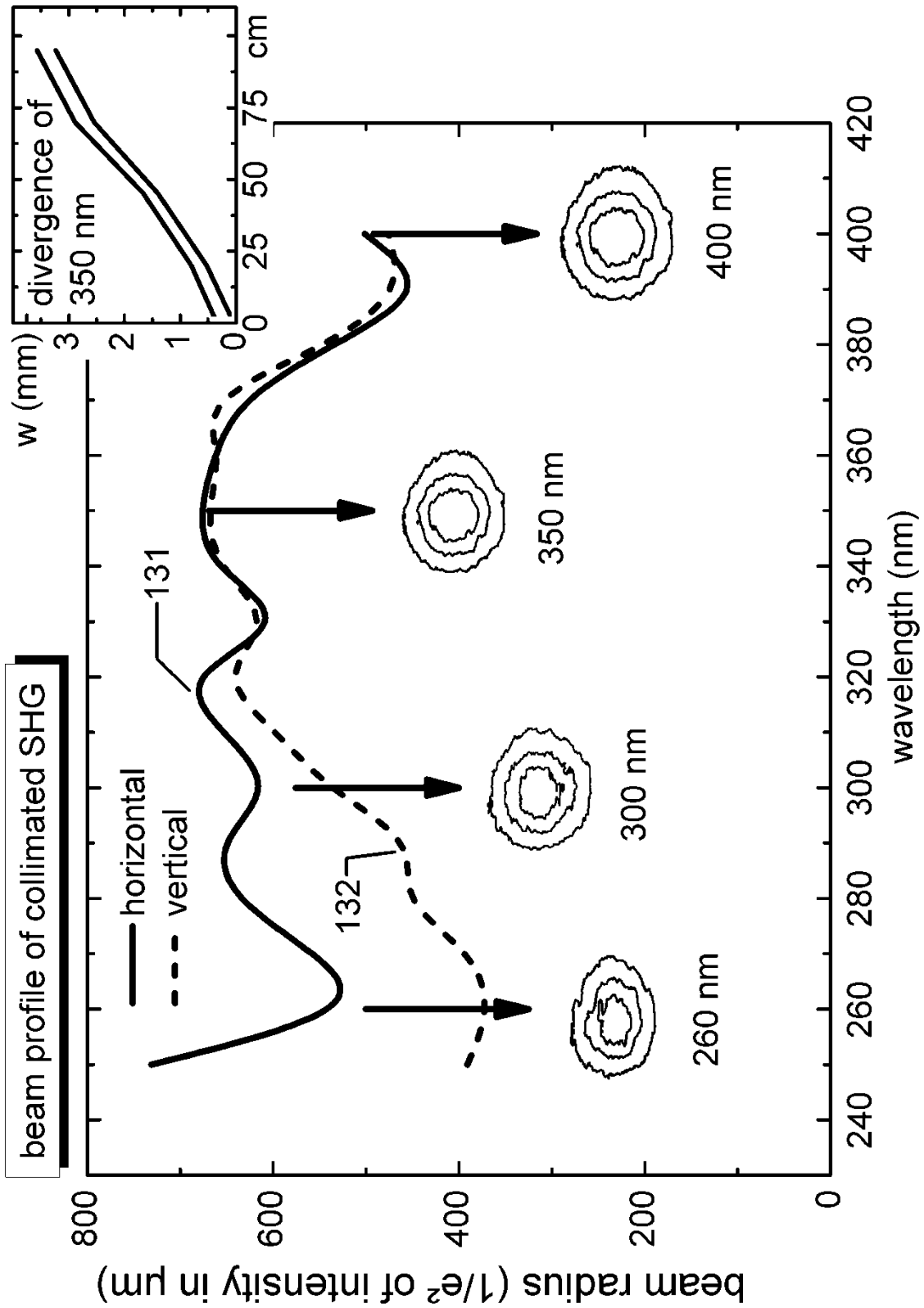
beam profile of collimated SHG
horizontal
vertical
131
132
260 nm
300 nm
350 nm
400 nm
beam radius (1/e² of intensity in µm)
wavelength (nm)
w (mm)
divergence of
350 nm
cm

Fig. 14

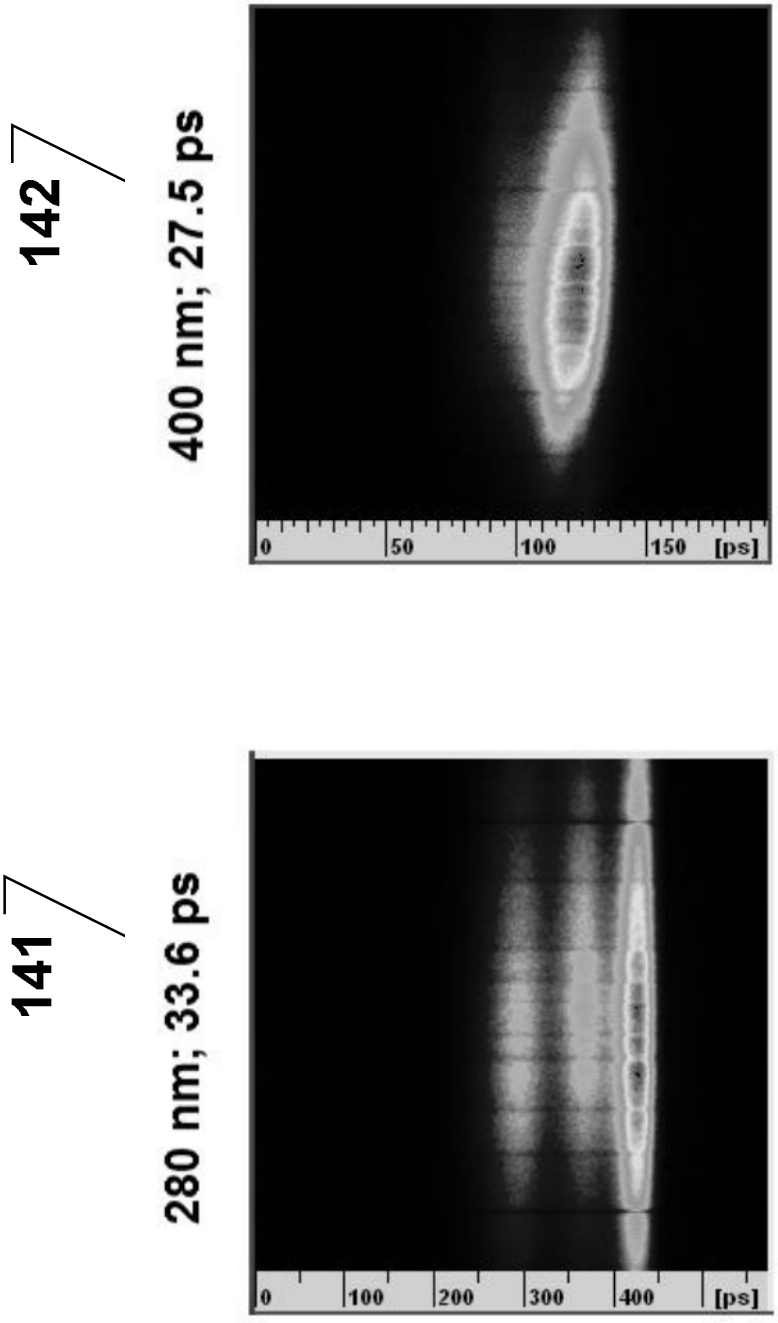
142
400 nm; 27.5 ps
0
50
100
150
[ps]
141
280 nm; 33.6 ps
0
100
200
300
400
[ps]

Fig. 15: SFM crystal

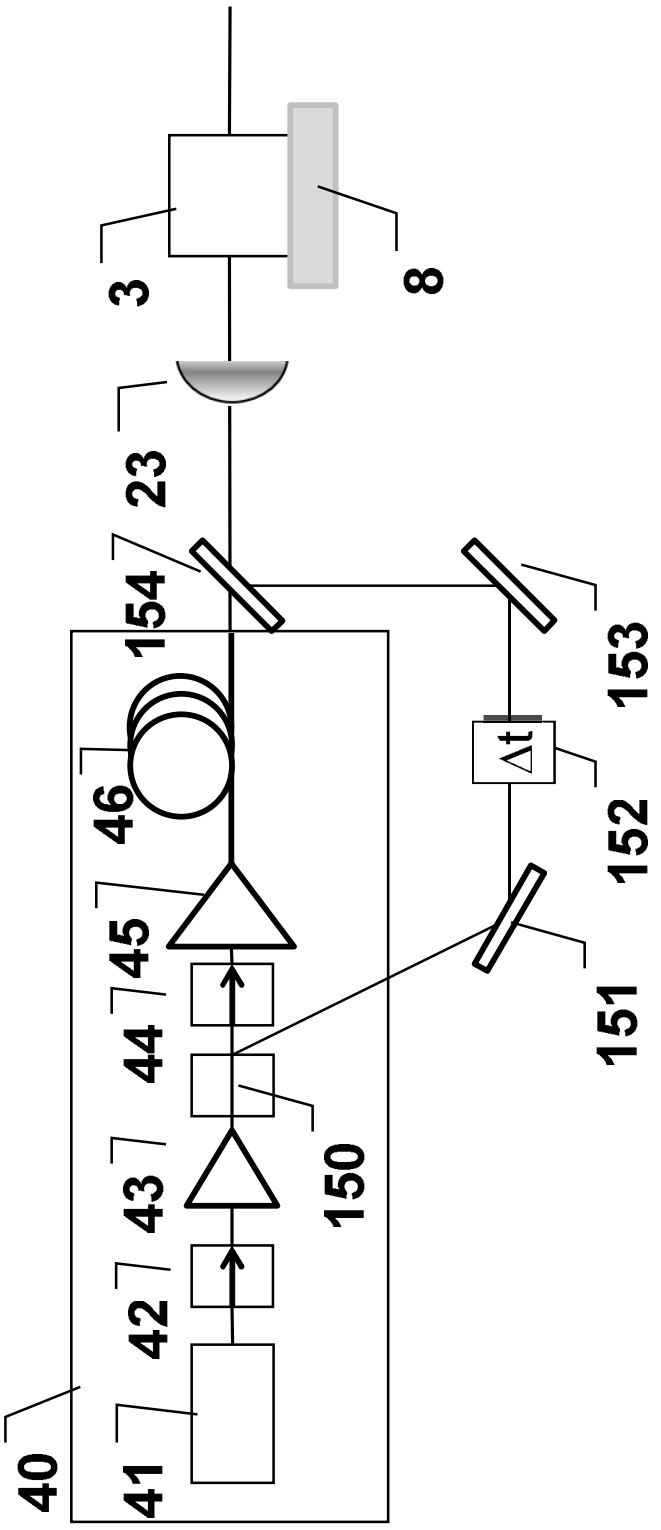

Fig. 16: Broadly tunable source

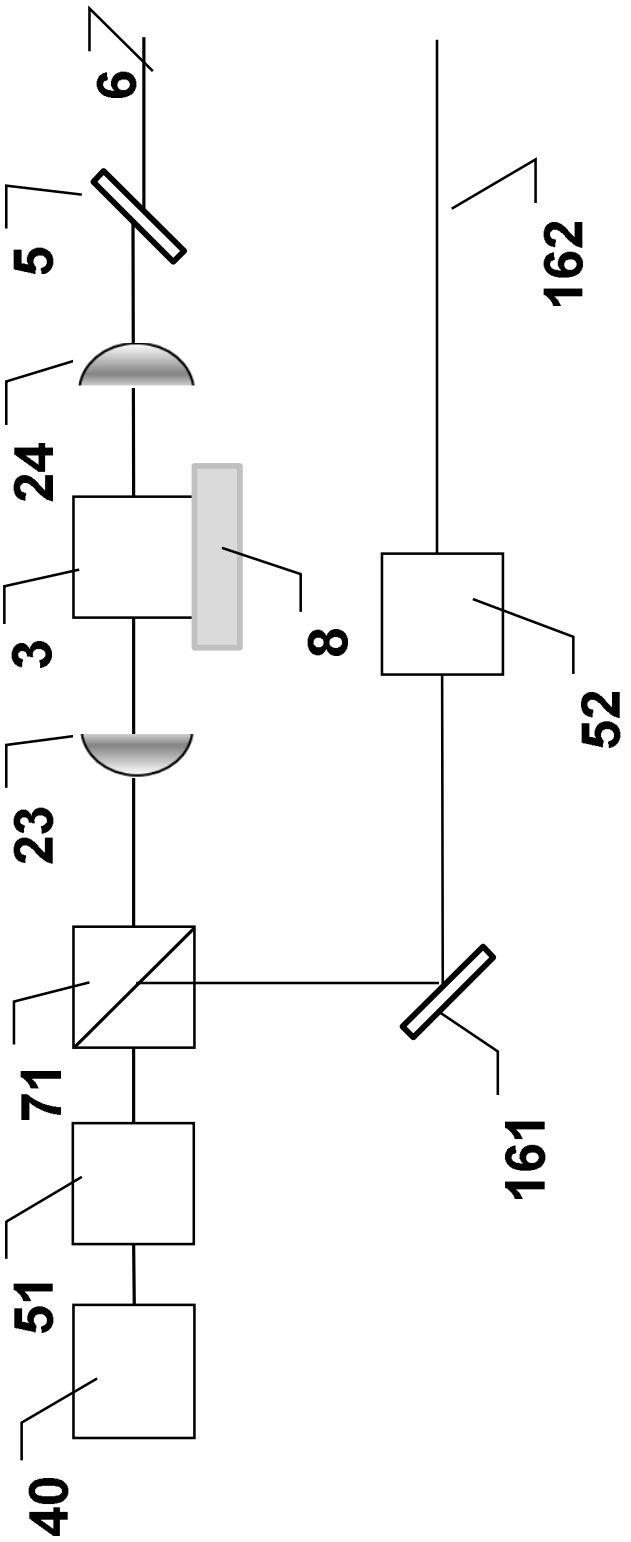

Appendix Video01

Multifilamentation in a 6 mm YAG plate and liberation of electrons from the surface for an increasing pump energy

M. Bradler

Appendix Video02

Spectrum, beam profile and side view of multiple refocusing in a 6 mm YAG plate for an increasing pump energy

M. Bradler

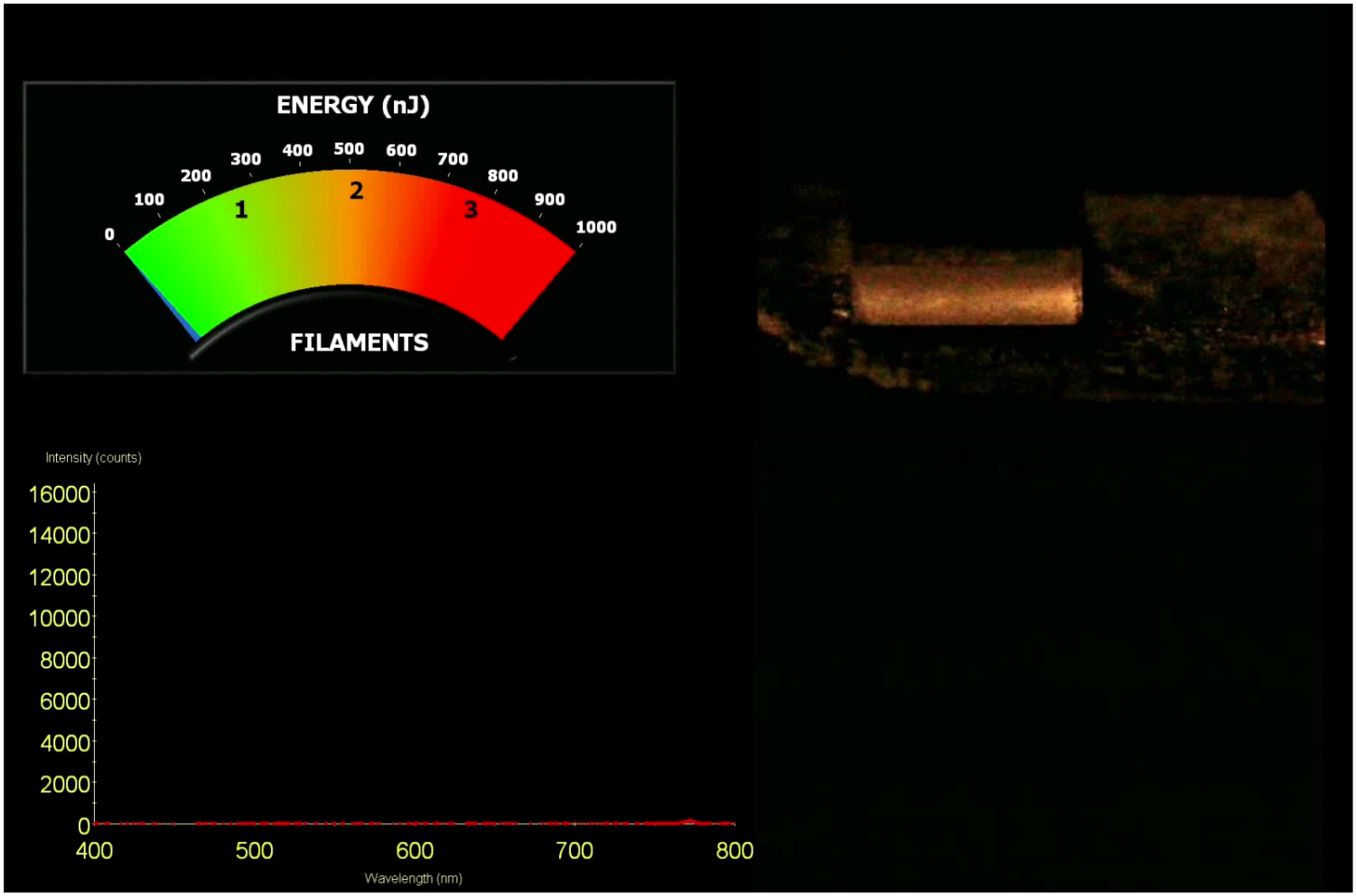

Danksagung

Diese Dissertation wäre nicht entstanden ohne die Unterstützung vieler Personen, denen ich an dieser Stelle danken möchte.

An erster Stelle möchte ich meinem Doktorvater **Herrn Prof. Dr. Eberhard Riedle** danken, der die Durchführung dieser Arbeit erst ermöglicht hat und sie stets bestens wissenschaftlich betreut hat. Sein hohes Engagement und großes Interesse an der Thematik haben mich zu unzähligen Experimenten motiviert, aus denen eine Vielfalt neuer Erkenntnisse entstanden sind. Doch auch alltägliche Hilfestellungen im Büro und Labor haben mir meine Arbeit hier am Institut erheblich erleichtert. Bei den zahlreichen Gesprächen und Diskussionen empfand ich zudem die „bayrische“ Atmosphäre sehr angenehm, die sich auch abseits der wissenschaftlichen Arbeit stets positiv bemerkbar gemacht hat.

Zudem möchte ich **Herrn Prof. Dr. Wolfgang Zinth** danken, mit dem ich oft über einzelne Aspekte meiner Arbeit diskutiert habe und der mir im Rahmen des internen Seminars wertvolle Fragen gestellt hat und auch hilfreiche Ratschläge gegeben hat.

Vielen Dank auch an **Herrn Prof. Dr. Peter Hommelhoff** und seinem Team für die angenehme und erfolgreiche Zusammenarbeit zur Untersuchung der Elektronenemissionen and Metallspitzen. Auch vielen Dank an **Dr. Hristo Iglev** und sein Team, im speziellen an **Dr. Jasper Werhahn**, mit dem ich zusammen in kürzester Zeit das schnellste Ultrakurzzeit Infrarotspektrometer der Welt aufgebaut habe. Außerdem danken möchte ich **Herrn Prof. Dr. Harald Kaufmann** und seinem Team, im speziellen **Jürgen Hauer**, für die erfolgreiche Zusammenarbeit zur Untersuchung des ultraschnellen Ladungstransfers. Außerdem danken möchte ich **Dr. Peter Baum**, der mir stets mit Rat und Tat geholfen hat und bis jetzt zusammen mit seinem Team immer wieder neue interessante Experimente ermöglicht. Ebenfalls danken möchte ich **Dr. Andreas Unterreiner** und seinem Team, für die schöne Kooperation zur Untersuchung verschiedener Metall-Porphyrenen.

Ich möchte an dieser Stelle noch einmal explizit auf die wirklich angenehme und konstruktive Zusammenarbeit mit den Kooperationspartnern in allen Fällen hinweisen, ohne die derart schöne Ergebnisse nicht möglich gewesen wären. Vor allem auch die gemeinsame Zeit außerhalb der wissenschaftlichen Tätigkeit waren in allen Fällen stets unterhaltsam und angenehm.

Neben den wissenschaftlichen Kooperationspartner möchte ich mich auch für die technische Unterstützung bei folgenden Personen bedanken. Sie waren maßgeblich daran beteiligt, dass die verwendeten Lasersysteme einwandfrei funktionierten. Mein Dank geht an **Gerald Jung**, und **Dr. Hans-Erik Swoboda** von Horiba Jobin, Yvon, **Bert Kremser** und **Rene Beilschmidt** von JenOptik, **Sascha Häuser** und **Frederique Nielsen** von NKT Photonics und an **Mark Drechsler** von Amplitude Systemes.

Besonderen Dank geht auch an **Dr. Christian Homann** – meinem langjährigen Bürokollegen – mit dem ich zusammen viele gemeinsame wissenschaftliche Projekte bestritten habe woraus zahlreiche Veröffentlichungen entstanden sind. Aber vor allem seine freundliche und nette Art machten ihn zu einem unschätzbaren Kollegen. Vielen Dank dafür!

Herzlichen Dank gilt auch allen anderen Kollegen am Lehrstuhl, die zu dem hervorragenden Betriebsklima und der tollen Atmosphäre hier am Institut geführt haben und mir immer mit Rat und Tat zur Seite standen. Stellvertretend für alle seien genannt **Dr. Christian Sailer**, **Dr. Nils Krebs**, **Matthias Wenninger**, **Dr. Igor Pugliesi**, **Elias Eckert**, **Christoph Grill**, **Dr. Daniel Herrmann, Dr. Uwe Megerle**, **Bastian Baudisch**, **Roland Wilcken**, **Andreas Welzmüller**, **Sebastian Wiegner**, **Mario Masetto**, **Dr. Oliver Schalk**, **Michael Michailov**, **Markus Breuer**, **Dr. Patrizia Krok** und **Andreas Böck**. Dies gilt natürlich auch für die Mitarbeiter aller Arbeitsgruppen am Lehrstuhl für BioMolekulare Optik und für die Mitarbeiter anderer Lehrstühle, mit denen ich zusammen gearbeitet habe.

Bedanken möchte ich mich auch bei „meinem“ Bachelor-Studenten **Emanuel Wittmann**, mit dem ich mich auf und abseits „des Platzes“ bestens verstehe und mit dem ich zusammen viele wertvolle Erkenntnisse über Weißlichterzeugung gewonnen habe und der meine Arbeit bestens weiterführen wird.

Besten Dank natürlich auch an das hervorragende Werkstatt-Team **Rudi Schwarz**, **Alfons Stork** und **Christian Hausmann**, die alle Arbeiten zuverlässig, schnell und höchst präzise erledigten. Und natürlich werde ich die Fachgespräche über den bayrischen Fußball aufs schmerzlichste vermissen. Vielem Dank gilt auch **Harald Hoppe** für die ausgezeichneten Optikarbeiten.

Zum Schluss möchte ich mich auch bei meiner **Familie** bedanken, die mich in jeder Hinsicht vollsten unterstützt hat, mir die nötige Ruhe und Gelassenheit in anstrengenden Zeiten gegeben hat und immer ein hervorragender Ausgleich zum Arbeitsleben war.

Curriculum vitae

PERSONAL DETAILS

Last name:	Bradler
First name:	Maximilian
Date of birth:	29.09.1982
Place of birth:	Burghausen, Germany
Nationality:	German
Marital status:	unmarried

EDUCATION

1989 – 1993	Primary school in Burghausen (Hans-Kammerer-Schule)
1993 – 1994	Secondary school “Franz-Xaver-Gruber-Schule” in Burghausen
1994 – 1998	Secondary school “Maria-Ward-Realschule” in Burghausen
1998 – 2003	Secondary school “Maria-Ward-Gymnasium” in Altötting
06/2003	Abitur with grade 1.2
09/2003 – 09/2007	Studies in physics at the LMU München
10/2007	Diploma in physics “with distinction”
since 11/2008	PhD student at the chair of BioMolecular Optics, LMU München

Hiermit erkläre ich, die vorliegende Arbeit selbstständig verfasst und keine anderen als die angegebenen Quellen und Hilfsmittel verwendet zu haben.

München, den 22. Juli 2014

Maximilian Bradler